DOC.20041025.0006

QA: QA

MDL-EBS-MD-000001 REV 00

October 2004

In-Drift Natural Convection and Condensation

Prepared for:
U.S. Department of Energy
Office of Civilian Radioactive Waste Management
Office of Repository Development
1551 Hillshire Drive
Las Vegas, Nevada 89134-6321

Prepared by:
Bechtel SAIC Company, LLC
1180 Town Center Drive
Las Vegas, Nevada 89144

Under Contract Number
DE-AC28-01RW12101

DISCLAIMER

This report was prepared as an account of work sponsored by an agency of the United States Government. Neither the United States Government nor any agency thereof, nor any of their employees, nor any of their contractors, subcontractors or their employees, makes any warranty, express or implied, or assumes any legal liability or responsibility for the accuracy, completeness, or any third party's use or the results of such use of any information, apparatus, product, or process disclosed, or represents that its use would not infringe privately owned rights. Reference herein to any specific commercial product, process, or service by trade name, trademark, manufacturer, or otherwise, does not necessarily constitute or imply its endorsement, recommendation, or favoring by the United States Government or any agency thereof or its contractors or subcontractors. The views and opinions of authors expressed herein do not necessarily state or reflect those of the United States Government or any agency thereof.

QA: QA

In-Drift Natural Convection and Condensation

MDL-EBS-MD-000001 REV 00

October 2004

OCRWM	MODEL SIGNATURE PAGE/CHANGE HISTORY	Page iii 1. Total Pages: 618

2. Type of Mathematical Model

☒ Process Model ☐ Abstraction Model ☐ System Model

Describe Intended Use of Model

The intended use of this model is the prediction of in-drift natural convection, water vapor transport, and subsequent condensation. The in-drift natural convection and condensation model results are limited to post-closure conditions and do not include rock fall, repository-wide natural circulation, natural ventilation, or barometric pumping. The equivalent thermal conductivity analysis and correlation results are subject to the same limitations. Parameter limits on the equivalent thermal conductivity correlations are explicitly listed.

3. Title

In-Drift Natural Convection and Condensation

4. DI (including Rev. No., if applicable):

MDL-EBS-MD-000001 REV 00

5. Total Appendices	6. No. of Pages in Each Appendix
Thirteen (13)	A-10; B-56; C-4; D-30; E-56; F-6; G-10; H-12; I-22; J-10; K-8; L-6; M-16

	Printed Name	Signature	Date
7. Originator	Stephen W. Webb	SIGNATURE ON FILE	10/25/04
8. Independent Technical Reviewer	Phillip Rogers	SIGNATURE ON FILE	10/25/04
9. Checker	John Del Mar	SIGNATURE ON FILE	10/25/04
10. QER	Darrell Svalstad	SIGNATURE ON FILE	10-25-04
11. Responsible Manager/Lead	Cliff Howard	SIGNATURE ON FILE	10-25-04
12. Responsible Manager	Ernest Hardin	SIGNATURE ON FILE	10/25/04

13. Remarks

Change History

14. Revision No.	15. Description of Change
REV 00	Initial Issue.

INTENTIONALLY LEFT BLANK

EXECUTIVE SUMMARY

The Yucca Mountain repository configuration consists of waste packages stored inside of underground tunnels, or drifts. The waste packages generate heat due to radioactive decay, and moisture flows into and out of the drifts in liquid and vapor form. Heat and mass transfer within the drifts, including interaction with the surrounding rock, are potentially important processes for the performance of the repository. The present report documents models for in-drift heat and mass transfer during the post-closure period. Pre-closure, or ventilated, conditions are documented in a separate report (BSC 2004 [DIRS 169862]).

Convection Model

In-drift heat transfer including natural convection and thermal radiation is modeled through the use of a computational fluid dynamics (CFD) code, FLUENT. In the present application, FLUENT solves the time-averaged Navier-Stokes equations including turbulence, and the energy equation including thermal radiation. The model resolves the boundary layer behavior in the drifts through fine discretization near the wall. The in-drift heat transfer model is thermally coupled to the surrounding rock. The variation of the rock temperature along the drift, or the "temperature tilt", is included and is a significant factor in the model results.

The important physical features including the drip shield, waste packages, and invert are individually represented in a three-dimensional grid. Due to computational limitations, only a portion of a drift is modeled. The grid is 71-m long encompassing 14 waste packages, or two 7-package sequences, while a full drift is approximately 600 m long. The spatial and temporal variation of the individual waste package power is included.

Two- and three-dimensional convection representations of the convection model are presented. The two-dimensional representation uses the line-averaged waste package power and considers various submodels, such as radiation and turbulence, to evaluate the effect of different assumptions and physics submodels. With these results, three-dimensional simulations were performed to produce detailed three-dimensional heat transfer characteristics and fluid flow velocities in the drift.

Axial mass transport in the drift environment is included in the three-dimensional convection simulations by specification of a trace gas. Cross-sectionally averaged trace gas concentrations are used along with the flow rate of the tracer and the geometry to specify an effective one-dimensional axial dispersion coefficient down the drift. Axial dispersion coefficients are calculated for the regions inside and outside the drip shield, which are a strong function of the temperature tilt. These dispersion coefficients are used in the condensation model as described in this report.

The convection model is partially validated by comparison to small-scale literature data for natural convection in horizontal concentric cylinders, which is a geometrically similar configuration to that of the repository at Yucca Mountain. The overall heat transfer from the horizontal concentric cylinder geometry predicted by FLUENT compares very well with the available literature data over a wide range of Rayleigh numbers including laminar and turbulent flow conditions and is well within the experimental uncertainty of the data.

The convection model has also been validated by comparison to experimental data from the 25% and 44% Yucca Mountain Natural Convection Tests conducted in the DOE Atlas Facility in North Las Vegas. The predicted component temperatures compare well within the uncertainty range of the experimental data.

The dispersion coefficients from the three-dimensional in-drift convection simulations are validated by independent peer review. Professor Ivan Catton of UCLA reviewed the convection and condensation models including the calculations of the dispersion coefficient presented in this report. His review is included in Appendix G.

The results from the convection model are not used directly in the Total System Performance Assessment for the Licence Application. The results are used to represent convective mixing and transport along the drift as an effective one-dimensional dispersion process, which is used directly in the condensation model.

Condensation Model

The condensation model is used to predict condensation and evaporation rates along the entire length of 7 selected drifts at different times (e.g., 300, 1,000, 3,000, and 10,000 years). As such, the model uses a much simpler representation of the drift geometry than the convection model discussed above. The condensation model uses single-node representations of each waste package along each drift, as well as separate nodes for the drip shield, invert, and drift wall at each waste package location. The drift wall temperature boundary conditions for the condensation model are derived from analytical line-source solutions.

Heat transfer between the nodes (waste package to drip shield, drip shield to drift wall, etc.) is based on literature correlations for natural convection heat and mass transfer for the particular geometry. Thermal radiation is calculated based on surface-to-surface radiation and the appropriate view factors. Only heat transfer in the radial direction is considered. The effect of axial heat transfer in the drip shield and waste packages is assumed to be small.

Sources of water are available at each waste package location at the drift wall and the invert. The local vapor pressure is the saturation pressure at the calculated temperature. The rate of water evaporation is based on the difference between the local vapor pressure on the evaporating surface and the local gas-phase vapor partial pressure, and the corresponding mass transfer correlation. The rate is limited by the availability of water to the surface by percolation in the host rock and capillary induction (pumping).

The water vapor is transported along the drift by one-dimensional axial dispersion using the dispersion coefficients calculated by the in-drift convection model as discussed above. These dispersion values are a function of time and temperature tilt due to the thermal evolution of the repository.

Water vapor evaporates and condenses based on the various component surface temperatures and the drift vapor pressure limited by the availability of water and axial transport. Axial transport equations are solved to predict the water vapor distribution and condensation on the various surfaces along each of the seven selected drifts at four selected times. From these results, the

location and rate of condensation on the drift walls, under the drip shield, and on individual waste packages is evaluated.

Two different representations of the drip shield are considered. They are: 1) unventilated cases in which the regions under the drip shield and outside the drip shield are isolated, and 2) the ventilated cases with a single well-mixed region. Use of the terms "ventilated" and "unventilated" does not imply active ventilation or special-purpose features in the present design. The "ventilated" case is an assumption in *Multiscale Thermohydrologic Model* (BSC 2004 [DIRS 169565]) and is the basis for abstraction information used in the Total System Performance Assessment for the Licence Application. The multiscale thermohydrologic model assumes that the partial pressure of water vapor P_v in the drift is uniform outside of the drip shield and that the drip shield is permeable to gas flow such that the vapor pressure inside and outside of the drip shield are equal. The "unventilated" case is not addressed in *Multiscale Thermohydrologic Model* (BSC 2004 [DIRS 169565]). The effect of these two drip shield representations on the condensation rate is evaluated in the present report.

Uncertainty analysis of the condensation rate has been performed for the following variables:

- Percolation Rate
- Dispersion Coefficient
- Water supply to the invert surface.

The condensation model is validated through independent peer review. Professor Ivan Catton reviewed the convection and condensation models included in this report; his review is included in Appendix G.

k_{eq} Correlations

Correlations are also developed to evaluate the effective thermal conductivity for the Yucca Mountain in-drift configuration. In this approach, the open space in the drift is modeled as a thermally-conductive and non-convecting medium with an enhanced thermal conductivity to simulate the increased heat transfer due to natural convection. The k_{eq} correlations are developed specifically to support *Multiscale Thermohydrologic Model* (BSC 2004 [DIRS 169565]), but they can be used in other applications as well.

INTENTIONALLY LEFT BLANK

CONTENTS

Page

ACRONYMS AND ABBREVIATIONS xxiii

1. PURPOSE 1-1

2. QUALITY ASSURANCE 2-1

3. USE OF SOFTWARE 3-1
   3.1 QUALIFIED SOFTWARE 3-1
   3.2 OTHER SOFTWARE 3-2

4. INPUTS 4-1
   4.1 DIRECT INPUT 4-1
      4.1.1 Two-Dimensional In-Drift Convection Simulations 4-1
      4.1.2 Three-Dimensional In-Drift Convection Simulations 4-3
      4.1.3 Condensation Model 4-7
      4.1.4 k_{eq} Analysis and Correlations 4-13
      4.1.5 Other Direct Input 4-14
   4.2 CRITERIA 4-15
      4.2.1 Acceptance Criterion 1: *System Description and Model Integration Are Adequate.* 4-15
      4.2.2 Acceptance Criterion 2: *Data Are Sufficient for Model Justification.* 4-17
      4.2.3 Acceptance Criterion 3: *Data Uncertainty Is Characterized and Propagated Through the Model Abstraction.* 4-17
      4.2.4 Acceptance Criterion 4: *Model Uncertainty Is Characterized and Propagated Through the Model Abstraction.* 4-18
      4.2.5 Acceptance Criterion 5: *Model Abstraction Output Is Supported by Objective Comparisons.* 4-18
   4.3 CODES, STANDARDS, AND REGULATIONS 4-19

5. ASSUMPTIONS 5-1
   5.1 TWO-DIMENSIONAL IN-DRIFT CONVECTION SIMULATIONS 5-1
   5.2 THREE-DIMENSIONAL IN-DRIFT CONVECTION SIMULATIONS 5-1
   5.3 CONDENSATION MODEL 5-2
   5.4 EQUIVALENT THERMAL CONDUCTIVITY (K_{EQ}) ANALYSIS 5-2

6. MODEL DISCUSSION 6-1
   6.1 TWO-DIMENSIONAL IN-DRIFT CONVECTION SIMULATIONS 6-4
      6.1.1 Simulation Objectives 6-4
      6.1.2 Features, Events, and Processes Included 6-5
      6.1.3 Base-Case Conceptual Model for Two-Dimensional Simulations 6-6
      6.1.4 Consideration of Alternative Conceptual Models for In-Drift Natural Convection 6-14

CONTENTS (Continued)

Page

6.1.5 Formulation for the Base-Case Convection Simulations 6-14
6.1.6 Formulation for Alternative Conceptual Models for In-Drift Natural Convection 6-28
6.1.7 Two-Dimensional Simulation Results 6-28
6.2 THREE-DIMENSIONAL IN-DRIFT CONVECTION SIMULATIONS 6-32
6.2.1 Simulation Objectives 6-32
6.2.2 Features, Events, and Processes Included 6-32
6.2.3 Base-Case Convection Conceptual Model 6-32
6.2.4 Consideration of Alternative Conceptual Models for In-Drift Natural Convection 6-34
6.2.5 Formulation for the Base-Case Convection Model 6-34
6.2.6 Formulation for Alternative Conceptual Models for In-Drift Natural Convection 6-42
6.2.7 Three-Dimensional Dispersion Calculations 6-42
6.3 IN-DRIFT CONDENSATION MODEL 6-53
6.3.1 Modeling Objectives 6-53
6.3.2 Features, Events, and Processes Included in the Condensation Model 6-55
6.3.3 Base-Case Conceptual Condensation Model 6-55
6.3.4 Consideration of Alternative Conceptual Models for In-Drift Condensation 6-68
6.3.5 Formulation for the Base-Case Condensation Model 6-69
6.3.6 Model Formulation for Alternative Conceptual Models for In-Drift Condensation 6-126
6.3.7 Base-Case Condensation Model Results 6-126
6.4 EQUIVALENT THERMAL CONDUCTIVITY ANALYSIS 6-157
6.4.1 Analysis Objectives 6-157
6.4.2 Features, Events, and Processes Included in the k_{eq} Analysis 6-158
6.4.3 Base-Case Conceptual k_{eq} Analysis 6-159
6.4.4 Consideration of Alternative Conceptual Models for the k_{eq} Analysis 6-159
6.4.6 Formulation for Alternative Conceptual Models for the k_{eq} Analysis 6-165
6.4.7 Results for the Two-Dimensional Equivalent Thermal Conductivity (k_{eq}) Analysis 6-165

7. MODEL VALIDATION 7-1
7.1 CONFIDENCE BUILDING DURING MODEL DEVELOPMENT TO ESTABLISH SCIENTIFIC BASIS AND ACCURACY FOR INTENDED USE 7-3
7.2 CONFIDENCE BUILDING AFTER MODEL DEVELOPMENT TO SUPPORT THE SCIENTIFIC BASIS OF THE MODEL 7-4
7.2.1 Convection Model 7-5
7.2.2 Condensation Model 7-6
7.3 SMALL-SCALE LITERATURE DATA VALIDATION 7-7
7.3.1 Kuehn and Goldstein Simulations 7-10
7.3.2 Repository-Scale Concentric Cylinder Simulations 7-13

CONTENTS (Continued)

Page

7.3.3 Correlation, Experimental Data, and CFD Code Comparison for Average Heat Transfer 7-16
7.4 THREE-DIMENSIONAL NATURAL CONVECTION TEST VALIDATION 7-19
7.4.1 Experiment 7-19
7.4.2 CFD Simulations 7-49
7.4.3 Results 7-67
7.4.4 Conclusions 7-93
7.5 DISPERSION COEFFICIENT VALIDATION 7-96
7.6 CONDENSATION MODEL VALIDATION 7-96

8. CONCLUSIONS 8-1
8.1 TWO-DIMENSIONAL IN-DRIFT CONVECTION 8-1
8.2 THREE-DIMENSIONAL IN-DRIFT CONVECTION 8-2
8.3 IN-DRIFT CONDENSATION MODEL 8-4
8.3.1 Condensation Model Abstraction Summary 8-5
8.3.2 Model Outputs – Condensation Model Summary 8-15
8.3.3 Restrictions For Subsequent Use – Condensation Model 8-18
8.4 K_{EQ} ANALYSIS AND CORRELATIONS 8-18
8.5 EVALUATION OF YUCCA MOUNTAIN REVIEW PLAN CRITERIA 8-20
8.5.1 Acceptance Criterion 1: *System Description and Model Integration Are Adequate.* 8-21
8.5.2 Acceptance Criterion 2: *Data Are Sufficient for Model Justification.* 8-24
8.5.3 Acceptance Criterion 3: *Data Uncertainty Is Characterized and Propagated Through the Model Abstraction.* 8-26
8.5.4 Acceptance Criterion 4: *Model Uncertainty Is Characterized and Propagated Through the Model Abstraction.* 8-27
8.5.5 Acceptance Criterion 5: *Model Abstraction Output Is Supported by Objective Comparisons.* 8-28

9. INPUTS AND REFERENCES 9-1
9.1 DOCUMENTS CITED 9-1
9.2 CODES, STANDARDS, REGULATIONS, AND PROCEDURES 9-10
9.3 SOURCE DATA, LISTED BY DATA TRACKING NUMBER 9-11
9.4 OUTPUT DATA, LISTED BY DATA TRACKING NUMBER 9-12
9.5 SOFTWARE CODES 9-13

APPENDIX A: KUEHN AND GOLDSTEIN CORRELATIONS A-1

APPENDIX B: BLIND ANALYSES OF EBS NATURAL CONVECTION TESTS B-1

APPENDIX C: NATURAL CONVECTION TEST DATA INFORMATION C-1

APPENDIX D: SOLUTION TO THE DISPERSION EQUATIONS D-1

CONTENTS (Continued)

Page

APPENDIX E: CALCULATION PLOTS FOR DRIFT CHOICE #7 ..... E-1

APPENDIX F: COMPARISON OF SOLUTIONS: LINE SOURCE VS. CYLINDER WITH PRESCRIBED WALL FLUX F-1

APPENDIX G: TECHNICAL REVIEWS G-1

APPENDIX H: CORRELATION SUMMARY OF VENTILATED CONDENSATION MODEL ABSTRACTION H-1

APPENDIX I: CORRELATION SUMMARY OF UNVENTILATED CONDENSATION MODEL ABSTRACTION I-1

APPENDIX J: VERIFICATION OF TWO-DIMENSIONAL HEAT TRANSFER MODEL FOR STRUCTURES WITHIN THE DRIFT J-1

APPENDIX K: JUSTIFICATION OF SUPERSEDED INPUT K-1

APPENDIX L: QUALIFICATION OF DIRECT INPUTS LISTED IN TABLE 4.1.5-1 ..... L-1

APPENDIX M: CALCULATION CORRECTION M-1

FIGURES

Page

6.1.3-1. Yucca Mountain Drift Configuration 6-7
6.1.3-2. Conceptual Model for Two- and Three-Dimensional CFD Simulations 6-8
6.1.5-1. Boundary Conditions Imposed on the Two-Dimensional Convection Simulations 6-25
6.1.5-2. Computational Grid for the Two-Dimensional In-Drift Convection Simulations 6-26
6.2.5-1. Schematic Diagram of Geometry of the Three-Dimensional Natural Convection Simulations 6-36
6.2.5-2. Boundary Conditions Imposed on the Three-Dimensional Natural Convection Simulations 6-37
6.2.5-3. Computational Grid for the Two-Dimensional In-Drift Convection Simulations 6-39
6.2.7-1. Cross-Sectionally Averaged Air2 Concentrations with Uniform Boundary Temperature 6-45
6.2.7-2. Iso-Velocity Contours Underneath the Drip Shield for Velocity Greater than 2 cm/s in the +Z Direction at 300 Years 6-47
6.2.7-3. Iso-Velocity Contours Underneath the Drip Shield for Velocity Greater than 2 cm/s in the –Z Direction at 300 Years 6-47
6.2.7-4. Iso-Velocity Contours above the Drip Shield for Velocity Greater than 2 cm/s in the +Z Direction at 300 Years 6-48
6.2.7-5. Iso-Velocity Contours above the Drip Shield for Velocity Greater than 2 cm/s in the –Z Direction at 300 Years 6-48
6.2.7-6. Cross-Sectionally Averaged Air2 Concentrations with Tilted Boundary Temperature 6-49
6.2.7-7. Iso-Velocity Contours Underneath the Drip Shield for Velocity Greater than 2 cm/s in the +Z Direction at 300 Years 6-51
6.2.7-8. Iso-Velocity Contours Underneath the Drip Shield for Velocity Greater than 2 cm/s in the –Z Direction at 300 Years 6-51
6.2.7-9. Iso-Velocity Contours Above the Drip Shield for Velocity Greater than 2 cm/s in the +Z Direction at 300 Years 6-52
6.2.7-10. Iso-Velocity Contours Above the Drip shield for Velocity Greater than 2 cm/s in the –Z Direction at 300 Years 6-52
6.3.3-1. Schematic of the Emplacement Drift Cross Section 6-57
6.3.3-2. Schematic of Invert Inter-Particle Contact 6-57
6.3.3-3. Seepage Migration to the Invert Surface 6-59
6.3.3-4. Two-Dimensional Annular Convection Pattern 6-59
6.3.3-5. Location of Gas Conduction Zone When Invert Temperature Is Less than Gas Temperature 6-60
6.3.3-6. Streamlines (Left) and Isotherms (Right) Calculated by Kuehn and Goldstein 6-61
6.3.3-7. Convective Cells Connecting Hotter and Colder Waste Packages 6-61
6.3.3-8. Three Stages of Evaporation/Condensation Inside an Emplacement Drift 6-63

FIGURES (Continued)

Page

6.3.5-1. Creation of an Isothermal Surface Using the Method of Images 6-73
6.3.5-2. Locations of Emplacement Drifts Chosen for Analysis 6-75
6.3.5-3. Centerpoint Temperatures for Chosen Drifts #1 and #2 6-76
6.3.5-4. Centerpoint Temperatures for Chosen Drifts #3 and #4 6-77
6.3.5-5. Centerpoint Temperatures for Chosen Drifts #5 and #6 6-77
6.3.5-6. Centerpoint Temperatures for Chosen Drift #7 6-78
6.3.5-7. Drift Wall Temperatures for Chosen Drift #1 6-79
6.3.5-8. Drift Wall Temperatures for Chosen Drift #2 6-79
6.3.5-9. Drift Wall Temperatures for Chosen Drift #3 6-80
6.3.5-10. Drift Wall Temperatures for Chosen Drift #4 6-80
6.3.5-11. Drift Wall Temperatures for Chosen Drift #5 6-81
6.3.5-12. Drift Wall Temperatures for Chosen Drift #6 6-81
6.3.5-13. Drift Wall Temperatures for Chosen Drift #7 6-82
6.3.5-14. Modern, Monsoon, and Glacial Percolation Rates for Chosen Drift #1 6-83
6.3.5-15. Modern, Monsoon, and Glacial Percolation Rates for Chosen Drift #2 6-84
6.3.5-16. Modern, Monsoon, and Glacial Percolation Rates for Chosen Drift #3 6-85
6.3.5-17. Modern, Monsoon, and Glacial Percolation Rates for Chosen Drift #4 6-86
6.3.5-18. Modern, Monsoon, and Glacial Percolation Rates for Chosen Drift #5 6-87
6.3.5-19. Modern, Monsoon, and Glacial Percolation Rates for Chosen Drift #6 6-88
6.3.5-20. Modern, Monsoon, and Glacial Percolation Rates for Chosen Drift #7 6-89
6.3.5-21. Illustration of Mass Fluxes 6-90
6.3.5-22. Approximate Angle for Drip Shield Top 6-99
6.3.5-23. Comparison of Cylindrical and Spherical Solutions for Capillary Pumping 6-112
6.3.5-24. Schematic of Barometric Pumping 6-113
6.3.5-25. Possible Effects of Barometric Pumping on Capillary Pumping 6-114
6.3.5-26. Repository Layout 6-116
6.3.5-27. Line-Averaged Power 6-117
6.3.5-28. Discrete Waste Package Powers 6-118
6.3.5-29. Line-Averaged Power with Ventilation Efficiency 6-119
6.3.5-30. Discrete Waste Package Powers with Ventilation Efficiency 6-119
6.3.5-31. Waste Package Sequence 6-120
6.3.5-32. Calculation of Drip Shield Perimeter 6-121
6.3.5-33. Calculation of Exposed Wall Perimeter 6-122
6.3.7-1. Numbering of Chosen Drifts 6-127
6.3.7-2. Vapor Mass Fraction in Gas and Condensation Rate on Drift Wall: Choice #7, 1,000 Years, Mean Percolation Rate, Well-Ventilated Drip Shield, Low Invert Transport, Low Dispersion Coefficient 6-130
6.3.7-3. Vapor Mass Fraction in Gas at 3,000 Years and 10,000 Years: Choice #7, Mean Percolation Rate, Well-Ventilated Drip Shield, Low Invert Transport, Low Dispersion Coefficient 6-131
6.3.7-4. Vapor Mass Fraction in Gas: Choice #7, 1,000 Years, Mean Percolation Rate, Well-Ventilated Drip Shield, Low Invert Transport, High Dispersion Coefficient 6-132

FIGURES (Continued)

Page

6.3.7-5. Vapor Mass Fraction in Gas at 3,000 Years and 10,000 Years: Choice #7, Mean Percolation Rate, Well-Ventilated Drip Shield, Low Invert Transport, High Dispersion Coefficient 6-133
6.3.7-6. Condensation Rate on the Underside of the Drip Shield: Choice #7, 1,000 Years, Mean Percolation Rate, Unventilated Drip Shield, High Invert Transport, Low Dispersion Coefficient 6-141
6.3.7-7. Vapor Mass Fraction in Gas under the Drip Shield: Choice #7, 1,000 Years, Mean Percolation Rate, Unventilated Drip Shield, High Invert Transport, Low Dispersion Coefficient 6-142
6.3.7-8. Condensation Rate on the Underside of the Drip Shield: Choice #7, 10,000 Years, Mean Percolation Rate, Unventilated Drip Shield, High Invert Transport, Low Dispersion Coefficient 6-143
6.3.7-9. Vapor Mass Fraction in Gas under the Drip Shield: Choice #7, 10,000 Years, Mean Percolation Rate, Unventilated Drip Shield, High Invert Transport, Low Dispersion Coefficient 6-143
6.3.7-10. Condensation Rate on the Waste Package: Choice #7, 10,000 Years, Mean Percolation Rate, Unventilated Drip Shield, High Invert Transport, Low Dispersion Coefficient 6-144
6.4.5-1. Diagram of Two-Dimensional k_{eq} CFD Domain with Boundary Conditions 6-160
6.4.5-2. Computational Grid for the Average Radius Two-Dimensional YMP Geometry k_{eq} Analysis 6-162
6.4.7-1. Correlation of the Equivalent Thermal Conductivity (k_{eq}) Inside the Drip Shield 6-166
6.4.7-2. Correlation of the Equivalent Thermal Conductivity (k_{eq}) Outside the Drip Shield 6-170
6.4.7-3. Comparison of Natural Convection Correlation Equations 6-173
7.3.2-1. Computational Grid for the Full-Scale YMP Concentric Cylinder Geometry 7-14
7.3.3-1. Comparison of CFD Simulation Results to the Kuehn and Goldstein Correlation Equation (1978) and the General Correlation in Kuehn and Goldstein (1976) for Concentric Cylinders..... 7-17
7.3.3-2. Comparison of CFD Simulation Results for Concentric Cylinders to Other Experimental Results, Simulation Results, and Heat Transfer Correlations 7-18
7.4.1-1. Schematic Presentation of a Cross-Section of an Emplacement Drift Showing Major Components of the Engineered Barrier System..... 7-21
7.4.1-2. Steel Support Pallets Design Drawing..... 7-22
7.4.1-3. Photographs of the 25% Scale Test Components 7-23
7.4.1-4. Schematic Depicting Relative Locations of Thermocouples and Relative Humidity Sensors for the Cases without a Drip Shield (Cases 1 and 2)..... 7-27
7.4.1-5. Schematic Depicting Relative Locations of Thermocouples and Relative Humidity Sensors for the Cases with a Drip Shield (Cases 3 and 4)..... 7-28
7.4.1-6. Design Layout and Power for Case 1 7-35
7.4.1-7. Design Layout and Power for Case 4 7-36
7.4.1-8. Design Layout and Power for Case 5 7-37

FIGURES (Continued)

Page

7.4.1-9. Design Layout and Power for Case 8 7-38
7.4.1-10. Example of Variations Recorded in Ambient Temperatures (Case 8) 7-40
7.4.1-11. Typical Changes in Ambient Conditions (Case 8) 7-41
7.4.2-1. Cross-Sectional Dimensions for Case 4 Simulations..... 7-51
7.4.2-2. Cross-Sectional Dimensions for Case 8 Simulations..... 7-52
7.4.2-3. Gridding (XY) of a Cross-Section through One of the Smaller Waste Packages for Case 4 (25% Scale)..... 7-55
7.4.2-4. Gridding (XY) of a Cross-Section through One of the Smaller Waste Packages for Case 8 (44% Scale)..... 7-56
7.4.2-5. Axial Gridding for Case 4..... 7-57
7.4.2-6. Axial Gridding for Case 8..... 7-58
7.4.3-1. Applied Temperature Boundary Condition to the Exterior Surface of the Concrete (Case 4)..... 7-68
7.4.3-2. Applied Temperature Boundary Condition to the Exterior Surface of the Concrete (Case 8)..... 7-68
7.4.3-3. Comparison of Experimentally Measured and Calculated Simulation Temperatures for the Interior Surface of the Concrete (Case 4)..... 7-69
7.4.3-4. Comparison of Experimentally Measured and Calculated Simulation Temperatures for the Interior Surface of the Concrete (Case 8)..... 7-70
7.4.3-5. Plot of Temperatures for All Cells on the Waste Packages (Case 4)..... 7-71
7.4.3-6. Plot of Temperatures for All Cells on the Waste Packages (Case 8)..... 7-71
7.4.3-7. Comparison of Experimentally Measured and Calculated Simulation Temperatures for the Invert (Case 4)..... 7-74
7.4.3-8. Comparison of Experimentally Measured and Calculated Simulation Temperatures for the Invert (Case 8)..... 7-75
7.4.3-9. Comparison of Experimentally Measured and Calculated Simulation Temperatures for the Drip Shield (Case 4)..... 7-76
7.4.3-10. Comparison of Experimentally Measured and Calculated Simulation Temperatures for the Drip Shield (Case 8)..... 7-76
7.4.3-11. Comparison of Simulation and Measured Fluid Temperatures for Position of (a) Top Sensor and (b) Side Sensor (Case 4)..... 7-78
7.4.3-12. Comparison of Simulation and Measured Fluid Temperatures for Positions of Bottom Sensors (Case 4) 7-79
7.4.3-13. Comparison of Simulation and Measured Fluid Temperatures for Position of (a) Top Sensor and (b) Side Sensor (Case 8)..... 7-80
7.4.3-14. Comparison of Simulation and Measured Fluid Temperatures for Positions of Bottom Sensors (Case 8) 7-81
7.4.3-15. FLUENT Temperature Contours for Case 4..... 7-83
7.4.3-16. FLUENT Temperature Contours for Case 8..... 7-84
7.4.3-17. FLUENT Velocity Vector Plots for Case 4 7-87
7.4.3-18. FLUENT Velocity Vector Plots for Case 8 7-88
7.4.3-19. Comparison of Experimental and Calculated Velocities at (a) Station 5 and (b) Station 11 (Case 4) 7-89

FIGURES (Continued)

Page

7.4.3-20. Comparison of Experimental and Calculated Velocities at (a) Station 5 and (b) Station 7 (Case 8) 7-90
7.4.3-21. Comparison of Experimental and Calculated Velocities along the Length of the Test Train (Case 4) 7-91
7.4.3-22. Comparison of Experimental and Calculated Velocities along the Length of the Test Train (Case 8) 7-92

INTENTIONALLY LEFT BLANK

TABLES

Page

2-1. Engineered Barrier System Components Addressed in This Report, Listed with Corresponding Safety Category (SC) Level 2-1
3-1. Software Used 3-1
4.1.1-1. Thermophysical Properties of Dry Air Used for the Two-Dimensional In-Drift Convection Simulations 4-1
4.1.1-2. Thermal Properties of Materials Used for the Base Case of the Two-Dimensional In-Drift Convection Simulations 4-2
4.1.1-3. Approximate In-Drift Geometries with Drip Shield 4-2
4.1.1-4. Absorption/Emission Thermal Radiation Input 4-3
4.1.2-1. Material Properties of Engineered Barrier System Components 4-4
4.1.2-2. Bulk Thermal Properties of Stratigraphic Unit Tsw35 (Tptpll) 4-5
4.1.2-3. Fluid Properties for Three-Dimensional In-Drift Convection Simulations 4-5
4.1.2-4. Waste Package Sequence and Waste Package Powers at Four Different Times Used in the Three-Dimensional In-Drift Convection Simulations 4-6
4.1.2-5. Design Inputs Required by Three-Dimensional In-Drift Simulations 4-6
4.1.2-6. Standard Atmosphere 4-7
4.1.3-1. Rock Properties 4-7
4.1.3-2. Thermal Radiation Properties 4-8
4.1.3-3. Air Properties 4-8
4.1.3-4. Water Vapor Properties 4-9
4.1.3-5. Water Vapor Pressures 4-10
4.1.3-6. Water Vapor Density at Saturation 4-11
4.1.3-7. Repository Layout and Sources for Percolation Data 4-12
4.1.3-8. Waste Package Dimensions 4-13
4.1.3-9. Drift/Drip Shield Dimensions 4-13
4.1.4-1. Thermophysical Properties of Dry Air Used for the k_{eq} Analysis 4-13
4.1.4-2. Rayleigh Number Property Group of Dry Air Used for the k_{eq} Analysis 4-14
4.1.5-1. Other Direct Input 4-14
4.2-1. Project Requirements for this Report 4-15
6.1.2-1. Included FEPs in TSPA-LA Addressed In This Document 6-5
6.1.2-2. Excluded FEPs Addressed In This Document 6-6
6.1.4-1. Alternative Conceptual Models Considered for In-Drift Natural Convection 6-14
6.1.7-1. Two-Dimensional YMP Geometry Sensitivity Studies Results 6-31
6.2.5-1. Five-Meter Boundary Conditions for the Three-Dimensional CFD Simulations 6-37
6.2.5-2. Information Needed to Calculate the Power Density Needed for Three-Dimensional Natural Convection Simulations at 300 Years 6-40
6.2.5-3. Information Needed to Calculate the Power Density Needed for Three-Dimensional Natural Convection Simulations at 1,000 Years 6-40
6.2.5-4. Information Needed to Calculate the Power Density Needed for Three-Dimensional Natural Convection Simulations at 3,000 Years 6-41
6.2.5-5. Information Needed to Calculate the Power Density Needed for Three-Dimensional Natural Convection Simulations at 10,000 Years 6-41

TABLES (Continued)

Page

6.2.7-1. Locations of Waste Packages in the Three-Dimensional Natural Convection Simulations 6-44
6.2.7-2. Results for Three-Dimensional Drift-Scale Natural Convection Simulations with a Uniform 350 K Boundary Temperature 6-46
6.2.7-3. Results for Three-Dimensional Drift-Scale Natural Convection Simulations with a Linearly Varying Boundary Temperature 6-50
6.3.5-1. Average Temperature "Tilt" 6-82
6.3.7-1. Condensation on the Drift Walls: Well-Ventilated Drip Shield, Low Invert Transport, Low Dispersion Coefficient 6-129
6.3.7-2. Condensation on the Drift Walls: Well-Ventilated Drip Shield, High Invert Transport, Low Dispersion Coefficient 6-134
6.3.7-3. Condensation on the Drift Walls: Well-Ventilated Drip Shield, High Invert Transport, High Dispersion Coefficient 6-135
6.3.7-4. Condensation on the Drift Walls: Unventilated Drip Shield, Low Invert Transport, Low Dispersion Coefficient 6-136
6.3.7-5. Condensation on the Drift Walls: Unventilated Drip Shield, High Invert Transport, Low Dispersion Coefficient 6-137
6.3.7-6. Condensation under the Drip Shield: Unventilated Drip Shield High Invert Transport, Low Dispersion Coefficient 6-139
6.3.7-7. Condensation under the Drip Shield: Unventilated Drip Shield, High Invert Transport, High Dispersion Coefficient 6-140
6.3.7-8. Axial Energy Flow to the Access and Exhaust Regions: Well-Ventilated Drip Shield, Low Invert Transport, Low Dispersion Coefficient 6-147
6.3.7-9. Axial Energy Flow to the Access and Exhaust Regions:: Well-Ventilated Drip Shield, Low Invert Transport, High Dispersion Coefficient 6-148
6.3.7-10. Axial Energy Flow to the Access and Exhaust Regions:: Well-Ventilated Drip Shield, High Invert Transport, Low Dispersion Coefficient 6-149
6.3.7-11. Axial Energy Flow to the Access and Exhaust Regions:: Well-Ventilated Drip Shield, High Invert Transport, High Dispersion Coefficient 6-150
6.3.7-12. Axial Energy Flow to the Access and Exhaust Regions:: Unventilated Drip Shield, Low Invert Transport, Low Dispersion Coefficient 6-151
6.3.7-13. Axial Energy Flow to the Access and Exhaust Regions:: Unventilated Drip Shield, Low Invert Transport, High Dispersion Coefficient 6-152
6.3.7-14. Axial Energy Flow to the Access and Exhaust Regions:: Unventilated Drip Shield, High Invert Transport, Low Dispersion Coefficient 6-153
6.3.7-15. Axial Energy Flow to the Access and Exhaust Regions:: Unventilated Drip Shield, High Invert Transport, High Dispersion Coefficient 6-154
6.4.5-1. Summary of Temperature Boundary Conditions for Two-Dimensional k_{eq} YMP Simulations 6-161
6.4.5-2. Approximate In-Drift Geometries with Drip Shield 6-162
6.4.5-3. Thermophysical Properties of Air Used in the Two-Dimensional k_{eq} In-Drift Geometry Simulations 6-164

TABLES (Continued)

Page

6.4.5-4. Operating Conditions for the Two-Dimensional k_{eq} In-Drift Geometry Simulations 6-165
6.4.7-1. CFD Equivalent Thermal Conductivity Simulations – Inside the Drip Shield Results 6-167
6.4.7-2. CFD Equivalent Thermal Conductivity Simulations – Outside the Drip Shield Results 6-170
6.4.7-3. Summary of Repository Correlation Equations for Natural Convection Heat Transfer in Enclosures[a] 6-173
7-1. Summary of Intended Uses, Confidence Building, Validation Results and Sections Where Details Are Found 7-2
7.3.1-1. Internal Natural Convection Heat Transfer in the Literature 7-9
7.3.1-2. Concentric Cylinder Geometries 7-10
7.3.1-3. Thermophysical Properties of N_2 used for the Two-Dimensional Concentric Cylinders Kuehn and Goldstein Simulations 7-12
7.3.1-4. Operating Conditions 7-12
7.3.2-1. Concentric Cylinder Geometries 7-13
7.3.2-2. Geometric information used in the Repository-Scale Concentric Cylinders Simulations 7-13
7.3.2-3. Thermophysical Properties of Dry Air Used in FLUENT for the Two-Dimensional Concentric Cylinders Simulations 7-15
7.3.2-4. Operating Conditions 7-15
7.3.3-1. Thermophysical Properties of Dry Air Used in the Two-Dimensional Kuehn and Goldstein Correlations 7-16
7.4.1-1. Postclosure Convection Test Matrix 7-20
7.4.1-2 Instrument Characteristics for the Natural Convection Tests 7-25
7.4.1-3. Case 4 Measured Velocities Along the Length of the Test Train 7-29
7.4.1-4. Case 4 Measured Velocities at Station 5 7-29
7.4.1-5. Case 4 Measured Velocities at Station 11 7-30
7.4.1-6. Case 8 Measured Velocities Along the Length of the Test Train 7-30
7.4.1-7. Case 8 Measured Velocities at Station 5 7-31
7.4.1-8. Case 8 Measured Velocities at Station 7 7-31
7.4.1-9. Relative Locations for the 25% Scale Drip Shield Temperature Sensors 7-33
7.4.1-10. Relative Locations for the 44% Scale Drip Shield Temperature Sensors 7-34
7.4.1-11. DTN Numbers for Data from the Scale Natural Convection Tests 7-39
7.4.1-12. Averaging Periods for Cases 4 and 8 7-39
7.4.1-13. Case 4 Average Waste Package Temperatures, C 7-42
7.4.1-14. Case 4 Average Concrete Inner Surface Temperatures, C 7-43
7.4.1-15. Case 4 Average Concrete Outer Surface Temperatures, C 7-43
7.4.1-16. Case 4 Average Air Temperatures Inside Test Train, C 7-44
7.4.1-17. Case 4 Average Invert Temperatures, C 7-44
7.4.1-18. Case 4 Average Drip Shield Temperatures, C 7-45
7.4.1-19. Case 8 Average Waste Package Temperatures, C 7-45
7.4.1-20. Case 8 Average Concrete Inner Surface Temperatures, C 7-46

TABLES (Continued)

Page

7.4.1-21. Case 8 Average Concrete Outer Surface Temperatures, C 7-46
7.4.1-22. Case 8 Average Air Temperatures Inside Test Train, C 7-47
7.4.1-23. Case 8 Average Invert Temperatures, C 7-47
7.4.1-24. Case 8 Average Drip Shield Temperatures, C 7-48
7.4.1-25. Measured Power Input from Test Cases 4 and 8 7-48
7.4.2-1. CFD Simulation Discretization 7-59
7.4.2-2. Thermophysical Properties of Introduced Materials 7-62
7.4.2-3. Emissivities of Materials 7-62
7.4.2-4. Thermal Conductivity of 4-10 Crushed Tuff 7-63
7.4.2-5. Thermophysical Properties of Air 7-63
7.4.2-6. Power Inputs for the Blind FLUENT Runs 7-65
7.4.2-7. Power Inputs for the Post-Test FLUENT Runs 7-65
7.4.2-8. Standard Atmosphere 7-66
7.4.3-1. Comparison of FLUENT and Experimental Temperature Data for the Waste Package Cylinders (Case 4) 7-72
7.4.3-2. Comparison of FLUENT and Experimental Temperature Data for the Waste Package End Plates (Case 4) 7-72
7.4.3-3. Comparison of FLUENT and Experimental Temperature Data for the Waste Package Cylinders (Case 8) 7-73
7.4.3-4. Comparison of FLUENT and Experimental Temperature Data for the Waste Package End Plates (Case 8) 7-73
8.1-1. Product Output DTNs for the Two-Dimensional Natural Convection Simulations 8-1
8.1-2. Product Output DTNs for the Two-Dimensional Natural Convection Validation Simulations 8-2
8.2-1. Product Output DTNs for the Three-Dimensional Natural Convection Simulations 8-3
8.2-2. Product Output DTNs for the Three-Dimensional Natural Convection Validation Data-Simulation Comparisons 8-4
8.3.1.2-1. Regression Models for Probability of Condensation Under the Drip Shield 8-12
8.3.2-1. Product Output DTNs for the In-Drift Condensation Model 8-15
8.3.2.1-1. Ventilated Drift Wall Condensation 8-16
8.3.2.2-1. Unventilated Drift Wall Condensation 8-17
8.3.2.2-2. Unventilated Drip Shield Condensation, HLW Waste Packages 8-17
8.3.2.2-3. Unventilated Drip Shield Condensation, Non-HLW Waste Packages 8-18
8.4-1. Product Output DTN for the k_{eq} Analysis and Correlations 8-20

ACRONYMS AND ABBREVIATIONS

ACM	Alternative Conceptual Model
BWR	boiling water reactor
CFD	computational fluid dynamics
CSNF	commercial spent nuclear fuel
DO	discrete ordinates
DOE	U.S. Department of Energy
DTN	data tracking number
EBS	Engineered Barrier System
ECRB	Enhanced Characterization of Repository Block
FEP(s)	features, events and process(es)
HLW	high-level (radioactive) waste
LA	License Application
MSTHM	multiscale thermohydrologic model
NRC	U.S. Nuclear Regulatory Commission
ODE	ordinary differential equation
PWR	pressurized water reactor
RANS	Reynolds-averaged-Navier Stokes equations
RNG	renormalized group
RSM	Reynolds Stress Model
RTE	radiative transfer equation
SIMPLE	Semi-Implicit Method for Pressure-Linked Equations
TC	Thermocouple
TDC	Top dead center
Tptpll	Lower Lithophysal Zone of the Topopah Spring Formation
TSPA	total system performance assessment
TSPA-LA	Total System Performance Assessment for the License Application
TWP	Technical Work Plan
UZ	Unsaturated Zone
YMP	Yucca Mountain Project

INTENTIONALLY LEFT BLANK

1. PURPOSE

Two models and one analysis are documented in this report. The two models are the in-drift convection model and the in-drift condensation model, which apply to the postclosure period of the repository after forced ventilation has ceased. The analysis correlates the natural convection heat transfer from computational fluid dynamics simulations for use in porous media codes to represent in-drift convective heat transfer. Preclosure forced ventilation aspects are addressed in *Ventilation Model and Analysis Report*. The technical work plan (TWP) for this activity is given by *Technical Work Plan for: Near-Field Environment and Transport In-Drift Heat and Mass Transfer Model and Analysis Reports Integration* (BSC 2004 [DIRS 170950]).

The two models and one analysis discussed in the report are:

1. In-drift convection model
2. In-drift condensation model
3. Equivalent thermal conductivity (k_{eq}) analysis and correlations.

The in-drift natural convection and condensation model results are limited to post-closure conditions and do not include rock fall, repository-wide natural circulation, natural ventilation, or barometric pumping. The equivalent thermal conductivity analysis and correlation results are subject to the same limitations. Parameter limits on the equivalent thermal conductivity correlations are explicitly listed.

A variation from the TWP (BSC 2004 [DIRS 170950]) is that the dispersion coefficient model mentioned on page 13 is not a model but a calculation. Dispersion coefficients are calculated from the output of the convection model as discussed in Section 6.2.7. Another variance from the TWP is that some features, events, and processes (FEPs) have been added to the Included list from what is listed in the TWP.

Convection Model

Two-dimensional and three-dimensional versions of the convection model are developed. The purpose of the two-dimensional in-drift convection simulations is to evaluate the sensitivity of waste package temperatures to the uncertainty in in-drift thermal properties, and to evaluate physics submodels, such as turbulence and thermal radiation, for subsequent use in the three-dimensional simulations.

The purpose of the three-dimensional convection simulations is to generate axial mass dispersion coefficients for water vapor transport down the drift for use in the in-drift condensation model. The appropriate physics submodels are based on the two-dimensional convection simulation results.

The convection model documentation includes:

- Description of the contributing phenomena
- Presentation of the appropriate relationships such as for turbulence and radiation that are implemented in FLUENT

- Sensitivity results using the two-dimensional convection representation
- Simulation results for the three-dimensional representation
- Evaluation of the axial mass dispersion coefficients from FLUENT results that are used in the condensation model
- Validation of the natural convection model including comparison to experimental data
- Validation of the dispersion coefficients by independent technical review.

Condensation Model

The purpose of the in-drift condensation model is to evaluate the location and rate of in-drift condensation on the drift walls, under the drip shield, and on individual waste packages for selected drifts. Two different drip shield configurations have been considered. The first configuration is where the regions inside and outside the drip shield are isolated from each other, which represents an unventilated and intact drip shield. The second configuration considers a single well-mixed region, which represents a ventilated drip shield.

The in-drift condensation model uses a calculated axial dispersion coefficient generated by the three-dimensional in-drift convection model (item 2 of this section) to estimate the rate of axial vapor transport. It also uses geometric parameters specific to the license application (LA) repository design, rock thermal properties, estimated percolation rates, and standard transport coefficients. All direct inputs are taken from qualified and/or accepted sources.

Two different representations of the drip shield are considered. They are: 1) unventilated cases in which the regions under the drip shield and outside the drip shield are isolated, and 2) the ventilated cases with a single well-mixed region. Use of the terms “ventilated” and “unventilated” does not imply active ventilation or special-purpose features in the present design. The “ventilated” case is an assumption in *Multiscale Thermohydrologic Model* (BSC 2004 [DIRS 169565]) and is the basis for abstraction information used in the Total System Performance Assessment for the Licence Application (TSPA-LA). The multiscale thermohydrologic model (MSTHM) assumes that the partial pressure of water vapor P_v in the drift is uniform outside of the drip shield and that the drip shield is permeable to gas flow such that the vapor pressure inside and outside of the drip shield are equal. The “unventilated” case is not addressed in the MSTHM (BSC 2004 [DIRS 169565]). The effect of these two drip shield representations on the condensation rate is evaluated in the present report.

Results of the condensation model are abstracted in the form of correlations where the percolation rate is the independent variable. Specific correlations produced are:

- Fraction of the waste package locations that receive condensation on the drift wall
- Rate of drift-wall condensation when such condensation occurs
- Fraction of the high-level waste (HLW) package locations where condensation occurs under the drip shield

- Rate of condensation for HLW packages when condensation occurs under the drip shield
- Fraction of the non-HLW package locations where condensation occurs under the drip shield
- Rate of condensation for non-HLW packages when condensation occurs under the adjacent drip shield.

The correlations produced by the in-drift condensation model are direct inputs to TSPA-LA model and are appropriate for the LA repository geometry and the range of anticipated percolation flux.

The condensation model documentation includes:

- Description of the contributing phenomena
- Development of the vapor transport equations and their solution
- Estimates of available water from the adjacent rock
- Transport correlations used
- Model scope limitations
- Model uncertainty
- Model abstraction development
- Validation of the dispersion coefficients by independent technical review.

Equivalent Thermal Conductivity (k_{eq}) Analysis and Correlations

The k_{eq} correlation is discussed separately from the convection and condensation models. The purpose of the k_{eq} analysis is to generate equivalent thermal conductivity correlations that can be used by a porous media code to represent in-drift conditions. These correlations are limited to the current Yucca Mountain Project (YMP) geometry including a drip shield. Specific ranges of applicability are documented in the development of the correlation. The output is used in the MSTHM. Therefore, the output from the k_{eq} analysis has an indirect feed to TSPA-LA through the MSTHM.

The information used for the correlation is based on the two-dimensional natural convection simulations developed in this report. Therefore, data and validation activities that support the two-dimensional convection simulations implicitly support the correlations. The natural convection heat transfer results are correlated as a function of the appropriate dimensionless number, or the Rayleigh number, to allow for general application of the results. This procedure is standard engineering practice and does not need to be validated.

The k_{eq} equivalent thermal conductivity analysis and correlation documentation includes:

- Development of the k_{eq} correlations for the regions inside and outside the drip shield including limits of applicability
- Comparison of the YMP-specific correlations to literature results.

Direct Sources and Users of the Output of the AMR

The in-drift condensation and convection model uses qualified data obtained from project information (i.e. data tracking numbers (DTNs) and IEDs as presented in Section 4.1 of this report. Information is also obtained from the following reports:

- *UZ Flow Models and Submodels*
- *Drift-Scale THC Seepage Model*
- *In Situ Field Testing of Processes*
- *Calibrated Properties Model*
- *Thermal Conductivity of the Potential Repository Horizon Model Report*
- *Ventilation Model and Analysis Report*
- *Heat Capacity Analysis Report*
- *The Multiscale Thermohydrologic Model*
- The *Engineered Barrier System: Physical and Chemical Environment Model*
- *EBS Radionuclide Transport Abstraction*

The in-drift condensation and convection model provides correlations for the TSPA-LA condensation rates that depend on the waste package heat evolution and changes in percolation rates from climate evolution. The TSPA-LA then uses the condensation rates to evaluate the following:

- General corrosion of the waste package
- Localized corrosion of the waste package
- Waste-form degradation
- Radionuclide solubility
- In-drift seepage evolution and thermal seepage
- Dust-leachate evolution
- Radionuclide transport in the Engineered Barrier System

Analysis and model reports that are directly downstream of this report include:

- *Total System Performance Assessment (TSPA) Model/Analysis for the License Application*
- *Engineered Barrier System Features, Events, and Processes*
- *The Multiscale Thermohydrologic Model*
- *Environment on the Surfaces of the Drip Shield and Waste Package Outer Barrier*
- *Drift-Scale Coupled Processes (DST and TH Seepage) Models*
- *Abstraction of Drift Seepage*
- *EBS Radionuclide Transport Abstraction*

- *Drift-Scale Radionuclide Transport*
- *Screening Analysis of Criticality Features, Events, and Processes for License Application*
- *Waste Form Features, Events and Processes*
- *Mineralogic Model (MM3.0) Report*
- *Dike/Drift Interactions*
- *Thermal Conductivity of Non-Repository Lithostratigraphic Layers*

INTENTIONALLY LEFT BLANK

2. QUALITY ASSURANCE

The Quality Assurance program applies to the development of this document (BSC 2004 [DIRS 170950], Section 8.1). This document was prepared in accordance with *Technical Work Plan for: Near-Field Environment and Transport In-Drift Heat and Mass Transfer Model and Analysis Reports Integration* (BSC 2004 [DIRS 170950]), which directs the work identified in work package ARTM02. The only variance from the TWP is discussed in Section 1. The methods used to control the electronic management of data are identified in the TWP (BSC 2004 [DIRS 170950], Section 8.4) and were implemented without variance. As directed in the TWP, this document was prepared in accordance with AP-SIII.10Q, *Models*; LP-SI.11Q-BSC, *Software Management*; and AP-3.15Q, *Managing Technical Product Inputs*, and reviewed in accordance with AP-2.14Q, *Document Review*.

The work scope of this report involves conducting investigations or analyses of Engineered Barrier System components including the determination of in-drift condensation conditions that are required by TSPA-LA. It provides in-drift condensation parameters that are important to the performance of the engineered barriers classified in *Q-List* (BSC 2004 [DIRS 168361]) as "Safety Category" because they are important to waste isolation as defined in AP-2.22Q, *Classification Analyses and Maintenance of the Q-List*. Safety Categories for the components are provided in Table 2-1.

Table 2-1. Engineered Barrier System Components Addressed in This Report, Listed with Corresponding Safety Category (SC) Level

Engineered Barrier System Component	Safety Category
Drip Shield	SC
Invert	SC
Emplacement Drift	Non SC
DOE and Commercial Waste Packages	SC
DOE Spent Nuclear Fuel Disposable Canister	SC
Naval Spent Nuclear Fuel Waste Package	SC

Source: BSC 2004 [DIRS 168361].

DOE = U.S. Department of Energy.

Furthermore, this report provides analysis of model results supporting performance assessment activities for the Total Systems Performance Assessment for License Application. The results of this report are important to the demonstration of compliance with the postclosure performance objectives prescribed in 10 CFR 63.113.

INTENTIONALLY LEFT BLANK

3. USE OF SOFTWARE

Table 3-1 lists the software used in this report.

Table 3-1. Software Used

Software Name	Software Tracking Number	Qualification Status	Description of Use	Operating Environment
FLUENT 6.0.12	10550-6.0.12-01 [DIRS 164315]	Qualified	Computational Fluid Dynamics (CFD) Calculations Convection Model	PC – Linux v 7.3
GAMBIT 2.0.4	N/A	Exempt per Section 2.1.2 of LP-SI.11Q-BSC	Visual Display of Data and Mesh	PC – Windows 2000
Ensight 7.4	N/A	Exempt per Section 2.1.2 of LP-SI.11Q-BSC	Visualization of CFD Results	PC – Windows 2000
MS Excel Version 2000 SP3	N/A	Exempt per Section 2.1.6 of LP-SI.11Q-BSC	Graphical Representation and Arithmetic Manipulation	PC – Windows 2000
MATHCAD Professional 11.2a	N/A	Exempt per Section 2.1.6 of LP-SI.11Q-BSC	Graphical Representation and Arithmetic Manipulation	PC – Windows 2000

3.1 QUALIFIED SOFTWARE

The computational fluid dynamics (CFD) computer code, FLUENT (FLUENT V6.0.12, STN: 10550-6.0.12-01 [DIRS 164315]), is used for the in-drift convection computational fluid dynamics model analyses. FLUENT is a commercial code that solves conservation of mass, momentum, energy (including a radiative transfer equation), species, and turbulence models using various means to obtain closure for the turbulent momentum equations. Transient or steady state formulations are also available. For this analysis, steady-state turbulent natural convection heat transfer and thermal radiation are considered.

FLUENT was selected because it is a state-of-the-art computational fluid dynamics code that has been successfully used on the Yucca Mountain Project. FLUENT includes the physics and features that are necessary to model in-drift convection. The application of FLUENT to YMP-scale in-drift convection and heat transfer including turbulence and thermal radiation is validated in Chapter 7. FLUENT was also validated for natural convection, turbulence, and thermal radiation prior to its use in this report as documented in the FLUENT Software Definition Report (SNL 2002 [DIRS 171415]) and Software Implementation Report (YMP 2003 [DIRS 166345]) for the Redhat Linux 7.3 Operating System.

The validation range of FLUENT for turbulent natural convection is further established in Section 7.3, Figure 7.3.3-2, by comparison of FLUENT predictions with experimental data. In this figure, FLUENT predictions agree within the experimental uncertainty of the data up to a Rayleigh number of 5.3×10^9. This validation range of up to a Rayleigh number of 5.3×10^9

will be discussed separately for the convection model and for the equivalent thermal conductivity correlations.

From the equivalent thermal conductivity analysis for the Yucca Mountain geometry including a drip shield, a temperature difference of 50°C between the waste package and the drift wall corresponds to a Rayleigh number of 4.05×10^9 (see Table 6.4.7-2), which in the range of validation presented above. Therefore, the range of validation for turbulent natural convection is up to a 50°C temperature difference between the waste package and the drift wall. FLUENT results for two-dimensional convection simulations are presented in Appendix J. These results show that the temperature difference between an average waste package with the line-averaged power and the drift wall from the convection simulations is a maximum of 8°C at 300 years, which decreases with increasing time. In addition, results from Table 6.3-6 in *Multiscale Thermohydrologic Model* (BSC 2004 [DIRS 169565]) show that the peak temperature difference is less then 30°C. Therefore, the FLUENT results for the convection model presented in this report are within the validation range established for turbulent natural convection conditions in Chapter 7.

FLUENT was run on seven dual processor PC computers running Redhat LINUX v 7.3. The computers used are SNL property numbers S839357, R436060, R436790, R436753, R436048, R404817, and R404818.

3.2 OTHER SOFTWARE

GAMBIT version 2.0.4 was used in this report to prepare input including the calculational mesh for the FLUENT models. The input was checked using engineering judgment and visual examination of the graphical display. The output from GAMBIT was used directly as input to FLUENT. GAMBIT meets the definition of exempt software in Section 2.1 of LP-SI.11Q-BSC, *Software Management*. GAMBIT was run on a Dell Precision 330 with 2 GB of RAM (SNL R435648) at Sandia National Laboratories in Albuquerque, NM. The Windows 2000 operating system was used.

Ensight 7.4 was used in this report to generate figures in Section 6. Ensight is a post-processing code that is used to visualize output from CFD codes like FLUENT. It was used only for the visual display of output and therefore meets the definition of exempt software in Section 2.1 of LP-SI.11Q-BSC. Ensight was run on a Dell Precision 330 with 2 GB of RAM (SNL R435648) at Sandia National Laboratories in Albuquerque, NM. The Windows 2000 operating system was used.

Mathcad (for Windows 2000, Version Mathcad 11.2a Professional) and Microsoft EXCEL 2000 (SP 3) are problem solving environments used in calculations and analyses. They are also used to tabulate and chart results. The user-defined expressions, inputs, and results are documented in sufficient detail to allow an independent repetition of computations. Thus, Mathcad and Excel are used as worksheets and not as software routines. Mathcad and Excel were run on a Dell Optiplex GX400 with 512MB of RAM (SNL R435705) at Sandia National Laboratories in Albuquerque, NM.

4. INPUTS

The direct inputs used in this report are listed in Section 4.1 below. The inputs for the validation problems are included in Chapter 7.

4.1 DIRECT INPUT

The direct inputs are broken up into several sections for the convection model (separate sections are provided for the two-dimensional and three-dimensional simulations), the condensation model, and the k_{eq} analysis as follows:

- 4.1.1 – Two-dimensional in-drift convection simulations
- 4.1.2 – Three-dimensional in-drift convection simulations
- 4.1.3 – Condensation model
- 4.1.4 – k_{eq} analysis and correlations.

The textbooks, book chapters, and technical papers used as references in this section have been qualified as discussed in Section 4.1.5 and Appendix L.

4.1.1 Two-Dimensional In-Drift Convection Simulations

Two-dimensional convection simulations are used to investigate the sensitivity of the results to uncertainty in material physical properties and physical submodels. The simulations require the following air properties: specific heat, thermal conductivity and dynamic viscosity. Table 4.1.1-1 contains the air property values used. The density is calculated by the incompressible-ideal-gas law in FLUENT as described in Section 6.1.5.2. Thermal properties, consisting of the emissivity and thermal conductivity of the invert, waste package, drip shield, and host rock are given in Table 4.1.1-2. Table 4.1.1-3 lists the geometry information for the simulations. Some of the geometry information in Table 4.1.1-3 was updated after the simulations were completed; the changes to this information are discussed in Appendix K. These small changes have a negligible impact on the results of this report as evaluated in Appendix K, thereby justifying the information for its intended use.

Table 4.1.1-1. Thermophysical Properties of Dry Air Used for the Two-Dimensional In-Drift Convection Simulations

Temperature (°K)	Specific Heat, c_p (J/kg-K)	Thermal Conductivity k_a, (W/m-K)	Dynamic Viscosity, μ (kg/m-s)	Density
300	1007	0.0263	$1.846x10^{-5}$	Incompressible-ideal-gas
350	1009	0.0300	$2.082x10^{-5}$	Incompressible-ideal-gas
400	1014	0.0338	$2.301x10^{-5}$	Incompressible-ideal-gas

Source: Incropera and DeWitt 1990 [DIRS 156693], Table A.4.

Table 4.1.1-2. Thermal Properties of Materials Used for the Base Case of the Two-Dimensional In-Drift Convection Simulations

Parameter Name	Parameter Source	Parameter Value	Units
Invert Thermal Conductivity	DTN: GS000483351030.003 [DIRS 152932]	0.14-0.17[a]	W/m-K
Invert Emissivity	Incropera and DeWitt 1990 [DIRS 156693], Table A.11 (“Rock”)	0.9 (0.88-0.95)	-
Drip Shield Thermal Conductivity	ASME 1995 [DIRS 108417], Section II-D, Table TCD, p. 611	20.708[b]	W/m-K
Drip Shield Emissivity	Lide 1995 [DIRS 101876], p. 10-298	0.63	-
Waste Package Thermal Conductivity	BSC 2004 [DIRS 169990], Table 20	1.5	W/m-K
Waste Package Emissivity	DTN: MO0003RIB00071.000 [DIRS 148850]	0.87	-
Host Rock Thermal Conductivity (Tptpll)	DTN: SN0404T0503102.011 [DIRS 169129]; Product Output of BSC 2004 [DIRS 169854], Table 7-10	1.8895	W/m-K
Host Rock Emissivity	Incropera and DeWitt 1990 [DIRS 156693], Table A.11 (“Rock”)	0.9 (0.88-0.95)	-
Gravitational Constant	Incropera and DeWitt 1990 [DIRS 156693], Inside Back Cover	9.81	m/s^2

[a] Range of thermal conductivity of invert material (4-10 crushed tuff) of the 11 samples listed in DTN: GS000483351030.003 [DIRS 152932].

[b] Thermal Conductivity at 212°F (100 °C). The value was found by linear interpolation between values at 200°F (12.00 BTU/hr-ft-° F) and 250°F (11.85 BTU-hr-ft-°F), as given in ASME 1995 [DIRS 108417], Section II-D, Table TCD, p. 611. Conversion is 1 BTU/hr-ft-°F = 1.7307 W/m-°C (Bird et al. 1960 [DIRS 103524], pg. 753).

Table 4.1.1-3. Approximate In-Drift Geometries with Drip Shield

Case	Inner Cylinder Diameter *Di* (m)	Outer Cylinder Diameter D_o (m)	Invert Height (mm)	Outside Width of Drip Shield (mm)	Height of Drip Shield (mm)
24-BWR waste package diameter (smallest)	1.318	5.5	806	2512	2521
DHLW waste package diameter (largest)	2.110	5.5	806	2512	2521

NOTES: Inner cylinder diameters are given in BSC 2003 [DIRS 164053].

Outer cylinder diameters are given in BSC 2003 [DIRS 164069].

Invert height is given in BSC 2004 [DIRS 164101].

Outside width of drip shield is given in BSC 2003 [DIRS 171024].

The height of the drip shield is given in BSC 2003 [DIRS 171024] as the distance from the invert to the top of the drip shield.

The sensitivity study presented in Section 6.1 includes sensitivity to absorption/emission of thermal radiation by a fluid medium (Case R11 and Worst Case). The input for these simulations is given in Table 4.1.1-4.

Table 4.1.1-4. Absorption/Emission Thermal Radiation Input

Simulation Input	Value	Units	Source
Peak CO_2 Pressure in Drifts	0.01	Bars	DTN MO0308SPACO2GL.001 [DIRS 168096]
Emissivity Pressure Correction for CO_2	Figure 13-14 in Siegel and Howell 1992 [DIRS 100687]	-	Siegel and Howell 1992 [DIRS 100687]
CO_2 Emittance	Figure 13-13 in Siegel and Howell 1992 [DIRS 100687]	-	
Emissivity Pressure Correction for H_2o	Figure 13-16 in Siegel and Howell 1992 [DIRS 100687]	-	
H_2O Emittance	Figure 13-15 in Siegel and Howell 1992 [DIRS 100687]	-	
Correction for Total Emittance	Figure 13-17 in Siegel and Howell 1992 [DIRS 100687]	-	

4.1.2 Three-Dimensional In-Drift Convection Simulations

The thermal properties of the host rock are required to estimate the thermal response in the Engineered Barrier System (EBS). These data sources contain analyses that provide thermal properties of the four different host rock units. These values are direct input to the simulations that include the host rock in their domain.

Thermal properties of the introduced materials are needed to simulate the in-drift thermal response. These values are direct inputs to the simulations that include the emplacement drift in their domain.

Material properties of the engineered barrier system components are given in Table 4.1.2-1 below. For the waste package, the homogeneous thermal properties of the waste package internal cylinder are used (BSC 2004, Table 20 [DIRS 169990]). The emissivity of the waste package is based on values for the outer shell material, which is Alloy 22 (DTN: MO0003RIB00071.000 [DIRS 148850]).

Table 4.1.2-1. Material Properties of Engineered Barrier System Components

Property	Value	Source
Waste Package Properties		
Density [kg/m^3]	3495	BSC 2004 [DIRS 169990], Table 20
Specific heat [J/kg-K]	378	BSC 2004 [DIRS 169990], Table 20
Thermal conductivity [W/m-K]	1.5	BSC 2004 [DIRS 169990], Table 20
Emissivity (Alloy 22)	0.87	DTN: MO0003RIB00071.000 [DIRS 148850]
Drip Shield Properties (Titanium grade 7)		
Density [kg/m^3]	4512[a]	ASME 1995 [DIRS 108417], Section II-D, Table NF-2, p. 620
Specific heat [J/kg-K]	540.82 at 100 ºC [b]	ASME 1995 [DIRS 108417], Section II-D, Table TCD, p. 611
Thermal conductivity [W/m-K]	20.708 at 100 ºC [c]	ASME 1995 [DIRS 108417], Section II-D, Table TCD, p. 611
Emissivity	0.63	Lide 1995 [DIRS 101876], p. 10-298
Invert Properties (Crushed tuff)		
Density [g/cm^3]	1.2-1.3 [d]	DTN: GS020183351030.001 [DIRS 163107]
Specific heat [J/cm^3-K]	0.82-1.06 [e]	DTN: GS000483351030.003 [DIRS 152932]
Thermal conductivity [W/m-K]	0.14-0.17[f]	DTN: GS000483351030.003 [DIRS 152932]
Emissivity	0.9 (0.88 - 0.95)	Incropera and DeWitt 1990 [DIRS 156693], Table A.11 values for “Rocks”

[a] The density of titanium grade 7 was found by taking the value of 0.163 lb/in^3 from ASME 1995 [DIRS 108417], Section II-D, Table NF-2, p. 620 and converting it to kg/m^3. Conversion factors are 1 lb=0.45359 kg and 1 inch = 0.0254 m (Bird et al. 1960 [DIRS 103524], pg. 748).

[b] The specific heat of titanium grade 7 at 212F (100 ºC) was found by linear interpolation between thermal diffusivity values of 0.331 ft^2/hr at 200°F and 0.322 ft^2/hr at 250°F from ASME 1995 [DIRS 108417], Section II-D, Table TCD, p. 611, the conversion factors 1 ft^2/hr = 2.5807 x 10^{-5} m^2/s (Bird et al 1960 [DIRS 103524], pg. 754), using the relationship specific heat = thermal conductivity / (density times thermal diffusivity) (Bird et al. 1960 [DIRS 103524], eq. 8.1-7), and the factor W = J/s.

[c] The thermal conductivity at 212°F (100 °C). The value was found by linear interpolation between values at 200°F (12.00 BTU/hr-ft-° F) and 250°F (11.85 BTU-hr-ft-°F) in ASME 1995 [DIRS 108417], Section II-D, Table TCD, p. 611. Conversion is 1 BTU/hr-ft-°F = 1.7307 W/m-°C (Bird et al. 1960 [DIRS 103524], pg. 753).

[d] Range of density of invert material (4-10 crushed tuff) of the 50 samples listed in DTN: GS020183351030.001 [DIRS 163107].

[e] Range of specific heat of invert material (4-10 crushed tuff) of the 11 samples listed in DTN: GS000483351030.003 [DIRS 152932].

[f] Range of thermal conductivity of invert material (4-10 crushed tuff) of the 11 samples listed in DTN: GS000483351030.003 [DIRS 152932].

Properties of the host rock are given in Table 4.1.2-2 below.

Table 4.1.2-2. Bulk Thermal Properties of Stratigraphic Unit Tsw35 (Tptpll)

Property	Value	Source
Wet bulk thermal conductivity [W/m °K] (Tptpll)	1.8895 [a]	DTN: SN0404T0503102.011 [DIRS 169129] is product output of BSC 2004 [DIRS 169854], Table 7-10
Drift wall emissivity	0.9 (0.88 - 0.95)	Incropera and DeWitt 1990 [DIRS 156693], Table A.11 values for "Rocks"

[a] Mean value for wet bulk thermal conductivity.

The fluid properties used in the three-dimensional natural convection simulations are listed in Table 4.1.2-3. FLUENT interpolates linearly between the data points. The fluid properties of the emplacement drift air are used to simulate the in-drift thermal response.

Table 4.1.2-3. Fluid Properties for Three-Dimensional In-Drift Convection Simulations

Data Name	Parameter Value	Units	Distribution
Air Heat Capacity at 280 K and 1 bar	1.006	kJ/kg-K	None
Air Heat Capacity at 300 K and 1 bar	1.007	kJ/kg-K	None
Air Heat Capacity at 350 K and 1 bar	1.009	kJ/kg-K	None
Air Heat Capacity at 400 K and 1 bar	1.014	kJ/kg-K	None
Air Heat Capacity at 450 K and 1 bar	1.021	kJ/kg-K	None
Air Dynamic Viscosity at 280 K and 1 bar	0.175×10^{-4}	Pa-s	None
Air Dynamic Viscosity at 300 K and 1 bar	0.185×10^{-4}	Pa-s	None
Air Dynamic Viscosity at 350 K and 1 bar	0.208×10^{-4}	Pa-s	None
Air Dynamic Viscosity at 400K and 1 bar	0.230×10^{-4}	Pa-s	None
Air Dynamic Viscosity at 450 K and 1 bar	0.251×10^{-4}	Pa-s	None
Air Thermal Conductivity at 280 K and 1 bar	0.0247	W/m-K	None
Air Thermal Conductivity at 300 K and 1 bar	0.0263	W/m-K	None
Air Thermal Conductivity at 350 K and 1 bar	0.0301	W/m-K	None
Air Thermal Conductivity at 400 K and 1 bar	0.0336	W/m-K	None
Air Thermal Conductivity at 450 K and 1 bar	0.0371	W/m-K	None

Source: Perry et al. 1984 [DIRS 125806], pp. 3-162 and 3-163.

The power inputs into the individual waste packages are found in *D&E / PA/C IED Typical Waste Package Components Assembly* (BSC 2004 [DIRS 167754], Table 12), as listed in Table 4.1.2-4. The three-dimensional natural convection simulations are conducted at 300, 1,000, 3,000, and 10,000 years. The powers listed for the two half packages are the heat generated by only half of a full package and not for a whole package. The order of the six full and two half-packages that are in a "seven-package segment" is listed in *D&E / PA/C IED Typical Waste Package Components Assembly* (BSC 2004 [DIRS 167754], Table 12). The segment consists of a half 21-PWR package, a 5-HLW long package, a 21-PWR, two 44-BWR packages, a 5-HLW short package, a 21-PWR package, and a half 44-BWR package. In order to investigate the dispersion coefficient, it is desirable to have a longer segment so that the edge effects can be minimized. Consequently, the simulations were extended by reflecting the segment at the half 44-BWR package. This resulted in simulations that had a half 21-PWR package at each end.

Table 4.1.2-4. Waste Package Sequence and Waste Package Powers at Four Different Times Used in the Three-Dimensional In-Drift Convection Simulations

Waste Package Type	Time [Years]			
	300	1,000	3,000	10,000
1/2 21-PWR AP [kW/Half-Package]	6.90E-01	2.92E-01	1.21E-01	7.20E-02
5-HLW Long [kW/Package]	4.64E-03	2.50E-03	1.79E-03	1.42E-03
21-PWR AP (Hot) [kW/Package]	1.41E+00	5.99E-01	2.47E-01	1.47E-01
44-BWR AP [kW/Package]	8.00E-01	3.56E-01	1.61E-01	9.42E-02
44-BWR AP (Adjusted) [kW/Package]	8.58E-01	3.72E-01	1.60E-01	9.51E-02
5-HLW Short [kW/Package]	3.18E-02	5.70E-03	3.11E-03	2.21E-03
21-PWR AP [kW/Package]	1.38E+00	5.85E-01	2.42E-01	1.44E-01
1/2 44-BWR AP [kW/Half-Package]	4.00E-01	1.78E-01	8.03E-02	4.71E-02

Source: BSC 2004 [DIRS 167754], Table 12.

Table 4.1.2-5 contains repository design information needed for development of the three-dimensional CFD simulations. These include properties of a representative waste package segment, waste stream characteristics (heat load), and drip shield and invert geometry. The information is contained in design drawings and these inputs are considered single values with no uncertainty. Some of the geometry information in Table 4.1.2-5 was updated after the simulations were completed; changes to this information are discussed in Appendix K. These small changes have a negligible impact on the results of this report as evaluated in Appendix K, thereby justifying the information for its intended use.

Table 4.1.2-5. Design Inputs Required by Three-Dimensional In-Drift Simulations

Input Description	Source	Value	Input Uncertainty
21-PWR Heat Output per Waste Package	BSC 2004 [DIRS 167754], Table 12	See Table 4.1.2-4	None
44-BWR Heat Output per Waste Package	BSC 2004 [DIRS 167754], Table 12	See Table 4.1.2-4	None
5-HLW Short Heat Output per Waste Package	BSC 2004 [DIRS 167754], Table 12	See Table 4.1.2-4	None
5-HLW Long Heat Output per Waste Package	BSC 2004 [DIRS 167754], Table 12	See Table 4.1.2-4	None
Waste Package Segment Layout	BSC 2004 [DIRS 167754], Table 12	See Table 4.1.2-4	None
Waste Package Spacing	BSC 2003 [DIRS 164069]	0.1 m	None
Length of 21-PWR Waste Package	BSC 2003 [DIRS 165406]	5165 mm	None
21-PWR Waste Package Diameter	BSC 2003 [DIRS 165406]	1644 mm	None
Length of 44-BWR Waste Package	BSC 2003 [DIRS 165406]	5165 mm	None
Length of 5-HLW Short Waste Package	BSC 2003 [DIRS 165406]	3590 mm	None
Length of 5-HLW Long Waste Package	BSC 2003 [DIRS 165406]	5217 mm	None
Drift Diameter	BSC 2004 [DIRS 168489]	5.5 m	None
Invert Height from Bottom of Drift	BSC 2003 [DIRS 164101]	0.806 m	None
Distance from Top of Invert to Center of 21-PWR Package	BSC 2003 [DIRS 164069]	1018 mm	None
Peak Height of Drip Shield	BSC 2003 [DIRS 171024]	2.521 m	None
Drip Shield Thickness	BSC 2004 [DIRS 169220]	0.015 m	None

Table 4.1.2-5. Design Inputs Required by Three-Dimensional In-Drift Simulations (Continued)

Input Description	Source	Value	Input Uncertainty
Width of Drip Shield at Base	BSC 2003 [DIRS 171024]	2.512 m	None
Height of Vertical Section of Drip Shield	BSC 2003 [DIRS 171024]	1.875 m	None
Max Elevation of Repository	BSC 2004 [DIRS 164519]	1107 m	None
Min Elevation of Repository	BSC 2004 [DIRS 164519]	1039 m	None

The operating pressure for the three-dimensional in-drift convection simulations is found by calculating the standard atmospheric pressure at the elevation of the repository. Table 4.1.2-6 contains standard atmosphere pressure at two elevations that bound the elevation of the repository. The elevation range of the repository is listed in Table 4.1.2-5.

Table 4.1.2-6. Standard Atmosphere

Elevation (m)	Pressure[a] (Pa)
1,000	89,889
1,500	84,565

[a] Source: White 1986 [DIRS 111015], Table A.6.

4.1.3 Condensation Model

Table 4.1.3-1 presents hydrologic and thermal properties that were used in the calculations. The thermal properties are used in Section 6.3.5.1.1 to calculate the repository temperature field. The hydrologic properties are used in Section 6.3.5.1.4 to compute the limits of evaporation at the drift wall surface.

Table 4.1.3-1. Rock Properties

Model Input	Value	Units	Source
TSW35 (Tptpll) bulk wet thermal conductivity	1.8895	W/m-K	DTN: SN0404T0503102.011 [DIRS 169129], ReadMe.doc
TSW35 (Tptpll) dry bulk density	1979.3	kg/m^3	DTN: SN0404T0503102.011 [DIRS 169129], ReadMe.doc
TSW35 (Tptpll) grain heat capacity	0.93	J/g-K	DTN: SN0307T0510902.003 [DIRS 164196], rock_grain_heat_capacity.xls, Row 10, Col Y
Matrix porosity (Tptpll)	0.1486	-	DTN: SN0404T0503102.011 [DIRS 169129], ReadMe.doc
Lithophysae porosity (Tptpll)	0.0883	-	DTN: SN0404T0503102.011 [DIRS 169129], ReadMe.doc
Intragranular permeability (tsw35 matrix continuum for mean infiltration case)	4.48E-18	m^2	DTN: LB0208UZDSCPMI.002 [DIRS 161243] (tswM5)
Intragranular van Genuchten α (tsw35 matrix continuum for mean infiltration case)	1.08E-05	Pa^{-1}	DTN: LB0208UZDSCPMI.002 [DIRS 161243] (tswM5)
Intragranular van Genuchten m (tsw35 matrix continuum for mean infiltration case)	0.216	-	DTN: LB0208UZDSCPMI.002 [DIRS 161243] (tswM5)
Intragranular residual saturation (tsw35 matrix continuum for mean infiltration case)	0.12	-	DTN: LB0208UZDSCPMI.002 [DIRS 161243] (tswM5)

Table 4.1.3-2 presents the Stefan-Boltzmann constant and the emissivities of the surfaces within the emplacement drift. These values are used in Section 6.3.5.1.2 to calculate surface temperatures.

Table 4.1.3-2. Thermal Radiation Properties

Model Input	Value	Units	Source
Stefan-Boltzmann constant	5.67051E-08	$W/m^2\text{-}K^4$	Siegel and Howell 1992 [DIRS 100687], p 970
Emissivity of drift wall (rock)	0.9 (0.88-0.95)	-	Incropera and Dewitt 1996 [DIRS 108184], Table A.11, value for “Rocks”
Emissivity of upper invert surface (rock)	0.9 (0.88-0.95)	-	Incropera and Dewitt 1996 [DIRS 108184], Table A.11, value for “Rocks”
Emissivity of drip shield (Titanium Grade 7)	0.63	-	Lide 1995 [DIRS 101876], p. 10-298
Emissivity of waste packages (Alloy 22)	0.87	-	DTN: MO0003RIB00071.000 [DIRS 148850]

Table 4.1.3-3 contains the transport properties of air. Table 4.1.3-4 contains the transport properties of water vapor. These properties are used in Section 6.3.5.2.8 to compute the transport properties of the vapor/air mixture.

Table 4.1.3-3. Air Properties

Data Name	Temp. (K)	Data Source	Parameter Value	Units	Distribution
Air Heat Capacity at 280 K and 1 bar	280	Perry et al. 1984 [DIRS 125806], pp. 3-162 and 3-163	1.006	kJ/kg-ºC	None
Air Heat Capacity at 300 K and 1 bar	300	Perry et al. 1984 [DIRS 125806], pp. 3-162 and 3-163	1.007	kJ/kg-ºC	None
Air Heat Capacity at 350 K and 1 bar	350	Perry et al. 1984 [DIRS 125806], pp. 3-162 and 3-163	1.009	kJ/kg-ºC	None
Air Heat Capacity at 400 K and 1 bar	400	Perry et al. 1984 [DIRS 125806], pp. 3-162 and 3-163	1.014	kJ/kg-ºC	None
Air Heat Capacity at 450 K and 1 bar	450	Perry et al. 1984 [DIRS 125806], pp. 3-162 and 3-163	1.021	kJ/kg-ºC	None
Air Dynamic Viscosity at 280 K and 1 bar	280	Perry et al. 1984 [DIRS 125806], pp. 3-162 and 3-163	0.175	10^{-4} Pa-s	None
Air Dynamic Viscosity at 300 K and 1 bar	300	Perry et al. 1984 [DIRS 125806], pp. 3-162 and 3-163	0.185	10^{-4} Pa-s	None
Air Dynamic Viscosity at 350 K and 1 bar	350	Perry et al. 1984 [DIRS 125806], pp. 3-162 and 3-163	0.208	10^{-4} Pa-s	None
Air Dynamic Viscosity at 400K and 1 bar	400	Perry et al. 1984 [DIRS 125806], pp. 3-162 and 3-163	0.23	10^{-4} Pa-s	None
Air Dynamic Viscosity at 450 K and 1 bar	450	Perry et al. 1984 [DIRS 125806], pp. 3-162 and 3-163	0.251	10^{-4} Pa-s	None
Air Thermal Conductivity at 280 K and 1 bar	280	Perry et al. 1984 [DIRS 125806], pp. 3-162 and 3-163	0.0247	W/m-ºC	None
Air Thermal Conductivity at 300 K and 1 bar	300	Perry et al. 1984 [DIRS 125806], pp. 3-162 and 3-163	0.0263	W/m-ºC	None

Table 4.1.3-3. Air Properties (Continued)

Data Name	Temp. (K)	Data Source	Parameter Value	Units	Distribution
Air Thermal Conductivity at 350 K and 1 bar	350	Perry et al. 1984 [DIRS 125806], pp. 3-162 and 3-163	0.0301	W/m-ºC	None
Air Thermal Conductivity at 400 K and 1 bar	400	Perry et al. 1984 [DIRS 125806], pp. 3-162 and 3-163	0.0336	W/m-ºC	None
Air Thermal Conductivity at 450 K and 1 bar	450	Perry et al. 1984 [DIRS 125806], pp. 3-162 and 3-163	0.0371	W/m-ºC	None
Molecular Weight of Air	-	Reynolds 1979 [DIRS 158410], p. ix	28.96	kg/kmole	None

Table 4.1.3-4. Water Vapor Properties

Data Name	Temp. (K)	Data Source	Parameter Value	Units	Distribution
Steam Heat Capacity at 100°C and 1 bar	373.15	Haar et. al. 1984 [DIRS 105175], p. 229	2.042	kJ/kg-ºC	None
Steam Latent Heat at 100°C and 1 bar	373.15	Haar et. al. 1984 [DIRS 105175], p. 10	2256.64	kJ/kg	None
Steam Dynamic Viscosity at 100°C and 1 bar	373.15	Haar et. al. 1984 [DIRS 105175], p. 263	12.28	10^{-6} kg/s-m	None
Steam Dynamic Viscosity at 150°C and 1 bar	423.15	Haar et. al. 1984 [DIRS 105175], p. 263	14.19	10^{-6} kg/s-m	None
Steam Dynamic Viscosity at 200°C and 1 bar	473.15	Haar et. al. 1984 [DIRS 105175], p. 263	16.18	10^{-6} kg/s-m	None
Steam Dynamic Viscosity at 250°C and 1 bar	523.15	Haar et. al. 1984 [DIRS 105175], p. 263	18.22	10^{-6} kg/s-m	None
Steam Dynamic Viscosity at 300°C and 1 bar	573.15	Haar et. al. 1984 [DIRS 105175], p. 263	20.29	10^{-6} kg/s-m	None
Steam Thermal Conductivity at 100°C and 1 bar	373.15	Haar et. al. 1984 [DIRS 105175], p. 264	25.08	10^{-3} W/m-ºC	None
Steam Thermal Conductivity at 150°C and 1 bar	423.15	Haar et. al. 1984 [DIRS 105175], p. 264	28.85	10^{-3} W/m-ºC	None
Steam Thermal Conductivity at 200°C and 1 bar	473.15	Haar et. al. 1984 [DIRS 105175], p. 264	33.28	10^{-3} W/m-ºC	None
Steam Thermal Conductivity at 250 K and 1 bar	523.15	Haar et. al. 1984 [DIRS 105175], p. 264	38.17	10^{-3} W/m-ºC	None
Steam Thermal Conductivity at 300°C and 1 bar	573.15	Haar et. al. 1984 [DIRS 105175], p. 264	43.42	10^{-3} W/m-ºC	None
Molecular Weight of Water	-	Reynolds 1979 [DIRS 158410], p. ix	18.016	kg/kmole	None
Liquid Water Saturation Density of 40°C	313.15	Haar et. al. 1984 [DIRS 105175], p. 9	992.17	kg/m^3	None
Liquid Water Dynamic Viscosity at 50°C	323.15	Haar et. al. 1984 [DIRS 105175], p. 263	547.1	10^{-6} kg/s-m	None
Liquid Water Specific Heat at 40°C and 1 bar	313.15	Haar et. al. 1984 [DIRS 105175], p. 229	4182	J/kg-K	None

Table 4.1.3-5 contains the water vapor pressure as a function of temperature. Table 4.1.3-6 contains the water saturation pressure as a function of temperature. These two tables are used in Section 6.3.5.1.3 to quantitatively describe the surface boundaries as a function of the surface temperature.

Table 4.1.3-5. Water Vapor Pressures

Data Name	Temp. (K)	Data Source	Parameter Value	Units	Distribution
Steam Saturation Pressure at 20 C	293.15	Haar et. al. 1984 [DIRS 105175], p. 9	0.023388	10^5 Pa	None
Steam Saturation Pressure at 25 C	298.15	Haar et. al. 1984 [DIRS 105175], p. 9	0.031691	10^5 Pa	None
Steam Saturation Pressure at 30 C	303.15	Haar et. al. 1984 [DIRS 105175], p. 9	0.042455	10^5 Pa	None
Steam Saturation Pressure at 35 C	308.15	Haar et. al. 1984 [DIRS 105175], p. 9	0.056267	10^5 Pa	None
Steam Saturation Pressure at 40 C	313.15	Haar et. al. 1984 [DIRS 105175], p. 9	0.073814	10^5 Pa	None
Steam Saturation Pressure at 45 C	318.15	Haar et. al. 1984 [DIRS 105175], p. 9	0.095898	10^5 Pa	None
Steam Saturation Pressure at 50 C	323.15	Haar et. al. 1984 [DIRS 105175], p. 9	0.12344	10^5 Pa	None
Steam Saturation Pressure at 55 C	328.15	Haar et. al. 1984 [DIRS 105175], p. 10	0.15752	10^5 Pa	None
Steam Saturation Pressure at 60 C	333.15	Haar et. al. 1984 [DIRS 105175], p. 10	0.19932	10^5 Pa	None
Steam Saturation Pressure at 65 C	338.15	Haar et. al. 1984 [DIRS 105175], p. 10	0.25022	10^5 Pa	None
Steam Saturation Pressure at 70 C	343.15	Haar et. al. 1984 [DIRS 105175], p. 10	0.31176	10^5 Pa	None
Steam Saturation Pressure at 75 C	348.15	Haar et. al. 1984 [DIRS 105175], p. 10	0.38563	10^5 Pa	None
Steam Saturation Pressure at 80 C	353.15	Haar et. al. 1984 [DIRS 105175], p. 10	0.47373	10^5 Pa	None
Steam Saturation Pressure at 85 C	358.15	Haar et. al. 1984 [DIRS 105175], p. 10	0.57815	10^5 Pa	None
Steam Saturation Pressure at 90 C	363.15	Haar et. al. 1984 [DIRS 105175], p. 10	0.70117	10^5 Pa	None
Steam Saturation Pressure at 95 C	368.15	Haar et. al. 1984 [DIRS 105175], p. 10	0.84529	10^5 Pa	None
Steam Saturation Pressure at 100 C	373.15	Haar et. al. 1984 [DIRS 105175], p. 10	1.0132	10^5 Pa	None

Table 4.1.3-6. Water Vapor Density at Saturation

Data Name	Temp. (K)	Data Source	Parameter Value	Units	Distribution
Steam Saturation Density at 20 C	293.15	Haar et. al. 1984 [DIRS 105175], p. 9	0.017308	kg/m^3	None
Steam Saturation Density at 25 C	298.15	Haar et. al. 1984 [DIRS 105175], p. 9	0.023065	kg/m^3	None
Steam Saturation Density at 30 C	303.15	Haar et. al. 1984 [DIRS 105175], p. 9	0.030399	kg/m^3	None
Steam Saturation Density at 35 C	308.15	Haar et. al. 1984 [DIRS 105175], p. 9	0.03965	kg/m^3	None
Steam Saturation Density at 40 C	313.15	Haar et. al. 1984 [DIRS 105175], p. 9	0.05121	kg/m^3	None
Steam Saturation Density at 45 C	318.15	Haar et. al. 1984 [DIRS 105175], p. 9	0.06552	kg/m^3	None
Steam Saturation Density at 50 C	323.15	Haar et. al. 1984 [DIRS 105175], p. 9	0.08308	kg/m^3	None
Steam Saturation Density at 55 C	328.15	Haar et. al. 1984 [DIRS 105175], p. 10	0.10446	kg/m^3	None
Steam Saturation Density at 60 C	333.15	Haar et. al. 1984 [DIRS 105175], p. 10	0.1303	kg/m^3	None
Steam Saturation Density at 65 C	338.15	Haar et. al. 1984 [DIRS 105175], p. 10	0.1613	kg/m^3	None
Steam Saturation Density at 70 C	343.15	Haar et. al. 1984 [DIRS 105175], p. 10	0.19823	kg/m^3	None
Steam Saturation Density at 75 C	348.15	Haar et. al. 1984 [DIRS 105175], p. 10	0.24194	kg/m^3	None
Steam Saturation Density at 80 C	353.15	Haar et. al. 1984 [DIRS 105175], p. 10	0.29336	kg/m^3	None
Steam Saturation Density at 85 C	358.15	Haar et. al. 1984 [DIRS 105175], p. 10	0.35349	kg/m^3	None
Steam Saturation Density at 90 C	363.15	Haar et. al. 1984 [DIRS 105175], p. 10	0.42343	kg/m^3	None
Steam Saturation Density at 95 C	368.15	Haar et. al. 1984 [DIRS 105175], p. 10	0.5043	kg/m^3	None
Steam Saturation Density at 100 C	373.15	Haar et. al. 1984 [DIRS 105175], p. 10	0.5975	kg/m^3	None

Table 4.1.3-7 presents the repository layout and sources for percolation data. The geometric data, line-averaged powers, and ventilation efficiencies are used in Section 6.3.5.1.1 to calculate the repository temperature field. The discrete waste package powers are used in Section 6.3.5.1.2 to compute waste package temperatures. The percolation rates and time intervals are used in Section 6.3.5.1.1 to compute average percolation rates for each chosen drift. Note that the YMP uses several different data sets to represent the lower, mean and upper percolation rates at the repository horizon that were developed for different purposes. *Multiscale Thermohydrologic Model* (BSC 2004 [DIRS 169565], Appendix XII) provides a comparison of these different data sets and concludes that, for the purpose of thermohydrologic analysis, the data sets are in reasonable agreement, and therefore can be used to assess in-drift condensation. Some of the geometry information in Table 4.1.3-7 was updated after the analyses were completed. The changes to this information are discussed in Appendix K. These small changes will have a negligible impact on the results of this report, thereby justifying the information for its intended use.

Table 4.1.3-7. Repository Layout and Sources for Percolation Data

Model Input	Value	Units	Source
Waste package endpoint coordinates	-	-	BSC 2003 [DIRS 161727]
Minimum exhaust standoff	15	m	BSC 2004 [DIRS 171424]
Turnout radius	61	m	BSC 2004 [DIRS 171423]
Line-averaged powers	-	-	BSC 2004 [DIRS 167754]
Waste package sequence	-	-	BSC 2004 [DIRS 167754]
Discrete waste package powers	-	-	BSC 2004 [DIRS 167754]
Ventilation efficiencies	-	-	DTN: MO0307MWDAC8MV.000 [DIRS 165395]
Lower Percolation Rate	-	-	DTN: LL030608723122.028 [DIRS 164510] (Nevada_SMT_percolation_BIN_la.txt)
Mean Percolation Rate	-	-	DTN: LL030610323122.029 [DIRS 164513] (Nevada_SMT_percolation_BIN_ma.txt)
Upper Percolation Rate	-	-	DTN: LL030602723122.027 [DIRS 164514] (Nevada_SMT_percolation_BIN_ua.txt)
Time Intervals for Percolation Rates	-	-	BSC 2004 [DIRS 169861]

Waste package dimension are shown in Table 4.1.3-8. Drip shield dimensions are shown in Table 4.1.3-9. Additional dimensions are derived from these dimensions in Section 6.3.5.2.7. These dimensions are used in the calculation of heat and mass transfer coefficients (Section 6.3.5.1.3) and in the actual transport calculations (Section 6.3.5.1.2). Some of the geometry information in Tables 4.1.3-8 and 4.1.3-9 was updated after the analyses were completed. The changes to this information are discussed in Appendix K. These small changes will have a negligible impact on the results of this report as evaluated in Appendix K, thereby justifying the information for its intended use.

Properties specific to the repository site are implemented in the analysis through the file **Repository Description LA 2.mcd**. Fluid properties are implemented in the analysis through the file **Fluid Properties.mcd**. Refer to Appendix D, Section D.7 for a list of Mathcad files used in the analysis as well as instructions for their use.

Table 4.1.3-8. Waste Package Dimensions

Model Input	Value	Units		Source
Waste Package Spacing	0.1	m	-	BSC 2004 [DIRS 168489], Table 1
Location of 21-PWR AP WP centerline above invert	1018	mm	-	BSC 2003 [DIRS 164069]
	Length	**Diameter**	**Units**	
21-PWR AP WP	5165	1644	mm	BSC 2003 [DIRS 165406]
44-BWR WP	5165	1674	mm	BSC 2003 [DIRS 165406]
5 DHLW/DOE SNF-LONG WP	5217	2110	mm	BSC 2003 [DIRS 165406]
5 DHLW/DOE SNF-SHORT WP	3590	2110	mm	BSC 2003 [DIRS 165406]

Table 4.1.3-9. Drift/Drip Shield Dimensions

Model Input	Value	Units	Source
Drift diameter	5.5	m	BSC 2004 [DIRS 168489]
Invert height from bottom of drift	806	mm	BSC 2003 [DIRS 164101]
Drip shield width	2512	mm	BSC 2003 [DIRS 171024]
Drip shield wall height	1875	mm	BSC 2003 [DIRS 171024]
Drip shield top radius	1365	mm	BSC 2003 [DIRS 171024]
Drip shield height	2521	mm	BSC 2003 [DIRS 171024]

4.1.4 k_{eq} Analysis and Correlations

The k_{eq} analysis used to generate the effective thermal conductivity correlations requires air properties. Table 4.1.4-1 contains the air properties used in this simulations. Table 4.1.1-3 (in Section 4.1.1) contains the geometric properties used in the analysis.

Table 4.1.4-1. Thermophysical Properties of Dry Air Used for the k_{eq} Analysis

Temperature (°C)	Specific Heat, c_p (kJ/kg-K)	Thermal Conductivity k_a, (W/m-K)	Dynamic Viscosity, μ (kg/m-s)
60	1.008	0.028	$2.00x10^{-5}$
100	1.011	0.032	$2.18x10^{-5}$

Source: Bejan 1995 [DIRS 152307], p. 603.

Table 4.1.4-2 summarizes the Rayleigh Number property group for dry air at atmospheric pressure used in the k_{eq} analysis and correlations.

Table 4.1.4-2. Rayleigh Number Property Group of Dry Air Used for the k_{eq} Analysis

Temperature (°C)	Rayleigh Number Property Group $\frac{g\beta}{\alpha\nu}$, cm^{-3} K^{-1}
20	107
30	90.7
60	57.1
100	34.8
200	9.53
300	4.96

Source: Bejan 1995 [DIRS 152307], p. 603.

4.1.5 Other Direct Input

This section presents other sources of direct input in the form of data and equations used in this report. Table 4.1.5-1 presents a summary of the direct input and the source references. These sources are demonstrated to be reliable in Appendix L.

Table 4.1.5-1. Other Direct Input

Information Used	Reference Identification
Data and equations for the physical properties of air; Basic concepts of natural convection	Bejan 1995 [DIRS 152307]
Heat and mass transfer relationships for dispersion/diffusion, conversion factors	Bird et al. 1960 [DIRS 103524]
Heat conduction relationships in the form of analytical/mathematical results	Carslaw and Jaeger 1959 [DIRS 100968]
Thermophysical properties of liquid/vapor water	Haar et al. 1984 [DIRS 105175]
Gas-phase diffusion coefficient dependence on temperature and pressure	Ho 1997 [DIRS 141521]
Radiant heat transfer relations and radiation view factors	Siegel and Howell 1992 [DIRS 100687]
Radiation view factors for specific in-drift geometries	Howell 1982 [DIRS 164711]
Natural convection heat and mass transfer correlations	Raithby and Hollands 1975 [DIRS 156726] Raithby and Hollands 1985 [DIRS 164700]
Heat transfer relations and physical properties for air, emissivity of solid surfaces; Basic concepts of natural convection	Incropera and DeWitt 1990 [DIRS 156693] Incropera and DeWitt 1996 [DIRS 108184] Incropera and DeWitt 2002 [DIRS 163337]
Natural convection heat transfer correlations between concentric cylinders based on experimental measurements for air; Basic concepts of natural convection	Kuehn and Goldstein 1976 [DIRS 100675]
Gas Properties and equations	Reid, Prausnitz, and Sherwood 1977 [DIRS 130310]
Physical properties, molecular weights of air and water	Reynolds 1979 [DIRS 158410]
Atmospheric properties as a function of elevation	White 1986 [DIRS 111015]

4.2 CRITERIA

The Yucca Mountain *Project Requirements Document* (Canori and Leitner 2003) [DIRS 166275] identifies the high-level requirements for the Yucca Mountain Project. The requirements that pertain to this report, and their link to 10 CFR 63 [DIRS 156605], are shown in Table 4.2-1. As described in *Technical Work Plan for: Near-Field Environment and Transport In-Drift Heat and Mass Transfer Model and Analysis Reports Integration*, (BSC 2004 [DIRS 170950]), specific acceptance criteria identified by the U.S. Nuclear Regulatory Commission (NRC) are applicable to this report. These criteria are listed in Table 4.2.-1 and described below.

Table 4.2-1. Project Requirements for this Report

Requirement Number	Requirement Title	10 CFR 63 Link [DIRS 156605]	Yucca Mountain Review Plan Acceptance Criteria
PRD-002/T-015	Requirements for Performance Assessment from Canori and Leitner 2003 [DIRS 166275].	10 CFR 63.114	2.2.1.3.3.3 Criteria 1 to 5 for *Quantity and Chemistry of Water Contacting Engineered Barriers and Waste Forms Model Abstraction* (NRC 2003 [DIRS 163274]).

The acceptance criteria identified in Section 2.2.1.3.3.3 of the *Yucca Mountain Review Plan, Final Report* (NRC 2003 [DIRS 163274]) are given below. The disposition of these criteria items is listed in Section 8.5. These acceptance criteria are based on meeting the requirements of 10 CFR 63.114(a)–(c) and (e)–(g), relating to the quantity and chemistry of water contacting engineered barriers and waste forms model abstraction. The sub-criteria from Quantity and Chemistry of Water Contacting the Waste Packages and Waste Forms (NRC 2003 [DIRS 163274], Section 2.2.1.3.3.3), from 10 CFR 63.114(a)-(c) and (e)-(g), are listed in Sections 4.2.1 through 4.2.5:

4.2.1 Acceptance Criterion 1: *System Description and Model Integration Are Adequate*.

(1) Total system performance assessment adequately incorporates important design features, physical phenomena, and couplings, and uses consistent and appropriate assumptions throughout the quantity and chemistry of water contacting engineered barriers and waste forms abstraction process;

(2) The abstraction of the quantity and chemistry of water contacting engineered barriers and waste forms uses assumptions, technical bases, data, and models, that are appropriate and consistent with other related U.S. Department of Energy abstractions. For example, the assumptions used for the quantity and chemistry of water contacting engineered barriers and waste forms are consistent with the abstractions of "Degradation of Engineered Barriers" (Section 2.2.1.3.1); "Mechanical Disruption of Engineered Barriers (Section 2.2.1.3.2); "Radionuclide Release Rates and Solubility Limits" (Section 2.2.1.3.4); "Climate and Infiltration" (Section 2.2.1.3.5); and "Flow Paths in the Unsaturated Zone" (Section 2.2.1.3.6). The descriptions and technical bases provide transparent and traceable support for the abstraction of quantity and chemistry of water contacting engineered barriers and waste forms;

(3) Important design features, such as waste package design and material selection, backfill, drip shield, ground support, thermal loading strategy, and degradation processes, are adequate to determine the initial and boundary conditions for calculations of the quantity and chemistry of water contacting engineered barriers and waste forms;

(4) Spatial and temporal abstractions appropriately address physical couplings (thermal-hydrologic-mechanical-chemical). For example, the U.S. Department of Energy evaluates the potential for focusing of water flow into drifts, caused by coupled thermal-hydrologic-mechanical-chemical processes;

(5) Sufficient technical bases and justification are provided for total system performance assessment assumptions and approximations for modeling coupled thermal-hydrologic-mechanical-chemical effects on seepage and flow, the waste package chemical environment, and the chemical environment for radionuclide release. The effects of distribution of flow on the amount of water contacting the engineered barriers and waste forms are consistently addressed, in all relevant abstractions;

(6) The expected ranges of environmental conditions within the waste package emplacement drifts, inside of breached waste packages, and contacting the waste forms and their evolution with time are identified. These ranges may be developed to include: (i) the effects of the drip shield and backfill on the quantity and chemistry of water (e.g., the potential for condensate formation and dripping from the underside of the shield); (ii) conditions that promote corrosion of engineered barriers and degradation of waste forms; (iii) irregular wet and dry cycles; (iv) gamma-radiolysis; and (v) size and distribution of penetrations of engineered barriers;

(7) The model abstraction for quantity and chemistry of water contacting engineered barriers and waste forms is consistent with the detailed information on engineered barrier design and other engineered features. For example, consistency is demonstrated for: (i) dimensionality of the abstractions; (ii) various design features and site characteristics; and (iii) alternative conceptual approaches. Analyses are adequate to demonstrate that no deleterious effects are caused by design or site features that the U.S. Department of Energy does not take into account in this abstraction;

(8) Adequate technical bases are provided, including activities such as independent modeling, laboratory or field data, or sensitivity studies, for inclusion of any thermal-hydrologic-mechanical-chemical couplings and features, events, and processes;

(9) Performance-affecting processes that have been observed in thermal-hydrologic tests and experiments are included into the performance assessment. For example, the U.S. Department of Energy either demonstrates that liquid water will not reflux into the underground facility or incorporates refluxing water into the performance assessment calculation, and bounds the potential adverse effects of alteration of the hydraulic pathway that result from refluxing water;

(12) Guidance in NUREG–1297 and NUREG–1298 (Altman, et al., 1988 [DIRS 103597 and 103750]), or other acceptable approaches, is followed.

4.2.2 Acceptance Criterion 2: *Data Are Sufficient for Model Justification.*

(1) Geological, hydrological, and geochemical values used in the license application are adequately justified. Adequate description of how the data were used, interpreted, and appropriately synthesized into the parameters is provided;

(2) Sufficient data were collected on the characteristics of the natural system and engineered materials to establish initial and boundary conditions for conceptual models of thermal-hydrologic-mechanical-chemical coupled processes, that affect seepage and flow and the engineered barrier chemical environment;

(3) Thermo-hydrologic tests were designed and conducted with the explicit objectives of observing thermal-hydrologic processes for the temperature ranges expected for repository conditions and making measurements for mathematical models. Data are sufficient to verify that thermal-hydrologic conceptual models address important thermal-hydrologic phenomena;

(4) Sufficient information to formulate the conceptual approach(es) for analyzing water contact with the drip shield, engineered barriers, and waste forms is provided; and

4.2.3 Acceptance Criterion 3: *Data Uncertainty Is Characterized and Propagated Through the Model Abstraction.*

(1) Models use parameter values, assumed ranges, probability distributions, and bounding assumptions that are technically defensible, reasonably account for uncertainties and variabilities, and do not result in an under-representation of the risk estimate;

(2) Parameter values, assumed ranges, probability distributions, and bounding assumptions used in the total system performance assessment calculations of quantity and chemistry of water contacting engineered barriers and waste forms are technically defensible and reasonable, based on data from the Yucca Mountain region (e.g., results from large block and drift-scale heater and niche tests), and a combination of techniques that may include laboratory experiments, field measurements, natural analog research, and process-level modeling studies;

(3) Input values used in the total system performance assessment calculations of quantity and chemistry of water contacting engineered barriers (e.g., drip shield and waste package) are consistent with the initial and boundary conditions and the assumptions of the conceptual models and design concepts for the Yucca Mountain site. Correlations between input values are appropriately established in the U.S. Department of Energy total system performance assessment. Parameters used to define initial conditions, boundary conditions, and computational domain in sensitivity analyses involving coupled thermal-hydrologic-mechanical-chemical effects on seepage and flow, the waste package chemical environment, and the chemical environment for radionuclide

release, are consistent with available data. Reasonable or conservative ranges of parameters or functional relations are established;

(4) Adequate representation of uncertainties in the characteristics of the natural system and engineered materials is provided in parameter development for conceptual models, process-level models, and alternative conceptual models. The U.S. Department of Energy may constrain these uncertainties using sensitivity analyses or conservative limits. For example, the U.S. Department of Energy demonstrates how parameters used to describe flow through the engineered barrier system bound the effects of backfill and excavation-induced changes;

4.2.4 Acceptance Criterion 4: *Model Uncertainty Is Characterized and Propagated Through the Model Abstraction*.

(2) Alternative modeling approaches are considered and the selected modeling approach is consistent with available data and current scientific understanding. A description that includes a discussion of alternative modeling approaches not considered in the final analysis and the limitations and uncertainties of the chosen model is provided;

(3) Consideration of conceptual model uncertainty is consistent with available site characterization data, laboratory experiments, field measurements, natural analog information and process-level modeling studies; and the treatment of conceptual model uncertainty does not result in an under-representation of the risk estimate;

4.2.5 Acceptance Criterion 5: *Model Abstraction Output Is Supported by Objective Comparisons*.

(1) The models implemented in this total system performance assessment abstraction provide results consistent with output from detailed process-level models and/or empirical observations (laboratory and field testings and/or natural analogs);

(2) Abstracted models for coupled thermal-hydrologic-mechanical-chemical effects on seepage and flow and the engineered barrier chemical environment, as well as on the chemical environment for radionuclide release, are based on the same assumptions and approximations demonstrated to be appropriate for process-level models or closely analogous natural or experimental systems. For example, abstractions of processes, such as thermally induced changes in hydrological properties, or estimated diversion of percolation away from the drifts, are adequately justified by comparison to results of process-level modeling, that are consistent with direct observations and field studies; and

(3) Accepted and well-documented procedures are used to construct and test the numerical models that simulate coupled thermal-hydrologic-mechanical-chemical effects on seepage and flow, engineered barrier chemical environment, and the chemical environment for radionuclide release. Analytical and numerical models are appropriately supported. Abstracted model results are compared with different mathematical models, to judge robustness of results.

4.3 CODES, STANDARDS, AND REGULATIONS

This report was prepared to comply with 10 CFR Part 63, the NRC rule on high-level radioactive waste. Subparts of this rule that are applicable to data include Subpart E, Section 114 (Requirements for Performance Assessment). The subpart applicable to models is also outlined in Subpart E Section 114. The subparts applicable to features, events, and processes (FEPs) are 10 CFR 63.114(d), (e), and (f). Section II of *1995 ASME Boiler and Pressure Vessel Code* (ASME 1995 [DIRS 108417]) was also used in this report.

INTENTIONALLY LEFT BLANK

5. ASSUMPTIONS

No assumptions were made in this report that did not have direct confirming data or evidence. Modeling and analysis assumptions are discussed in Section 6. For convenience, the assumptions discussed in Section 6 are listed below.

The modeling and analysis assumptions are broken up into several sections for the convection model (separate sections are provided for the two-dimensional and three-dimensional simulations), condensation model, and the k_{eq} analysis as follows:

- 5.1 – Two-dimensional in-drift convection simulations
- 5.2 – Three-dimensional in-drift convection simulations
- 5.3 – Condensation model
- 5.4 – k_{eq} analysis and correlations.

5.1 TWO-DIMENSIONAL IN-DRIFT CONVECTION SIMULATIONS

The assumptions listed below are used in the two-dimensional in-drift convection simulations presented in Section 6.1. Refer to Section 6.1.3.2.x (where x is the number of the assumption listed below) for further details.

1. Natural Convection in the Drifts Assumes Pure Air Conditions

2. Steady-State Conditions

3. Conduction-Only Heat Transfer in the Surrounding Host Rock and Invert

4. Use of Constant Thermophysical Properties of the Introduced Materials in the Drift

5. Neglect of Barometric Pumping

6. Mean Beam Length.

5.2 THREE-DIMENSIONAL IN-DRIFT CONVECTION SIMULATIONS

The assumptions listed below are used in the three-dimensional in-drift convection simulations presented in Section 6.2. Refer to Section 6.2.3.2.x (where x is the number of the assumption listed below) for further details.

1. Natural Convection In The Drifts Assumes Pure Air Conditions

2. Steady-State Conditions

3. Use of Renormalized Group (RNG) k-ε Turbulence Flow Model

4. Use of the Discrete Ordinates (DO) Thermal Radiation Model and a Nonparticipating Medium

5. Conduction-Only in the Surrounding Host Rock
6. Use of Constant Thermophysical Properties of the Introduced Materials in the Drift
7. Neglect of Barometric Pumping
8. Use of a Non-Buoyant Trace Gas to Evaluate Dispersion Coefficient.

5.3 CONDENSATION MODEL

The modeling assumptions listed below are used in the condensation model developed in Section 6.3. Refer to Section 6.3.3.2.x (where x is the number of the assumption listed below) for further details.

1. Vapor Pressure at Invert Surface Underneath the Drip Shield
2. Vapor Pressure on the Drift Wall, Drip Shield, and Waste Packages
3. Partitioning of Available Water
4. Neglect of Barometric Pumping
5. Neglect of Axial Energy Transport Terms
6. Neglect of the Axial Relocation of Energy in the Calculation of Rock Temperatures
7. Drip Shield Ventilation
8. Water Available for Evaporation in the Drift
9. Disposition of Condensate after Formation.

5.4 EQUIVALENT THERMAL CONDUCTIVITY (K_{EQ}) ANALYSIS

The analysis assumptions listed below are used in the equivalent thermal conductivity (k_{eq}) analysis developed in Section 6.4. Refer to Section 6.4.3.2.x (where x is the number of the assumption listed below) for further details.

1. Natural Convection In The Drifts Assumes Pure Air Conditions
2. Steady-State Conditions
3. Use of Renormalized Group (RNG) k-ε Turbulence Flow Model
4. Neglect of Barometric Pumping.

6. MODEL DISCUSSION

The Yucca Mountain repository configuration consists of waste packages stored inside underground tunnels, or drifts. The waste packages generate heat due to decay of fission products, and water flows into and out of the drifts in liquid and vapor form. Heat and mass transfer within the drifts, including interaction with the surrounding rock, are important processes for the performance of the repository. The present report documents the models for in-drift heat and mass transfer during the postclosure period. The models for in-drift heat transfer, or convection, and in-drift mass transfer, or condensation, are discussed in the present report.

The model discussion is broken up into several sections for the convection model (separate sections are provided for the two-dimensional and three-dimensional simulations), condensation model, and the k_{eq} analysis as follows:

- 6.1 – Two-dimensional in-drift convection simulations
- 6.2 – Three-dimensional in-drift convection simulations
- 6.3 – Condensation model
- 6.4 – k_{eq} analysis and correlations.

In-Drift Convection Model

Natural convection heat transfer in the post-closure repository emplacement drift environment is analyzed using a computational fluid dynamics code. A drift-scale analysis using CFD is necessary to determine the heat transfer and fluid flow patterns in the drift. Other process-level thermal-hydrologic (TH) models currently used by the project, as exemplified by *Multiscale Thermohydrologic Model* (BSC 2004 [DIRS 169565]), approximate the emplacement drift as a porous medium using an equivalent thermal conductivity to evaluate the in-drift heat transfer by natural convection.

In-drift heat transfer and natural convection are modeled in this report through the use of a computational fluid dynamics (CFD) code, FLUENT (Fluent 2001 [DIRS 164453]). In the present application, FLUENT solves the time-averaged Navier-Stokes equations including turbulence, and the energy equation including thermal radiation. The model resolves the boundary layer behavior in the drifts through fine discretization near the wall. The in-drift heat transfer model is thermally coupled to the surrounding rock. The variation of the rock temperature along the drift, or the temperature tilt, is included and is a significant factor in the model results. The development of the in-drift convection model did not rely on corroborating/supporting data, models, or product output.

The CFD simulations include the in-drift components such as the invert, drip shield, waste packages, and drift wall. The in-drift geometric representation of each component is accurately depicted. The model include some surrounding host rock. The limited surrounding host rock is treated as a conduction-only solid because it primarily serves as a temperature boundary condition in the CFD simulations (e.g., the purpose of the CFD simulations is to ascertain the physics occurring in the emplacement drifts, not in the host rock). The invert is also treated as an impermeable conduction-only solid.

Two- and three-dimensional convection simulations are conducted. The two-dimensional simulations discussed in Section 6.1 use a line-averaged waste package power and consider various submodels, such as radiation and turbulence, to evaluate the effect of different submodel options and introduced material property variations. With these results, the three-dimensional simulations with appropriate submodels are developed to produce detailed heat transfer and fluid flow velocities in the drift.

For computational reasons, only a portion of a drift is simulated in the three-dimensional calculations as detailed in Section 6.2. The domain is 71-m long encompassing 14 waste packages, or two 7-package sequences, representing a section of a full drift that is approximately 600 m long. The spatial and temporal variation of the power output for individual waste packages is included in the CFD simulations.

Axial mass transfer in the drift environment is included in the three-dimensional convection simulations by specification of a trace gas. Cross-sectionally averaged trace gas concentrations are used along with the mass flux of the tracer and the geometry to specify an effective one-dimensional axial dispersion coefficient along the drift. Axial dispersion coefficients are calculated separately for the regions inside and outside the drip shield, and are functions of temperature tilt. These dispersion coefficients are subsequently used in the in-drift condensation model.

The results from the in-drift convection model are not used directly in TSPA-LA.

In-Drift Condensation Model

The condensation model discussed in Section 6.3 is used to predict condensation and evaporation rates along the entire length of selected drifts at different times (e.g., 300, 1,000, 3,000, and 10,000 years). As such, the model uses a simpler representation of the drift geometry than the convection model discussed above. The condensation model uses single-node representations of each waste package along the drifts as well as separate nodes for the drip shield, invert, and drift wall. The drift wall temperature boundary conditions for the condensation model are derived from analytical line-source solutions.

Heat and mass transfer between the nodes (waste package to drip shield, drip shield to drift wall, etc.) is based on literature correlations for natural convection heat and mass transfer for the particular geometry. Thermal radiation is calculated based on surface-to-surface radiation and the appropriate view factors. Only heat transfer in the radial direction is considered. The effect of axial heat transfer in the drip shields and the waste packages is assumed to be small.

Sources of water are available at each waste package location at the drift wall and the invert. The local vapor pressure is the saturation pressure at the calculated temperature. The rate of water evaporation is based on the difference between the local vapor pressure on the evaporating surface and the local gas-phase vapor partial pressure, and the corresponding mass transfer correlation. The rate is limited by the availability of water to the surface by percolation in the host rock and capillary induction (pumping).

The water vapor is transported along the drift by one-dimensional axial dispersion using the dispersion coefficients calculated by the in-drift convection model as discussed above. These

dispersion values are a function of time and temperature tilt due to the thermal evolution of the repository.

Based on the local temperatures and vapor pressures, the availability of water, and the axial dispersion of water vapor, water vapor evaporates, is transported, and condenses based on the various component surface temperatures. Axial transport equations are solved to predict the water vapor distribution and condensation on the various surfaces along each of the 7 selected drifts at four selected times. From these results, the location and rate of condensation on the drift walls, under the drip shield, and on individual waste packages is evaluated.

Two different representations of the drip shield are considered. They are: 1) unventilated cases in which the regions under the drip shield and outside the drip shield are isolated, and 2) the ventilated cases with a single well-mixed region. Use of the terms "ventilated" and "unventilated" does not imply active ventilation or special-purpose features in the present design. The "ventilated" case is an assumption in *Multiscale Thermohydrologic Model* (BSC 2004 [DIRS 169565]) and is the basis for abstraction information used in TSPA-LA. The MSTHM assumes that the partial pressure of water vapor P_v in the drift is uniform outside of the drip shield and that the drip shield is permeable to gas flow such that the vapor pressure inside and outside of the drip shield are equal. The "unventilated" case is not addressed in the MSTHM (BSC 2004 [DIRS 169565]). The effect of these two drip shield representations on the condensation rate is evaluated in the present report.

Uncertainty analysis of the condensation rate has been performed for the following variables:

- Percolation Rate
- Dispersion Coefficient
- Water supply to the invert surface.

The in-drift condensation model was validated by independent peer review as given in Appendix G.

k_{eq} Analysis

An analysis is performed to evaluate the effective thermal conductivity for the Yucca Mountain in-drift configuration for use in porous media codes and models such as those developed in *Multiscale Thermohydrologic Model* (BSC 2004 [DIRS 169565]). In this approach, the open space in the drift is simulated as a thermally-conductive and non-convecting medium with an enhanced thermal conductivity to simulate the increased heat transfer due to natural convection. The k_{eq} correlations are developed specifically to support the MSTHM (BSC 2004 [DIRS 169565]), but they can be used in other applications as well.

The k_{eq} analysis developed in Section 6.4 is based on a two-dimensional representation of a drift including the drip shield and only considers conduction and natural convection. The analysis is based on the two-dimensional convection simulations developed in Section 6.1. Constant but different surface temperatures are used for the waste package, drip shield, and drift wall to develop the value of k_{eq} and the corresponding correlation.

6.1 TWO-DIMENSIONAL IN-DRIFT CONVECTION SIMULATIONS

6.1.1 Simulation Objectives

The purpose of the two-dimensional simulations is to determine the sensitivity of the waste package surface temperature to thermal properties of materials in the drift environment and to evaluate physics submodels for use in the three-dimensional simulations. A suite of one-off sensitivity studies is performed to demonstrate the potential uncertainty in the waste package surface temperature. The sensitivity studies are based on ranges of thermal properties of the waste package, drip shield, invert, and drift wall host rock. This investigation primarily considers material thermal conductivities and surface emissivities. In addition, submodels for turbulence and thermal radiation are investigated. The submodel sensitivity studies are used to select appropriate submodels for the three-dimensional in-drift convection simulations discussed in Section 6.2.

6.1.1.1 Problem Statement

Two-dimensional in-drift CFD simulations are developed to analyze a large number of cases stemming from uncertainties in thermal properties associated with introduced materials in the emplacement drifts. Heat transfer by conduction, turbulent natural convection, and thermal radiation are all included. The simulations use an average waste package diameter and heat output.

6.1.1.2 Performance Measures Used in Downstream Models or Analyses

The two-dimensional simulations are used to assess the uncertainty in waste package temperature associated with uncertainties in thermal properties and calculational submodels. Because the two-dimensional CFD simulations are more computationally efficient than the three-dimensional simulations, many more sensitivities can be examined. These sensitivity study results are used to select the calculational submodels for turbulence and thermal radiation used in the three-dimensional simulations presented in Section 6.2.

6.1.1.3 Inputs

Refer to Section 4.1.1 for inputs required by the two-dimensional drift CFD simulations.

6.1.1.4 Description of How Output Quantities Are Used

The results from the two-dimensional in-drift convection simulations are used to evaluate uncertainties in introduced material properties and to select appropriate submodels for the three-dimensional in-drift convection simulations.

6.1.1.5 Direct Use in TSPA System Model

The CFD simulation results are not directly used in the total system performance assessment (TSPA) model.

6.1.2 Features, Events, and Processes Included

This section summarizes the features, events, and processes included in the two-dimensional and the three-dimensional in-drift convection simulations.

The development of a comprehensive list of features, events, and processes (FEPs) potentially relevant to post-closure performance of the Yucca Mountain repository, is based on site-specific information, design, and regulations. The approach for developing an initial list of FEPs, in support of TSPA-SR (CRWMS M&O 2000 [DIRS 153246]), is documented in *The Development of Information Catalogued in REV00 of the YMP FEP Database* (Freeze et al. 2001 [DIRS 154365]). To support TSPA-LA, the FEP list was re-evaluated in accordance with *The Development of the Total System Performance Assessment License Application Features, Events, and Processes* (BSC 2004 [DIRS 168706], Section 3). The list of FEPs for LA is given in *LA FEP List* (MO0407SEPFEPLA.000 [DIRS 170760]).

Table 6.1.2-1 provides a list of included FEPs associated with this report, while Table 6.1.2-2 lists the excluded FEPs. The in-drift convection model results described in this report are not used directly in TSPA models.

Table 6.1.2-1. Included FEPs in TSPA-LA Addressed In This Document

FEP No.	FEP Name	Description	Section Where Disposition is Described
2.1.06.06.0A	Effects of drip shield on flow	The drip shield will affect the amount of water reaching the waste package. Effects of the drip shield on the disposal region environment (for example, changes in relative humidity and temperature below the shield) should be considered for both intact and degraded conditions.	See Sections 6.1, 6.2 and 6.4
2.1.08.04.0A	Condensation forms on roofs of drifts (drift-scale cold traps)	Emplacement of waste in drifts creates thermal gradients within the repository. Such thermal gradients can lead to drift-scale cold traps characterized by latent heat transfer from warmer to cooler locations. This mechanism can result in condensation forming on the roof or other parts of the drifts, leading to enhanced dripping on the drip shields, waste packages, or exposed waste material.	See Section 6.3
2.1.08.04.0B	Condensation forms at repository edges (repository-scale cold traps)	Emplacement of waste in drifts creates thermal gradients within the repository. Such thermal gradients can lead to repository-scale cold traps characterized by latent heat transfer from warmer to cooler locations. This mechanism can result in condensation forming at repository edges or elsewhere in the EBS, leading to enhanced dripping on the drip shields, waste packages, or exposed waste material.	See Section 6.3

Table 6.1.2-1. Included FEPs in TSPA-LA Addressed In This Document (Continued)

FEP No.	FEP Name	Description	Section Where Disposition is Described
2.1.11.01.0A	Heat generation in EBS	Temperature in the waste and EBS will vary through time. Heat from radioactive decay will be the primary cause of temperature change, but other factors to be considered in determining the temperature history include the in-situ geothermal gradient, thermal properties of the rock, EBS, and waste materials, hydrological effects, and the possibility of exothermic reactions. Considerations of the heat generated by radioactive decay should take different properties of different waste types, including DSNF, into account.	See Sections 6.2, 6.3 and 6.4
2.1.11.02.0A	Non-uniform heat distribution in EBS	Uneven heating and cooling at edges of the repository lead to non-uniform thermal effects during both the thermal peak and the cool-down period.	See Section 6.3
2.1.11.09.0A	Thermal effects on flow in the EBS	High temperatures in the EBS may influence seepage into and flow within the waste and EBS. Thermally-induced changes to fluid saturation and/or relative humidity could influence in-package chemistry. Thermal gradients in the repository could lead to localized accumulation of moisture. Wet zones form below the areas of moisture accumulation.	See Sections 6.1, 6.2, 6.3 and 6.4
2.1.11.09.0C	Thermally driven flow (convection) in drifts	Temperature differentials may result in convective flow in the EBS. Convective flow within drifts could influence in-drift chemistry.	See Sections 6.1, 6.2, 6.3, and 6.4.

Table 6.1.2-2. Excluded FEPs Addressed In This Document

FEP No.	FEP Name	Description	Section Where Disposition is Described
2.1.08.14.0A	Condensation on underside of drip shield	Condensation of water on the underside of drip shield affects waste package hydrologic and chemical environment.	See Section 6.3

6.1.3 Base-Case Conceptual Model for Two-Dimensional Simulations

6.1.3.1 Conceptual Model

The physical subsystem that is the primary subject of this report is the region inside of the emplacement drifts as shown in Figure 6.1.3-1. Heat is generated inside the waste canisters due to the decay of the radioactive materials. This heat generation rate decreases with time. The waste packages are emplaced on metal pallets with small gaps between waste packages. The waste packages vary in length and diameter depending on the type of waste in the waste package. The pallets sit on top of a crushed tuff invert. A relatively thin metallic drip shield covers the waste packages. The emplacement drifts are drilled at regularly spaced intervals into the host

rock. The host rock, invert, waste packages, and drip shield are physically represented in the natural convection simulations.

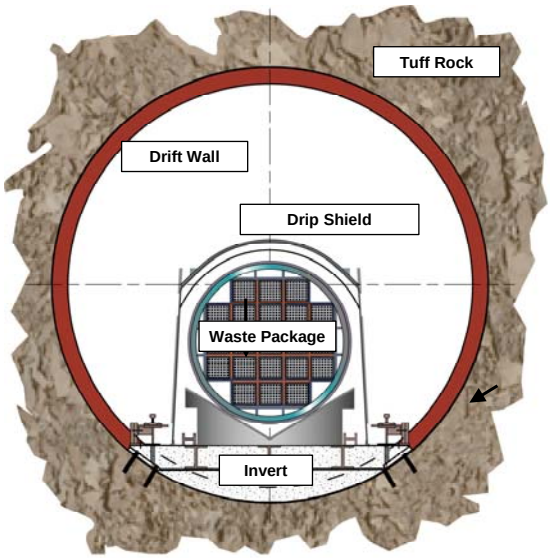

NOTE: Not to scale.

Figure 6.1.3-1. Yucca Mountain Drift Configuration

After emplacement of the waste, the drift is ventilated for a period of up to 50 years, which removes a large fraction of the waste heat as well as some moisture from the drift. The amount of time that a drift is ventilated varies depending on when the drift is loaded and when the repository is finally closed. At closure, drip shields are installed to cover the waste packages. The natural convection simulations are run at specific times after closure of the repository. The linkage of the natural convection simulations to the environment is through the boundary conditions of the simulation. The temperature five meters into the host rock from the drift wall is used as a constant temperature boundary condition for the natural convection simulations as discussed in Section 6.1.3.2.3.

The conceptual model considers an intact drift and drip shield configuration with no rockfall. Natural convection within a drift is considered; natural convection between drifts and natural ventilation are not included.

The movement of heat and mass within the drift are the important processes that are simulated. Conduction, convection, and radiation are all important thermal processes that are contained within the simulations. Conduction is simulated in all solid materials, and turbulent thermal convection and thermal radiation are simulated in the gas phase. In order to develop a dispersion coefficient, the flux of a tracer is calculated between a constant concentration source at one end of the drift segment and a constant concentration sink at the other end of the drift.

Uncertainties in the fluid flow pattern associated with natural ventilation and barometric pumping are not evaluated for the in-drift convection simulations. Uncertainties associated with the future state of the system include drift degradation that could partially fill the volume outside

of the drip shield with rock. Such effects that could change the geometry of the in-drift simulations are not investigated in this report.

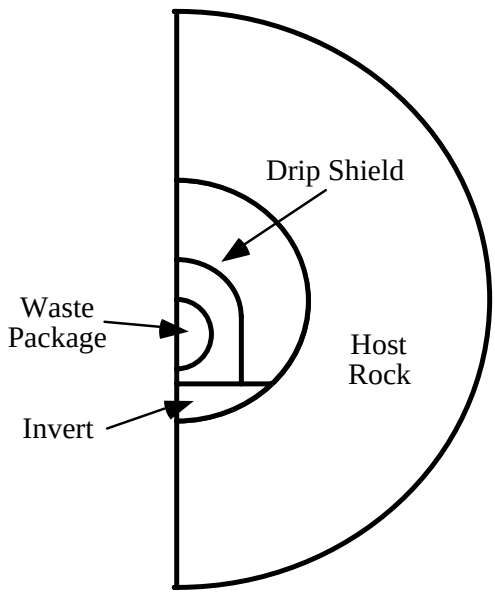

NOTE: Not to scale.

Figure 6.1.3-2. Conceptual Model for Two- and Three-Dimensional CFD Simulations

The two- and three-dimensional base case natural convection simulations contain some simplifications as indicated in Figure 6.1.3-2. The waste package pallet is not represented in the two-dimensional simulations because including the pallet in the two-dimensional simulations would create an artificial flow blockage. The three-dimensional drift geometry is simplified in that the package pallet is not represented, and the waste package is suspended above the invert. The structural supports on the surface of the drip shield are also not represented. An average waste package diameter has also been implemented into the two-dimensional simulations. The 21-PWR waste package diameter is used in the three-dimensional simulations. The drip shield is simulated as a continuous sheet of metal without any way for fluid to flow between the volume under and over the drip shield. The last simplification is that the invert and host rock are simulated as conduction-only solids and not as porous media.

Condensation and evaporation in the drift are not simulated. Condensation and evaporation have the potential to modify the flow patterns and temperatures in the drift due to axial transport. Condensation and evaporation are expected to increase the axial transport compared to the present simulations, so the present calculations are conservative similar to neglecting barometric pumping and repository natural convection. Latent heat effects of this phase change are expected to occur mostly on the drift wall. The large heat capacity of the drift wall is expected to minimize drift wall temperature perturbations.

There are no elements of the subsystem or environment that are treated as uncertain. The base case uses only average properties. Uncertainties in material properties are treated in sensitivity studies to determine how sensitive the system is to uncertainties in the material properties.

6.1.3.2 Simulation Assumptions

6.1.3.2.1 Natural Convection in the Drifts Assumes Pure Air Conditions

Assumption: The FLUENT natural convection calculations for in-drift conditions performed in Sections 6.1, 6.2, and 6.4 are based on pure air with no water vapor.

Rationale: For pure natural convection, the Rayleigh number is a measure of the energy state of the system; the higher the Rayleigh number, the more vigorous the fluid motion. As given in Equation 6.1-8, the Rayleigh number is a product of various fluid properties, gravity, a length scale, and a temperature difference. For given conditions (length scale and temperature difference), the fluid properties determine the Rayleigh number. The Rayleigh number divided by the length scale cubed and the temperature difference is (see Section 6.1.5 for Nomenclature)

$$\frac{Ra_L}{L^3 \Delta T} = \frac{g\beta}{\nu\,\alpha} \qquad \text{(Eq. 6.1-1)}$$

Using $\alpha = k_a/\rho c_p$ (Bird et al. 1960 [DIRS 103524], eq. 8.1-7) and $\nu = \mu/\rho$ (Bird et al. 1960 [DIRS 103524], eq. 1.1-3) this equation can be rewritten as

$$\frac{Ra_L}{L^3 \Delta T} = \frac{g\beta\rho^2 c_p}{\mu\, k_a} \qquad \text{(Eq. 6.1-2)}$$

The right-hand side will be evaluated for 1 atmosphere pressure and 100°C for air and pure steam conditions. The absolute value of the pressure is not significant because a ratio of the Rayleigh numbers is important, not the absolute values. A temperature of 100°C is used so the properties would correspond to a pressure of 1 atmosphere consistent with the air properties.

For air, perfect gas approximations can be used for density and β (=1/T, T in K) (Incropera and DeWitt 2002 [DIRS 163337], Equation 9.9). The specific heat, dynamic viscosity, and thermal conductivity can be interpolated from Table 4.1.3-3. For air, this equation becomes

$$\frac{g\beta\rho^2 c_p}{\mu k_a} = 3.8\,x10^7\ \frac{1}{m^3 K}\ \textit{for air} \qquad \text{(Eq. 6.1-3)}$$

For steam, again assuming a perfect gas, and using properties given in Table 4.1.3-4, the equation becomes

$$\frac{g\beta\rho^2 c_p}{\mu k_a} = 6.2\,x10^7\ \frac{1}{m^3 K}\ \textit{for water vapor} \qquad \text{(Eq. 6.1-4)}$$

Therefore, the Rayleigh number is 63% higher for pure water vapor than for pure air. From the k_{eq} analysis is Section 6.4.7, the heat transfer is approximately proportional to the Rayleigh number to the 0.26 power, or less than 14% in this case.

The Rayleigh number is a measure of the intensity of natural convection. A higher Rayleigh number implies more heat transfer and more mixing than a lower Rayleigh number. By extension, a lower Rayleigh number is conservative because it leads to decreased axial transport of vapor (See Section 6.1.3.2.5). Therefore, pure air conditions can be used to simulate natural convection in the drifts because the Rayleigh number for air is lower than the Rayleigh number for water vapor.

Confirmation Status: No further confirmation required.

Use in this Calculation: This assumption is used in the two-dimensional and three-dimensional convection simulations described in Sections 6.1.5.2 and 6.2.5.2, and in the k_{eq} analysis described in Section 6.4.5.2.

6.1.3.2.2 Steady-State Conditions

Assumption: The two- and three-dimensional convection simulations assume steady-state conditions.

Rationale: The time scale for in-drift flow is discussed below. Additional justification is that steady-state calculations produce very good data-simulation comparisons as shown in Section 7.

The time scale for natural convection can be estimated from the time scale for internal natural convection for heating from the side walls. According to Bejan (1995 [DIRS 152307], pg. 223, Equation 5.13'), the time scale for development of the natural convection boundary layers is given by

$$t_f \sim \left(\frac{\nu H}{g\beta \Delta T \alpha} \right)^{1/2} \qquad \text{(Eq. 6.1-5)}$$

Using Pr = ν/α (Incropera and DeWitt 2002 [DIRS 163337], Equation 6.46), the equation can be written as

$$t_f \sim \left(\frac{H}{g\beta \Delta T} \Pr \right)^{1/2} \qquad \text{(Eq. 6.1-6)}$$

For air, perfect gas approximations can be used for β (=1/T, T in K) (Incropera and DeWitt 2002 [DIRS 163337], Equation 9.9). The height for natural convection is the gap width, or a maximum of 2.75 m, the drift radius. A small ΔT of 1°C can be used for this initial estimation of the time constant. The Pr number for air is approximately 0.7. Therefore, the estimated time

constant for development of the natural convection boundary layers at a temperature of 350 K (~77°C) is approximately 10 seconds.

This time estimate is based on vertical boundary layers. In the repository, horizontal boundary layers will also develop due to the difference in waste package powers and the temperature gradient in the drift wall temperatures. These time scales will be longer than those calculated above but are expected to be in the range of a minute or less.

Based on these time scales, and the long time scale for significant temperature changes in the repository and decay heat levels of years, a steady-state fluid flow and heat transfer analysis is justified.

Confirmation Status: No further confirmation required.

Use in this Calculation: This assumption is used in the two-dimensional and three-dimensional convection simulations described in Sections 6.1.5.1.4 and 6.2.5.1.4 and in the k_{eq} analysis described in Section 6.4.5.1.4.

6.1.3.2.3 Conduction-Only Heat Transfer in the Surrounding Host Rock and Invert

Assumption: Conduction-only heat transfer using a constant thermal conductivity in the rock and in the invert is assumed. The surrounding rock and the invert are simulated as solids. A uniform temperature boundary at 5 m into the rock is used as the simulation boundary condition. The effects of fluid flow on the effective thermal conductivity are not included, and there is no fluid exchange between the drift and the surrounding rock or invert.

Rationale: This assumption is broken down into two separate topics, 1) heat transfer in the rock and 2) fluid exchange between the drift and the rock.

1. Heat Transfer in the Rock

   Heat transfer through the rock is primarily by conduction. The effective thermal conductivity in the rock may vary significantly due to rock dryout and rewetting and the heat pipe effect in the rock due to condensation and evaporation in the rock. For a given rock boundary temperature, this change in effective thermal conductivity influences the calculated waste package temperatures. However, the convection simulations developed in Sections 6.1 and 6.2 are not used to predict absolute waste package temperatures. Rather, the simulations are used to evaluate differential temperatures in the drifts for the evaluation of sensitivities (Section 6.1) and to calculate an effective dispersion coefficient (Section 6.2). In Sections 6.1 and 6.2, approximate boundary rock temperatures are used because the exact value is not important for natural convection calculations.

   The rationale for the 5-m boundary is given by the calculation "Repository Twelve Waste Package Segment Thermal Calculation," (BSC 2003 [DIRS 164726]), which calculates the temperature at various distances into the rock for a given waste package sequence. The calculation shows that the maximum difference in the rock temperature 5 m into the rock along the entire drift segment at any given time is less than 1°C after

500 years (25 years of pre-closure, 475 years of post-closure) (output DTN: SN0406T0507803.023). The waste package sequence assumed in the referenced calculation is similar, but not identical to, the waste package sequence in the present simulations. The linear powers are similar (1.4 kW/m in the referenced calculation (Section 5.3.3); 1.45 kW/m in the present simulations (Section 6.3.5.2.4)). Based on these similarities, the results from the referenced calculation are considered to be appropriate for the present simulations. Therefore, for the purposes of this calculation, the 5-m rock boundary temperatures are assumed to be uniform circumferentially. In general, axial uniformity of temperature is also assumed except when a temperature "tilt" boundary condition is imposed on the problem as discussed in Section 6.2.5.1.3.

The invert thermal conductivity is a function of moisture content, which affects the temperature distribution in the drifts. The sensitivity of the results to the invert thermal conductivity is evaluated in Section 6.1 (Table 6.1.7-1, Cases R6 and R7), and the effect on the peak waste package temperature is smaller than a number of uncertainties such as the emissivity of the waste package and the drip shield. Therefore, the invert thermal conductivity is assumed to be a constant value.

2. Fluid Exchange Between the Drift and the Rock

Fluid flow and exchange between the drift and the rock and invert, and implicitly between the fluid regions inside and outside the drip shield, are assumed to be insignificant. The fluid exchange between the drift and the surrounding rock can be evaluated by comparing the permeability of each medium. For the drift, a theoretical effective permeability can be derived based on natural convection heat transfer as given by Webb (2001 [DIRS 156409]). For a square enclosure 0.25 m on a side and a 1ºC temperature difference between the vertical walls, Webb (2001 [DIRS 156409]) reports a theoretical equivalent permeability of 2.65 x 10^{-5} m^2 for the open drift based on natural convection considerations. The equivalent permeability is proportional to (Webb 2001 [DIRS 156409], Equation 7,8)

$$k \sim \left(\frac{H}{\Delta T} \right)^{1/2} \qquad \text{(Eq. 6.1-7)}$$

For a larger length scale of 2.75 m (drift radius) and a ΔT of 20ºC, the equivalent permeability of the drift becomes approximately 2.0 x 10^{-5} m^2. Even if the ΔT is 1ºC, the value only decreases to 4 x 10^{-6} m^2.

This equivalent permeability of the drift can be compared to fracture permeabilities of approximately 10^{-8} to 10^{-10} m^2 in the invert (BSC 2004 [DIRS 169565]) and lower values in the surrounding rock. Because the drift equivalent permeability is higher than that of the invert and rock by at least two orders of magnitude, natural convection fluid exchange between the drift and the surrounding rock and the invert can be neglected.

The fluid exchange between the regions inside and outside the drip shield through the invert, and implicitly through any gaps in the drip shield, are assumed to be insignificant in this analysis. Exchange of fluids and the associated heat will decrease the temperature difference between the two regions and the waste package temperatures. Therefore, this assumption is bounding for calculation of waste package temperatures.

Confirmation Status: No further confirmation required.

Use in this Calculation: This assumption is used in the two-dimensional and three-dimensional convection simulations described in Sections 6.1.5.1.3 and 6.2.5.1.3.

6.1.3.2.4 Use of Constant Thermophysical Properties of the Introduced Materials in the Drift

Assumption: Constant thermophysical properties are assumed for material properties in the drift.

Rationale: Sensitivity studies results described in Section 6.1 demonstrate that the waste package surface temperatures are not significantly affected by the range in expected thermal properties of the introduced materials.

Confirmation Status: No further confirmation required.

Use in this Calculation: This assumption is used in the two-dimensional and three-dimensional convection simulations described in Sections 6.1.5.2 and 6.2.5.2, in the k_{eq} analysis described in Section 6.4.5.2, and in the validation presented in Section 7.3.

6.1.3.2.5 Neglect of Barometric Pumping

See Section 6.3.3.2.4 – Neglect of Barometric Pumping – for a discussion of this assumption.

6.1.3.2.6 Mean Beam Length

Assumption: The mean beam length, L_e, for the in-drift geometry is assumed to be 3 meters.

Rationale: As shown in Table 6.4.5-4, the maximum characteristic gap width is 1.5 meters for the two-dimensional YMP geometry. To account for the third dimension, a value twice the gap width was selected for L_e. This parameter is only used in a sensitivity study in Section 6.1.7, and is not used for the base case simulations in Sections 6.1 and 6.2, nor in the analysis presented in Section 6.4.

Confirmation Status: No further confirmation required.

Use in this Calculation: This assumption is used in the two-dimensional convection sensitivity studies presented in Section 6.1.7, Case R11. L_e is the length scale used to determine the gas absorption coefficient, α, required as input to FLUENT. This mean beam length is used to

calculate the high value of α used in two cases of the two-dimensional YMP geometry sensitivity study.

6.1.4 Consideration of Alternative Conceptual Models for In-Drift Natural Convection

Two alternative conceptual models (ACMs) of in-drift natural convection have been considered and are summarized in Table 6.1.4-1. An alternative conceptual model is to treat the air phase as a solid material. To account for the higher heat transfer between surfaces due to convection, the effective thermal conductivity of the solid (air) can be increased so that the same amount of heat can transfer from one surface to another for the same temperature difference. This alternative conceptual model is essentially what is done in the MSTHM (BSC 2004 [DIRS 169565]). Section 6.4 of this AMR develops the equivalent thermal conductivity for this approach. This alternative conceptual model is not considered further because it is implemented in Section 6.4 of this report and in the MSTHM (BSC 2004 [DIRS 169565]).

Another alternative conceptual model is to simulate the drift with a CFD code and the surrounding rock with porous media code. The CFD code FLUENT contains limited porous media capabilities that only consider single-phase flow. To more rigorously simulate the rock physical processes, the software would need to be able to simulate partially saturated flow as well as phase change in the porous media. However, as discussed in Assumption 6.1.3.2.3, conduction-only heat transfer in the surrounding rock and the invert is acceptable, and this ACM is not considered further in this report.

Table 6.1.4-1. Alternative Conceptual Models Considered for In-Drift Natural Convection

Alternative Conceptual Model	Key Assumptions	Screening Assessment and Basis
Use porous media code to model heat transfer in drift.	The heat flux inside of the drift can be modeled as quiescent (solid) air with a higher thermal conductivity to account for natural convection.	This general approach has already been investigated in Section 6.4 of the present report and in the MSTHM (BSC 2004 [DIRS 169565]). Therefore, this ACM is not considered further in this report.
Couple thermal-hydrologic and CFD code	Porous media code allows flow of water through invert and host rock. CFD codes model the heat transfer modes from waste package to drift wall or invert. Heat and mass fluxes at air-solid interfaces can be matched between separate porous media zone and CFD zone.	Conduction-only heat transfer in the surrounding rock and invert is acceptable as discussed in Assumption 6.1.3.2.3.

6.1.5 Formulation for the Base-Case Convection Simulations

Nomenclature

A flow area (m^2)
A_c cross-sectional area (m^2)
B empirical constant (9.81)
c local mass fraction (-)

C	volume-averaged mass fraction (-)
c_p	specific heat (J/kg-K)
C_μ	RNG theory determined constant (0.0845)
D	dispersion coefficient (m^2/s)
D_i	inner cylinder wall diameter (m)
D_o	outer cylinder wall diameter (m)
E	total energy per unit mass (J/kg)
g	acceleration due to gravity (m/s^2)
H	drip shield height (m)
$\overline{h}_i$	mean overall heat transfer coefficient (W/m^2-K)
I	radiation intensity (W/m^2-solid angle)
k_{eq}	average equivalent thermal conductivity for natural convection (-)
k_{eff}	effective thermal conductivity (W/m-K)
k	turbulent kinetic energy (m^2/s^2)
k_p	turbulent kinetic energy at wall adjacent cell center (m^2/s^2)
k_{perm}	permeability (m^2)
k_a	air thermal conductivity (W/m-K)
L	annulus gap width, $R_o - R_i$ (m)
L_c	characteristic gap-width (m)
M_w	molecular weight of air (kg/kmol)
n	refractive index (-)
Ra_{L_c}	Rayleigh number based on characteristic gap-width (-)
Nu_i	Nusselt number for natural convection from the inner cylinder (-)
Nu_o	Nusselt number for natural convection from the outer cylinder (-)
$\overline{Nu}_{D_i}$	average overall Nusselt number (-)
Nu_{cond}	Nusselt number for conduction (-)
Nu_{conv}	Nusselt number for convection between concentric cylinders (-)
P	wetted perimeter (m)
p	pressure (N/m^2)
Pr	Prandtl number (-)
Pr_t	turbulent Prandtl number (-)
q''	wall heat flux (W/m^2)
Q	mass flow rate in the dispersion model (kg/s)
Q	overall heat transfer rate from the CFD simulations (W)
Q_{cond}	conduction heat transfer rate from the CFD simulations (W)
q_i	component heat flux on the inside surface of an enclosure (W/m^2)
q_o	component heat flux on the outside surface of an enclosure (W/m^2)

q_{cond_i} component conduction heat flux on the inside surface of an enclosure (W/m^2)
q_{cond_o} component conduction heat flux on the outside surface of an enclosure (W/m^2)
r* dimensionless radial distance $\frac{R - R_i}{L}$ (-)
$\vec{r}$ position vector (m)
R drip shield radius (m)
R_g universal gas constant (N-m/kmol-K)
Re_y turbulent Reynolds number (-)
Ra_L Rayleigh number based on gap-width (-)
R radial distance (m)
R_o outside radius (m)
R_i inside radius (m)
$\vec{s}$ direction vector (m)
$\vec{s}'$ scattering direction vector (m)
T_c cold cylinder (outer) wall temperature (K or °C)
T_h hot cylinder (inner) wall temperature (K or °C)
ΔT temperature difference (K or °C)
T_p fluid temperature at wall adjacent cell center (K or °C)
T_w wall temperature (K or °C)
$\overline{T}$ average fluid temperature (K or °C)
u velocity (m/s)
u_c characteristic velocity for natural convection (m/s)
y normal distance to nearest wall (m)
y_p distance from wall adjacent cell center to the wall (m).

Greek

α fluid thermal diffusivity, $k_a/\rho c_p$ (m^2/s), thermal radiation absorption coefficient (m^{-1})
$\alpha_{k,\varepsilon,T}$ inverse effective Prandtl numbers (-)
β volumetric thermal expansion coefficient (K^{-1})
δ_T laminar thermal boundary layer thickness for a plane wall (m)
δ_v laminar viscous boundary layer thickness for a plane wall (m)
ε dissipation rate of turbulent kinetic energy (m^2/s^3), eccentricity (m), thermal radiation emissivity (-)
θ angular position (0° vertical up, 180° vertical down) (degrees)
μ molecular fluid viscosity (kg/m-s)
μ_t turbulent viscosity (kg/m-s)
μ_{eff} effective viscosity, $\mu_t + \mu$ (kg/m-s)

ν	fluid kinematic viscosity, μ/ρ (m^2/s)
ρ	fluid density (kg/m^3)
σ_s	scattering coefficient (m^{-1})
σ	Stefan-Boltzmann constant ($W/m^2\text{-}K^4$)
τ_w	wall shear stress (N/m^2)
$\hat{\upsilon}$	viscosity ratio, μ_{eff}/μ (-)
ϕ	dimensionless temperature, $\frac{T-T_c}{T_h-T_c}$ (-)
Φ	phase function (-)
ω	specific dissipation rate (s^{-1})
Ω'	solid angle (radians)

6.1.5.1 Mathematical Description of the Base-Case Conceptual Model

The computer code FLUENT is used for the CFD analyses for the two- and three-dimensional drift simulations. FLUENT is a computational fluid dynamics code that solves conservation of mass, momentum, energy (including a radiative transfer equation) and species and turbulence submodels using various means to obtain closure for the turbulent momentum equations (Fluent 2001 [DIRS 164453]). Transient and steady state formulations are available. For this heat transfer analysis, steady-state conduction, turbulent natural convection, and thermal radiation are treated in the in-drift environment. The solution of these equations provides in-drift component temperatures as well as the encompassing flow field.

The general flow features for natural convection can be ascertained from the flow features for natural convection in horizontal concentric cylinders, which is a geometrically similar system. In the horizontal concentric cylinder configuration with a heated inner cylinder, the flow is characterized by an upward moving plume above the inner cylinder and turbulent downward flow on the outer wall. For internal natural convection in a horizontal concentric annulus, a Rayleigh number based on gap-width, Ra_L,

$$Ra_L = \frac{g\beta\Delta T L^3}{\nu\alpha} \qquad \text{(Eq. 6.1-8)}$$

is normally used to determine if the internal flow is laminar or turbulent (Kuehn and Goldstein 1978 [DIRS 130084]). The transition gap-width Rayleigh number for turbulence is about 10^6 (Kuehn and Goldstein 1978 [DIRS 130084]; Desai and Vafai 1994 [DIRS 156702]; Char and Hsu 1998 [DIRS 156701]). For Rayleigh numbers less than 10^6, the flow is laminar.

For internal natural convection, the Rayleigh number, Ra_{L_c}, is based on a characteristic gap-width, L_c,

$$Ra_{L_c} = \frac{g\beta\Delta T L_c^{\ 3}}{\nu\alpha} = \frac{g\beta\rho^2 c_p\,\Delta T\,L_c^3}{k\mu} \qquad \text{(Eq. 6.1-9)}$$

where the characteristic gap-width is half the hydraulic diameter (Perry et al. 1984 [DIRS 125806], pp. 5 to 6) and is given by the following relationship:

$$L_c = \frac{2A_c}{P} \qquad \text{(Eq. 6.1-10)}$$

where A_c is the cross-sectional area and P is the wetted perimeter. It is noted that the characteristic gap-width reduces to the standard gap-width definition, $R_o - R_i$, for a concentric cylinder annulus.

6.1.5.1.1 Turbulence Modeling

Turbulence is characterized by fluctuating quantities (e.g., velocity, temperature, etc.). The velocity fluctuations impact transport of quantities such as mass, momentum, and energy. Direct simulation of all scales of a velocity fluctuation is not computationally practical. Therefore, simplifications for turbulent flow solutions are necessary. Typical approaches for handling turbulent flows are through Reynolds averaging or filtering the Navier-Stokes equations. However, both methods introduce unknown terms into the Navier-Stokes equations; therefore, additional turbulence modeling is required to achieve closure of the flow equations. Reynolds-averaged Navier-Stokes equations (RANS) are written in terms of mean quantities and unknown terms with respect to the time-averaged fluctuating components that are generally referred to as the turbulent Reynolds stresses (Fluent 2001 [DIRS 164453], Section 10.2.2). The RANS approach is used in the following turbulence models available in FLUENT (Fluent 2001 [DIRS 164453], Chapter 10):

One equation model:

- Spalart-Allmaras (Fluent 2001 [DIRS 164453], Section 10.3)

Two equation models:

- k-ε models including standard, realizable, and renormalization-group (RNG) (Fluent 2001 [DIRS 164453], Section 10.4)
- k-ω models including standard and shear-stress transport (Fluent 2001[DIRS 164453], Section 10.5)

Five-equation model (in two dimensions) and a seven-equation model (in three dimensions)

- Reynolds Stress Model (RSM) (Fluent 2001 [DIRS 164453], Section 10.6)

In the RANS approach, unsteadiness is removed by casting all variables (e.g., velocity, temperature, and pressure) into mean and fluctuating components and time-averaging the

subsequent governing equations. The governing flow equations, written in terms of mean velocity and temperature components, for mass, momentum, and energy take the following forms after averaging:

Conservation of Mass (Continuity) (Fluent 2001 [DIRS 164453], Equation 10.2-3):

$$\frac{\partial \rho}{\partial t} + \frac{\partial}{\partial x_i}(\rho u_i) = 0 \qquad \text{(Eq. 6.1-11)}$$

Conservation of Momentum (Navier-Stokes) (Fluent 2001 [DIRS 164453], Equation 10.2-4):

$$\frac{\partial}{\partial t}(\rho u_i) + \frac{\partial}{\partial x_j}(\rho u_i u_j) = -\frac{\partial p}{\partial x_i} + \frac{\partial}{\partial x_j}\left[\mu\left(\frac{\partial u_i}{\partial x_j} + \frac{\partial u_j}{\partial x_i} - \frac{2}{3}\delta_{ij}\frac{\partial u_l}{\partial x_l}\right)\right] + \frac{\partial}{\partial x_j}\left(-\rho\overline{u_i' u_j'}\right) \qquad \text{(Eq. 6.1-12)}$$

All of the terms in Equation 6.1-12, with the exception of the last term, are written with respect to mean velocities or pressure. The last term on the right hand side of the momentum equation contains the turbulent Reynolds stresses.

Conservation of Energy (Fluent 2001 [DIRS 164453], Equation 10.4-29):

$$\frac{\partial}{\partial t}(\rho E) + \frac{\partial}{\partial x_i}(u_i(\rho E + p)) = \frac{\partial}{\partial x_j}\left(k_{eff}\frac{\partial T}{\partial x_j}\right) \qquad \text{(Eq. 6.1-13)}$$

where viscous heating and source terms are neglected and $k_{eff} = \alpha_T c_p \mu_{eff}$. The α_T term is computed in a manner similar to the inverse effective Prandtl numbers in the turbulence equations described below. The turbulent Prandtl number for energy is a function of the molecular Prandtl number and the effective viscosity described below.

The Boussinesq hypothesis (an assumption applied by the Spallart-Allmaras, k-ε, and k-ω turbulence models) can be used to relate the Reynolds stresses to the mean velocity gradients and other turbulence quantities including the turbulent viscosity (Fluent 2001 [DIRS 164453], Equation 10.2-5).

$$-\rho\overline{u_i' u_j'} = \mu_t\left(\frac{\partial u_i}{\partial x_j} + \frac{\partial u_j}{\partial x_i}\right) - \frac{2}{3}\delta_{ij}\left(\rho k + \mu_t\frac{\partial u_i}{\partial x_i}\right) \qquad \text{(Eq. 6.1-14)}$$

As described above, a number of different turbulence models can be applied when solving turbulent flow fields. The RNG k-ε is selected for this analysis for the two- and three-dimensional convection models and k_{eq} analysis. The primary reasons for using the RNG k-ε turbulence model are that it allows for variation in the turbulent Prandtl number as a function of flow conditions, it provides a means for including low-Reynolds number effects in the effective

viscosity formulation, and it includes an extra term, R_ε, in the ε-equation to better model separated flows. The conservation equations for the RNG k-ε turbulence (two-equation) model are given below.

k – turbulent kinetic energy (Fluent 2001 [DIRS 164453], Equation 10.4-4):

$$\frac{\partial}{\partial t}(\rho k) + \frac{\partial}{\partial x_i}(\rho k u_i) = \frac{\partial}{\partial x_j}\left(\alpha_k \mu_{eff} \frac{\partial k}{\partial x_j}\right) + G_k + G_b - \rho\varepsilon - Y_M \qquad \text{(Eq. 6.1-15)}$$

ε – dissipation of turbulent kinetic energy (Fluent 2001 [DIRS 164453], Equation 10.4-5):

$$\frac{\partial}{\partial t}(\rho \varepsilon) + \frac{\partial}{\partial x_i}(\rho \varepsilon u_i) = \frac{\partial}{\partial x_j}\left(\alpha_\varepsilon \mu_{eff} \frac{\partial \varepsilon}{\partial x_j}\right) + C_{1\varepsilon}\frac{\varepsilon}{k}(G_k + C_{3\varepsilon} G_b) - C_{2\varepsilon}\rho\frac{\varepsilon^2}{k} - R_\varepsilon \qquad \text{(Eq. 6.1-16)}$$

where α_k and α_ε are inverse effective Prandtl numbers derived analytically by the RNG theory, G_k is the generation of turbulent kinetic energy due to mean velocity gradients, G_b is the generation of turbulent kinetic energy due to buoyancy (a function of gravity and temperature gradient), Y_M is the contribution of fluctuating dilation to the dissipation rate, $C_{1\varepsilon}$ and $C_{2\varepsilon}$ are constants, $C_{3\varepsilon}$ is a (calculated) factor related to how the buoyant shear layer is aligned with gravity, and R_ε is a strain rate term written as a function of the mean rate-of-strain tensor. Including full buoyancy effects in the equations is related to inclusion of the generation of turbulence due to a buoyancy term in the transport equation for the dissipation rate of turbulent kinetic energy (e.g., in the ε-equation). The source terms are neglected. In the governing equations, the subscripts i, j, and l refer to values in the various directions (i = x, y, and z directions; j = x, y, and z directions, l = x, y, and z directions).

The RNG k-ε turbulence model provides an analytically derived differential formula for the effective viscosity that accounts for low-Reynolds number effects in the flow domain. It is written in terms of the effective viscosity, μ_{eff}.

$$d\left(\frac{\rho^2 k}{\sqrt{\varepsilon\mu}}\right) = 1.72\frac{\hat{\upsilon}}{\sqrt{\hat{\upsilon}^3 - 1 + C_\upsilon}}\, d\hat{\upsilon} \qquad \text{(Eq. 6.1-17)}$$

where $\hat{\upsilon} = \mu_{eff}/\mu$ and C_υ is a constant (≈100) (Fluent 2001 [DIRS 164453], Equation 10.4-6). The differential equation for viscosity is applicable to low-Reynolds number and near-wall flows. In the high Reynolds number limit, the turbulent viscosity produced by the differential equation is given by (Fluent 2001 [DIRS 164453], Equation 10.4-7):

$$\mu_t = \rho C_\mu \frac{k^2}{\varepsilon} \qquad \text{(Eq. 6.1-18)}$$

The various model constants are $C_{1\varepsilon}$ = 1.42, $C_{2\varepsilon}$ = 1.68, and C_μ = 0.0845, which are the default values in FLUENT (Fluent 2001 [DIRS 164453], pp. 10-21 and 10-24). For complete details, refer to the FLUENT documentation on modeling turbulence (Fluent 2001 [DIRS 164453], Section 10).

Use of the differential formula for the viscosity requires an appropriate treatment of the near-wall region. Specifically, it requires that the viscous sublayer (the laminar region nearest the wall) and the buffer layer (e.g., the near-wall region between the viscous sublayer and the fully turbulent region) are resolved (meshed) all the way to the wall surface (Fluent 2001 [DIRS 164453], pp. 10-60 to 10-61). The use of hydrodynamic wall functions (e.g., an alternative approach using semi-empirical modeling of the near-wall velocity behavior) is not appropriate when low-Reynolds number effects are pervasive within the flow domain (Fluent 2001 [DIRS 164453], p. 10-70). Additionally, the hydrodynamic wall function approach is not applicable in the presence of strong body forces (as in the case of buoyancy-driven flows) (Fluent 2001 [DIRS 164453], p. 10-70). Finally, hydrodynamic wall functions are not appropriate for natural convection conditions. In this case, hydrodynamic wall functions assume a monotonically increasing velocity profile as one goes from the wall to the core flow. In natural convection, the velocity profile has a local peak near the wall, so the monotonic velocity profile assumption implicit in wall functions is not met.

As an example, Desai and Vafai (1994 [DIRS 156702]) applied standard wall functions through the viscous sublayer in their analysis of internal natural convection. Their resulting heat transfer rates tend to underpredict the experimental data and other literature results (see Figure 7.3.3-2). Therefore, the boundary layer must be adequately resolved by the grid in order to obtain the correct surface heat transfer fluxes (the quantity used to determine the heat transfer characteristics previously described).

A wall function approach is used for the near-wall mean temperature. The temperature wall function is monotonic similar to the hydrodynamic wall functions. Because the temperature profile is monotonic in natural convection flow, temperature wall functions are appropriate. In the viscous sublayer, neglecting viscous heating effects (for incompressible flow), the linear law is written in terms of the molecular Prandtl number (Fluent 2001 [DIRS 164453], Equation 10.8-5 and unnumbered equations following Equation 10.8-6):

$$T^* = \Pr y^* \left(y^* < y_T^* \right) \qquad \text{(Eq. 6.1-19)}$$

while in the turbulent sublayer, a logarithmic law is written in terms of the turbulent Prandtl number, neglecting viscous heating effects and for incompressible flow conditions (Fluent 2001, [DIRS 164453], Equations 10.8-5 and 10.8-6 and unnumbered equations following Equation 10.8-6):

$$T^* = \mathrm{Pr}_t\left[\frac{1}{\kappa}\ln\left(Ey^*\right)+P\right]$$

$$P = 9.24\left[\left(\frac{\mathrm{Pr}}{\mathrm{Pr}_t}\right)^{3/4}-1\right]\left[1+0.28e^{-0.007\mathrm{Pr}/\mathrm{Pr}_t}\right] \qquad \left(y^* > y_T^*\right) \qquad \text{(Eq. 6.1-20)}$$

where κ is von Karman's constant (0.4187) (Fluent 2001 [DIRS 164453], p. 10-65) and P is a function of the molecular and turbulent Prandtl numbers, Pr and Pr_t respectively. The dimensionless quantities, T^* and y^*, in the above equations are defined as (Fluent 2001, [DIRS 164453], Equation 10.8-5):

$$T^* = \frac{\left(T_w - T_P\right)\rho c_p C_\mu^{1/4} k_P^{1/2}}{q''} \qquad \text{(Eq. 6.1-21)}$$

and (Fluent 2001 [DIRS 164453], Equation 10.8-3):

$$y^* = \frac{\rho C_\mu^{1/4} k_P^{1/2} y_P}{\mu} \qquad \text{(Eq. 6.1-22)}$$

The selection of linear or logarithmic laws is based on the computation of y_T^*. This quantity is computed as the y^* value at which the linear law and the logarithmic law intersect. For a refined grid (e.g., $y^+ = \frac{y_p}{\nu}\sqrt{\frac{\tau_w}{\rho}}$ <10, which is a result of the model results), the linear law (Equation 6.1-19) is selected based on the intersection of the two curves. It is noted that in equilibrium turbulent boundary layers, y^* and y^+ are approximately equal. The use of wall functions for temperature is acceptable in this analysis because the near-wall treatment for velocity places grid points inside the viscous sublayer. Subsequently, the natural convection boundary layer is resolved for both velocity and temperature.

6.1.5.1.2 Thermal Radiation Modeling

The thermal radiation model used in the three-dimensional drift models and two-dimensional sensitivity models is based on the radiative transfer equation (RTE) (Fluent 2001 [DIRS 164453], Equation 11.3-1):

$$\nabla\cdot\left(I\left(\vec{r},\vec{s}\right)\vec{s}\right)+\left(a+\sigma_s\right)I\left(\vec{r},\vec{s}\right) = an^2\frac{\sigma T^4}{\pi}+\frac{\sigma_s}{4\pi}\int_0^{4\pi} I\left(\vec{r},\vec{s}'\right)\Phi\left(\vec{s}\cdot\vec{s}'\right)d\Omega' \qquad \text{(Eq. 6.1-23)}$$

Thermal radiation heat transfer is accounted for by solving Equation 6.1-23 using the discrete ordinates (DO) model included as an option in FLUENT (Fluent 2001 [DIRS 164453], Section 11.3.6). The DO model solves the RTE for a finite number of discrete solid angles (called control angles). Division of a domain occurs as N_θ x N_ϕ solid angles. In two-dimensional calculations, four octants are required making a total of $4N_\theta N_\phi$ directions solved, one RTE for each direction. In three-dimensional calculations, eight octants are required making a total of $8N_\theta N_\phi$ directions solved, one RTE for each direction. Control angles are further subdivided into $N_{\theta p}$ x $N_{\phi p}$ pixels, in order to account for the possibility of incoming and outgoing radiation occurring within the same control angle. The DO model allows one to solve surface-to-surface radiation and fluid participation radiation. This model is restricted to either gray or non-gray thermal radiation using a banded gray model. The RTE accounts for scattering, gas emission, and absorption. The surfaces are treated as gray, diffuse surfaces.

The DO settings used in these CFD simulations are theta divisions, phi divisions, theta pixels, and phi pixels. These settings vary from two- and three-dimensional models. Three-dimensional models typically apply 3,3,3,3 for the DO model. This results in the solution of 72 RTEs at each radiation iteration. Two-dimensional models typically apply 6,6,6,6 for the DO model. This results in the solution of 144 RTEs at each radiation iteration. The gray radiation model is applied as a constant emissivity over all wavelengths. For the three-dimensional simulations, the default air absorptivity of 0.01 m^{-1} defined in FLUENT is used for all simulations. The sensitivity study includes sensitivity to absorption/emission of radiation by a fluid medium (Case R11 and Worst Case). In this case, the fluid in the emplacement drift participates in thermal radiation. FLUENT requires an absorption coefficient α (m^{-1}) for gas participation. The following is an analysis to evaluate a high value for the coefficient. The two gases that can participate in thermal radiation in air are water vapor and carbon dioxide (CO_2). Because both water vapor and carbon dioxide participate in radiation, both components must be considered when computing the total gas emissivity. The process of calculating the overall gas absorption coefficient is a multi-step process. The first step is to adjust the partial pressure of each type of gas for pressure effects. The emittance for both gases has to be evaluated. The emissivities are then added together and the bandwidth overlap between the two emissivities is subtracted from the sum. Because the two-dimensional base case simulation used a gas absorption coefficient of 0 m^{-1}, a higher value of α is desired for the sensitivity study. Higher values are achieved with higher water vapor and CO_2 concentrations.

The partial pressure of CO_2 will vary in magnitude as the chemistry of the air inside the drift evolves as a function of time and temperature. The partial pressure of CO_2 as a function of time in the repository is reported in DTN:MO0308SPACO2GL.001 [DIRS 168096]. These values vary with time and peak at a value of approximately 0.01 bars, or 0.01 atmospheres (1 atmosphere = 1.013 bars; see Bejan 1995 [DIRS 152307], pg. 582) as given in Table 4.1.1-4. Siegel and Howell (1992 [DIRS 100687], Figure 13-14) show that the pressure correction for CO_2 at a total pressure of 0.89 kPa, the approximate atmospheric pressure at the repository elevation (see Section 6.2.5.2), is small so it will be neglected. The length scale (L_e) for a full scale YMP simulation is assumed to be 3 meters (see Assumption 6.1.3.2.5). Thus,

$$P_{CO_2} L_e = (0.01 \text{ atm})\ (3.0 \text{ m}) = 0.03 \text{ atm-m} \qquad \text{(Eq. 6.1-24)}$$

For temperatures in the range 300 to 350 K and for a $P_{CO_2}L_e$ value of 0.03 atm-m, Siegel and Howell (1992 [DIRS 100687], Figure 13-13) give a CO_2 emittance (ε_{CO_2}) value of 0.085.

For the emittance of water vapor, the water vapor partial pressure is 1/3 atmospheres, which corresponds to the saturation vapor pressure at 345K (72 ºC). The pressure correction for water vapor can be evaluated using Figure 13-16 of Siegel and Howell (1992 [DIRS 100687]). The average pressure is:

$$(P + P_{H_2O})/2 = (0.9 \text{ atm} + 0.33 \text{ atm})/2 = 0.6 \text{ atm} \qquad \text{(Eq. 6.1-25)}$$

For

$$P_{H_2O}L_e = (0.33 \text{ atm})\ (3.0 \text{ m}) = 1.0 \text{ atm-m} \qquad \text{(Eq. 6.1-26)}$$

the pressure correction value from Figure 13-16 is 1.1. The corrected water vapor pressure is P_{H_2O} = 1.1*(0.33 atm) = 0.36 atm. This changes $P_{H_2O}L_e$ to 1.1 atm-m.

For temperatures in the range 300 to 350 K and at a $P_{H_2O}L_e$ value of 1.1 atm-m, Siegel and Howell (1992 [DIRS 100687], Figure 13-15) give a total emittance of water vapor (ε_{H_2O}) of 0.46.

Figure 13-17 of Siegel and Howell (1992 [DIRS 100687]) is then used to evaluate the correction on total emittance for band overlap when both CO_2 and water vapor are present.

Using

$$P_{H_2O}/(P_{CO_2} + P_{H_2O}) = .36/(.01 + .36) = 0.97 \qquad \text{(Eq. 6.1-27)}$$

Figure 13-17 of Siegel and Howell (1992 [DIRS 100687]) gives the band overlap correction value of $\Delta\varepsilon = 0.04$. The sum of the emittances for CO_2, H_2O and the overlap is then

$$0.085 + 0.46 - 0.04 = 0.5 \qquad \text{(Eq. 6.1-28)}$$

The absorption coefficient, α, used in FLUENT is then

$$\alpha = \frac{\varepsilon}{L_e} = 0.5/(3 \text{ m}) = 0.17 \text{ m}^{-1} \qquad \text{(Eq. 6.1-29)}$$

6.1.5.1.3 Boundary Conditions

The domain for the drift CFD simulations is a half-cylinder 15.5 m in diameter including the rock. A shell of host rock five meters thick is on the outer surface of the cylinder. To reduce computational costs, only half of the drift was simulated. A symmetry plane was created located at the center of the drift.

Figure 6.1.5-1 illustrates the boundary conditions for the two-dimensional natural convection simulations. For the waste package, invert, and the host rock, a no-heat-flux boundary condition is imposed on the center-line symmetry faces. For the inner and outer drip shield air volumes, no-heat-flux, no-mass-flux, and velocity slip condition (symmetry) boundary conditions are imposed on the centerline symmetry face. For the solid-air interfaces, a no mass flux, no-slip boundary conditions are imposed. The FLUENT code balances heat flux at those solid-air interfaces. The heat is introduced into the simulation through a volumetric heat generation rate inside the waste packages. Heat is removed from the simulation as a result of the constant temperature boundary condition imposed.

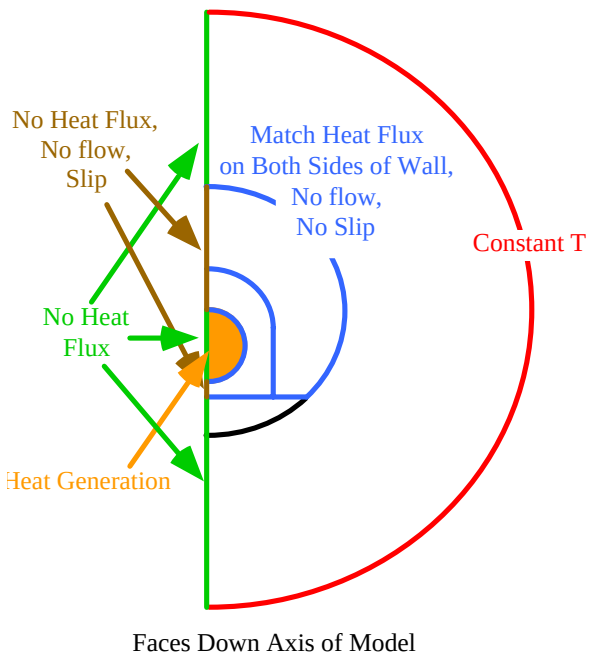

Figure 6.1.5-1. Boundary Conditions Imposed on the Two-Dimensional Convection Simulations

For the two-dimensional simulations, a heat generation rate of 68.1 W/m^3 and a 5-meter host rock boundary temperature of 59.6ºC are used. These values are approximate and produce reasonable temperatures in the drift. For the average waste package diameter of 1.714 meters (average of 24-BWR and DHLW waste package diameters in Table 4.1.1-3), the heat generation rate corresponds to a linear heat load of approximately 157 W/m, or the value just after 300 years in the current design (BSC 2004, [DIRS 167754], Table 12) assuming zero waste package spacing.

Thermal radiation is calculated inside the air domains. The base case surface radiation emissivities used in the two-dimensional CFD simulations are given in Table 4.1.1-2.

6.1.5.1.4 Initial Conditions

The CFD simulations are run in steady-state mode so initial conditions are not specified.

6.1.5.2 Base-Case Inputs

Geometry

The geometric information used in the simulations is listed in Table 4.1.1.3. This table contains the relevant drift cross-section information.

The FLUENT mesh is shown in Figure 6.1.5-2. The mesh consists of about 5500 cells including the surrounding rock.

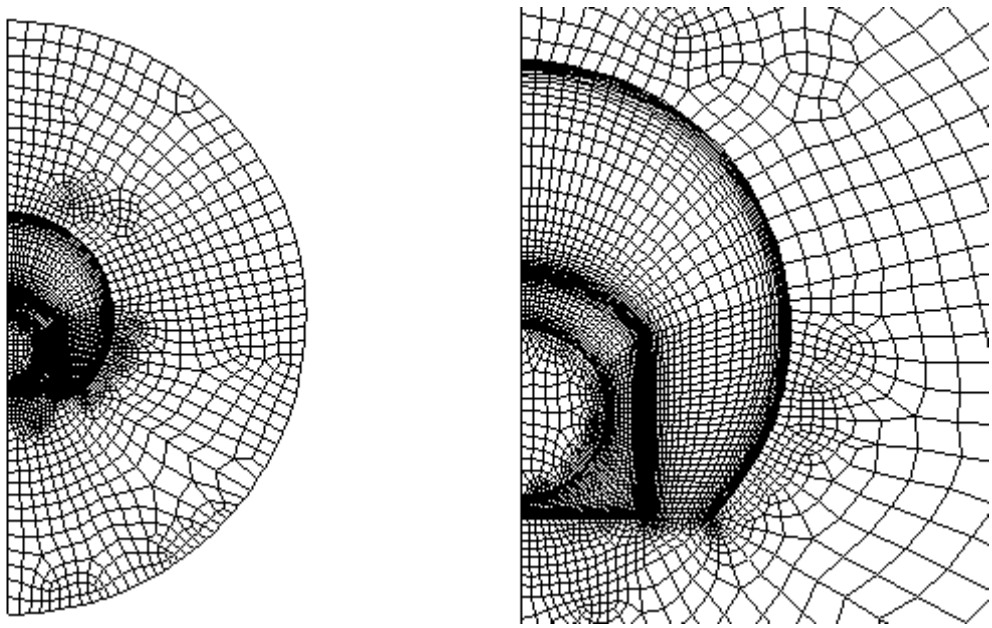

(a) Total Grid (b) In-Drift Region

DTN: SN0312T0507803.022.

Figure 6.1.5-2. Computational Grid for the Two-Dimensional In-Drift Convection Simulations

Properties

The air properties used in the FLUENT simulations is found in Table 4.1.1-1. The air properties are linearly interpolated between temperatures by the code. The fluid density is computed internally by FLUENT (Fluent 2001 [DIRS 164453], Equation 7.2-5), using the incompressible-ideal-gas law:

$$\rho = \frac{P_o}{\frac{R_g}{M_w} T} \qquad \text{(Eq. 6.1-30)}$$

where P_o is the operating pressure described in the next section and T is the fluid temperature.

The base case thermal properties are listed in Table 4.1.1-2. The measured invert thermal conductivity has a range of 0.14 to 0.17 W/m-K for dry material. The invert thermal conductivity is rounded up to a value of 0.2 W/m-K to approximately account for greater thermal conductivity of wet material. This value is the same as reported in Table IV-9 in *Multiscale Thermohydrologic Model* (BSC 2004 [DIRS 169565]).

The nominal invert and host rock surface emissivities are 0.9. The waste package and drip shield emissivities are 0.87 and 0.63, respectively. These are the same values used in the three-dimensional natural convection simulations. Average waste package and invert thermal conductivities used in the base case simulation are 1.5 and 0.2 W/m-K. These are typical values used in the three-dimensional natural convection simulations.

Operating Conditions

The two-dimensional convection simulations use a heat generation rate of 68.1 W/m^3 as discussed in Section 6.1.5.1.3, an average waste package diameter of 1.714 m (see Table 4.1.1-3), and a total (operating) pressure of 101.3 kPa. The total pressure is approximate and produces reasonable temperatures in the drift. Because the results of the two-dimensional simulations are just used to evaluate the sensitivity of the results to various parameters, and the absolute value is not used in this report, an approximate operating pressure is adequate. In any event, the difference in heat transfer between the assumed operating pressure of 101.3 kPa and the repository pressure of 89.05 kPa (Section 6.2.5.2) is only about 6.5% based on the equivalent thermal conductivity analysis results (Equation 6.4-10 and 6.4-15).

The heat generation in the simulations is based on the simulation depth of one meter, which makes the heat generation correspond to a lineal heat loading of 157 W/m. The gravitational constant is specified in each of the simulations as 9.81 m/s^2 (Table 4.1.1-2).

6.1.5.3 Summary of the Computational Simulations

The CFD numerical simulation settings and runtime monitoring for equation residuals, discretization, convergence, and steady-state energy balance are described in this section for all the simulations.

The steady-state segregated solver (Fluent 2001 [DIRS 164453], Section 22.3) is used in this work. The segregated solver approach results in the governing equations being solved sequentially. An implicit linearization technique is applied in the segregated solution of the modeled equations previously described. This results in a linear system of equations at each computational cell. The equations are coupled and non-linear; therefore, several iterations of the equation set are required to obtain a converged solution.

FLUENT uses a control-volume method to solve the governing equations (Fluent 2001 [DIRS 164453], Section 22.2). The equations are discrete for each computational cell. In applying this solution method the CFD simulation stores flow properties (e.g., dependent variables) at cell centers. However, face values are required for the convection terms in the discretized equations. Face values are obtained by interpolation from the cell centers using a second-order upwind scheme for the momentum and energy equations and a first-order upwind scheme for the turbulence equations. It is noted that the diffusion terms in the equations are central-differenced and are second-order accurate. The body-force-weighted pressure interpolation scheme is applied to this analysis (Fluent 2001 [DIRS 164453], pp. 22-21 and 22-22). The pressure interpolation scheme is used to compute face pressures from cell center values. A body-force-weighted pressure interpolation scheme is applicable to buoyancy driven flows. Pressure-velocity coupling is achieved through the Semi-Implicit Method for Pressure-Linked Equations (SIMPLE) algorithm (Fluent 2001 [DIRS 164453], pp. 22-24 and 22-25). The SIMPLE algorithm uses the discrete continuity equation to determine a cell pressure correction equation. Once a solution to the cell pressure correction equation is obtained the cell pressure and face mass fluxes are then corrected using the cell pressure correction term.

The flow solution is given an arbitrary initial starting point for fluid velocity, temperature, and turbulence quantities. Additional iterations are required for solution convergence. A flow solution is considered to have converged after all equation residuals have been reduced by several orders of magnitude. A final convergence criterion specified in the CFD simulations is based on an overall steady-state energy balance. When the energy imbalance between cylinders is at or below about 2%, the flow simulation is assumed to be at steady-state. Therefore, when the residuals are reduced by several orders of magnitude and the energy imbalance is about 2% or less, the flow simulation is complete.

6.1.6 Formulation for Alternative Conceptual Models for In-Drift Natural Convection

Each of the Alternate Conceptual Models (ACMs) discussed in Section 6.1.4 have been screened out.

6.1.7 Two-Dimensional Simulation Results

Base Case (R1)

A sensitivity study was performed to investigate the variation in peak waste package temperature due to changes in some of the physical input parameters that are used in the simulations. To do this, a base case two-dimensional CFD simulation is defined. The base case uses “average” thermal properties for radiation emissivities and constant material thermal conductivities of the introduced materials (see Table 4.1.1-2).

Cases R2 and R3

The base case host rock and crushed tuff invert emissivity is 0.9 (Incropera and DeWitt 1990 [DIRS 156693], Table A.11). In Case R2, the host rock and invert emissivities are specified to be 0.88. This is the minimum rock emissivity as taken from Incropera and DeWitt (1990 [DIRS 156693], Table A.11). In Case R3, the host rock and invert emissivities are specified to be 0.95,

the maximum rock emissivity as taken from Incropera and DeWitt (1990 [DIRS 156693], Table A.11).

Cases R4 and R5

The base case waste package thermal conductivity is 1.5 W/m-K. The range of waste package thermal conductivities evaluated is 1.0 to 2.0 W/m-K. In Case R4, the minimum waste package thermal conductivity is 1.0 W/m-K. In Case R5, the maximum waste package thermal conductivity is 2.0 W/m-K.

Cases R6 and R7

The base case invert thermal conductivity is 0.20 W/m-K. The range of invert thermal conductivities is plus/minus 10 percent in line with the variability in the data as indicated in Table 4.1.1-2. In Case R6, the minimum invert thermal conductivity is 0.18 W/m-K. In Case R7, the maximum invert thermal conductivity is 0.22 W/m-K.

Cases R8 through R10

Cases R8 through R10 consider alternative turbulence flow models to the RNG k-ε model used in the base case. Case R8 uses a Reynolds Stress Model (RSM) as the turbulent flow model (Fluent 2001 [DIRS 164453], Section 10.6). Unlike the base case turbulence model, the RSM does not assume an isotropic eddy-viscosity to close the Reynolds-averaged Navier-Stokes (RANS) equations solved in the fluid domain. The RSM closes the RANS equations by solving transport equations for the Reynolds stresses together with a transport equation for the dissipation rate of turbulent kinetic energy. The RSM requires more computational resources than the RNG k-ε because it is a five equation model. Case R9 uses a standard k-ε two equation turbulence model (Fluent 2001 [DIRS 164453], Section 10.4.1). It differs from the base case turbulence model by not including a mean rate-of-strain term in the ε-equation. It also does not include a means of accounting for low-Reynolds-number impacts on the turbulent viscosity. Unlike the base case turbulence model, the turbulent Prandtl number used in this turbulence model is constant. Finally, Case R10 uses a standard k-ω turbulence model (Fluent 2001 [DIRS 164453], Section 10.5.1). Like the base case turbulence model, the k-ω model includes a low-Reynolds-number correction for the turbulent viscosity. This turbulence model is similar to the base case model; however, it is written in terms of a specific dissipation rate (ω) instead of the dissipation rate of turbulent kinetic energy. The specific dissipation rate can be thought of as the ratio of the dissipation rate of turbulent kinetic energy to the turbulent kinetic energy.

Case R11

This case includes a participating fluid medium in the radiation intensity transport equation. The base case did not implement a participating gas. In this case, the fluid domain in the emplacement drift cavity participates in the thermal radiation occurring between walls. It contains pressure-corrected components for both H_2O and CO_2 at a temperature of 350 K. The participating fluid medium can both absorb and emit radiant energy. The fluid absorptivity for this case, as discussed in Section 4.1.2, was 0.17 m^{-1}.

Cases R12 through R15

Case R12 applies a maximum emissivity of 1.0 (e.g., black body thermal radiation) for the waste package surface (Alloy 22). Case R13 applies a minimum emissivity of 0.74 for the waste package surface where the emissivity of Inconel X, whose surface condition was listed "as received and cleaned," at the lowest temperature for which data are presented (~1500ºF) is used as a surrogate for Alloy 22 (Wood et al. 1964 [DIRS 164664], p. 118). Case R14 uses a maximum emissivity of 1.0 for the drip shield surface (titanium). Case R15 assumes a minimum emissivity of 0.54 for the drip shield surface at the lowest temperature for which data are presented, (~1400ºF) (Wood et al. 1964 [DIRS 164664], p. 36).

Worst Case

One additional case is also examined. It is the worst-case combination of effects considered in this CFD analysis. Instead of changing one variable in this simulation, five variables are changed in the direction expected to produce the highest peak waste package surface temperature. This involved running the low invert thermal conductivity, the RSM, gas participation, and low emissivities for the waste package and drip shield.

Results

The results of the sensitivity simulations are found in Table 6.1.7-1 below. The variation in invert and waste package thermal conductivity resulted in peak waste package temperature changes of less than 0.1 K. The peak temperature rose only 0.1 K for the lower invert thermal conductivity and when the Reynolds Stress Turbulence model was selected. The largest increase in peak temperature was 0.7 K when the waste package emissivity was reduced to 0.54. When each of the settings was changed to maximize waste package temperatures, the peak temperature rose 1.4 K.

The results show that the waste package surface temperatures are not changed significantly by the uncertainty in input parameters into the natural convection simulations. Because the thermally driven flow and the surface temperatures are linked, the change in waste package thermal temperatures should not change the flow fields and, consequently, the dispersion coefficient.

The results from this study that are used in the three-dimensional simulations refer to the turbulence model and thermal radiation. Based on the present results, the RNG k-ε turbulence model is appropriate for the three-dimensional in-drift simulations. The influence of the various turbulence models is small as shown in Table 6.1.7-1. In addition, thermal radiation in the drift does not need to simulate the gas as a participating medium. The impact of treating the gas as a participating medium is well within the uncertainty of other parameters such as the emissivity of various surfaces.

Table 6.1.7-1. Two-Dimensional YMP Geometry Sensitivity Studies Results

CFD Case	Emissivity of Host Rock and Invert	Emissivity of Drip Shield	Emissivity of waste Package	Thermal Conductivity of Waste Package (W/m-K)	Thermal Conductivity of Invert (W/m-K)	Turbulence Model	Absorption Coefficient α (m^{-1})	Average Waste Package Surface Temperature (K)	Peak Waste Package ΔT (K)
BC1	0.9	0.63	0.87	1.5	0.2	RNG k-ε	0	355.49	-
R2	0.88	0.63	0.87	1.5	0.2	RNG k-ε	0	355.51	0.0
R3	0.95	0.63	0.87	1.5	0.2	RNG k-ε	0	355.44	0.0
R4	0.9	0.63	0.87	1.0	0.2	RNG k-ε	0	355.50	0.0
R5	0.9	0.63	0.87	2.0	0.2	RNG k-ε	0	355.48	0.0
R6	0.9	0.63	0.87	1.5	0.18	RNG k-ε	0	355.57	0.1
R7	0.9	0.63	0.87	1.5	0.22	RNG k-ε	0	355.40	-0.1
R8	0.9	0.63	0.87	1.5	0.2	RSM	0	355.54	0.1
R9	0.9	0.63	0.87	1.5	0.2	Standard k-ε	0	355.50	0.0
R10	0.9	0.63	0.87	1.5	0.2	k-ω	0	355.51	0.0
R11	0.9	0.63	0.87	1.5	0.2	RNG k-ε	0.17	355.66	0.2
R12	0.9	0.63	1.0	1.5	0.2	RNG k-ε	0	355.17	-0.3
R13	0.9	0.63	0.74	1.5	0.2	RNG k-ε	0	355.90	0.4
R14	0.9	1.0	0.87	1.5	0.2	RNG k-ε	0	353.68	-1.8
R15	0.9	0.54	0.87	1.5	0.2	RNG k-ε	0	356.21	0.7
Worst Case	0.9	0.54	0.74	1.5	0.18	RSM	0.17	356.93	1.4

DTN: SN0312T0507803.022.

6.2 THREE-DIMENSIONAL IN-DRIFT CONVECTION SIMULATIONS

6.2.1 Simulation Objectives

The objective of the three-dimensional convection simulations is to predict the heat transfer and fluid flow patterns in a section of a Yucca Mountain drift. As a result of these fluid flow patterns, an effective dispersion coefficient for mass transfer along the drift, both under and outside the drip shield, is evaluated as a function of time and temperature tilt of the rock boundary temperature. This effective dispersion coefficient is used directly in the condensation model discussed in Section 6.3.

6.2.1.1 Problem Statement

Three-dimensional in-drift CFD simulations are developed to determine the temperature and flow field due to variability in waste package heat output and spacing. This simulation domain is 71 m long and includes 14 waste packages of different types. Heat transfer by conduction, turbulent natural convection, and thermal radiation are all included. These simulations calculate the turbulent natural convection flow field in the emplacement drifts and interactions with the emplaced components.

6.2.1.2 Performance Measures Used in Downstream Models or Analyses

The three-dimensional CFD simulations evaluate variabilities in drift component temperatures and fluid flow patterns. The three-dimensional simulations are also used to develop a mass dispersion coefficient, which is used in the condensation model in this report.

6.2.1.3 Inputs

Refer to Section 4.1.2 for inputs required by the three-dimensional drift CFD simulations.

6.2.1.4 Description of How Output Quantities are Used

The three-dimensional CFD simulations provide the dispersion coefficient in the drift, both inside and outside the drip shield, for the condensation model.

6.2.1.5 Direct Use in TSPA System Model

The three-dimensional CFD simulation results are not directly used in the TSPA model.

6.2.2 Features, Events, and Processes Included

The features, events, and processes (FEPs) included in the three-dimensional convection simulations are discussed in Section 6.1.2.

6.2.3 Base-Case Convection Conceptual Model

6.2.3.1 Conceptual Model

The base-case three-dimensional conceptual simulation is discussed in Section 6.1.3.

6.2.3.2 Simulation Assumptions

6.2.3.2.1 Natural Convection In The Drifts Assumes Pure Air Conditions

See Section 6.1.3.2.1 - Natural Convection In The Drifts Assumes Pure Air Conditions.

6.2.3.2.2 Steady-State Conditions

See Section 6.1.3.2.2 - Steady-State Conditions

6.2.3.2.3 Use of Renormalized Group (RNG) k-ε Turbulence Flow Model

Assumption: Turbulence is represented by the RNG k-ε turbulence approach in the three-dimensional convection simulations.

Rationale: A number of different turbulence models can be applied when solving turbulent flow fields. The RNG k-ε is selected for the three-dimensional convection simulations. The two-dimensional convection simulation results in Section 6.1 show a small influence of the turbulence submodel on the convection model results. The primary reasons for using the RNG k-ε turbulence model are that it allows for variation in the turbulent Prandtl number as a function of flow conditions, it provides a means for including low-Reynolds number effects in the effective viscosity formulation, and it includes an extra term, R_ε, in the ε-equation to better model separated flows as discussed in Section 6.1.5.1.1.

Confirmation Status: The assumption does not require further confirmation because it is reasonable engineering submodel for turbulence, and the influence on the results is small as determined by the two-dimensional simulation results shown in Section 6.1.

Use in this Calculation: This assumption is used in each CFD simulation discussed in Sections 6.1.7, 6.2.5.1.1, and 6.4.5.1 with the exception of four cases considered in the two-dimensional sensitivity study.

6.2.3.2.4 Use of the Discrete Ordinates (DO) Thermal Radiation Model and a Nonparticipating Medium

Assumption: Diffuse, gray, thermal radiation is represented by the discrete ordinates (DO) thermal radiation model with air simulated as a nonparticipating medium.

Rationale: Diffuse thermal radiation is a reasonable engineering approach for oxidized surfaces. The gray surface assumption should be reasonable because the surface radiation properties are independent of wavelength over the spectral regions of irradiation and surface emission (e.g., temperatures of emitting and receiving surfaces are similar). The DO model with a nonparticipating medium is used in the three-dimensional convection simulations. The two-dimensional convection simulations evaluated the effect of including the atmosphere as a participating medium and found that the effect was small on the results. Therefore, a nonparticipating medium is appropriate for the three-dimensional convection simulations and for the condensation model.

Confirmation Status: The assumption does not require further confirmation because it is reasonable engineering submodel for thermal radiation, and the influence on the results are small as determined by the two-dimensional simulation results shown in Section 6.1.

Use in this Calculation: This assumption is used in the CFD simulations discussed in Sections 6.1.5.1.2 and 6.2.5.1.2 except for some cases in the two-dimensional sensitivity study simulations.

6.2.3.2.5 Conduction-Only in the Surrounding Host Rock

See Section 6.1.3.2.3 Conduction-Only Heat Transfer in the Surrounding Host Rock and Invert

6.2.3.2.6 Use of Constant Thermophysical Properties of the Introduced Materials in the Drift

See Section 6.1.3.2.4 - Use of Constant Thermophysical Properties of the Introduced Materials in the Drift.

6.2.3.2.7 Neglect of Barometric Pumping

See Section 6.3.3.2.4 – Neglect of Barometric Pumping - for a discussion of this assumption.

6.2.3.2.8 Use of a Non-Buoyant Trace Gas to Evaluate Dispersion Coefficient

Assumption: A non-buoyant trace gas is employed in the dispersion calculations to calculate the dispersion of water vapor in the condensation model.

Rationale: A neutrally-buoyant trace gas (air) is used so that the calculated dispersion coefficient is only that due to air movement inside the drift and not due to buoyancy effects. It is recognized that in the actual situation, a buoyant gas (water vapor) will be dispersed along the drift, and that the dispersion coefficient will likely be a function of the mass fraction of water vapor. However, as shown in the Rationale for Assumption 6.1.3.2.1, Natural Convection in the Drifts Assumes Pure Air Conditions, the difference in Rayleigh number for air and water vapor under natural convection conditions is small. If a buoyant gas were considered, the dispersion coefficient would likely increase. Ignoring this augmentation of the dispersion coefficient is conservative in the condensation model because a larger value of the dispersion coefficient will decrease local condensation rates.

Confirmation Status: This assumption is conservative and requires no further confirmation.

Use in this Calculation: This assumption is used in Section 6.2.7.

6.2.4 Consideration of Alternative Conceptual Models for In-Drift Natural Convection

The alternate conceptual models are discussed in Section 6.1.4.

6.2.5 Formulation for the Base-Case Convection Model

The nomenclature is given in Section 6.1.5.

6.2.5.1 Mathematical Description of the Base-Case Conceptual Model

The mathematical description is given in Section 6.1.5.1.

6.2.5.1.1 Turbulence Modeling

The general features of the turbulence modeling are discussed in Section 6.1.5.1.1. Based on the two-dimensional sensitivity studies presented in Section 6.1, the RNG k-ε turbulence model is appropriate and has been selected for the three-dimensional convection simulations.

6.2.5.1.2 Thermal Radiation Modeling

The general features of thermal radiation modeling are discussed in Section 6.1.5.1.2. Based on the two-dimensional sensitivity studies presented in Section 6.1, the gas is treated as a non-participating medium. In fact, the default absorbtivity of 0.01 m^{-1} has been used in the simulations as discussed in Section 6.1.5.1.2. Based on the two-dimensional sensitivity results where an absorbtivity of 0.17 m^{-1} is used, this default value results in essentially the same results as treating the gas as a non-participating medium.

6.2.5.1.3 Boundary Conditions

The domain for the three-dimensional in-drift CFD simulations is a half-cylinder 15.5 m in diameter including the rock. A shell of host rock five meters thick is on the outer surface of the cylinder. An illustration of the simulation geometry is found in Figure 6.2.5-1. To reduce computational costs, only half of the drift is simulated. A symmetry plane is located through the center of the drift. For the three-dimensional simulations, the domain is 71 meters long and contains 13 full waste packages and two half-packages. Due to computational restrictions on the number of elements, the variability in waste package diameters is not included in the three-dimensional simulations. Instead, the waste packages have a uniform diameter of 1.644 meters, which corresponds to the diameter of the most common waste package in the repository – the 21-PWR (see Table 4.1.2-5).

Figure 6.2.5-2 illustrates the boundary conditions for the three-dimensional natural convection simulations. To create a mass gradient needed to calculate a dispersion coefficient, a second air component, air2, is incorporated into the simulations. This second air component is assigned the same properties as air. At the symmetry plane, symmetry boundary conditions (no heat flux, no flow, and velocity slip) are specified. The inner and outer air boundaries on the two ends of the simulation are walls with constant mass fraction of air2, no heat flux, and no flow. For the solid materials at the end of the domain (invert, host rock, and waste packages), a no-heat-flux and no flow boundary condition is specified.

For the waste package, invert, and the host rock, a no-heat-flux boundary condition is imposed on the centerline symmetry faces. For the inner and outer drip shield air volumes, no-heat flux, no-flow, and velocity-slip boundary conditions are imposed on the center-line symmetry face. For the solid-air interfaces, no flow, no-slip boundary conditions are imposed. The FLUENT code balances heat flux at those solid-air interfaces within the simulation. The heat is introduced

into the simulation through a volumetric heat generation rate inside the waste packages. Heat is removed from the simulation as a result of the constant temperature boundary condition imposed.

Specification of no-flow boundaries at the ends minimizes the axial movement of air and water vapor, and these boundary conditions minimize the resulting axial dispersion coefficient. Similar to other assumptions used in this report (neglect of barometric pumping and repository natural circulation), this set of boundary conditions is conservative (see Section 6.2.3.2.7).

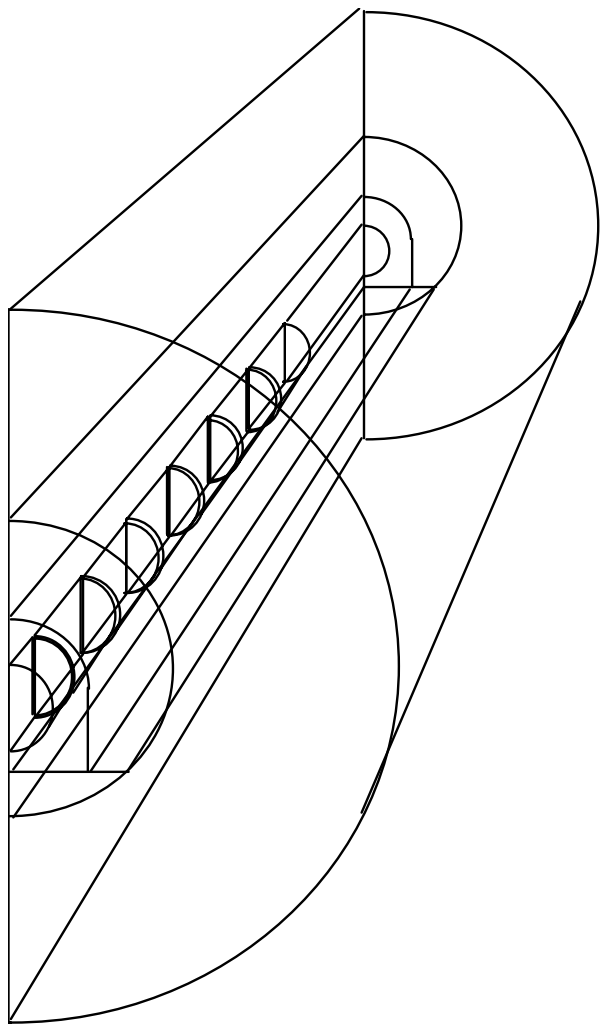

NOTE: Not to scale and all waste packages not shown.

Figure 6.2.5-1. Schematic Diagram of Geometry of the Three-Dimensional Natural Convection Simulations

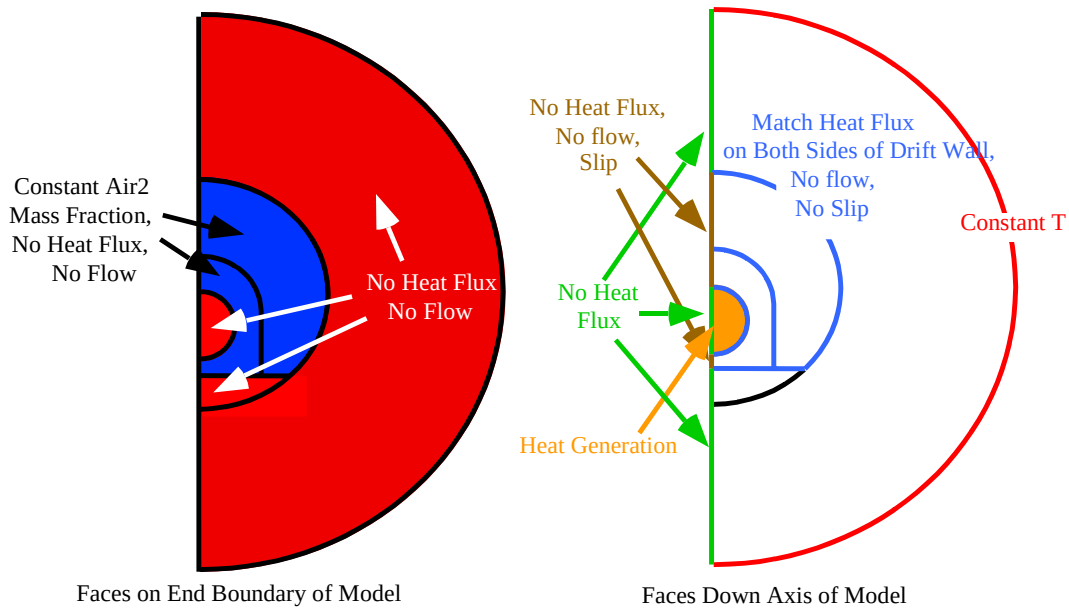

Figure 6.2.5-2. Boundary Conditions Imposed on the Three-Dimensional Natural Convection Simulations

The boundary conditions on the ends of the domain are on the left of Figure 6.2.5-2 and those on the faces down the drift are on the right of Figure 6.2.5-2.

A total of eight simulations are performed to calculate the drift dispersion coefficients. The boundary conditions are shown below in Table 6.2.5-1 for the four simulation times of 300, 1,000, 3,000, and 10,000 years. Temperatures vary linearly from one end of the domain to the other and are different at each time. The temperature tilt values are based on line source solutions as given by the condensation model (Table 6.3.5-1). The waste package thermal output is also different as summarized in Tables 6.2.5-2 through 6.2.5-5. Selection of 350 K (77ºC) as the mean temperature for all eight simulations is not significant. A constant mean temperature is appropriate because evaporation and condensation mechanisms are not considered. Therefore, the actual mean temperature is not significant as along as it is a reasonable value. By not varying the mean temperature for these simulations, more direct comparisons between cases are possible.

Table 6.2.5-1. Five-Meter Boundary Conditions for the Three-Dimensional CFD Simulations

Case	Temperature (Z=0 meters) (K)	Temperature (Z=71 meters) (K)	Product Output DTN
300 Year	350.0	350.0	SN0406T0507803.025
1,000 Year	350.0	350.0	
3,000 Year	350.0	350.0	
10,000 Year	350.0	350.0	
300 Year - Variable	348.0	352.0	
1,000 Year - Variable	348.5	351.5	
3,000 Year - Variable	349.0	351.0	
10,000 Year - Variable	349.5	350.5	

Thermal radiation is calculated inside of the air domains. The surface radiation emissivities used in the three-dimensional CFD simulations are shown in Table 4.1.2-1.

In order to simulate the changing thermal environment as a function of time, the heat flux into each waste package decreases as the nuclear material in the waste packages decays. The quantity of heat input into the simulation is based on the power output listed in Table 4.1.2-4.

6.2.5.1.4 Initial Conditions

The CFD simulations are run in steady-state mode so initial conditions are not specified.

6.2.5.2 Base-Case Inputs

Geometry

The three-dimensional in-drift simulations require geometry information, thermal properties for the solids and air, radiation emission properties for the surfaces, and power input.

The geometric information used in the simulations is listed in Table 4.1.2-5 of this report. This table contains the relevant drift cross-section information. The simulation domain is presented graphically in the Figure 6.2.5-1. The drift segment is based on *D&E / PA/C IED Typical Waste Package Components Assembly* (BSC 2004 [DIRS 167754], Table 12). The representative drift segment described in the design document contains six full and two half packages in the following order: ½ 21-PWR, 5-HLW-Long, 21-PWR, 44-BWR, 44-BWR-Adjusted, 5-HLW-Short, 21-PWR, and ½ 44-BWR. The representative drift segment is reflected on the 44-BWR side of the segment to create the FLUENT domain that contains 13 full waste packages with two half-packages (21-PWR) at the ends. Due to computational restrictions on the number of elements, the variability in waste package diameters is not included. Instead, all of the waste packages had a diameter of 1.644 m, which corresponds to the diameter of the most common waste package in the repository – the 21-PWR (see Table 4.1.2-5).

The FLUENT mesh is shown in Figure 6.2.5-3. The mesh consists of about 4.0 million cells including the surrounding rock.

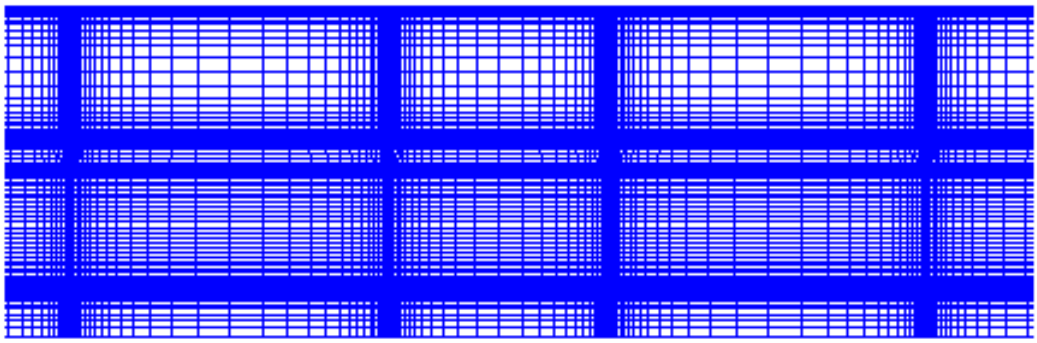

(a) Side View of Symmetry Plane Showing Three Full Waste Packages

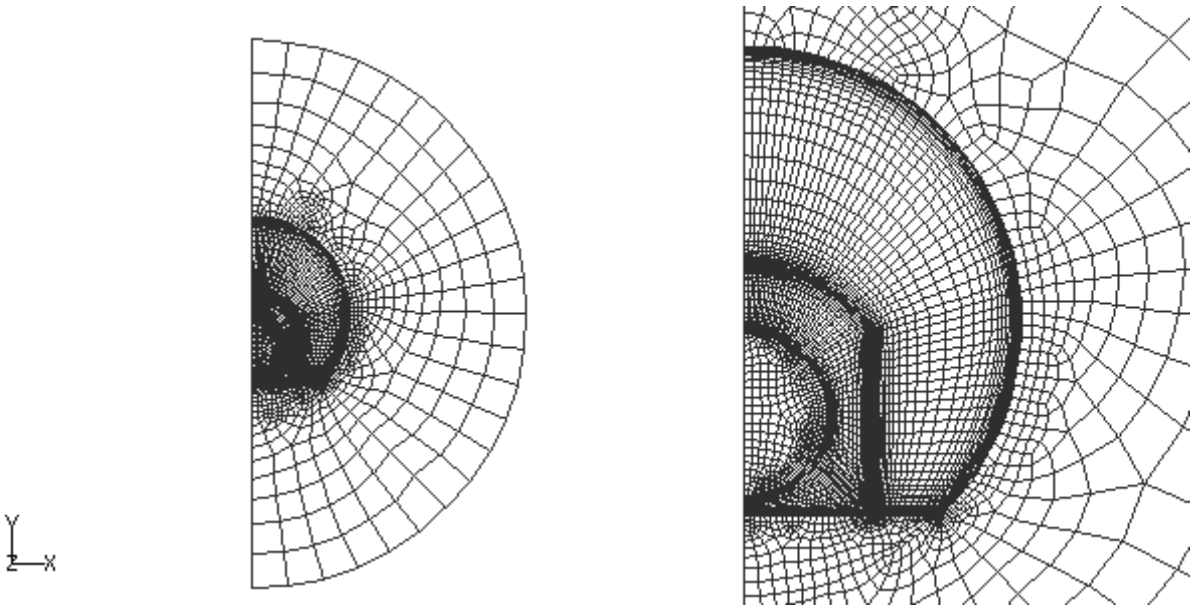

(b) End View - Total Grid (b) End View - In-Drift Region

DTN: SN0312T0507803.022.

Figure 6.2.5-3. Computational Grid for the Two-Dimensional In-Drift Convection Simulations

The units for volumetric heat generation input values for FLUENT are W/m^3. To achieve this, the power per package listed in Table 4.1.2-4 is converted to Watts and is divided by the volume of each waste package. Tables 6.2.5-2 through 6.2.5-5 contain the information needed to calculate the power generation for the waste packages for 300, 1,000, 3,000, and 10,000 years. The heater power for the middle 44-BWR has been multiplied by two to account for it being a full waste package in the simulated segment rather than a half package in the representative segment. The values input to the simulations are shown in the final column. Significant figures to the third decimal place are retained for all waste packages in the simulations.

Table 6.2.5-2. Information Needed to Calculate the Power Density Needed for Three-Dimensional Natural Convection Simulations at 300 Years

Waste Package Type	Power (W/WP)[a]	Length (m)[b]	Diameter (m)[b]	Volume (m^3)	Power Density (W/m3)
1/2 21-PWR	6.90E+2	2.5825	1.644	5.482	125.868
5-HLW-Long	4.64E+0	5.217	1.644	11.074	0.419
21-PWR	1.41E+3	5.165	1.644	10.964	128.604
44-BWR	8.00E+2	5.165	1.644	10.964	72.967
44-BWR-Adj	8.58E+2	5.165	1.644	10.964	78.257
5-HLW-Short	3.18E+1	3.590	1.644	7.621	4.173
21-PWR	1.38E+3	5.165	1.644	10.964	125.868
44-BWR	8.00E+2	5.165	1.644	10.964	72.967
21-PWR	1.38E+3	5.165	1.644	10.964	125.868
5-HLW-Short	3.18E+1	3.590	1.644	7.621	4.173
44-BWR-Adj	8.58E+2	5.165	1.644	10.964	78.257
44-BWR	8.00E+2	5.165	1.644	10.964	72.967
21-PWR	1.41E+3	5.165	1.644	10.964	128.604
5-HLW-Long	4.64E+0	5.217	1.644	11.074	0.419
1/2 21-PWR	6.90E+2	2.5825	1.644	5.482	125.868

[a] Source: Table 4.1.2-4.
[b] Source: Table 4.1.2-5.

Table 6.2.5-3. Information Needed to Calculate the Power Density Needed for Three-Dimensional Natural Convection Simulations at 1,000 Years

Waste Package Type	Power (W/WP)[a]	Length (m)[b]	Diameter (m)[b]	Volume (m^3)	Power Density (W/m3)
1/2 21-PWR	2.92E+2	2.5825	1.644	5.482	53.266
5-HLW-Long	2.50E+0	5.217	1.644	11.074	0.226
21-PWR	5.99E+2	5.165	1.644	10.964	54.634
44-BWR	3.56E+2	5.165	1.644	10.964	32.470
44-BWR-Adj	3.72E+2	5.165	1.644	10.964	33.930
5-HLW-Short	5.70E+0	3.590	1.644	7.621	0.748
21-PWR	5.85E+2	5.165	1.644	10.964	53.357
44-BWR	3.56E+2	5.165	1.644	10.964	32.470
21-PWR	5.85E+2	5.165	1.644	10.964	53.357
5-HLW-Short	5.70E+0	3.590	1.644	7.621	0.748
44-BWR-Adj	3.72E+2	5.165	1.644	10.964	33.930
44-BWR	3.56E+2	5.165	1.644	10.964	32.470
21-PWR	5.99E+2	5.165	1.644	10.964	54.634
5-HLW-Long	2.50E+0	5.217	1.644	11.074	0.226
1/2 21-PWR	2.92E+2	2.5825	1.644	5.482	53.266

[a] Source: Table 4.1.2-4.
[b] Source: Table 4.1.2-5.

Table 6.2.5-4. Information Needed to Calculate the Power Density Needed for Three-Dimensional Natural Convection Simulations at 3,000 Years

Waste Package Type	Power (W/WP)[a]	Length (m)[b]	Diameter (m)[b]	Volume (m^3)	Power Density (W/m3)
1/2 21-PWR	1.21E+2	2.5825	1.644	5.482	22.073
5-HLW-Long	1.79E+0	5.217	1.644	11.074	0.162
21-PWR	2.47E+2	5.165	1.644	10.964	22.529
44-BWR	1.61E+2	5.165	1.644	10.964	14.685
44-BWR-Adj	1.60E+2	5.165	1.644	10.964	14.593
5-HLW-Short	3.11E+0	3.590	1.644	7.621	0.408
21-PWR	2.42E+2	5.165	1.644	10.964	22.073
1/2 44-BWR	1.606E+2	5.165	1.644	10.964	14.648
21-PWR	2.42E+2	5.165	1.644	10.964	22.073
5-HLW-Short	3.11E+0	3.590	1.644	7.621	0.408
44-BWR-Adj	1.60E+2	5.165	1.644	10.964	14.593
44-BWR	1.61E+2	5.165	1.644	10.964	14.685
21-PWR	2.47E+2	5.165	1.644	10.964	22.529
5-HLW-Long	1.79E+0	5.217	1.644	11.074	0.162
1/2 21-PWR	1.21E+2	2.5825	1.644	5.482	22.073

[a] Source: Table 4.1.2-4.
[b] Source: Table 4.1.2-5.

Table 6.2.5-5. Information Needed to Calculate the Power Density Needed for Three-Dimensional Natural Convection Simulations at 10,000 Years

Waste Package Type	Power (W/WP)[a]	Length (m)[b]	Diameter (m)[b]	Volume (m^3)	Power Density (W/m3)
1/2 21-PWR	7.20E+1	2.5825	1.644	5.482	13.134
5-HLW-Long	1.42E+0	5.217	1.644	11.074	0.128
21-PWR	1.47E+2	5.165	1.644	10.964	13.408
44-BWR	9.42E+1	5.165	1.644	10.964	8.592
44-BWR-Adj	9.51E+1	5.165	1.644	10.964	8.674
5-HLW-Short	2.21E+0	3.590	1.644	7.621	0.290
21-PWR	1.44E+2	5.165	1.644	10.964	13.134
44-BWR	9.42E+1	5.165	1.644	10.964	8.592
21-PWR	1.44E+2	5.165	1.644	10.964	13.134
5-HLW-Short	2.21E+0	3.590	1.644	7.621	0.290
44-BWR-Adj	9.51E+1	5.165	1.644	10.964	8.674
44-BWR	9.42E+1	5.165	1.644	10.964	8.592
21-PWR	1.47E+2	5.165	1.644	10.964	13.408
5-HLW-Long	1.42E+0	5.217	1.644	11.074	0.128
1/2 21-PWR	7.20E+1	2.5825	1.644	5.482	13.134

[a] Source: Table 4.1.2-4.
[b] Source: Table 4.1.2-5.

Properties

The air properties used in the FLUENT simulations are listed in Table 4.1.2-3. The air properties are linearly interpolated between temperatures by the code. The fluid density is computed internally by FLUENT (Fluent 2001 [DIRS 164453], Equation 7.2-5), using the incompressible-ideal-gas law as discussed in Section 6.1.5.2. The simulations use radiation emissivities and constant material thermal conductivities of the introduced materials as given in Table 4.1.2-2.

The thermal properties are listed in Table 4.1.2-1. The measured invert thermal conductivity has a range of 0.14 to 0.17 W/m-K for dry material. The invert thermal conductivity is rounded up to a value of 0.2 W/m-K to approximately account for greater thermal conductivity of wet material. This value is the same as reported in Table IV-9 in *Multiscale Thermohydrologic Model* (BSC 2004 [DIRS 169565]).

The measured invert density and specific heat listed in Table 4.1.2-1 have a range based on the data. These data are averaged, and the resulting average values of invert density and specific heat used in these simulations are 1.27 g/cm^3 (50 samples) and 0.93 J/cm^3-K (11 samples). These average values and the data used for averaging are the same as reported in Tables IV-8 and IV-9 in *Multiscale Thermohydrologic Model* (BSC 2004 [DIRS 169565]). Note that because the three-dimensional simulations are run in the steady-state mode as discussed in Section 6.2.5.1.4, the density and specific heat properties do not affect the final converged solution.

Operating Conditions

The three-dimensional simulations are run at an operating pressure of 89.05 kPa. The data used to linearly interpolate the operating pressure are listed in Table 4.1.2-6. This corresponds to the standard atmospheric pressure at 1,080 meters elevation. The elevations for the repository drifts range from 1,039 to 1,107 meters (See Table 4.1.2-5). The gravitational constant is specified in each of the simulations as 9.81 m/s^2 (Table 4.1.1-2).

6.2.5.3 Summary of the Computational Simulations

The summary of the computational simulations is discussed in Section 6.1.5.3.

6.2.6 Formulation for Alternative Conceptual Models for In-Drift Natural Convection

The Alternate Conceptual Models are discussed in Section 6.1.6.

6.2.7 Three-Dimensional Dispersion Calculations

For calculation of the dispersion coefficient, the heat transfer and fluid flow portion of the simulation is run until the conditions are at steady state. Simulations are run at 300, 1,000, 3,000, and 10,000 years, accounting for time-varying waste package power generation rates. A pair of simulations is run at each time period to evaluate the effect of the rock boundary temperature variation along the drift, or temperature tilt. The outer boundary of the domain is either set to a uniform value of 350 K (zero tilt) or a linear variation in temperature from one end of the domain to the other end to represent the variation in temperatures expected in the drifts.

This linear variation is given in Table 6.3.5-1 as generated in the condensation model. The variation over the 71-m length of the simulated drift is 4°C (348 to 352 K boundary values) for the 300-year simulation, 3°C (348.5 to 351.5 K) for the 1,000-year simulation, 2°C (349 to 351 K) for the 3,000-year simulation, and 1°C (349.5 to 350.5 K) for the 10,000 year simulation. The average boundary temperature for all eight cases was kept at 350 K to allow direct comparison between the four times simulated.

To calculate a dispersion coefficient, the concentration gradient and flux of a tracer in the gas phase material is used. A second air species (air2) is introduced in the domain and assigned identical physical properties to that of air. The concentration of air2 is 0.01 mass fraction on one side of the drift segment and 0.02 mass fraction on the other side of the drift segment. From continuity, the mass fraction of air is 0.99 and 0.98 because the mass fractions must sum to 1.0 on both surfaces. The choice of using a second air component is made to eliminate mass-based buoyancy effects (Assumption 6.2.3.2.8).

The mass dispersion coefficient, D, is defined using the following relationship for mass flux based on the diffusion equation for stationary coordinates (Bird et al. 1960 [DIRS 103524], p. 502, Equation A, Table 16.2-1) where the diffusing species have equal molecular weights:

$$Q / A = \rho D \nabla C \qquad \text{(Eq. 6.2.7-1)}$$

where Q is the mass flow rate [kg/s], A is the cross section area [m^2], D is the dispersion coefficient [m^2/s], ρ is the density [kg/m^3], and ∇C is the mass fraction gradient [1/m]. Solving for the dispersion coefficient, D:

$$D = Q / (A \rho \nabla C) \qquad \text{(Eq. 6.2.7-2)}$$

Two dispersion coefficients are calculated; one for the region inside the drip shield and one for the region outside the drip shield. The ends of the air regions at the two sides of the domain are thermally insulated, no-slip, constant mass fraction walls. This wall boundary condition is the only option available in Fluent that allows the user to specify the mass fraction of the species. Because the presence of the wall will alter the flow locally, portions of the domain near the wall are not considered in calculating the dispersion coefficients. There are 14 waste packages (13 full- and 2 half-packages) in the domain. They are numbered from 1 to 15 as indicated in Table 6.2.7-1. The location of each waste package is summarized in Table 6.2.7-1.

Table 6.2.7-1. Locations of Waste Packages in the Three-Dimensional Natural Convection Simulations

Waste Package	Numbering	Start Z Location (meter)	Stop Z Location (meter)
½ 21-PWR	1	0.000	2.583
5-HLW-Long	2	2.683	7.900
21-PWR	3	8.000	13.165
44-BWR	4	13.265	18.430
44-BWR-Adj	5	18.530	23.695
5-HLW-Short	6	23.795	27.385
21-PWR	7	27.485	32.650
44-BWR	8	32.750	37.915
21-PWR	9	38.015	43.180
5-HLW-Short	10	43.280	46.870
44-BWR-Adj	11	46.970	52.135
44-BWR	12	52.235	57.400
21-PWR	13	57.500	62.665
5-HLW-Long	14	62.765	67.982
½ 21-PWR	15	68.082	70.664

Source: Table 4.1.2-5.

The air gaps between the third and fourth waste packages and between the twelfth and thirteenth waste packages are used to calculate the dispersion coefficient. These locations are chosen as being far enough from the ends of the domain to avoid end wall effects, yet far enough apart (9 waste packages) to give a representative value of the concentration gradient in the drift. The concentration of air2 used in the calculation of the dispersion coefficient is the volume-averaged concentration in the air gap in between these waste packages. The z-locations for these two air volumes are 13.215 and 57.45 meters, or a difference of approximately 44.2 meters. The magnitude of the mass flow rates of air2 can differ slightly over the length of the domain so the values at either end are averaged to get the mass flow rate, Q. The areas of the inner and outer air regions are reported by FLUENT as 1.838 and 7.897 m^2, respectively. The inner air region does not include the cross section area of the waste package. The density, ρ, is calculated internally by the FLUENT code and corresponds to the volume-averaged density of the volumes inside and outside the drip shield. The equation above can then be written as follows:

$$D = \frac{(Q_{z=0m} + Q_{z=70.6m})}{2} / (A\rho \frac{C_{WP-12/13gap} - C_{WP-3/4gap}}{L_{WP-12/13gap} - L_{WP-3/4gap}}) \qquad \text{(Eq. 6.2.7-3)}$$

where the local value of the concentration, or mass fraction, is a volume-averaged value in the gap between the waste packages. The values under the drip shield consider the volume-averaged value in the gap between the waste packages extended over the entire cross section under the drip shield. The volumes outside the drip shield are an extension of those under the drip shield. The volume-averaged mass fraction values are:

$$C = \frac{\int c\rho \, dV}{\int \rho \, dV} \qquad \text{(Eq. 6.2.7-4)}$$

where c is the local value of the mass fraction, and C is the volume-averaged value.

The variation of the air2 mass fraction, or concentration, along the drift is shown in Figure 6.2.7-1 for the uniform temperature boundary condition. The air2 mass fractions at the location between the waste packages are plotted in this figure. The mass fraction variation along the drift is remarkably similar for the various years and for inside and outside the drip shield. The mass fraction profile is symmetric around the middle of the drift as expected. The one exception is the mass fraction profile under the drip shield at 10,000 years. The reason the mass fraction is lower than the rest of the values is unknown. This behavior did not affect the value of the effective dispersion coefficient as shown in the next paragraph.

The concentration between waste packages varies widely. In some instances, the concentration changes only slightly. In other situations, the change in concentration is much greater. The significant changes in concentration usually occur where two hot packages are next to each other (PWR and/or BWR). The reason for this large increase in concentration is probably due to a rising plume, which under steady-state conditions acts as a significant resistance to gas flow. In actuality, the plume may be unsteady and be a less significant barrier to flow due to the oscillatory nature of the plume.

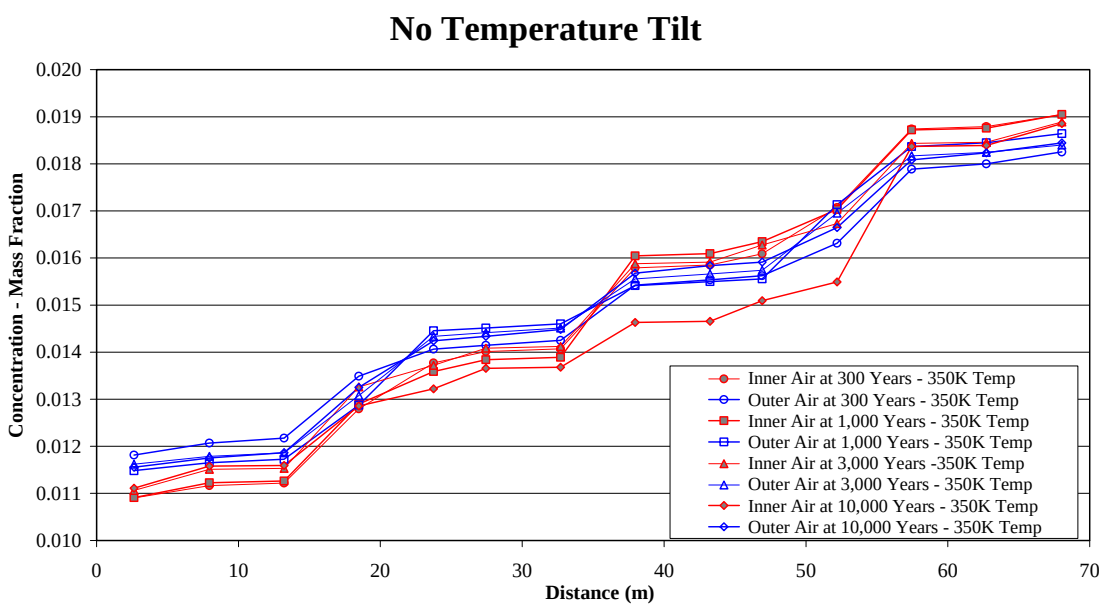

DTN: SN0406T0507803.025.

Figure 6.2.7-1. Cross-Sectionally Averaged Air2 Concentrations with Uniform Boundary Temperature

The output from the four simulations with the uniform temperature boundary condition is shown in Table 6.2.7-2. The inner dispersion coefficient ranges from 0.006 to 0.007 m^2/s for the four runs. The outer dispersion coefficient ranges from 0.004 to 0.008 m^2/s. The diffusion

coefficient for air in an air-vapor mixture at STP is 2.13 x 10^{-5} m^2/s (Pruess 1987 [DIRS 100684], p.6). Therefore, the calculated dispersion coefficients for these runs are several hundred times greater than for pure diffusion.

Table 6.2.7-2. Results for Three-Dimensional Drift-Scale Natural Convection Simulations with a Uniform 350 K Boundary Temperature

	300 Year	**1,000 Year**	**3,000 Year**	**10,000 Year**
WP 3/4 Location (m)	13.215	13.215	13.215	13.215
WP 12/13 Location (m)	57.45	57.45	57.45	57.45
Inner Air Mass Flow Rate at WP 1 (kg/s)	1.8E-06	1.6E-06	1.7E-06	1.6E-06
Inner Air Mass Flow Rate at WP 15 (kg/s)	1.7E-06	1.6E-06	1.7E-06	1.6E-06
Inner Air Mass Fraction at WP 3/4 (kg/kg)	0.0112	0.0113	0.0115	0.0116
Inner Air Mass Fraction at WP 12/13 (kg/kg)	0.0187	0.0187	0.0184	0.0184
Inner Area (m2)	1.838	1.838	1.838	1.838
Average Inner Air Density (kg/m3)	0.841	0.866	0.877	0.881
Inner Dispersion Coefficient (m2/s)	**0.007**	**0.006**	**0.007**	**0.006**
Outer Air Mass Flow Rate at WP 1 (kg/s)	7.3E-06	4.5E-06	4.1E-06	3.5E-06
Outer Air Mass Flow Rate at WP 15 (kg/s)	7.2E-06	4.5E-06	4.1E-06	3.5E-06
Outer Air Mass Fraction at WP ¾ (kg/kg)	0.0122	0.0117	0.0119	0.0119
Outer Air Mass Fraction at WP 12/13 (kg/kg)	0.0179	0.0184	0.0182	0.0181
Outer Area (m2)	7.897	7.897	7.897	7.897
Average Outer Air Density (kg/m3)	0.848	0.869	0.879	0.882
Outer Dispersion Coefficient (m2/s)	**0.008**	**0.004**	**0.004**	**0.004**

DTN: SN0406T0507803.025.

The reason that the dispersion coefficient is higher than the diffusion coefficient is that buoyantly driven circulation cells develop within the domain. Figures 6.2.7-2 and 6.2.7-3 below show the iso-velocity contours for the region underneath the drip shield at one end of the domain for the 300 year simulation. The volume of gas that has a velocity greater than 2 cm/s either up or down the length of the drift is highlighted in the two figures. The locations of the gaps between the waste packages are labeled for clarity. Looking at the final few meters of the results, there is a circulation cell that moves flow towards the end at the bottom of the region and returns the flow towards the center at the top of the region. The end waste package is a hot 21-PWR and the fourteenth package is a cold HLW waste package. The power output of the PWR is over 300 times that of the HLW. Consequently, hot air rises up above the end package and flows toward the colder package. Around the gap in between the thirteenth and fourteenth waste packages, another circulation cell exists but it flows in the opposite direction. The thirteenth waste package is also a hot 21-PWR package, so the hot air rises above the hot package and flows towards the cool package. The twelfth and thirteenth packages are both similar 44-BWR packages so the axial velocities are smaller near those waste packages. This pattern of local re-circulation zones alternating direction exists throughout the drift.

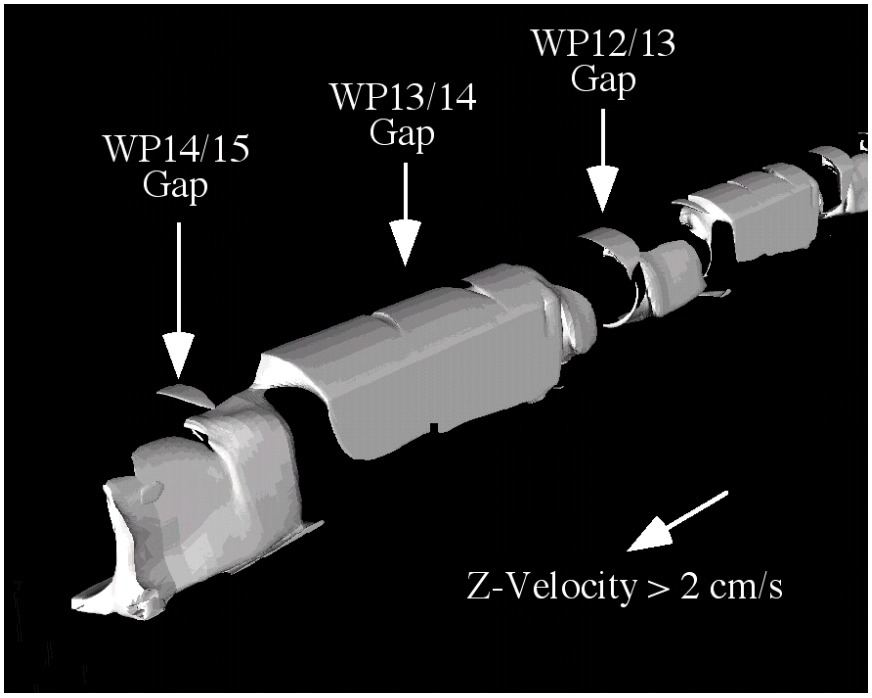

DTN: SN0406T0507803.025.

NOTE: Simulation boundary condition is a uniform 350 K.

Figure 6.2.7-2. Iso-Velocity Contours Underneath the Drip Shield for Velocity Greater than 2 cm/s in the +Z Direction at 300 Years

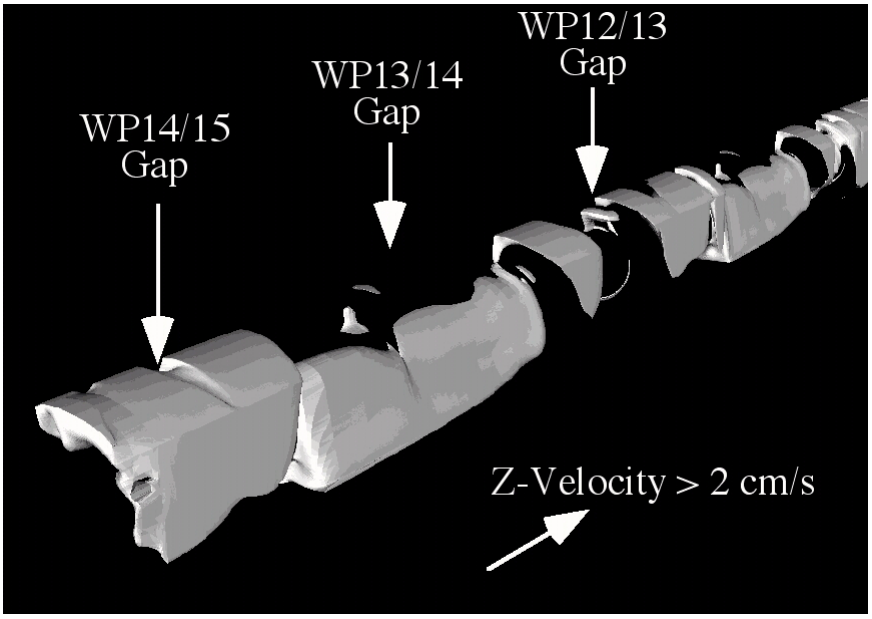

DTN: SN0406T0507803.025.

NOTE: Simulation boundary condition is a uniform 350 K.

Figure 6.2.7-3. Iso-Velocity Contours Underneath the Drip Shield for Velocity Greater than 2 cm/s in the –Z Direction at 300 Years

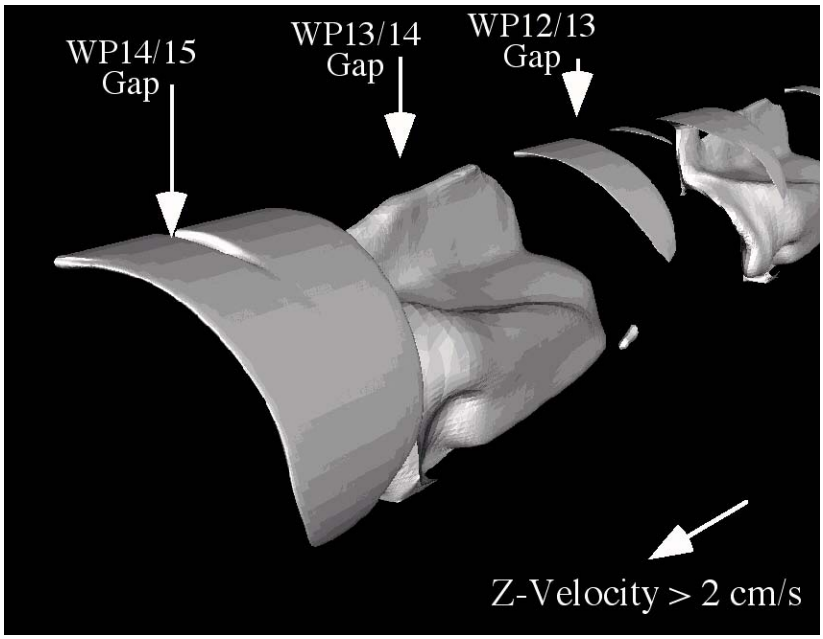

DTN: SN0406T0507803.025.

NOTE: Simulation boundary condition is a uniform 350 K.

Figure 6.2.7-4. Iso-Velocity Contours above the Drip Shield for Velocity Greater than 2 cm/s in the +Z Direction at 300 Years

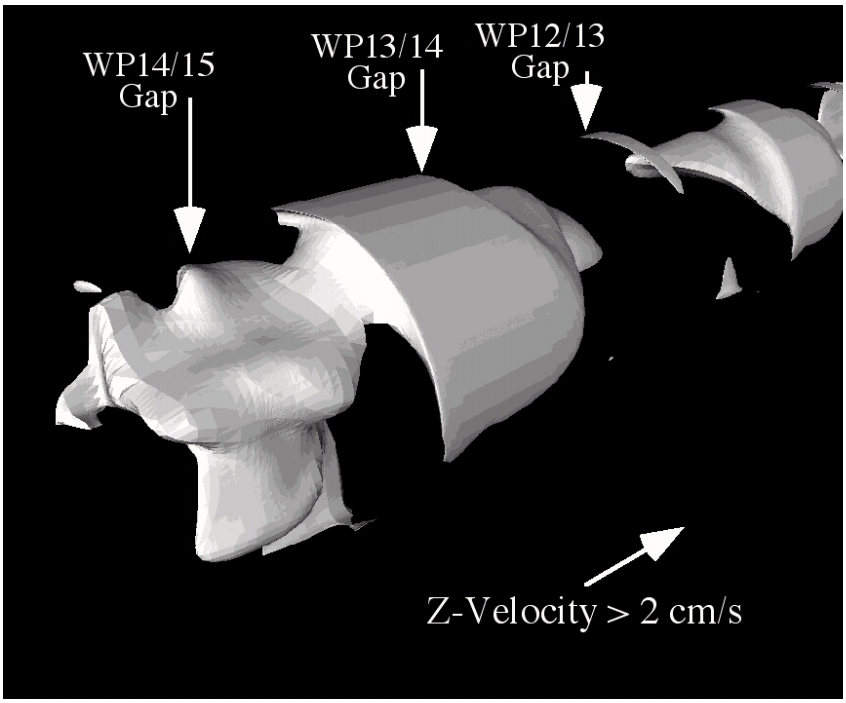

DTN: SN0406T0507803.025.

NOTE: Simulation boundary condition is a uniform 350 K.

Figure 6.2.7-5. Iso-Velocity Contours above the Drip Shield for Velocity Greater than 2 cm/s in the –Z Direction at 300 Years

The iso-velocity contours for the upper air region are shown in Figures 6.2.7-4 and 6.2.7-5. A similar pattern to that seen below the drip shield is seen above the drip shield. A re-circulation zone moves from above WP-15 towards WP-14 and the return flow is closer to the bottom of the outer region. Near the gap between WP-13 and WP-14, a circulation pattern in the opposite direction exists. This pattern continues down the drift.

A second set of four simulations is run at the same four times except with the boundary temperature tilted linearly from one end of the drift segment to the other. This temperature tilt destroys the natural symmetry of the simulation and is a more realistic boundary condition near the edges of the repository, which are expected to be cooler than locations in the center of the repository.

The variation of the air2 mass fraction, or concentration along the drift is shown in Figure 6.2.7-6 for the tilted boundary temperature condition. The mass fraction variation along the drift inside and outside the drip shield is significantly different but consistent with each other for all the simulations. The values are not symmetrical around the center of the drift due to the imposition of temperature tilt in the boundary conditions.

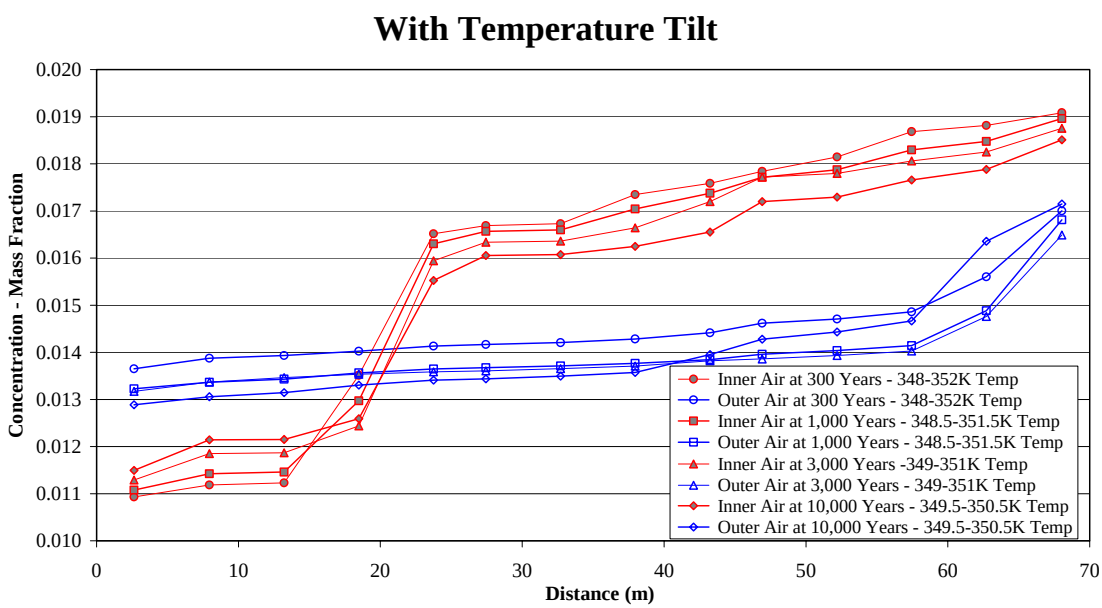

DTN : SN0406T0507803.025.

Figure 6.2.7-6. Cross-Sectionally Averaged Air2 Concentrations with Tilted Boundary Temperature

The simulation results are shown in Table 6.2.7-3. The dispersion coefficients are higher for these cases than for the uniform temperature cases. The inner dispersion coefficients ranged from 0.007 to 0.01 m^2/s while the outer dispersion coefficients ranged from 0.03 to 0.1 m^2/s. The inner values are slightly higher when compared with the previous simulations. The outer values are a few orders of magnitude higher than for the uniform temperature case. Explanation for the different behavior is found by looking at the axial iso-velocity plots for the second set of simulations.

Table 6.2.7-3. Results for Three-Dimensional Drift-Scale Natural Convection Simulations with a Linearly Varying Boundary Temperature

	300 Year	**1,000 Year**	**3,000 Year**	**10,000 Year**
WP 3/4 Location (m)	13.215	13.215	13.215	13.215
WP 12/13 Location (m)	57.45	57.45	57.45	57.45
Inner Air Mass Flow Rate at WP 1 (kg/s)	1.8E-06	1.8E-06	2.0E-06	2.1E-06
Inner Air Mass Flow Rate at WP 15 (kg/s)	1.7E-06	1.8E-06	2.0E-06	2.1E-06
Inner Air Mass Fraction at WP 3/4 (kg/kg)	0.0112	0.0115	0.0119	0.0122
Inner Air Mass Fraction at WP 12/13 (kg/kg)	0.0187	0.0183	0.0181	0.0177
Inner Area (m2)	1.838	1.838	1.838	1.838
Average Inner Air Density (kg/m3)	0.841	0.866	0.877	0.881
Inner Dispersion Coefficient (m2/s)	**0.007**	**0.007**	**0.009**	**0.01**
Outer Air Mass Flow Rate at WP 1 (kg/s)	1.4E-05	1.3E-05	1.2E-05	7.3E-06
Outer Air Mass Flow Rate at WP 15 (kg/s)	1.4E-05	1.3E-05	1.2E-05	7.3E-06
Outer Air Mass Fraction at WP 3/4 (kg/kg)	0.0139	0.0134	0.0135	0.0131
Outer Air Mass Fraction at WP 12/13 (kg/kg)	0.0149	0.0141	0.0140	0.0147
Outer Area (m2)	7.897	7.897	7.897	7.897
Average Outer Air Density (kg/m3)	0.848	0.869	0.879	0.882
Outer Dispersion Coefficient (m2/s)	**0.1**	**0.1**	**0.1**	**0.03**

DTN: SN0406T0507803.025.

The iso-velocity contours for the variable temperature boundary condition cases for the volume below the drip shield at 300 years are shown in Figures 6.2.7-7 and 6.2.7-8. Similar flow patterns are seen here that are also seen in the uniform temperature cases. The flow at the top of the region flows from the tops of hot waste packages towards the tops of cold waste packages. At the bottom of the region, the flow moves from the bottom of cold waste packages towards the bottom of hot waste packages. The alternating re-circulation zones continue down the drift segment.

The iso-velocity contours for the region above the drip shield for the variable boundary simulation at 300 years are shown in Figures 6.2.7-9 and 6.2.7-10. Unlike the other iso-velocity contours, this pair of figures shows one extremely long re-circulation zone. The boundary condition had higher temperatures on the WP-15 side than on the WP-1 side. The flow of air from the cold side to the hot side can be seen in Figure 6.2.7-9. Note that much of the flux occurs in the lower part of the region. The flow from the hot side of the segment to the cold side is shown in Figure 6.2.7-10. Note that the region of flow is predominantly at the top of the region. It is because the flow is more affected by the temperature boundary condition rather than the temperature variability caused by the waste packages that there is one large re-circulation zone rather than many smaller re-circulation zones. The higher dispersion coefficient is a result of this large re-circulation zone.

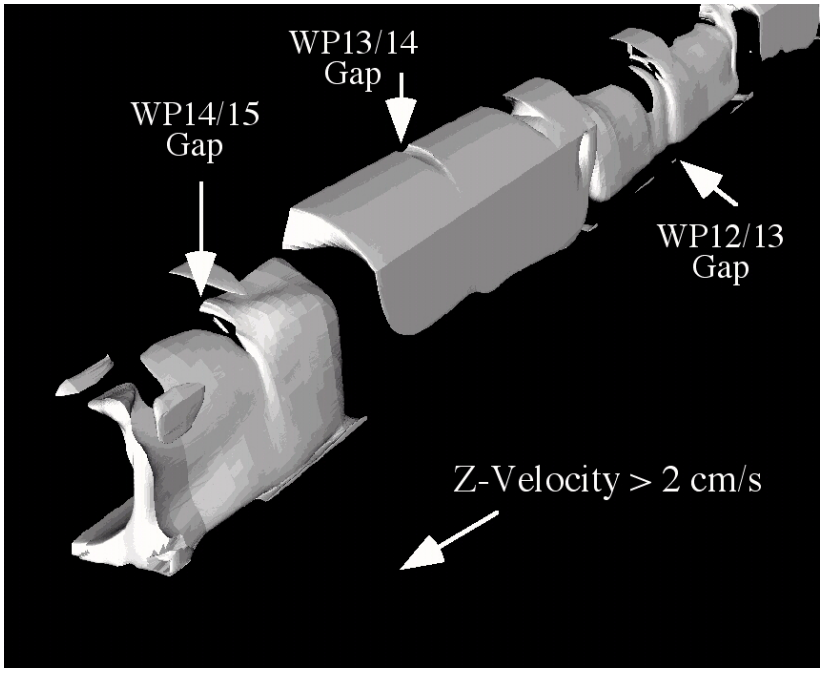

DTN: SN0406T0507803.025.

NOTE: Simulation boundary condition varied linearly from 348 K on WP-1 to 352 K on WP-15.

Figure 6.2.7-7. Iso-Velocity Contours Underneath the Drip Shield for Velocity Greater than 2 cm/s in the +Z Direction at 300 Years

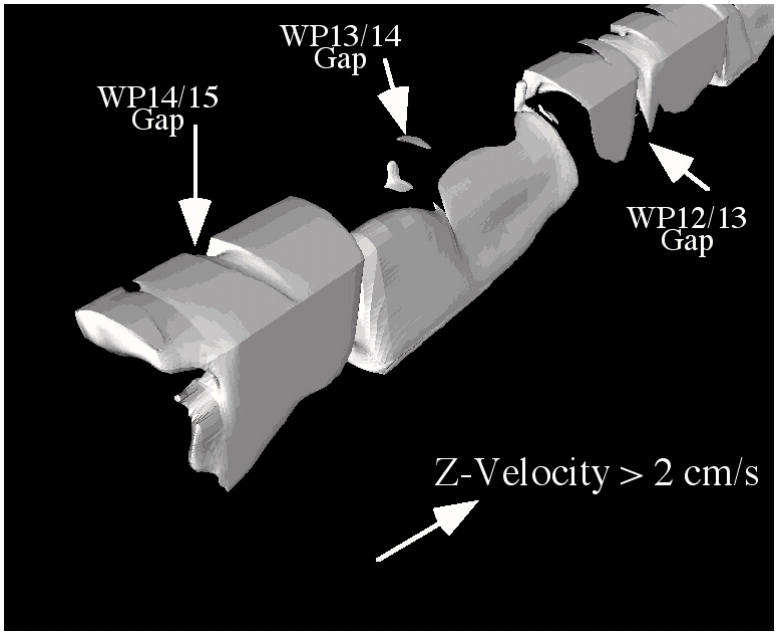

DTN: SN0406T0507803.025.

NOTE: Simulation boundary condition varied linearly from 348 K on WP-1 to 352 K on WP-15.

Figure 6.2.7-8. Iso-Velocity Contours Underneath the Drip Shield for Velocity Greater than 2 cm/s in the –Z Direction at 300 Years

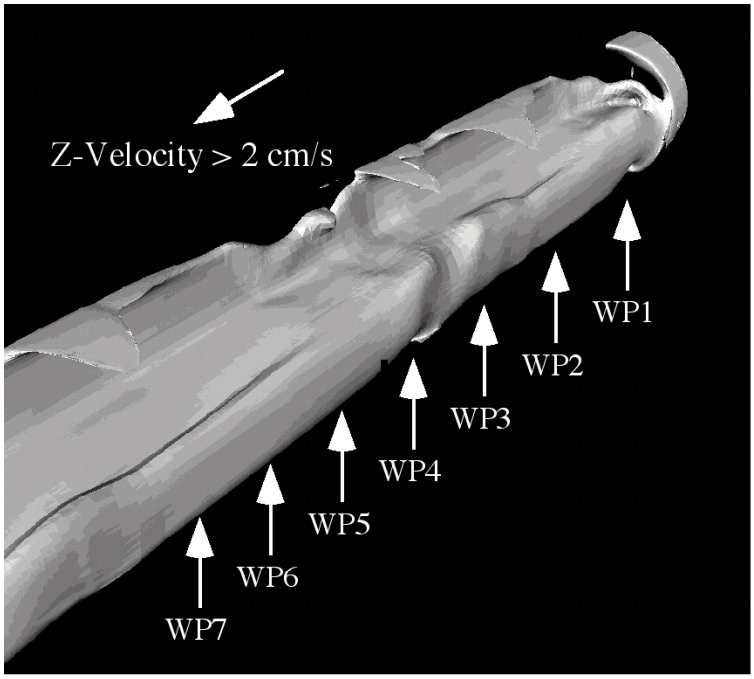

DTN: SN0406T0507803.025.

NOTE: Simulation boundary condition varied linearly from 348 K on WP-1 to 352 K on WP-15.

Figure 6.2.7-9. Iso-Velocity Contours Above the Drip Shield for Velocity Greater than 2 cm/s in the +Z Direction at 300 Years

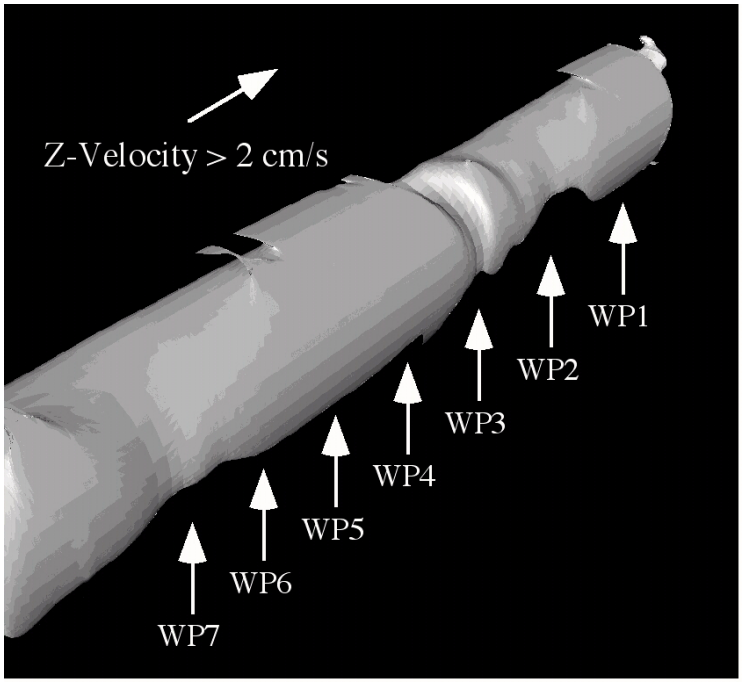

DTN: SN0406T0507803.025.

NOTE: Simulation boundary condition varied linearly from 348 K on WP-1 to 352 K on WP-15.

Figure 6.2.7-10. Iso-Velocity Contours Above the Drip shield for Velocity Greater than 2 cm/s in the –Z Direction at 300 Years

The simulation results show that the dispersion coefficient can vary depending on the size and shape of the re-circulation zones. At center locations of the repository where the temperatures in the rock may be uniform at any particular time, the dispersion coefficient will be several orders of magnitude greater than the diffusion coefficient. At edge locations, temperature gradients caused by edge effects may result in larger dispersion coefficients. Consequently, the actual repository will behave on average somewhere in between the two extremes simulated here, and the simulation results provide reasonable upper and lower bounds for the dispersion coefficient. The range of dispersion coefficients for the inner region is 0.006 to 0.007 m^2/s for a uniform boundary temperature and 0.007 to 0.01 m^2/s with a tilted boundary temperature. The outer region values are much more sensitive to the boundary temperature variation, ranging from 0.004 to 0.008 m^2/s for a uniform boundary temperature to 0.03 to 0.1 m^2/s for tilted boundary temperature.

6.3 IN-DRIFT CONDENSATION MODEL

6.3.1 Modeling Objectives

Temperature-driven vapor migration has been observed in two field tests. Water was observed to accumulate on structures in the Enhanced Characterization of Repository Block (ECRB) Cross Drift after the bulkhead doors had been closed for long periods of time (BSC 2004 [DIRS 170004] Section 6.10.2.2). Extensive logs were kept of the water formation. Dry regions in the drift were located in the vicinity of heat sources; the wet regions in the drift were removed from the heat sources. This is consistent with vapor migration away from the heat source and condensation in a cooler region.

A similar phenomenon was observed in the Drift-Scale Test (Blair et al., 1998 [DIRS 133836], Section 8). Condensate was observed on the cool side of the bulkhead. The apparent source of the water vapor was the heated test region on the hot side of the bulkhead. Again, water vapor appears be migrating from a hot region to a cooler region where it condenses.

Vapor migration in drifts and caves is a commonly observed and documented phenomenon. Stuckless and Toomey (2003 [DIRS 171855]) cite numerous examples in which natural circulation and barometric pumping result in the drying of caves that would otherwise be wet. Such natural analogues suggest that the same vapor transport processes observed in nature will be present in emplacement drifts containing nuclear waste. However, the decay heat produced by the nuclear waste will produce additional thermal and convective flow effects that will interact with these naturally occurring processes.

Condensation on the drift wall in the emplacement regions will have the same effect as drift seepage. It will contribute to the inflow to the EBS and affect the rates of radionuclide releases to the unsaturated zone (UZ). This inflow can flow through the EBS along eight pathways (BSC 2004 [DIRS 169868], Section 6.3.1.1): (1) seepage flux, (2) flux through the drip shield, (3) diversion around the drip shield, (4) flux through the waste package, (5) diversion around the waste package, (6) flux from the waste package into the invert, (7) imbibition flux from the unsaturated zone matrix to the invert, and (8) flux from the invert to the unsaturated zone fractures. These pathways are time dependent because drip shield penetrations, and waste package penetrations will vary with time and local conditions in the repository.

The condensation model describes the phenomena of evaporation of water from the drift wall and invert, transport of water along the drift, and condensation in cooler locations. There are two bounding possibilities for the condensation, or "coldtrap" phenomenon. If the axial transport of vapor is sufficiently high and the amount of water available for evaporation is sufficiently low, the air in the emplacement drifts will have a low humidity, and condensation in the emplacement area will not occur. Alternatively, if the axial transport of vapor is low, the humidity will be higher and local condensation in the emplacement area will be possible.

This calculation answers three questions:

1. Does water condense on the drift walls?
2. Does water condense on the underside of the drip shield?
3. Does water condense on the outside of the drip shield?

NOTE: The condensation model described in this Section (6.3) and the solution technique described in Appendix D are implemented in a collection of Mathcad files. Appendix D, Section D.7, contains a list of these files. The file **TOC.mcd** is a table of contents that is hyperlinked to Mathcad files covering specific topics. To compare the contents of this report to the implementation in the calculation, simply "click" on the appropriate topic in **TOC.mcd**, and the appropriate Mathcad file will be activated.

6.3.1.1 Problem Being Modeled

The condensation model addresses the transport of water vapor within individual emplacement drifts. The domain of the calculation is an individual emplacement drift and the adjacent exhaust standoff and access turnout; seven different emplacement drifts are analyzed. The model is based upon a one-dimensional dispersion formulation in which water that is evaporated from hotter drift wall and invert surfaces is transported axially to cooler surfaces in the emplacement drift where it condenses. The axial dispersion coefficient is taken from the three-dimensional convection model calculations presented in this report (Section 6.2.7).

The drip shield within each emplacement drift partitions the gas into two regions. The two regions (inside and outside the drip shield) combine into common regions in the exhaust standoff and the access turnout. The drift wall and the drip shield provide the thermal boundary conditions for the gas outside the drip shield; the drip shield, invert surface, and waste package surfaces provide the thermal boundary conditions for the gas inside of the drip shield.

Two drip shield bounding cases are considered in this model. The first case is one in which the drip shield completely separates the gas on either side. The second case is one in which the gas regions on either side are completely mixed.

The axial wall temperature profile of the drift is estimated using the analytic solution for line sources arranged according to the LA design. The line source solution does not include the effect of pore water vaporization in the rock. Heat transfer between the solid surfaces (wall, drip shield, invert, and waste package) is calculated using standard natural convection correlations. Surface temperatures (drip shield, invert, and waste package) are computed using these standard heat transfer correlations combined with simple surface-to-surface thermal radiation form factors.

Mass transfer between the inner and outer gas regions and the surfaces is computed using mass transfer correlations that are analogous to the heat transfer correlations. Evaporation from the drift wall and invert surfaces is limited by percolation and capillary pumping in the fractured rock. Condensation is allowed on waste package and drip shield surfaces when the surface vapor pressure drops below the vapor pressure of the adjacent gas. The latent heat of condensation is included in the calculation of these surface temperatures

6.3.1.2 Performance Measures Used in Downstream Models or Analyses

The condensation process model and abstraction are developed in this report, which feeds the TSPA-LA directly (Section 6.3.1.5).

6.3.1.3 Model Inputs

Refer to Section 4.1.3 for inputs required by the condensation calculation.

6.3.1.4 Description of How Model Output Quantities are Used

Model results represent condensation on the drift walls and on the drip shield (outside and inside).

6.3.1.5 Direct Use in TSPA System Model

The condensation calculation results are directly used in the TSPA model. The abstraction is described in detail in Appendices H (ventilated drip shield) and I (unventilated drip shield).

6.3.2 Features, Events, and Processes Included in the Condensation Model

The features, events, and processes included in the condensation model are discussed in Section 6.1.2.

6.3.3 Base-Case Conceptual Condensation Model

6.3.3.1 Conceptual Model

Consider the simple thought experiment in which a pan of water is placed in a room, which is then sealed. The pan of water is kept a few degrees hotter than the walls of the room. Over time, water evaporates from the pan. If there is enough water in the pan, the vapor pressure in the room reaches that associated with the temperature of the walls and water begins to condense on the walls. The evaporation/condensation processes continue until all of the water in the pan has evaporated.

A similar process takes place within the repository emplacement drifts. Water from the rock evaporates from the hotter portions of the drift walls and condense on colder surfaces. Those surfaces may include the drip shield, cold waste packages, and cold portions of the invert and drift wall. The rates of evaporation and condensation determine the relative humidity in the drift, the presence of water on engineered barriers such as the drip shield and waste package, and may affect radionuclide transport through the invert.

The temperature differences that drive this process occur on two different length scales. The current seven package segment (BSC 2004 [DIRS 167754]) calls for waste packages producing the majority of heat to be adjacent to waste packages that produce relatively little heat. This arrangement is assumed in the multiscale model as a means of promoting more uniform thermal condition in the emplacement drifts. Water evaporated in the vicinity of hotter packages can condense near colder packages; this is the "local scale."

At each end of each drift is a section containing no waste packages. One end is the exhaust standoff. This is set to a minimum of 15 m from the end of the waste package to the centerline of the exhaust drift (BSC 2004 [DIRS 171424]). On the other end is the turnout with a radius of 61 m (BSC 2004 [DIRS 171423]). Both of these regions are substantially cooler than the populated portion of the emplacement drift. Vapor from the emplacement area will migrate to these cooler zones and condense. This is the "drift scale." It includes both the "repository-scale" effect of cooling at the outer periphery of the repository, and the cooling effect that occurs due to the unheated drifts interior to the repository.

The relative humidity in the emplacement drifts and the condensation rates in the vicinity of the waste packages are highly dependent on the "drift scale" rate of in-drift axial vapor transport. If the axial vapor transport is sufficiently large, all of the water vapor produced in the heated region will be transported to the unoccupied cold regions at each end of each drift. Conversely, if the axial vapor transport is sufficiently small, the condensation rates will be largely independent of the "drift scale" temperature gradients.

A schematic of the emplacement drift cross section is shown in Figure 6.3.3-1. The major structures consist of the waste package, the drip shield, and the invert. The invert is of particular interest. Because of its low thermal conductivity, the invert is likely to have a surface temperature greater than that of the drip shield. Water at the invert surface is expected to evaporate and condense on the drip shield (CRWMS M&O 2001 [DIRS 152016], Section 6.4) if the vapor pressure at the invert surface exceeds the equilibrium vapor pressure at the drip shield temperature (Section 6.3.3.2.1).

The invert is composed of sand-sized particles derived from the surrounding rock (BSC 2004 [DIRS 169565], Appendix X). The interstices between the particles will be too large to imbibe water from the surrounding rock. However, individual each particle will have the same porosity as the surrounding rock layer and will have a comparable characteristic pore size. Capillary flow is possible within each invert particle; capillary flow from particle to particle is more uncertain.

Figure 6.3.3-2 is a schematic of invert inter-particle contact. One possible mode of water transport across the contact points is by pendular rings of water that might exist at the contact points. Liquid pressure equilibrium requires that the menisci of these rings have the same radii as the largest filled pores inside the invert particles if the particles are not fully saturated. This is a very small radius and the surface roughness of the particles might prevent their formation. Intuitively, one suspects that the rate of capillary pumping in the invert will be less than that in the undisturbed rock. In the absence of definitive measurements to confirm this suspicion, the conservative bound is made for this analysis: capillary pumping in the invert is unimpaired by the discontinuous nature of the particulate that compose the invert. For this bound, the invert surface should rewet at about the same time that the drift walls rewet. This leads to the upper

bound of the first modeling assumption (Section 6.3.3.2.1, high invert transport): the vapor pressure at the invert surface is the equilibrium vapor pressure for the invert surface temperature. This is conservative because it maximizes the evaporation rate at the invert surface and thereby makes more water vapor available for condensation. The lower bound of this assumption (Section 6.3.3.2.1, low invert transport) is that the vapor pressure at the invert surface is the equilibrium vapor pressure for the temperature at the bottom of the invert.

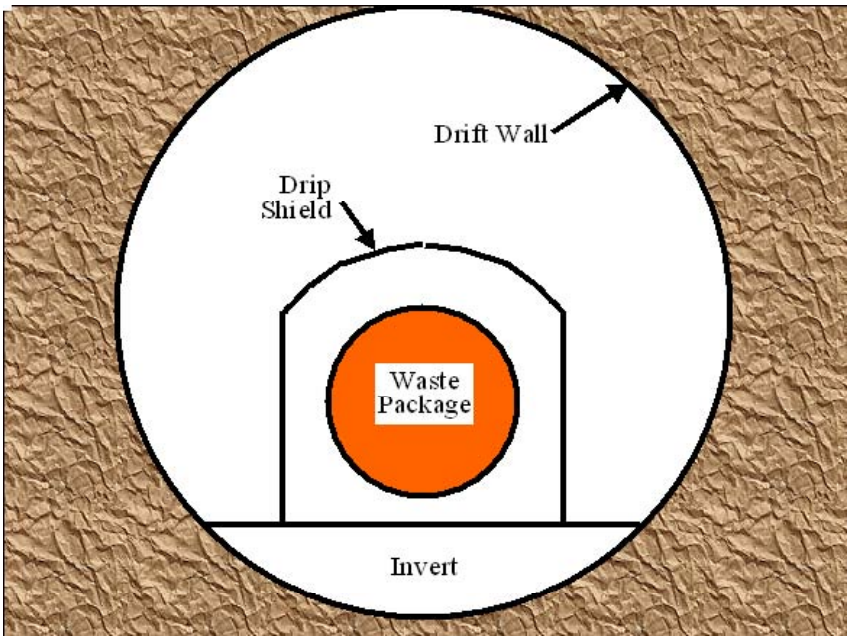

Figure 6.3.3-1. Schematic of the Emplacement Drift Cross Section

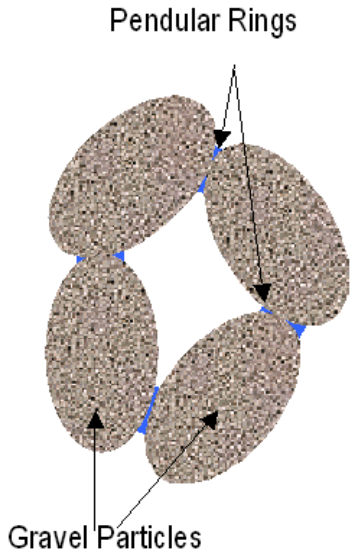

Figure 6.3.3-2. Schematic of Invert Inter-Particle Contact

Another possible source of water under the invert is seepage water that penetrates into the drift. Some of the water may fall onto the invert surface outside of the drip shield. More of the seepage may fall onto the drip shield where it might flow down the side until it reaches the invert immediately outside the vertical wall of the drip shield. Capillary flow through the interstices between the invert particles will cause some of that water to flow laterally, bringing it under the drip shield and, possibly, to the invert surface. The degree of lateral spreading will increase with smaller invert particle sizes (Figure 6.3.3-3). Lateral migration of seepage also motivates the low and high invert transport bounds stated in Section 6.3.3.2.1.

The prediction of moisture migration rates requires quantitative knowledge of the convection pattern in the drift. The convection pattern is governed by the combined effects of natural convection induced by the alternating hot/cold waste package configuration of the current repository design, barometric pumping, and repository-scale natural circulation. Each of these contributors increases the air speed in the drifts, which in turn increases the axial transport of vapor in the drifts.

The simplest and most analytically accessible of these contributors is the inter-package natural convection. The scale of this process is compatible with CFD capabilities and experimental observation produces a basis for the discussion of circulation patterns. Both natural circulation and barometric pumping require a repository-scale analysis that would be more difficult to analyze because of the scale of the phenomena. Therefore, the treatment of air circulation in this report is confined to inter-package natural convection with the expectation that both barometric pumping and natural convection will enhance the axial transport of vapor.

The nature of the two-dimensional annular convective pattern (Figure 6.3.3-4) varies with the temperature difference between the bounding surfaces. Just after incipient gas motion, large roll cells form in the gas. Thermal and viscous boundary layer thicknesses are on the same order as the cavity dimensions. This makes the gas temperature dependent upon location in the cavity. Rising gases above the heat source (i.e., above the waste package and above the top of drip shield) are hotter than descending gases (i.e., along the drip shield sides and the drift walls).

As the driving temperature differences increase, laminar flow instabilities form above the waste package and above the top of the drift shield. The large roll cells begin to divide into smaller cells. These processes begin to homogenize the gas temperatures within the roll cells.

When the driving temperature differences are sufficiently large, the large-scale roll cell structure becomes completely transient. Cell breakdown and oscillation combine to make the bulk of the gas nearly isothermal. Under these conditions, the local heat transfer between a bounding surface and the gas is a function of the local conditions: local wall temperature, wall inclination, and gas temperature.

The deposition of the heat by natural convection on the cooling surfaces is not uniform (Kuehn and Goldstein 1976 [DIRS 156722] and 1978 [DIRS 130084]). Most of the convected heat is carried upward to the top of the drip shield and the drift crown. When the invert surface temperature is less than or equal to the overlying gas temperature, the temperature gradient above the invert favors fluid stability (cold below and warm above). Downward convective heat

transfer below the waste package in this gas zone approaches the conduction limit with little enhancement due to gas motion (Figure 6.3.3-5).

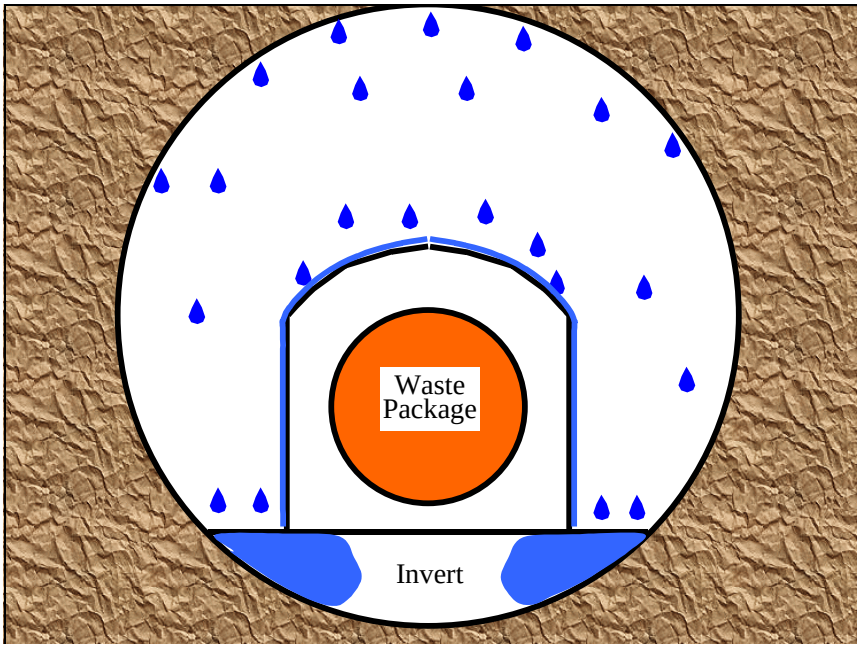

Figure 6.3.3-3. Seepage Migration to the Invert Surface

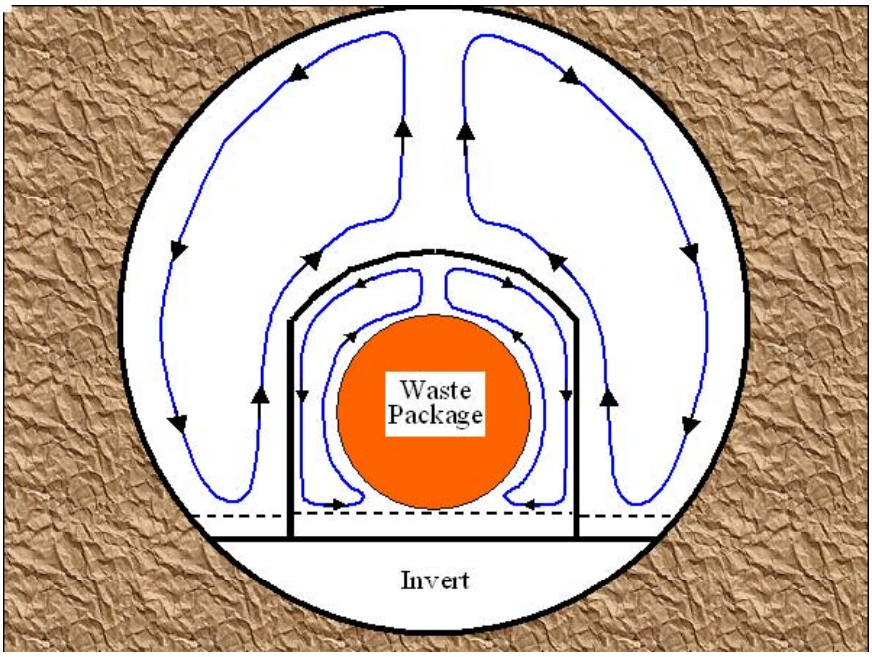

Figure 6.3.3-4. Two-Dimensional Annular Convection Pattern

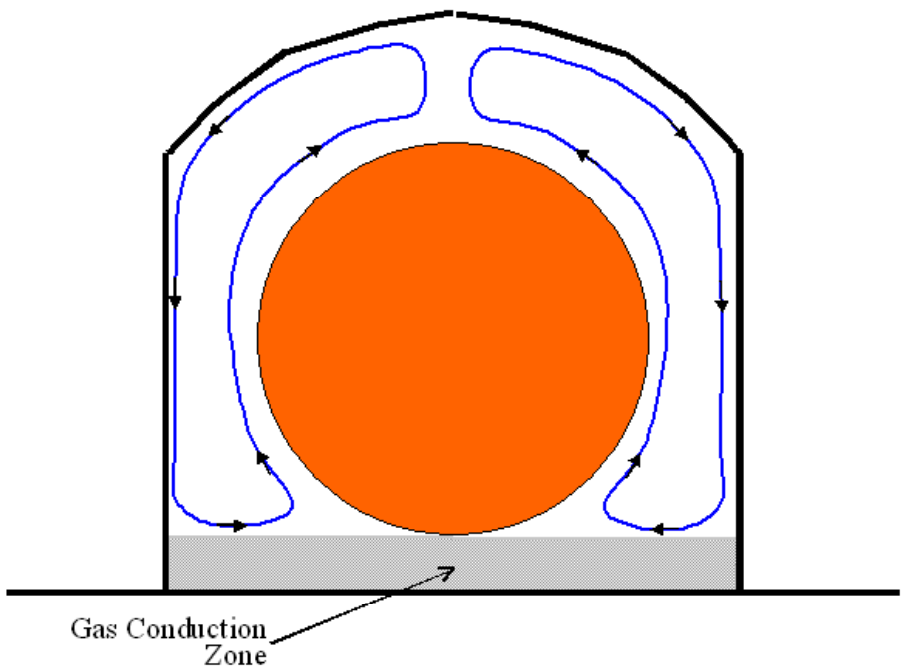

Figure 6.3.3-5. Location of Gas Conduction Zone When Invert Temperature Is Less than Gas Temperature

The partitioning of convective heat flux is corroborated directly by the experimental and analytical work of Kuehn and Goldstein (1976 [DIRS 156722] and 1978 [DIRS 130084]). Figure 6.3.3-6 is one of the contour maps calculated by Kuehn and Goldstein (1976 [DIRS 156722], Figure 12) for an isothermal annulus at a relative high Rayleigh number (indicating a strong convection pattern). The left side of the map shows the streamlines. Note that the highest velocities are located in the plume at the top of the inner cylinder. Little circulation exists below the boundary layer at the bottom of the inner cylinder.

The isotherms are shown on the right of the contour map (Figure 6.3.3-6). Closely grouped isotherms indicate high heat fluxes perpendicular to the isotherm. The isotherms show that the greatest cooling of the inner cylinder occurs on the lower half. The lowest cooling rate of the inner cylinder occurs at the very top of the cylinder, which is at the base of the plume. The highest heating rate of the outer cylinder occurs at the top where the plume impacts the outer cylinder. The lowest heating rate of the outer cylinder occurs at the base where the fluid velocities are lowest. The diagram indicates that, below the boundary layer of the inner cylinder, the heat transfer between the gas and the outer annulus is dominated by conduction.

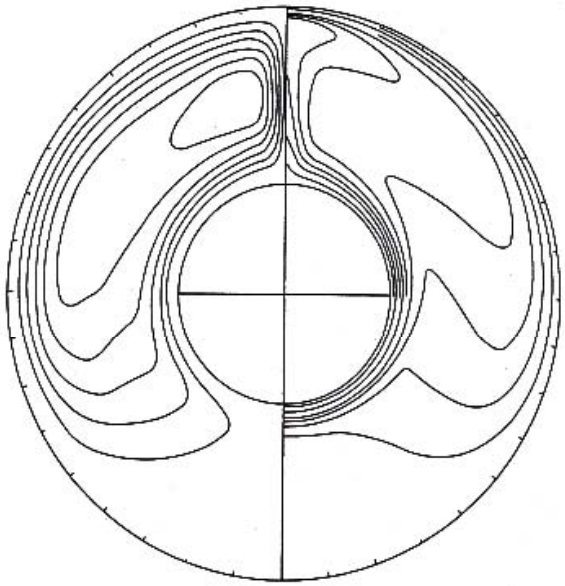

Source: Kuehn and Goldstein 1976 [DIRS 156722], Figure 12.

Figure 6.3.3-6. Streamlines (Left) and Isotherms (Right) Calculated by Kuehn and Goldstein

If the temperature difference between the inner and outer cylinders is sufficiently high and the distance between them sufficiently large, the flow field will form roll cells in the axial direction (Choi and Kim 1993 [DIRS 164647]). This comes about from instabilities in the two-dimensional flow field. An additional contributor to these axial roll cells is the temperature variation between packages (Figure 6.3.3-7). Strong upward flow plumes will form above the hotter waste packages. This air will move axially to the cooler surfaces in the vicinity of the cooler waste packages. After transfer of heat to the cooler surfaces, the air will return to the hotter waste packages.

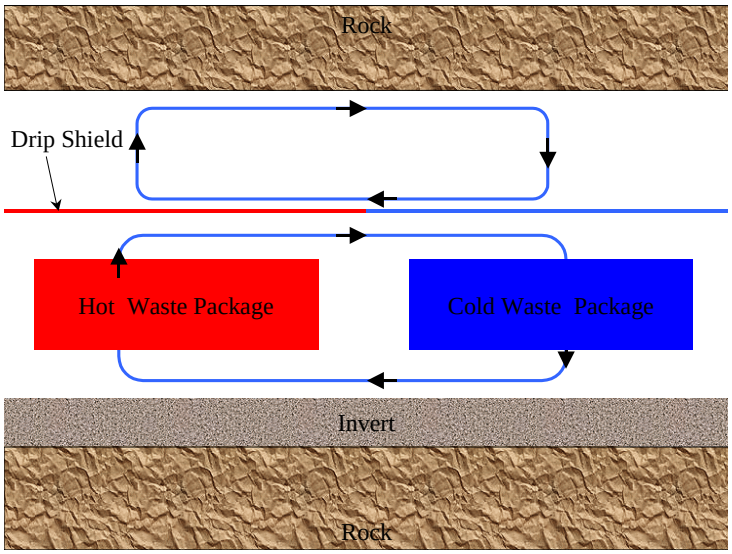

Figure 6.3.3-7. Convective Cells Connecting Hotter and Colder Waste Packages

The drift-scale axial temperature gradient should also contribute to the structure of these roll cells. If the temperature differences between the interior of a drift and the unheated ends are larger than the package-to-package temperature differences, large roll cells may span the entire drift. The total flow field will reflect all of these contributions.

Unlike the two-dimensional flow field, there are no correlations that incorporate these axial flow fields. Yet it is this axial roll cell that governs the axial transport of vapor. The axial advective transport of vapor is expected to be significantly greater than that governed by molecular diffusion. Capturing the axial transport of vapor is central to the coldtrap analysis.

Condensation inside the emplacement drifts is possible only when the surfaces within the drift cool to the saturation temperature. This means that the location of condensation will vary with time. After the drift temperature peaks, the drift will pass through three stages. In the first stage, the entire emplacement region will exceed the saturation region. A dry zone will surround the drift surface and extend some distance into the rock (Figure 6.3.3-8 top). Water vapor that flow from the rock into the drift will be transported along the entire length of the emplacement drift and into the access or exhaust drifts until it reaches a temperature lower than the saturation temperature.

As time passes, the ends of the emplacement drift will drop below the saturation temperature first. A portion of the drift will remain above the saturation temperature (Figure 6.3.3-8 middle). Vapor will evolve from both the region above the saturation temperature and a portion of the region below the saturation temperature. Condensation will occur in the balance of the emplacement region and in the adjacent access/exhaust region.

In the final stage, the entire emplacement drift will lie below the saturation temperature (Figure 6.3.3-8 bottom). Vapor will evolve in the hotter center of the drift and will condense in the cooler ends of the emplacement region and in the adjacent access/exhaust region. In general, the rock at the drift wall surface will not be dry in this final state.

Only the final stage is addressed in this model. It describes the repository state for the longest interval of the time of interest. The presence of water at the drift wall permits a bounding approach to the coupling between the evaporation in the rock and the axial vapor transport in the drift. The first stage is of no consequence because condensate cannot form in the emplacement region of the drift. The second stage occurs for a finite period of time and will require a more advanced description of the interaction between the drift and the rock than is developed here.

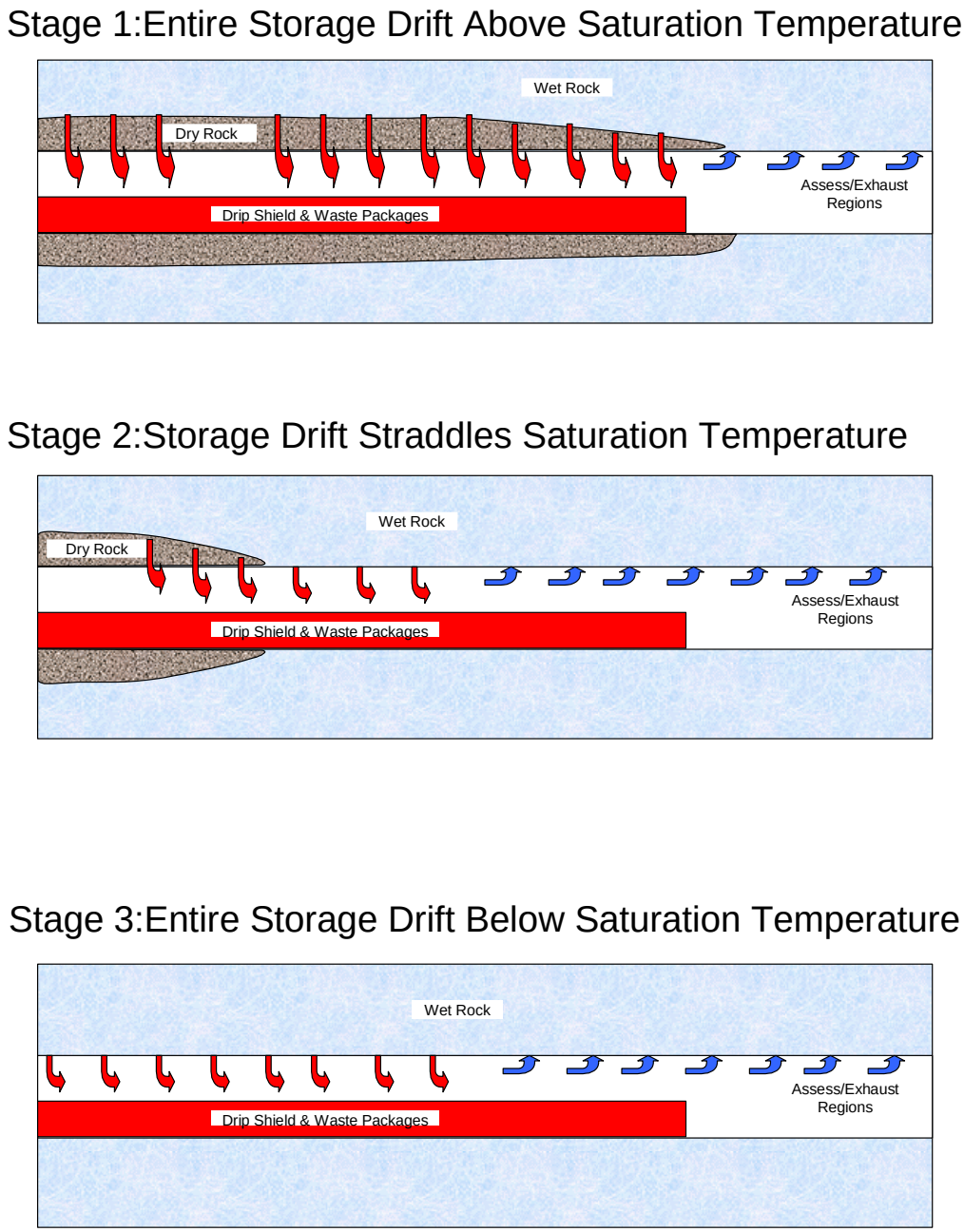

Figure 6.3.3-8. Three Stages of Evaporation/Condensation Inside an Emplacement Drift

In principle, the complete evaporation/condensation process could be modeled in a computational fluid dynamics (CFD) code like FLUENT (Fluent 2001 [DIRS 164453]). In reality, the dimensions of the prototypic problem are sufficiently large that the required computational resources needed to model the process are prohibitive, especially for sensitivity analyses involving repeated simulations. For this reason, a one-dimensional axial dispersion calculation is used to estimate the axial transport of vapor. In this approach, the axial advection

is described by a dispersion process analogous to diffusion, in which the advective transport is characterized by the dispersion coefficient. This formulation is valid as long as the composition variations in the cross-section are small compared to those in the axial direction. The dispersion coefficient is determined from Fluent CFD calculations for a "unit cell" in an emplacement drift that contains the repeated pattern of hot and cold waste packages (Section 6.2.7).

FEPs 2.1.08.04.0A (condensation on drift roof), 2.1.08.04.0B (condensation at repository edges), and 2.1.08.14.0A (condensation on underside of drip shield) are all facets of the same problem and are all addressed by this model. Condensation rates are explicitly calculated for the drift wall, the outer surface of the drip shield, the inner surface of the drip shield, and the surface of the waste package as functions of location along the chosen emplacement drifts. There is no distinction made in the calculation between the crown of the drift and the wall of the drift.

FEP 2.1.11.01.0A (heat generation in EBS) is included in the condensation model by modeling individual waste packages in the chosen drifts. Each waste package is characterized by a thermal output that reflects the waste type and the age of the waste.

FEP 2.1.11.02.0A (non-uniform heat distribution in EBS) is included by modeling the different output of individual waste packages. It is also addressed by including the contributions of all of the emplacement drifts to the axial wall temperature profile of the chosen drifts. This is accomplished by superposition in the conduction solution for the temperature field. The calculated temperature profiles reflect the lower temperatures at the repository edge as well as the lower temperatures near the unheated regions in the interior of the repository layout.

FEP 2.1.11.09.0A (thermal effects on flow in the EBS) is also directly addressed by the condensation model, which calculates the potential flux of condensate which can affect transport of radionuclides in the invert and coupling to transport in the unsaturated zone.

6.3.3.2 Modeling Assumptions

6.3.3.2.1 Vapor Pressure at Invert Surface Underneath the Drip Shield

Assumption: Two cases are examined in this report. The low-invert transport case assumes that the vapor pressure at the invert surface underneath the drip shield is the equilibrium vapor pressure at the drift wall temperature. The high-invert transport case assumes that the vapor pressure at the invert surface underneath the drip shield is the equilibrium vapor pressure for the invert surface temperature.

Rationale: The vapor pressure at the invert surface depends upon the location of the evaporation process within the invert. If water does not make its way into the invert under the drip shield, either by lateral seepage migration or capillary pumping from the drift wall through the invert particles (Section 6.3.3.1), then the evaporation will take place at or near the bottom of the invert. The temperature of this interface is lower than that of the drift wall. Therefore, the drift wall temperature is an upper bound for the drift surface temperature under the invert; pinning the vapor pressure at the invert surface to the drift wall temperature provides a reasonable lower bound to the vapor evolution at the invert surface (low invert transport case).

Alternatively, water might make its way to the invert surface by capillary flow through the invert particles. Additionally, seepage water might work its way under the drip shield through the invert. The vapor pressure at the invert surface would be greater than if the water evaporates at the bottom of the invert. The upper bound for the vapor pressure at the invert surface is therefore the equilibrium vapor pressure at the invert surface temperature (high invert transport case).

The invert is partially saturated with liquid water, and therefore exhibits a capillary response that can lower the equilibrium partial pressure of water. This capillary effect is greatest within the invert particles at the top of the invert, which is warmer than the bottom, and can be substantial if the invert saturation is sufficiently small. For simplicity in this model, the invert saturation and capillary response are not considered. Instead, the local partial pressure of water vapor is conservatively assumed to be independent of invert saturation. The vapor pressure-lowering effects of adsorption to mineral surfaces is also ignored in calculation of vapor pressure.

Confirmation Status: The assumption covers the credible range of vapor pressures at the invert surface. The high-invert transport limit leads to the greatest amount of evaporation under the drip shield. The low-invert transport limit leads to the least amount of evaporation under the drip shield. Since the full range is addressed, this assumption requires no further confirmation.

Use in this Calculation: This assumption is used in Section 6.3.5.1.3.

6.3.3.2.2 Vapor Pressure on the Drift Wall, Drip Shield, and Waste Packages

Assumption: The vapor pressure on the drift wall, drip shield, and waste packages is the equilibrium vapor pressure at the local temperature.

Rationale: The vapor pressure at the drift wall depends upon the location of the evaporation and condensation processes within the surrounding rock and on the drift wall. The drift wall may be partially saturated with liquid water, which would lower the equilibrium partial pressure of water due to capillary effects. For simplicity in this model, the drift wall saturation and capillary response are not considered. Instead, the local partial pressure of water vapor is conservatively assumed to be independent of saturation and simply dependent on the local temperature. This assumption maximizes the evaporation rate at the drift surface, making more water available for condensation in the drift. The assumption that the local partial pressure of water vapor is simply a function of the local temperature is also used for the drip shield and the waste packages.

The vapor pressure-lowering effects of adsorption to mineral surfaces are also ignored in calculation of vapor pressure for all of these surfaces.

Confirmation Status: This assumption is conservative by making more water available for condensation and requires no further confirmation.

Use in this Calculation: This assumption is used in Section 6.3.5.2.9.

6.3.3.2.3 Partitioning of Available Water

Assumption: The water supplied to the drift from the host rock is prorated between the invert and the drift wall according to the ratio of the drift wall and invert perimeters.

Rationale: The evaporation rate within the emplacement drift is limited by the rate at which water can flow to the drift wall and invert surface through the rock (Section 6.3.5.1.4). In this calculation, the total fluence of water available to the emplacement drift is calculated as the sum of the radial capillary flow through the host rock matrix and the percolation flux incident on the drift footprint. The partitioning of this available water between the drift wall and the invert surface requires a detailed knowledge of how percolation water enters the drift, evaporates or drips into the invert, and flows through the invert. Models for these processes do not exist.

Partitioning according to surface area implies no distinction between the invert surface and the drift wall. The physical processes that govern water partitioning are likely to decrease the water available to the invert surface below that indicated by the partitioning rule. Hence the partitioning rule likely overestimates the water available for evaporation under the drip shield and therefore maximizes the condensation rate under the drip shield. Therefore, the partitioning rule used in this analysis is conservative.

Confirmation Status: The assumption is conservative and requires no further confirmation.

Use in this Calculation: This assumption is used in Sections 6.3.5.1.3 and 6.3.5.1.4.

6.3.3.2.4 Neglect of Barometric Pumping

Assumption: Barometric pumping is ignored.

Rationale: Barometric pumping will augment the axial dispersion coefficient, promoting condensation in unheated regions. Ignoring its contribution is conservative. Additional discussion is included in Section 6.3.5.1.4.

Confirmation Status: The assumption is conservative and requires no further confirmation.

Use in this Calculation: This assumption is used in Section 6.3.5.1.2.

6.3.3.2.5 Neglect of Axial Energy Transport Terms

Assumption: Inter-package thermal radiation and axial conduction in the drip shield are ignored in the condensation model.

Rationale: This serves to overstate the temperature differences between adjacent waste packages and drip shield sections. This, in turn, maximizes the evaporation rates under the hottest waste packages and the condensation rates in the vicinity of the coolest waste packages. Hence, this assumption is conservative with respect to EBS transport and requires no further confirmation.

Confirmation Status: The assumption is conservative and requires no further confirmation.

Use in this Calculation: This assumption is used in Section 6.3.5.1.2.

6.3.3.2.6 Neglect of the Axial Relocation of Energy in the Calculation of Rock Temperatures

Assumption: The latent heat associated with the axial transport of water vapor causes a spatially nonuniform deposition of energy in the rock. This axial redistribution of energy in the rock is ignored.

Rationale: Water evaporated in the middle of the drift carries with it a latent heat that is released at the point of condensation. This modifies the spatially uniform line source used to estimate the drift wall temperatures (Section 6.3.5.1.1). The fully coupled problem that integrates this axial redistribution of energy represents a significant computational complication. The procedure used in this calculation is to calculate the rock temperature profiles using average line source representations for the decay heat. The axial redistribution of energy is then derived from the axial vapor fluxes. The appropriateness of the assumption is assessed at that point.

Confirmation Status: The assumption is assessed in Section 6.3.7.2.4.

Use in this Calculation: This assumption is used in Section 6.3.5.1.1.

6.3.3.2.7 Drip Shield Ventilation

Assumption: Two limits to the drip shield features are considered. The first limit (ventilated drip shield) presumes that the drip shield is designed to promote mixing of the gas from under the drip shield with gas outside the drip shield. Perfect mixing is used in this case. The second limit (unventilated drip shield) presumes that the drip shield is designed to prevent mixing of the gases inside and outside of the drip shield.

Rationale: These are the two extremes of gas mixing. By addressing both extremes, the analysis captures the full range of possibilities.

Confirmation Status: Because the two extremes capture the full range of possibilities, no further confirmation is needed.

Use in this Calculation: This assumption is used in Section 6.3 and Appendices D.1 and D.2.

6.3.3.2.8 Water Available for Evaporation in the Drift

Assumption: The water available for evaporation in the drift is limited by the percolation rate rather than the seepage rate.

Rationale: Water can enter the drift by evaporation from the drift wall and by liquid seepage (the portion of the liquid percolation that enters the drift) from the fractures. The two processes are coupled. The current thermal THC seepage model is two-dimensional (BSC 2004 [DIRS 169856], Table 6-1, pg. 6-1) and accounts for fracture-matrix interactions. Because of the two-dimensional nature of the model, the drift vapor pressure in the current seepage analysis will be very close to saturation and the evaporation into the drift will be close to zero. This means that the matrix saturation near the drift wall in the current seepage model will be high, and the imbibition of water from the fracture into the matrix will be low.

In the condensation model, evaporation limits are realized when the drift vapor pressure is significantly lower than the saturation value. When this occurs, the rock matrix will desaturate in the vicinity of the drift wall. A portion of the percolated water will be imbibed into this desaturated rock matrix and pumped by capillary forces to the drift wall surface where it will evaporate. The resulting flow of liquid and vapor into the drift will be larger than the sum of the currently predicted liquid seepage and the matrix capillary pumping limit in the absence of percolation.

A complete calculation that includes the coupling between the rock flow and the vapor dispersion within the drift is beyond the scope of this document. An approximate bounding argument is used in its place: the amount of water than can enter into the drift by seepage and evaporation is reasonably bounded by the sum of the capillary pumping fluence in the absence of fractures and the percolation flux over the shadow of the drift.

Confirmation Status: This assumption is conservative and requires no further confirmation.

Use in this Calculation: This assumption is used in the calculation of evaporation limits in the condensation model (Section 6.3.5.1.4).

6.3.3.2.9 Disposition of Condensate after Formation

Assumption The fraction of drift-wall condensate that forms over the drip shield can drip down on the drip shield. The fraction of drip shield condensate that forms over the waste package can drip down onto the waste package.

Rationale The condensation model makes no attempt to analyze the motion of condensate once it is formed. In addition to dripping, capillary flows along the drift and drip shield surfaces are possible. Furthermore, for sufficiently low condensation rates, condensate may be imbibed into the drift wall. Since neither of these mechanisms is examined, it is assumed that the condensate drips. Specifically, condensate that overlies the drip shield can drip onto the drip shield; condensate that overlies the waste package can drip onto the waste package.

Confirmation Status: This assumption is conservative and requires no further confirmation.

Use in this Calculation: This assumption is used in the abstraction of the condensation model results (Section 8.3).

6.3.4 Consideration of Alternative Conceptual Models for In-Drift Condensation

There are no completely analogous alternative conceptual models for in-drift condensation. Some limited alternate conceptual models for in-drift condensation do exist. In particular, Danko and Bahrami (2004 [DIRS 171417 and 171418]) present an alternate conceptual model for repository condensation. However, their model is only appropriate for natural ventilation, not natural convection. In addition, their model does not include a drip shield, even for post-closure conditions. Therefore, the results for this alternate conceptual model can not be compared to the results from this report because they are for different situations.

6.3.5 Formulation for the Base-Case Condensation Model

Nomenclature

Symbol	Meaning	Units
Ac	cross-sectional area	m^2
d	diameter	m
D	diameter	m
D_{va}	air/vapor gas diffusion coefficient	m^2/s
DY	length increment	m
F	view factor	-
g	gravitational constant	m/s^2
h	height	m
h	enthalpy	J/kg-K
hc	convective heat transfer coefficient	W/m^2-K
h_{fg}	latent heat of water	J/kg
k (context sensitive)	thermal conductivity or	W/m-K
	permeability	m^2
k_L	liquid relative permeability	-
L	length	m
m	mass flux	kg/m^2-s
MW	molecular weight	kg/kmole
Nu	Nusselt number	-
P	pressure	Pa
P (with subscript)	perimeter	m
Pr	Prandtl number	-
q (context sensitive: based upon subscript)	power	W
Q	power	W
q (context sensitive: based upon subscript)	mass flux	kg/m^2-s
qL	linear power density	W/m
qr	radiation heat flux	W/m^2
R	radius	m
r	radius	m
Ra	Rayleigh number	-
S	saturation	-
Sc	Schmidt number	-
T	temperature	K
t	time	s
V	speed	m/s
x	position along x axis	m
X	mass fraction	-
y	position along y axis	m
z	position along z axis	m
ZG	distance to ground surface	m
α (context sensitive: based upon subscript)	Angle	-
α (context sensitive: based upon subscript)	thermal diffusivity	m^2/s
β	coefficient of thermal expansion	K^{-1}

Symbol	Meaning	Units
χ	mole fraction	-
δ	Kronecker delta	-
ε	surface emissivity	-
ϕ	porosity	-
λ	van Genuchten parameter	-
μ	absolute viscosity	poise
ν	dynamic viscosity	m^2/s
ρ	density	kg/m^3
σ	Stefan-Boltzmann constant	$W/m^2\text{-}K^4$

Subscript	Meaning
C	center
c	capillary
cond	condensation
ds	drip shield
eff	effective
in	inside the drip shield
inv	invert
out	outside the drip shield
perc	percolation
st	vapor (steam)
wp	waste package

6.3.5.1 Mathematical Description of the Base-Case Conceptual Model

The axial transport of water vapor in the gas is described as a steady-state one-dimensional dispersion/diffusion process described by two coupled second-order ordinary differential equations (ODEs). One ODE describes vapor dispersion in the y (axial) direction outside of the drip shield; the other ODE describes vapor dispersion inside the drip shield. Energy dispersion in the gas is also described by two coupled second-order ODEs for the same two regions. The gas energy transport equations are coupled with the gas vapor transport equations. The domain of the 4 coupled ODEs consists of a single emplacement drift, the 15 m long exhaust standoff, and 60 m of the access turnout. Zero-flux conditions at each end of the drift for energy and vapor in each region (inside and outside of the drip shield) provide the four boundary conditions for the problem.

The boundary of the region outside of the drip shield consists of the drift wall and the outside surface of the drip shield. Heat transfer between the gas in this region and the two surfaces is calculated using standard heat transfer coefficients. The drift wall is a source of water vapor. Evaporation and condensation at the drift wall are described by mass transfer coefficients that are direct analogues of the heat transfer coefficients. Condensation on the outside surface of the drip shield is included in the calculation when the saturation vapor mass fraction at the drip shield is lower than the vapor mass fraction of the adjacent gas.

The boundary of the region inside of the drip shield consists of the invert surface, the waste package surfaces, and the inside surface of the drip shield. Heat and mass transfer between the gas of this region and the bounding surfaces are described by standard heat and mass transfer coefficients. The invert surface is the source of water vapor for this region; both evaporation and condensation are possible on the invert surface. Only condensation, not evaporation, is possible on the waste packages and the underside of the drip shield.

The amount of water that can be evaporated from the drift wall surface and the invert surface is limited by the supply of water in the surrounding rock. An estimate of that supply is calculated from bounds on capillary flow through the rock matrix and from the percolation flux. The sum of these contributions is prorated over the combined perimeter of the drift wall and the invert surface to arrive at a limiting evaporation mass flux. Calculation of the surface temperatures provides mathematical closure to the problem.

The drift wall temperature profiles are approximated using conduction line source solutions and superposition. Drip shield, invert, and waste package surface temperatures are calculated by accounting for the convected heat, thermal radiation, and evaporation/condensation rates.

The differential equations are discretized so that each node contains a specific waste package. Condensation rates in the immediate vicinity of each waste package are calculated as part of the solution to the four coupled ODEs. The calculation provides estimates of the condensation rate 1) on the outside of the drip shield, 2) on the drift walls, and 3) on the inside surface of the drip shield and on the waste packages.

The mathematical description of the base case begins with the calculation of the drift wall temperatures (Section 6.3.5.1.1). First, the equation for the repository temperature field is developed from line source solutions. The seven representative drifts from the LA design are chosen for analysis. The wall temperatures at the centers of these drifts are then calculated as functions of time in order to choose the appropriate analysis times. Then the axial temperature profiles for each of the seven chosen drifts at each of the selected times are calculated. Finally, the average percolation rate for each of the chosen drifts is determined for each of the chosen times based upon the values developed in *Multiscale Thermohydrologic Model* (BSC 2004 [DIRS 169565]).

The four ODEs for mass and energy dispersion in the gas are developed in Section 6.3.5.1.2. This section also includes the energy equations for the three structural surfaces (drip shield, waste package, and invert), from which the surface temperatures are calculated. The heat and mass transfer correlations used in the calculation are documented in Section 6.3.5.1.3. The limits to evaporation from the drift wall and the invert are developed in Section 6.3.5.1.4.

6.3.5.1.1 Calculation of the Repository Temperature Field and Average Percolation Rates

Single Line Source in an Infinite Homogeneous Medium

The line source solution is derived from the transient solution for a continuous point source (q(t)) in an infinite homogeneous medium (Carslaw and Jaeger 1959 [DIRS 100968], p. 261, Equation 1). The radial distance from the point source is r. The initial temperature is zero.

$$T_{point}(t,r) = \frac{1}{8\,\rho\,Cp\,(\pi\,\alpha)^{3/2}} \int_0^t \frac{q(t')}{(t-t')^{3/2}} e^{\frac{-r^2}{4\alpha(t-t')}} dt' \qquad \text{(Eq. 6.3-4)}$$

The conversion from the spherical coordinates of the solution to the Cartesian coordinates of the repository is:

$$r^2 = (x - x0)^2 + (y - y0)^2 + (z - z0)^2 \qquad \text{(Eq. 6.3-5)}$$

where the source is located at (x0, y0, z0).

The line source solution is obtained by applying the differential transform:

$$qL(t)\,dy0 = q(t) \qquad \text{(Eq. 6.3-6)}$$

(where the coordinate y is collinear with the line source) and integrating y0 over the length of the line source (L). When the line source is centered at (x_C, y_C, z_C), the line source solutio becomes:

$$T_{line}(t,x,y,z) = \frac{1}{8\,\rho\,Cp\,(\pi\,\alpha)^{3/2}} \int_0^t \left[\frac{qL(t')}{(t-t')^{3/2}} e^{\frac{-\left[(x-x_C)^2+(z-z_C)^2\right]}{4\alpha(t-t')}} \int_{y_C-L/2}^{y_C+L/2} e^{\frac{-(y-y0)^2}{4\alpha(t-t')}} dy0 \right] dt' \qquad \text{(Eq. 6.3-7)}$$

The definite integral over dy0 is recognized as a form of the error function.

$$T_{line}(t,x,y,z) = \frac{1}{8\,\pi\,k} \int_0^t \frac{qL(t')}{t-t'} e^{\frac{-\left[(x-x_C)^2+(z-z_C)^2\right]}{4\alpha(t-t')}} \left[\operatorname{erf}\frac{\left((y-y_C)+\frac{L}{2}\right)}{\sqrt{4\alpha(t-t')}} - \operatorname{erf}\frac{\left((y-y_C)-\frac{L}{2}\right)}{\sqrt{4\alpha(t-t')}} \right] dt' \qquad \text{(Eq. 6.3-8)}$$

Extension of the Line Source Solution to a Semi-infinite Domain Bounded by One Isothermal Surface

The analytic solution for an infinite domain is extended to the case of a semi-infinite domain by the method of images. A sink of strength equal to the source is reflected across the isothermal plane (Figure 6.3.5-1) at z=ZG (ground surface). The solution is the sum of the source and sink fields (superposition).

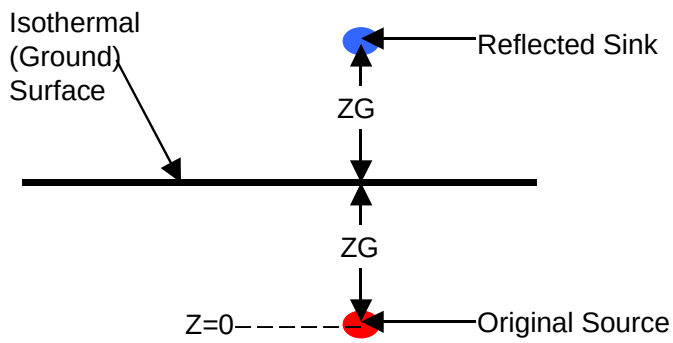

Figure 6.3.5-1. Creation of an Isothermal Surface Using the Method of Images

The technique is applicable to all of the line and solutions derived above. Hence,

$$T_{line_1iso}(t,x,y,z) = T_{line}(t,x,y,z) - T_{line}(t,x,y,z-2\,ZG) \qquad \text{(Eq. 6.3-9)}$$

where the temperature contribution from the sink is evaluated with respect to the sink location. The temperature increase due to a single line in the presence of the isothermal surface becomes:

$$T_{line}(t,x,y,z) = \frac{1}{8\,\pi\,k}\int_0^t \frac{qL(t')}{t-t'}\frac{\left[e^{\frac{-(z-z_C)^2}{4\alpha(t-t')}} - e^{\frac{-(z-2\,ZG-z_C)^2}{4\alpha(t-t')}}\right]}{e^{\frac{(x-x_C)^2}{4\alpha(t-t')}}}\left[\operatorname{erf}\frac{\left((y-y_C)+\frac{L}{2}\right)}{\sqrt{4\alpha(t-t')}} - \operatorname{erf}\frac{\left((y-y_C)-\frac{L}{2}\right)}{\sqrt{4\alpha(t-t')}}\right]dt' \qquad \text{(Eq. 6.3-10)}$$

The total temperature increase is the sum of the individual contributions from each of the line sources (superposition).

$$T_{line}(t,x,y,z) = \frac{\displaystyle\int_0^t \left[\sum_{n=1}^{N_{lines}} \frac{qL_n(t')}{t-t'}\frac{e^{\frac{-(z-z_{C_n})^2}{4\alpha(t-t')}} - e^{\frac{-(z-2\,ZG-z_{C_n})^2}{4\alpha(t-t')}}}{e^{\frac{(x-x_{C_n})^2}{4\alpha(t-t')}}}\left[\operatorname{erf}\frac{\left(y-y_{C_n}+\frac{L}{2}\right)}{\sqrt{4\alpha(t-t')}} - \operatorname{erf}\frac{\left(y-y_{C_n}-\frac{L}{2}\right)}{\sqrt{4\alpha(t-t')}}\right]\right]dt'}{8\,\pi\,k} \qquad \text{(Eq. 6.3-11)}$$

When the heating histories of each line are identical, this equation reduces to:

$$T_{line}(t,x,y,z) = \frac{\displaystyle\int_0^t \frac{qL(t')}{t-t'} \sum_{n=1}^{N_{lines}} \left[\frac{e^{\frac{-(z-z_{C_n})^2}{4\alpha(t-t')}} - e^{\frac{-(z-2ZG-z_{C_n})^2}{4\alpha(t-t')}}}{e^{\frac{(x-x_{C_n})^2}{4\alpha(t-t')}}} \left[\operatorname{erf}\frac{\left(y-y_{C_n}+\frac{L}{2}\right)}{\sqrt{4\alpha(t-t')}} - \operatorname{erf}\frac{\left(y-y_{C_n}-\frac{L}{2}\right)}{\sqrt{4\alpha(t-t')}} \right] \right] dt'}{8\pi k} \quad \text{(Eq. 6.3-12)}$$

The temperatures of interest are those of the drift wall. The circumferential temperature gradients along the drift wall above the invert should be small compared to the axial gradients. Therefore the drift wall temperature will be calculated at the apex of the drift as applied to the entire circumference of the drift above the invert. For drift j, the coordinates of interest are:

$$z = z_{C_j} + \frac{D_{drift}}{2} \quad x = x_{C_j} \quad y = y_{C_j} + \Delta y \quad \text{(Eq. 6.3-13)}$$

where Δy is the axial distance of the point of interest from the center (designated by the subscript *C*) of drift j. This makes the temperature equation:

$$T_{wall}(t,j,\Delta y) = \frac{1}{8\pi k} \int_0^t \frac{qL(t')}{t-t'} \sum_{n=1}^{N_{lines}} \left[\frac{e^{-\frac{\left(\Delta z_{C_{j,n}}+\frac{D_{drift}}{2}\right)^2}{4\alpha(t-t')}} - e^{-\frac{\left(\Delta z_{C_{j,n}}+\frac{D_{drift}}{2}-2ZG\right)^2}{4\alpha(t-t')}}}{e^{\frac{(\Delta x_{C_{j,n}})^2}{4\alpha(t-t')}}} \left[\operatorname{erf}\frac{\left(\Delta y_{C_{j,n}}+\Delta y+\frac{L}{2}\right)}{\sqrt{4\alpha(t-t')}} - \operatorname{erf}\frac{\left(\Delta y_{C_{j,n}}+\Delta y-\frac{L}{2}\right)}{\sqrt{4\alpha(t-t')}} \right] \right] dt'$$

(Eq. 6.3-14)

where the spatial distance between the line sources j and n are:

$$\Delta x_{j,n} = x_{C_j} - x_{C_n} \quad \Delta y_{j,n} = y_{C_j} - y_{C_n} \quad \Delta z_{j,n} = z_{C_j} - z_{C_n} \quad \text{(Eq. 6.3-15)}$$

Analyzed Drifts

Seven drifts are chosen for the condensation/evaporation analysis (Figure 6.3.5-2). Two sets of three drifts span the width of the repository. The three drifts at the north of the drift reflect the cooler portion of the repository layout. The three drifts at the middle of the drift capture the hotter portion of the layout. The seventh drift is in the narrowest portion of the repository.

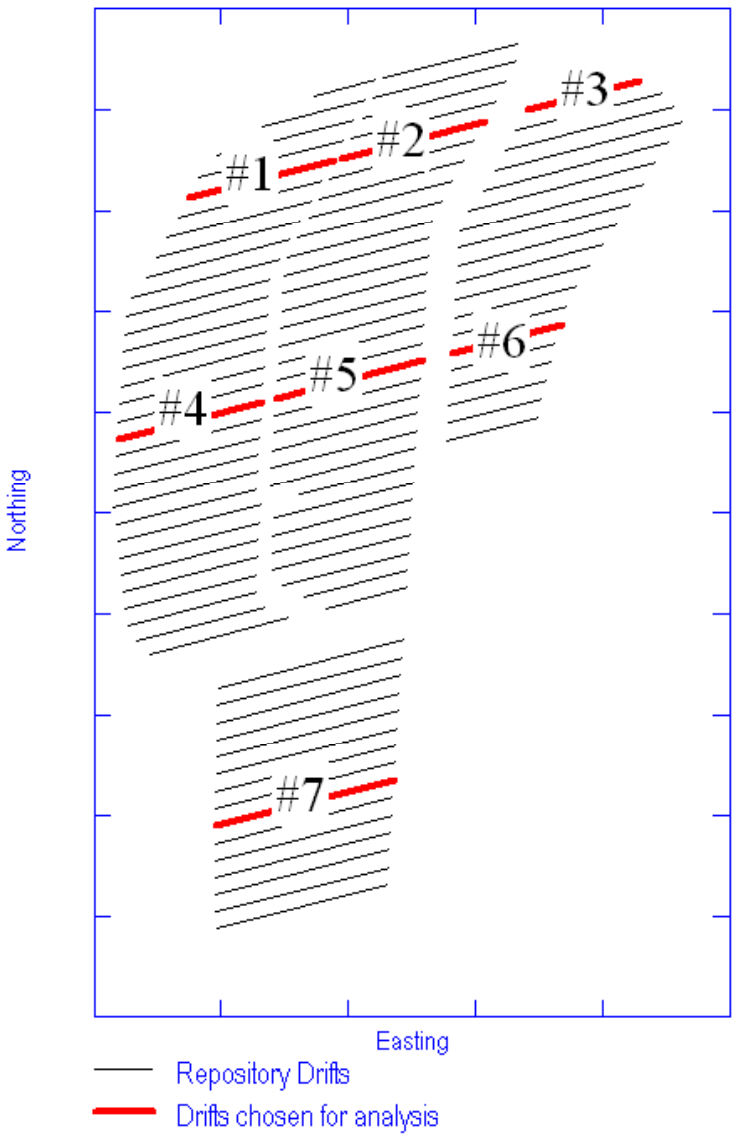

Source: BSC 2003 [DIRS 161727].

Figure 6.3.5-2. Locations of Emplacement Drifts Chosen for Analysis

Analysis Times

For condensation to take place on the structures in the drift, those structures must have a temperature lower than the saturation temperature at the repository elevation (~96ºC, Buscheck et. al. 2002 [DIRS 160749], p. 10-2). Since these structures are expected to be hotter than the drift wall temperature, the wall temperature must also be lower than the saturation temperature where condensation might take place.

This cold trap analysis is limited to the case where the drift wall is saturated throughout the drift. This means that the maximum wall temperature in the drift of interest is less than the saturation temperature (96°C). To determine the times when this condition occurs for each drift, the center temperatures of the drifts of interest are first calculated. Although these are not the maximum temperatures in the drifts, they are adequate for this purpose; the complete temperature profiles, including the maximum drift temperature, are calculated in the next step (**Calculated Wall Temperatures**).

Based on the calculation of drift wall temperature at the center of the emplacement regions (centerpoint temperature in Figures 6.3.5-3 through 6.3.5-6), all seven of the selected drifts are evaluated at 1,000, 3,000, and 10,000 years. This represents a roughly linear interpolation over the log of time suggested by the shape of the temperature-time plots below. Selected drift 3 is also evaluated at 300 years. Also note that there is little difference between the temperatures calculated at 300 m (red lines) and 400 m (blue lines) of depth. In the absence of a significant difference, a representative depth of 300 m is used for the condensation model.

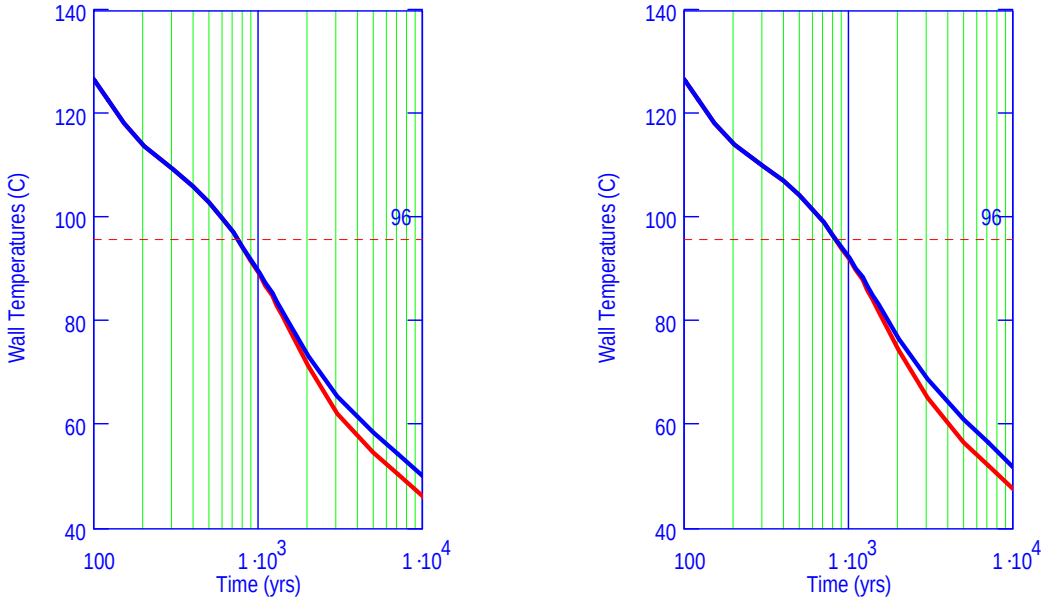

DTN: SN0408T0509903.007; file TOC.mcd; hyperlink 6.2.5, Percolation Rates for Chosen Drifts.

NOTE: Left: Choice #1; right: Choice #2. Red line: 300 m deep; blue line: 400 m deep.

Figure 6.3.5-3. Centerpoint Temperatures for Chosen Drifts #1 and #2

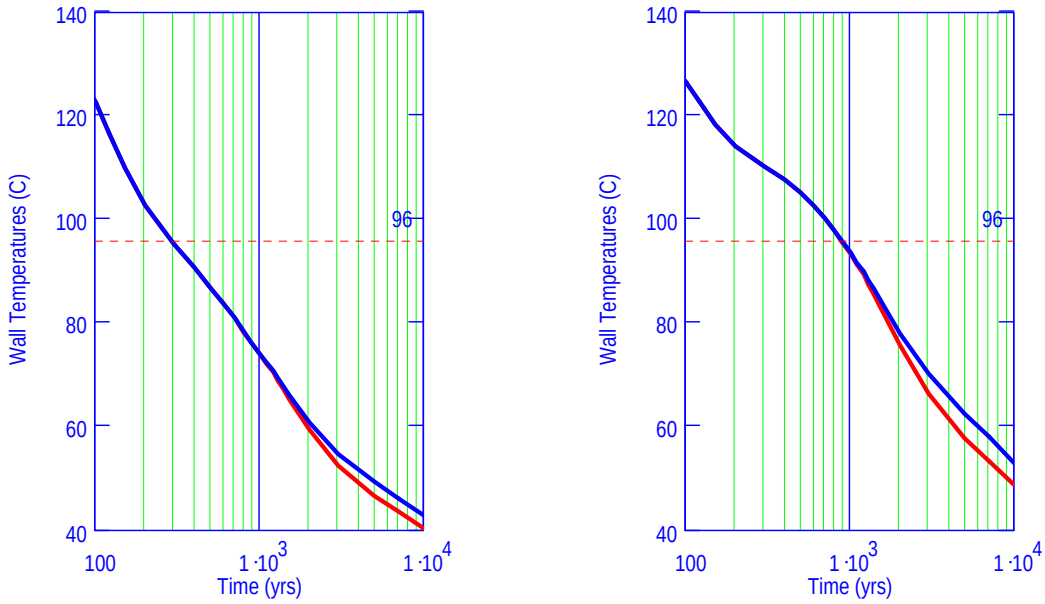

DTN: SN0408T0509903.007; file TOC.mcd; hyperlink 6.2.5, Percolation Rates for Chosen Drifts.

NOTE: Left:: Choice #3; right: Choice #4. Red line: 300 m deep; blue line: 400 m deep.

Figure 6.3.5-4. Centerpoint Temperatures for Chosen Drifts #3 and #4

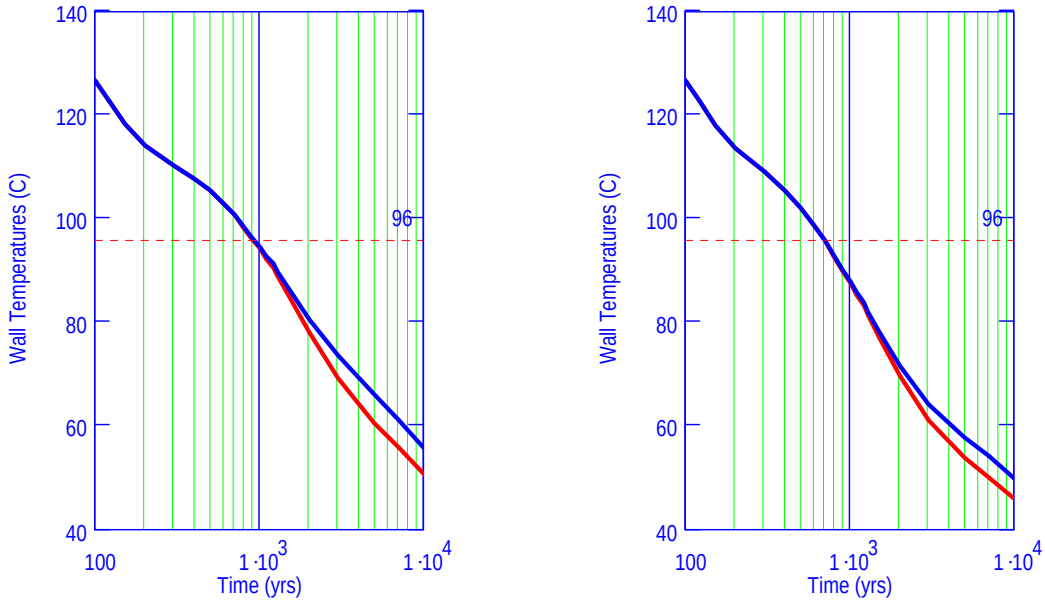

DTN: SN0408T0509903.007; file TOC.mcd; hyperlink 6.2.5, Percolation Rates for Chosen Drifts.

NOTE: Left:: Choice #5; right: Choice #6. Red line: 300 m deep; blue line: 400 m deep.

Figure 6.3.5-5. Centerpoint Temperatures for Chosen Drifts #5 and #6

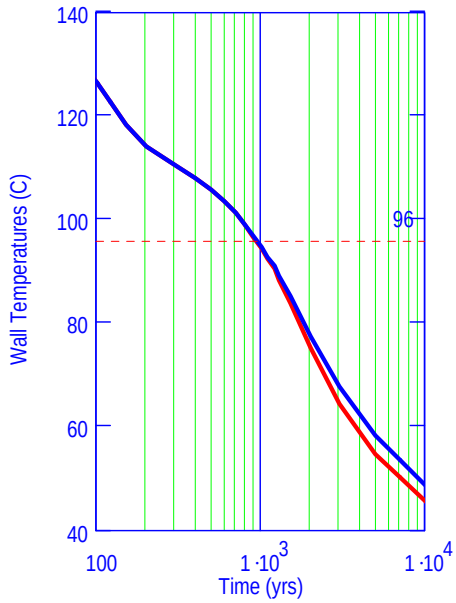

DTN: SN0408T0509903.007; file TOC.mcd; hyperlink 6.2.5, Percolation Rates for Chosen Drifts.
NOTE: Red line: 300 m deep; blue line: 400 m deep.

Figure 6.3.5-6. Centerpoint Temperatures for Chosen Drift #7

Calculated Wall Temperatures

The calculated wall temperatures for the seven chosen emplacement drifts are shown in Figures 6.3.5-7 through 6.3.5-13. The temperature calculation accounts for the contributions from all of the drifts in the repository. They are obtained by evaluating the line source solution (Equation 6.3-14) at a radius of 2.75 m. The two vertical lines mark the ends of the waste package emplacement area. The horizontal dashed line marks the 96ºC limit. All of the calculated temperature profiles lie below the saturation temperature of the repository.

Of particular note are the cooler regions within the center of the repository. Both the exhaust standoffs (between chosen drifts 1 and 2 and between 4 and 5) and the access turnouts (between chosen drifts 2 and 3 and between 5 and 6) are cool enough for vapor condensation. This means that axial vapor transport will not be directed solely towards the outer edges of the repository; vapor will condense in the connecting drifts within the middle of the repository.

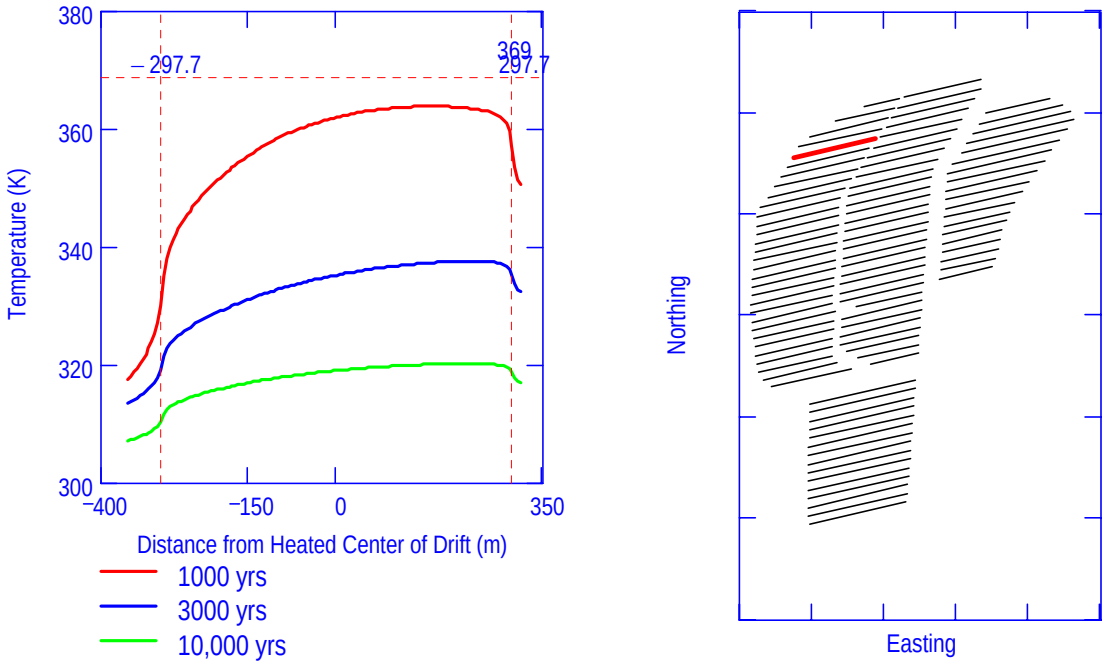

DTN: SN0408T0509903.007; file TOC.mcd; hyperlink 6.2.4, Calculated Wall Temperatures.

Figure 6.3.5-7. Drift Wall Temperatures for Chosen Drift #1

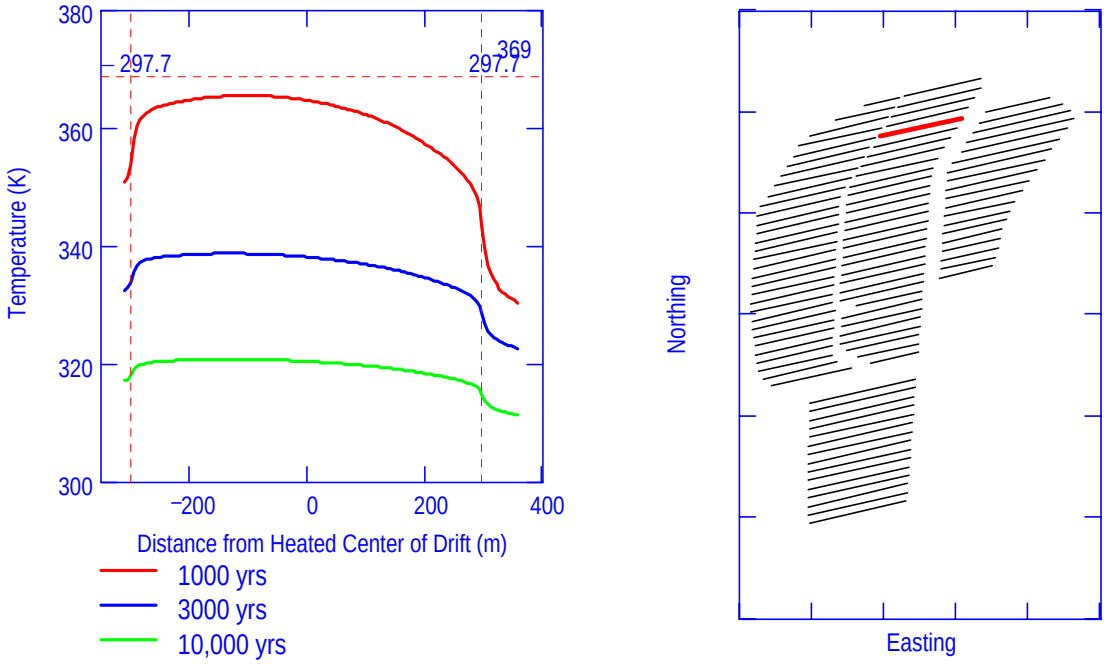

DTN: SN0408T0509903.007; file TOC.mcd; hyperlink 6.2.4, Calculated Wall Temperatures.

Figure 6.3.5-8. Drift Wall Temperatures for Chosen Drift #2

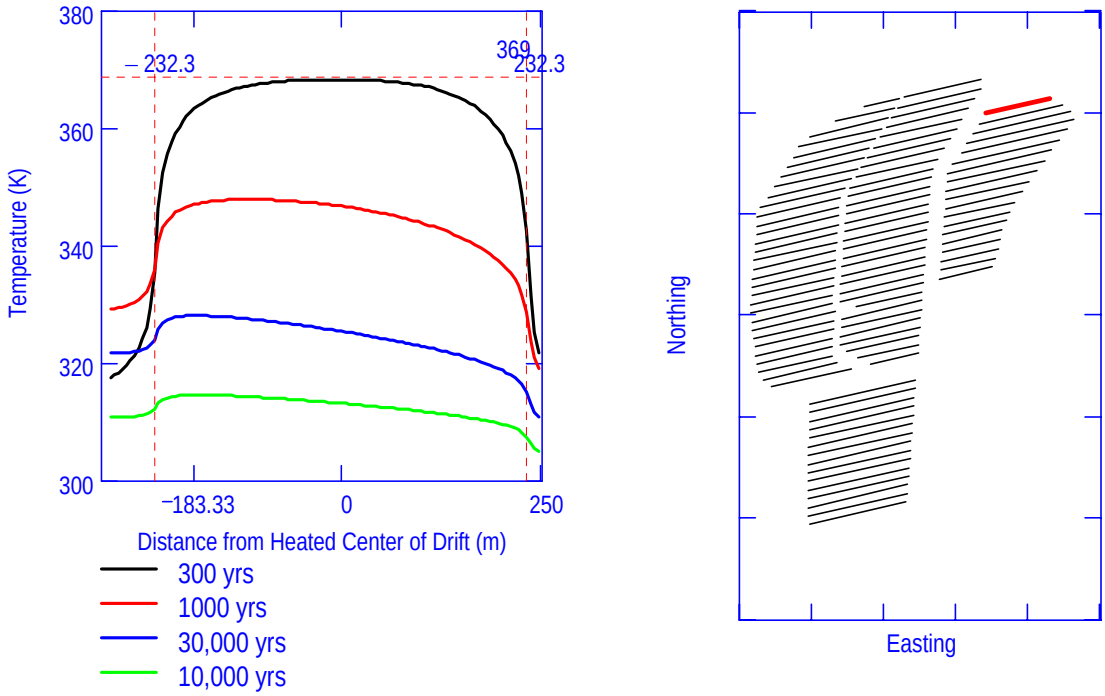

DTN: SN0408T0509903.007; file TOC.mcd; hyperlink 6.2.4, Calculated Wall Temperatures.

Figure 6.3.5-9. Drift Wall Temperatures for Chosen Drift #3

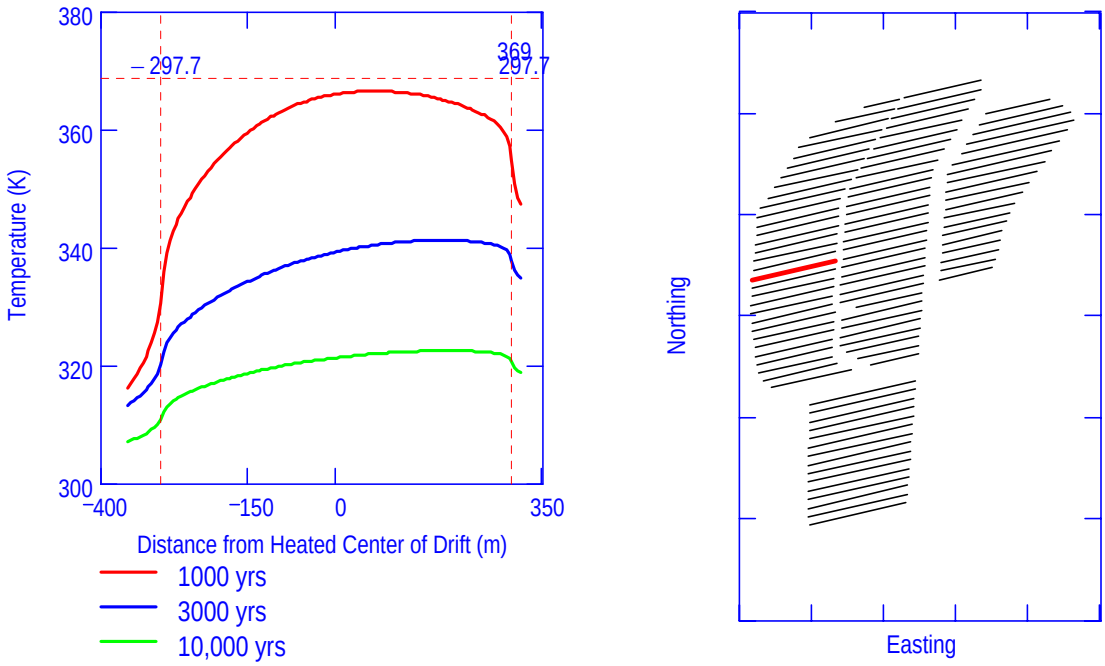

DTN: SN0408T0509903.007; file TOC.mcd; hyperlink 6.2.4, Calculated Wall Temperatures.

Figure 6.3.5-10. Drift Wall Temperatures for Chosen Drift #4

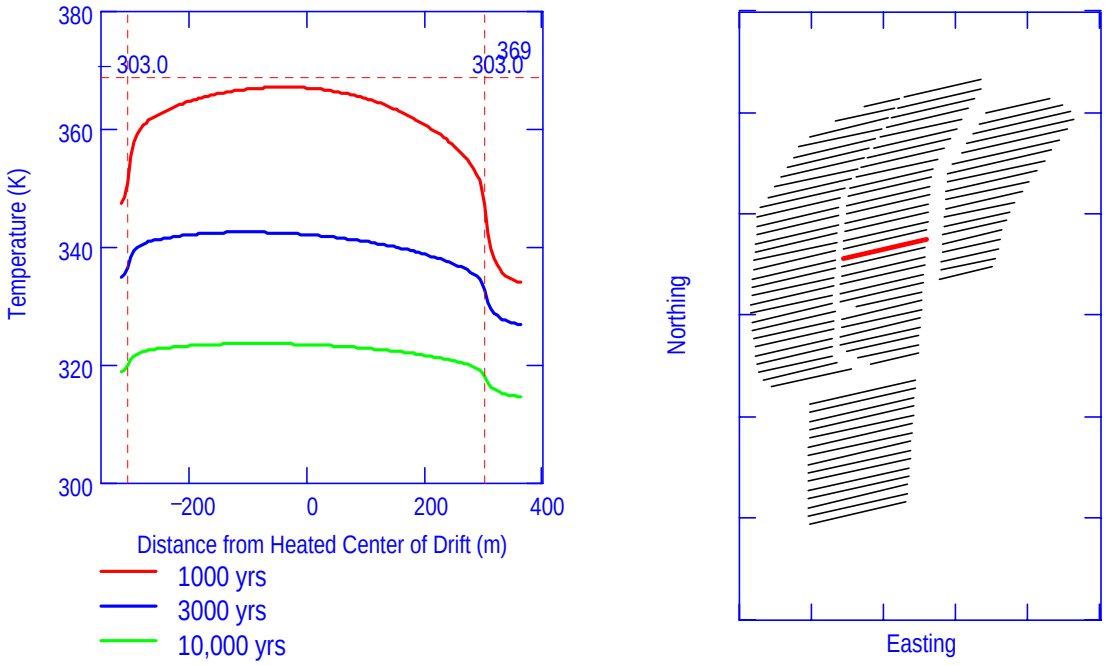

DTN: SN0408T0509903.007; file TOC.mcd; hyperlink 6.2.4, Calculated Wall Temperatures.

Figure 6.3.5-11. Drift Wall Temperatures for Chosen Drift #5

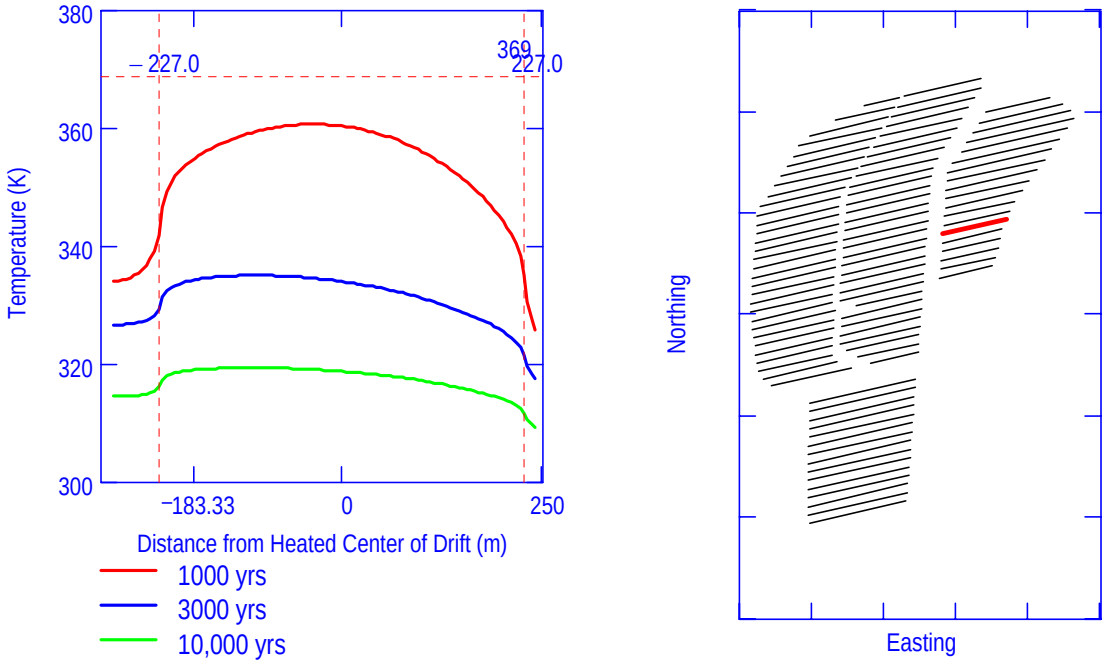

DTN: SN0408T0509903.007; file TOC.mcd; hyperlink 6.2.4, Calculated Wall Temperatures.

Figure 6.3.5-12. Drift Wall Temperatures for Chosen Drift #6

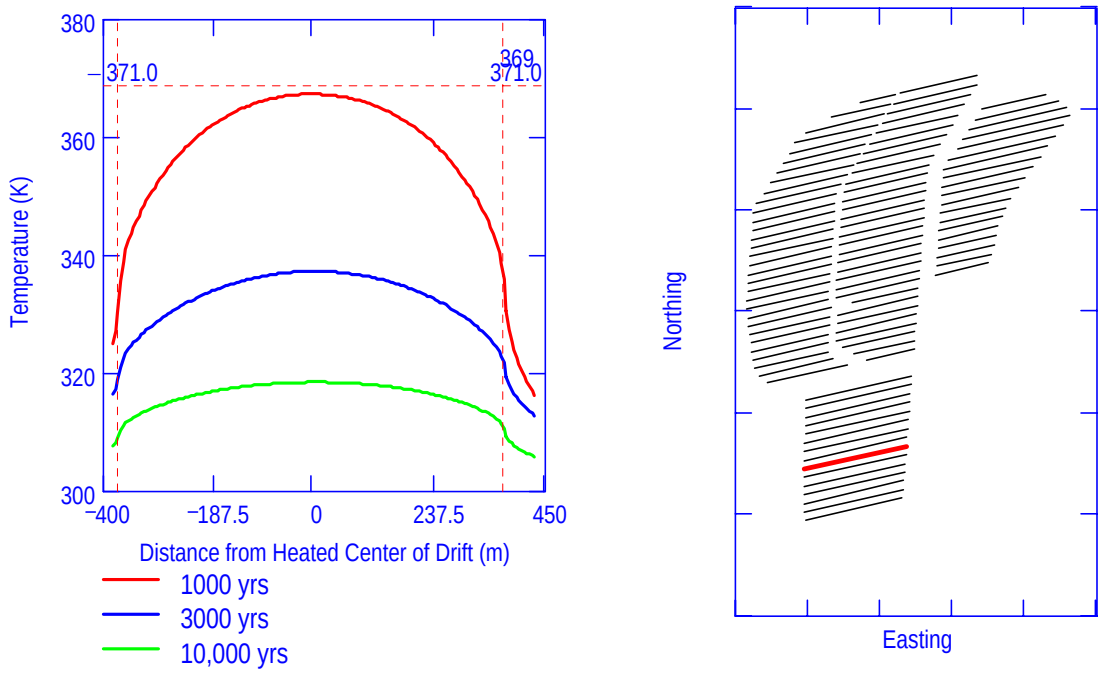

DTN: SN0408T0509903.007; file TOC.mcd; hyperlink 6.2.4, Calculated Wall Temperatures.

Figure 6.3.5-13. Drift Wall Temperatures for Chosen Drift #7

An estimate of the average axial temperature gradient in the emplacement drifts is obtained by taking the difference between the minimum and maximum wall temperatures of a particular drift and dividing by the length of the emplacement region. This gradient is multiplied by the 71-m length used in the FLUENT calculation to arrive at the temperature "tilt" used in the calculation of dispersion coefficient. The average temperature tilt for each of the analysis times is shown in Table 6.3.5-1.

Table 6.3.5-1. Average Temperature "Tilt"

Time (yrs)	Temperature Tilt (°C)
300	4
1,000	3
3,000	2
10,000	1

DTN : SN0408T0509903.007; file TOC.mcd; hyperlink 6.2.4 Calculated Wall Temperatures.

Percolation Rates for Chosen Drifts

The current analysis uses the lower limit, mean, and upper limit values of the percolation in the evaporation/condensation analysis. The local percolation rates for each drift (DTNs: LL030610323122.029 [DIRS 164513]; LL030602623122.027 [DIRS 164514]; LL030602623122.028 [DIRS 164510]) are shown in Figures 6.3.5-14 through 6.3.5-20. The averages for each of the percolation rates for each of the chosen drifts are shown on the same plot. Lower limits are shown in red. Mean values are shown in blue. Upper limits are shown in

green. The extraction of percolation rates for the drifts is located in the Mathcad file **Repository Temperature Field 3.mcd**.

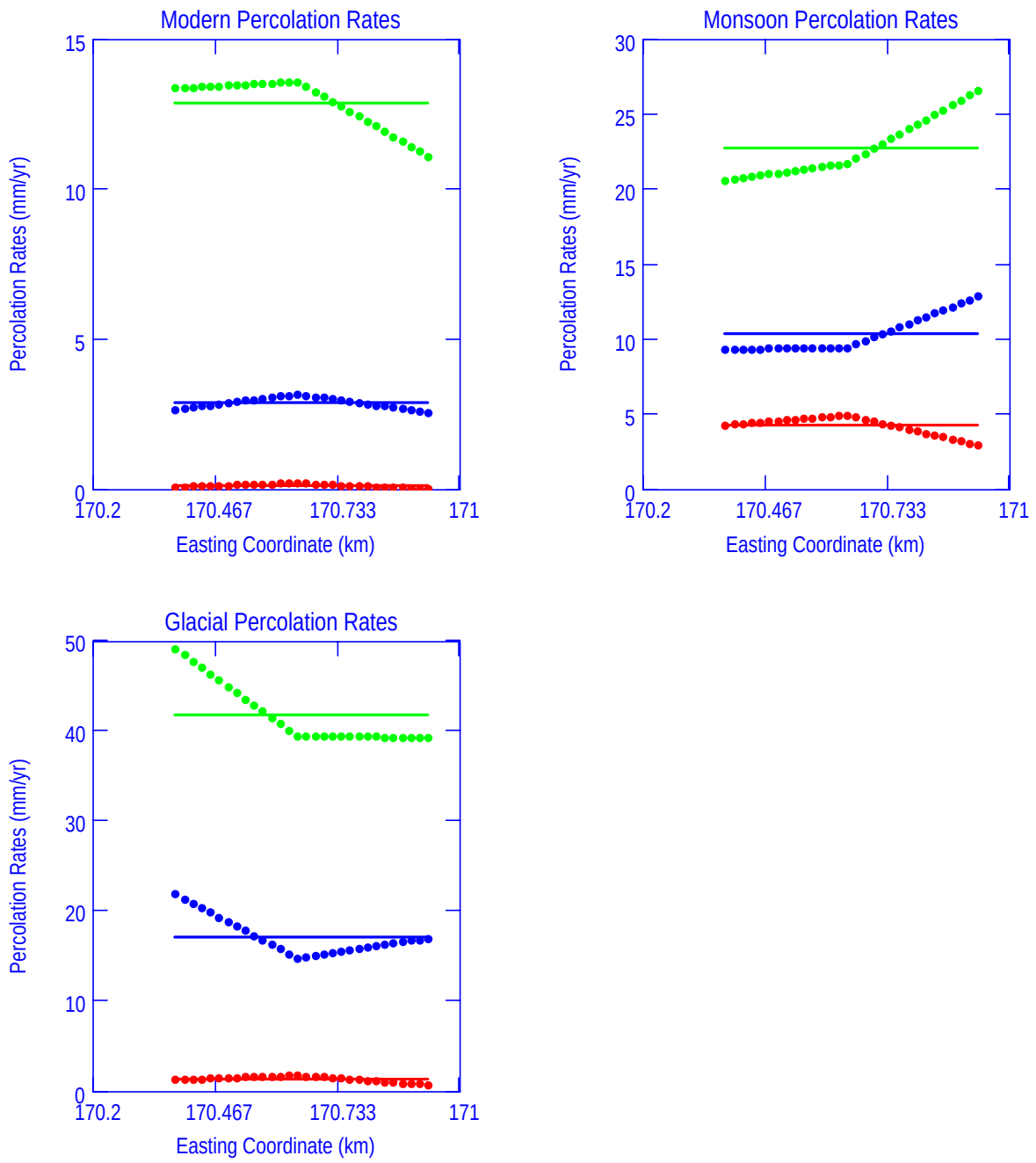

DTN: SN0408T0509903.007; file TOC.mcd; hyperlink 6.2.5, Percolation Rates for Chosen Drifts.

NOTE: Lower Limit (red); Mean (blue); Upper Limit (green); Averages (lines).

Figure 6.3.5-14. Modern, Monsoon, and Glacial Percolation Rates for Chosen Drift #1

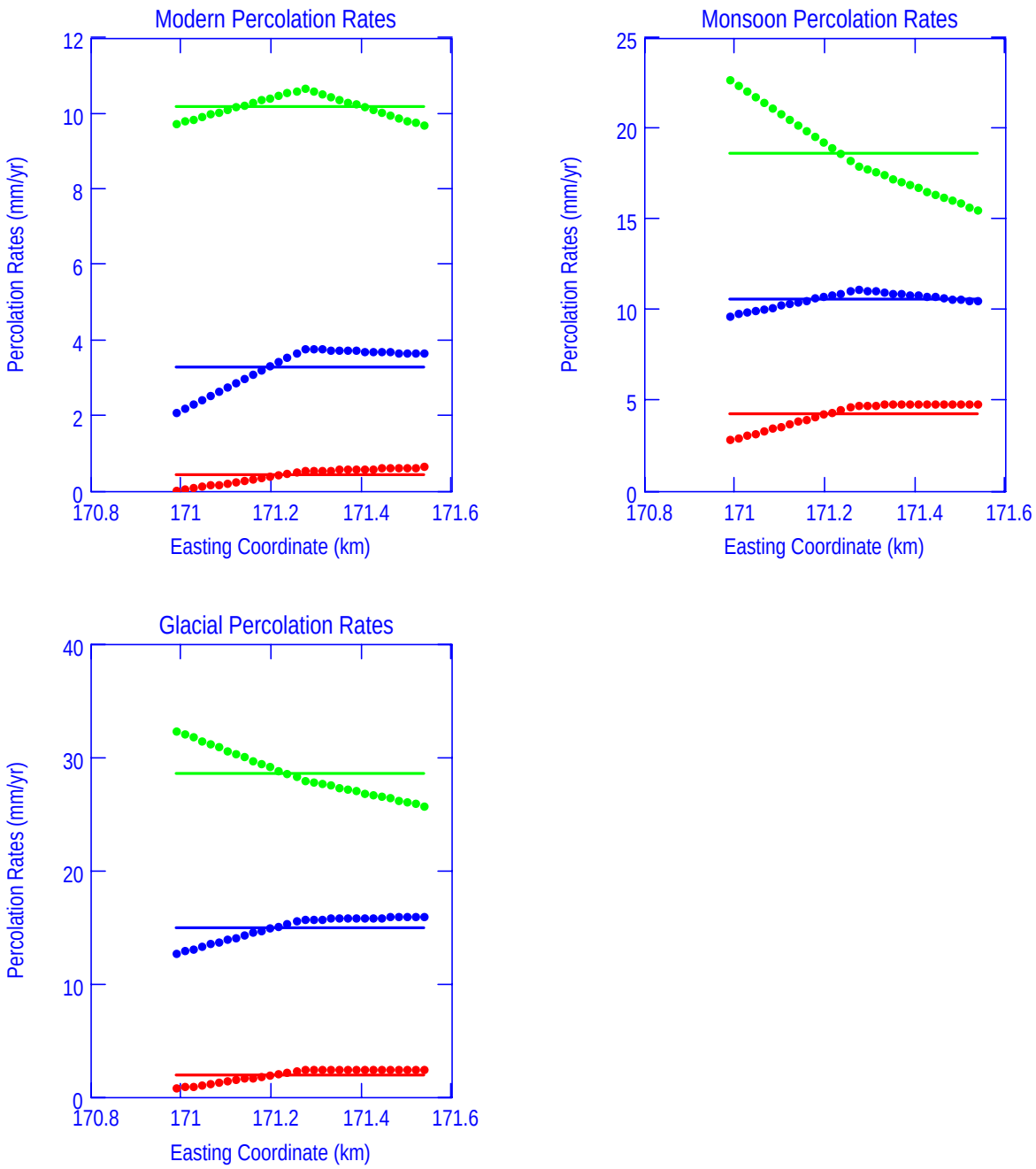

DTN: SN0408T0509903.007; file TOC.mcd; hyperlink 6.2.5, Percolation Rates for Chosen Drifts.

NOTE: Lower Limit (red); Mean (blue); Upper Limit (green); Averages (lines).

Figure 6.3.5-15. Modern, Monsoon, and Glacial Percolation Rates for Chosen Drift #2

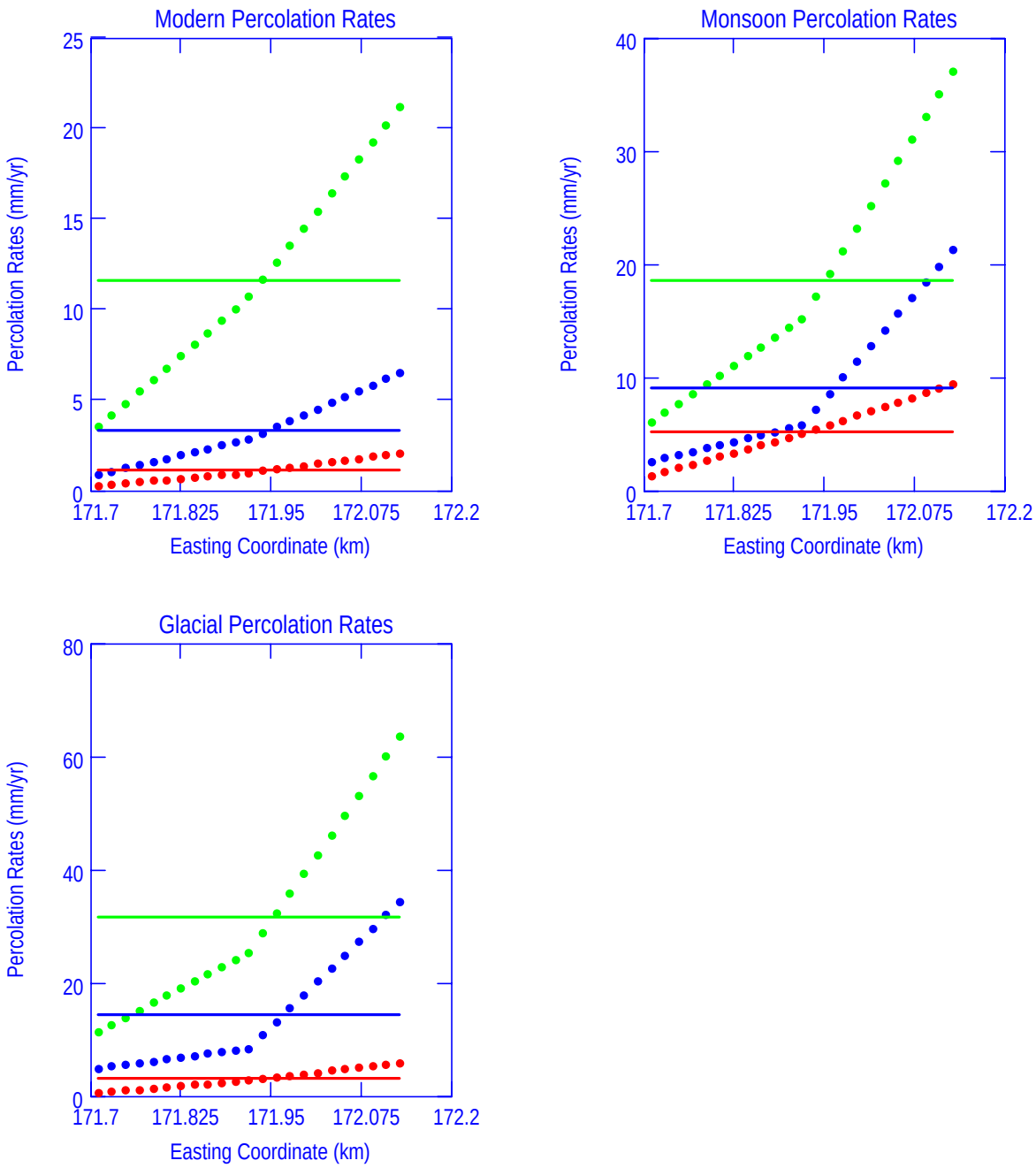

DTN: SN0408T0509903.007; file TOC.mcd; hyperlink 6.2.5 Percolation Rates for Chosen Drifts.

NOTE: Lower Limit (red); Mean (blue); Upper Limit (green); Averages (lines).

Figure 6.3.5-16. Modern, Monsoon, and Glacial Percolation Rates for Chosen Drift #3

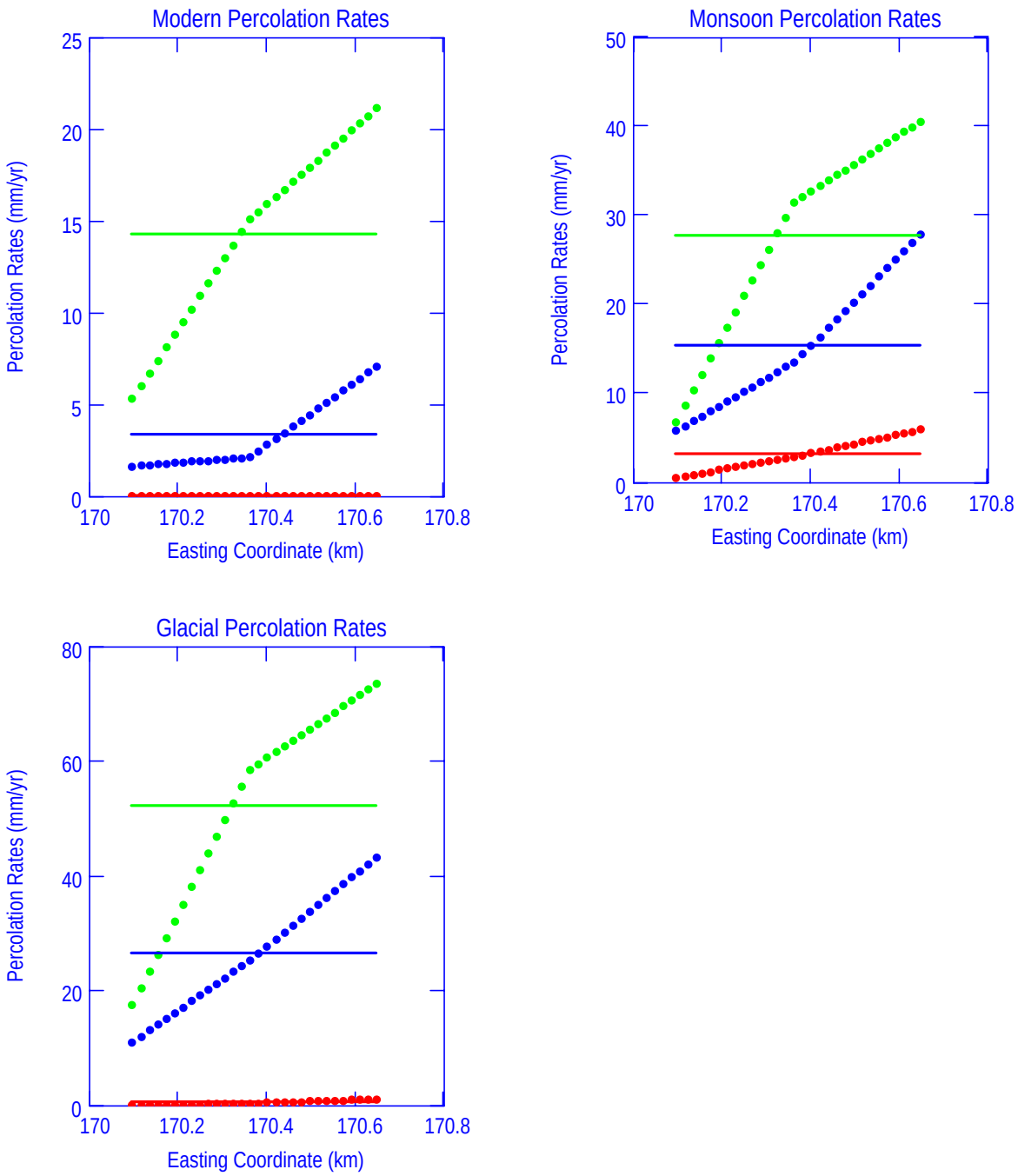

DTN: SN0408T0509903.007; file TOC.mcd; hyperlink 6.2.5, Percolation Rates for Chosen Drifts.

NOTE: Lower Limit (red); Mean (blue); Upper Limit (green); Averages (lines).

Figure 6.3.5-17. Modern, Monsoon, and Glacial Percolation Rates for Chosen Drift #4

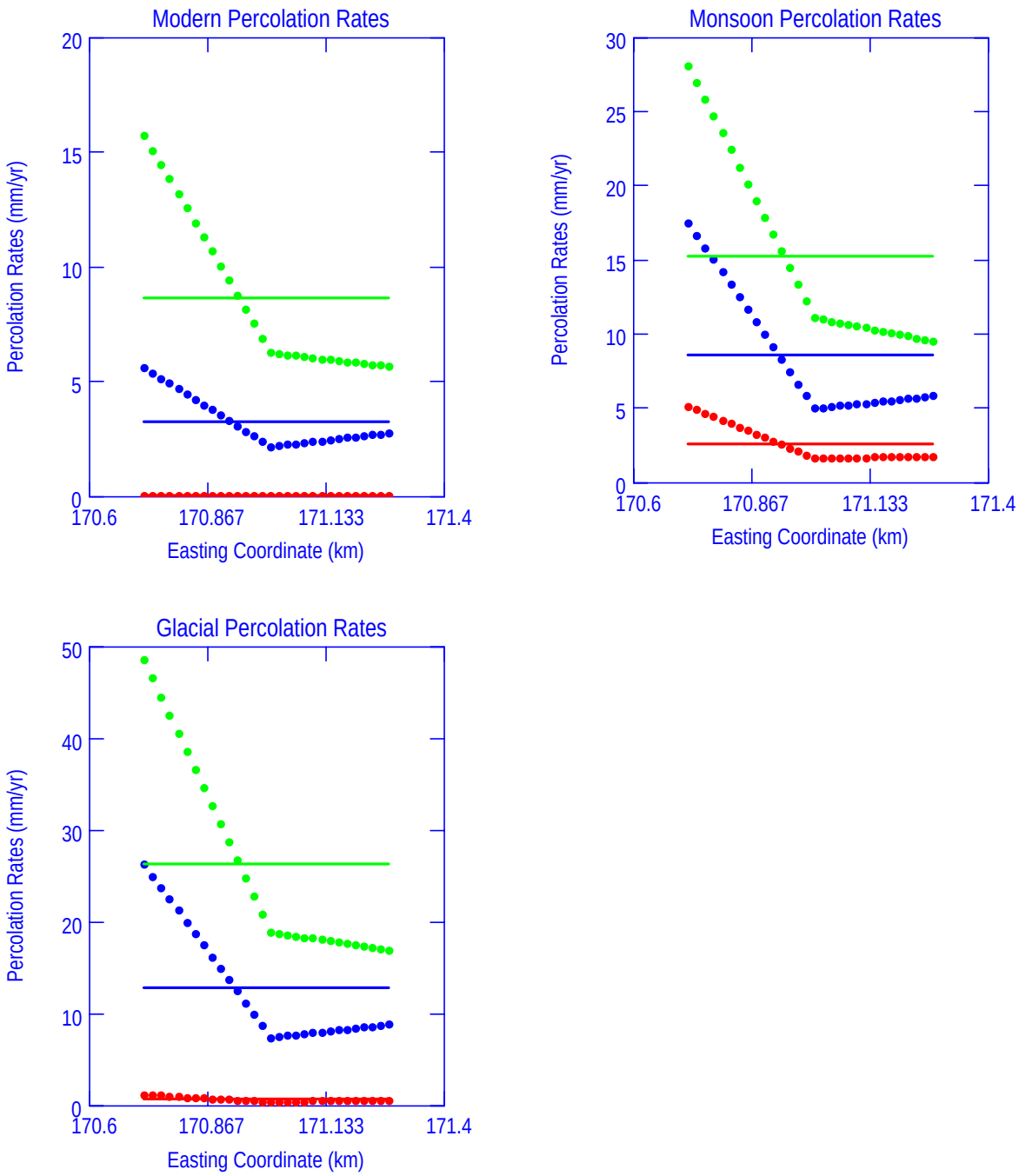

DTN: SN0408T0509903.007; file TOC.mcd; hyperlink 6.2.5, Percolation Rates for Chosen Drifts.

NOTE: Lower Limit (red); Mean (blue); Upper Limit (green); Averages (lines).

Figure 6.3.5-18. Modern, Monsoon, and Glacial Percolation Rates for Chosen Drift #5

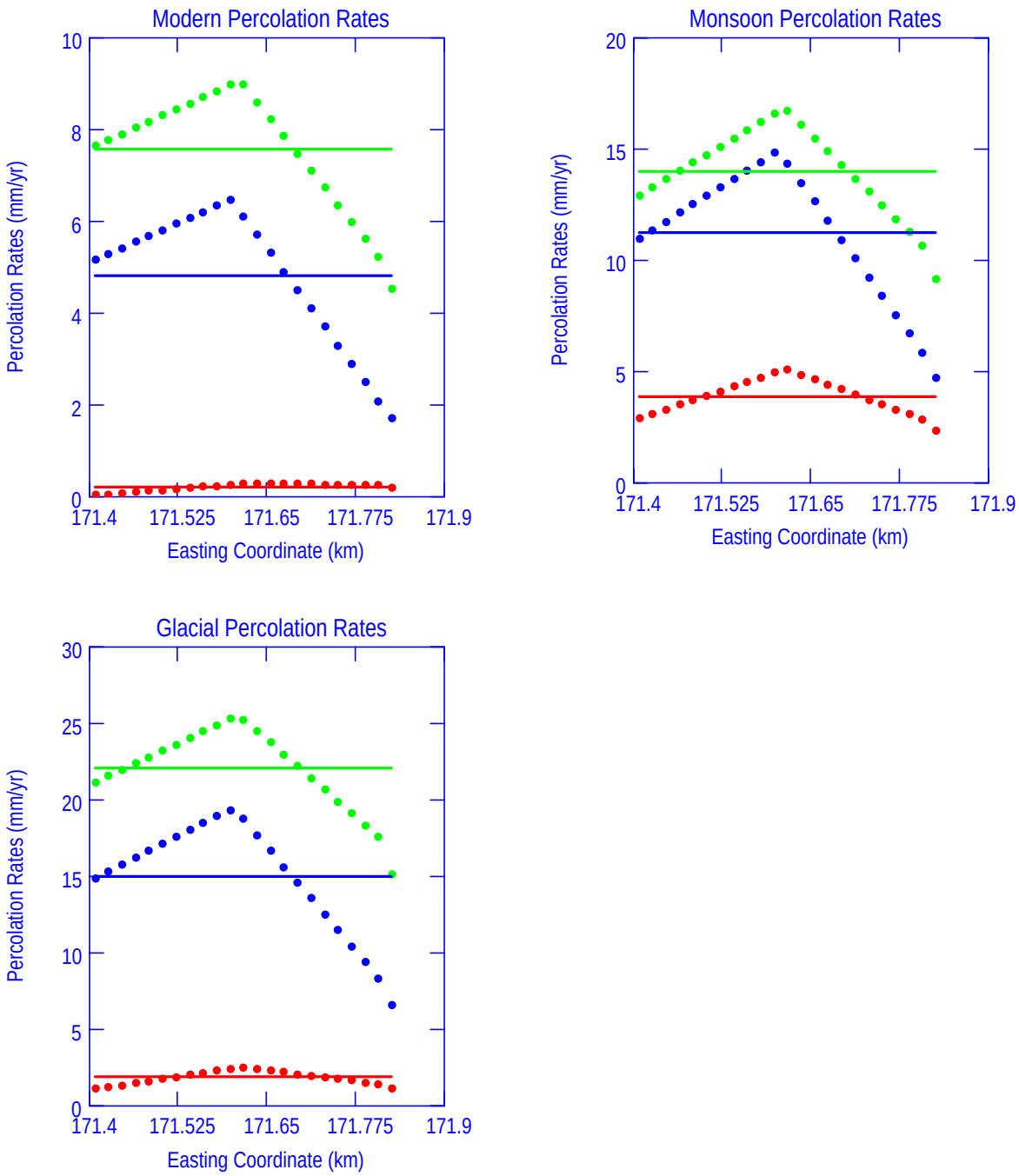

DTN: SN0408T0509903.007; file TOC.mcd; hyperlink 6.2.5, Percolation Rates for Chosen Drifts.

NOTE: Lower Limit (red); Mean (blue); Upper Limit (green); Averages (lines).

Figure 6.3.5-19. Modern, Monsoon, and Glacial Percolation Rates for Chosen Drift #6

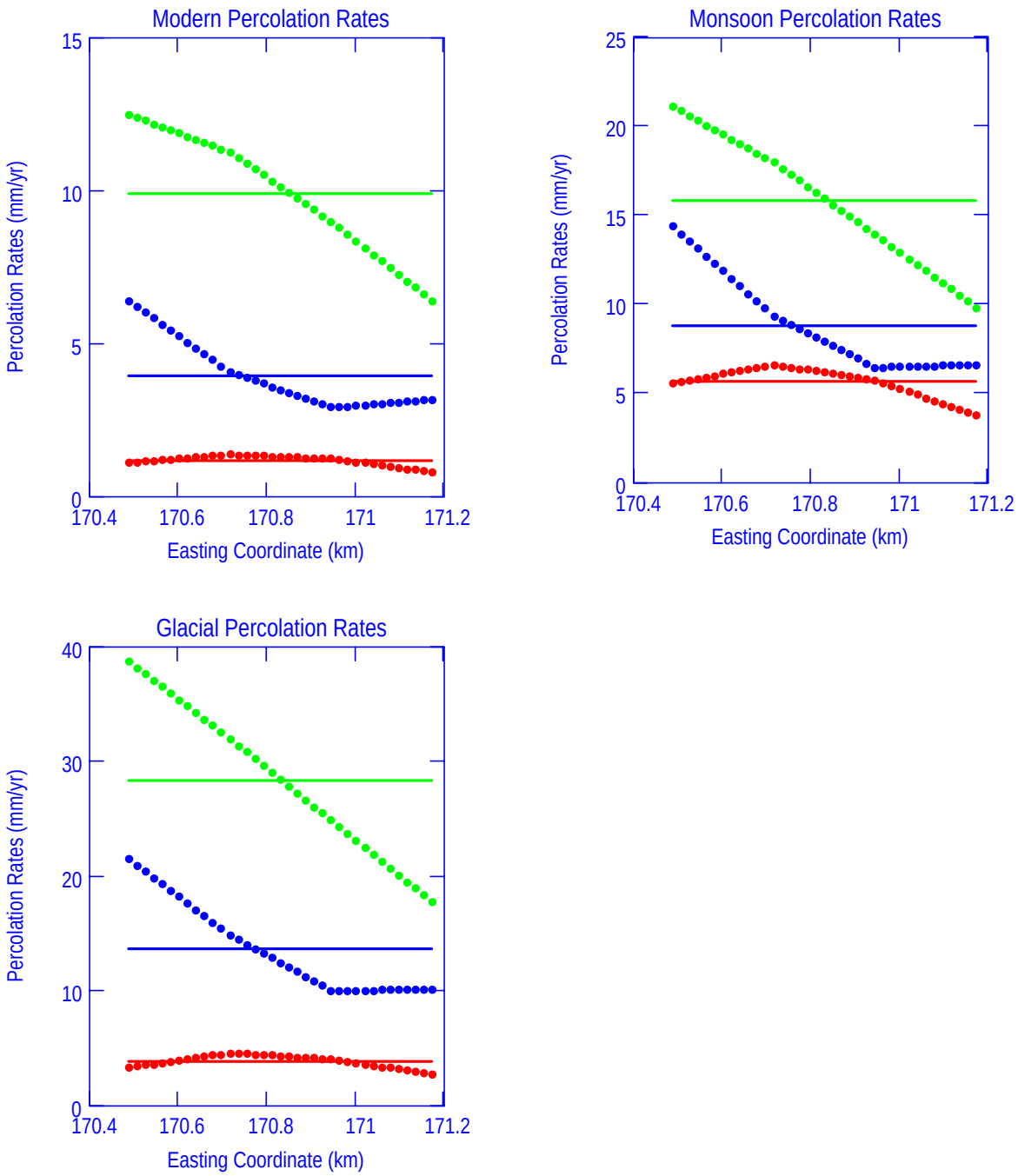

DTN: SN0408T0509903.007; file TOC.mcd; hyperlink 6.2.5, Percolation Rates for Chosen Drifts.

NOTE: Lower Limit (red); Mean (blue); Upper Limit (green); Averages (lines).

Figure 6.3.5-20. Modern, Monsoon, and Glacial Percolation Rates for Chosen Drift #7

6.3.5.1.2 Dispersion Problem Formulation

Mass and Energy Transport in the Gas

The mathematical description begins with the vapor mass conservation equation for the regions inside and outside of the drip shield. Water can evaporate (positive flux) from hotter locations, at the drift wall and invert surface, and condense at cooler portions. Additionally, condensate (negative flux) can form on both sides of the drip shield and on the waste package directly if these surfaces are sufficiently cool. These surface vapor mass fluxes (m_{wall}, m_{invert}, m_{ds_in}, m_{ds_out}, m_{wp}) add to and subtract from the axial vapor fluxes on both sides of the drip shield (m_{y_in}, m_{y_out})

$$Ac_{in}\frac{d}{dy}m_{y_in} = P_{wp}\ m_{wp} + P_{ds}\ m_{ds_in} + P_{invert}\ m_{invert}$$

$$Ac_{out}\frac{d}{dy}m_{y_out} = P_{wall}\ m_{wall} + P_{ds}\ m_{ds_out}$$

where

$Ac = \text{cross} - \text{sectional area}$

$P = \text{Perimeter}$ (Eq. 6.3-16)

Note that the contribution from the invert surface to the gas outside the drip shield is lumped with the contribution from the drift wall (Section 6.3.5.2.7, Equation 6.3-69).

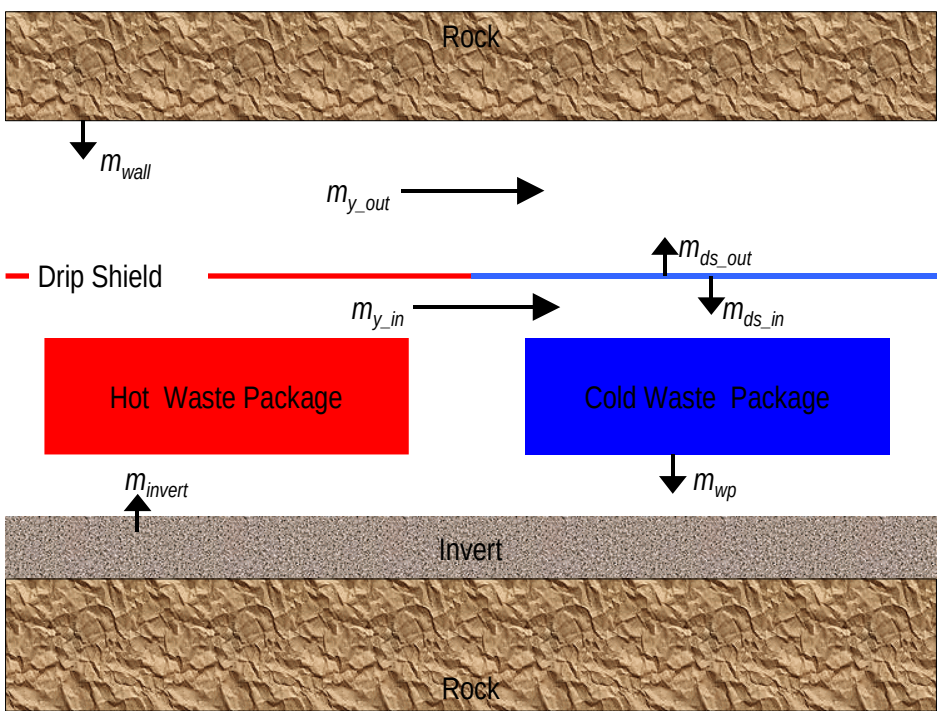

Figure 6.3.5-21. Illustration of Mass Fluxes

The vapor transport equations are derived from Fick's first law for binary mixtures in stationary coordinates (Bird et al. 1960 [DIRS 103524], p. 502, Equation A, Table 16.2-1):

$$m_{st} - X_{st}\left(m_{st} + m_{air}\right) = -\rho_{gas} D_{eff} \frac{d}{dy} X_{st}$$
$$m_{air} - X_{air}\left(m_{st} + m_{air}\right) = -\rho_{gas} D_{eff} \frac{d}{dy} X_{air} \qquad \text{(Eq. 6.3-17)}$$

where m is the mass flux in stationary coordinates, X is the component (air or vapor) mass fraction, ρ_{total} is the density of the air-vapor mixture, and D_{eff} is the vapor-air dispersion coefficient. The mass flux of air is equal to zero ($m_{air}=0$) because the drift is represented as a sealed volume without an air source or sink. The equations for the vapor mass flux down the drift (inside and outside the drip shield) become:

$$m_{y_in} = -\rho_{gas} \frac{D_{eff}}{1 - X_{st_in}} \frac{d}{dy} X_{st_in}$$
$$m_{y_out} = -\rho_{gas} \frac{D_{eff}}{1 - X_{st_out}} \frac{d}{dy} X_{st_out} \qquad \text{(Eq. 6.3-18)}$$

where the subscript for steam (st) in the axial steam mass flux (m_y) is implied. Note that this formulation accounts for the bulk advection of steam (vapor) that will occur in the drift.

The heat flow down the drift is the sum of the conduction/advection flow of heat and the enthalpy flux associated with the steam mass flux. The axial rate of change of these quantities is equal to the sum of two contributions: 1) the convective transfer of heat from the bounding surfaces, and 2) the addition and subtraction of energy via the evaporation and condensation of vapor from/on the bounding surfaces. The energy equations for the air inside and outside the drip shield are:

$$Ac_{in}\frac{d}{dy}\begin{bmatrix} q_{cond_in} \\ +h_{st}\left(T_{gas_in}\right)m_{y_in}\end{bmatrix} = P_{wp}\ hc_{wp}\left(T_{wp}-T_{gas_in}\right)+P_{ds}\ hc_{ds}\left(T_{ds}-T_{gas_in}\right)$$
$$+P_{invert}\ hc_{invert}\left(T_{invert}-T_{gas_in}\right)$$
$$+P_{wp}\ m_{wp}h_{st}\left(T_{gas_in}\right)+P_{ds}\ m_{ds_in}h_{st}\left(T_{gas_in}\right)$$
$$+P_{invert}\ m_{invert}h_{st}\left(T_{gas_in}\right)$$
$$Ac_{out}\frac{d}{dy}\begin{bmatrix} q_{cond_out} \\ +h_{st}\left(T_{gas_out}\right)m_{y_out}\end{bmatrix} = P_{wall}\ hc_{wall}\left(T_{wall}-T_{gas_out}\right)$$
$$+P_{ds}\ hc_{ds}\left(T_{ds}-T_{gas_out}\right)$$
$$+P_{wp}\ m_{wp}h_{st}\left(T_{gas_out}\right)+P_{ds}\ m_{ds_out}h_{st}\left(T_{gas_out}\right)$$

$$q_{cond_in} = -k_{eff_in}\frac{dT_{gas_in}}{dy} \quad q_{cond_out} = -k_{eff_out}\frac{dT_{gas_out}}{dy}$$

(Eq. 6.3-19)

where $h_{st}(T)$ is the enthalpy of steam at temperature T, hc is the convective heat transfer coefficient at the bounding surface, and q_{cond} is the axial heat conduction. The dispersive axial thermal conductivities (k_{eff}) are calculated based upon a dispersive Lewis number of unity. We employ the convention that surface mass flux is positive for evaporation and negative for condensation. Hence the surface mass fluxes for the waste package and the drip shield (m_{wp}, m_{dp_in}, m_{dp_out}) must always be negative because neither surface has a water source; surface mass fluxes for the invert and the drift wall can be either positive or negative.

Conservation of Energy: **Waste Packages**

Decay heat from the waste packages radiates to the drip shield and the invert, or convects to the surrounding air. Additionally, water vapor can condense on the waste package if the package temperature is sufficiently low. Conservation of energy for the waste package is:

$$Q_{wp} = Qr_{wp} + P_{wp}hc_{wp}\left(T_{wp}-T_{gas_in}\right)+P_{wp}m_{wp}h_{fg} \qquad \text{(Eq. 6.3-20)}$$

where Q_{wp} is the waste package decay heat, Qr_{wp} is the net heat radiated from the waste package to the surrounding surfaces, and m_{wp} is the condensation flux on the waste package surface (negative). Note that the sensible heat difference in the steam ($Cp_{st}\ (T_{wp}-T_{gas_in})$) is small compared to the latent heat (h_{fg}), so it is neglected. The heat radiated from the waste package (Qr_{wp}) is calculated as part of a 3-gray-surface radiation problem.

Conservation of Energy: **Drip Shield**

The drip shield produces no heat internally. Therefore the sum of the heat fluxes on both sides of the drip shield must equal zero. The thermal radiation transport from the drip shield to the

drift wall is approximated as a 2-gray-surface problem; this means that the radiation fluxes outside the drip shield can be written explicitly (Bird et al. 1960 [DIRS 103524], p. 453, Problem 14.G2). Conservation of energy for the drip shield is:

$$0 = Qr_{ds} + P_{ds} hc_{ds_in}\left(T_{ds} - T_{gas_in}\right) + P_{ds} m_{ds_in} h_{fg} + P_{ds} \frac{\sigma\left(T_{ds}^{\ 4} - T_{wall}^{\ 4}\right)}{\frac{1}{\varepsilon_{ds}} + \frac{P_{ds}}{P_{wall}}\left(\frac{1}{\varepsilon_{wall}} - 1\right)} + P_{ds} hc_{ds_out}\left(T_{ds} - T_{gas_out}\right) + P_{ds} m_{ds_out} h_{fg} \qquad \text{(Eq. 6.3-21)}$$

Conservation of Energy: **Invert**

The significant thermal characteristic of the invert is its low thermal conductivity. The measured values of dry crushed tuff are an order of magnitude smaller than those of intact tuff (DTN: GS000483351030.003 [DIRS 152932]). This means that it acts as a thermal insulator and retards the flow of heat downward into the underlying rock. The analytic approximation for the drift wall temperature does not provide any information about the invert surface temperature. In the absence of a rock/invert conduction component, the invert surface temperature cannot be calculated directly.

If the invert were a perfect insulator, the net heat flux on its surface would be zero; no heat would diffuse into the underlying rock. All of the heat radiated to it from the waste package would be either re-radiated to the drip shield or convected to the adjacent air. For this limiting case, one concludes that the invert surface temperature lies between the waste package temperature and the drip shield temperature, and the energy equation is:

$$0 = Qr_{invert} + P_{invert} hc_{invert}\left(T_{invert} - T_{gas_in}\right) + P_{invert} m_{invert} h_{fg} \qquad \text{(Eq. 6.3-22)}$$

Thermal Radiation Under the Drip Shield: **The Enclosure Problem**

To simplify the calculation, the radiation is approximated as two-dimensional; each waste package radiates only to the portions of the drip shield and invert that occupy the same axial location. Inter-package radiation is ignored. The mathematical verification of the two-dimensional heat transfer model within the drift wall is documented in Appendix J.

This two-dimensional thermal radiation simplification serves to overstate the temperature difference between adjacent waste packages. This, in turn, maximizes the evaporation rate under the hottest waste packages and the condensation rate in the vicinity of the coolest waste packages. Hence, this simplification produces an upper bound to the “local scale” condensation rate.

The radiation problem under the drip shield is a 3- gray-surface enclosure problem. The system of equations describing this problem is (Siegel and Howell 1992 [DIRS 100687], p. 271, Equation 7-31):

$$\sum_{j=1}^{3}\left(\frac{\delta_{kj}}{\varepsilon_j}-F_{k-j}\frac{1-\varepsilon_j}{\varepsilon_j}\right)qr_j=\sigma\sum_{j=1}^{3}\left(\delta_{kj}-F_{k-j}\right)T_j^4 \qquad \text{(Eq. 6.3-23)}$$

where δ is the Kronecker delta, $F_{k\text{-}j}$ is the view factor from surface k to surface *j*, and qr_j is the net radiation flux leaving surface *j*. Expanding this produces a set of three coupled equations for the surfaces under the drip shield:

$$\begin{bmatrix}\left(\frac{1}{\varepsilon_{wp}}-F_{wp-wp}\frac{1-\varepsilon_{wp}}{\varepsilon_{wp}}\right)qr_{wp}- \\ \left(F_{wp-ds}\frac{1-\varepsilon_{ds}}{\varepsilon_{ds}}\right)qr_{ds}-\left(F_{wp-invert}\frac{1-\varepsilon_{invert}}{\varepsilon_{invert}}\right)qr_{invert}\end{bmatrix}=\sigma\begin{bmatrix}\left(1-F_{wp-wp}\right)T_{wp}^4- \\ F_{wp-ds}\,T_{ds}^4-F_{wp-invert}\,T_{invert}^4\end{bmatrix}$$

$$\begin{bmatrix}\left(-F_{ds-wp}\frac{1-\varepsilon_{wp}}{\varepsilon_{wp}}\right)qr_{wp}+ \\ \left(\frac{1}{\varepsilon_{ds}}-F_{ds-ds}\frac{1-\varepsilon_{ds}}{\varepsilon_{ds}}\right)qr_{ds}-\left(F_{ds-invert}\frac{1-\varepsilon_{invert}}{\varepsilon_{invert}}\right)qr_{invert}\end{bmatrix}=\sigma\begin{bmatrix}-F_{ds-wp}\,T_{wp}^4+ \\ \left(1-F_{ds-ds}\right)T_{ds}^4 \\ -F_{ds-invert}\,T_{invert}^4\end{bmatrix}$$

$$\begin{bmatrix}\left(-F_{invert-wp}\frac{1-\varepsilon_{wp}}{\varepsilon_{wp}}\right)qr_{wp}- \\ \left(F_{invert-ds}\frac{1-\varepsilon_{ds}}{\varepsilon_{ds}}\right)qr_{ds}+\left(\frac{1}{\varepsilon_{invert}}-F_{invert-invert}\frac{1-\varepsilon_{invert}}{\varepsilon_{invert}}\right)qr_{invert}\end{bmatrix}=\sigma\begin{bmatrix}-F_{invert-wp}\,T_{wp}^4- \\ F_{invert-ds}\,T_{ds}^4+ \\ \left(1-F_{invert-invert}\right)T_{invert}^4\end{bmatrix}$$

(Eq. 6.3-24)

The geometric view factors must now be calculated. Because neither the waste package nor the invert can "see" themselves:

$$F_{wp-wp}=0$$
$$F_{invert-invert}=0 \qquad \text{(Eq. 6.3-25)}$$

The view factor from the waste package to the invert is (Howell 1982 [DIRS 164711], p. 143):

$$F_{wp-invert}=\frac{1}{\pi}\tan^{-1}\left(\frac{\frac{P_{invert}}{2}}{\frac{D_{wp}}{2}+h_{wp}}\right)$$

(Eq. 6.3-26)

where D_{wp} is the waste package diameter, h_{wp} is the vertical distance separating the waste package and the invert, and P_{invert} is the width of the invert under the drip shield. The reciprocal view factor is found by area weighting:

$$F_{invert-wp} = \frac{\pi\, D_{wp}}{P_{invert}} F_{wp-invert} \qquad \text{(Eq. 6.3-27)}$$

Because the sum of the view factors for an individual surface must sum to unity:

$$\begin{aligned} F_{wp-ds} &= 1 - F_{wp-invert} \\ F_{invert-ds} &= 1 - F_{invert-wp} \end{aligned} \qquad \text{(Eq. 6.3-28)}$$

By area weighting:

$$\begin{aligned} F_{ds-wp} &= \frac{\pi\, D_{wp}}{P_{ds}} F_{wp-ds} \\ F_{ds-invert} &= \frac{P_{invert}}{P_{ds}} F_{invert-ds} \end{aligned} \qquad \text{(Eq. 6.3-29)}$$

where P_{ds} is the perimeter length of the invert. Finally, the drip shield "self" view factor is calculated as the complement of the sum of its other view factors:

$$F_{ds-ds} = 1 - F_{ds-wp} - F_{ds-invert} \qquad \text{(Eq. 6.3-30)}$$

The surface radiation fluxes (*qr*) are taken from the energy conservation equations for the waste package surface, invert surface, and drip shield surface. View factors equal to zero are left out:

$$\sigma\begin{bmatrix} T_{wp}^4 - \\ F_{wp-ds}\,T_{ds}^4 - F_{wp-invert}\,T_{invert}^4 \end{bmatrix} = \begin{bmatrix} \left(\dfrac{1}{\varepsilon_{wp}}\right) qr_{wp} - \\ \left(F_{wp-ds}\dfrac{1-\varepsilon_{ds}}{\varepsilon_{ds}}\right) qr_{ds} - \\ \left(F_{wp-invert}\dfrac{1-\varepsilon_{invert}}{\varepsilon_{invert}}\right) qr_{invert} \end{bmatrix}$$

$$\sigma\begin{bmatrix} -F_{ds-wp}\,T_{wp}^4 + \left(1-F_{ds-ds}\right)T_{ds}^4 \\ -F_{ds-invert}\,T_{invert}^4 \end{bmatrix} = \begin{bmatrix} \left(-F_{ds-wp}\dfrac{1-\varepsilon_{wp}}{\varepsilon_{wp}}\right) qr_{wp} + \\ \left(\dfrac{1}{\varepsilon_{ds}} - F_{ds-ds}\dfrac{1-\varepsilon_{ds}}{\varepsilon_{ds}}\right) qr_{ds} - \\ \left(F_{ds-invert}\dfrac{1-\varepsilon_{invert}}{\varepsilon_{invert}}\right) qr_{invert} \end{bmatrix}$$

$$\sigma\begin{bmatrix} -F_{invert-wp}\,T_{wp}^4 - \\ F_{invert-ds}\,T_{ds}^4 + T_{invert}^4 \end{bmatrix} = \begin{bmatrix} \left(-F_{invert-wp}\dfrac{1-\varepsilon_{wp}}{\varepsilon_{wp}}\right) qr_{wp} \\ -\left(F_{invert-ds}\dfrac{1-\varepsilon_{ds}}{\varepsilon_{ds}}\right) qr_{ds} \\ +\left(\dfrac{1}{\varepsilon_{invert}}\right) qr_{invert} \end{bmatrix} \qquad \text{(Eq. 6.3-31)}$$

6.3.5.1.3 Heat and Mass Transfer Correlations

Heat Transfer Correlations

Waste Package

In their development of a convection correlation for annular regions, Kuehn and Goldstein modified previously developed correlations for a cylinder in a fluid to account for the thickness of the boundary layer. This analysis uses their modified correlation for a cylinder in a fluid (Kuehn and Goldstein 1976 [DIRS 100675], Equation 12; Kuehn and Goldstein 1978 [DIRS 130084], nomenclature).

$$hc_{wp} = \frac{Nu_{wp} k_{gas}}{D_{wp}}$$

$$Nu_{wp} = \frac{2}{\ln\left[1 + \frac{2}{\left[\left(0.518 Ra_{wp}^{1/4}\left[1 + \left(\frac{0.559}{\mathrm{Pr}_{gas}}\right)^{3/5}\right]^{-5/12}\right)^{15} + \left(0.1 Ra_{wp}^{1/3}\right)^{15}\right]^{1/15}}\right]}$$

$$Ra_{wp} = g \frac{\beta_{gas}}{\nu_{gas}^2} \mathrm{Pr}_{gas} D_{wp}^3 \left|T_{wp} - T_{gas}\right|$$

(Eq. 6.3-32)

Invert

Heat transfer from the invert surface to the overlying gas depends on the invert-gas temperature difference. When the invert surface is hotter than the overlying gas, the gas layer will become unstable and a convection pattern will form. This calculation uses the correlation for horizontal heated upward-facing plates (Raithby and Hollands 1985 [DIRS 164700], p. 6-19).

When the invert is cooler than the overlying gas, the gas is reasonably stable. Heat must conduct through a thick nearly stagnant gas layer; the thickness of this layer is estimated to be equal to the distance between the invert surface and the bottom of the waste package (H_{wp}).

$$hc_{invert} = \begin{cases} \dfrac{Nu_{invert} k_{gas}}{P_{invert}} & \text{if} \quad T_{invert} > T_{gas} \\ \dfrac{k_{gas}}{H_{wp}} & \text{if} \quad T_{invert} < T_{gas} \end{cases}$$

$$Nu_{invert} = \left[Nu_l^{10} + Nu_t^{10} \right]^{0.1}$$ [Raithby & Hollands 1985 [DIRS 164700], Eq. 52]

$$Nu_t = C_t^H Ra_{invert}^{1/3}$$ [Raithby & Hollands 1985 [DIRS 164700], Eq. 51]

$$Nu_l = \frac{1.4}{\ln\left(1 + 1.4 / Nu^T\right)}$$ [Raithby & Hollands 1985 [DIRS 164700], Eq. 50]

$$Nu^T = 0.835\, \overline{C}_l\, Ra_{invert}^{1/4}$$ [Raithby & Hollands 1985 [DIRS 164700], Eq. 49]

$$C_t^H = 0.14$$ [Raithby & Hollands 1985 [DIRS 164700], Eq. 30]

$$\overline{C}_l = \frac{4}{3} C_l$$ [Raithby & Hollands 1985 [DIRS 164700], Eq. 22]

$$C_l = \frac{0.503}{\left[1 + \left(\dfrac{0.492}{\Pr_{gas}} \right)^{9/16} \right]^{4/9}}$$ [Raithby & Hollands 1985 [DIRS 164700], Eq. 16]

$$Ra_{invert} = g \frac{\beta}{\nu_{gas}^2} \Pr_{gas} P_{invert}^3 \left| T_{invert} - T_{gas} \right|$$ [Raithby & Hollands 1985 [DIRS 164700], Eq. 15]

(Eq. 6.3-33)

where P_{invert} is the width of the invert under the drip shield.

Drip Shield

The drip shield is represented with a single temperature; a single heat transfer coefficient is used to describe it. For the purpose of this model, the drip shield is composed of two (2) vertical sides and a curvilinear top. The correlation for a vertical flat plate is used for the sides. The correlation for an inclined plate is used to approximate the convection from the top surface.

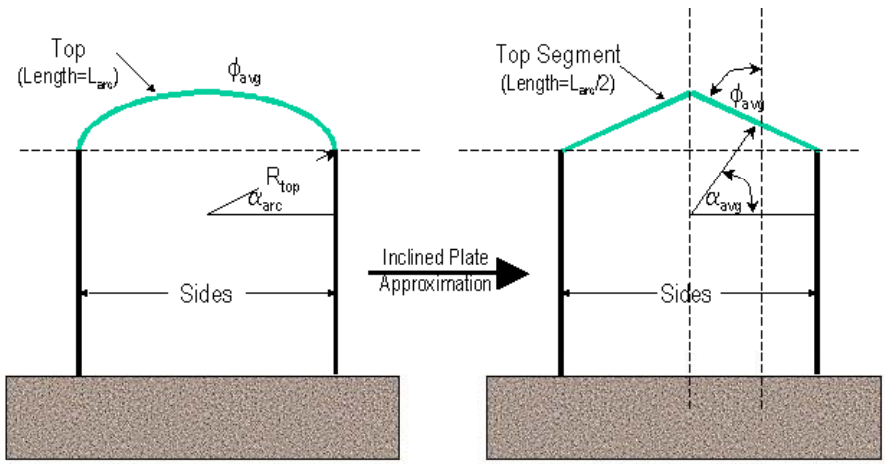

Figure 6.3.5-22. Approximate Angle for Drip Shield Top

The vertical sides are represented with the vertical plate correlation (Raithby and Hollands 1985 [DIRS 164700], p. 6-17).

$$hc_{ds_sides} = \frac{Nu_{ds_sides} k_{gas}}{L_{ds_sides}}$$

$$Nu_{ds_sides} = \left[Nu_l^{\,6} + Nu_t^{\,6}\right]^{1/6}$$ [Raithby & Hollands 1985 [DIRS 164700], Eq. 42]

$$Nu_t = C_t^V Ra_{ds_sides}^{1/3}$$ [Raithby & Hollands 1985 [DIRS 164700], Eq. 41]

$$Nu_l = \frac{2.8}{\ln\left(1 + 2.8/Nu^T\right)}$$ [Raithby & Hollands 1985 [DIRS 164700], Eq. 40]

$$Nu^T = \overline{C}_l Ra_{ds_sides}^{1/4}$$ [Raithby & Hollands 1985 [DIRS 164700], Eq. 39]

$$C_t^V = \frac{0.13 \Pr_{gas}^{\;0.22}}{\left(1 + 0.61 \Pr_{gas}^{\;0.81}\right)^{0.42}}$$ [Raithby & Hollands 1985 [DIRS 164700], Eq. 29]

$$\overline{C}_l = \frac{4}{3} C_l$$ [Raithby & Hollands 1985 [DIRS 164700], Eq. 22]

$$C_l = \frac{0.503}{\left[1 + \left(\frac{0.492}{\Pr_{gas}}\right)^{9/16}\right]^{4/9}}$$ [Raithby & Hollands 1985 [DIRS 164700], Eq. 16]

$$Ra_{ds_sides} = g \frac{\beta_{gas}}{\nu_{gas}^2} \Pr_{gas} L_{ds_sides}^3 \left|T_{ds} - T_{gas}\right|$$ [Raithby & Hollands 1985 [DIRS 164700], Eq. 15]

(Eq. 6.3-34)

Convection from the cap of the drip shield is approximated by the correlation for an inclined plate (Raithby and Hollands 1985 [DIRS 164700], p. 6-21). The average angle of inclination (ϕ_{avg}) is computed from the arc angle (α_{arc}) (Section 6.3, Equation 6.3-62). The angle describing the top of the drip shield varies from α_{arc} to π/2. The average inclination angle (ϕ_{avg}) is the average of the descriptive angle:

$$\phi_{avg} = \frac{1}{2}\left(\frac{\pi}{2} + \alpha_{arc}\right) \qquad \text{(Eq. 6.3-35)}$$

For this drip shield design (Section 6.3.5.2.7), the average inclination angle is 56.5º.

The total Nusselt number is computed using the same averaging for laminar and turbulent components as for the vertical plate:

$$hc_{ds_top} = \frac{Nu_{ds_sides} k_{gas}}{\left(\frac{P_{ds_top}}{2}\right)}$$

$$Nu_{ds_top} = \left[Nu_l^{\,6} + Nu_t^{\,6}\right]^{1/6} \qquad \text{[Raithby \& Hollands 1985 [DIRS 164700], Eq. 42]}$$

(Eq. 6.3-36)

where P_{ds_top} is the arc-length of the drip shield cap and α_{avg} is the average angle of the drip shield top.

The laminar Nusselt number (Nu_l) is obtained by multiplying the Rayleigh number by the cosine of the inclination angle (ϕ_{avg}) in the correlation for a vertical plate.

$$Nu_l = \max\left(Nu_{lH}, Nu_{lV}\right)$$

$$Nu_l = \frac{2.8}{\ln\left(1+\frac{2.8}{Nu^T}\right)}$$ [Raithby & Hollands 1985 [DIRS 164700], Eq. 40]

$$Nu^T = \overline{C}_l\left(\cos\left(\phi_{avg}\right) Ra_{ds_top}\right)^{1/4}$$ [Raithby & Hollands 1985 [DIRS 164700], Eq. 39, modified per p. 6.21]

$$\overline{C}_l = \frac{4}{3}C_l$$ [Raithby & Hollands 1985 [DIRS 164700], Eq. 22]

$$C_l = \frac{0.503}{\left[1+\left(\frac{0.492}{\Pr_{gas}}\right)^{9/16}\right]^{4/9}}$$ [Raithby & Hollands 1985 [DIRS 164700], Eq. 16]

$$Ra_{ds_top} = g\frac{\beta_{gas}}{\nu_{gas}^2}\Pr_{gas}\left(\frac{P_{ds_top}}{2}\right)^3\left|T_{ds}-T_{gas}\right|$$ [Raithby & Hollands 1985 [DIRS 164700], Eq. 15]

(Eq. 6.3-37)

The turbulent Nusselt is given by the relationship:

$$Nu_t = C_t\, Ra_{ds_top}^{1/3}$$ [Raithby & Hollands 1985 [DIRS 164700], p. 6 - 21]

$$C_t = \begin{cases} C_{tV}\left[\cos\left(\phi_{avg}\right)\right]^{1/3} & -90^o \le \phi_{avg} \le \operatorname{atan}\left[\left(\frac{C_{tV}}{C_{tH}}\right)^3\right] \\ C_{tH}\left[\sin\left(\phi_{avg}\right)\right]^{1/3} & \operatorname{atan}\left[\left(\frac{C_{tV}}{C_{tH}}\right)^3\right] \le \phi_{avg} \le 90^o \end{cases}$$ [Raithby & Hollands 1985 [DIRS 164700], Eq. 28]

$$C_{tV} = \frac{0.13\Pr_{gas}^{0.22}}{\left(1+0.61\Pr_{gas}^{0.81}\right)^{0.42}}$$ [Raithby & Hollands 1985 [DIRS 164700], Eq. 29]

$$C_{tH} = 0.14 \quad \Pr_{gas} < 100$$ [Raithby & Hollands 1985 [DIRS 164700], Eq. 30]

(Eq. 6.3-38)

For a Prandtl number of 0.7, the arctan of $(C_{tV}/C_{tH})^3$ is about 22º.

The sign attributed to the inclination angle is dependent upon the orientation of the surface with respect to the gas (Raithby and Hollands 1985 [DIRS 164700], p. 6-11). The drip shield will be cooler than the gas inside of the drip shield and hotter than the gas outside the drip shield. For both of these cases, ϕ_{avg} is positive. This means that the correct turbulent Nusselt number for this analysis is:

$$Nu_t = C_t \, Ra_{ds_top}^{1/3} \qquad \left[\text{Raithby \& Hollands 1985 [DIRS 164700], p. 6-21 in text}\right]$$

$$C_t = C_{tH}\left[\sin\left(\phi_{avg}\right)\right]^{1/3} \qquad \left[\text{Raithby \& Hollands [DIRS 164700], Eq. 28}\right]$$

$$C_{tH} = 0.14 \qquad \left[\text{Raithby \& Hollands [DIRS 164700], Eq. 30}\right]$$

(Eq. 6.3-39)

The average heat transfer coefficient for the entire drip shield is the area-weighted average of the vertical plate correlation and the inclined plate correlation.

$$hc_{ds_top} = \frac{hc_{ds_top} P_{ds_top} + 2\, hc_{ds_sides} L_{ds_sides}}{P_{ds}}$$

where

$$P_{ds} = P_{ds_top} + 2\, L_{ds_sides}$$

(Eq. 6.3-40)

Drift Wall

In their development of a convection correlation for annular regions, Kuehn and Goldstein modified previously developed correlations for convection within a horizontal cylinder in a fluid to account for the thickness of the boundary layer. This analysis uses their modified correlation (Kuehn and Goldstein 1976 [DIRS 100675], Equation 22):

$$hc_{wall} = \frac{Nu_{wall} k_{gas}}{D_{drift}}$$

$$Nu_{wall} = \frac{2}{-\ln\left[1 - \frac{2}{\left[\left(\left[\left(\frac{2}{1-e^{-0.25}}\right)^{5/3} + \left(0.587\, G\, Ra_{wall}^{1/4}\right)^{5/3}\right]^{3/5}\right)^{15} + \left(0.1 Ra_{wall}^{1/3}\right)^{15}\right]^{\frac{1}{15}}}\right]}$$

$$G = \left[\left(1 + \frac{0.6}{\Pr_{gas}^{0.7}}\right)^{-5} + \left(0.4 + 2.6 \Pr_{gas}^{0.7}\right)^{-5}\right]^{-1/5}$$

$$Ra_{wall} = g \frac{\beta_{gas}}{\nu_{gas}^2} \Pr_{gas} D_{wall}^3 \left|T_{wall} - T_{gas}\right|$$

(Eq. 6.3-41)

Mass Transfer Correlations

Correlations for vapor transport to and from the bounding surfaces are derived from the heat transfer coefficients by adjusting the correlating equations for gas diffusion instead of heat diffusion. Specifically, 1) the Schmidt number of the gas (Sc_{gas}) is substituted for the Prandtl number (Pr_{gas}) in the calculation of the Rayleigh number, and 2) the product of the density (ρ_{gas}) and the gas diffusion coefficient (Dva) is substituted for the gas thermal conductivity (k_{gas}) in the equation for the mass transfer coefficient (Bird et al. 1960 [DIRS 103524], p. 646, Table 21.2-1). For clarity, the vapor mass fluxes (m) are written directly in terms of the Rayleigh numbers (Ra), thereby eliminating the mass transfer coefficient itself. The mass transfer rate is adjusted for the vapor mass fraction (X_{st}) in the same way that the axial diffusion equations were corrected: by dividing by the complement of the vapor mass fraction.

Waste Package

The waste package mass transfer Nusselt number (Nu_mass_{wp}) is derived from the waste package heat transfer Nusselt number. Evaporation from the waste package is not possible, so the difference between the equilibrium vapor fraction at the waste package temperature ($Xst_{sat}(Twp)$) and the vapor mass fraction in the gas under the drip shield (Xst_{in}) is tested to see if condensation is possible.

$$m_{wp} = \begin{cases} \dfrac{Nu_mass_{wp}\rho_{gas}Dva}{D_{wp}}\left(\dfrac{Xst_{sat}\left(T_{wp}\right) - Xst_{in}}{1 - Xst_{in}}\right) & \text{if} \quad Xst_{sat}\left(T_{wp}\right) < Xst_{in} \\ 0 & \text{if} \quad Xst_{sat}\left(T_{wp}\right) > Xst_{in} \end{cases}$$

$$Nu_mass_{wp} = \frac{2}{\ln\left[1 + \dfrac{2}{\left[\left(0.518\, Ra_{wp}^{1/4}\left[1 + \left(\dfrac{0.559}{Sc_{gas}}\right)^{3/5}\right]^{-5/12}\right)^{15} + \left(0.1\, Ra_{wp}^{1/3}\right)^{15}\right]^{1/15}}\right]}$$

$$Ra_{wp} = g\frac{\beta_{gas}}{\nu_{gas}^2}\Pr_{gas} D_{wp}^3 \left|T_{wp} - T_{gas}\right|$$

(Eq. 6.3-42)

Invert

The invert mass transfer Nusselt number (Nu_mass_{invert}) is derived from the invert heat transfer Nusselt number. In the low invert transport case, the vapor pressure at the invert surface is tied to the drift wall temperature. In the high invert transport case, the vapor pressure at the invert surface is tied to the invert surface temperature (Assumption 6.3.3.2.1).

$$m_{invert} = \begin{cases} \dfrac{Nu_mass_{invert}\ \rho_{gas}\ Dva}{P_{invert}} \left(\dfrac{Xst_{invert} - Xst_{in}}{1 - Xst_{in}} \right) & \text{if} \quad T_{invert} > T_{gas} \\ \dfrac{\rho_{gas}\ Dva}{H_{wp}} & \text{if} \quad T_{invert} < T_{gas} \end{cases}$$

$$Xst_{invert} = \begin{matrix} Xst_{sat}(T_{wall}) & \text{for low invert transport case} \\ Xst_{sat}(T_{invert}) & \text{for high invert transport case} \end{matrix}$$

$$Nu_mass_{invert} = \left[Nu_mass_l^{\ 10} + Nu_mass_g^{\ 10} \right]^{0.1}$$

$$Nu_mass_l = C_t^H\ Ra_{invert}^{1/3}$$

$$Nu_mass_l = \frac{1.4}{\ln\left(1 + 1.4 / Nu^T\right)}$$

$$Nu^T = 0.835\ \overline{C}_l\ Ra_{invert}^{1/4}$$

$$C_t^H = 0.14$$

$$\overline{C}_l = \frac{4}{3} C_l$$

$$C_l = \frac{0.503}{\left[1 + \left(\dfrac{0.492}{Sc_{gas}} \right)^{9/16} \right]^{4/9}}$$

$$Ra_{invert} = g \frac{\beta_{gas}}{\nu_{gas}^2} \Pr_{gas}\ P_{invert}^3 \left| T_{invert} - T_{gas} \right|$$

(Eq. 6.3-43)

Drip Shield

The drip shield mass transfer Nusselt number (Nu_mass_{ds}) is derived from the drip shield heat transfer Nusselt number. Evaporation from the drip shield is not possible, so the difference between the equilibrium vapor fraction at the drip shield temperature ($Xst_{sat}(T_{ds})$) and the vapor mass fraction in the gas (Xst_{in}, Xst_{out}) is tested to see if condensation is possible.

$$m_{ds_sides} = \begin{cases} \dfrac{Nu_mass_{ds_sides}\,\rho_{gas}\,Dva}{L_{ds_sides}}\left(\dfrac{Xst_{sat}(T_{ds}) - Xst_{in}}{1 - Xst}\right) & \text{if} \quad Xst_{sat}(T_{ds}) < Xst \\ 0 & \text{if} \quad Xst_{sat}(T_{ds}) > Xst \end{cases}$$

$$Nu_mass_{ds_sides} = \left[Nu_l^{\,6} + Nu_t^{\,6}\right]^{1/6}$$

$$Nu_t = C_t^V\, Ra_{ds_sides}^{1/3}$$

$$Nu_l = \frac{2.8}{\ln\left(1 + 2.8 / Nu^T\right)}$$

$$Nu^T = \overline{C}_l\; Ra_{ds_sides}^{1/4}$$

$$C_t^V = \frac{0.13\, Sc^{0.22}}{\left(1 + 0.61 Sc_{gas}^{\;0.81}\right)^{0.42}}$$

$$\overline{C}_l = \frac{4}{3} C_l$$

$$C_l = \frac{0.503}{\left[1 + \left(\dfrac{0.492}{Sc_{gas}}\right)^{9/16}\right]^{4/9}}$$

$$Ra_{ds_sides} = g\,\frac{\beta_{gas}}{\nu_{gas}^2}\,\mathrm{Pr}_{gas}\; L_{ds_sides}^3 \left|T_{ds} - T_{gas}\right|$$

(Eq. 6.3-44)

$$m_{ds_top} = \begin{cases} \dfrac{Nu_mass_{ds_top}\rho_{gas}Dva}{\dfrac{P_{ds_top}}{2}}\left(\dfrac{Xst_{sat}(T_{ds}) - Xst_{in}}{1 - Xst}\right) & \text{if} \quad Xst_{sat}(T_{ds}) < Xst \\ 0 & \text{if} \quad Xst_{sat}(T_{ds}) > Xst \end{cases}$$

$$Nu_{ds_top} = \left[Nu_l^{\,6} + Nu_t^{\,6}\right]^{1/6}$$

$$Nu_l = \frac{2.8}{\ln\left(1 + 2.8/Nu^T\right)}$$

$$Nu^T = \overline{C}_l\left[\cos(\phi_{avg})Ra_{ds_top}\right]^{1/4}$$

$$\overline{C}_l = \frac{4}{3}C_l$$

$$C_l = \frac{0.503}{\left[1 + \left(\dfrac{0.492}{Sc_{gas}}\right)^{9/16}\right]^{4/9}}$$

$$Nu_t = C_t\ Ra_{ds_top}^{1/3}$$

$$C_t = C_{tH}\left[\sin(\phi_{avg})\right]^{1/3}$$

$$C_{tH} = 0.14$$

$$Ra_{ds_top} = g\cos(\alpha)\frac{\beta_{gas}}{\nu_{gas}^2}Sc_{gas}\left(\frac{P_{ds_top}}{2}\right)^3\left|T_{ds} - T_{gas}\right|$$

(Eq. 6.3-45)

The average mass flux for the entire drip shield (m_{ds}) is the area-weighted average of the vertical plate correlation and the inclined plate correlation.

$$m_{ds} = \frac{m_{ds_top}P_{ds_top} + 2\ m_{ds_sides}L_{ds_sides}}{P_{ds}}$$

$$\text{where} \quad P_{ds} = P_{ds_top} + 2\ L_{ds_sides}$$

(Eq. 6.3-46)

Drift Wall

The drift wall mass transfer Nusselt number (Nu_mass_{wall}) is derived from the wall heat transfer Nusselt number.

$$m_{invert} = \frac{Nu_mass_{wall}\ \rho_{gas}\ Dva}{D_{wall}} \left(\frac{Xst_{sat}(T_{invert}) - Xst_{in}}{1 - Xst_{in}} \right)$$

$$Nu_mass_{wall} = \frac{2}{-\ln\left[1 - \frac{2}{\left[\left(\left[\left(\frac{2}{1-e^{-0.25}}\right)^{5/3} + \left(0.587\ G\ Ra_{wall}^{1/4}\right)^{5/3}\right]^{5/3}\right)^{15} + \left(0.1\ Ra_{wall}^{1/3}\right)^{15}\right]^{1/15}}\right]}$$

$$G = \left[\left(1 + \frac{0.6}{Sc_{gas}^{0.7}}\right)^{-5} + \left(0.4 + 2.6\,Sc_{gas}^{0.7}\right)^{-5}\right]^{-1/5}$$

$$Ra_{wall} = g\,\frac{\beta_{gas}}{\nu_{gas}^{2}}\,Sc_{gas}\ D_{wall}^{3}\left|T_{wall} - T_{gas}\right|$$

(Eq. 6.3-47)

6.3.5.1.4 Evaporation Limits

The discussion of water entry into the drift begins by restating the conditions of interest. We are interested in the period when condensation can occur within the drift. At any axial location in the drift, the coolest surface will be the drift wall. The drip shield and waste packages will be hotter than the drift wall. Hence, for condensation to take place on any surface within the drift, the drift wall must be less than or equal to the saturation temperature (96ºC). At early times, the entire repository will be above the saturation temperature and condensation will be impossible. At sufficiently later times, the entire length of some or all of the emplacement drifts will be cooler than the saturation temperature, and condensation will be possible. The condensation model addresses this time period.

Water can enter the drift by evaporation from the drift wall and by liquid seepage (the portion of the liquid percolation that enters the drift) from the fractures. The two processes are coupled. The current thermohydraulic seepage model does not account for evaporation at the drift surface caused by axial vapor transport (BSC 2004 [DIRS 169856], p. 59). This means that the matrix saturation near the drift wall is high and the imbibition of water from the fracture into the rock matrix is low.

For this vapor dispersion analysis, upper evaporation limits are realized when the drift vapor pressure is significantly lower than the saturation value. When this occurs, the rock matrix desaturates in the vicinity of the drift wall. A portion of the percolated water will be imbibed into this desaturated rock matrix and “pumped” by capillary forces to the drift wall surface where it will evaporate. The resulting flow of liquid and vapor into the drift will be larger than the sum

of the currently predicted liquid seepage and the matrix capillary pumping limit in the absence of water flow in the fractures.

A complete calculation that includes the coupling between the rock flow and the vapor dispersion within the drift is beyond the scope of this document. An approximate bounding argument is used in its place: the amount of water than can enter into the drift by seepage and evaporation is reasonably bounded by the sum of the capillary flow and the percolation flux incident over the footprint of the drift.

The capillary pumping limit through the rock matrix in the absence of fractures is obtained from two solutions to Darcy's equation with an isobaric gas. The first solution is for a cylindrical drift of infinite extent. The far field saturation is approximately unity (1) and the saturation at the drift surface is the irreducible saturation (S_{ir}). There is no steady solution, so the transient equation is addressed.

The one-dimensional transient flow equations in cylindrical coordinates are derived from the conservation of mass (Equation 6.3-48) and Darcy flow (Equation 6.3-49) equations for the liquid phase:

$$\phi\, \rho_L \frac{\partial S}{\partial t} = -\frac{\rho_L}{r}\frac{\partial}{\partial r}\left(r\, q_L\right) \qquad \text{(Eq. 6.3-48)}$$

$$q_L = -\frac{k\, k_L}{\mu}\rho_L \frac{d}{dr}\left(P_L\right) \qquad \text{(Eq. 6.3-49)}$$

In the absence of significant gas flows, the gas phase is nearly isobaric. The radial gradient of the liquid pressure (P_L) becomes equal to the negative of the radial gradient of the capillary pressure (P_c). Combining the conservation of mass and Darcy flow equations with the isobaric gas constraint in cylindrical coordinates produces Equation 6.3-50:

$$\phi \frac{\partial S}{\partial t} = \frac{-k}{\mu}\frac{1}{r}\frac{\partial}{\partial r}\left(r\, k_L\left(S_{eff}\right)\frac{\partial P_c\left(S_{eff}\right)}{\partial r}\right) \quad ; P_c = P_{gas} - P_L \qquad \text{(Eq. 6.3-50)}$$

The capillary pressure and the liquid relative permeability (k_L) are related to the effective saturation (S_{eff}) through the van Genuchten parameters (Pruess 1988 [DIRS 100684], p. 75 IRP=7, p. 78 ICP=7).

$$k_L\left(S_{eff}\right) = \sqrt{S_{eff}}\left[1-\left(1-S_{eff}^{\frac{1}{\lambda}}\right)^{\lambda}\right]^2 \qquad S_{eff} = \frac{S-S_{ir}}{1-S_{ir}}$$

$$P_c\left(S_{eff}\right) = P0_c\left(S_{eff}^{\frac{-1}{\lambda}} - 1\right)^{1-\lambda} \qquad \text{(Eq. 6.3-51)}$$

The differential is rewritten in terms of the effective saturation (S_{eff}).

$$\frac{\partial S_{eff}}{\partial t} = \frac{-k}{\mu\,\phi\,(1-S_{ir})}\frac{1}{r}\frac{\partial}{\partial r}\left(r\,G(S_{eff})\frac{\partial S_{eff}}{\partial r}\right)$$

$$\text{where}\quad G(S_{eff}) = k_L(S_{eff})\frac{d}{dS_{eff}}P_c(S_{eff})$$

$$\frac{d}{dS_{eff}}P_c(S_{eff}) = -P0_c\left(S_{eff}^{\frac{-1}{\lambda}}-1\right)^{\lambda}\frac{(1-\lambda)}{\lambda}S_{eff}^{\frac{-(1+\lambda)}{\lambda}}$$

(Eq. 6.3-52)

The variable coefficient G(S_{eff}) makes the equation nonlinear. Instead of solving the equation numerically, we find the solution to an approximation of this equation that uses an average value for G(S_{eff}).

$$\frac{\partial S_{eff}}{\partial t} = \frac{-k\,G_{avg}}{\mu\,\phi\,(1-S_{ir})}\frac{1}{r}\frac{\partial}{\partial r}\left(r\,\frac{\partial S_{eff}}{\partial r}\right)$$

$$\text{where}\quad G_{avg} = \frac{1}{S0_{eff}}\int_0^{S0_{eff}}\left[k_L(S_{eff})\frac{d}{dS_{eff}}P_c(S_{eff})\right]dS_{eff}$$

(Eq. 6.3-53)

Here, the effective saturation at the drift wall is set to zero; the upper bound of the integral ($S0_{eff}$) reflects the undisturbed far field saturation.

The superficial velocity (q_{matrix_limit}) at the drift surface ($r=R_{drift}$) for the approximate equation is calculated from the derivative of the effective saturation:

$$q_{\text{matrix_limit_cyl}} = -q(r=R_{drift}) = \frac{-k}{\mu}G_{avg}\frac{\partial S_{eff}}{\partial r}$$

(Eq. 6.3-54)

The solution for the liquid flux at the drift wall is analogous to the solution for heat flow (Carslaw and Jaeger 1959 [DIRS 100968], p. 336, Equation 8):

$$q_{\text{matrix_limit_cyl}} = \frac{4\left(\frac{-k}{\mu}G_{avg}\right)S0_{eff}}{R_{drift}\pi^2}\int_0^{\infty}e^{-\left(\frac{-k\,G_{avg}}{\mu\,\phi\,(1-S_{ir})}\right)u^2\,t}\frac{du}{u\left[J_0^2(R_{drift}\,u)+Y_0^2(R_{drift}\,u)\right]}$$

(Eq. 6.3-55)

Next we examine the flux limit for a spherical geometry; the radius of the sphere is set equal to the drift radius. In this case, a steady solution exists and can be computed without any

approximations. Continuity requires that the spherical fluence be independent of radial position. Hence:

$$q_{\text{matrix_limit_shp}}\, R_{drift}{}^{2} = q(r)\, r^{2} \qquad \text{(Eq. 6.3-56)}$$

This relationship is substituted into Darcy's law:

$$q(r) = q_{\text{matrix_limit_shp}} \frac{R_{drift}{}^{2}}{r^{2}} = -\frac{k\, k_L(S_{eff})}{\mu} \frac{dP_L}{dr} \qquad \text{(Eq. 6.3-57)}$$

We enforce the isobaric gas phase and write the liquid pressure in terms of the capillary pressure and effective saturation.

$$q_{\text{matrix_limit_shp}} \frac{R_{drift}{}^{2}}{r^{2}} = -\frac{k\, k_L(S_{eff})}{\mu} \frac{dP_c(S_{eff})}{dS_{eff}} \frac{dS_{eff}}{dr} \qquad \text{(Eq. 6.3-58)}$$

The dependence upon r and S_{eff} is separated and the equation is integrated.

$$q_{\text{matrix_limit_shp}} R_{drift}{}^{2} \left[\frac{1}{r}\right]_{r=R_{drift}}^{r=\infty} = -\frac{k}{\mu} \int_{0}^{S0_{eff}} k_L(S_{eff}) \frac{dP_c(S_{eff})}{dS_{eff}} dS_{eff} \qquad \text{(Eq. 6.3-59)}$$

The equation is rearranged to find the capillary pumping limit.

$$q_{\text{matrix_limit_shp}} = \frac{k}{\mu\, R_{drift}} \int_{0}^{S0_{eff}} k_L(S_{eff}) \frac{dP_c(S_{eff})}{dS_{eff}} dS_{eff} \qquad \text{(Eq. 6.3-60)}$$

Figure 6.3.5-23 compares the cylindrical and spherical solutions to the capillary pumping problem. The effective far field saturation ($S0_{eff}$) is set to unity to maximize the capillary pumping bound. After about 400 years, the cylindrical solution lies below the spherical solution. In the current analysis, nearly all of the times of interest are greater than or equal to 1,000 years. For these times, the spherical solution is greater than the cylindrical solution. Only one drift is analyzed at 300 years. At 300 years, the cylindrical solution is slightly larger than the spherical solution. For ease of implementation, the spherical solution is used as the upper bound for the capillary-drawn flux into the emplacement drifts.

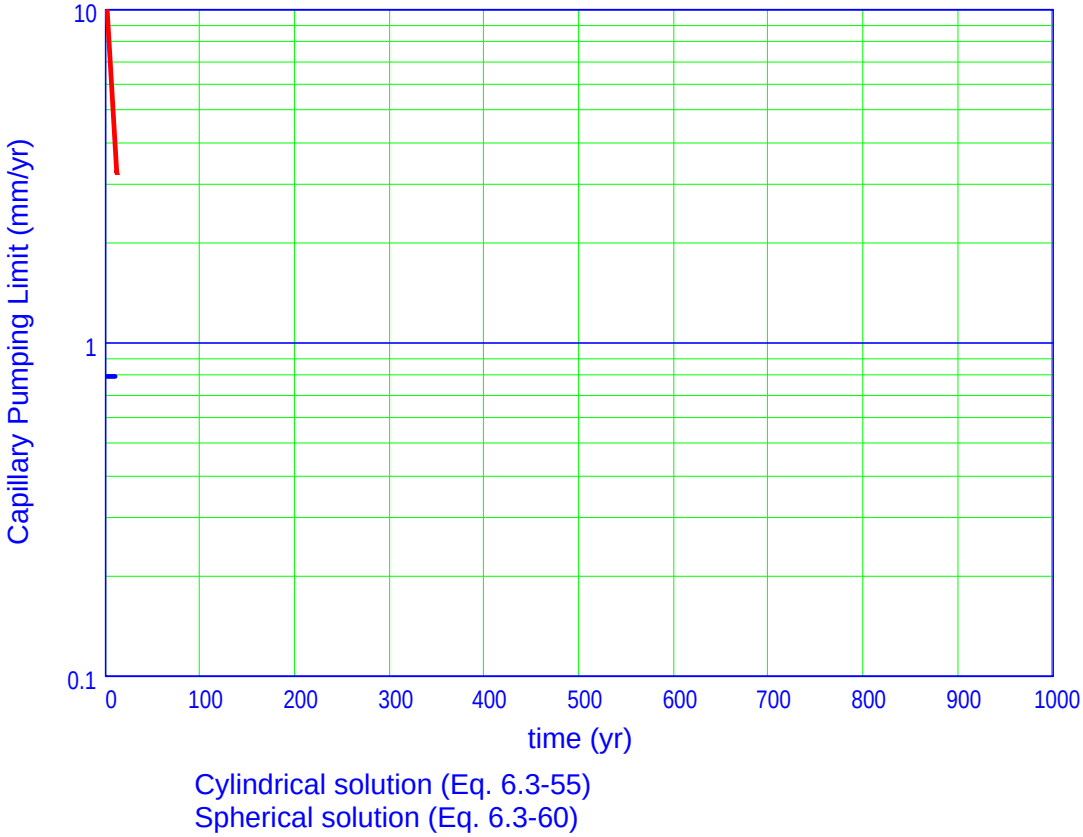

DTN: SN0408T0509903.007; file TOC.mcd; hyperlink 6.3.8 Evaporation Limits

Figure 6.3.5-23. Comparison of Cylindrical and Spherical Solutions for Capillary Pumping

As mentioned above, the influence of percolation on the evaporation at the drift wall is bounded by the product of the percolation flux (V_{perc}) and the drift diameter (D_{drift}). For the purposes of this analysis, the percolation flux is modeled as though it is uniform throughout the length of the drift. The total water fluence is "spread" over the combined perimeter of the drift wall (P_{drift}, including the invert) and the perimeter of the invert under the drift (P_{invert}) to produce a maximum mass evaporation rate at the drift wall and at the invert surface:

$$mmax_{wall} = mmax_{inv} = \rho_{liquid}\left[q_{\text{matrix_limit_shp}} + \frac{D_{drift}V_{perc}}{P_{drift} + P_{inv}}\right] \qquad \text{(Eq. 6.3-61)}$$

The effect of barometric pumping on the capillary pumping limit in the rock matrix is not included in this analysis. However, a discussion on its potential effect is in order. Barometric pumping is driven by the cyclic nature of the barometric pressure. When the barometric pressure increases, air from the drift flows into the rock fractures. When the barometric pressure decreases, air is sucked from the rock fractures into the drifts.

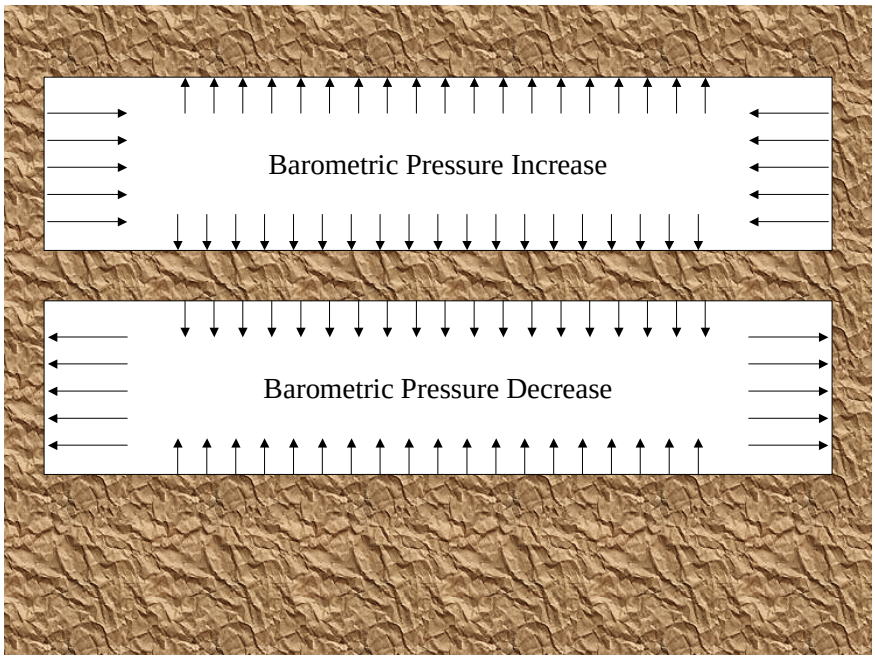

Figure 6.3.5-24. Schematic of Barometric Pumping

Both the radial and axial temperature gradients in the rock will combine with the barometric pumping to affect the flow of water vapor. When the barometric pressure increases, cooler air with less water vapor moves from the ends of the drift towards the center of the drift and then into the surrounding rock fractures. As it moves into the fractures, water will evaporate from the adjacent hot rock, increasing the moisture content of the air. As the vapor-laden air penetrates further into the rock, it encounters lower rock temperatures. Part of the water vapor will condense in the cooler rock.

When the barometric pressure decreases, air from the rock fractures will be pulled into the drifts. As it passes the hottest rock near the drift wall, water will evaporate from the rock into the passing air that then enters the drift center and moves towards the cooler ends where it will condense. Both directions of the barometric pressure oscillation should work to dry out the drift wall.

The capillary pumping limit for cylindrical coordinates is inversely proportional to the drift radius. The capillary pumping limit will still apply in the presence of barometric pumping, but the radius of the evaporating surface will be expanded beyond the actual drift radius. Water evaporated between the drift radius and the effective evaporation radius will be transported into the drift.

While this document does not include this analysis, some sense of its impact can be intuited by substituting an effective evaporation radius for the drift radius in the equation for the capillary pumping limit. Figure 6.3.5-25 shows the maximum amount of water than can enter the drift (m^3/m/yr) based upon the cylindrical solution when the effective evaporation radius is larger than the drift radius. The cylindrical solution limit for an evaporation radius three times larger than the drift radius is not dramatically larger than the spherical solution used in this analysis. The

span of uncertainty in the percolation rate is typically larger. This suggests that barometric pumping will not greatly affect the calculation of the evaporation limit.

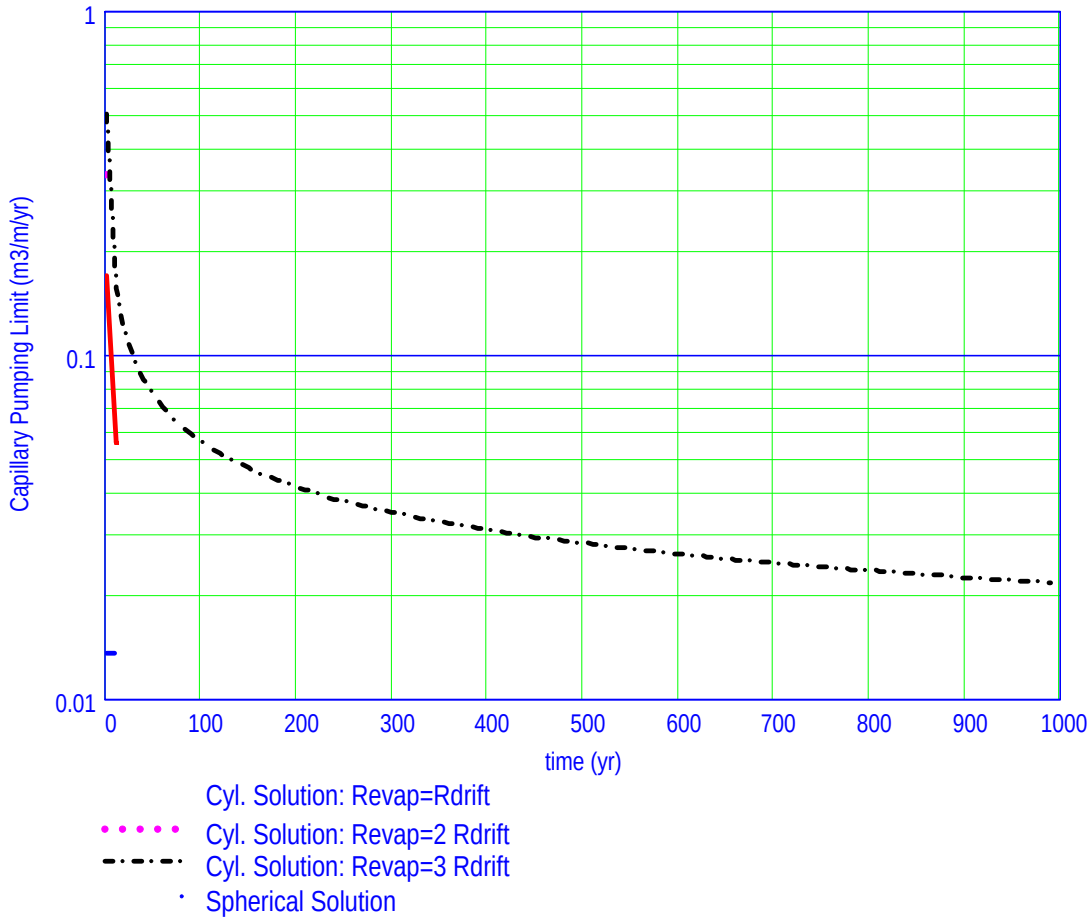

DTN: SN0408T0509903.007; file TOC.mcd; hyperlink 6.3.8 Evaporation Limits.

Figure 6.3.5-25. Possible Effects of Barometric Pumping on Capillary Pumping

6.3.5.2 Base-Case Model Inputs

6.3.5.2.1 Drift Locations

The repository (Figure 6.3.5-26) is composed of parallel emplacement drifts, on 81 m centers (BSC 2003 [DIRS 164069]). The emplacement drifts are connected to each other with an access drift and an exhaust drift. The minimum standoff distance between the end of the waste canisters and the center of the exhaust drift is 15 m. (BSC 2004 [DIRS 171424]). Waste canisters are to be loaded into the emplacement drifts through a curved "turnout" having a radius of 61 m (BSC 2004 [DIRS 171423]). Both the exhaust drift standoff and the access drift are cooler than the loaded region of the emplacement drift, and condensate will accumulate in both areas. In order to standardize this analysis, the length of the exhaust drift standoff is set to 15 m for all of the examined drifts. The length of the turnout is set to 60 m for all of the examined drifts. This excludes the lengths of the exhaust and access drifts associated with the 81-m spacing, and

understates the actual curvilinear distance of the turnout, but provides a lower bound for the length of this "super coldtrap" region. Repository layout data are cited in Table 4.1.3-7. These data are used in Section 6.3.5.1.1, "Calculation of the Repository Temperature Field."

6.3.5.2.2 Rock Properties

The bulk of the repository is located in the lower lithophysal unit (Tptpll). The thermal and flow properties of this layer are used in this analysis to approximate the temperature distribution and near-field water flow. The flow properties are documented in DTN: LB0208UZDSCPMI.002 [DIRS 161243]. Thermal properties are documented in DTNs: SN0307T0510902.002 [DIRS 164196] and SN0404T0503102.011 [DIRS 169129]. The thermal diffusivity of the rock is calculated with an approximated saturation value of unity (1). Rock properties are listed in Table 4.1.3-1. Thermal rock properties are used in Section 6.3.5.1.1, "Calculation of the Repository Temperature Field." Matrix permeability and capillary pressure properties are used in Section 6.3.5.1.4, "Evaporation Limits."

6.3.5.2.3 Percolation Rates

Percolation rates are used to calculate the maximum amount of water available for evaporation at the drift and invert surfaces. Percolation rates vary with the expected climate (BSC 2004 [DIRS 169861], Table 6.9-1). The "modern" climate is projected to last until 600 years after emplacement. The "monsoon" climate extends from 600 to 2,000 years. The "glacial" climate begins at 2000 years and extends throughout the balance of the repository life (BSC 2004 [DIRS 169565], Table 6.3-4). Three percolation rates are associated with each climate: the lower bound (DTN: LL030608723122.028 [DIRS 164510]), the upper bound (DTN: LL030602723122.027 [DIRS 164514]), and the mean (DTN: LL030610323122.029 [DIRS 164513]). Percolation rates are cited in Table 4.1.3-7 and are used Section 6.3.5.1.4, "Evaporation Limits."

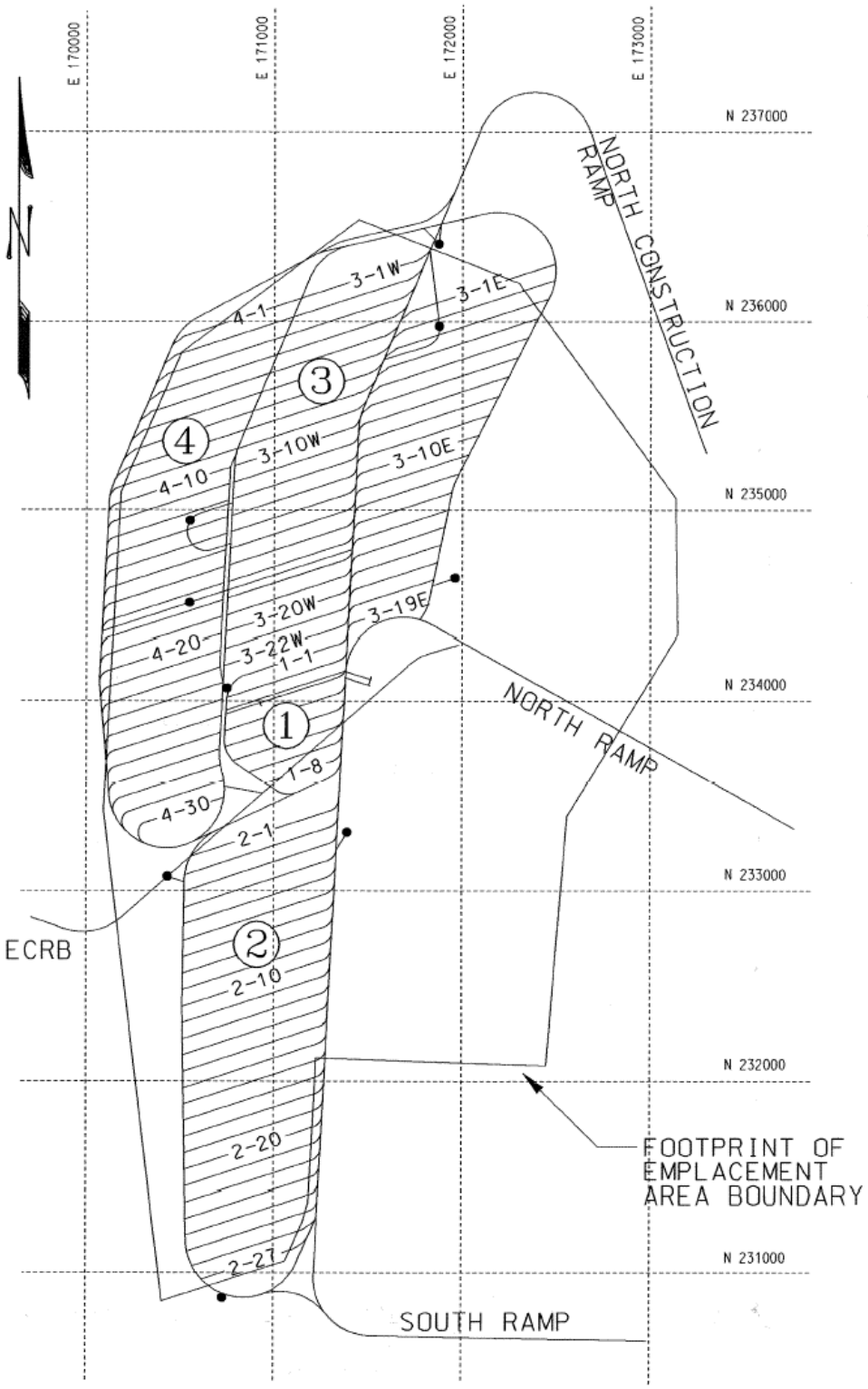

Source: BSC 2003 [DIRS 164519].

Figure 6.3.5-26. Repository Layout

6.3.5.2.4 Waste Package Power

The LA repository design is based upon a 1.45 kW/m line loading at the time of emplacement. The line-averaged power density in the repository as a function of time (BSC 2004 [DIRS 167754]) is shown in Figure 6.3.5-27. Line-averaged powers are cited in Table 4.1.3-7 and are used in Section 6.3.5.1.1, "Calculation of the Repository Temperature Field."

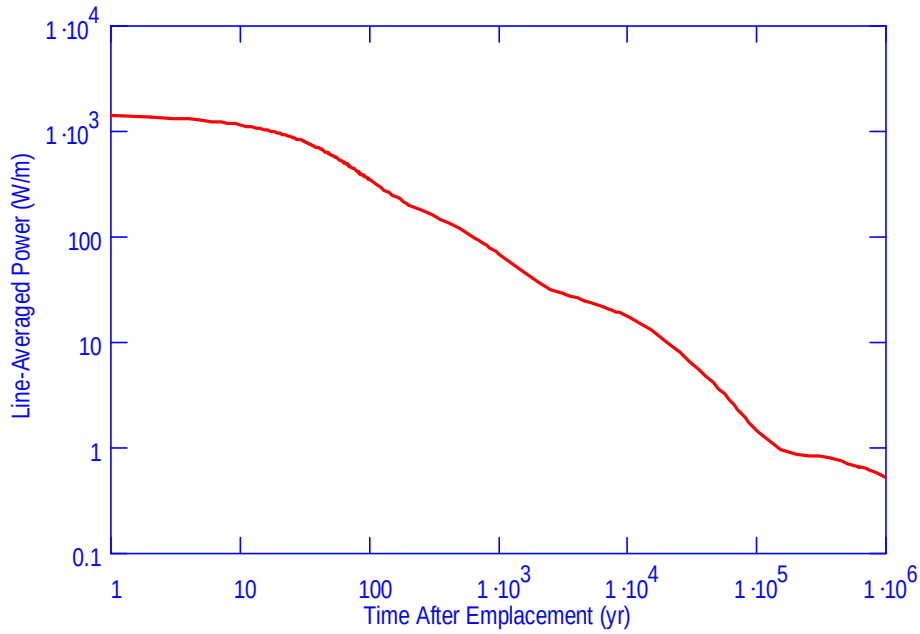

Source: BSC 2004 [DIRS 167754]; DTN: SN0408T0509903.007; file TOC.mcd; hyperlink 6.1.4 Waste Package Powers.

Figure 6.3.5-27. Line-Averaged Power

Discrete waste package power output for the packages used in this analysis are found in *D&E / PA/C IED Typical Waste Package Components Assembly* (BSC 2004 [DIRS 167754], Table 12) and shown in Figure 6.3.5-28. Discrete waste package powers are cited in Table 4.1.3-7 and are used in Section 6.3.5.1.2, "Dispersion Problem Formulation."

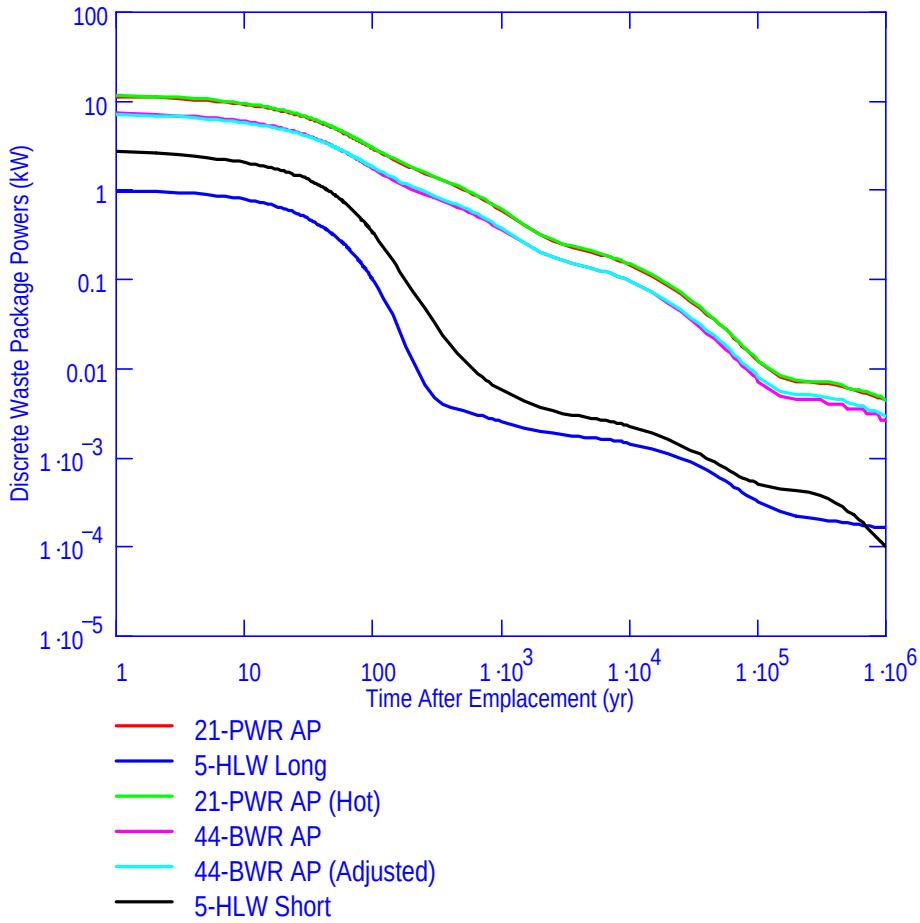

Source: BSC 2004 [DIRS 167754]; DTN: SN0408T0509903.007; file TOC.mcd; hyperlink 6.1.4 Waste Package Powers.

Figure 6.3.5-28. Discrete Waste Package Powers

6.3.5.2.5 Ventilation Efficiency

The ventilation period for the LA design is 50 years. During that time, a substantial amount of the decay heat is removed by the ventilation system. The balance of the heat is transferred into the rock. Ventilation efficiency is calculated in *Ventilation Model and Analysis Report* (BSC 2004 [DIRS 169862]; DTN: MO0307MWDAC8MV.000 [DIRS 165395]). The waste package power outputs (line-averaged and discrete waste package) are modified by multiplying them by the complement of the ventilation efficiency over the 50-year ventilation time. The resultant powers are shown in Figure 6.3.5-29 (line-averaged power) and Figure 6.3.5-30 (discrete waste package powers). Ventilation efficiencies are cited in Table 4.1.3-7 and are used in Section 6.3.5.1.1, "Calculation of the Repository Temperature Field," and in Section 6.3.5.1.2, "Dispersion Problem Formulation."

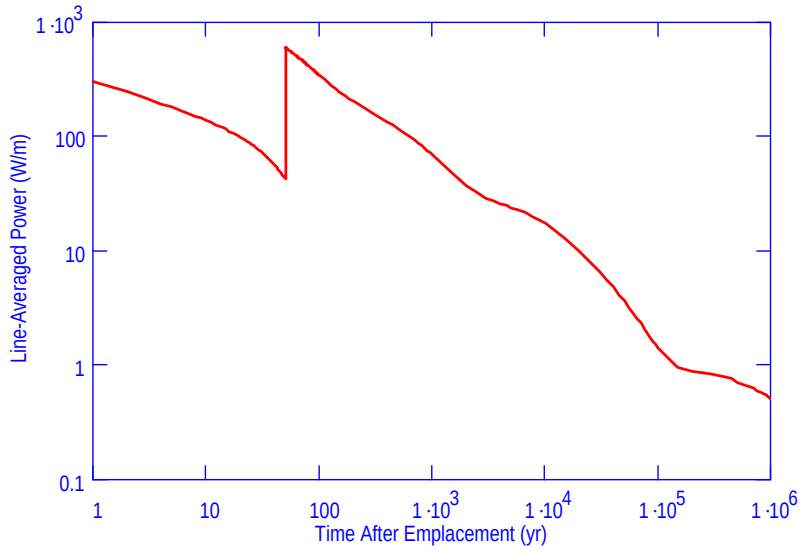

Sources: BSC 2004 [DIRS 167754], BSC 2004 [DIRS 169862]; DTN: SN0408T0509903.007; file TOC.mcd; hyperlink 6.1.5 Ventilation Efficiency.

Figure 6.3.5-29. Line-Averaged Power with Ventilation Efficiency

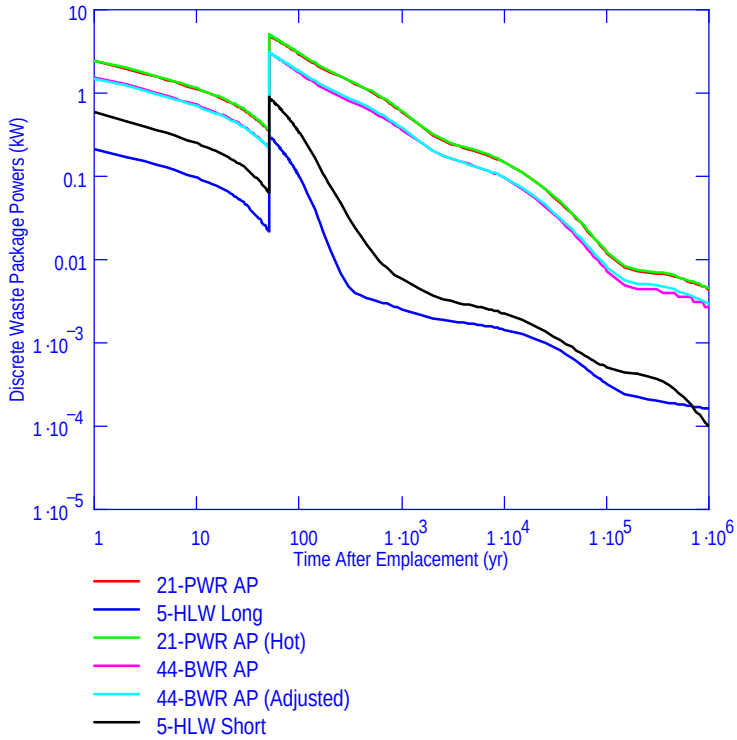

Sources: BSC 2004 [DIRS 167754], BSC 2004 [DIRS 169862]; DTN: SN0408T0509903.007; file TOC.mcd; hyperlink 6.1.5 Ventilation Efficiency.

Figure 6.3.5-30. Discrete Waste Package Powers with Ventilation Efficiency

6.3.5.2.6 Waste Package Arrangement

The waste package sequence is represented by the 7-package segment. The package sequence of this segment is: 21-PWR AP, 5-HLW LONG, 21-PWR AP (Hot), 44-BWR AP, 44-BWR AP (Adjusted), 5-HLW Short, 21-PWR AP, 44-BWR AP (BSC 2004 [DIRS 167754]). The end packages of this segment are half-packages. This 7-package segment is illustrated in Figure 6.3.5-31 (not to scale).

Figure 6.3.5-31. Waste Package Sequence

This 7-package sequence is actually 1/2 of a unit cell; it must be reflected about one of the end packages to achieve unit cell symmetry. Further, it does not indicate which of the packages is loaded into the drift first. For the purposes of this calculation, the package at the west end of the emplacement drift is always the 21-PWR AP (full size). The package sequence of the 7-package segment is then followed, with the proper reflection about the 1/2 44-BWR AP package on the right.

The inter-package spacing is 0.1 m (BSC 2003 [DIRS 164069]). This relatively small gap is not included separately, but is lumped into the waste packages. Hence, the length of each waste package is increased by this amount. Waste package dimensions are given in *Repository Design Project, RDP/PA IED Typical Waste Package Components Assembly (3)* (BSC 2003 [DIRS 165406]).

The waste package sequence is cited in Table 4.1.3-7. The inter package spacing is listed in Table 4.1.3-8. The sequence and spacing are used in Section 6.3.5.1.1, “Calculation of the Repository Temperature Field” and in Section 6.3.5.1.2, “Dispersion Problem Formulation.”

6.3.5.2.7 Emplacement Drift Configuration

This analysis requires that a number of dimensions for the structures inside of the emplacement drift be calculated. The drip shield and waste package dimensions for the repository design are located in Tables 4.1.3-8 and 4.1.3-9. These listed dimensions and those computed below are used in Section 6.3.5.1.2, “Dispersion Problem Formulation.”

The nominal perimeter of the drip shield (P_{ds}, Figure 6.3.5-32) is needed. The height of the drip shield walls (h_{side}), the height of the drip shield (h_{ds}), and the radius of the drip shield top (R_{ds}) are known. First, the arc length of the top (L_{arc}) must be computed.

$$L_{arc} = 2R_{top}\left(\frac{\pi}{2} - \alpha_{\text{arc}}\right)$$

$$\text{where} \quad \alpha_{\text{arc}} = \text{acos}\left(\frac{P_{inv}}{2\,R_{top}}\right) \qquad \text{(Eq. 6.3-62)}$$

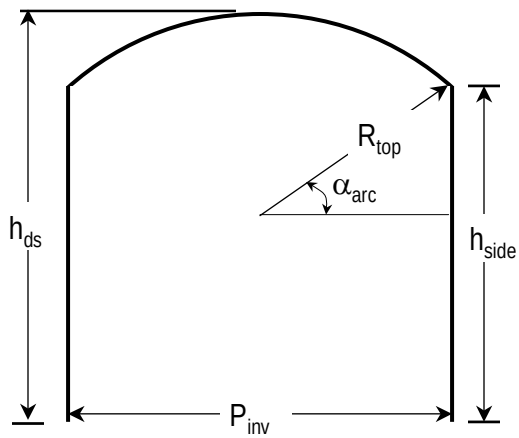

Figure 6.3.5-32. Calculation of Drip Shield Perimeter

The drip shield perimeter is the sum of the arc length of the top and the height of the sides.

$$P_{ds} = 2\,h_{side} + L_{arc} \qquad \text{(Eq. 6.3-63)}$$

The cross-sectional area under the drip shield (Ac_{ds}) is:

$$Ac_{ds} = h_{side}\;P_{inv} + \left[\left(\pi\;R_{top}{}^{2}\;\frac{2\left(\frac{\pi}{2} - \alpha_{arc}\right)}{2\,\pi}\right) - \frac{P_{inv}R_{top}\sin(\alpha_{arc})}{2}\right] \qquad \text{(Eq. 6.3-64)}$$

The average flow area under the drip shield (Ac_{in}) is the cross-sectional area under the drip shield minus the length-weighted cross-sectional areas of the waste packages.

$$Ac_{in} = Ac_{ds} \frac{\frac{\pi}{4}\left[\frac{1}{2} d_{wp_1}{}^2 DY_{wp_1} + \sum_{n=2}^{7} d_{wp_n}{}^2 DY_{wp_n} + \frac{1}{2} d_{wp_8}{}^2 DY_{wp_8}\right]}{\frac{1}{2} DY_{wp_1} + \sum_{n=2}^{7} DY_{wp_n} + \frac{1}{2} DY_{wp_8}}$$

where d_{wp} = waste package diameter

DY_{wp} = waste package length

(Eq. 6.3-65)

The invert covers a portion of the drift wall. The exposed perimeter of the drift wall (P_{drift}) and the cross-sectional area of the drift (Ac_{drift}) is now calculated.

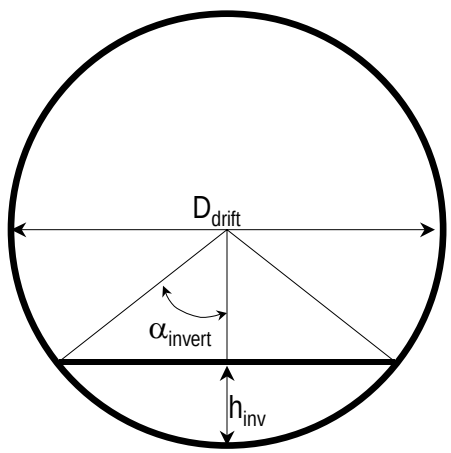

Figure 6.3.5-33. Calculation of Exposed Wall Perimeter

The half-angle that is defined by the invert (α_{invert}) is:

$$\alpha_{invert} = \operatorname{acos}\left(\frac{\frac{D_{drift}}{2} - h_{inv}}{\frac{D_{drift}}{2}}\right)$$

(Eq. 6.3-66)

The exposed perimeter of the drift (P_{drift}) is calculated:

$$P_{drift} = \frac{D_{drift}}{2} 2(\pi - \alpha_{invert}) \qquad \text{(Eq. 6.3-67)}$$

Because the portion of the invert that is outside the drip shield is relatively small, its exposed surface is lumped with the exposed drift perimeter:

$$P_{drift} = \frac{D_{drift}}{2} 2(\pi - \alpha_{invert}) + 2\left(\frac{D_{drift}}{2}\sin(\alpha_{invert}) - \frac{P_{inv}}{2}\right) \qquad \text{(Eq. 6.3-68)}$$

The cross-sectional area of the drift is:

$$Ac_{drift} = \pi\left(\frac{D_{drift}}{2}\right)^2\left(\frac{\pi - \alpha_{invert}}{\pi}\right) + \frac{1}{2}D_{drift}\sin(\alpha_{invert})\left(\frac{D_{drift}}{2} - h_{inv}\right) \qquad \text{(Eq. 6.3-69)}$$

The flow area outside the drip shield is the difference between the cross-sectional areas of the drift and the drip shield.

$$Ac_{out} = Ac_{drift} - Ac_{ds} \qquad \text{(Eq. 6.3-70)}$$

The fraction of the exposed perimeter of the drift that is directly above the drip shield (f_{drift}) is:

$$f_{drift} = \frac{2\arcsin\left(P_{inv}/D_{drift}\right)}{P_{drift}} = 0.36395 \qquad \text{(Eq. 6.3-71)}$$

The fraction of the drip shield that is directly above the waste package (f_{wp}) is:

$$f_{wp} = \frac{2\arcsin\left(D_{wp}/2R_{top}\right)}{P_{ds}} = \begin{matrix} 0.34751 & \text{for HLW waste packages} \\ 0.25966 & \text{for BWR waste packages} \end{matrix} \qquad \text{(Eq. 6.3-72)}$$

6.3.5.2.8 Variation of Gas Properties with Composition

The humidity inside the drift varies both spatially and temporally. The transport properties used in the calculation are a function of the vapor mass fraction of the air. Calculation of the transport properties is performed according to well-established mixing formulas. The air and vapor transport properties used in these mixing formulae are tabulated in Tables 4.1.3-3 and 4.1.3-4. Mixture properties are used in Section 6.3.5.1.3, "Heat and Mass Transfer Correlation."

Gas Density

Both the air and the water vapor are treated as ideal gases. Therefore, the density of the binary mixture is computed from the ideal gas laws in terms of the vapor mole fraction χ_{st}.

$$\rho_{gas} = \rho_{air}\left(T_{gas}, (1-\chi_{st})\, P_{gas}\right) + \rho_{st}\left(T_{gas}, \chi_{st}\, P_{gas}\right) \qquad \text{(Eq. 6.3-73)}$$

The mole fraction of steam is related to the mass fraction of steam (X_{st}) by the molecular weights of each component (MW_{st}, MW_{air}).

$$\chi_{st} = \frac{\dfrac{MW_{air}}{MW_{st}} X_{st}}{1 + \left(\dfrac{MW_{air}}{MW_{st}} - 1\right) X_{st}} \qquad \text{(Eq. 6.3-74)}$$

Gas Viscosity

The method of Wilke (Reid et. al. 1977 [DIRS 130310], Equations 9-5.1 and 9-5.2) is used to compute the mixture viscosity of the air/vapor mixture.

$$\mu_{gas} = \frac{\chi_{air}}{\chi_{air} + \chi_{st}\, \phi_{air-st}} \mu_{air} + \frac{\chi_{st}}{\chi_{air}\, \phi_{st-air} + \chi_{st}} \mu_{st}$$

where

$$\phi_{air-st} = \frac{1}{\sqrt{8}} \left(1 + \frac{MW_{air}}{MW_{st}}\right)^{-1/2} \left[1 + \left(\frac{\mu_{air}}{\mu_{st}}\right)^{1/2} \left(\frac{MW_{st}}{MW_{air}}\right)^{1/4}\right]^2$$

$$\phi_{st-air} = \frac{1}{\sqrt{8}} \left(1 + \frac{MW_{st}}{MW_{air}}\right)^{-1/2} \left[1 + \left(\frac{\mu_{st}}{\mu_{air}}\right)^{1/2} \left(\frac{MW_{air}}{MW_{st}}\right)^{1/4}\right]^2 \qquad \text{(Eq. 6.3-75)}$$

Gas Thermal Conductivity

The thermal conductivity of the gas mixture is computed using the same formula as that for the mixture gas viscosity (Bird et al. 1960 [DIRS 103524], p. 258, Equations 8.3-17 and 8.3-18):

$$k_{gas} = \frac{\chi_{air}}{\chi_{air} + \chi_{st}\,\phi_{air-st}} k_{air} + \frac{\chi_{st}}{\chi_{air}\,\phi_{st-air} + \chi_{st}} k_{st} \qquad \text{(Eq. 6.3-76)}$$

The values of $\phi_{air\text{-}st}$ and $\phi_{st\text{-}air}$ are identical to those of Equation 6.3-75.

Gas Specific Heat

The specific heat of the gas mixture is the mass-weighted average of the air and vapor specific heats.

$$Cp_{gas} = X_{st} Cp_{st} + (1 - X_{st}) Cp_{air} \qquad \text{(Eq. 6.3-77)}$$

Air/Vapor Molecular Diffusion Coefficient

The air/vapor molecular diffusion coefficient is the same used by Ho (1997 [DIRS 141521], Equation 2).

$$D_{va}(T,P) = D0_{va} \frac{P0}{P} \left(\frac{T}{T0} \right)^{\theta}$$

$$\text{where} \quad D0_{va} = (2.13e-5)\frac{m^2}{s}$$

$$T0 = 273.15\,K$$

$$\theta = 1.8 \qquad \text{(Eq. 6.3-78)}$$

6.3.5.2.9 Vapor Saturation Properties

The vapor mass fraction boundary conditions at each of the surfaces (drift wall, invert, drip shield, and waste packages) are computed by applying saturation conditions for the local surface temperature (Sections 6.3.3.2.1 and 6.3.3.2.2). The vapor saturation properties are tabulated in Tables 4.1.3-5 and 4.1.3-6. The mass fraction boundary conditions are used in Section 6.3.5.1.2, "Dispersion Problem Formulation."

6.3.5.2.10 Surface Radiation Properties

Both thermal radiation and natural convection contribute to the calculation of the structure surface temperatures (drip shield, invert, waste packages). Surface emissivities and the Stefan-

Boltzmann constant are tabulated in Table 4.1.3-2. These are used in Section 6.3.5.1.2, "Dispersion Problem Formulation."

6.3.5.3 Summary of the Computational Model

The surface energy equations (Equation 6.3-21, 6.3-22, and 6.3-23) (3), gas energy dispersion equations (Equation 6.3-19) (2), and gas vapor dispersion equations (Equation 6.3-18 combined with Equation 6.3-16) (2) form a set of seven (7) coupled equations for each axial location in the drift. The solution of these equations is detailed in Appendix IV.

6.3.6 Model Formulation for Alternative Conceptual Models for In-Drift Condensation

All the Alternate Conceptual Models (ACMs) for in-drift condensation identified in Section 6.3.4 have been screened out.

6.3.7 Base-Case Condensation Model Results

6.3.7.1 Overview

Seven drifts in the repository are analyzed for condensation location and quantity in this calculation as shown in Figure 6.3.7.1. These drifts are chosen to reflect the range of conditions expected in the repository. Choices #1, #2, and #3 are colinear and cut across the northern end of the drift. Choice #3 is shorter than most emplacement drifts and is at the edge of the repository. Choices #4, #5, and #6 are collinear and cut across the middle of the repository. Choice #7 is in the southern section of the repository.

All seven drifts are analyzed at times of 1,000, 3,000, and 10,000 years after emplacement. Choice #3 decreases to the saturation temperature of the repository sooner than the other six analyzed because it lies on the edge of the repository. It is analyzed at 300 years.

The inputs presented in Section 4.1.3 include repository layout, percolation data, rock thermal properties, waste package and drip shield dimensions, and standard thermodynamic properties for air and water. These inputs were used to make predictions of condensation as presented in Section 6.3.7.2. Three percolation rates (lower, mean, and upper) are incorporated for each of the times and each of the emplacement drifts. The percolation rates vary with both location and time.

Lower and upper reasonable bound values for the axial dispersion coefficients, computed in the FLUENT computational fluid dynamics (CFD) code, are used in the simulations. The lower bound dispersion coefficients are computed without any axial gradients in the wall temperature; the upper bound dispersion coefficients are computed with axial gradients in the wall temperature that are representative of those computed in this calculation.

6.3.7.2 Base-Case Model Results

The sections that follow contain several plots and tables that are used to illustrate specific points. A complete set of plots and tables for drift choice #7 is contained in Appendix E. Complete sets

of plots and tables for all the seven drift choices are contained in the accompanying electronic files (Appendix F).

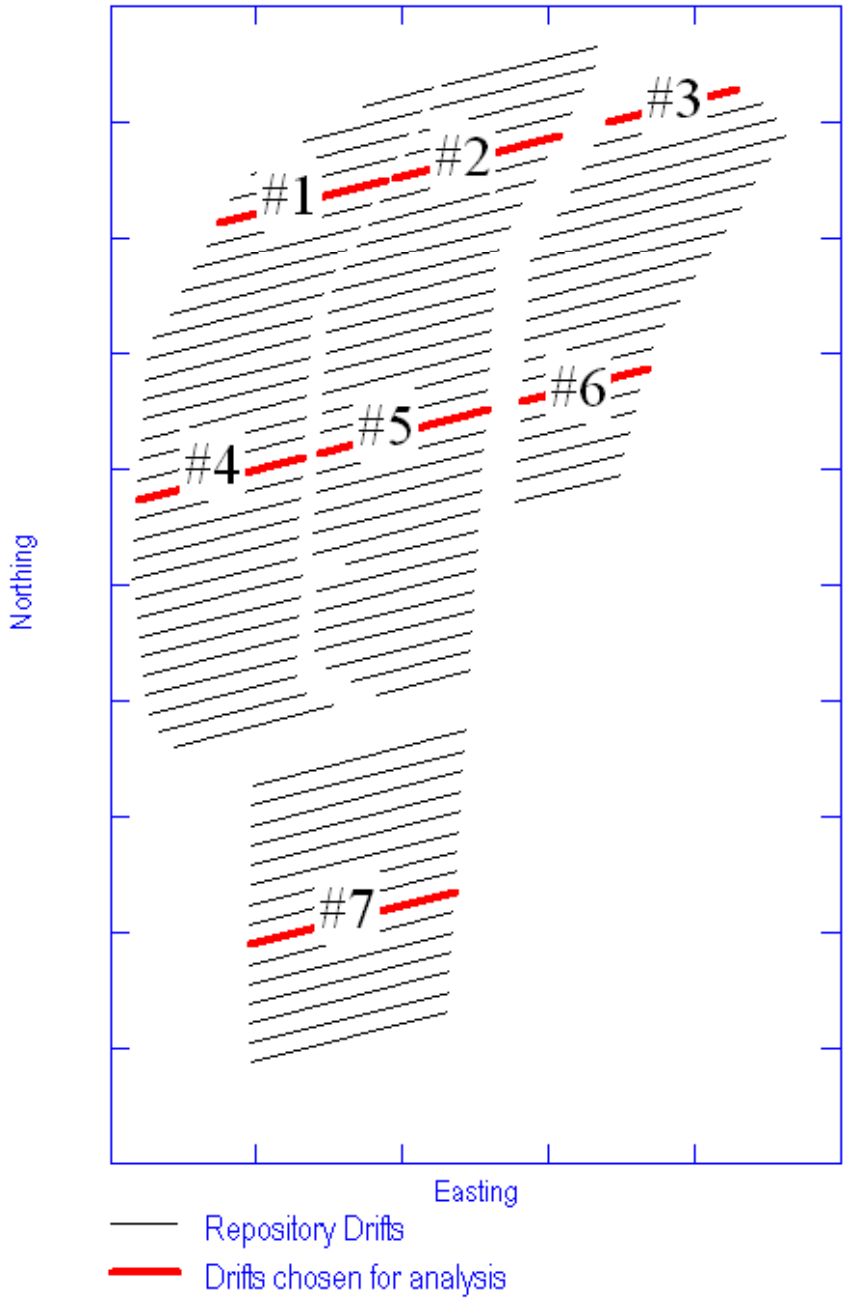

Figure 6.3.7-1. Numbering of Chosen Drifts

6.3.7.2.1 Condensation on the Outside Surface of the Drip Shield

No condensation is predicted to form on the outside of the drip shield in any of the analyzed drifts at any time for any percolation rate. This is because the drift wall temperature is always lower than the drip shield temperature. Condensation, if it occurs, is located on the cooler of the two (drift wall or drip shield) surfaces.

6.3.7.2.2 Condensation on the Drift Walls

Condensate forms on the drift wall when water evaporates in a hotter portion of the drift and moves axially to a cooler portion of the drift where it condenses on the drift wall. This will always occur where water is available in the rock and where there is an axial temperature gradient. At early times and low percolation rates, the majority of the wall condensate occurs in the cool exhaust standoff and access turnout where no waste packages are emplaced. This effect is desirable because it transports water away from the waste packages to unheated regions of the repository where it resumes its downward migration towards the water table. Radionuclides cannot be transported with this evaporated water because their lower vapor pressures preclude significant migration by vapor dispersion.

In some cases, the axially transported water vapor encounters a section of the occupied emplacement drift that is cool enough to initiate condensation. When this occurs, the condensate might drip on the drip shield or, if the drip shield is displaced, drip directly onto the waste package.

Condensation on the Drift Walls: Well-Ventilated Drip Shield

Table 6.3.7-1 summarizes the wall condensation rates in the emplacement region for the case of a well ventilated drip shield, with low-invert transport (Section 6.3.3.2.1) and a low axial dispersion coefficient. The first column in the table refers to the percolation level (lower, mean, upper). The second column indicates the chosen drift. Next, there are two columns for each of the analyzed times. The first of these columns shows the total length of the wall condensation zone(s). The second column is the total condensation rate (kg/yr) occurring on the drift wall in the emplacement region. This is the summation over all of the nodes in the chosen drift. Modest amounts of wall condensate are predicted to form at 1,000 years; none is predicted to form at 3,000 or 10,000 years. No condensate is predicted to form on the drift wall for the case of a well ventilated drip shield with low-invert transport and a high axial dispersion (output DTN: SN0408T0509903.007; file Mixed_LowInvertTransport\Summary Tables.mcd).

Table 6.3.7-1. Condensation on the Drift Walls: Well-Ventilated Drip Shield, Low Invert Transport, Low Dispersion Coefficient

Perc. Level	Drift Choice	300 Years		1,000 Years		3,000 Years		10,000 Years	
		Length (m)	Total Cond (kg/yr)	Length (m)	Total Cond (kg/yr)	Length (m)	Total Cond (kg/yr)	Length (m)	Total Cond (kg/yr)
Low	#1:	—	—	34	40	0	0	0	0
	#2:	—	—	9	15	0	0	0	0
	#3:	0	0	0	0	0	0	0	0
	#4:	—	—	0	0	0	0	0	0
	#5:	—	—	0	0	0	0	0	0
	#6:	—	—	0	0	0	0	0	0
	#7:	—	—	152	2834	0	0	0	0
	Total:	**0**		**195**		**0**		**0**	
Mean	#1:	—	—	55	106	0	0	0	0
	#2:	—	—	39	70	0	0	0	0
	#3:	0	0	0	0	0	0	0	0
	#4:	—	—	147	1855	0	0	0	0
	#5:	—	—	71	563	0	0	0	0
	#6:	—	—	14	17	0	0	0	0
	#7:	—	—	258	4787	0	0	0	0
	Total:	**0**		**583**		**0**		**0**	
Upper	#1:	—	—	65	127	0	0	0	0
	#2:	—	—	55	114	0	0	0	0
	#3:	0	0	0	0	0	0	0	0
	#4:	—	—	156	1921	0	0	0	0
	#5:	—	—	106	748	0	0	0	0
	#6:	—	—	19	26	0	0	0	0
	#7:	—	—	373	6062	0	0	0	0
	Total:	**0**		**774**		**0**		**0**	

DTN: SN0408T0509903.007; file Mixed_LowInvertTransport\Summary Tables.mcd.

An examination of the condensation locations and the vapor mass fraction profiles helps the visualization of the process. The top portion of Figure 6.3.7-2 shows the vapor mass fraction in the gas (red dashed line) and the equilibrium vapor mass fraction for the drift wall based upon the drift wall temperature (solid blue line). In the center of the drift, the axial transport causes the gas vapor pressure to be lower than the equilibrium vapor pressure at the drift wall. This is where water is evaporating from the drift wall.

Progressing from the drift center, the gas vapor pressure reaches a point where it is slightly higher than the equilibrium vapor pressure at the drift wall. A portion of the axially transported water vapor condenses on the drift wall in these two regions. The rate of condensation on the drift wall in these regions is determined by the vapor mass fraction difference between the gas and the wall and the thickness of the gas boundary layer.

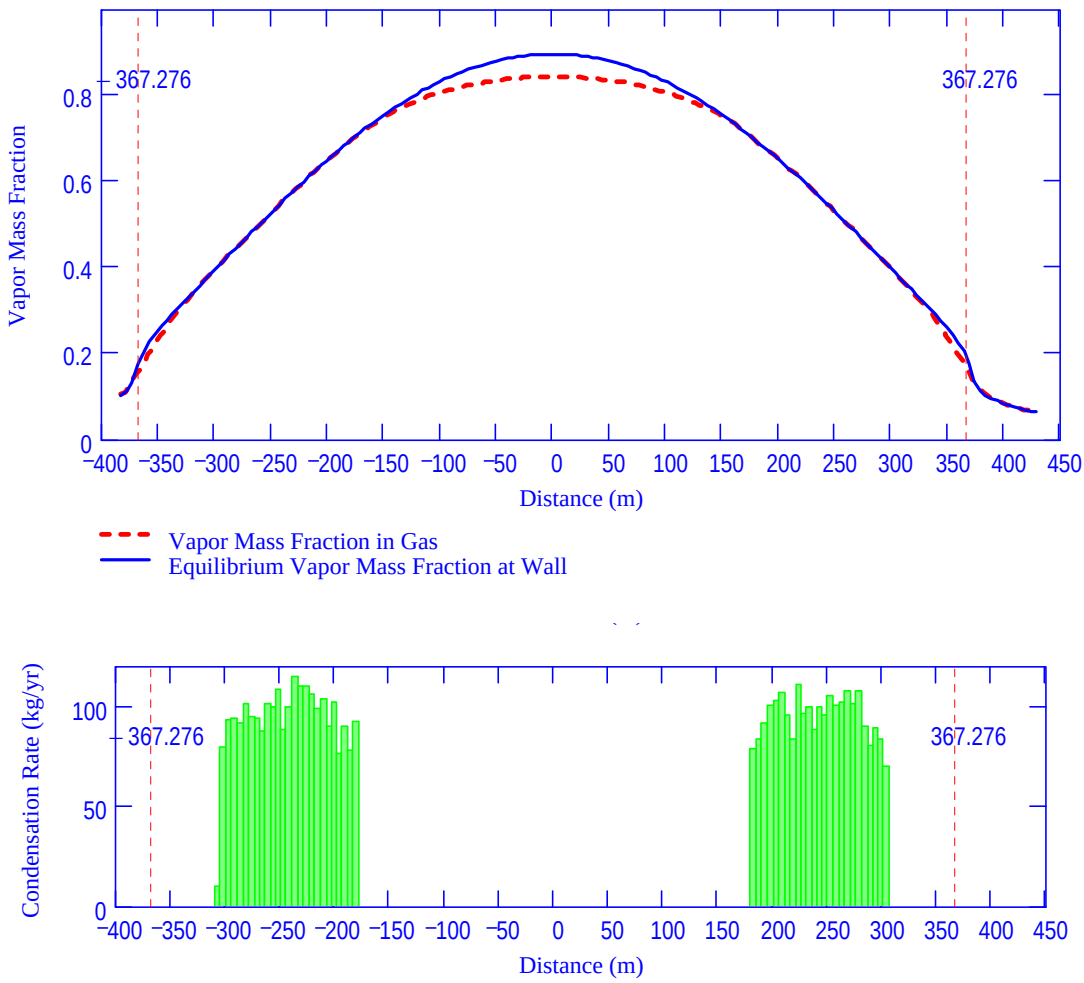

DTN: SN0408T0509903.007; file TOC.mcd; hyperlink 7.1.7, Calculated Results for Drift Choice #7.

NOTE: Top: vapor mass fraction in gas; bottom: condensation rate on drift wall (condensation in access/exhaust regions not shown).

Figure 6.3.7-2. Vapor Mass Fraction in Gas and Condensation Rate on Drift Wall: Choice #7, 1,000 Years, Mean Percolation Rate, Well-Ventilated Drip Shield, Low Invert Transport, Low Dispersion Coefficient

In the regions between the two condensation zones and the non-emplacement portions of the drift (the access turnout and the exhaust standoff, indicated by the vertical dashed lines), the vapor mass fraction in the gas again dips below the equilibrium mass fraction at the wall. As in the center of the drift, water evaporates from the drift wall in these two regions. This evaporated water combines with the axially transported water vapor that made it through the condensation zones and condenses in the non-emplacement regions of the drift.

The axial transport of water vapor is smaller at 3,000 and 10,000 years than at 1,000 years because the axial temperature gradient of the drift wall is smaller. In the absence of significant axial vapor transport, the gas vapor mass fraction is slightly lower than the vapor equilibrium mass fraction at the drift wall (Figure 6.3.7-3; the gas and equilibrium vapor mass fractions are

imperceptibly different). In these cases, no condensation occurs on the drift walls of the emplacement region. Wall condensation occurs only in the access turnout and the exhaust standoff.

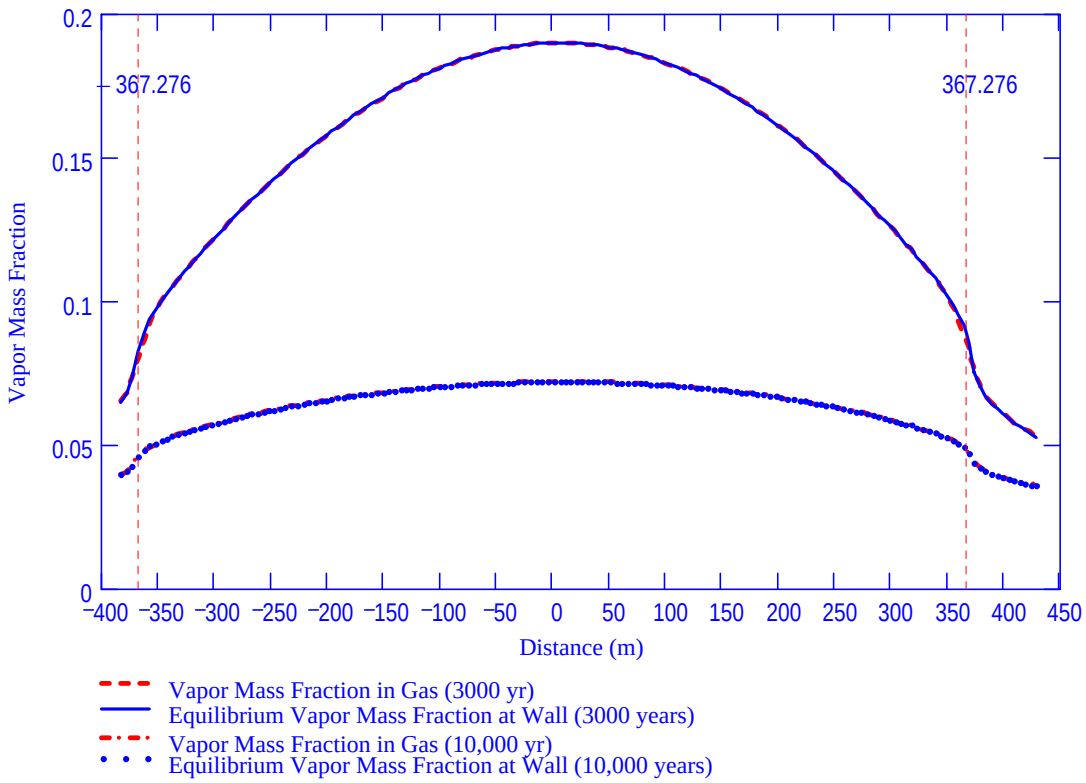

DTN: SN0408T0509903.007; file TOC.mcd; hyperlink 7.1.7, Calculated Results for Drift Choice #7.

NOTE: Top lines: vapor mass fraction in gas at 3,000 years; bottom lines: vapor mass in gas at 10,000 years.

Figure 6.3.7-3. Vapor Mass Fraction in Gas at 3,000 Years and 10,000 Years: Choice #7, Mean Percolation Rate, Well-Ventilated Drip Shield, Low Invert Transport, Low Dispersion Coefficient

When the high axial dispersion coefficient is applied to the same case (Choice #7, Mean Percolation Rate, Well Ventilated Drip Shield, Low Invert Transport) at 1,000 years, the higher axial transport of water vapor results in a substantial reduction in the vapor mass fraction of the gas (Figure 6.3.7-4). The drift-wall condensation that was observed for the low axial dispersion case is completely eliminated. Wall condensation occurs only in the exhaust standoff and the access turnout.

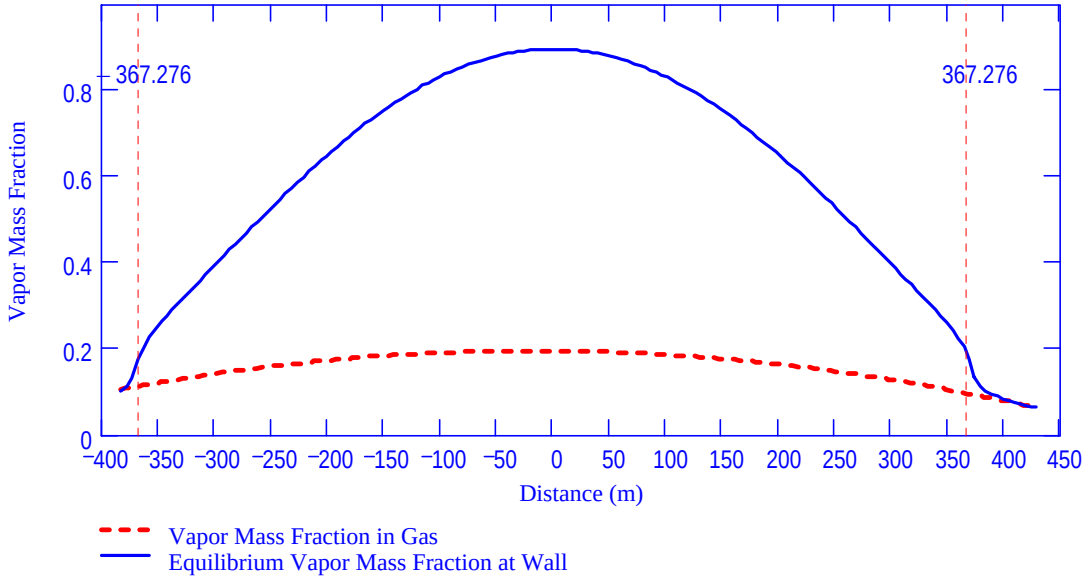

DTN: SN0408T0509903.007; file TOC.mcd; hyperlink 7.1.7, Calculated Results for Drift Choice #7.

Figure 6.3.7-4. Vapor Mass Fraction in Gas: Choice #7, 1,000 Years, Mean Percolation Rate, Well-Ventilated Drip Shield, Low Invert Transport, High Dispersion Coefficient

Vapor mass fraction profiles for 3,000 and 10,000 years for the high dispersion coefficient (Figure 6.3.7-5) differ only marginally for those of the low dispersion coefficient (Figure 6.3.7-3). At 3,000 years, the difference between the gas and wall vapor mass fractions is discernible near the axial edges of the emplacement region; at 10,000 years, the difference is imperceptible. In both cases, wall condensation occurs only in the exhaust standoff and the access turnout.

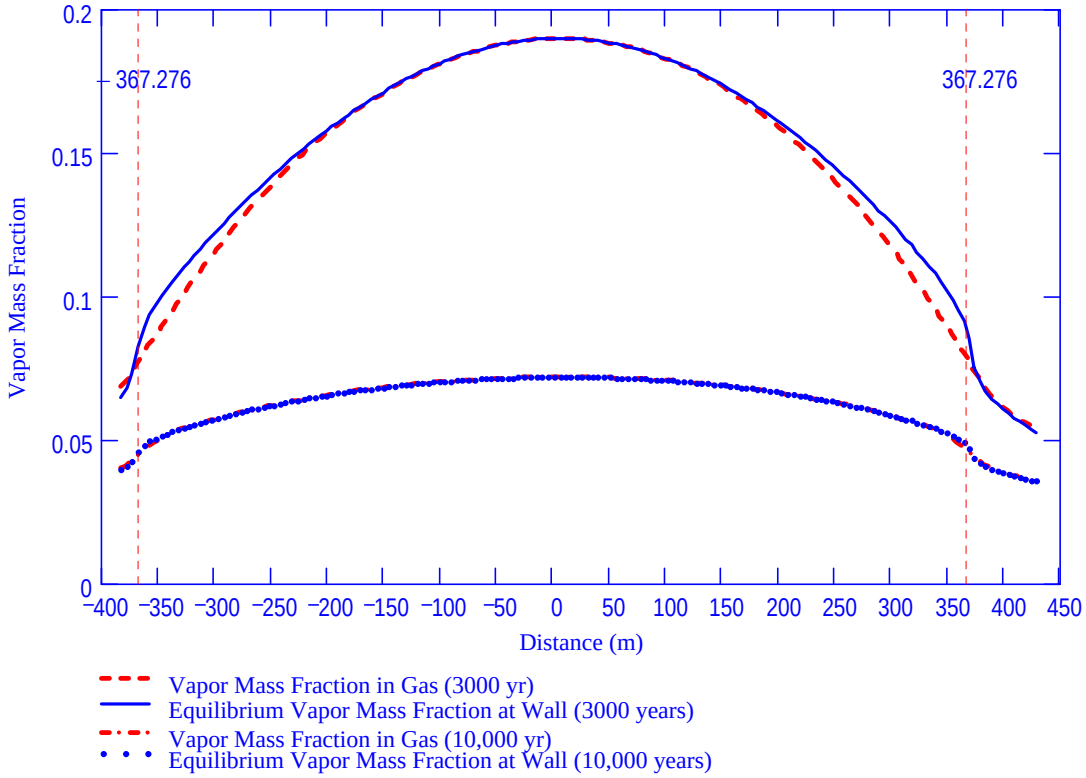

DTN: SN0408T0509903.007; file TOC.mcd; hyperlink 7.1.7, Calculated Results for Drift Choice #7.

NOTE: Top curves: vapor mass fraction in gas at 3,000 years; bottom curves: vapor mass fraction in gas at 10,000 years.

Figure 6.3.7-5. Vapor Mass Fraction in Gas at 3,000 Years and 10,000 Years: Choice #7, Mean Percolation Rate, Well-Ventilated Drip Shield, Low Invert Transport, High Dispersion Coefficient

The high-invert transport model relates the source vapor pressure with the invert surface temperature rather than the drift wall temperature. Since the invert surface temperature is higher than the drift wall temperature, the evaporation rate from the invert surface will be higher. The greater abundance of water vapor in the gas results in larger condensation rates (Tables 6.3.7-2, low dispersion coefficient, and 6.3.7-3, high dispersion coefficient.). For the low dispersion case, wall condensation in the emplacement region occurs at 1,000, 3,000, and 10,000 years. The higher axial transport of the high dispersion case completely eliminates wall condensation at 1,000 years, nearly eliminates it at 3,000 years, reduces it at 10,000 years.

Table 6.3.7-2. Condensation on the Drift Walls: Well-Ventilated Drip Shield, High Invert Transport, Low Dispersion Coefficient

Perc. Level	Drift Choice	300 Years		1,000 Years		3,000 Years		10,000 Years	
		Length (m)	Total Cond (kg/yr)	Length (m)	Total Cond (kg/yr)	Length (m)	Total Cond (kg/yr)	Length (m)	Total Cond (kg/yr)
Low	#1:	—	—	99	403	419	510	505	1062
	#2:	—	—	30	121	413	612	509	1266
	#3:	0	0	90	37	337	1002	380	1188
	#4:	—	—	0	0	5	0	475	645
	#5:	—	—	0	0	142	18	489	762
	#6:	—	—	0	0	137	23	359	661
	#7:	—	—	156	4204	600	705	666	2146
	Total:	**0**		**374**		**2055**		**3383**	
Mean	#1:	—	—	173	1309	525	5522	540	6212
	#2:	—	—	131	1120	505	4667	540	5479
	#3:	0	0	219	555	380	3541	415	3975
	#4:	—	—	178	4389	521	7805	549	9193
	#5:	—	—	76	1288	495	3576	540	4697
	#6:	—	—	56	433	358	2722	399	3780
	#7:	—	—	263	7724	666	4643	687	6192
	Total:	**0**		**1097**		**3449**		**3672**	
Upper	#1:	—	—	270	3483	535	13549	560	14537
	#2:	—	—	177	2356	525	9014	555	10011
	#3:	0	0	313	2382	410	7775	435	8501
	#4:	—	—	212	6193	535	16217	565	17932
	#5:	—	—	140	2563	521	7822	556	9261
	#6:	—	—	62	625	374	4339	399	5514
	#7:	—	—	404	12488	677	10711	707	12475
	Total:	**0**		**1577**		**3577**		**3777**	

DTN: SN0408T0509903.007; file Mixed_HighInvertTransport\Summary Tables.mcd.

Table 6.3.7-3. Condensation on the Drift Walls: Well-Ventilated Drip Shield, High Invert Transport, High Dispersion Coefficient

Perc. Level	Drift Choice	300 Years		1,000 Years		3,000 Years		10,000 Years	
		Length (m)	Total Cond (kg/yr)	Length (m)	Total Cond (kg/yr)	Length (m)	Total Cond (kg/yr)	Length (m)	Total Cond (kg/yr)
Low	#1:	—	—	0	0	0	0	228	112
	#2:	—	—	0	0	0	0	288	242
	#3:	0	0	0	0	0	0	263	601
	#4:	—	—	0	0	0	0	0	0
	#5:	—	—	0	0	0	0	0	0
	#6:	—	—	0	0	0	0	0	0
	#7:	—	—	0	0	0	0	208	75
	Total:	**0**		**0**		**0**		**987**	
Mean	#1:	—	—	0	0	0	0	486	4369
	#2:	—	—	0	0	0	0	475	3744
	#3:	0	0	0	0	55	84	348	2809
	#4:	—	—	0	0	0	0	491	6293
	#5:	—	—	0	0	0	0	454	2625
	#6:	—	—	0	0	0	0	313	1562
	#7:	—	—	0	0	0	0	586	3079
	Total:	**0**		**0**		**55**		**3153**	
Upper	#1:	—	—	0	0	111	171	519	12022
	#2:	—	—	0	0	0	0	500	7869
	#3:	0	0	0	0	196	1909	378	6687
	#4:	—	—	0	0	0	0	519	14315
	#5:	—	—	0	0	0	0	505	6595
	#6:	—	—	0	0	0	0	344	2968
	#7:	—	—	0	0	0	0	652	8735
	Total:	**0**		**0**		**307**		**3418**	

DTN: SN0408T0509903.007; file Mixed_HighInvertTransport\Summary Tables.mcd.

Condensation on the Drift Walls: Unventilated Drip Shield

Condensation on the drift wall for the unventilated drip shield, low-invert transport case (Table 6.3.7-4) is very close to that for the ventilated drip shield low-invert transport case (Table 6.3.7-4) for low axial dispersion. Because the invert contribution is comparatively small for the low-invert transport case, the difference in wall condensation between the ventilated and unventilated drip shield is minor.

Table 6.3.7-4. Condensation on the Drift Walls: Unventilated Drip Shield, Low Invert Transport, Low Dispersion Coefficient

Perc. Level	Drift Choice	300 Years		1,000 Years		3,000 Years		10,000 Years	
		Length (m)	Total Cond (kg/yr)	Length (m)	Total Cond (kg/yr)	Length (m)	Total Cond (kg/yr)	Length (m)	Total Cond (kg/yr)
Low	#1:	—	—	34	45	0	0	0	0
	#2:	—	—	13	16	0	0	0	0
	#3:	0	0	0	0	0	0	0	0
	#4:	—	—	5	46	0	0	0	0
	#5:	—	—	0	0	0	0	0	0
	#6:	—	—	0	0	0	0	0	0
	#7:	—	—	198	3064	0	0	0	0
	Total:	**0**		**249**		**0**		**0**	
Mean	#1:	—	—	55	92	0	0	0	0
	#2:	—	—	44	69	0	0	0	0
	#3:	0	0	0	0	0	0	0	0
	#4:	—	—	152	1557	0	0	0	0
	#5:	—	—	92	541	0	0	0	0
	#6:	—	—	19	18	0	0	0	0
	#7:	—	—	304	4515	0	0	0	0
	Total:	**0**		**666**		**0**		**0**	
Upper	#1:	—	—	60	102	0	0	0	0
	#2:	—	—	64	100	0	0	0	0
	#3:	0	0	0	0	0	0	0	0
	#4:	—	—	156	1598	0	0	0	0
	#5:	—	—	106	639	0	0	0	0
	#6:	—	—	25	22	0	0	0	0
	#7:	—	—	378	5068	0	0	0	0
	Total:	**0**		**788**		**0**		**0**	

DTN: SN0408T0509903.007; file Unmixed_LowInvertTransport\Summary Tables.mcd.

The impact of an unventilated drip shield on wall condensation is substantially larger for the high-invert transport case with low axial dispersion (compare Table 6.3.7-5 to Table 6.3.7-2). Wall condensation in the emplacement area for the low dispersion case is lower at 1,000 years and completely eliminated at 3,000 and 10,000 years.

Table 6.3.7-5. Condensation on the Drift Walls: Unventilated Drip Shield, High Invert Transport, Low Dispersion Coefficient

Perc. Level	Drift Choice	300 Years		1,000 Years		3,000 Years		10,000 Years	
		Length (m)	Total Cond (kg/yr)	Length (m)	Total Cond (kg/yr)	Length (m)	Total Cond (kg/yr)	Length (m)	Total Cond (kg/yr)
Low	#1:	—	—	34	45	0	0	0	0
	#2:	—	—	13	16	0	0	0	0
	#3:	0	0	0	0	0	0	0	0
	#4:	—	—	5	46	0	0	0	0
	#5:	—	—	0	0	0	0	0	0
	#6:	—	—	0	0	0	0	0	0
	#7:	—	—	198	3064	0	0	0	0
	Total:	**0**		**249**		**0**		**0**	
Mean	#1:	—	—	55	92	0	0	0	0
	#2:	—	—	44	69	0	0	0	0
	#3:	0	0	0	0	0	0	0	0
	#4:	—	—	152	1557	0	0	0	0
	#5:	—	—	92	540	0	0	0	0
	#6:	—	—	19	18	0	0	0	0
	#7:	—	—	304	4514	0	0	0	0
	Total:	**0**		**666**		**0**		**0**	
Upper	#1:	—	—	60	102	0	0	0	0
	#2:	—	—	64	100	0	0	0	0
	#3:	0	0	0	0	0	0	0	0
	#4:	—	—	156	1599	0	0	0	0
	#5:	—	—	106	639	0	0	0	0
	#6:	—	—	25	22	0	0	0	0
	#7:	—	—	378	5068	0	0	0	0
	Total:	**0**		**788**		**0**		**0**	

DTN: SN0408T0509903.007; file Unmixed_HighInvertTransport\Summary Tables.mcd.

The unventilated drip shield with high axial dispersion produces no wall condensation for either the low or high invert cases. In both cases, the axial transport is sufficiently high to keep the local vapor pressure from exceeding the saturation pressure at the local drift wall temperature.

6.3.7.2.3 Condensation Underneath the Drip Shield

Condensation takes place under the drip shield only for the high-invert transport case in the presence of an unventilated drip shield. The reason for this is straightforward. The low-invert transport model assumes that the vapor pressure at the invert surface is no greater than the equilibrium vapor pressure at the wall (Section 6.3.3.2.1). The drip shield temperature is always greater than the wall temperature at any axial location. Hence, the equilibrium vapor pressure at the drip shield surface will always be greater than the vapor pressure of the gas under the drip shield, which prevents drip shield condensation. The ventilation characteristics of the drip shield are unimportant for the low-invert transport case.

The ventilation characteristics of the drip shield are important for the high invert transport case. The temperature of the invert surface under a hot PWR package is always greater than the drip shield temperature above an adjacent HLW package. Condensate will form on this cooler drip shield surface unless 1) the axial vapor dispersion is sufficiently high, or 2) a cooler surface is accessible. A ventilated drip shield allows the vapor evolved from the invert surface to contact the drift wall, which is cooler than the drip shield. This precludes condensation on the underside of the drip shield.

Predicted condensation rates under the drip shield are tabulated in Table 6.3.7-6 (low dispersion coefficient) and Table 6.3.7-7 (high dispersion coefficient). The incidence and magnitude of drip shield condensation increases with time and percolation rate. Increased percolation rate makes more water available for evaporation. Decreasing decay heat (increasing time) decreases the axial temperature gradient and, consequently, the axial vapor transport.

An examination of the condensation locations and the vapor mass fraction profiles helps the visualization of the process. Figure 6.3.7-6 shows the location and magnitude of condensation on the underside of the drip shield for each of the waste packages at 1,000 years for the mean percolation case (also itemized in Table 6.3.7-6). Drip shield condensation occurs in the vicinity of only seven packages that are located near the ends of the drift emplacement region (indicated by the vertical dashed lines). All seven of the waste packages are high level waste packages. No condensate forms on the underside of the drip shield over most of the emplacement region.

Table 6.3.7-6. Condensation under the Drip Shield: Unventilated Drip Shield High Invert Transport, Low Dispersion Coefficient

Perc. Level	Drift Choice	300 Years		1,000 Years		3,000 Years		10,000 Years	
		Length (m)	Total Cond (kg/yr)	Length (m)	Total Cond (kg/yr)	Length (m)	Total Cond (kg/yr)	Length (m)	Total Cond (kg/yr)
Low	#1:	—	—	0	0	21	820	29	1095
	#2:	—	—	0	0	20	938	28	1285
	#3:	0	0	8	507	18	1009	22	1216
	#4:	—	—	0	0	14	352	27	784
	#5:	—	—	0	0	14	379	27	854
	#6:	—	—	0	0	13	440	20	834
	#7:	—	—	0	0	34	1945	39	2385
	Total:	**0**		**8**		**134**		**192**	
Mean	#1:	—	—	11	1421	30	5692	55	6252
	#2:	—	—	6	648	28	4907	36	5500
	#3:	0	0	13	1352	23	3644	42	4077
	#4:	—	—	7	1754	30	8501	73	8825
	#5:	—	—	0	0	28	4112	32	4807
	#6:	—	—	1	43	21	3357	33	4025
	#7:	—	—	7	1050	38	5837	48	6429
	Total:	**0**		**45**		**198**		**319**	
Upper	#1:	—	—	20	4831	35	13712	73	11694
	#2:	—	—	14	2690	30	9206	71	9318
	#3:	0	0	18	3459	25	7975	58	7540
	#4:	—	—	19	4704	41	16805	73	13037
	#5:	—	—	5	856	30	8399	72	8932
	#6:	—	—	4	519	22	5043	52	5682
	#7:	—	—	16	4461	40	11855	93	11728
	Total:	**0**		**96**		**223**		**492**	

DTN: SN0408T0509903.007; file Unmixed_HighInvertTransport\Summary Tables.mcd.

Table 6.3.7-7. Condensation under the Drip Shield: Unventilated Drip Shield, High Invert Transport, High Dispersion Coefficient

Perc. Level	Drift Choice	300 Years		1,000 Years		3,000 Years		10,000 Years	
		Length (m)	Total Cond (kg/yr)	Length (m)	Total Cond (kg/yr)	Length (m)	Total Cond (kg/yr)	Length (m)	Total Cond (kg/yr)
Low	#1:	—	—	0	0	16	603	25	990
	#2:	—	—	0	0	16	719	26	1173
	#3:	0	0	4	166	15	860	21	1121
	#4:	—	—	0	0	1	12	23	666
	#5:	—	—	0	0	6	141	24	734
	#6:	—	—	0	0	8	233	18	703
	#7:	—	—	0	0	31	1657	37	2243
	Total:	**0**		**4**		**93**		**174**	
Mean	#1:	—	—	7	845	28	5447	31	6037
	#2:	—	—	0	0	28	4594	31	5283
	#3:	0	0	10	962	21	3468	24	3893
	#4:	—	—	5	979	30	8109	62	8423
	#5:	—	—	0	0	25	3766	30	4555
	#6:	—	—	0	0	19	3080	23	3781
	#7:	—	—	0	0	37	5568	40	6204
	Total:	**0**		**22**		**188**		**241**	
Upper	#1:	—	—	18	4100	31	13362	72	11333
	#2:	—	—	9	1916	29	8874	70	9003
	#3:	0	0	15	2990	23	7706	54	7247
	#4:	—	—	11	3997	34	16367	73	13106
	#5:	—	—	0	0	29	7993	49	8574
	#6:	—	—	0	0	21	4711	37	5354
	#7:	—	—	13	3246	39	11541	88	11272
	Total:	**0**		**66**		**206**		**443**	

DTN: SN0408T0509903.007; file Unmixed_HighInvertTransport\Summary Tables.mcd.

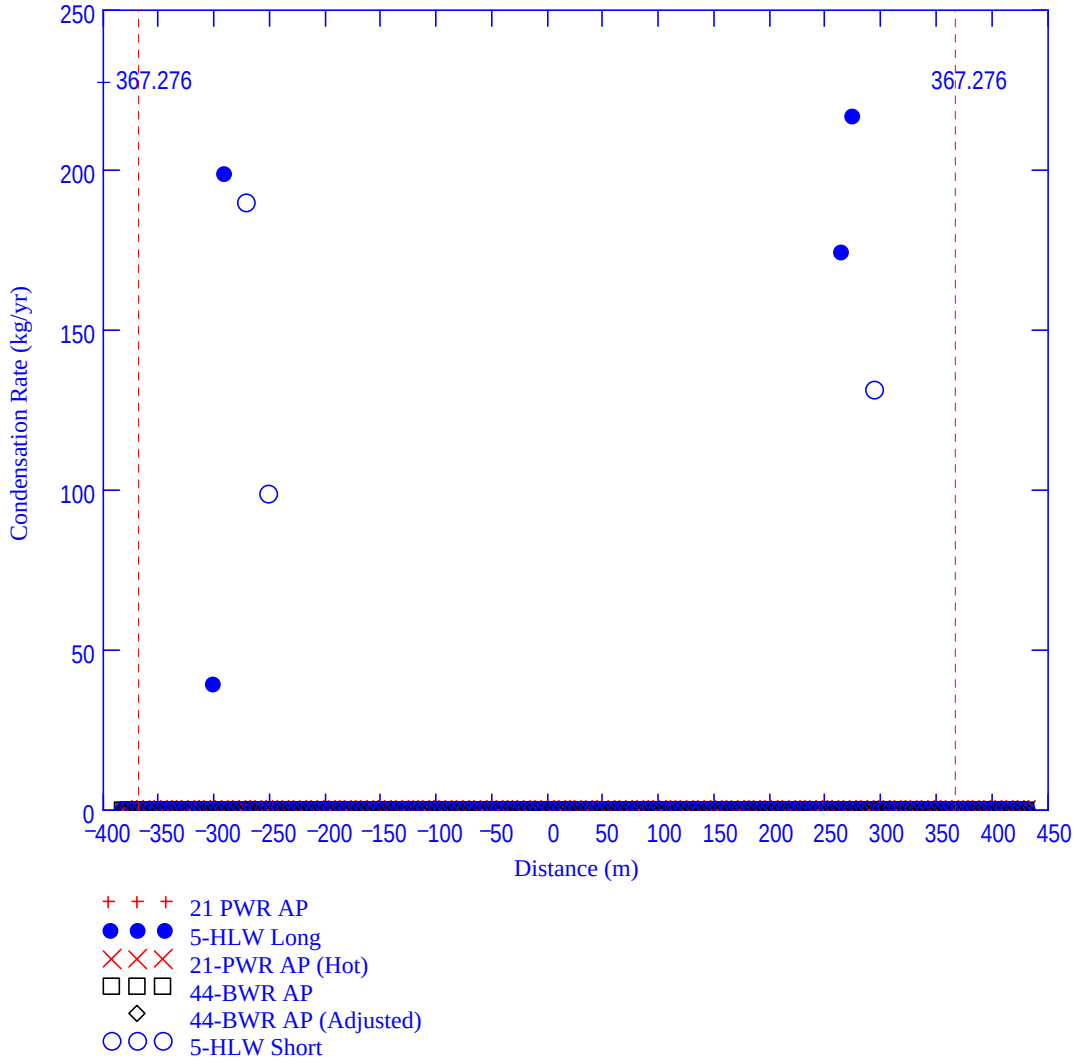

DTN: SN0408T0509903.007; file TOC.mcd; hyperlink 7.4.7, Calculated Results for Drift Choice #7.

Figure 6.3.7-6. Condensation Rate on the Underside of the Drip Shield: Choice #7, 1,000 Years, Mean Percolation Rate, Unventilated Drip Shield, High Invert Transport, Low Dispersion Coefficient

Figure 6.3.7-7 shows the vapor mass fraction of the gas under the drip shield (dashed red line) and the equilibrium vapor mass fraction for the drip shield surface (solid blue line). The "stepped" appearance of the drip shield line reflects the temperature differences between adjacent waste packages. High level waste (HLW) packages produce the smallest amount of decay heat and have the lowest temperatures. Pressurized water reactor (PWR) waste packages produce the greatest amount of decay heat and have the highest temperatures. Boiling water reactor (BWR) waste packages have decay heats and temperatures that lie in the middle.

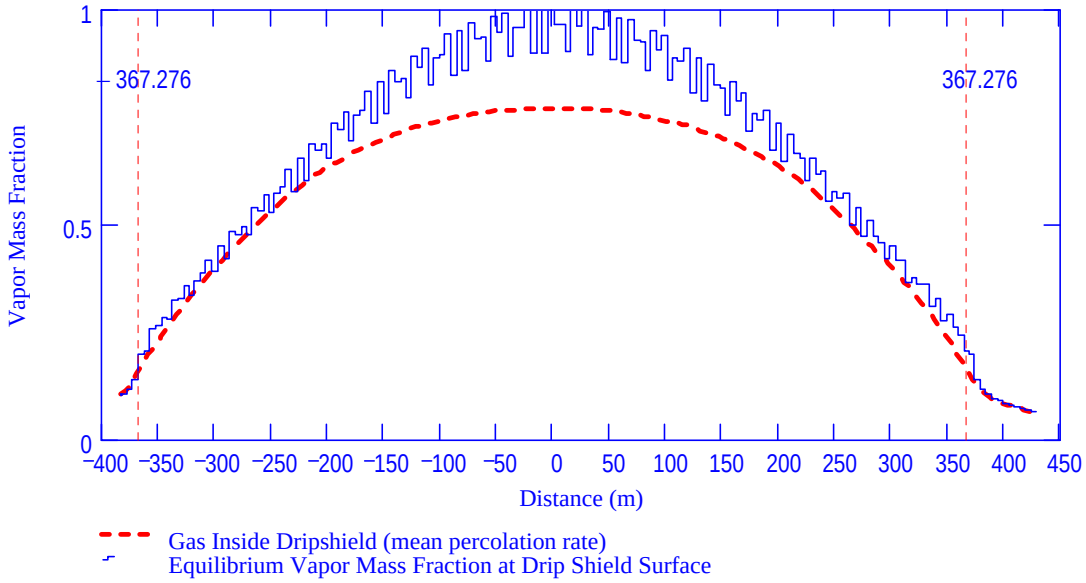

DTN: SN0408T0509903.007; file TOC.mcd; hyperlink 7.4.7, Calculated Results for Drift Choice #7.

Figure 6.3.7-7. Vapor Mass Fraction in Gas under the Drip Shield: Choice #7, 1,000 Years, Mean Percolation Rate, Unventilated Drip Shield, High Invert Transport, Low Dispersion Coefficient

In the center of the drift, the vapor mass fraction of the gas is below the equilibrium values of the drip shield surface. No condensation on the drip shield occurs in this region. The vapor mass fraction difference decreases near the ends of the drift. Near the drift ends, the gas vapor mass fraction exceeds the equilibrium vapor fraction for the coolest of the waste packages (HLWs) and condensate forms.

The extent of condensation on the underside of the drip shield is substantially increased at 10,000 years. Virtually all of the HLW packages have condensate forming on the adjacent drip shield (Figure 6.3.7-8). Comparatively minor amounts of drip shield condensate form in the vicinity of a small number of BWR packages near the drift ends. The vapor mass fraction profiles (Figure 6.3.7-9) for this case are consistent with this picture.

If the percolation rate is sufficiently high and the axial dispersion is sufficiently low, condensate can form directly on some of the waste packages. When this occurs, the condensation rate on the waste packages is much lower than that on the adjacent drip shield surface. It is predicted to occur only on HLW packages as shown in Figure 6.3.7-10. The combination of condensation on the underside of the drip shield and the condensate that forms directly on the waste packages is reported in Tables 6.3.7-6 and 6.3.7-7.

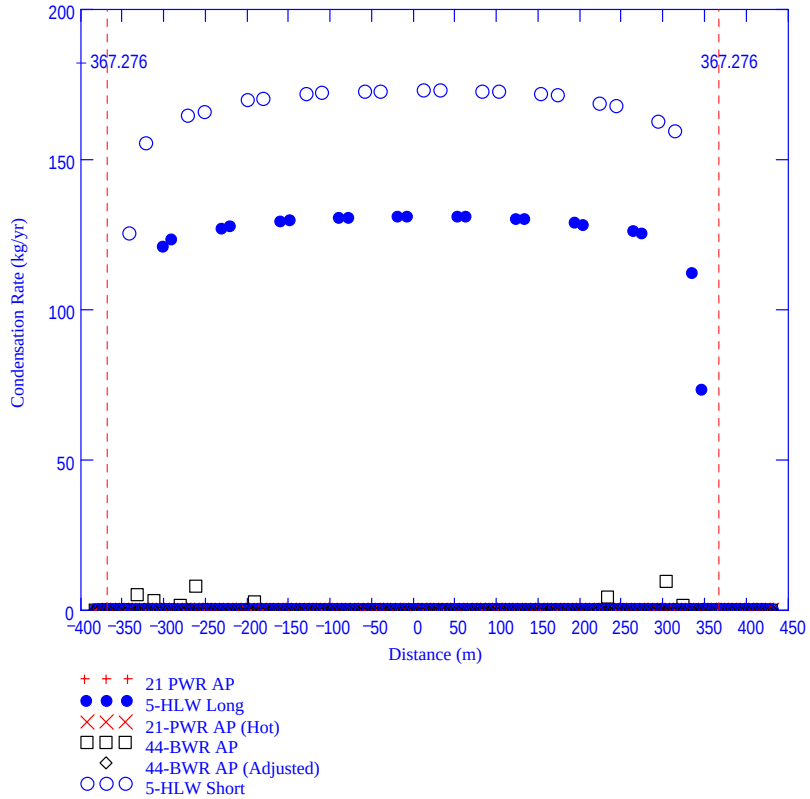

DTN: SN0408T0509903.007; file TOC.mcd; hyperlink 7.4.7, Calculated Results for Drift Choice #7.

Figure 6.3.7-8. Condensation Rate on the Underside of the Drip Shield: Choice #7, 10,000 Years, Mean Percolation Rate, Unventilated Drip Shield, High Invert Transport, Low Dispersion Coefficient

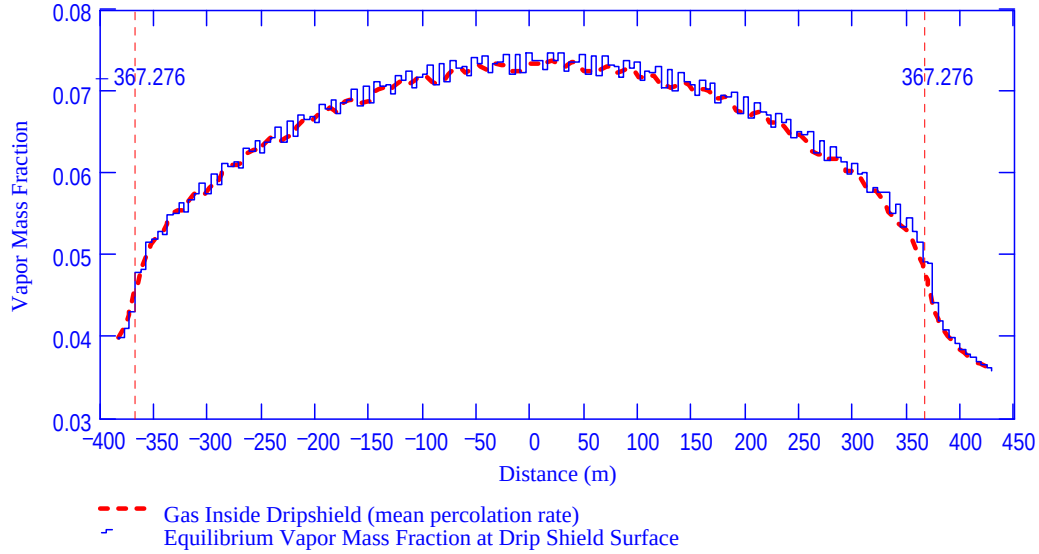

DTN: SN0408T0509903.007; file TOC.mcd; hyperlink 7.4.7, Calculated Results for Drift Choice #7.

Figure 6.3.7-9. Vapor Mass Fraction in Gas under the Drip Shield: Choice #7, 10,000 Years, Mean Percolation Rate, Unventilated Drip Shield, High Invert Transport, Low Dispersion Coefficient

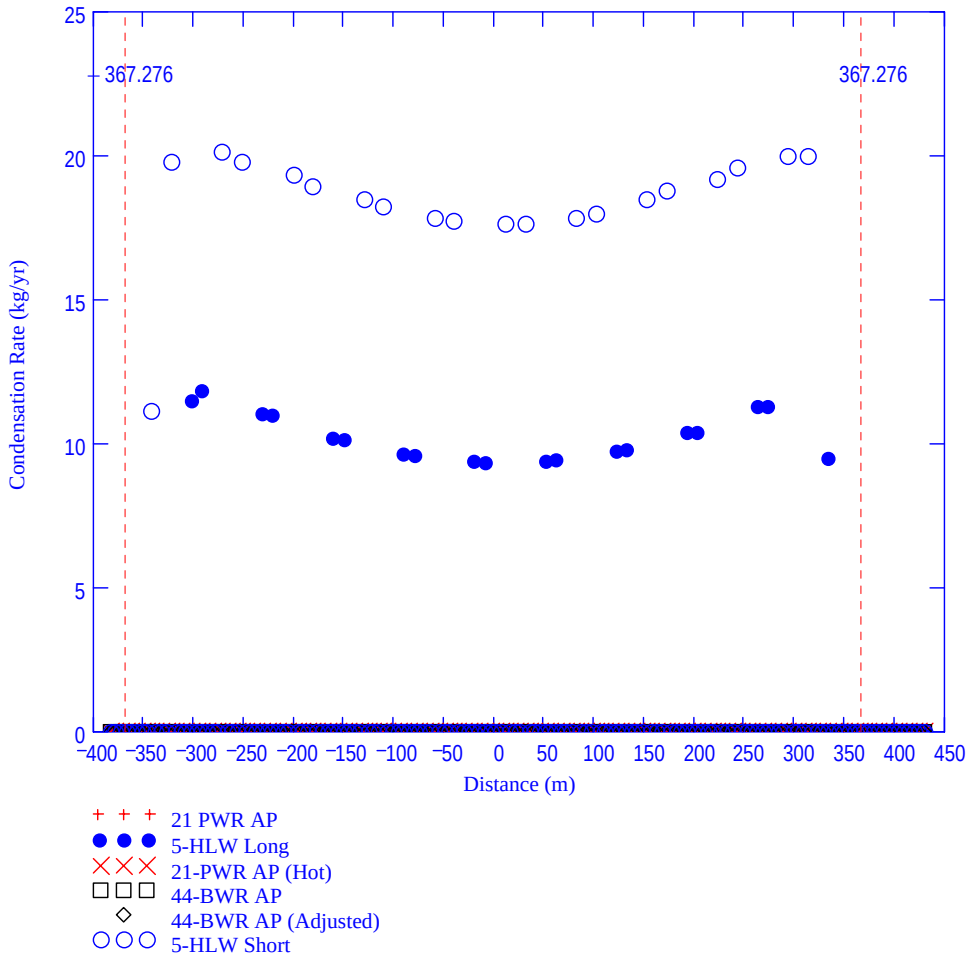

DTN: SN0408T0509903.007; file TOC.mcd; hyperlink 7.4.7, Calculated Results for Drift Choice #7.

Figure 6.3.7-10. Condensation Rate on the Waste Package: Choice #7, 10,000 Years, Mean Percolation Rate, Unventilated Drip Shield, High Invert Transport, Low Dispersion Coefficient

6.3.7.2.4 Impact of Assumptions

This calculation uses several bounding-type assumptions for purposes of calculating condensation. The result of the calculation is a predicted range for the condensation rates on the various structures within the emplacement drift. These ranges are suitable for their intended application of assessing the impacts of in-drift condensation on radionuclide migration.

The vapor pressure at the invert surface (Section 6.3.3.2.1) has a strong impact on the calculated results. Condensation under the drip shield can take place only when the water source for vapor under the drip shield is hotter than the drip shield. The high-invert bound is realized only when water can flow to the invert surface. If water evaporation under the drip shield is limited to a lower point in the invert, the vapor pressure at the invert surface will reflect that cooler location.

There are two components to water flow in the invert: 1) capillary flow through the small pores of the individual invert particles, and 2) seepage water augmented by local condensate that migrates laterally underneath the drip shield. Intuitively, one is inclined to think that capillary pumping through the small pores of the invert particles (component 1, Figure 6.3.3.2) is reduced or eliminated at the particle contact points. There are, however, no data to prove this. It is important to emphasize that the determination of the invert capillary pumping characteristics is not simply a matter of modeling. Data are required to clarify the nature and magnitude of water flow across particle contacts if such flows even exist. Without such data, a defensible model for invert flow reduction cannot be formulated.

The lateral migration of seepage water from the outside of the drip shield (component 2) is controlled by the capillary characteristics of the packed bed that comprises the invert. No attempt was made in this analysis to quantify this flow. It is worth noting, however, that the lateral capillary flow in the invert can be reduced by increasing the invert particle size. If the particle size is sufficiently large, seepage water will flow straight down without significant lateral migration. This would work to reduce the vapor pressure at the invert surface.

The partitioning of the available water (Section 6.3.3.2.3) is less important than the assumption about the invert vapor pressure (Section 6.3.3.2.1). The details of water partitioning between the drift and the invert depend on the flow characteristics of the invert and the behavior of seepage water once it enters the drift.

Barometric pumping (Section 6.3.3.2.4) is expected to increase the axial dispersion coefficient and thereby decrease the vapor mass fraction in the gas. This, in turn, should reduce condensation rates. A quantitative estimate of the impact of barometric pumping is not addressed in this report.

Drip shield ventilation (Section 6.3.3.2.5) can preclude condensation under the drip shield by providing a pathway for water vapor to move from the invert surface to the drift wall. The impact of drip shield ventilation is dependent upon the vapor pressure at the invert surface. If the vapor pressure at the invert surface is sufficiently low (Section 6.3.3.2.1), the impact of a ventilated drip shield is small. If, however, the vapor pressure at the invert surface is high, drip shield ventilation will have a substantial impact.

The axial redistribution of heat is neglected in the model calculation of drift wall temperatures (Section 6.3.3.2.6). The impact of axial energy redistribution can now be assessed. Tables 6.3.7-8 through 6.3.7-15 present an accounting of condensation in the exhaust standoff and the access turnout. The drift choice (#1 through #7) and time occupy the first two columns. The integrated decay heat (W) and the average line source strength (W/m) occupy the next two columns (labeled “Decay Heat”). The next six columns (labeled “Heat Deposited in Access/Exhaust Regions”) are arranged in pairs for each percolation level. The first column of each pair is the integral latent heat of the vapor that condenses in the exhaust standoff and the access turnout. The second column of each pair is the linear average of the latent heat deposited in the exhaust standoff and access turnout.

The fraction of the decay heat that is transported axially is obtained by dividing the heat condensed in the unoccupied regions by the decay heat generated within the drift. For instance,

for the mean percolation case of drift choice #1 at 1,000 years in Table 6.3.7-8, the total decay heat generation in the drift is 40289 W and the heat deposited in the unoccupied regions is 1646 W. Approximately 4% of the decay heat is transported axially by vapor transport. In all the low axial dispersion cases, the axial redistribution of heat is less than 7%. For these cases, ignoring the axial redistribution of energy is acceptable.

In some of the high axial dispersion cases, the axial redistribution of energy may be important. For instance, for the high percolation case of drift choice #4 at 3,000 years in Table 6.3.7-9, the total decay heat generation in the drift is 17113 W and the heat deposited in the unoccupied regions is 5976 W. Approximately 35% of the decay heat is transported axially by vapor transport. Ignoring the axial transport of energy in the calculation of the wall temperatures is more problematic in this case. It is noted that other assumptions, such as that assigning source vapor pressure based only on temperature (Section 6.3.3.2.1), are bounding and tend to maximize the amount of moisture transport and thus the heat transported as latent heat.

The energy deposited in the unheated regions of the drifts will heat the surrounding rock just like the waste packages heat the rock that surrounds them. The equivalent average line power of the condensate (W/m) is also tabulated in Tables 6.3.7-8 through 6.3.7-15. In some cases this equivalent source strength is actually higher than the line source strength in the emplacement region. These equivalent line average power values are overestimated because the length of unheated drift available for condensation is greater than represented in the model.

Axial transport of heat will have two impacts. First, it will tend to flatten the axial temperature profile and, consequently, decrease the axial transport of vapor and energy. This is a stabilizing mechanism that will tend to increase the condensation rate in the emplacement region. The second impact will be to decrease the temperature differences that drive the evaporation and condensation processes; this will tend to decrease the condensation rate in the emplacement region.

The net impact of the redistribution of energy on the calculated wall temperature cannot be quantitatively determined on the basis of these calculations alone. Had the axial transport been shown to be a small percentage of the total decay heat at all times and in all cases, the argument for the insignificance of heat relocation would have been strong. However, the strength of the axial relocation term at individual times for some of the cases analyzed does not, *ipso facto*, prove that axial transport significantly modifies the wall temperature profile. The wall temperature is a function of the entire power history rather than the instantaneous value. All that can be stated now is that the fractional change in condensation rate within the emplacement region is likely to be less than the fraction of the decay heat that is transported to the access and exhaust regions. This is within the uncertainty bounds of the current analysis.

Table 6.3.7-8. Axial Energy Flow to the Access and Exhaust Regions: Well-Ventilated Drip Shield, Low Invert Transport, Low Dispersion Coefficient

Drift Choice	Time (yr)	Decay Heat		Heat Deposited in Access/Exhaust Regions					
				Low Perc.		Mean Perc.		High Perc.	
		W	W/m	W	W/m	W	W/m	W	W/m
#1	1,000	40289	67.7	1227	16.4	1646	21.9	2161	28.8
	3,000	17113	28.7	303	4.0	554	7.4	719	9.6
	10,000	10170	17.1	142	1.9	236	3.1	238	3.2
#2	1,000	40289	67.7	1463	19.5	2002	26.7	2415	32.2
	3,000	17113	28.7	354	4.7	589	7.9	724	9.7
	10,000	10170	17.1	155	2.1	242	3.2	255	3.4
#3	300	73327	157.8	636	8.5	1036	13.8	2534	33.8
	1,000	31438	67.7	826	11.0	971	12.9	1225	16.3
	3,000	13354	28.7	271	3.6	412	5.5	513	6.8
	10,000	7935	17.1	140	1.9	191	2.6	195	2.6
#4	1,000	40289	67.7	1290	17.2	2361	31.5	2704	36.1
	3,000	17113	28.7	334	4.4	727	9.7	861	11.5
	10,000	10170	17.1	145	1.9	265	3.5	265	3.5
#5	1,000	41002	67.7	1186	15.8	2213	29.5	2621	34.9
	3,000	17416	28.7	365	4.9	651	8.7	816	10.9
	10,000	10349	17.1	154	2.0	266	3.5	302	4.0
#6	1,000	30726	67.7	1114	14.9	1742	23.2	1830	24.4
	3,000	13051	28.7	338	4.5	545	7.3	609	8.1
	10,000	7756	17.1	157	2.1	235	3.1	244	3.3
#7	1,000	50209	67.7	1606	21.4	1684	22.5	1826	24.3
	3,000	21327	28.7	411	5.5	527	7.0	616	8.2
	10,000	12673	17.1	177	2.4	220	2.9	222	3.0

DTN: SN0408T0509903.007; file Mixed_LowInvertTransport\Summary Tables.mcd.

Table 6.3.7-9. Axial Energy Flow to the Access and Exhaust Regions: Well-Ventilated Drip Shield, Low Invert Transport, High Dispersion Coefficient

Drift Choice	Time (yr)	Decay Heat		Heat Deposited in Access/Exhaust Regions					
				Low Perc.		Mean Perc.		High Perc.	
		W	W/m	W	W/m	W	W/m	W	W/m
#1	1,000	40289	67.7	1546	20.6	2961	39.5	5846	78.0
	3,000	17113	28.7	879	11.7	3347	44.6	4541	60.5
	10,000	10170	17.1	435	5.8	789	10.5	1019	13.6
#2	1,000	40289	67.7	1548	20.6	3017	40.2	4886	65.1
	3,000	17113	28.7	1022	13.6	3478	46.4	4393	58.6
	10,000	10170	17.1	471	6.3	783	10.4	957	12.8
#3	300	31438	67.7	1383	18.4	2069	27.6	3798	50.6
	1,000	31438	67.7	1383	18.4	2069	27.6	3798	50.6
	3,000	13354	28.7	993	13.2	2291	30.5	3102	41.4
	10,000	7935	17.1	416	5.5	641	8.5	808	10.8
#4	1,000	40289	67.7	1290	17.2	4147	55.3	7014	93.5
	3,000	17113	28.7	675	9.0	4782	63.8	5976	79.7
	10,000	10170	17.1	457	6.1	1008	13.4	1196	16.0
#5	1,000	41002	67.7	1186	15.8	2588	34.5	4171	55.6
	3,000	17416	28.7	723	9.6	3595	47.9	5034	67.1
	10,000	10349	17.1	471	6.3	851	11.3	1061	14.1
#6	1,000	30726	67.7	1114	14.9	2411	32.1	2907	38.8
	3,000	13051	28.7	753	10.0	3078	41.0	3896	51.9
	10,000	7756	17.1	493	6.6	809	10.8	904	12.1
#7	1,000	50209	67.7	2337	31.2	3254	43.4	5271	70.3
	3,000	21327	28.7	1817	24.2	4432	59.1	5262	70.2
	10,000	12673	17.1	619	8.3	810	10.8	960	12.8

DTN: SN0408T0509903.007; file Mixed_LowInvertTransport\Summary Tables.mcd.

Table 6.3.7-10. Axial Energy Flow to the Access and Exhaust Regions:: Well-Ventilated Drip Shield, High Invert Transport, Low Dispersion Coefficient

Drift Choice	Time (yr)	Decay Heat		Heat Deposited in Access/Exhaust Regions					
				Low Perc.		Mean Perc.		High Perc.	
		W	W/m	W	W/m	W	W/m	W	W/m
#1	1,000	40289	67.7	1227	16.4	1646	21.9	2161	28.8
	3,000	17113	28.7	303	4.0	554	7.4	717	9.6
	10,000	10170	17.1	142	1.9	234	3.1	238	3.2
#2	1,000	40289	67.7	1464	19.5	2002	26.7	2415	32.2
	3,000	17113	28.7	354	4.7	589	7.9	723	9.6
	10,000	10170	17.1	155	2.1	240	3.2	255	3.4
#3	300	73327	157.8	636	8.5	1036	13.8	2534	33.8
	1,000	31438	67.7	826	11.0	971	12.9	1226	16.3
	3,000	13354	28.7	271	3.6	412	5.5	512	6.8
	10,000	7935	17.1	140	1.9	191	2.6	196	2.6
#4	1,000	40289	67.6	1290	17.2	2361	31.5	2704	36.1
	3,000	17113	28.7	334	4.4	726	9.7	858	11.4
	10,000	10170	17.1	145	1.9	265	3.5	267	3.6
#5	1,000	41002	67.7	1186	15.8	2213	29.5	2621	34.9
	3,000	17416	28.7	365	4.9	651	8.7	816	10.9
	10,000	10349	17.1	154	2.0	266	3.5	306	4.0
#6	1,000	30726	67.7	1114	14.9	1742	23.2	1831	24.4
	3,000	13051	28.7	338	4.5	545	7.3	608	8.1
	10,000	7756	17.1	157	2.1	233	3.1	243	3.2
#7	1,000	50209	67.7	1606	21.4	1684	22.5	1826	24.3
	3,000	21327	28.7	411	5.5	528	7.0	616	8.2
	10,000	12673	17.1	177	2.4	220	2.9	222	3.0

DTN: SN0408T0509903.007; file Mixed_HighInvertTransport\Summary Tables.mcd.

Table 6.3.7-11. Axial Energy Flow to the Access and Exhaust Regions:: Well-Ventilated Drip Shield, High Invert Transport, High Dispersion Coefficient

Drift Choice	Time (yr)	Decay Heat		Heat Deposited in Access/Exhaust Regions					
				Low Perc.		Mean Perc.		High Perc.	
		W	W/m	W	W/m	W	W/m	W	W/m
#1	1,000	40289	67.7	1546	20.6	2961	39.5	5846	78.0
	3,000	17113	28.7	879	11.7	3348	44.6	4542	60.6
	10,000	10170	17.1	435	5.8	789	10.5	1015	13.5
#2	1,000	40289	67.7	1548	20.6	3017	40.2	4886	65.1
	3,000	17113	28.7	1022	13.6	3479	46.4	4394	58.6
	10,000	10170	17.1	472	6.3	783	10.4	954	12.7
#3	300	31438	67.7	1383	18.4	2069	27.6	3798	50.6
	1,000	31438	67.7	1383	18.4	2069	27.6	3798	50.6
	3,000	13354	28.7	993	13.2	2292	30.6	3103	41.4
	10,000	7935	17.1	416	5.5	641	8.5	808	10.8
#4	1,000	40289	67.7	1290	17.2	4147	55.3	7014	93.5
	3,000	17113	28.7	675	9.0	4783	63.8	5977	79.7
	10,000	10170	17.1	457	6.1	1006	13.4	1189	15.9
#5	1,000	41002	67.7	1186	15.8	2588	34.5	4171	55.6
	3,000	17416	28.7	723	9.6	3595	47.9	5035	67.1
	10,000	10349	17.1	471	6.3	851	11.4	1061	14.1
#6	1,000	30726	67.7	1114	14.9	2411	32.1	2907	38.8
	3,000	13051	28.7	753	10.0	3078	41.0	3898	52.0
	10,000	7756	17.1	494	6.6	809	10.8	902	12.0
#7	1,000	50209	67.7	2337	31.2	3254	43.4	5271	70.3
	3,000	21327	28.7	1817	24.2	4434	59.1	5264	70.2
	10,000	12673	17.1	619	8.3	811	10.8	960	12.8

DTN: SN0408T0509903.007; file Mixed_HighInvertTransport\Summary Tables.mcd.

Table 6.3.7-12. Axial Energy Flow to the Access and Exhaust Regions:: Unventilated Drip Shield, Low Invert Transport, Low Dispersion Coefficient

Drift Choice	Time (yr)	Decay Heat		Heat Deposited in Access/Exhaust Regions					
				Low Perc.		Mean Perc.		High Perc.	
		W	W/m	W	W/m	W	W/m	W	W/m
#1	1,000	40289	67.7	1203	16.0	1626	21.7	2138	28.5
	3,000	17113	28.7	298	4.0	544	7.3	698	9.3
	10,000	10170	17.1	140	1.9	229	3.1	234	3.1
#2	1,000	40289	67.7	1395	18.6	1973	26.3	2385	31.8
	3,000	17113	28.7	349	4.6	580	7.7	710	9.5
	10,000	10170	17.1	154	2.0	239	3.2	249	3.3
#3	300	73327	157.8	636	8.5	1036	13.8	2534	33.8
	1,000	31438	67.7	817	10.9	961	12.8	1213	16.2
	3,000	13354	28.7	266	3.5	405	5.4	497	6.6
	10,000	7935	17.1	139	1.8	186	2.5	191	2.6
#4	1,000	40289	67.7	1267	16.9	2293	30.6	2687	35.8
	3,000	17113	28.7	328	4.4	719	9.5	837	11.2
	10,000	10170	17.1	143	1.9	260	3.5	262	3.5
#5	1,000	41002	67.7	1186	15.8	2149	28.6	2567	34.2
	3,000	17416	28.7	359	4.8	642	8.6	802	10.7
	10,000	10349	17.1	152	2.0	263	3.5	292	3.9
#6	1,000	30726	67.7	1114	14.9	1697	22.6	1797	24.0
	3,000	13051	28.7	332	4.4	537	7.2	597	8.0
	10,000	7756	17.1	155	2.1	231	3.1	237	3.2
#7	1,000	50209	67.7	1565	20.9	1680	22.4	1820	24.3
	3,000	21327	28.7	406	5.4	520	6.9	608	8.1
	10,000	12673	17.1	175	2.3	213	2.8	218	2.9

DTN: SN0408T0509903.007; file Unmixed_LowInvertTransport\Summary Tables.mcd.

Table 6.3.7-13. Axial Energy Flow to the Access and Exhaust Regions:: Unventilated Drip Shield, Low Invert Transport, High Dispersion Coefficient

Drift Choice	Time (yr)	Decay Heat		Heat Deposited in Access/Exhaust Regions					
				Low Perc.		Mean Perc.		High Perc.	
		W	W/m	W	W/m	W	W/m	W	W/m
#1	1,000	40289	67.7	1546	20.6	2893	38.6	5482	73.1
	3,000	17113	28.7	833	11.1	3243	43.2	4418	58.9
	10,000	10170	17.1	431	5.7	781	10.4	996	13.3
#2	1,000	40289	67.7	1548	20.6	3015	40.2	4723	63.0
	3,000	17113	28.7	967	12.9	3358	44.8	4265	56.9
	10,000	10170	17.1	467	6.2	775	10.3	944	12.6
#3	300	31438	67.7	1369	18.3	1991	26.5	3527	47.0
	1,000	31438	67.7	1369	18.3	1991	26.5	3527	47.0
	3,000	13354	28.7	917	12.2	2216	29.5	3002	40.0
	10,000	7935	17.1	412	5.5	634	8.5	791	10.5
#4	1,000	40289	67.7	1290	17.2	4062	54.2	6665	88.9
	3,000	17113	28.7	673	9.0	4636	61.8	5816	77.5
	10,000	10170	17.1	453	6.0	997	13.3	1158	15.4
#5	1,000	41002	67.7	1186	15.8	2588	34.5	4166	55.5
	3,000	17416	28.7	713	9.5	3239	43.2	4873	65.0
	10,000	10349	17.1	467	6.2	844	11.3	1049	14.0
#6	1,000	30726	67.7	1114	14.9	2411	32.1	2907	38.8
	3,000	13051	28.7	734	9.8	2772	37.0	3751	50.0
	10,000	7756	17.1	489	6.5	801	10.7	894	11.9
#7	1,000	50209	67.6	2337	31.2	3254	43.4	5005	66.7
	3,000	21327	28.7	1673	22.3	4106	54.7	5159	68.8
	10,000	12673	17.1	615	8.2	805	10.7	950	12.7

DTN: SN0408T0509903.007; file Unmixed_LowInvertTransport\Summary Tables.mcd.

Table 6.3.7-14. Axial Energy Flow to the Access and Exhaust Regions:: Unventilated Drip Shield, High Invert Transport, Low Dispersion Coefficient

Drift Choice	Time (yr)	Decay Heat		Heat Deposited in Access/Exhaust Regions					
				Low Perc.		Mean Perc.		High Perc.	
		W	W/m	W	W/m	W	W/m	W	W/m
#1	1,000	40289	67.7	1203	16.0	1629	21.7	2143	28.6
	3,000	17113	28.7	299	4.0	548	7.3	702	9.4
	10,000	10170	17.1	141	1.9	232	3.1	243	3.2
#2	1,000	40289	67.7	1395	18.6	1977	26.4	2389	31.9
	3,000	17113	28.7	349	4.7	583	7.8	714	9.5
	10,000	10170	17.1	154	2.1	240	3.2	255	3.4
#3	300	73327	157.8	636	8.5	1036	13.8	2534	33.8
	1,000	31438	67.7	818	10.9	963	12.8	1217	16.2
	3,000	13354	28.7	267	3.6	407	5.4	503	6.7
	10,000	7935	17.1	139	1.9	188	2.5	200	2.7
#4	1,000	40289	67.7	1267	16.9	2297	30.6	2698	36.0
	3,000	17113	28.7	328	4.4	719	9.6	843	11.2
	10,000	10170	17.1	144	1.9	265	3.5	273	3.6
#5	1,000	41002	67.7	1186	15.8	2149	28.6	2572	34.3
	3,000	17416	28.7	359	4.8	644	8.6	805	10.7
	10,000	10349	17.1	153	2.0	265	3.5	296	3.9
#6	1,000	30726	67.7	1114	14.9	1699	22.7	1801	24.0
	3,000	13051	28.7	332	4.4	539	7.2	600	8.0
	10,000	7756	17.1	156	2.1	233	3.1	241	3.2
#7	1,000	50209	67.7	1565	20.9	1685	22.5	1827	24.4
	3,000	21327	28.7	407	5.4	523	7.0	611	8.1
	10,000	12673	17.1	176	2.3	216	2.9	224	3.0

DTN: SN0408T0509903.007; file Unmixed_HighInvertTransport\Summary Tables.mcd.

Table 6.3.7-15. Axial Energy Flow to the Access and Exhaust Regions:: Unventilated Drip Shield, High Invert Transport, High Dispersion Coefficient

Drift Choice	Time (yr)	Decay Heat		Heat Deposited in Access/Exhaust Regions					
				Low Perc.		Mean Perc.		High Perc.	
		W	W/m	W	W/m	W	W/m	W	W/m
#1	1,000	40289	67.7	1546	20.6	2897	38.6	5488	73.2
	3,000	17113	28.7	834	11.1	3247	43.3	4423	59.0
	10,000	10170	17.1	432	5.8	783	10.4	1002	13.4
#2	1,000	40289	67.7	1548	20.6	3017	40.2	4729	63.1
	3,000	17113	28.7	968	12.9	3361	44.8	4271	56.9
	10,000	10170	17.1	468	6.2	778	10.4	948	12.6
#3	300	31438	67.7	1371	18.3	1994	26.6	3531	47.1
	1,000	31438	67.7	1371	18.3	1994	26.6	3531	47.1
	3,000	13354	28.7	918	12.2	2218	29.6	3008	40.1
	10,000	7935	17.1	413	5.5	637	8.5	799	10.7
#4	1,000	40289	67.7	1290	17.2	4067	54.2	6672	89.0
	3,000	17113	28.7	674	9.0	4642	61.9	5823	77.6
	10,000	10170	17.1	453	6.0	1001	13.4	1168	15.6
#5	1,000	41002	67.7	1186	15.8	2588	34.5	4170	55.6
	3,000	17416	28.7	713	9.5	3242	43.2	4878	65.0
	10,000	10349	17.1	467	6.2	847	11.3	1054	14.1
#6	1,000	30726	67.7	1114	14.9	2411	32.1	2907	38.8
	3,000	13051	28.7	735	9.8	2775	37.0	3755	50.1
	10,000	7756	17.1	490	6.5	804	10.7	897	12.0
#7	1,000	50209	67.7	2337	31.2	3254	43.4	5013	66.8
	3,000	21327	28.7	1675	22.3	4109	54.8	5163	68.8
	10,000	12673	17.1	616	8.2	807	10.8	949	12.7

DTN: SN0408T0509903.007; file Unmixed_HighInvertTransport\Summary Tables.mcd.

6.3.7.3 Uncertainty Associated with the Condensation Model Analysis

Uncertainty Due to the Axial Dispersion Coefficient Calculation

The axial migration of water vapor through the drift is governed by the gas flow field within that drift. There are four contributors to that flow field:

1. Hot/cold package arrangement in the drift that creates package-scale axial flow patterns

2. Axial temperature profile that creates drift-scale flow patterns

3. Barometric pumping that creates drift-scale flow patterns

4. Natural circulation that creates drift-scale and repository-scale flow patterns.

As discussed below, the progressive inclusion of these flow field contributors results in progressively larger calculated values of the axial dispersion coefficient.

The hot/cold package arrangement creates a natural convection flow field that connects adjacent hot and cold waste packages. Air near a hot structure (waste package or drip shield) rises upward until it reaches a solid surface (drip shield or drift wall). It then travels axially until it reaches the vicinity of a cold surface. At this point, the air moves downward as it cools. It then returns axially to its original location by a counter flow path along the bottom of the volume. The unit cell actually contains packages at three different heat levels. This causes multiple coupled convection cells to form rather than simple pairings. This convection pattern is captured by the basic CFD calculation. The axial dispersion coefficient based on the simple flow description is used as the "lower bound" for this parameter in this analysis.

Drift-scale in-drift temperature differences elongate the natural circulation cells established by the hot/cold package arrangement, and in so doing, increase the axial dispersion coefficient. If the axial temperature difference were large enough, it might dominate the axial flow pattern; the convection cells could be as long as the drift itself.

The contribution of the axial temperature difference to the dispersion coefficient cannot be properly formulated in terms of the instantaneous slope of the temperature profile. The prototypic temperature gradient will vary from zero at the point of maximum drift temperature to its maximum value at the end of the emplacement drift. However, the convection cells that contribute to the axial dispersion span a range of local temperature gradients. Hence, it is the integral structure of the flow, and not the local temperature gradient, that controls the impact of the axial temperature gradient.

Calculations for this analysis use a unit-cell of 14 waste packages (13 full- and 2 half-packages), rather than an explicit representation of an entire drift, for computational efficiency. A linear temperature profile is applied to the unit-cell that reflects a representative average gradient across the entire drift. The dispersion coefficient based on this configuration is used as the upper bound for this parameter in the model.

Barometric pumping and repository-scale natural ventilation will couple with the natural circulation flow fields generated by in-drift temperature differences. These additional sources of gas momentum will cause gas speeds to increase and convection loops to elongate. The net effect will be to increase the axial dispersion of water vapor from the hotter regions of the repository to the cooler regions.

The lower bound value on the dispersion coefficient approximates a physical lower bound. However, the upper value for the dispersion coefficient is a bound only for the range of calculations performed for this report. The phenomena listed above are not included in the calculation of the upper dispersion bound, and should increase the axial dispersion. Additionally, transient flow oscillations not captured in the steady-state CFD calculation may serve to break down stable flow structures that, at specific points, retard the advection of water vapor. This also provides the potential for augmenting the dispersion coefficient.

The likelihood of condensation within the emplacement region decreases with increasing dispersion coefficient. The "lower bound" maximizes the formation of condensate. The "upper bound" is an estimate based on one of several factors that could contribute to axial transport.

Use of these values provides a conservative bound on condensation rates but should not be construed as providing an upper bound on the drying effect of axial transport in the drift.

Uncertainty Due to the Computed Temperature Profiles

Repository temperature profiles are computed using line source conduction solutions for a homogeneous domain. In reality, the rock is composed of strata with a range of thermal properties. Hence, one can expect some difference between the approximation used in this calculation and the prototypic situation.

The temperature calculation is used in the condensation model in two ways. First, it predicts the axial temperature profile and the associated peak/end temperature differences that drive the axial vapor transport. The line source solution used in this calculation does not capture temperature variations due to small scale inhomogenities in the rock thermal properties, nor does it capture the large-scale perturbation in the temperature profile due to the tilt in the strata. It is expected that these effects will result in local perturbations of the predicted values without significantly impacting the global averages of condensation and evaporation.

The time at which a specific peak drift temperature is realized is also predicted by the temperature calculation. This is of secondary importance. If one misses the timing of the peak temperature, it merely results in a corresponding raising or lowering of the decay heat. Given the long half-lives of the decay processes, this is not an important uncertainty.

Uncertainty Due to Invert Vapor Pressure and Water Partitioning

The uncertainty due to the vapor pressure at the invert surface (Assumption 6.3.3.2.1) and the partitioning of the available water in the rock (Assumption 6.3.3.2.3) both result from the fact that the details of water flow in the rock and in the invert are not coupled to the vapor dispersion calculation. Only a portion of this uncertainty might be reduced by coupling the two calculations. Uncertainties in certain underlying phenomenological processes (Section 6.3.3) are not addressed in the current vapor dispersion and rock flow calculations.

Setting the vapor pressure at the invert surface to correspond to the invert surface temperature (high-invert transport) produces the true theoretical upper bound on the invert evaporation rate. Setting the vapor pressure at the invert surface to correspond to the exposed wall temperature (low-invert transport) is not a true lower bound; the drift wall beneath the invert will be cooler than the exposed drift wall. However, the invert evaporation rate is sufficiently low at this point, that it provides a reasonable estimate. Neither vapor pressure bound accounts for vapor pressure lowering due to capillarity (Section 6.3.3.2.1).

The partitioning of the available water based upon the perimeter (Section 6.3.3.2.3) does not differentiate between the invert surface and the drift wall. The attempt here is to set forth the simplest and most transparent partitioning rule that does not imply a bias about the water flow. The effect of the water partitioning rule is dependent upon the invert vapor pressure. It will have little effect on condensation for the low-invert transport case because the invert vapor pressure will be the limiting factor. In the high-invert transport case, the partitioning argument affects the rate of evaporation from the invert and the subsequent condensation rate.

Uncertainty in the Equation of State for Water

The equation of state for pure water is used to calculate the water vapor pressure at rock surfaces. Actual water vapor pressures at these surfaces will be dependent upon the chemical state of the water. If the solutions are sufficiently dilute, they will have negligible effect on the vapor pressure. Stronger solutions, which might form from the cumulative effect of evaporation, would lower the evaporation rate at the rock surface by lowering the vapor pressure.

Uncertainty in the Dispersion Equation Formulation

The axial transport equations for vapor are obtained by substituting a dispersion coefficient in place of the molecular diffusion coefficient in Ficks's first law for binary mixtures (Eq. 6.3-17). This results in a factor of $(1-X_{st})$ in the denominator of the equation for the axial mass flux in Eq. 6.3-18. There is, in fact, some ambiguity in this formulation.

The $(1-X_{st})$ term that comes out of Fick's first law accounts for the molecular flux of the diffusing species in the stationary coordinate frame when the second species is stagnant. It serves to augment the transport when the fraction of the diffusing species is high. The dispersion coefficient, which captures the advective component the natural convection, was calculated from the three-dimensional CFD calculations with a low component fraction (Section 6.2.7). It has not yet been proven that the axial vapor transport will increase with increasing vapor fraction. The FLUENT calculations from which the axial dispersion coefficients are derived do not address this source of uncertainty.

Model Implementation of Uncertainty

The uncertainty of the two major contributors is incorporated into the model results. Correlated results are given for the two major contributors to uncertainty: the axial dispersion coefficient and the vapor pressure at the invert surface. Each is modeled using a low and high "bound," which are to be given equal weight in the performance assessment analysis. Use of these bounds will provide clear insight into the relative importance of the underlying phenomena to the safety case.

6.4 EQUIVALENT THERMAL CONDUCTIVITY ANALYSIS

6.4.1 Analysis Objectives

The objective of the equivalent thermal conductivity (k_{eq}) analysis is the development of correlations to support *Multiscale Thermohydrologic Model* (BSC 2004 [DIRS 169565]).

6.4.1.1 Problem Statement

The problem being analyzed is a two-dimensional representation of a repository emplacement drift based on the two-dimensional convection simulations developed in Section 6.1. In the present analysis, isothermal surfaces are employed in order to develop heat transfer correlation equations that supply effective thermal conductivities for in-drift geometries required by the porous media flow models. Unlike the convection model described in Sections 6.1 and 6.2, the k_{eq} analysis and correlations only include heat transfer by conduction and turbulent natural

convection. Thermal radiation is not included because the intent of this heat transfer analysis is to compute an effective thermal conductivity that approximates heat transfer by natural convection only. The CFD simulations used to create repository-specific heat transfer correlation equations include different waste package diameters and the in-drift components (e.g., drip shield) previously discussed. These k_{eq} correlation equations for natural convection heat transfer are a function of Rayleigh number (Equation 6.1-8), which is standard scientific practice for natural convection heat transfer as evident in numerous references (Incropera and DeWitt, 2002 [DIRS 163337], pg. 545 and 562; Bejan 1995 [DIRS 152307] pg. 232; Kuehn and Goldstein 1976 [DIRS 100675]).

6.4.1.2 Performance Measures Used in Downstream Models or Analyses

The output from this analysis is correlations of k_{eq} as a function of Rayleigh number that can be used in porous media codes such as the MSTHM.

6.4.1.3 Inputs

Refer to Section 4.1.4 for inputs required by the two-dimensional k_{eq} CFD simulations.

6.4.1.4 Description of How Output Quantities are Used

The effective thermal conductivities are developed in this section using FLUENT. The analysis results are used to develop correlations that can be used to approximate turbulent natural convection heat transfer in repository drifts in porous media codes.

6.4.1.5 Direct Use in TSPA System Model

The k_{eq} analysis and correlations support the MSTHM (BSC 2004 [DIRS 169565]), which uses these parameters within its submodel formulation.

6.4.2 Features, Events, and Processes Included in the k_{eq} Analysis

See Section 6.1.2 for a general discussion of the features, events, and processes for the convection model and the k_{eq} analysis. The specifics as applied to the k_{eq} analysis are summarized in Table 6.1.2-1.

The treatment of FEP 2.1.06.06.0A (Effects of drip shield on flow) is explicitly included in the k_{eq} analysis. The drip shield serves as a flow barrier and k_{eq} is correlated for the regions inside and outside of the drip shield. The k_{eq} correlations feed TSPA by providing an input for the drift thermal conductivity into the thermal-hydrologic models.

The treatment of FEP 2.1.11.01.0A (Heat generation in EBS) is implemented in the k_{eq} analysis. The range in Rayleigh number in the analysis serves as a proxy for the variable heat flux through the temperature difference between various surfaces. The k_{eq} correlations feed TSPA by providing an input for the drift thermal conductivity into the thermal-hydrologic models.

The treatment of FEP 2.1.11.09.0A (Thermal effects on flow in EBS) is implemented in the k_{eq} analysis. The premise behind using an effective thermal conductivity is to represent the effects

of natural convection in a thermal-hydrologic porous medium model. Natural convection is included in the CFD simulations. Heat transfer rates are calculated and correlated as a function of Rayleigh number, the appropriate dimensionless number for natural convection heat transfer.

6.4.3 Base-Case Conceptual k_{eq} Analysis

6.4.3.1 Conceptual Basis

The k_{eq} analysis uses the two-dimensional convection conceptual model described in Section 6.1.3. The differences are that the waste package, drip shield, and drift wall temperatures are each isothermal so dimensionless correlations can be easily developed. In addition, thermal radiation is not considered because the value of k_{eq} from natural convection is desired.

There are no elements of the subsystem or environment that are treated as uncertain. The base case uses average properties.

6.4.3.2 Analysis Assumptions

6.4.3.2.1 Natural Convection In The Drifts Assumes Pure Air Conditions

See Section 6.1.3.2.1 - Natural Convection In The Drifts Assumes Pure Air Conditions.

6.4.3.2.2 Steady-State Conditions

See Section 6.1.3.2.2 - Steady-State Conditions

6.4.3.2.3 Use of Renormalized Group (RNG) k-ε Turbulence Flow Model

See Section 6.1.3.2.3 - Use of Renormalized Group (RNG) k-ε turbulence flow model

6.4.3.2.4 Neglect of Barometric Pumping

See Section 6.3.3.2.4 – Neglect of Barometric Pumping - for a discussion of this assumption.

6.4.4 Consideration of Alternative Conceptual Models for the k_{eq} Analysis

Not Applicable. The two-dimensional convection conceptual model developed in Section 6.1 is used to develop the k_{eq} correlations. Alternate conceptual models for the two-dimensional convection conceptual model are discussed in Section 6.1.4.

6.4.5.1 Mathematical Description of the Base-Case k_{eq} Analysis

6.4.5.1.1 Turbulence Modeling

Based on the results of the two-dimensional convection model as presented in Section 6.1, the RNG k-ε turbulence model has been used.

6.4.5.1.2 Thermal Radiation Modeling

Thermal radiation is not included in the k_{eq} analysis as discussed above.

6.4.5.1.3 Boundary Conditions

The domain for the k_{eq} analysis contains the two air volumes that exist on both sides of the drip shield; the host rock is not in the analysis domain. The domain is depicted schematically in Figure 6.4.5-1. Because the correlations are intended only to account for convective heat transfer and not thermal radiation, boundary conditions such as surface emissivities are not needed. No-flow and no-slip boundary conditions are imposed on all walls (T_h, T_m and T_c walls). A symmetry boundary (no heat flux, no flow, slip) is imposed on the fluid symmetry planes. The only thermal boundary conditions imposed on the domain are temperature boundary conditions on all walls.

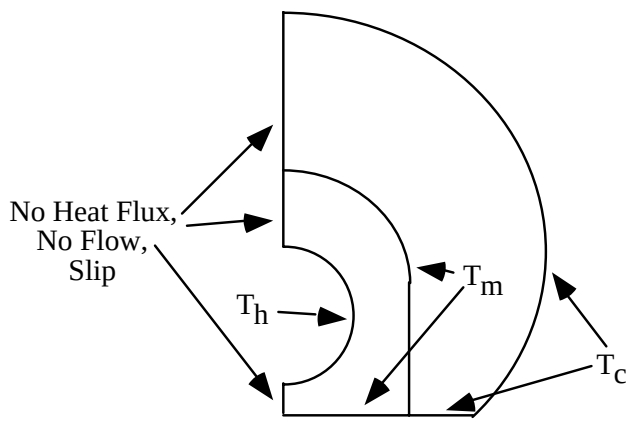

Figure 6.4.5-1. Diagram of Two-Dimensional k_{eq} CFD Domain with Boundary Conditions

Constant temperature boundary conditions are applied to the geometries. The inner cylinder is maintained at a constant temperature, T_h. The drip shield and inner invert surfaces under the drip shield are specified at a constant temperature, T_m. The outer cylinder surface and outer invert surface are maintained at a constant temperature, T_c. The numerical simulations for all three different waste package radii (Table 6.4.5-2) apply the same 20 K overall temperature difference. Additionally, the in-drift geometry is also evaluated at smaller and larger overall temperature differences of 5 and 50 K. The overall temperature difference is defined between T_h and T_c. The split in the total temperature drop between the inner cylinder surface to the drip shield and the temperature drop from the drip shield to the outer cylinder surface is arbitrarily specified (e.g., for an overall temperature change, ΔT = 20 K, a 10.8 K change is between the inner cylinder and drip shield and a 9.2 K change is between the drip shield and the outer cylinder). Separate correlation equations are created for the inner and outer air regions. Consequently, the individual temperature ranges ultimately define the range of applicability of the correlation equations. The primary goal of this section of the report is to establish a reasonable range of potential temperature differences so that the ensuing heat transfer correlation equations developed for specific in-drift geometries can be applied over a broad range of temperature conditions.

Constant temperature boundaries are specified such that the fluid space inside the drip shield is always maintained at the same average temperature (367.6 K) for any ΔT. The average fluid temperature outside the drip shield is not a constant for different ΔT values. For a 20 K overall temperature difference, the temperature drop inside the drip shield (from the inner cylinder to the drip shield and inner invert) is 10.8 K; the temperature drop between the drip shield and the outer cylinder and outer invert is 9.2 K. The inner and outer boundary temperatures are (T_h=) 373 K (100°C) and (T_c=) 353 K (80°C), respectively. Therefore, the temperature denoted as T_m in Figure 6.2.5-2 is equal to 373 K – 10.8 K = 362.2 K. For this specified temperature drop, the average fluid temperature inside the drip shield is indeed 367.6 K. Likewise, for an overall temperature difference of 5 K, the same percentage temperature drop inside the drip shield (from the inner cylinder to the drip shield and inner invert) results in a 2.7 K drop; the temperature drop outside the drip shield (from the drip shield to the outer cylinder and outer invert) is 2.3 K. In order to maintain an average fluid temperature of 367.6 K inside the drip shield, the temperature denoted as T_m in Figure 6.2.5-2 is specified to be 366.25 K. Finally, for an overall temperature difference of 50 K, the same fractional temperature drop inside the drip shield (from the inner cylinder to the drip shield and inner invert) is 27 K; the temperature drop outside the drip shield (from the drip shield to the outer cylinder and outer invert) is 23 K. In order to maintain an average fluid temperature of 367.6 K inside the drip shield, the temperature denoted as T_m in Figure 6.2.5-2 is set equal to 354.1 K. The constant temperature boundary conditions applied in the CFD simulations are listed in Table 6.4.5-1.

Table 6.4.5-1. Summary of Temperature Boundary Conditions for Two-Dimensional k_{eq} YMP Simulations

Overall ΔT (K)	ΔT_{inside} (K)	$\Delta T_{outside}$ (K)	T_h (K)	T_m (K)	T_c (K)
5	2.7	2.3	368.95	366.25	363.95
20	10.8	9.2	373	362.2	353
50	27	23	381.1	354.1	331.1

DTN: SN0407T0507803.026.

6.4.5.1.4 Initial Conditions

The CFD simulations are all run in steady state mode. Consequently, no initial conditions are required for the analyses.

6.4.5.2 Base-Case Inputs

Geometry

The analysis uses the two-dimensional natural convection simulation approach presented in Section 6.1 with the geometries listed in Table 6.4.5-2 below. Note that the waste package diameters used in these simulations represent average, small and large waste packages but do not correspond exactly to any particular waste package size. For example, the smallest waste package (24-BWR) has a diameter of 1.318 m while the smallest waste package considered is 1.24 m. The largest waste package is the DHLW with a diameter of 2.11 m, which is slightly larger than the diameter of the largest package used in these simulations (2 m).

Table 6.4.5-2. Approximate In-Drift Geometries with Drip Shield

Case	Inner Cylinder Diameter D_i (m)	Outer Cylinder Diameter[a] D_o (m)	Diameter Ratio D_o/D_i	Flow Blockage (Invert) Height[b] (m)	L_c (m) (inside drip shield)	L_c (m) (outside drip shield)
Average Radius	1.71[c]	5.5	3.2	0.8	0.485	1.5
Small Radius	1.24	5.5	4.4	0.8	0.708	1.5
Large Radius	2	5.5	2.7	0.8	0.334	1.5

[a] Table 4.1.1-3.
[b] Table 4.1.2-5.
[c] Table 4.1.1-3 (Average of DHLW and 24-BWR waste package diameters).

The characteristic gap width parameters, L_c (Equation 6.1-3), given in Table 6.4.5-2 were evaluated using postprocessing capabilities of FLUENT to evaluate the computational grid flow areas and wetted perimeters for the regions inside and outside the drip shield. The area used in the inside gap width formula is the area bounded by the inner drip shield surface and the inner invert surface minus the waste package area. The wetted perimeter is the sum of the inner drip shield surface length, waste package surface length, and the length of invert surface inside the drip shield. The area used in the outside gap width formula is the area bounded by the drift wall, the outer surface of the drip shield and the invert surface outside the drip shield. The wetted perimeter is the sum of the drip shield outer surface length, the drift wall surface length and the length of the invert surface outside the drip shield. The computational grid for the average radius case is shown in Figure 6.4.5-2 and consists of about 12,000 cells. Boundary conditions applied to this analysis are shown in Figure 6.4.5-1.

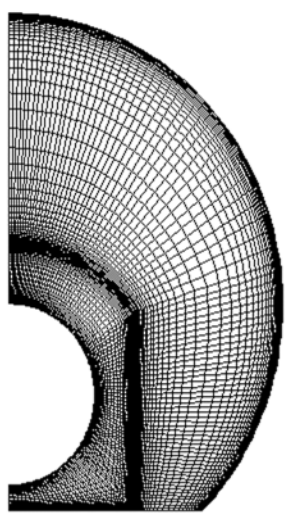

DTN: SN0407T0507803.026.

Figure 6.4.5-2. Computational Grid for the Average Radius Two-Dimensional YMP Geometry k_{eq} Analysis

Properties

Constant thermal properties for dry air are applied in the numerical simulations. Air properties inside the drip shield are calculated at a temperature corresponding to the average of the waste package surface and drip shield temperatures. The air properties outside the drip shield are calculated at the temperature corresponding to the average of the drip shield and drift wall temperatures.

The average fluid temperatures of 367.6 K inside the drip shield and 357.6 K outside the drip shield are used to determine the fluid properties subject to an overall temperature difference of 20 K. For the analyses that also included 5 and 50 K temperature differences, the average fluid temperature inside the drip shield remains 367.6 K. The average fluid temperatures outside the drip shield are 365.1 K and 342.6 K for the 5 and 50 K temperature difference cases, respectively.

Table 6.4.5-3 provides air thermal properties evaluated at the average (constant) fluid temperature. These properties are based on those listed in Table 4.1.4-4 at 60ºC and 100ºC using linear interpolation. The volumetric thermal expansion coefficient, β, is defined by Equation 6.4-1 (Bejan 1995 [DIRS 152307], Equation. 1.35).

$$\beta = -\frac{1}{\rho}\frac{\partial \rho}{\partial T}\bigg|_p \qquad \text{(Eq. 6.4-1)}$$

For an ideal gas, Equation 6.4-1 becomes

$$\beta = \frac{1}{T} \qquad \text{(Eq. 6.4-2)}$$

The fluid Prandtl number, Pr, is defined by Equation 6.4-3 (Bejan 1995 [DIRS 152307], p. xxiii).

$$\mathrm{Pr} = \frac{\nu}{\alpha} \qquad \text{(Eq. 6.4-3)}$$

The Prandtl number for air at the different average temperatures, calculated from the information in Table 6.4.5-3, is approximately 0.7.

Table 6.4.5-3. Thermophysical Properties of Air Used in the Two-Dimensional k_{eq} In-Drift Geometry Simulations

Property	367.6 K (Inside Drip Shield), All ΔT	365.1 K (Outside Drip Shield), ΔT = 5 K	357.6 K (Outside Drip Shield), ΔT = 20 K	342.6 K (Outside Drip Shield), ΔT = 50 K
Density, ρ (kg/m^3)	0.96	0.97	0.99	1.03
Specific heat, c_p (J/kg-K)	1010.58	1010.40	1009.83	1008.71
Thermal conductivity, k_a (W/m-K)	0.0314	0.0312	0.0304	0.0289
Dynamic viscosity, μ (kg/m-s)	$2.155x10^{-5}$	$2.144x10^{-5}$	$2.11x10^{-5}$	$2.043x10^{-5}$
Volumetric thermal expansion coefficient, β (K^{-1})	$2.72x10^{-3}$	$2.74\ x10^{-3}$	$2.8x10^{-3}$	$2.92x10^{-3}$

NOTES: Interpolated from Bejan 1995 [DIRS 152307], Appendix D. Values listed in Table 4.1.4-1.
Density used to compute Rayleigh numbers given in Table 6.4.5-4.
Volumetric thermal expansion coefficient calculated using Equation 6.4-2.

The dynamic viscosity, molecular thermal conductivity, and specific heat are inputs in the numerical simulations as specified in Table 6.4.5-3. Each thermal quantity except the fluid density is treated as a constant. The fluid density is computed using the incompressible-ideal-gas law (Fluent 2001 [DIRS 164453], Equation 7.2-5). The incompressible-ideal-gas law is identified in Section 6.1.5.2 (Equation 6.1-30).

The incompressible-ideal-gas law is used when pressure variations are small enough such that the overall internal flow conditions are essentially incompressible, but a relationship between density and temperature is required because this is the driving force for flow (buoyancy), as in the case of natural convection.

Operating Conditions

The operating pressure selected for the numerical simulations is 101.3 kPa. The pressure used in these simulations is discussed further in Section 6.4.7. The gravitational constant is specified in each of the simulations as 9.81 m/s^2 (Table 4.1.1-2). It is noted that a wide range of Rayleigh numbers result from the temperature difference (ΔT = 5, 20, 50 K) and characteristic gap-widths used in this analysis. Additionally, the range of Rayleigh number applicability is further increased by scaling gravity as indicated in Table 6.4.5-4. To achieve lower Rayleigh numbers for a given geometry and temperature difference, the gravity vector is simply scaled below its nominal value through the Rayleigh number. For instance, if for a given geometry and temperature difference a gravity vector (-g) of 9.81 m/s^2 results in a Rayleigh number of $1x10^8$, a gravity vector of 0.981 m/s^2 results in a Rayleigh number of $1x10^7$ for the same temperature difference and length scale. Using characteristic gap-widths, $L_{c,in}$ *and* $L_{c,out}$ (Equation 6.1-3), as the length scale, with the thermophysical properties of air given in Table 6.4.5-3, the Rayleigh numbers, $Ra_{L_{c,in}}$ and $Ra_{L_{c,out}}$ are computed using Equation 6.1-9. The three values of $L_{c,in}$, 0.485, 0.334, and 0.708, correspond to the average, largest and smallest simulated waste packages, respectively (Table 6.4.5-2). The operating conditions for each of the in-drift geometry cases are given in Table 6.4.5-4.

Table 6.4.5-4. Operating Conditions for the Two-Dimensional k_{eq} In-Drift Geometry Simulations

Case	Gravity, -g (m/s^2)	ΔT (K)	ΔT_{in} (K)	ΔT_{out} (K)	$L_{c,\,in}$ (m)	$L_{c,out}$ (m)	$Ra_{L_{c,\,in}}$	$Ra_{L_{c,out}}$
1	0.00981	20	10.8	9.2	0.485	1.5	$4.55x10^4$	$1.32x10^6$
2	0.0981	20	10.8	9.2	0.485	1.5	$4.55x10^5$	$1.32x10^7$
3	0.981	20	10.8	9.2	0.485	1.5	$4.55x10^6$	$1.32x10^8$
4	9.81	20	10.8	9.2	0.485	1.5	$4.55x10^7$	$1.32x10^9$
5	9.81	5	2.7	2.3	0.334	1.5	$3.69x10^6$	$2.96x10^8$
6	9.81	5	2.7	2.3	0.485	1.5	$1.14x10^7$	$2.96x10^8$
7	9.81	5	2.7	2.3	0.708	1.5	$3.53x10^7$	$2.96x10^8$
8	9.81	20	10.8	9.2	0.334	1.5	$1.48x10^7$	$1.32x10^9$
9	9.81	20	10.8	9.2	0.708	1.5	$1.41x10^8$	$1.32x10^9$
10	9.81	50	27	23	0.334	1.5	$3.69x10^7$	$4.05x10^9$
11	9.81	50	27	23	0.485	1.5	$1.14x10^8$	$4.05x10^9$
12	9.81	50	27	23	0.708	1.5	$3.53x10^8$	$4.05x10^9$

DTN: SN0407T0507803.026.

Based on Table 6.4.5-4 and the laminar-to-turbulent transition Rayleigh number of 10^6, most of the flow conditions are turbulent for the gap-widths and temperature differences considered in this report. Therefore, a turbulence flow model is required when solving the governing conservation equations as described in Section 6.4.5.1. For the lower Rayleigh number flows, laminar flow equations are solved.

6.4.5.3 Summary of the Computational Approach

The computational information used in the present analysis is the same as for the two-dimensional convection simulations given in Section 6.1.5.3.

6.4.6 Formulation for Alternative Conceptual Models for the k_{eq} Analysis

Not Applicable. Any alternate conceptual approaches are addressed in the two-dimensional convection simulations discussed in Section 6.1.6.

6.4.7 Results for the Two-Dimensional Equivalent Thermal Conductivity (k_{eq}) Analysis

6.4.7.1 Average Equivalent Thermal Conductivity Inside the Drip Shield

This section details the development of the k_{eq} analysis and correlation for natural convection heat transfer inside the drip shield. Section 6.4.7.2 discusses the results for natural convection heat transfer outside the drip shield. An equivalent thermal conductivity simulates natural convection heat transfer by specifying an enhanced fluid thermal conductivity for use in a model that simulates conduction but not free-space convection. For each geometry and ΔT, CFD simulations are run in conduction-only mode to get the baseline conduction heat transfer. The total heat flux for natural convection is then determined in a CFD simulation. The equivalent thermal conductivity is then be found using the following equation.

$$k_{eq} = \frac{Q}{Q_{cond}} \qquad \text{(Eq. 6.4-4)}$$

where Q is the total heat transfer rate for natural convection, and Q_{cond} is the total heat transfer for conduction only using air properties. Heat transfer correlation equations for k_{eq} are derived for flow conditions inside the drip shield.

Twelve cases are simulated as listed previously in Table 6.4.5-4 including the appropriate Rayleigh number, Ra_{Lc}. The results from these simulations for inside the drip shield are shown in Table 6.4.7-1. Figure 6.4.7-1 presents the correlation of the results from these twelve cases as a function of the Rayleigh number, Ra_{L_c}. A simple linear fit on a log-log plot is used to generate a repository-specific correlation equation for natural convection heat transfer inside the drip shield. This equation is a function of the Rayleigh number, which is a function of the temperature, temperature difference, and characteristic gap width.

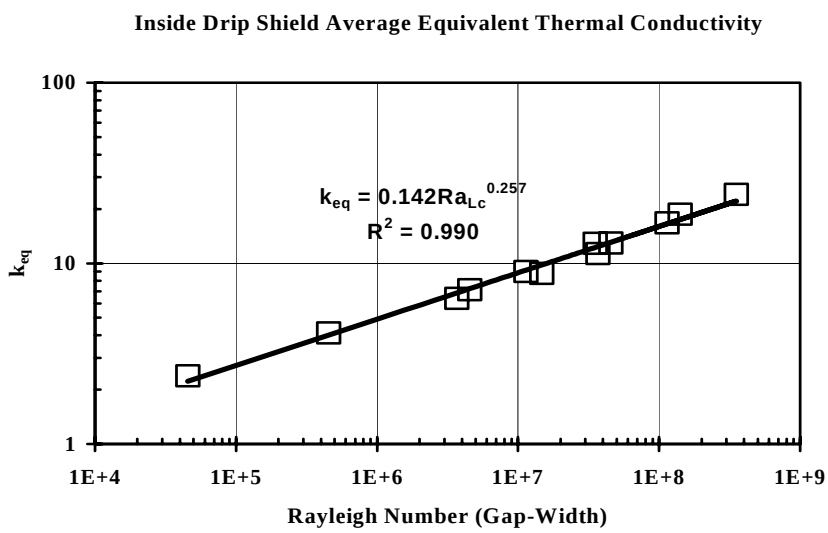

DTN: SN0407T0507803.026.

Figure 6.4.7-1. Correlation of the Equivalent Thermal Conductivity (k_{eq}) Inside the Drip Shield

Table 6.4.7-1. CFD Equivalent Thermal Conductivity Simulations – Inside the Drip Shield Results

CFD Run	Conduction Run	Gravity [m/s^2]	Overall ΔT [K]	Ra_{L_c}	Qtot [W]	Qcond [W]	Keq
flscl_a_bcpp	flscl_d_bcpp-cond	0.00981	20	4.55E+4	6.04	2.53	2.39
flscl_b_bcpp	flscl_d_bcpp-cond	0.0981	20	4.55E+5	10.40	2.53	4.11
flscl_c_bcpp	flscl_d_bcpp-cond	0.981	20	4.55E+6	18.09	2.53	7.15
flscl_d_bcpp	flscl_d_bcpp-cond	9.81	20	4.55E+7	32.78	2.53	12.96
fullscl_max_d5	fullscl_max_d5-cond	9.81	5	3.69E+6	6.55	1.02	6.40
flscl_v_d5	flscl_v_d5-cond	9.81	5	1.14E+7	5.71	0.63	9.03
fullscl_min_d5	fullscl_min_d5-cond	9.81	5	3.53E+7	4.68	0.36	12.91
fullscl_max_d20	fullscl_max_d20-cond	9.81	20	1.48E+7	35.92	4.09	8.78
fullscl_min_d20	fullscl_min_d20-cond	9.81	20	1.41E+8	27.15	1.45	18.71
fullscl_max_d50	fullscl_max_d50-cond	9.81	50	3.69E+7	115.93	10.23	11.33
flscl_v_d50	flscl_v_d50-cond	9.81	50	1.14E+8	105.83	6.32	16.74
fullscl_min_d50	fullscl_min_d50-cond	9.81	50	3.53E+8	87.21	3.63	24.05

DTN: SN0407T0507803.026.

The k_{eq} correlation equation inside the drip shield is given by Equation 6.4-5 as a function of the Rayleigh number.

$$k_{eq} = 0.142 Ra_{Lc}^{0.257} \qquad \text{(Eq. 6.4-5)}$$

Using equation 6.1-8, the above expression can be written as

$$k_{eq} = 0.142 \left(\frac{g\beta}{\nu\alpha} \right)^{0.257} \left(\Delta T \, L_c^3 \right)^{0.257} \qquad \text{(Eq. 6.4-6)}$$

The first part of this expression, $g\beta / \nu\alpha$, is simply a combination of the gravitational constant and fluid properties. This part of the Rayleigh number has been curve fit as a function of the average fluid temperature for ease of use. Using fluid properties from Bejan (1995 [DIRS 152307], Appendix D) from 20°C to 300°C (see Table 4.1.4-2), the resulting curve fit equation is

$$0.142 \left(\frac{g\beta}{\alpha\nu} \right)^{0.257} = 15567 \overline{T}^{-1.207} \qquad \text{(Eq. 6.4-7)}$$

The properties used for this curve fit are at 1 atmosphere pressure. The effect of pressure can be evaluated by looking at the property group rewritten as (Equations 6.1-1 and 6.1-2)

$$\frac{g\beta}{\alpha\nu} = \frac{g\beta\rho^2 c_p}{\mu k_a} \qquad \text{(Eq. 6.4-8)}$$

The gravitational constant, g, and the volumetric thermal expansion coefficient, β, are not a function of pressure. The density, ρ, is directly proportional to pressure based on the perfect gas law. The specific heat, c_p, is not a function of pressure (Reid et. al. 1977 [DIRS 130310], pg. 223). The viscosity of air is a weak function of pressure (< 1% increase per atmosphere increase) (Reid et. al. 1977 [DIRS 130310], pg. 420, Figure 9-8). Similarly, the variation of thermal conductivity with pressure is small (~1% increase per atmosphere increase between 1 mm Hg and 10 atmospheres) (Reid et. al. 1977 [DIRS 130310], pg. 499-500). Note that 1 atmosphere is equal to 760 mm Hg (Bird et al. 1960 [DIRS 103524], pg. 750), so 1 mm Hg = 0.0013 atmospheres. Therefore, the pressure variation of this property term can be expressed as

$$\frac{g\beta}{\alpha\nu} = \frac{g\beta\rho^2 c_p}{\mu k_a} \sim P^2 \qquad \text{(Eq. 6.4-9)}$$

Substituting Equations 6.4-7 and 6.4-9 into Equation 6.4-6 gives

$$k_{eq} = 1450\,\overline{T}^{-1.207}\left(\Delta T\, L_c^3\, P^2\right)^{0.257} \qquad \text{(Eq. 6.4-10)}$$

where $\overline{T}$ is in K, ΔT is in °C, L_c is in meters, P is in kPa, and 101.3 kPa has been used for atmospheric pressure conditions.

The effective thermal conductivity of the porous media is the equivalent thermal conductivity, which is a ratio, times the molecular thermal conductivity, $k_a(\overline{T})$, or

$$k_{eff,th} = k_{eq} * k_a(\overline{T}) \qquad \text{(Eq. 6.4-11)}$$

Note that the average equivalent thermal conductivity (k_{eq}) is a dimensionless quantity, while the effective thermal conductivity, $k_{eff,th}$, includes the effects of natural convection and has units of thermal conductivity. The two terms should not be confused. The stagnant air thermal conductivity is a function of the average fluid temperature. The coefficient of determination for correlation equation 6.4-5 is r^2 = 0.990. The limitations for the YMP-specific correlation equation for natural convection heat transfer are:

1. The applicable temperature difference range is 0.0108ºC ≤ ΔT ≤ 27°C. The minimum temperature refers to 10.8ºC/1000, where 10.8ºC is ΔT_{in} for the 20ºC overall temperature case (Table 6.4.5-4), and the division by 1,000 refers to the use of gravity/1000. As seen in equation 6.1-8 for the Rayleigh number, the gravity times the temperature difference is important. If the gravity is artificially lowered by a factor of 1,000 to obtain a lower Rayleigh number, this operation is equivalent to dividing the temperature difference by a factor of 1,000 for full gravity conditions. The maximum temperature is the ΔT_{in} for the 50ºC overall temperature case (Table 6.4.5-4).

2. Thermal properties are evaluated at an average fluid temperature (Note: when using equation 6.4-10, $\overline{T}$ is the average fluid temperature in absolute temperature, K.) The applicable range of $\overline{T}$ is from 20ºC to 300ºC.

3. The applicable pressure range is between 0.0013 and 10 atmospheres.

4. The applicable characteristic length range is 0.334 m $\leq L_c \leq$ 0.708m (see Table 6.4.5-4).

5. The correlations are only applicable inside the drip shield.

6. The applicable Rayleigh number range is $4.55 \times 10^4 \leq Ra_{L_c} \leq 3.53 \times 10^8$.

7. Fluid motion is suppressed. If the above correlation is used in a porous media code, the fluid motion must be suppressed by a low or zero value of the permeability. If this constraint is not followed, natural convection may be "double counted" by specification of the equivalent thermal conductivity, which is based on no fluid motion, and any calculated fluid motion.

Equations 6.4-5 and 6.4-10 should be applied within the above constraints when evaluating the equivalent thermal conductivity for full-scale repository geometries inside the drip shield (eccentric placement with invert and drip shield).

Francis et al. (2003 [DIRS 164602], Equation 8) solved the same geometry for the equivalent thermal conductivity. An error in the evaluation of the characteristic gap width led to several data points being plotted incorrectly resulting in a slightly different correlation equation. Their equation is

$$k_{eq} = 0.171 Ra_{Lc}^{0.243} \qquad \text{(Eq. 6.4-12)}$$

A comparison of the two expressions shows that the equivalent thermal conductivity for the new correlation is only about 7.5 percent higher at $Ra=10^8$ and only about 4 percent higher at $Ra=10^7$ than Equation 8 of Francis et al. (2003 [DIRS 164602]).

6.4.7.2 Average Equivalent Thermal Conductivity Outside the Drip Shield

A similar correlation equation is obtained for the equivalent thermal conductivity outside the drip shield. Twelve cases are simulated as listed previously in Table 6.4.5-4 including the appropriate Rayleigh number, Ra_{Lc}. The results from these simulations for outside the drip shield are shown in Table 6.4.7-2. Figure 6.4.7-2 presents the correlation of the results from these twelve cases as a function of the Rayleigh number, Ra_{L_c}. A simple linear fit on a log-log plot is used to generate a YMP-specific correlation equation for natural convection heat transfer outside the drip shield. This equation is a function of the Rayleigh number, which is a function of the temperature, temperature difference, and characteristic gap width.

Table 6.4.7-2. CFD Equivalent Thermal Conductivity Simulations – Outside the Drip Shield Results

CFD Run	Conduction Run	Gravity (m/s^2)	ΔT (K)	Ra_{Lc} (-)	Qtot (W)	Qcond (W)	Keq (-)
Flscl_a_bcpp	flscl_d_bcpp-cond	0.00981	20	1.32E+6	6.80	1.60	4.24
Flscl_b_bcpp	flscl_d_bcpp-cond	0.0981	20	1.32E+7	11.34	1.60	7.07
Flscl_c_bcpp	flscl_d_bcpp-cond	0.981	20	1.32E+8	20.56	1.60	12.82
Flscl_d_bcpp	flscl_d_bcpp-cond	9.81	20	1.32E+9	39.08	1.60	24.36
fullscl_max_d5	fullscl_max_d5-cond	9.81	5	2.96E+8	6.60	0.41	16.03
Flscl_v_d5	flscl_v_d5-cond	9.81	5	2.96E+8	6.60	0.41	16.03
fullscl_min_d5	fullscl_min_d5-cond	9.81	5	2.96E+8	6.60	0.42	15.61
fullscl_max_d20	fullscl_max_d20-cond	9.81	20	1.32E+9	39.08	1.60	24.37
fullscl_min_d20	fullscl_min_d20-cond	9.81	20	1.32E+9	39.27	1.65	23.82
fullscl_max_d50	fullscl_max_d50-cond	9.81	50	4.05E+9	130.77	3.81	34.31
Flscl_v_d50	flscl_v_d50-cond	9.81	50	4.05E+9	130.30	3.81	34.18
fullscl_min_d50	fullscl_min_d50-cond	9.81	50	4.05E+9	130.34	3.92	33.27

DTN: SN0407T0507803.026.

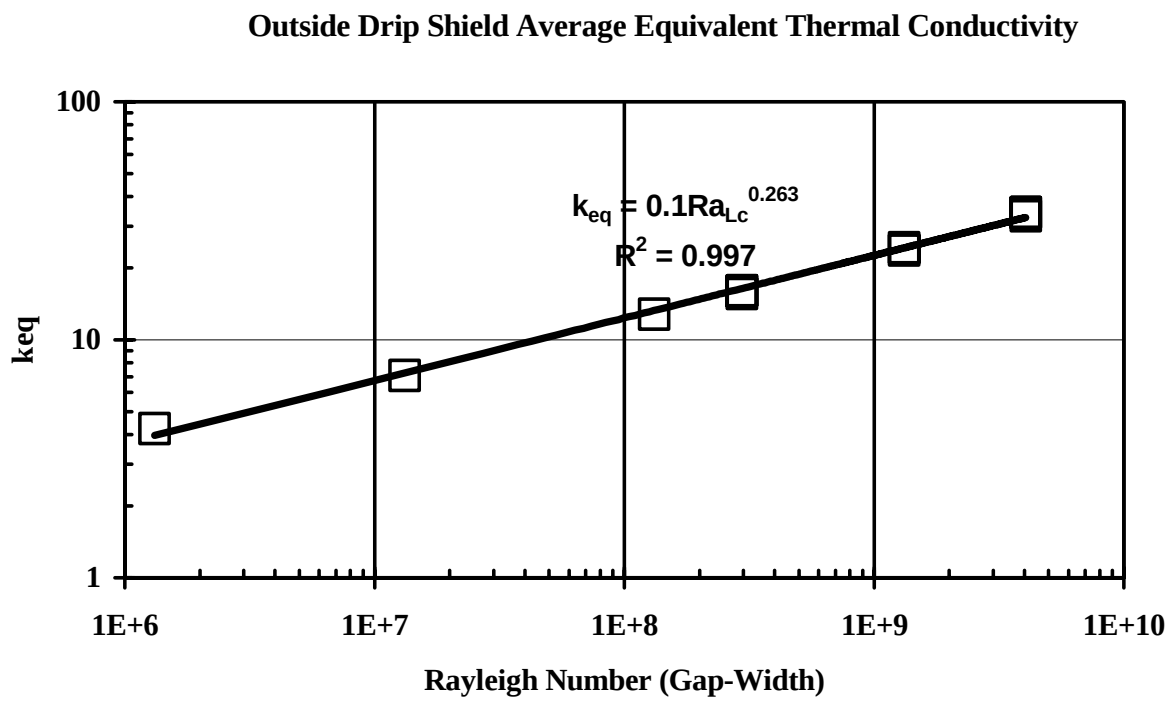

DTN: SN0407T0507803.026.

Figure 6.4.7-2. Correlation of the Equivalent Thermal Conductivity (k_{eq}) Outside the Drip Shield

The k_{eq} correlation equation outside the drip shield is given by Equation 6.4-11 as a function of the Rayleigh number.

$$k_{eq} = 0.100 Ra_{Lc}^{0.263} \qquad \text{(Eq. 6.4-13)}$$

As described earlier, the term $g\beta / \nu\alpha$, which is part of the Rayleigh number, is curve fit as a function of temperature, or

$$0.1\left(\frac{g\beta}{\alpha\nu}\right)^{0.263} = 14374\overline{T}^{-1.236} \qquad \text{(Eq. 6.4-14)}$$

The k_{eq} correlation equation becomes:

$$k_{eq} = 1267\overline{T}^{-1.236}\left(\Delta T\, L_c^3\, P^2\right)^{0.263} \qquad \text{(Eq. 6.4-15)}$$

where $\overline{T}$ is in K, ΔT is in °C, L_c is in meters, and P is in kPa, and 101.3 kPa has been used for atmospheric pressure conditions.

The effective thermal conductivity of the porous media is the equivalent thermal conductivity, which is a ratio, times the molecular thermal conductivity, $k_a(\overline{T})$, or

$$k_{eff,th} = k_{eq} * k_a(\overline{T}) \qquad \text{(Eq. 6.4-16)}$$

Note that the average equivalent thermal conductivity (k_{eq}) is a dimensionless quantity, while the effective thermal conductivity, $k_{eff,th}$, includes the effects of natural convection and has units of thermal conductivity. The two terms should not be confused. The stagnant air thermal conductivity is a function of the average fluid temperature. The coefficient of determination for this correlation equation is $r^2 = 0.997$. The limitations for the YMP-specific correlation equation for natural convection heat transfer are:

1. The applicable temperature difference range is 0.0092ºC ≤ ΔT ≤ 23ºC. The minimum temperature refers to 9.2ºC /1000, where 9.2ºC is ΔT_{in} for the 20ºC overall temperature case (Table 6.4.5-4), and the division by 1,000 refers to the use of gravity/1000. Dividing gravity is here taken to be equivalent to dividing temperature as discussed earlier. The maximum temperature refers to ΔT_{in} for the 50ºC overall temperature case (Table 6.4.5-4).

2. Thermal properties are evaluated at an average fluid temperature (Note: when using equation 6.4-15, $\overline{T}$ is the average fluid temperature in absolute temperature, K.) The applicable range of $\overline{T}$ is from 20ºC to 300ºC.

3. The applicable pressure range is between 0.0013 and 10 atmospheres.

4. The applicable characteristic length, L_c, is 1.5m (the characteristic length is constant because the drip shield geometry was not changed).

5. The correlations are only applicable outside drip shield.

6. The applicable Rayleigh number range is $1.32x10^6 \leq Ra_{L_c} \leq 4.05x10^9$.

7. Fluid motion is suppressed. If the above correlation is used in a porous media code, the fluid motion must be suppressed by a low or zero value of the permeability. If this constraint is not followed, natural convection may be "double counted" by specification of the equivalent thermal conductivity, which is based on no fluid motion, and any calculated fluid motion.

Equations 6.4-13 and 6.4-15 should be applied within the above constraints when evaluating the equivalent thermal conductivity for full-scale repository geometries outside the drip shield (eccentric placement with invert and drip shield).

Francis et al. (2003 [DIRS 164602], Equation 9) solved the same geometry for the equivalent thermal conductivity. His correlation for the equivalent thermal conductivity outside the drip shield is

$$k_{eq} = 0.097\, Ra_{Lc}^{0.263} \qquad \text{(Eq. 6.4-17)}$$

The results presented here are approximately 3 percent higher than the above equation. The difference is that the present simulations have a higher level of precision than those of Francis et al. (2003 [DIRS 164602]) resulting in a slight change in the correlation.

Table 6.4.7-3 summarizes each of the natural convection heat transfer correlation equations developed for full-scale repository geometries. Figure 6.4.7-3 illustrates the Kuehn and Goldstein correlation equations (1976 [DIRS 156722] and 1978 [DIRS 130084]) for natural convection heat transfer together with Equation 6.4-5 and Equation 6.4-13. The evaluation of the Kuehn and Goldstein correlation equations is shown in Appendix I. The curve labeled "Kuehn & Goldstein 1978-YMP" is the Kuehn and Goldstein (1978 [DIRS 130084]) correlation equations applied to the geometry and conditions expected at Yucca Mountain.

Table 6.4.7-3. Summary of Repository Correlation Equations for Natural Convection Heat Transfer in Enclosures

Location	Correlation Equation	Comments	Equation
Inside Drip Shield	$k_{eq} = 1450\,\overline{T}^{-1.207}\left(\Delta T\, L_c^3\, P^2\right)^{0.257}$	0.0108 K ≤ ΔT ≤ 27 K, 0.3m ≤ L_c ≤ 0.7m 0.0013 atm ≤ P ≤ 10 atm $\overline{T}$ is the average fluid temperature in K and is between 20°C and 300°C	6.4-10
	$k_{eq} = 0.142 Ra_{Lc}^{0.257}$	$4.55x10^4 \le Ra_{L_c} \le 3.53x10^8$	6.4-5
Outside Drip Shield	$k_{eq} = 1267\,\overline{T}^{-1.236}\left(\Delta T\, L_c^3\, P^2\right)^{0.263}$	0.0092 K ≤ ΔT ≤ 23 K, L_c =1.5m 0.0013 atm ≤ P ≤ 10 atm $\overline{T}$ is the average fluid temperature in K and is between 20°C and 300°C	6.4-15
	$k_{eq} = 0.100 Ra_{Lc}^{0.263}$	$1.32x10^6 \le Ra_{L_c} \le 4.05x10^9$	6.4-13

NOTE: *keff,th* = *keq* * *ka*($\overline{T}$).

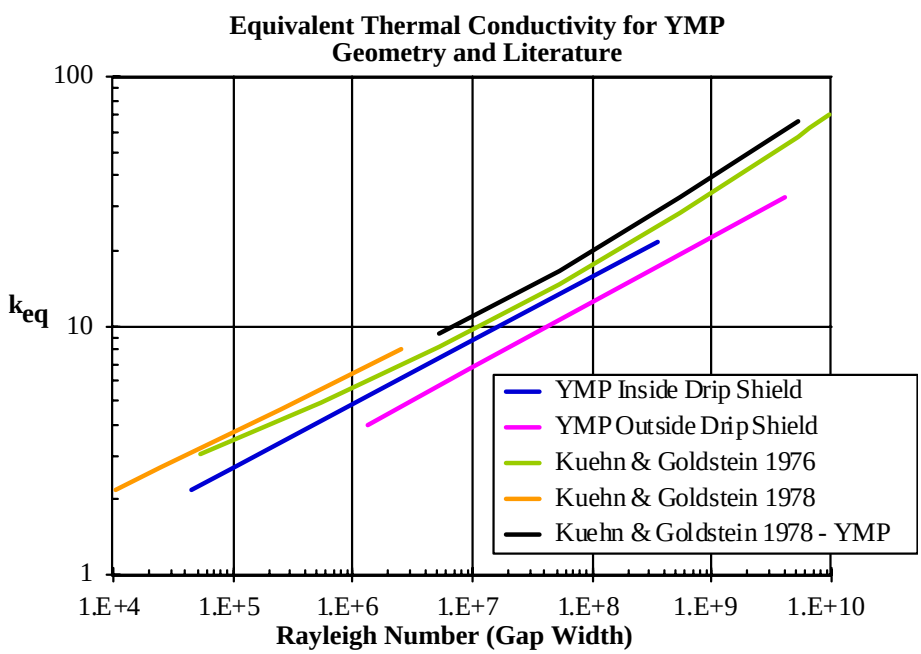

DTN: SN0407T0507803.026.

Figure 6.4.7-3. Comparison of Natural Convection Correlation Equations

It is evident that geometry indeed affects the average equivalent thermal conductivity associated with the YMP annulus. The heat transfer correlation equations developed in the literature are specifically for the annulus formed by horizontal concentric cylinders. In some instances allowances are made for eccentric placement of the inner cylinder in the correlation equations in the literature. However, these expressions do not account for changes in heat transfer due to

flow blockages (e.g., invert, drip shield). It is clear that the repository geometry with invert and drip shield can only be approximated by literature correlation equations developed for an annulus formed by horizontal concentric cylinders. The correlations have been modified to account for repository-specific geometry as shown above.

7. MODEL VALIDATION

AP-SIII.10Q requires that TSPA model components be validated for their intended purpose and stated limitations, and to the level of confidence required by a component's relative importance to the performance of the repository.

The two models discussed in the report are

1. in-drift convection model (two-dimensional and three-dimensional simulations).
2. in-drift condensation model.

Table 7-1 summarizes the intended use, confidence during and after model development, model validation, and sections where detailed discussion is provided for the two models. For purposes of this discussion, the two- and three-dimensional convection simulations are discussed together. The condensation model is discussed separately.

The equivalent thermal conductivity (k_{eq}) correlations developed in Section 6.4 are determined by an analysis involving numerical manipulation of results of the two-dimensional in-drift convection simulation approach, which is validated in Sections 7.3 and 7.4 of this report. These numerical manipulations produce a correlation for natural convection heat transfer as a function of Rayleigh number (Equation 6.1-8) that is standard scientific practice as evident in numerous references (Incropera and DeWitt 2002 [DIRS 163337], pp. 545 and 562; Bejan 1995 [DIRS 152307], p. 232; Kuehn and Goldstein 1976 [DIRS 100675]). The equivalent thermal conductivity correlation work is a scientific analysis that does not need to be validated and is not discussed further in this section.

The governing technical work plan (BSC 2004 [DIRS 170950], Section 2.3.2) identifies Level I as the appropriate level of confidence for the convection and condensation models. The criteria for ensuring that the appropriate level of confidence has been obtained as required by AP-SIII.10Q are based on recognition of the model's contribution to the demonstration of compliance with postclosure performance objectives. Variation in the output of the convection and condensation models is estimated to have only a small effect on the estimated mean annual dose (less than 0.1 mrem/year) because condensation can occur only when the local drift wall temperature is below boiling, and because the effects of condensation are very similar to the effects of seepage for such conditions. Like seepage, for the nominal scenario in-drift condensation will affect only the drift wall, the invert, and the partitioning of flow and transport between the EBS and the unsaturated zone host rock. Condensation under the drip shield may be addressed by the report, but is not included in the model results provided for TSPA, and is excluded as a FEP (BSC 2004 [DIRS 169898]).

Table 7-1. Summary of Intended Uses, Confidence Building, Validation Results and Sections Where Details Are Found

Model or Analysis	Intended Use	Confidence Building during Development	Confidence Building after Development	Validation Criteria and Results
Convection Model	2-D Simulations: The intended use of the two-dimensional in-drift convection simulations is to evaluate the sensitivity of waste package temperatures to the uncertainty in in-drift thermal properties, and to evaluate physics submodels, such as turbulence and thermal radiation, for subsequent use in the three-dimensional in-drift convection simulations. 3-D Simulations: The intended use of the three-dimensional in-drift convection simulations is to generate axial mass dispersion coefficients for water vapor transport down the drift for use in the in-drift condensation model.	(See Section 7.1)	1. Comparison of simulation results to small-scale literature data and 2. Comparison of simulation results to acquired experimental data from 25% and 44 % of full-scale dimension tests (See Section 7.2.1) 3. Technical review (AP-SIII.10Q, Section 5.3.2,c,5) (See Section 7.2.1).	**Small-scale:** Comparison between simulation and literature data for total heat transfer must agree within 25 percent (no parameter specified in the TWP) (BSC 2004 [DIRS 170950], Section 2.3.4). (See Section 7.3 for results.) **Natural Convection Tests**: Comparison between simulation and literature data (temperature) must agree within 35 percent (BSC 2004 [DIRS 170950], Section 2.3.4). (See Section 7.4 for results.) **Fluid Velocities:** Data inadequate for validation. Validation implicit in technical review of dispersion coefficients. **Dispersion Coefficients:** No appropriate experimental data available. Technical review with affirmative answer to all 6 questions in TWP (BSC 2004 [DIRS 170950], Section 2.3.3 and 2.3.4.). (See Section 7.5 and Appendix G for results.)
Condensation Model including dispersion coefficient calculation	The intended use of the in-drift condensation model is to evaluate the location and rate of in-drift condensation on the drift walls, under the drip shield, and on individual waste packages for selected drifts.	(See Section 7.1)	Technical review (AP-SIII.10Q, Section 5.3.2,c,5) (See Section 7.2.2).	No appropriate experimental data available. Technical review with affirmative answer to all 6 questions in TWP (BSC 2004 [DIRS 170950], Section 2.3.3 and 2.3.4). (See Section 7.6 and Appendix G for results).

7.1 CONFIDENCE BUILDING DURING MODEL DEVELOPMENT TO ESTABLISH SCIENTIFIC BASIS AND ACCURACY FOR INTENDED USE

In accordance with AP-2.27Q, *Planning for Science Activities*, Level I validation includes a discussion of model development. In particular, this report documents decisions implemented during model development that build confidence and verify that a reasonable, credible technical approach using scientific and engineering principles was taken. The development of the model should be documented in accordance with the requirements of Section 5.3.2(b) of AP-SIII.10Q and Attachment 3 of AP-2.27Q.

The confidence building during model development discussed in this section applies to the convection model and the in-drift condensation model. The development of the convection and condensation models has been conducted according to these criteria, as follows:

1. *Selection of input parameters and/or input data, and a discussion of how the selection process builds confidence in the model. [AP-SIII.10Q 5.3.2(b) (1) and AP-2.27Q Attachment 3 Level I (a)]*

   The inputs to the convection and condensation models have been obtained from controlled sources. Sections 4.1.1 and 4.1.2 summarize the direct input parameters for the convection model, while Section 4.1.3 presents the direct input parameters for the condensation model. Other direct input for both models, such as data and equations, are listed in Section 4.1.5 and justified in Appendix L. All design information is from IEDs. Appendix K summarizes changes to the in-drift information that occurred during model development including an evaluation of the impact of these changes, which are determined to be insignificant for the present results.

2. *Description of calibration activities, and/or initial boundary condition runs, and/or run convergences, simulation conditions set up to span the range of intended use and avoid inconsistent outputs, and a discussion of how the activity or activities build confidence in the model. Inclusion of a discussion of impacts of any non-convergence runs[(AP-SIII.10Q 5.3.2(b)(2) and AP-2.27Q Attachment 3 Level I (e)].*

   The convection model uses steady-state simulations of in-drift conditions (See Section 6.1.3.2.2), so initial conditions are not necessary. The boundary conditions are the host rock dimensions surrounding the drift and the conditions at that boundary, which are discussed in Section 6.1.3.2.3. There were no calibration activities performed for the convection model.

   The condensation model is a steady-state model, so initial conditions are not necessary. The thermal boundary condition at the drift wall is obtained from analytic line source solutions for conduction (Section 6.3.5.1.1). The mass fraction boundary condition at the wall comes from the temperature boundary condition and the equation of state for pure water (Section 6.3.5.1.3; Mass Transfer Correlations). Limitations on evaporation at the drift wall are provided by estimates of available water in the host rock (Section 6.3.5.1.4). There are no calibration activities associated with the condensation model. All calculations converged in the condensation model.

3. *Discussion of the impacts of uncertainties to the model results including how the model results represent the range of possible outcomes consistent with important uncertainties.[(AP-SIII.10Q 5.3.2(b)(3) and AP-2.27Q Attachment 3 Level 1 (d) and (f)].*

   Sensitivity studies are documented in Section 6.1, which evaluate the impact of various submodels, such as turbulence and thermal radiation, on the convection simulations as well as the sensitivity to various properties. The uncertainty in input parameters did not have a significant effect on the results.

   The mass dispersion coefficient, which is the major link between the convection and condensation models, is a strong function of the variability of the drift wall temperature, or temperature tilt. This temperature tilt was varied over appropriate ranges based on analytical line source solutions discussed in Section 6.3.5.1.1.

   The uncertainty in the condensation model is described in Section 6.3.7.3. The bounds in the invert vapor pressure (invert transport) are designed to capture the full range of physical possibility and associated condensation rates. The uncertainty in the water partitioning is conservative because it presumes that seepage water can readily make its way under the drip shield. The balance of the uncertainties described in Section 6.3.7.3 are conservative in that they tend to maximize the amount of predicted condensate.

4. *Formulation of defensible assumptions and simplifications. [AP-2.27Q Attachment 3 Level I (b)].*

   Assumptions, including their rationale, are discussed in Sections 6.1.3.2 and 6.2.3.2 for the convection simulations, and in Section 6.3.3.2 for the condensation model.

5. *Consistency with physical principles, such as conservation of mass, energy, and momentum. [AP-2.27Q Attachment 3 Level I (c)]*

   The convection model uses the computer code FLUENT [DIRS 164315]. FLUENT is based on the basic conservation equations for mass, momentum (Navier-Stokes), and energy as summarized in Section 6.1.5.1.1. Various submodels such as turbulence and thermal radiation, which are significant factors in the simulations, are discussed in Sections 6.1.5.1.1 and 6.1.5.1.2. The selection of the turbulence and thermal radiation submodels is based on the sensitivity results discussed above and presented in Section 6.1.

   The condensation model is formulated directly upon the physical principles of conservation of mass and conservation of energy (Section 6.3.5.1.2). The momentum equation is not solved in the condensation model.

7.2 CONFIDENCE BUILDING AFTER MODEL DEVELOPMENT TO SUPPORT THE SCIENTIFIC BASIS OF THE MODEL

Level I validation must include at least one post-development method described in Paragraph 5.3.2c of AP-SIII.10Q. The validation activities for the convection and condensation models as

well as the acceptance criteria are from the governing TWP (BSC 2004 [DIRS 170950], Sections 2.3.3 and 2.3.4).

7.2.1 Convection Model

The validation activities for the convection portion of the *Convection and Condensation Model* report are accomplished by model-data comparison with existing experimental data and correlations in the open literature and refereed journals, and model-data comparisons with acquired data.

The convection model is validated in two ways. The model is validated by comparison to small-scale (centimeter dimensions) literature data for natural convection in horizontal concentric cylinders, which is a geometrically similar configuration to that of Yucca Mountain. The convection model is also validated by comparison to acquired experimental data from the three-dimensional Natural Convection Tests (25% and 44% of full-scale dimensions) conducted in Las Vegas.

The development of appropriate validation criteria for the natural convection model is discussed below:

<u>Small-Scale Literature Data Validation</u> - For the comparison to small-scale horizontal concentric cylinder literature data, there are a number of questions. First, the estimated uncertainty of the original experimental data is about 10 to 15 percent based on the various experimental references. For those simulation results that directly replicate an experimental configuration, such as Kuehn and Goldstein (1978 [DIRS 130084]), additional uncertainty exists such as the exact experimental configuration, boundary conditions (i.e., whether the boundary temperatures really isothermal), end losses, corrections for thermal radiation, and other factors that are estimated as 5 to 10 percent. Thus, the overall uncertainty is estimated to be 15 to 25 percent. Additional uncertainty exists where dimensionless number scaling is employed, such as using the repository-scale concentric cylinder geometry, which has a length scale about three orders of magnitude larger than the experimental data. For these data-simulation comparisons, the overall uncertainty is greater than 15 to 25 percent. Based on these arguments, the small-scale literature data-simulation comparison is acceptable if the simulation results are within 25 percent of the experimental data. (BSC 2004 [DIRS 170950], Section 2.3.4). This uncertainty is applied to the overall heat transfer rate of the experiments.

<u>Three-Dimensional Natural Convection Test Validation</u> - For comparison to the Natural Convection Tests, the same 15 to 25 percent uncertainty exists for the original experimental data and the configuration issues. Due to the scale of the tests, which are much larger than small-scale experiments, and the difficulty controlling boundary conditions such as the environmental temperature (diurnal and weather-related variations), the variability in local insulation thickness, and other issues associated with the scale of the test, the uncertainty is 25 to 35 percent. Note that if this uncertainty is applied to temperatures, the appropriate scale is the temperature difference between the structures and the inside of the concrete wall. The difference in the measured and simulated temperature drop across the concrete wall is not important in the validation of the present simulations. Based on these arguments, the Natural Convection Tests

data-simulation comparison is acceptable if the temperature difference simulation results are within 35 percent of the experimental data (BSC 2004 [DIRS 170950], Section 2.3.4).

The same validation criteria are not appropriate for the measurement of fluid velocities. The experimental data have a much higher uncertainty because they were manually collected, the data do not discriminate the flow direction, and the data are often below the calibration range of the detectors. The more important feature to note is that the flow velocities are important in evaluating mixing in the drift, both under the drip shield and outside the drip shield. Because there are no small-scale flow velocity natural convection data in a similar horizontal concentric cylinder configuration, and limitations on the measurements as discussed above, the velocity component data from the Natural Convection Tests are not sufficient to validate the velocity predictions from FLUENT. Instead, validation for this aspect of the FLUENT predictions is accomplished by an affirmative result from evaluation of the criteria given in Section 2.3.3 of the TWP (BSC 2004 [DIRS 170950]) for the independent technical review, including a statement from the reviewer that the model is valid for its intended use (refer to AP-SIII.10Q, Section 5.3.2(c)5) (BSC 2004 [DIRS 170950], Sections 2.3.3 and 2.3.4).

7.2.2 Condensation Model

The validation activities for the condensation model and for the dispersion coefficient developed from the convection model results are accomplished by independent technical review (as allowed by AP-SIII.10Q). Because of the close relationship between the convection and condensation phenomena, the convection model is also reviewed. Professor Ivan Catton of UCLA was selected to perform this review. The reviewer is independent of the development, checking, and internal review of this model. The reviewer is knowledgeable in transport phenomena involving heat, mass, and momentum transfer as related to natural convection.

The criteria for independent technical review of the condensation model and the dispersion calculations of the *Convection and Condensation Model* report are as follows:

1. Is the condensation model based on generally accepted transport phenomena concepts that pertain to heat and mass transfer in the drift? Are the transport equations appropriate for the purpose of the condensation model, which is to provide bounding calculations?

2. Does the model pertain specifically to the length and time scales for heat and mass transfer within the drifts in the repository design concept at Yucca Mountain? This question may be difficult to address in that few experimental data used in formulating the heat and mass transfer correlations are expected to be available. In the absence of such data, the review shall consider if the appropriate scaling parameters have been used (Rayleigh number, etc.) and if the proper flow regime (laminar, turbulent) has been employed.

3. Are the mathematical solution techniques appropriate and adequate to solve the problem of interest?

4. Are the problem formulation and the resulting calculations reasonable?

5. Are the scope and purpose (intended use) for the model defined, and is the model a valid representation of repository performance given this scope and purpose?

6. Are the uncertainties in the model, and their impact on the model output, adequately described?

The results of the technical review are to be considered acceptable for model validation if the reviewer answers the above questions (1 through 6) affirmatively (suggestions for model improvement or specification of model limitations may be consistent with model validation), and provides a statement that the model is valid for its intended use (BSC 2004 [DIRS 170950], Section 2.3.3). The results of the independent technical review by Professor Catton are summarized in the following sections (7.3 and 7.4) and are presented in Appendix G.

In addition to the independent technical review, results from the condensation model have been compared to those of the convection model. Structure temperatures within the drift (drip shield, invert surface, waste package) predicted by the condensation model are compared to those predicted by the two-dimensional FLUENT simulations in Appendix J. The two approaches predict nearly identical drip shield temperatures. The condensation model predicts waste package and invert surface temperatures that lie near the middle of the ranges predicted by FLUENT. The good comparison between the approaches indicates that the drift heat transfer module in the condensation model is adequate for its intended use.

7.3 SMALL-SCALE LITERATURE DATA VALIDATION

This section documents a comparison of computational fluid dynamics (CFD) simulations of natural convection in the annulus formed between horizontal concentric cylinders with experimental data and other numerical simulations available in the heat transfer literature. CFD simulations are used to compute both overall and local heat transfer rates for concentric cylinder arrangements. The CFD calculated heat transfer rates are then used directly in comparisons with data, correlation equations, and other numerical simulations.

These data were selected because they are geometrically similar to the Yucca Mountain configuration, and there are significant data available in the literature including data in the turbulent region expected in Yucca Mountain postclosure operation. These data will be used to validate the general computational fluid dynamics approach for natural convection using FLUENT. This general methodology can then be used with repository-specific geometry to calculate repository-specific conditions.

The effects of an imposed temperature difference and system geometry on CFD calculations of internal natural convection heat transfer in a horizontal annulus are considered in this section. Comparisons to established heat transfer correlation equations and experimental heat transfer measurements described in the literature are performed. An investigation of this type provides an evaluation of the capability of the CFD code to predict heat transfer in a known geometry as a precursor to calculating conditions for geometries specific to Yucca Mountain.

The following is a brief discussion of previous natural convection heat transfer experiments, correlation equations, and numerical simulations. In the literature, a variety of heat transfer expressions have been developed for horizontal concentric cylinders. However, these

expressions are typically based on experimental results using very small inner and outer cylinder radii (on the order of a few centimeters) and gap-widths (1.9 cm $\leq L \leq$ 7.1 cm). In the present natural convection heat transfer study, the correlation equations are applied to much larger gap-widths (0.5 m $\leq L \leq$ 1.9 m) and cylinder radii (0.2 m $\leq R_i, R_o \leq$ 2.75 m).

Previous experimental and theoretical studies of internal natural convection in the annulus between horizontal cylinders have been largely restricted to simple geometries such as concentric or eccentric horizontal cylinders. In many of these cases, the geometries have small (~ 3 cm) gap widths ($L = R_o - R_i$). Typically, a single radius ratio was considered (e.g., Kuehn and Goldstein 1976 [DIRS 156722], p. 697, and Kuehn and Goldstein 1978 [DIRS 130084], Figure 1, considered a radius ratio of 2.6; Bishop (1988 [DIRS 156511], p. 310) and McLeod and Bishop 1989 [DIRS 156725], p. 1969, considered a radius ratio of 3.37; Vafai et al. 1997 [DIRS 156727], p. 484, considered a radius ratio of 1.1). A limited number of numerical and experimental studies have investigated the influence of the radius ratio on internal flow characteristics (e.g., Lis 1966 [DIRS 156513]; Bishop et al. 1968 [DIRS 164423]; Desai and Vafai 1994 [DIRS 156702]; Char and Hsu 1998 [DIRS 156701]). Some investigators developed heat transfer correlation equations for their experimental results (e.g., Lis 1966 [DIRS 156513]; Bishop et al. 1968 [DIRS 164423]; Kuehn and Goldstein 1976 [DIRS 156722]; Kuehn and Goldstein 1978 [DIRS 130084]; Bishop 1988 [DIRS 156511]). In the experimental studies, the range of radius ratios considered was $1.1 \leq R_o/R_i \leq 4$. In the numerical studies, a wide range of radius ratios was considered ($1.5 \leq R_o/R_i \leq 11$), including a radius ratio of 3.5, which is similar to that of the repository geometry (Webb et al. 2003 [DIRS 164366]). In the present comparative study, interest is focused on large gap widths (on the order of 0.5 m or greater) and larger radius ratios ($R_o/R_i \approx$ 3.2-3.5) than used in most of the experimental studies.

Most of the concentric cylinder simulation studies consider gases (Pr $\approx$ 0.7) as the working fluid in the annulus (e.g., Kuehn and Goldstein 1976 [DIRS 156722]; Kuehn and Goldstein 1978 [DIRS 130084]; Farouk and Guceri 1982 [DIRS 156715]; Desai and Vafai 1994 [DIRS 156702]); although, some investigated a larger range of Prandtl numbers (e.g., Kuehn and Goldstein 1976 [DIRS 156722]; Desai and Vafai 1994 [DIRS 156702]). An experimental analysis used water (Pr $\approx$ 5) as the working fluid in the annulus (Kuehn and Goldstein 1976 [DIRS 156722]). Some numerical studies considered Prandtl numbers as high as 5,000 (engine oil at room temperature) and as low as about 0.01 (liquid metals). The present study considers gases with a Prandtl number of approximately 0.7 (e.g., air, nitrogen).

Table 7.3.1-1 lists the investigators and the form in which their natural convection heat transfer investigation was presented (experiment, correlation equation, and numerical simulations). The investigations in bold have been used for model validation as presented later in this report.

Table 7.3.1-1. Internal Natural Convection Heat Transfer in the Literature

Investigators	Experimental Data	Correlation Equation	Numerical Simulation
Bishop 1988 [DIRS 156511]	X	X	-
Bishop et al. 1968 [DIRS 164423]	X	X	-
Char and Hsu 1998 [DIRS 156701]	-	-	X
Desai and Vafai 1994 [DIRS 156702]	-	-	X
Farouk and Guceri 1982 [DIRS 156715]	-	-	X
Fusegi and Farouk 1986 [DIRS 156719]	-	-	X
Kuehn 1976 [DIRS 156720]	X	X	X
Kuehn and Goldstein 1976 [DIRS 156722]	X	X	X
Kuehn and Goldstein 1976 [DIRS 100675]	-	X	-
Kuehn and Goldstein 1978 [DIRS 130084]	X	X	-
Lis 1966 [DIRS 156513]	X	X	-
McLeod and Bishop 1989 [DIRS 156725]	X	X	-
Raithby and Hollands 1975 [DIRS 156726]	-	X	X
Vafai et al. 1997 [DIRS 156727]	X	X	X
Webb et al. 2003 [DIRS 164366]	X	-	X

NOTE: **Bold** indicates data used in model validation.

As discussed in Section 6.1.5.1, the transition gap-width Rayleigh number for turbulence is about 10^6 (Kuehn and Goldstein 1978 [DIRS 130084]; Desai and Vafai 1994 [DIRS 156702]; Char and Hsu 1998 [DIRS 156701]). For Rayleigh numbers less than 10^6, the flow is laminar. For Rayleigh numbers greater than the transition value, the annulus internal flow conditions are characterized by a turbulent upward moving plume above the inner cylinder and a turbulent downward flow against the outer wall. Stagnation regions exist near the top where the plume impinges on the outer cylinder and over the entire bottom of the annulus. A low velocity laminar region exists in the annulus away from the walls. Turbulent flow conditions in the annulus are typically obtained either through the length scale (e.g., gap width) or the operating conditions (e.g., temperature difference and operating pressure) of the configuration. For the very small gap widths (~ 3 cm) considered in the experiments presented in the literature, air at atmospheric temperatures and pressures would not result in turbulent flow (e.g., $Ra_L < 10^6$). Pressurized gases such as nitrogen were often used in experiments to obtain the fluid properties necessary to achieve turbulent Rayleigh numbers for very small gap widths and small temperature differences (Kuehn and Goldstein 1978 [DIRS 130084]). The results of the experiments were then used to establish correlation equations that relate fluid properties and apparatus geometry to average heat transfer rates, as discussed in an upcoming section. Numerical simulations have been developed for some of the experimental geometries to compare simulation predictions to measured temperatures and heat transfer coefficients. Most of the numerical simulations are two-dimensional, but a limited number of three-dimensional studies have been conducted (e.g., Fusegi and Farouk 1986 [DIRS 156719]; Desai and Vafai 1994 [DIRS 156702]).

Most of the experimental data discussed above and presented in the literature are restricted to heat transfer results such as temperature and equivalent thermal conductivity. Experimental measurements of fluid velocity and turbulence quantities for the horizontal annulus configuration have not been published in the literature.

Two-dimensional simulations are developed to compare directly to the existing heat transfer correlations and experimental data developed in the literature. The two-dimensional CFD simulations are applied for both laminar and turbulent flow Rayleigh numbers.

The Kuehn and Goldstein experimental setup (1978 [DIRS 130084]) is simulated in this section in a two-dimensional configuration. Kuehn and Goldstein used pressurized nitrogen as the fluid, and they conducted experiments under laminar and turbulent conditions. In addition, two-dimensional simulations using appropriate Yucca Mountain dimensions and air at the appropriate pressure have been developed. These simulations are used to confirm the dimensionless scaling typically used in existing correlations even when the length scale is much larger than the existing experimental data. These results also serve to establish the approximate range of dimensionless parameters expected in Yucca Mountain drifts.

7.3.1 Kuehn and Goldstein Simulations

Geometry

The geometry of the Kuehn and Goldstein experiment is summarized in Table 7.3.1-2.

Table 7.3.1-2. Concentric Cylinder Geometries

Case	Inner Cylinder Diameter, D_i (m)	Outer Cylinder Diameter, D_o (m)	Diameter Ratio, D_o/D_i	Gap-Width $L=(D_o-D_i)/2$ (m)
Kuehn and Goldstein 1978 [DIRS 130084], Figure 1	0.0356	0.0925	2.6	0.0284

The mesh for the Kuehn and Goldstein problem was refined near the walls to simulate near-wall boundary layer effects, both turbulence and heat. Because of symmetry, the mesh represents only one-half of the cross-section geometry. The Kuehn and Goldstein FLUENT simulations use 1200 computational elements.

For the Kuehn and Goldstein numerical simulation, the inner cylinder temperature (T_h) is 28.1°C and the outer cylinder temperature (T_c) is 27.2°C, for a temperature difference of 0.91°C (Kuehn and Goldstein 1978 [DIRS 130084], Table 1), consistent with the experimental data reported in their paper. The specified wall temperatures for all simulations are maintained as constants during the steady state simulations.

A vertical plane through the geometric center forms a symmetry boundary (half domain simulated due to symmetry) as illustrated earlier in Figure 7.3.2-1. The existence of a steady-state solution is tacitly implied since symmetry boundary conditions are imposed on the numerical simulations. Steady laminar flow has been found experimentally for low Rayleigh numbers (Kuehn and Goldstein 1976 [DIRS 156722]). At Rayleigh numbers of the order of 10^7, the wall boundary layers are steady (Kuehn and Goldstein 1978 [DIRS 130084], p. 638). For larger Rayleigh numbers ($5 \times 10^8 \leq Ra_L \leq 5 \times 10^9$), it is assumed that a steady-state solution is achievable since the solutions converged. However, it is possible that some flow regimes (presumably at high Rayleigh numbers) may not exhibit steady-state behavior.

The dynamic viscosity, thermal conductivity, and specific heat are inputs in the numerical simulations. Each thermal quantity except the fluid density is treated as a constant. The fluid density is computed internally by FLUENT (Fluent 2001 [DIRS 164453], Equation 7.2-5), using the incompressible-ideal-gas law. The incompressible-ideal-gas law is discussed in Section 6.1.5.2 (Equation 6.1-30).

Internal natural convection occurs when a density variation (due to a temperature variation) exists in a gravitational field. The incompressible-ideal-gas law is applied in the density calculation when pressure variations are small enough such that the overall internal flow conditions are essentially incompressible, but a relationship between density and temperature is required as the driving force for fluid flow. The internal density variation is based on the input ambient operating pressure and the computed fluid temperature.

The working fluid used in the Kuehn and Goldstein (1978 [DIRS 130084]) experiment is pressurized nitrogen. Using an average fluid temperature of 27.7°C (300.85 K), the density of nitrogen is computed using the ideal gas law as 39.3 kg/m^3 for an operating pressure of 3,500 kPa (34.6 atm in the paper). Reference to compressibility-factor data for nitrogen at this temperature and pressure indicates a compressibility factor of one (Van Wylen and Sonntag 1986 [DIRS 108881]), so that the ideal gas law is applicable at this temperature and pressure.

Other properties of nitrogen at high pressure were obtained from the original source (Kuehn 1976 [DIRS 156720]). The thermal conductivity, dynamic viscosity and specific heat of nitrogen are computed as functions of temperature and pressure, as described by Kuehn (1976 [DIRS 156720], Appendix A and Tables A.1, A.3 and A.4) and summarized in Table 7.3.1-3. Evaluating Equation A.1 in Appendix A at two temperatures, 26.85°C and 46.85°C (300 K and 320 K), and interpolating at the average temperature 27.7 °C (300.85 K), gives temperature and pressure dependent thermal conductivity, dynamic viscosity and specific heat of nitrogen of 0.0274 W/m-K, 1.828 x 10^{-5} kg/m s, and 1094.66 J/kg K, respectively. As in the case for air, the volumetric thermal expansion coefficient is evaluated using $1/T_{ave}$ (= 1/300.85 K). The dynamic viscosity, thermal conductivity, and specific heat are inputs in the simulations. The density is computed internally using the incompressible-ideal-gas law as previously described.

The operating pressure for the Kuehn and Goldstein (1978 [DIRS 130084]) simulation is 3,500 kPa. The gauge pressure is specified during solution initialization as 0 Pa for all numerical simulations. The absolute pressure is the operating pressure plus the gage pressure. Gravity is specified as 9.81 m/s^2. To achieve lower Rayleigh numbers for a given geometry and temperature difference, the gravity vector is simply scaled below its normal value. For instance, if for a given geometry and temperature difference a gravity vector (-g) of 9.81 m/s^2 results in a Rayleigh number of 1 x 10^8, a gravity vector of (9.81/10) m/s^2 results in a Rayleigh number of 1 x 10^7 for the same temperature difference and length scale. Using gap widths as the length scale in the Rayleigh numbers, the operating conditions for each geometry are given in Table 7.3.1-4.

Table 7.3.1-3. Thermophysical Properties of N_2 used for the Two-Dimensional Concentric Cylinders Kuehn and Goldstein Simulations

Temperature (°K)	Specific Heat, C_p (J/g-K)	Thermal Conductivity k_a, (W/cm-K)	Dynamic Viscosity, μ (g/cm-s)
300	1.095	2.731×10^{-4}	1.824×10^{-4}
320	1.088	2.856×10^{-4}	1.911×10^{-4}

Source: Kuehn 1976 [DIRS 156720], Appendix A, Equation A.1, and Tables A.1, A.3, and A.4.

NOTES: At T = 300K:

$C_p = 1.0394835 + 1.5820333 \times 10^{-3} P + 6.1787435 \times 10^{-7} P^2$

$K_a = 2.58051719 \times 10^{-4} + 4.51689926 \times 10^{-7} P - 5.30137942 \times 10^{-9} P^2 + 2.26889212 \times 10^{-10} P^3 - 2.55417410 \times 10^{-12} P^4$

$\mu = 1.7855493 \times 10^{-4} + 4.0334031 \times 10^{-8} P + 7.2008260 \times 10^{-9} P^2 - 2.8518373 \times 10^{-10} P^3 + 3.9604790 \times 10^{-12} P^4$

At T = 320K:

$C_p = 1.0400164 + 1.3578376 \times 10^{-3} P - 3.3228820 \times 10^{-7} P^2 + 1.3040655 \times 10^{-7} P^3 - 2.8875749 \times 10^{-9} P^4$

$K_a = 2.71659171 \times 10^{-4} + 4.43356829 \times 10^{-7} P - 7.00542461 \times 10^{-9} P^2 + 2.74970020 \times 10^{-10} P^3 - 3.08055493 \times 10^{-12} P^4$

$\mu = 1.8733579 \times 10^{-4} + 5.4692604 \times 10^{-8} P + 4.2674852 \times 10^{-9} P^2 - 1.4378423 \times 10^{-10} P^3 + 1.9167756 \times 10^{-12} P^4$

Values in Table 7.3.1-3 are the result of evaluating these equations at P=34.6 atm.

The following properties obtained from Reid et al. 1977 [DIRS 130310] were also used:
Universal gas constant (R) = 8314 J/kmol-K (p. 27)

Molecular weight of nitrogen = 28.013 kg/kmol (p. 630).

Table 7.3.1-4. Operating Conditions

Case	Gravity, -g (m/s^2)	Tave (C)	ΔT (C)	L (m)	Ra_L	Internal Flow Conditions
Kuehn and Goldstein 1978 [DIRS 130084]	0.09810	27.7	0.91	0.02845	2.31×10^4	Laminar
Kuehn and Goldstein 1978 [DIRS 130084]	0.98100	27.7	0.91	0.02845	2.31×10^5	Laminar
Kuehn and Goldstein 1978 [DIRS 130084]	9.81000	27.7	0.91	0.02845	2.31×10^6	Turbulent

Output DTN: SN0308T0507803.015.

The Kuehn and Goldstein simulations include laminar and turbulent flow conditions.

The steady-state segregated solver is used in this work. Pressure-velocity coupling is achieved through the SIMPLE algorithm. The SIMPLE algorithm uses the discrete continuity equation to determine a cell pressure correction equation. Once a solution to the cell pressure correction equation is obtained, the cell pressure and face mass fluxes are then corrected using the cell pressure correction term.

A final convergence criteria specified in the CFD simulations is based on an overall steady-state energy balance. When the energy imbalance between cylinders is at or below about 2%, the flow simulation is assumed to be complete.

7.3.2 Repository-Scale Concentric Cylinder Simulations

Geometry

The geometry, which is based on the repository scale, is given in Table 7.3.2-1. These simulations are two-dimensional. The inner cylinder diameter is based on the average of the waste package diameters listed in Table 7.3.2-2.

Table 7.3.2-1. Concentric Cylinder Geometries

Case	Inner Cylinder Diameter, D_i (m)	Outer Cylinder Diameter, D_o (m)	Diameter Ratio, D_o/D_i	Gap-Width $L=(D_o-D_i)/2$ (m)
Full-Scale Repository	1.71[a]	5.5[b]	3.2	1.895

[a] Average of DHLW and 24-BWR waste package diameters (BSC 2003 [DIRS 165406]). See Table 7.3.2-2.
[b] BSC 2003 [DIRS 164069].

The average diameter used in the repository scale simulations is the average of the largest and smallest diameter waste packages listed in Table 7.3.2-2. The value used in the simulations is 1.71 m = (2.11m+1.318m)/2.

Table 7.3.2-2. Geometric information used in the Repository-Scale Concentric Cylinders Simulations

Information	Value	Source
Outer Diameter (Drift diameter)	5.5 m	BSC 2003 [DIRS 164069]
DHLW waste package diameter (largest)	2110 mm	BSC 2003 [DIRS 165406]
24-BWR waste package diameter (smallest)	1318 mm	BSC 2003 [DIRS 165406]

The computational mesh, shown in Figure 7.3.2-1 for the full scale repository-type geometry, uses 3,111 computational elements (cells). The mesh is refined near the walls to simulate near-wall boundary layer effects for turbulence and heat transfer. Because of symmetry the mesh represents only one-half of the cross-section geometry.

The temperature boundary conditions are specified to give a temperature difference (ΔT) across the inner and outer cylinders similar to that expected at early times between the waste package and the drift wall at the Yucca Mountain repository during high temperature operation. The hot temperature (T_h) of the inner cylinder is assumed to be 100°C (373 K) and the cold temperature (T_c) of the outer cylinder is assumed to be 80°C (353 K), which results in a ΔT of 20°C. The temperature difference is more important than the actual temperatures in the natural convection calculations because it, along with the geometry, has the greatest influence on the Rayleigh number.

This assumed temperature difference is just used to establish an appropriate range of Rayleigh numbers. The validation range of turbulent natural convection will be established in Section 7.3, Figure 7.3.3-2, by comparison of FLUENT predictions with experimental data. In this figure, FLUENT predictions agree within the experimental uncertainty of the data up to a Rayleigh

number of 5.3×10^9. This Rayleigh number corresponds to a temperature difference of 20°C for the Yucca Mountain scale geometry as listed in Table 7.3.2-4. Therefore, the range of validation for turbulent natural convection is up to a 20°C temperature difference between the waste package and the drift wall. FLUENT results in Appendix J show that the temperature difference between the waste package and the drift wall are a maximum of 8°C, which decreases with increasing time. Therefore, the FLUENT results presented in this report are within the validation range established for turbulent natural convection conditions in Section 7.

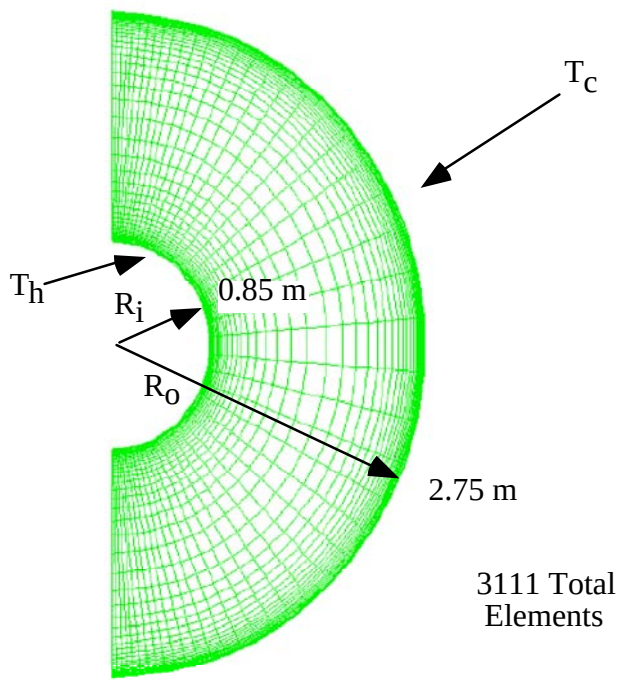

DTN: SN0308T0507803.014.

Figure 7.3.2-1. Computational Grid for the Full-Scale YMP Concentric Cylinder Geometry

Thermal property inputs for air are required in the CFD simulations. For air, thermophysical properties are evaluated at the average fluid temperature, T_{ave}, defined as the average of the inner and outer cylinder surface temperatures, of 90°C for the YMP-scale geometries. The average air temperature is different from the inner and outer cylinder film temperatures defined by Kuehn and Goldstein (1978 [DIRS 130084]) (see Appendix I for the definition of film temperature). The inner cylinder film temperature is about 2 to 3 degrees higher than the average fluid temperature while the outer cylinder film temperature is about 5 to 7 degrees lower than the average fluid temperature. Using the inner film temperature of 93°C to calculate the fluid thermal conductivity gives 0.0313 W/m-K while using the average fluid temperature of 90°C gives 0.0310 W/m-K (Bejan 1995 [DIRS 152307], Appendix D). This small difference does not influence the CFD simulations presented in this document.

Using Bejan (1995 [DIRS 152307], Appendix D), for air evaluated at 90°C, the following thermophysical property values for the density, dynamic viscosity, thermal conductivity, and specific heat are 0.9745 kg/m^3, $2.135x10^{-5}$ kg/s-m, 0.031 W/m-K, and 1010.25 J/kg-K,

respectively, based on the properties listed in Table 7.3.2-3. The fluid kinematic viscosity is 2.19×10^{-5} m^2/s and the fluid thermal diffusivity is 3.15×10^{-5} m^2/s. The Prandtl number is 0.7. The volumetric thermal expansion coefficient is $1/T_{ave}$ (= 1/363 K) for an ideal gas. The dynamic viscosity, thermal conductivity, and specific heat are inputs in the numerical simulations. Each thermal quantity except the fluid density is treated as a constant. The fluid density is computed internally by FLUENT (Fluent 2001 [DIRS 164453], Equation 7.2-5), using the incompressible-ideal-gas law. The incompressible-ideal-gas law is discussed in Section 6 (Equation 6.1-17).

Table 7.3.2-3. Thermophysical Properties of Dry Air Used in FLUENT for the Two-Dimensional Concentric Cylinders Simulations

Temperature (°C)	Specific Heat, c_p (kJ/kg-K)	Thermal Conductivity k_a, (W/m-K)	Dynamic Viscosity, μ (kg/m-s)	Density
60	1.008	0.028	2.00×10^{-5}	Incompressible-ideal-gas
100	1.011	0.032	2.18×10^{-5}	Incompressible-ideal-gas

Source: Bejan 1995 [DIRS 152307], Appendix D.

The operating pressure selected for the large-scale geometries is 101.3 kPa. A standard atmospheric pressure at sea level is selected to perform a comparison to literature heat transfer results for natural convection (both data and correlation equations). The absolute value of the pressure is unimportant because the results are presented as a function of Rayleigh number. The gauge pressure is specified during solution initialization as 0 Pa for all numerical simulations. The absolute pressure is the operating pressure plus the gage pressure. The gravitational constant is specified as 9.81 m/s^2. To achieve lower Rayleigh numbers for a given geometry and temperature difference, the gravity vector is simply scaled below its normal value. For instance, if for a given geometry and temperature difference a gravity vector (-g) of 9.81 m/s^2 results in a Rayleigh number of 1×10^8, a gravity vector of (9.81/10) m/s^2 results in a Rayleigh number of 1×10^7 for the same temperature difference and length scale. Using gap widths as the length scale in the Rayleigh numbers, the operating conditions for each geometry are given in Table 7.3.2-4.

Table 7.3.2-4. Operating Conditions

Case	Gravity, -g (m/s2)	Tave (C)	ΔT (C)	*L* (m)	Ra_L	Internal Flow Conditions
Full Scale 0.1% Gravity	0.00981	90.0	20.00	1.89450	5.30×10^6	Turbulent
Full Scale 1% Gravity	0.09810	90.0	20.00	1.89450	5.30×10^7	Turbulent
Full Scale 10% Gravity	0.98100	90.0	20.00	1.89450	5.30×10^8	Turbulent
Full Scale Full Gravity	9.81000	90.0	20.00	1.89450	5.30×10^9	Turbulent

Output DTN: SN0308T0507803.014.

Based on Table 7.3.2-4, the flow conditions are turbulent for these gap widths and a temperature difference of 20°C.

The CFD numerical simulation settings are the same as described in the Kuehn and Goldstein section.

7.3.3 Correlation, Experimental Data, and CFD Code Comparison for Average Heat Transfer

The CFD simulation predictions, experimental data, and the results from the Kuehn and Goldstein correlations are compared in this section. Table 7.3.3-1 lists the physical properties used to evaluate the Kuehn and Goldstein correlations for this section.

Table 7.3.3-1. Thermophysical Properties of Dry Air Used in the Two-Dimensional Kuehn and Goldstein Correlations

Temperature (°K)	Specific Heat, c_p (J/kg-K)	Thermal Conductivity k_a, (W/m-K)	Dynamic Viscosity, μ (kg/m-s)	Kinematic Viscosity, ν (m^2/s)	Thermal Diffusivity, α (m^2/s)	Density
300	1007	0.0263	1.846×10^{-5}	1.589×10^{-5}	2.25×10^{-5}	Incompressible-ideal-gas
350	1009	0.0300	2.082×10^{-5}	2.092×10^{-5}	2.99×10^{-5}	Incompressible-ideal-gas
400	1014	0.0338	2.301×10^{-5}	2.641×10^{-5}	3.83×10^{-5}	Incompressible-ideal-gas

Source: Incropera and DeWitt 1990 [DIRS 156693], Table A.4.

Figure 7.3.3-1 illustrates a comparison of the average equivalent thermal conductivity evaluated using the correlation equations of Kuehn and Goldstein (1976 [DIRS 100675]; 1978 [DIRS 130084]), and the FLUENT CFD simulations of concentric cylinders in two dimensions. Recall that the average equivalent thermal conductivity is defined as the ratio of the total heat transfer to that of pure conduction. When the average equivalent thermal conductivity is equal to one, the mode of heat transfer is pure conduction. The lines in the figure represent the evaluation of the correlation equations. The procedure for evaluating the correlation equations is described in Appendix A. The data points represent the average equivalent thermal conductivity based on CFD numerical simulation results from the FLUENT data files contained in DTNs: N0308T0507803.014 and SN0308T0507803.015. The CFD and correlation evaluations are contained in the MS Excel file “keqcorrelations&simulations.xls” submitted as part of these DTNs. The procedure used in the spreadsheet to evaluate average equivalent thermal conductivity from the CFD results are described below. Figure 7.3.3-2 illustrates, in addition to the information given in Figure 7.3.3-1, other literature data points representing either experimental or simulation results as indicated in the figure legend.

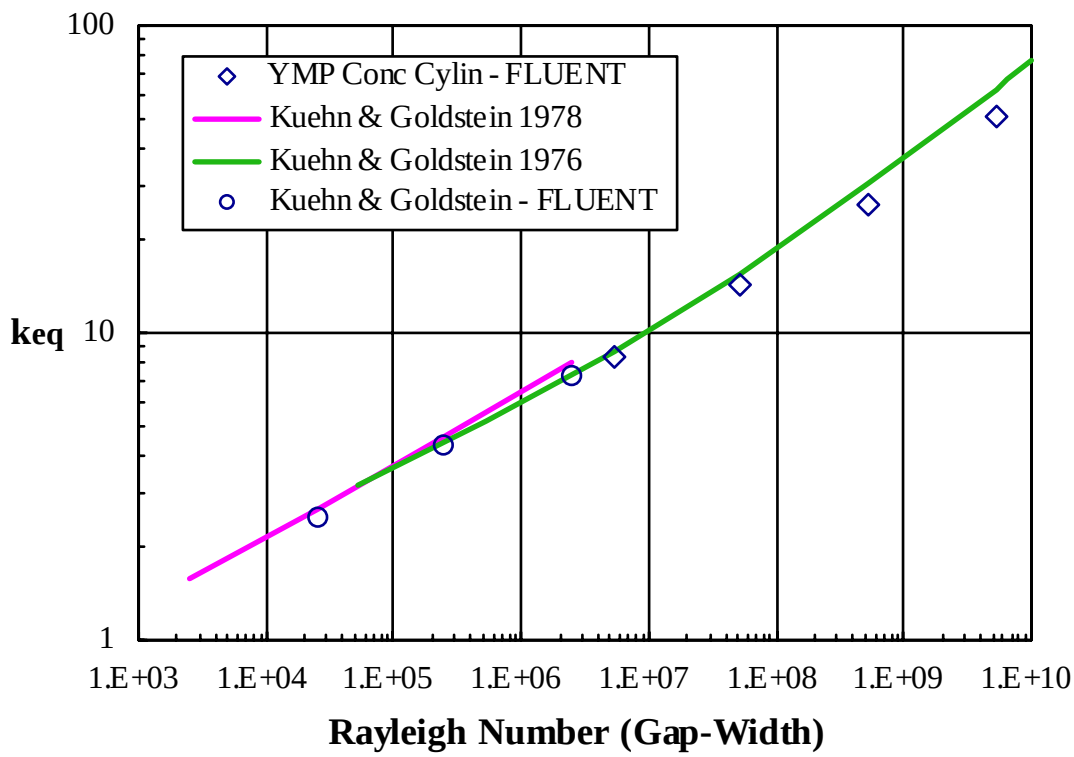

DTNs: SN0308T0507803.014; SN0308T0507803.015.

Source: Kuehn and Goldstein 1978 [DIRS 130084]; Kuehn and Goldstein 1976 [DIRS 100675].

Figure 7.3.3-1. Comparison of CFD Simulation Results to the Kuehn and Goldstein Correlation Equation (1978) and the General Correlation in Kuehn and Goldstein (1976) for Concentric Cylinders

The Rayleigh number in Figure 7.3.3-1 is based on the gap-width (L) between cylinders. The values of k_{eq} for the numerical simulations are found by taking the ratio of total heat flux for a natural convection run and the total heat flux from the conduction-only simulation.

$$k_{eq} = \frac{\overline{Nu}_{D_i}}{\overline{Nu}_{cond}} = \frac{Q_{FLUENT\ conv}}{Q_{FLUENT\ cond}} \qquad \text{(Eq. 7.1-2)}$$

The total heat flux from a surface is a direct output of FLUENT.

The average equivalent conductivity from Equation 7.1-2 is plotted in Figure 7.3.3-1 for each of the concentric cylinder geometries considered. Figure 7.3.3-2 provides a comparison to other experimental data and numerical simulation results. These figures show that for laminar flow with a Rayleigh number of 10^5, the total heat transfer is approximately two to four times larger than for conduction only. For a moderately turbulent regime with a Rayleigh number of 10^7, the total heat transfer is approximately ten times higher than conduction only. Based on this initial comparison in Figure 7.3.3-1, the numerical results at higher Rayleigh numbers ($>10^8$) are slightly low when compared to the Kuehn and Goldstein (1976 [DIRS 100675] and 1978 [DIRS 130084]) correlations.

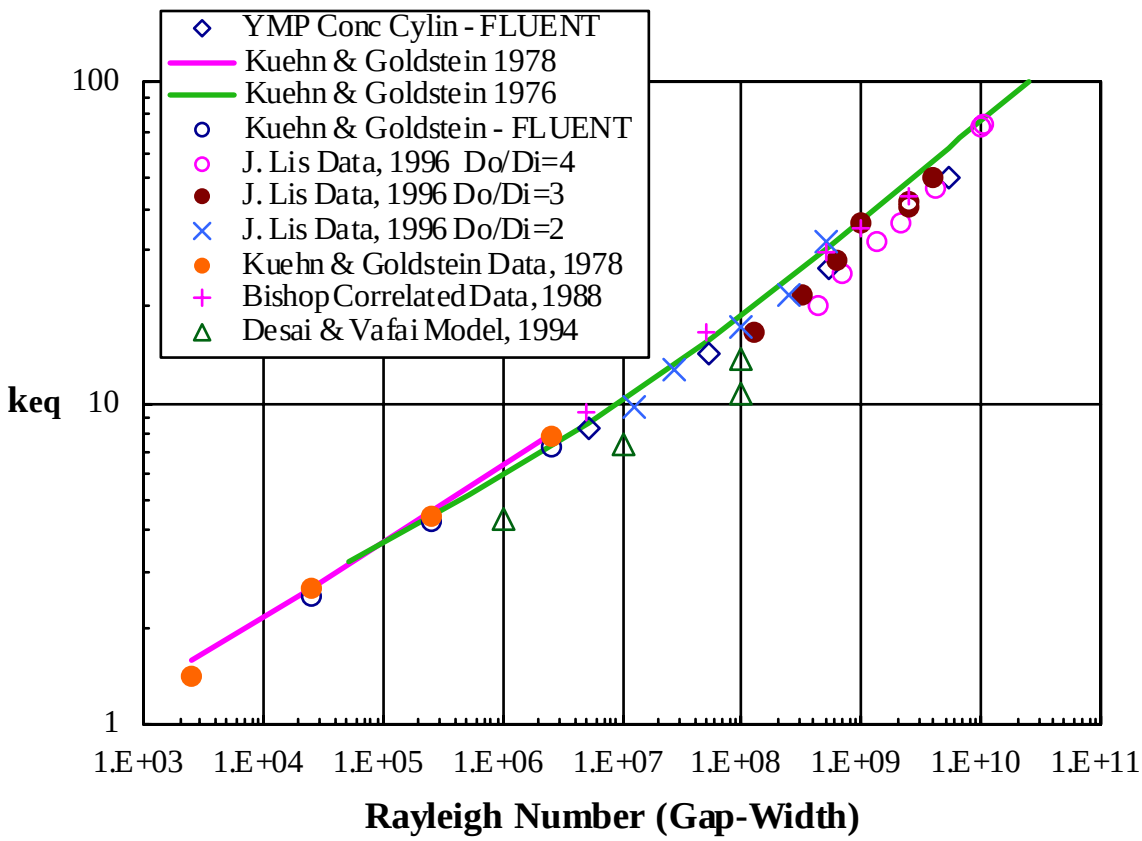

DTNs: SN0308T0507803.014; SN0308T0507803.015.

Figure 7.3.3-2. Comparison of CFD Simulation Results for Concentric Cylinders to Other Experimental Results, Simulation Results, and Heat Transfer Correlations

Figure 7.3.3-2 contains the results of the correlation equations (Kuehn and Goldstein 1976 [DIRS 100675]; Kuehn and Goldstein 1978 [DIRS 130084]), numerical simulation (FLUENT) results for concentric cylinders, experimental data from the literature, and other numerical simulation studies from the literature. Experimental and correlated heat transfer data from the literature included results from Kuehn and Goldstein (1978 [DIRS 130084], "Kuehn & Goldstein Data, 1978"), Bishop (1988 [DIRS 156511], "Bishop Correlated Data, 1988"), and Lis (1966 [DIRS 156513], "J. Lis Data, Do/Di = 4, 3, and 2, 1966"). Numerical simulation results from the literature included Desai and Vafai (1994 [DIRS 156702], "Desai & Vafai Model, 1994"). The Bishop correlation data are valid for Rayleigh numbers between 6×10^6 and 2×10^9. Figure 7.3.3-2 illustrates the Bishop correlation data slightly on either side of its range of investigated validity (e.g., evaluated at 5×10^6 and 2.5×10^9). The estimated uncertainty for the experimental data is about 10 to 15 percent.

From the figure it is noted that the range of Rayleigh numbers investigated both numerically and experimentally encompass both laminar and turbulent flow conditions. From the figures it can be deduced that the numerical simulations and experimental data agree very well for all ranges of Rayleigh number. In contrast, Kuehn and Goldstein (1976 [DIRS 100675] and 1978 [DIRS 130084]) slightly overpredict the average equivalent thermal conductivity for Rayleigh numbers greater than 10^8. This trend is consistent among the different geometries considered.

The numerical simulations agree within 10% or less of the experimental data, well within the validation criteria discussed earlier in Section 7. Therefore, based on the above comparisons, the FLUENT natural convection methodology is validated because it is able to match open literature natural convection data as well as correlations for a concentric cylinder geometry, which is similar to the YMP configuration. This methodology can be confidently used to predict repository-specific natural convection conditions using repository-specific geometry and boundary conditions.

7.4 THREE-DIMENSIONAL NATURAL CONVECTION TEST VALIDATION

The Engineered Barrier Systems (EBS) Department performed a series of scaled tests designed to support modeling activities in the EBS department. These tests were conducted at the DOE Atlas Facility in North Las Vegas. The tests evaluated the three dimensional effects of a distributed heat load in a scaled drift environment, under post-closure (without forced ventilation) conditions. The tests were conducted at two geometric scales (25% and 44% scales based on the repository design), with and without drip shields, and under both uniform and distributed heat loads (See Table 7.4.1-1). Data from these tests are used to validate the computational fluid dynamics (CFD) computer code, FLUENT.

Comparison between the FLUENT calculational results and measured test data for the two most relevant configurations from the test series is provided in this section.

7.4.1 Experiment

Experiment Overview

The natural convection tests were designed to evaluate fluid flow and heat transfer processes under conditions similar to repository post-closure conditions. During the post-closure period, all of the energy from the waste packages is disseminated into the surrounding rock mass. Hence, the conduction of the heat into the surrounding rock mass determines the maximum temperatures within the drift. The primary mechanisms for energy transfer from the waste packages to the emplacement drift walls are turbulent natural convection and thermal radiation. The natural convection tests were designed to recreate these processes at a smaller scale than the full-scale repository (Kalia 2001 [DIRS 156939]). Because it was not practical to maintain Rayleigh numbers between the scaled test and full-scale repository (the temperature difference in the 25%-scale experiment would have to be 64 times the temperature difference in the repository), scaling was based on maintaining equal heat fluxes and direct geometric scaling. Tests at two different geometric scales (25 and 44%) were conducted to provide confidence in extrapolation to full-scale conditions. Note that the purpose of the natural convection tests is to validate the FLUENT code and methodology for use in full-scale simulations, not to provide prototypical drift conditions. The Scientific Investigation Test Plan, *Atlas Natural Convection Test Plan* (BSC 2002 [DIRS 158192]), provides the complete scaling analysis.

The general objective of the test matrix design considered three variables:

- Power distributions of both uniform line load and scaled distributed load
- Presence and absence of a drip shield
- Physical scales of 25% and 44%, with power scaled to provide uniform flux from the waste packages

The overall test matrix created to incorporate the design variables included eight tests, four each for the 25% and 44% power levels (Table 7.4.1-1).

Table 7.4.1-1. Postclosure Convection Test Matrix

Case #	Scale	Drip Shield	WP Spacing	Power
1	25%	No	Uniform	Uniform
2	25%	No	Non-uniform	Distributed
3	25%	Yes	Uniform	Uniform
4	25%	Yes	Non-uniform	Distributed
5	44%	No	Uniform	Uniform
6	44%	No	Non-uniform	Distributed
7	44%	Yes	Uniform	Uniform
8	44%	Yes	Non-uniform	Distributed

Source: BSC 2002 [DIRS 158192], Table 2.

The controlled input for the test series was the waste package heater power. As a baseline, uniform loads were tested. In the uniform heat load cases, the total power generation of all the canisters equals the total power generated by the distributed canisters, but is distributed uniformly over the length of the string of canisters. Because the canisters have different lengths, their individual power levels vary.

For the cases with uniform heating (Cases 1, 3, 5, and 7), seven waste packages were evenly spaced within the test train. For non-uniform power cases, six waste packages were distributed within the test train. A continuous drip shield over the waste packages was incorporated in half of the cases.

The cases were simulated with FLUENT. The blind predictions discussed in Appendix B were performed without knowledge of the experimental data. The post-test predictions used information from the experiments to determine waste package powers, environmental conditions, and other parameters. Results from the two configurations most closely matching the repository design (Cases 4 and 8) are presented here.

Experiment Setup

Figure 7.4.1-1 is a schematic of the proposed repository, showing the major components of the EBS, including the drift wall, invert, waste package and drip shield. The experiment was designed to represent each of these major features. The natural convection test apparatus was built in the EBS Test Facility in North Las Vegas.

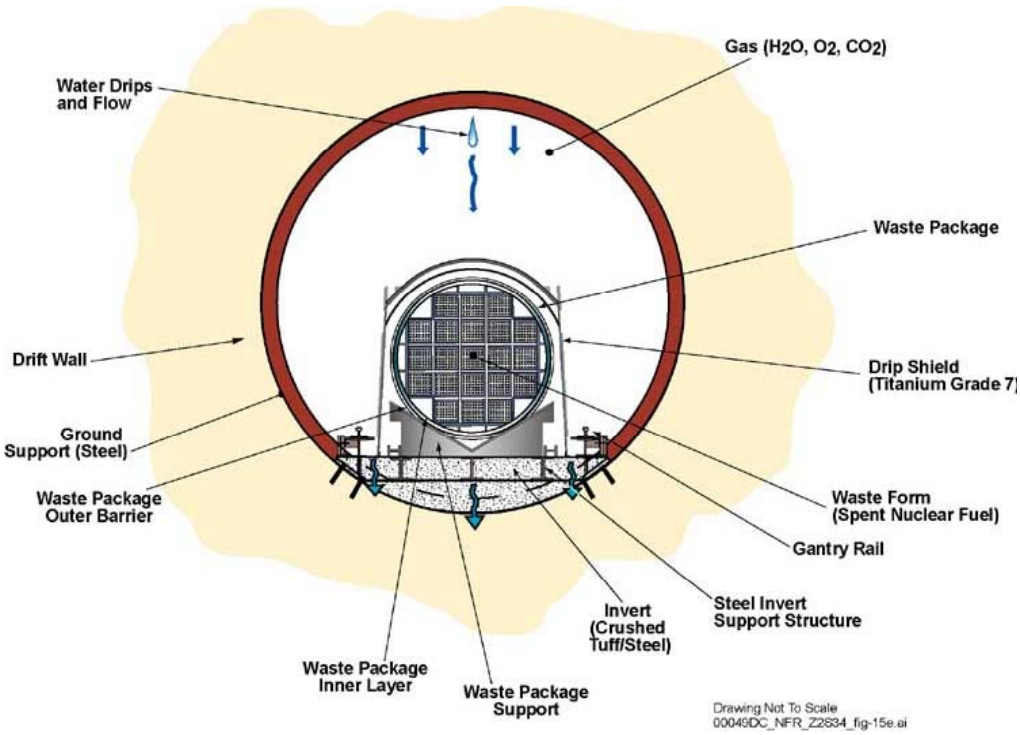

Source: DOE 2002 [DIRS 156958], Figure 3-45.

Figure 7.4.1-1. Schematic Presentation of a Cross-Section of an Emplacement Drift Showing Major Components of the Engineered Barrier System

The drift wall was simulated by connected segments of concrete pipes wrapped with standard spun fiberglass insulation. The concrete joints were sealed. The insulation was coated with reflective foil, which was exposed directly to the ambient air in the high bay. For economy, standard size concrete pipe was chosen to provide roughly the desired scales, resulting in tests of 25% and 44% of full scale. The overall lengths of the test trains were determined by the total length of the minimum number of concrete pipes needed to enclose the desired heated length based on the distributed waste package configuration, and the space available in the test facility. For the 25% scale tests the length of the concrete pipes was about 1.5 m longer than the desired heated length, while for the 44% scale tests the concrete pipes were only about 0.5 m longer than the desired heated length.

Crushed tuff formed the invert. The material was added to the bottom of the test train until it reached the top of the steel rail system used to emplace the waste packages and drip shields (described below).

Waste packages were fabricated from steel pipe and heated with electric heaters. The heaters were designed to provide a uniform flux over the surface of the packages (Howard 2002 [DIRS 161009], p. 18). The endplates of the packages were controlled separately such that they could be heated at the same flux as the cylindrical surface or could be turned off. Dimensions and power input to the waste packages were based on a lower temperature operating mode (LTOM) repository design (BSC 2002 [DIRS 158192], Section 3.1). This configuration used a nine-package segment for the emplacement drift, which included four distinct waste package types

(44-BWR, 21-PWR, 5-DHLW Short, and 5-DHLW Long). Because of the limited floor space in the low bay, the entire nine-package segment could not be incorporated. Instead, enough of the waste packages in the design sequence (six) were chosen to encompass the largest power gradients in the design. The power generation histories of the four waste packages types specified in the cool repository design were evaluated, and the generation rate at 300 years after emplacement was the baseline condition from which these tests were scaled (BSC 2002 [DIRS 158192], Section 3.1). Tests were scaled on heat transfer coefficients, resulting in a waste package power output for the 25% scale tests of 0.0625 times and the 44% scales tests of 0.194 times the full power output of the waste package (BSC 2002 [DIRS 158192], Section 5.2.2).

The power controllers could not accurately control the very low input powers for some of the waste packages in the distributed power cases. For these tests, no power was input to the "cold" canisters. The exterior surfaces of the packages were covered with a flat black paint of known emissivity. Each package was assembled on a steel pallet. Packages were cradled in two V-notched endplates such that the package and the support were in direct contact at only four points (Figure 7.4.1-2) to minimize energy transfer from the packages into the pallets via conduction. The pallets were pushed into place within the test train on steel rails that were supported by steel I-beams (Figure 7.4.1-2). Photographs of the 25% scale test are provided in Figure 7.4.1-3. These photos show both the inner and outer cylinders which made up the waste packages, a waste package support, and the interior of the test train with the steel rails and invert.

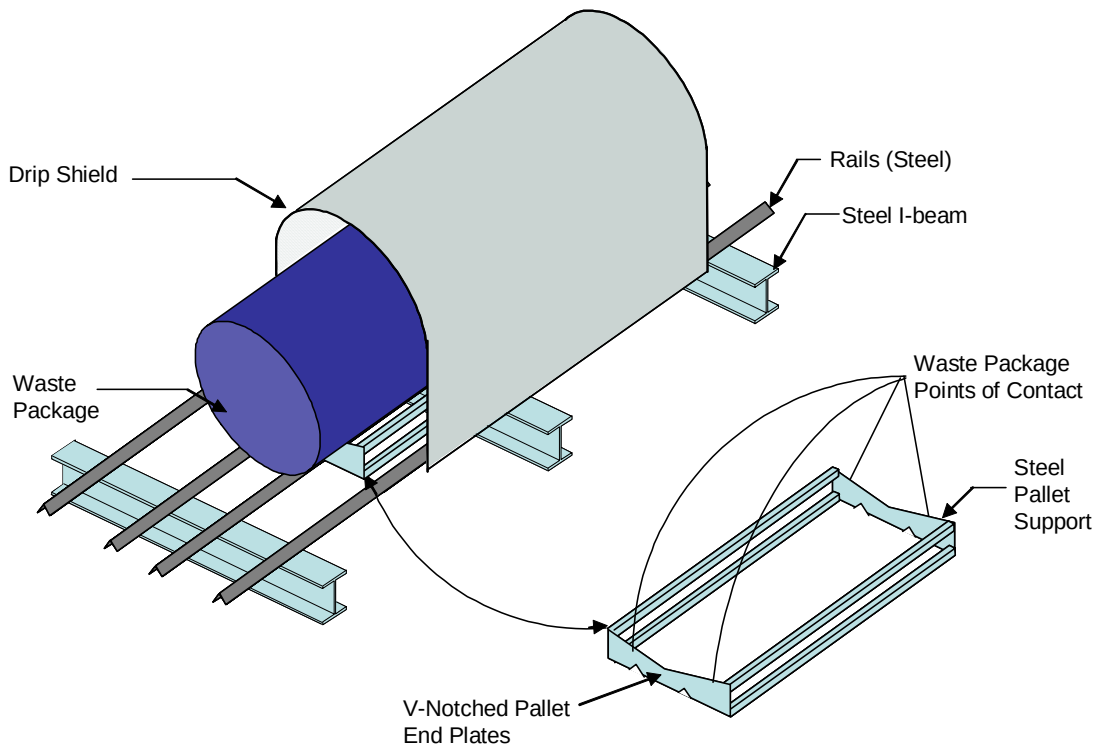

Source: Howard 2002 [DIRS 161009], p. 28.

Figure 7.4.1-2. Steel Support Pallets Design Drawing

Figure 7.4.1-3. Photographs of the 25% Scale Test Components

Drip shields were also fabricated from steel and painted the same color as the waste packages and test cell endplates. The sections were assembled end-to-end to provide a continuous shield over the assembly of waste packages. The joints between the shields were sealed to prevent air circulation. Cover plates were installed at both ends of the drip shield assembly (Figure 7.4.1-5).

The end conditions of the tests were designed to provide readily simulated heat transfer conditions. A reflective boundary with minimal heat loss was created on one end of the test train. The exterior surface of the end plate was heavily insulated while the inner surface of the steel plate was covered with a reflective aluminum tape, thus providing a very low emissivity. Throughout this report, this end is referred to as the "hot" or "reflective" end of the test train. The other end of the test setup was designed to be thermally "cold" like the test section walls. The exterior surface of this end plate was insulated with the same thickness of fiberglass as the concrete pipe, while the inner surface of the end plate was coated with the same paint used on the waste packages (this paint had a similar emissivity to the concrete surface). Throughout this report this end is referred to as the "cold" or "non-reflective" end of the test train.

Experiment Instrumentation

The key parameters monitored during the test included surface temperatures of the simulated waste packages, drip shields, invert and emplacement drift, the fluid temperatures and relative humidity, the power input to the simulated waste packages, and atmospheric conditions. In all, almost 300 sensors were automatically monitored and recorded every hour throughout the duration of the test. Figures 7.4.1-4 and 7.4.1-5 provide schematics of the sensor locations, which are discussed in greater detail below. The instrument types, ranges and accuracy for the air velocity, temperature, RH, and power measurements are listed in Table 7.4.1-2.

In addition to the above measurements that were collected automatically throughout the test duration, ports were added at a number of locations within the test train allowing temperature and velocity profiles in the annulus between the waste package (or drip shield, if present) and drift wall to be collected manually.

The number of test data automatically collected during the natural convection test series prohibits the data from being presented in tabular format. A summary of the data from these tests, which were used in validating the model (Section 7), is provided in Appendix C.

Average measured values were used for comparison to FLUENT results. A three-day period was chosen as representative of steady-state conditions for each case. An extended period was used in order to minimize the effects of diurnal variations as well as changing atmospheric conditions (i.e., changes in ambient conditions due to weather patterns). Each three-day period was selected during the most stable ambient conditions after steady state was reached. Average values as well as standard deviations are presented later in this section. The use of average values reduces the uncertainty due to random effects for a given sensor, but has no effect of systematic errors that could fall within the accuracy ranges presented in Table 7.4.1-2.

Table 7.4.1-2 Instrument Characteristics for the Natural Convection Tests

Instrument	Range	Accuracy
Air Velocity Meter (Sierra Instruments)	0 – 250 SCFM	+/- 2% @10 – 100% of Full Scale +/-0.5% FS below 10% of Full Scale
Temperature / Relative Humidity Probe (Vaisala)	10 – 100% RH 0 - 100°C	+/- 2% RH @ 10 – 90% RH +/- 3% RH above 90% +/- 2°C
Thermocouple, Type T (Omega)	15 - 100°C	+/- 0.5°C
Power Monitor (Ohio Semitronics)	0 – 4kW	+/- 0.5% of Full Scale

Source: BSC 2002 [DIRS 158192], p. 12.

Surface Temperature Measurements

Fifteen measurement stations were specified within the test train. The first and last stations (1 and 15) were at either end of the test train. At these two stations, six thermocouples (TCs) were located at each station – five surface-mounted in a cross pattern on the interior face of the end plate (top, right, bottom, left, and center) and the sixth surface mounted in the center of the plate on the exterior surface of the insulation (Figure 7.4.1-4). The remaining thirteen stations were all instrumented as depicted in Figure 7.4.1-4. Surface-mounted TCs were located in four places (top, right, bottom and left) on the interior surface of the concrete pipe and the interface between the concrete and insulation. Three TCs were embedded in the invert. All three of the TCs were approximately 2 cm below the surface of the invert, one at the centerline of the test train and the other two slightly outside the edges of the waste package (Howard 2002 [DIRS 161009], p. 57). The outside TCs were located below the outer steel rails. Three of the stations (3, 9, and 13) had surface mounted TCs on the exterior surface of the insulation at the top, right, bottom and left positions. For tests with a drip shield, one TC was located at the top of the drip shield at each station. Side sensors were placed on the drip shield at every other station. Each of the end plates of the drip shield assembly was instrumented with three TCs as shown in Figure 7.4.1-5.

Each waste package and waste package support was instrumented with eight surface mounted TCs. Four sensors were placed circumferentially around the center of the waste package, a TC was placed in the center of each waste package end plate, and a TC was placed at the center of the support end plate (Figure 7.4.1-4). Because the spacing and thus position of the waste packages moved between tests, these sensors were not defined with a specific station. A complete description of the as-built sensor locations for all tests can be found in Sánchez (2002 [DIRS 166231], [DIRS 166232], [DIRS 166233], [DIRS 166234], [DIRS 166235], [DIRS 166236], [DIRS 166237], [DIRS 166238]).

Fluid Temperature and Relative Humidity Measurements

Fluid temperature and relative humidity measurements were taken at each of the thirteen interior stations (stations 2 through 14), as shown in Figure 7.4.1-4 for cases without a drip shield and Figure 7.4.1-5 for cases with a drip shield. TCs recorded temperatures near the crown and at the right and left sides of the test train. Another TC measured the temperature below and to one side

of the waste package. For cases with a drip shield another TC was located near this lower sensor, but on the opposite side of the drip shield. Two relative humidity/temperature sensors were located at the stations, one near the crown and the other below and to one side of the waste package (this sensor was inside the drip shield for those cases having a drip shield).

Power Input

The power input to each of the waste packages was independently controlled. The heater control system was designed to allow variable power input. The ends of the waste packages could either be heated with the cylinder of the package (in the cases of non-uniform spacing) or turned off (to eliminate localized hot spots in cases of uniform spacing). For the uniform load cases, a constant line load was applied to each of the packages (power input per package varied based on the length of the package). The total power input (defined as the sum of the measured power input for each waste package) was constant for all four cases.

Atmospheric Measurements

Ambient temperature and relative humidity within the test bay were monitored throughout the tests. In addition to these sensors, 14 TC sensors were located on the exterior surfaces of the test, 12 on the exterior surface of the insulation (four each at stations 3, 9, and 13), and one on the outside surface of the insulation on either end plate.

Fluid Velocity Profiles

Air velocity and temperature profile data for the annulus between the waste package (or drip shield, if present) and drift wall were collected after steady-state conditions were reached for each test. The air velocity profiles were measured by traversing selected locations in the test section with a velocity probe. Stations were selected based on the waste package layout and heat distribution of the tests. Holes and guide tubes were located in the concrete pipe sections to allow insertion of the probe. Axial velocity profiles along the length of the test were also measured by inserting the probe to a location directly over the centerline of the waste package or drip shield (when present).

Velocity data were obtained by inserting the probe to the desired location and manually observing the sensor output over a time period typically lasting more than a minute. Note that the velocity probe only measures the magnitude of the velocity, not the direction. Indicated velocities were typically oscillatory, except in cases where a constant zero velocity was observed. Because of this unsteady velocity, minimum and maximum velocities were manually reported at each measurement location. In general, constant zero velocities were observed near the walls. In the region between the wall and waste package, the velocity varied from zero to the maximum recorded value. Over the waste package, velocities typically ranged from a non-zero value to the maximum value.

Velocity data are provided in Tables 7.4.1-3 through 7.4.1-8 below. Data were collected in reference to the insertion depth of the probe from the end of the guide tube. Conversion between this datum and the coordinates used in the FLUENT simulations is presented in Appendix C.

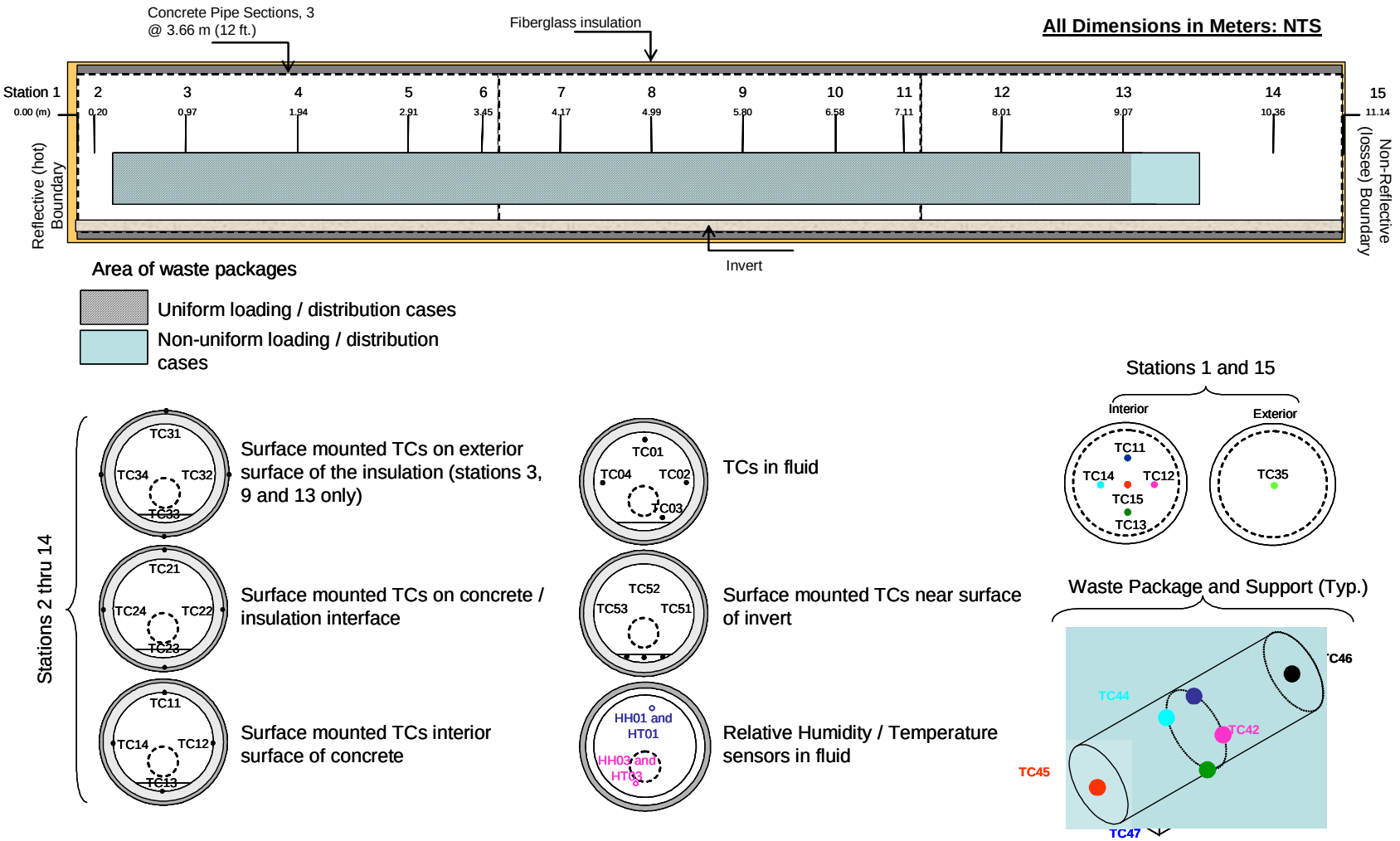

Source: Sánchez 2002 [DIRS 166231], pp. 6-12; [DIRS 166232].

Figure 7.4.1-4. Schematic Depicting Relative Locations of Thermocouples and Relative Humidity Sensors for the Cases without a Drip Shield (Cases 1 and 2)

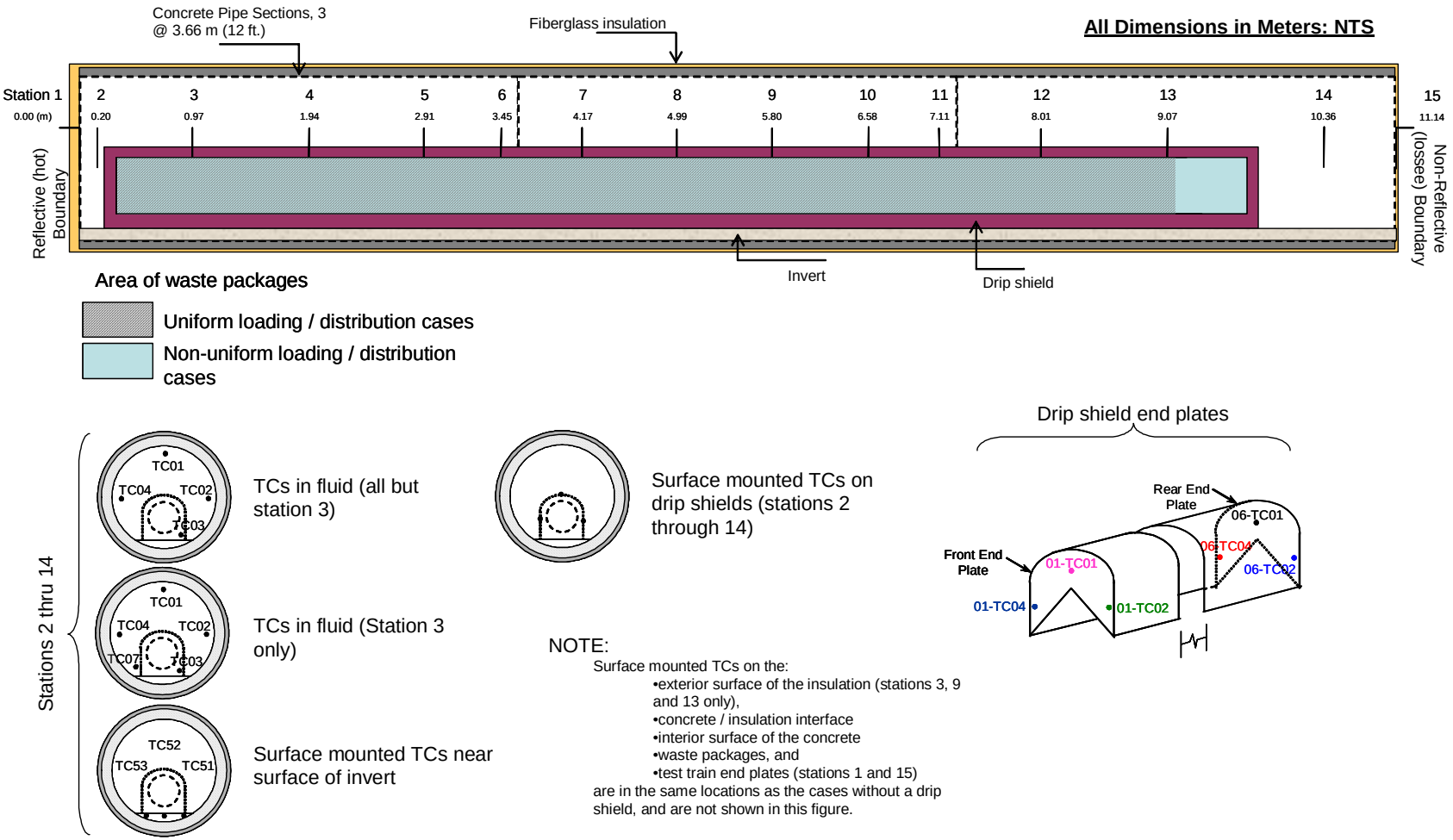

Source: Sánchez 2002, pp. 6-13 [DIRS 166233], [DIRS 166234]

Figure 7.4.1-5. Schematic Depicting Relative Locations of Thermocouples and Relative Humidity Sensors for the Cases with a Drip Shield (Cases 3 and 4)

Table 7.4.1-3. Case 4 Measured Velocities Along the Length of the Test Train

Test Cell Stations 2-14, Top 4/15/02		
Station #	**Measured Air Velocity, M/S**	**Comments**
2	0.076-0.086	Insertion depth : 40 cm
2	0.060-0.078	Insertion depth : 60 cm
3	0.000-0.044	Insertion depth : 60 cm
4	0.000-0.004	Insertion depth : 60 cm
5	0.044-0.056	Insertion depth : 60 cm
5	0.013-0.027	Insertion depth : 40 cm
6	0.017-0.047	Insertion depth : 60 cm
7	0.041-0.047	Insertion depth : 40 cm
7	0.000-0.014	Insertion depth : 60 cm
8	0.000-0.002	Insertion depth : 60 cm
9	0.019-0.047	Insertion depth : 60 cm
10	0	Insertion depth : 60 cm
11	0	Insertion depth : 60 cm
12	0	Insertion depth : 60 cm
12	0	Insertion depth : 40 cm
13	0.059-0.066	Insertion depth : 60 cm
13	0.046-0.061	Insertion depth : 40 cm
14	0.059-0.067	Insertion depth : 40 cm
14	0.079-0.094	Insertion depth : 60 cm

DTN: SN0208F3407102.009 [DIRS 161063].

NOTE: A range of air velocity values indicate oscillation during measurement. All sensor insertion depths are measured from outside edge of guide pipe.

Table 7.4.1-4. Case 4 Measured Velocities at Station 5

Test Cell Station 5 4/16/02		
Sensor Distance in from Outside Edge of Guide Pipe (cm)	**Measured Air Velocity, m/s**	
	Right Rib	**Left Rib**
30	0.000	0.000
35	0.000	0.000
40	0.000	0.000
45	0.000	0.000-0.011
50	0.000	0.000-0.038
55	0.003-0.021	0.000-0.020
60	0.003-0.017	0.000-0.024
65	0.000-0.013	0.001-0.009

DTN: SN0208F3407102.009 [DIRS 161063].

NOTE: A range of air velocity values indicate oscillation during measurement. All sensor insertion depths are measured from outside edge of guide pipe.

Table 7.4.1-5. Case 4 Measured Velocities at Station 11

Test Cell Station 11 4/16/02		
Sensor Distance in from Outside Edge of Guide Pipe (cm)	**Measured Air Velocity, m/s**	
	Right Rib	**Left Rib**
30	0.000	0.000
35	0.000	0.000
40	0.000	0.000
45	0.000	0.000
50	0.000	0.000
55	0.000	0.000
60	0.000	0.000
65	0.000	0.000

DTN: SN0208F3407102.009 [DIRS 161063].

NOTE: A range of air velocity values indicate oscillation during measurement. All sensor insertion depths are measured from outside edge of guide pipe.

Table 7.4.1-6. Case 8 Measured Velocities Along the Length of the Test Train

Test Cell Stations 2-14,Top 4/15/02		
Station #	**Measured Air Velocity, m/s**	**Comments**
2	0.050-0.078	Insertion depth : 100 cm
2	0.063-0.081	Insertion depth : 60 cm
3	0.043-0.056	Insertion depth : 100 cm
4	0.041-0.053	Insertion depth : 100 cm
5	0.067-0.081	Insertion depth : 100 cm
5	0.063-0.074	Insertion depth : 60 cm
6	0.041-0.055	Insertion depth : 100 cm
7	0.043-0.052	Insertion depth : 60 cm
7	0.000	Insertion depth : 100 cm
8	0.000	Insertion depth : 100 cm
9	0.031-0.057	Insertion depth : 100 cm
10	0.000	Insertion depth : 100 cm
11	0.000	Insertion depth : 100 cm
12	0.000	Insertion depth : 100 cm
12	0.000	Insertion depth : 60 cm
13	0.055-0.073	Insertion depth : 100 cm
13	0.046-0.063	Insertion depth : 60 cm
14	0.006-0.042	Insertion depth : 100 cm
14	0.000-0.002	Insertion depth : 60 cm

DTN: SN0208F3407102.009 [DIRS 161063].

NOTE: A range of air velocity values indicate oscillation during measurement. All sensor insertion depths are measured from outside edge of guide pipe.

Table 7.4.1-7. Case 8 Measured Velocities at Station 5

Test Cell Station 5 4/16/02		
Sensor Distance in from Outside Edge of Guide Pipe (cm)	**Measured Air Velocity, m/s**	
	Right Rib	**Left Rib**
40	0.000	0.000-0.023
45	0.000	0.000-0.002
50	0.000	0.000-0.001
60	0.000-0.032	0.000-0.025
80	0.040-0.059	0.018-0.046
100	0.001-0.057	0.020-0.053
120	0.000-0.018	0.000-0.043
130	0.000-0.046	-
140	-	0.019-0.047
160	-	0.000-0.007

DTN: SN0208F3407102.009 [DIRS 161063].

NOTE: A range of air velocity values indicate oscillation during measurement. All sensor insertion depths are measured from outside edge of guide pipe.

Table 7.4.1-8. Case 8 Measured Velocities at Station 7

Test Cell Station 7 4/16/02		
Sensor Distance in from Outside Edge of Guide Pipe (cm)	**Measured Air Velocity, m/s**	
	Right Rib	**Left Rib**
40	0.000	0.045-0.051
45	0.000	0.000
50	0.001-0.041	0.000
60	0.000-0.049	0.000
80	0.000-0.005	0.000
100	0.000	0.000
120	0.000	0.000-0.002
130	0.000-0.009	0.000-0.040

DTN: SN0208F3407102.009 [DIRS 161063].

NOTE: A range of air velocity values indicate oscillation during measurement. All sensor insertion depths are measured from outside edge of guide pipe.

Sensor Naming Convention

Sensor designations were made such that the test, sensor type, and sensor location could be determined from the name of each sensor. The naming convention is as follows:

Nx(S,P,M)yy-(TC, HH, HT, PW)nn

N = Natural Convection Test
x = H or Q, for quarter or half scale
S = Stationary gauge
M = Movable sensor
P = Package sensor
yy = Station number. For stationary gauges, 01-15 according to position along the test train
TC = Thermocouple
HH = Relative Humidity
HT = Temperature data taken with the relative humidity sensor
PW = Power sensor
nn = gauge location and number

1st n= Location of sensor, varies between 1 and 5

- 0 = Sensor hanging in air
- 1 = Sensor on inside surface of concrete pipe
- 2 = Sensor on outside surface of concrete pipe
- 3 = Sensor on outside surface of insulation
- 4 = Waste package sensor
- 5 = Invert sensor

2nd n = Position of sensor, varies between 1 and 8

- 1 – 4, clockwise from Top Dead Center (TDC) in 90 degree increments, ending at -90 degrees from TDC. Invert sensors are designated 1-right, 2-center, 3-left
- 5 – 6, are center, front and back, respectively
- 7 – 8, are the front and back in cases where additional sensors are installed next to existing sensors.

For example, NHS03-TC11 is a stationary thermocouple sensor for the 44% scale test located on the interior surface of the concrete pipe (top dead center position) at station 3. Data in Appendix C are provided using the sensor naming convention.

There was no set-numbering convention for the drip shield sensors. Table 7.4.1-9 provides the sensor designations and a relative description of the location for the 25% scale tests. Table 7.4.1-10 provides the same information for the 44% scale tests.

Table 7.4.1-9. Relative Locations for the 25% Scale Drip Shield Temperature Sensors

	Sensor Designation	Relative Location
End Plates	NQD06-TC01	Drip shield exterior rear end plate, top position
	NQD06-TC02	Drip shield exterior rear end plate, left position
	NQD07-TC01	Drip shield exterior rear end plate, right position
	NQD01-TC05	Station 2 drip shield exterior front end plate, top position
	NQD01-TC06	Station 2 drip shield exterior front end plate, right side position
	NQD03-TC04	Station 2 drip shield exterior front end plate, left side position
Top	NQD01-TC01	Station 3 drip shield exterior top position
	NQD02-TC01	Station 4 drip shield exterior top position
	NQD02-TC04	Station 5 drip shield exterior top position
	NQD02-TC06	Station 6 drip shield exterior top position
	NQD03-TC01	Station 7 drip shield exterior top position
	NQD03-TC06	Station 8 drip shield exterior top position
	NQD04-TC01	Station 9 drip shield exterior top position
	NQD04-TC02	Station 10 drip shield exterior top position
	NQD05-TC01	Station 11 drip shield exterior top position
	NQD05-TC06	Station 12 drip shield exterior top position
	NQD06-TC04	Station 13 drip shield exterior top position
Right Side	NQD01-TC04	Station 3 drip shield exterior right position
	NQD02-TC02	Station 5 drip shield exterior right position
	NQD03-TC05	Station 7 drip shield exterior right position
	NQD04-TC05	Station 9 drip shield exterior right position
	NQD05-TC02	Station 11 drip shield exterior right position
	NQD06-TC06	Station 13 drip shield exterior right position
Left Side	NQD05-TC05	Station 11 drip shield exterior left position
	NQD06-TC05	Station 13 drip shield exterior left position
	NQD01-TC02	Station 3 drip shield exterior left position
	NQD02-TC05	Station 5 drip shield exterior left position
	NQD03-TC02	Station 7 drip shield exterior left position
	NQD04-TC04	Station 9 drip shield exterior left position

Source: Sánchez 2002 [DIRS 166233], p. 13; Sánchez 2002 [DIRS 166234].

Table 7.4.1-10. Relative Locations for the 44% Scale Drip Shield Temperature Sensors

	Sensor Designation	Relative Location
End Plates	NHD01-TC01	Station 2 drip shield exterior front end plate, top position
	NHD01-TC02	Station 2 drip shield exterior front end plate, right side position
	NHD01-TC04	Station 2 drip shield exterior front end plate, left side position
	NHD06-TC01	Station 14 drip shield exterior rear end plate, top position
	NHD06-TC02	Station 14 drip shield exterior rear end plate, right side position
	NHD06-TC04	Station 14 drip shield exterior rear end plate, left side position
Top	NHD02-TC01	Station 3 drip shield exterior top position
	NHD02-TC02	Station 4 drip shield exterior top position
	NHD02-TC04	Station 5 drip shield exterior top position
	NHD03-TC01	Station 7 drip shield exterior top position
	NHD03-TC02	Station 6 drip shield exterior top position
	NHD03-TC04	Station 8 drip shield exterior top position
	NHD07-TC01	Station 9 drip shield exterior top position
	NHD05-TC01	Station 12 drip shield exterior top position
	NHD05-TC06	Station 13 drip shield exterior top position
	NHD07-TC05	Station 10 drip shield exterior top position
	NHD07-TC06	Station 11 drip shield exterior top position
Right Side	NHD01-TC05	Station 3 drip shield exterior right position
	NHD02-TC05	Station 5 drip shield exterior right position
	NHD03-TC05	Station 7 drip shield exterior right position
	NHD07-TC02	Station 9 drip shield exterior right position
	NHD05-TC02	Station 11 drip shield exterior right position
	NHD06-TC06	Station 13 drip shield exterior right position
Left Side	NHD01-TC06	Station 3 drip shield exterior left position
	NHD02-TC06	Station 5 drip shield exterior left position
	NHD03-TC06	Station 7 drip shield exterior left position
	NHD07-TC04	Station 9 drip shield exterior left position
	NHD05-TC04	Station 11 drip shield exterior left position
	NHD06-TC05	Station 13 drip shield exterior left position

Source: Sánchez 2002 [DIRS 166237], p. 13; Sánchez 2002 [DIRS 166238].

Experiment Layout

The tests that most closely represent the repository during the post-closure period were those having a drip shield, and where the waste packages were distributed non-uniformly along the length of the test train and were powered with non-uniform loads (Cases 4 and 8). This configuration causes the most complex heat transfer within the test train of all the cases, and was chosen to be presented in this report as validation of the ability of FLUENT to adequately model the repository. The two cases differ only by their relative scale (25 and 44% scales). In addition, the geometry for Cases 1 and 5 that are for uniform line load without a drip shield are included for reference by Appendix B. Figures 7.4.1-6 through 7.4.1-9 provide schematics of the cases (BSC 2002 [DIRS 158192], pp. 21 and 25). The CFD simulations are based on these layouts.

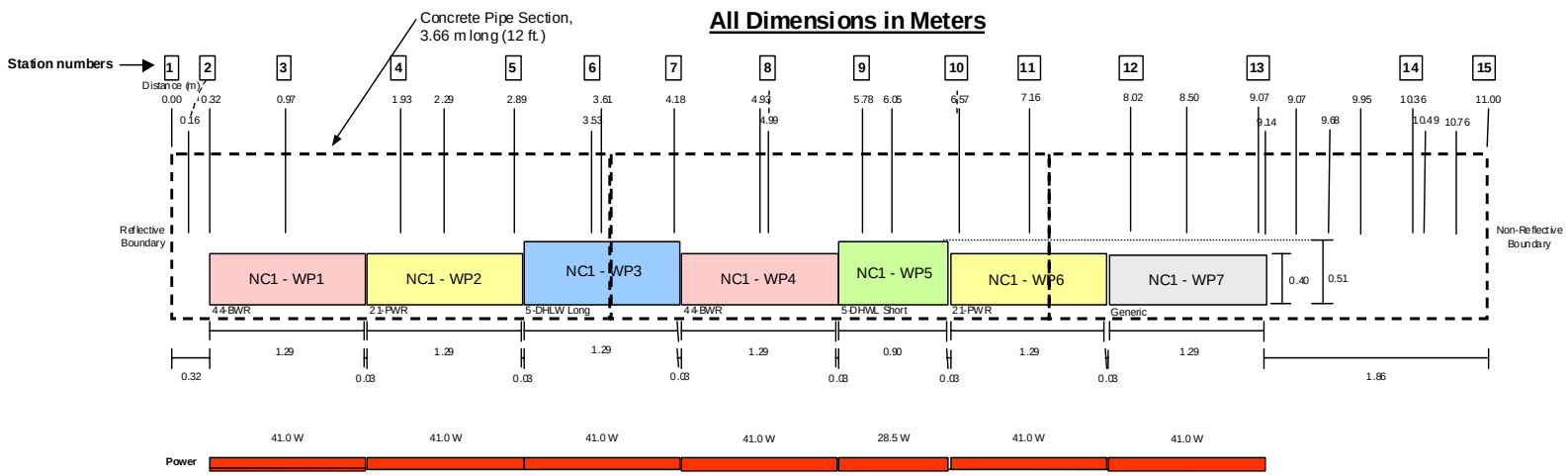

Source: BSC 2002 [DIRS 158192], p. 18.

NOTE: Packages uniformly powered and uniformly spaced in test train, without a drip shield.

Figure 7.4.1-6. Design Layout and Power for Case 1

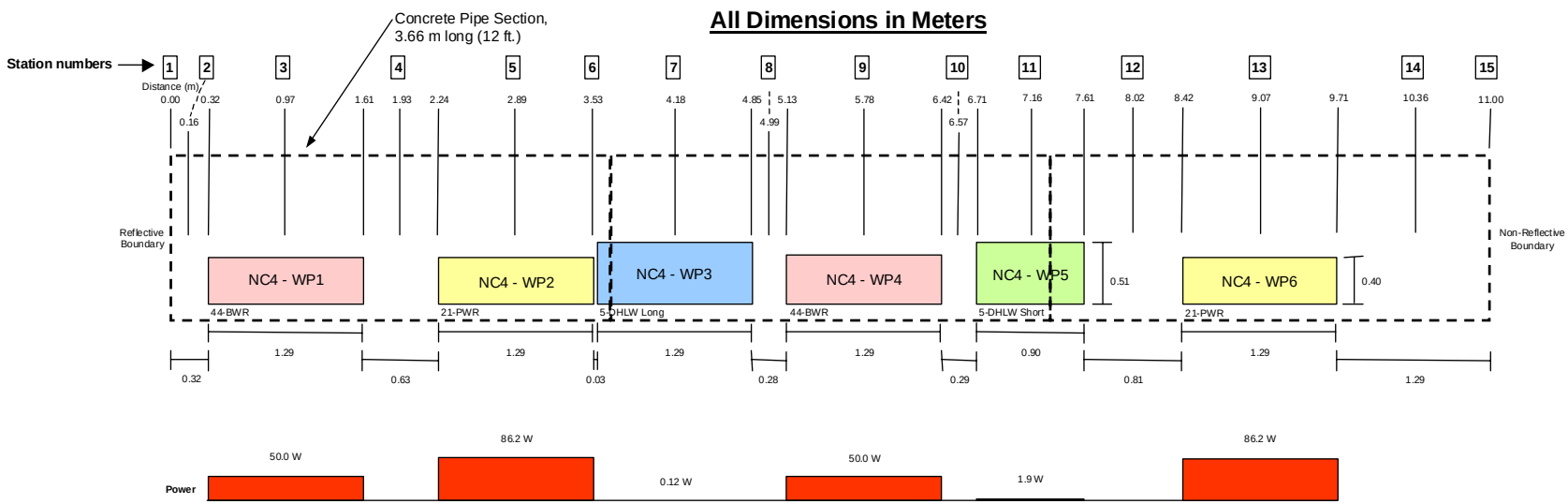

Source: BSC 2002 [DIRS 158192], p. 21.

NOTE: Packages non-uniformly powered and non-uniformly spaced in test train, with a drip shield. An inverted V shaped end plate is placed on both ends of the drip shield. The drip shield is made up of carbon steel. It starts at Station 2 and ends at Station 14.

Figure 7.4.1-7. Design Layout and Power for Case 4

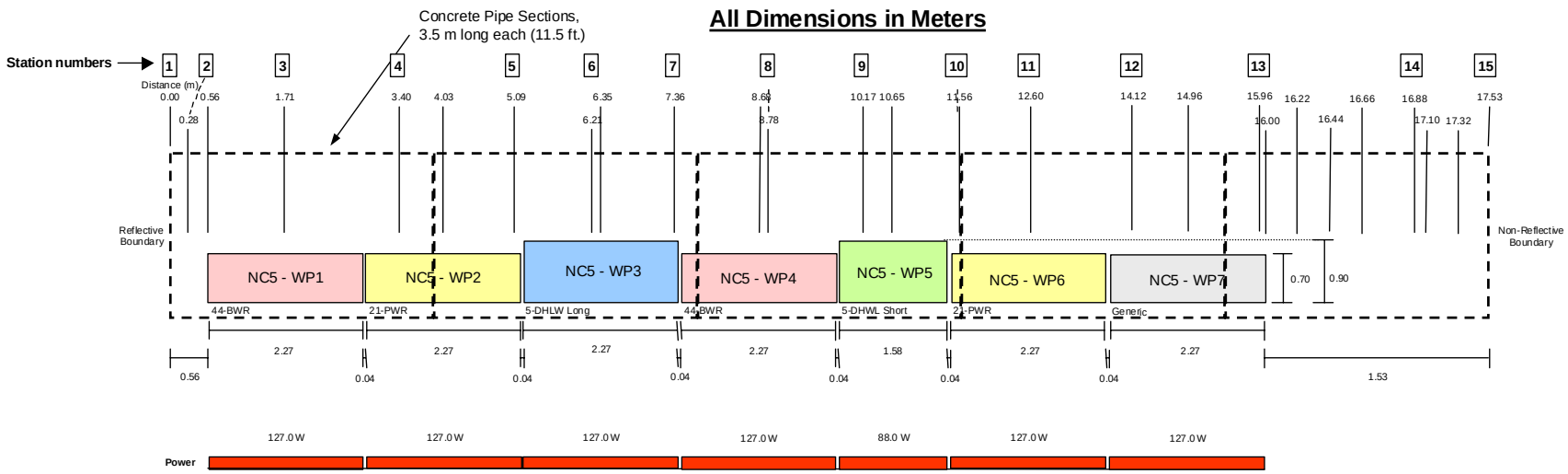

Source: BSC 2002 [DIRS 158192], p. 22.

NOTE: Packages uniformly powered and uniformly spaced in test train, without a drip shield.

Figure 7.4.1-8. Design Layout and Power for Case 5

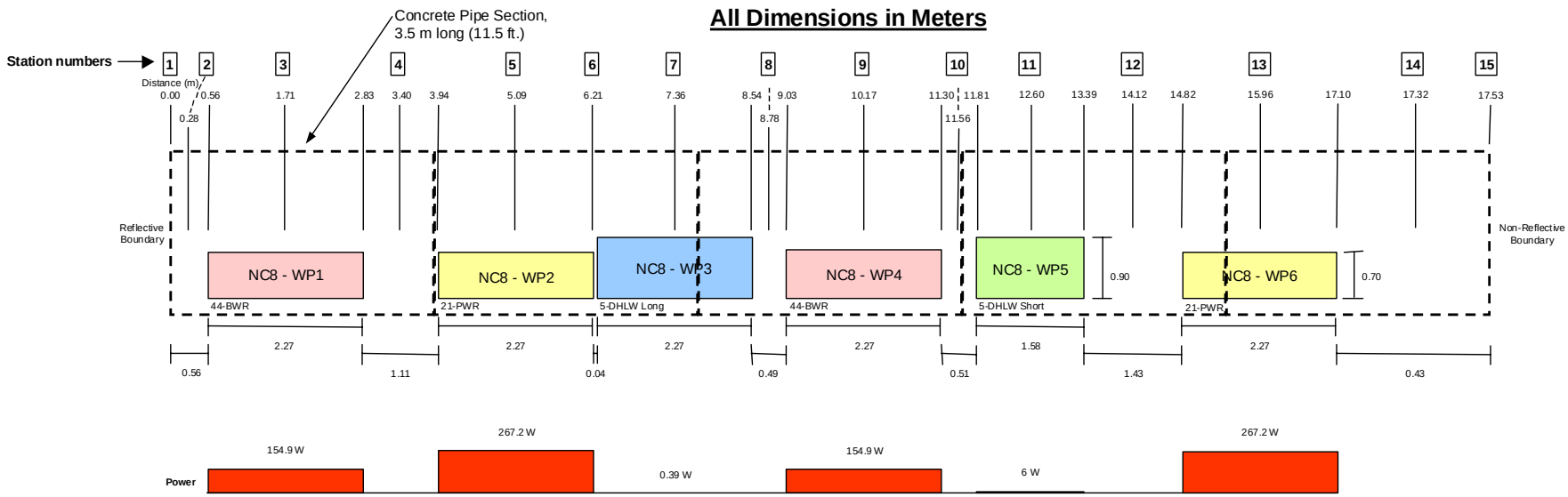

Source: BSC 2002 [DIRS 158192], p. 25.

NOTE: Packages non-uniformly powered and non-uniformly spaced in test train, with a drip shield. An inverted V shaped end plate is placed on both ends of the drip shield. The drip shield is made up of carbon steel. It starts at Station 2 and ends at Station 14 (note that the schematic is not to scale – in particular, the distance between Stations 14 and 15).

Figure 7.4.1-9. Design Layout and Power for Case 8

Experimental Results

All test data are available from the YMP Automated Technical Data Tracking System which is a master indexing sub-system of the Technical Data Management System. The data tracking number (DTN) for each data set is provided in Table 7.4.1-11.

Table 7.4.1-11. DTN Numbers for Data from the Scale Natural Convection Tests

Data	YMP Data Tracking Number (DTN)
Case 4	SN0208F3407102.004 [DIRS 161056]
Velocity Profiles for 25% Scale Cases	SN0208F3407102.009 [DIRS 161063]
Case 8	SN0208F3407102.008 [DIRS 161062]
Velocity Profiles for 44% Scale Cases	SN0208F3407102.009 [DIRS 161063]

Each test ran for a period of two to four weeks, and all data, with the exception of the velocity profiles, were collected continuously. The fluid velocity was manually measured at selected stations once during each test.

A three-day period of data was chosen as representative of steady-state conditions for each case. An extended period was used in order to minimize the effects of diurnal variations as well as changing atmospheric conditions (i.e., changes in ambient conditions due to weather patterns.) Figure 7.4.1-10 shows the temperature variations on the exterior surface of the insulation for Case 8. The graph shows both day-to-day weather related trends and diurnal variations. Reviews of the data showed there were lags of approximately 24 hours for external temperature variations to affect the inner temperatures of the test train. Using an averaging period of several times the associated time lag reduces the sensitivity of the relationship between the conditions within the test train to the test environment. Table 7.4.1-12 gives a summary of relevant dates for each case.

Table 7.4.1-12. Averaging Periods for Cases 4 and 8

Case	Test Start Date	Test End Date	Data Analysis Dates	Velocity and Temperature Profile Data
4	3/12/02	4/17/02	4/7 – 4/10	4/15 – 4/16
8	3/20/02	4/17/02	4/12 – 4/15	4/15 – 4/16

DTN: SN0307T057803.001.

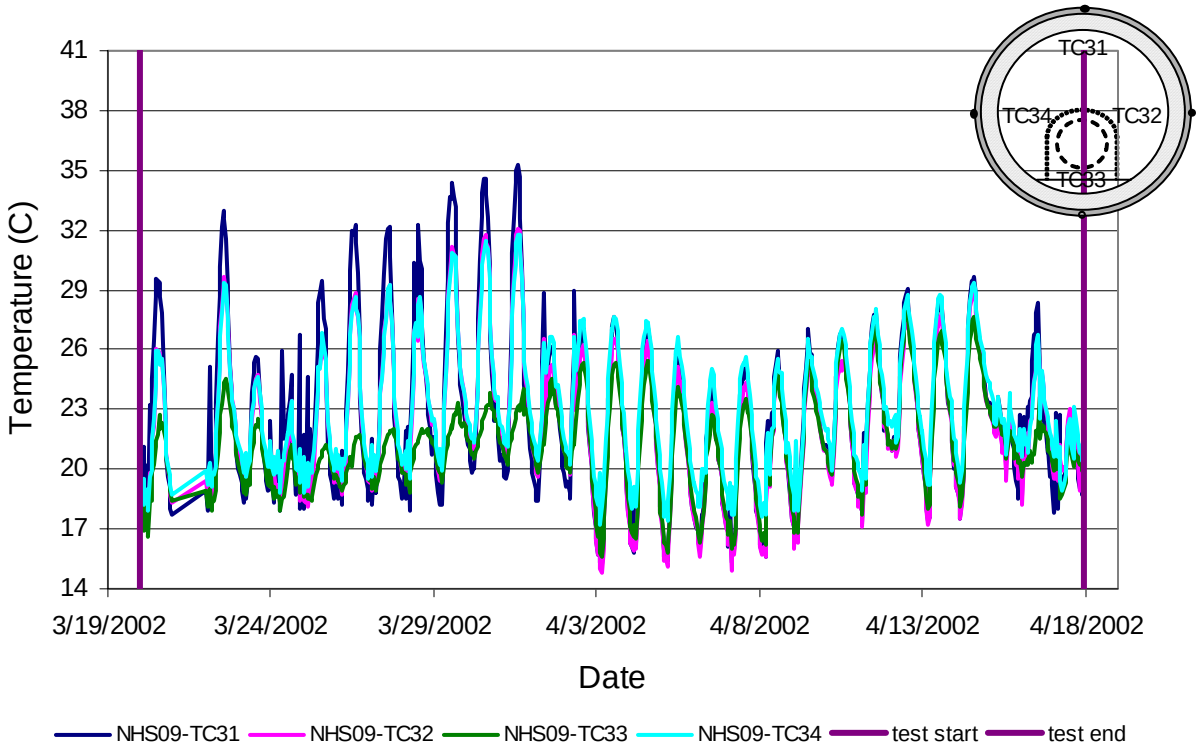

DTN: SN0208F3407102.008 [DIRS 161062].

Figure 7.4.1-10. Example of Variations Recorded in Ambient Temperatures (Case 8)

Atmospheric Conditions

Ambient temperature and relative humidity were monitored throughout the tests. In addition to these sensors, 14 TC sensors were located on the exterior surfaces of the test, 12 on the exterior surface of the insulation (four each at stations 3, 9, and 13), and one on either end plate. Sensors on the exterior surface of the test train closely followed the ambient temperature trend, but were generally 1 to 1.5 degrees above the measured ambient temperature.

Daily oscillations of 10 to 20ºC were typical throughout the tests, with the average ambient temperature varying about 5ºC over the test duration due to changing weather patterns. Figure 7.4.1-11 shows the ambient temperature, average 24-hr temperature and relative humidity for a typical case (Case 8).

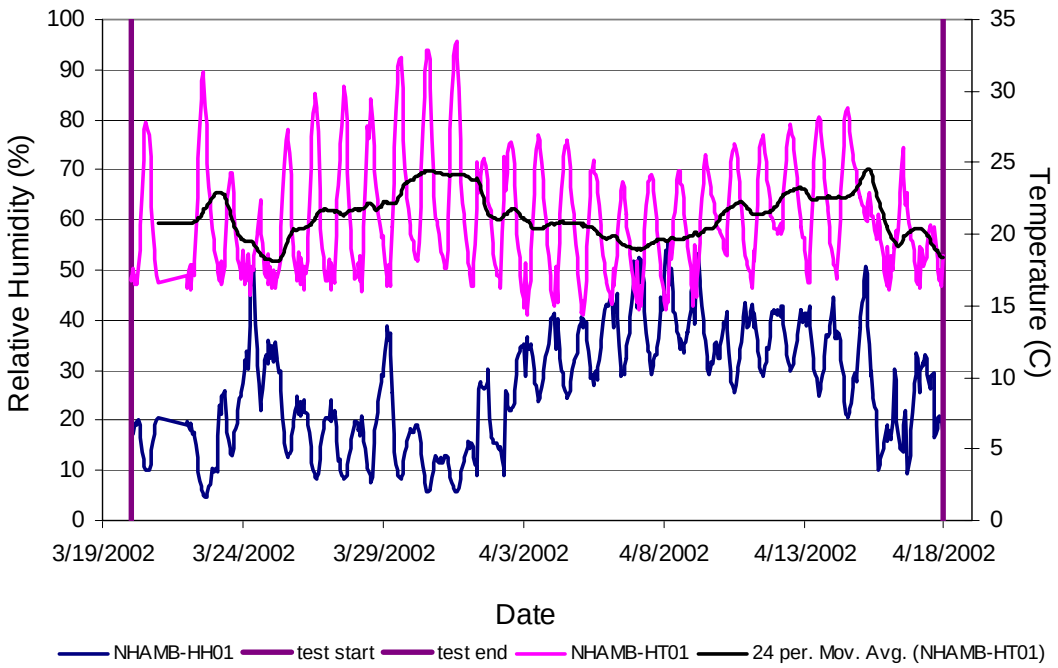

DTN SN0208F3407102.008 [DIRS 161062].

Figure 7.4.1-11. Typical Changes in Ambient Conditions (Case 8)

Temperatures

The following section includes tabulated temperature data for each of the cases. Tables 7.4.1-13 through 7.4.1-18 are for Case 4, while Tables 7.4.1-19 through 7.4.1-24 are for Case 8. The temperatures reported are the average temperatures over the three-day periods shown in Table 7.4.1-12. The data are presented graphically as comparisons to the simulation results in Section 7.4.3. Standard deviations of the data for this same period are also provided. The averages and standard deviations were calculated using standard EXCEL functions. These calculations are provided in Appendix C.

Case 4 Temperatures

Table 7.4.1-13. Case 4 Average Waste Package Temperatures, C

	WP	1	2	3	4	5	6
Top	Temp	32.3	34.6	28.2	31.6	27.6	33.3
	Std Dev.	0.2	0.4	0.2	0.3	0.2	0.3
Right	Temp	32.3	34.0	27.9	31.3	27.4	32.9
	Std Dev.	0.3	0.3	0.2	0.3	0.2	0.4
Bottom	Temp	31.9	34.0	27.5	30.9	27.2	33.7
	Std Dev.	0.2	0.4	0.3	0.4	0.3	0.3
Left	Temp	31.9	33.9	27.9	31.3	27.5	33.1
	Std Dev.	0.3	0.3	0.3	0.3	0.2	0.3
Front Plate	Temp	31.8	33.6	29.8	30.6	28.0	32.7
	Std Dev.	0.2	0.4	0.3	0.3	0.2	0.3
Back Plate	Temp	32.2	34.2	28.2	30.8	27.6	32.0
	Std Dev.	0.2	0.3	0.3	0.3	0.2	0.3

DTN: SN0307T0507803.001. Case 4 temp data Stations 2 thru 8.xls.

Table 7.4.1-14. Case 4 Average Concrete Inner Surface Temperatures, C

	Top		Right		Bottom		Left	
Station	**Temp**	**Std Dev.**	**Temp**	**Std Dev.**	**Temp**	**Std Dev.**	**Temp**	**Std Dev.**
2	27.4	0.3	26.8	0.2	25.9	0.3	27.0	0.2
3	26.9	0.3	26.7	0.2	25.5	0.3	26.6	0.3
4	26.7	0.3	26.7	0.3	25.4	0.3	26.6	0.3
5	26.6	0.2	26.0	0.2	25.0	0.3	26.3	0.3
6	26.4	0.3	26.1	0.2	24.6	0.3	26.1	0.2
7	26.3	0.2	26.1	0.3	24.5	0.3	26.0	0.3
8	26.7	0.2	26.6	0.3	25.6	0.3	26.6	0.3
9	27.0	0.3	26.7	0.3	25.9	0.4	26.8	0.3
10	26.8	0.3	26.6	0.3	25.8	0.3	26.7	0.3
11	26.9	0.2	26.8	0.2	25.9	0.2	26.7	0.3
12	27.1	0.2	27.0	0.3	26.2	0.3	26.8	0.3
13	27.6	0.3	27.3	0.3	26.7	0.4	27.2	0.4
14	27.1	0.3	N/A	N/A	25.5	0.3	26.5	0.3

DTN: SN0307T0507803.001. Case 4 temp data Stations 2 thru 8.xls and Case 4 temp data Stations 9 thru 15.xls.

Table 7.4.1-15. Case 4 Average Concrete Outer Surface Temperatures, C

	Top		Right		Bottom		Left	
Station	**Temp**	**Std Dev.**	**Temp**	**Std Dev.**	**Temp**	**Std Dev.**	**Temp**	**Std Dev.**
2	26.8	0.4	26.3	0.4	25.5	0.3	26.5	0.4
3	26.2	0.4	26.1	0.4	25.0	0.3	26.1	0.4
4	24.8	0.9	26.2	0.2	24.7	0.4	26.1	0.3
5	25.4	0.5	25.8	0.2	24.5	0.3	25.5	0.3
6	25.4	0.4	25.7	0.2	24.0	0.4	25.4	0.2
7	25.4	0.3	25.5	0.4	24.2	0.5	25.5	0.3
8	26.1	0.3	26.0	0.3	25.2	0.3	26.0	0.4
9	26.5	0.3	26.1	0.3	25.5	0.3	26.2	0.4
10	26.3	0.3	26.1	0.3	25.2	0.5	26.2	0.4
11	26.4	0.2	26.2	0.2	25.6	0.2	26.2	0.2
12	26.5	0.3	26.4	0.4	25.9	0.3	26.4	0.3
13	27.1	0.3	26.9	0.3	26.3	0.3	26.7	0.3
14	26.5	0.3	N/A	N/A	25.2	0.3	25.9	0.3

DTN: SN0307T0507803.001. Case 4 temp data Stations 2 thru 8.xls and Case 4 temp data Stations 9 thru 15.xls.

Table 7.4.1-16. Case 4 Average Air Temperatures Inside Test Train, C

	Top		Right		Bottom		Left	
Station	**Temp**	**Std Dev.**	**Temp**	**Std Dev.**	**Temp**	**Std Dev.**	**Temp**	**Std Dev.**
2	27.7	0.5	27.4	0.5	28.6	0.2	27.4	0.4
3	27.4	0.2	27.3	0.2	29.3	0.2	27.2	0.3
4	27.3	0.2	27.2	0.3	27.5	0.3	27.2	0.3
5	27.1	0.2	26.9	0.2	29.0	0.2	26.8	0.2
6	27.0	0.3	26.7	0.3	28.6	0.2	26.7	0.2
7	26.8	0.3	26.6	0.3	27.3	0.3	26.5	0.2
8	27.3	0.3	27.1	0.3	28.4	0.3	27.1	0.4
9	27.4	0.3	27.2	0.3	29.1	0.5	27.2	0.3
10	27.3	0.3	27.1	0.3	28.1	0.4	27.1	0.4
11	27.1	0.4	27.0	0.4	27.8	0.5	26.9	0.5
12	27.5	0.2	27.4	0.3	28.3	0.2	27.4	0.2
13	27.9	0.4	27.7	0.3	30.0	0.3	27.7	0.4
14	27.3	0.3	27.1	0.3	27.0	0.3	26.9	0.3

DTN: SN0307T0507803.001. Case 4 temp data Stations 2 thru 8.xls and Case 4 temp data Stations 9 thru 15.xls.

Table 7.4.1-17. Case 4 Average Invert Temperatures, C

	Right		Center		Left	
Station	**Temp**	**Std Dev.**	**Temp**	**Std Dev.**	**Temp**	**Std Dev.**
2	27.6	0.2	27.9	0.2	27.5	0.4
3	27.6	0.2	28.9	0.3	27.5	0.3
4	27.2	0.3	28.3	0.3	27.3	0.3
5	27.4	0.2	29.1	0.2	27.2	0.2
6	26.9	0.2	28.6	0.2	26.9	0.2
7	26.5	0.4	26.9	0.3	26.3	0.3
8	27.3	0.3	27.6	0.3	27.4	0.5
9	27.4	0.4	28.9	0.3	27.5	0.3
10	27.2	0.3	27.7	0.5	27.2	0.4
11	26.9	0.2	27.5	0.3	27.2	0.2
12	27.4	0.5	28.0	0.3	27.5	0.3
13	28.3	0.3	30.6	0.2	28.4	0.3
14	26.6	0.3	26.5	0.4	26.5	0.5

DTN: SN0307T0507803.001. Case 4 temp data Stations 2 thru 8.xls and Case 4 temp data Stations 9 thru 15.xls.

Table 7.4.1-18. Case 4 Average Drip Shield Temperatures, C

Station	TOP SENSORS	Average Temp	LEFT SENSORS	Average Temp	RIGHT SENSORS	Average Temp
3	NQD01-TC01	28.9	NQD01-TC02	28.2	NQD01-TC04	28.4
4	NQD02-TC01	28.5				
5	NQD02-TC04	29.4	NQD02-TC05	28.4	NQD02-TC02	28.5
6	NQD02-TC06	29.1				
7	NQD03-TC01	27.6	NQD03-TC02	26.9	NQD03-TC05	27.0
8	NQD03-TC06	27.4				
9	NQD04-TC01	28.3	NQD04-TC04	27.7	NQD04-TC05	27.4
10	NQD04-TC02	27.6				
11	NQD05-TC01	27.3	NQD05-TC05	26.8	NQD05-TC02	26.8
12	NQD05-TC06	27.6				
13	NQD06-TC04	28.5	NQD06-TC05	27.5	NQD06-TC06	27.5

DTN: SN0307T0507803.001. Case 4 Power and drip shield temp data.xls.

Case 8 Temperatures

Table 7.4.1-19. Case 8 Average Waste Package Temperatures, C

	WP	1	2	3	4	5	6
Top	Temp	33.5	35.9	30.2	33.9	29.9	36.4
	Std Dev.	0.2	0.2	0.2	0.4	0.3	0.3
Right	Temp	33.2	35.3	29.7	33.7	29.7	35.7
	Std Dev.	0.2	0.2	0.2	0.3	0.3	0.3
Bottom	Temp	33.4	36.1	29.2	33.7	29.4	36.0
	Std Dev.	0.2	0.3	0.2	0.3	0.2	0.3
Left	Temp	33.2	35.8	29.6	33.6	29.7	36.3
	Std Dev.	0.2	0.3	0.3	0.3	0.2	0.3
Front Plate	Temp	32.5	35.5	33.4	33.2	30.6	35.3
	Std Dev.	0.3	0.3	0.2	0.3	0.2	0.3
Back Plate	Temp	32.4	36.0	30.4	32.9	30.1	34.1
	Std Dev.	0.3	0.3	0.3	0.3	0.2	0.3

DTN: SN0307T0507803.001. Case 8 temp data Stations 2 thru 8 and WP temp data.xls.

Table 7.4.1-20. Case 8 Average Concrete Inner Surface Temperatures, C

	Top		Right		Bottom		Left	
Station	**Temp**	**Std Dev.**	**Temp**	**Std Dev.**	**Temp**	**Std Dev.**	**Temp**	**Std Dev.**
1								
2	27.9	0.3	27.6	0.3	25.4	0.3	27.6	0.3
3	28.6	0.2	28.4	0.3	26.1	0.3	28.5	0.3
4	28.4	0.3	28.3	0.4	26.1	0.4	28.4	0.4
5	28.8	0.3	28.6	0.3	26.4	0.4	28.7	0.2
6	28.5	0.3	28.3	0.3	N/A	N/A	28.4	0.3
7	28.3	0.3	28.0	0.3	25.5	0.3	28.2	0.3
8	27.8	0.2	27.7	0.3	25.3	0.3	27.7	0.3
9	27.9	0.2	27.7	0.3	25.5	0.3	27.8	0.2
10	27.7	0.3	27.5	0.3	25.4	0.3	27.7	0.3
11	27.2	0.4	27.0	0.4	25.0	0.3	27.1	0.3
12	27.2	0.3	27.1	0.3	N/A	N/A	27.2	0.3
13	27.7	0.3	27.5	0.3	25.2	0.3	27.6	0.3
14	27.4	0.4	N/A	N/A	24.9	0.4	27.2	0.3

DTN: SN0307T0507803.001. Case 8 temp data Stations 2 thru 8 and WP temp data.xls and Case 8 temp data Stations 9 thru 15.xls.

Table 7.4.1-21. Case 8 Average Concrete Outer Surface Temperatures, C

	Top		Right		Bottom		Left	
Station	**Temp**	**Std Dev.**	**Temp**	**Std Dev.**	**Temp**	**Std Dev.**	**Temp**	**Std Dev.**
2	27.2	0.5	27.0	0.3	25.0	0.6	27.2	0.3
3	27.9	0.4	27.8	0.4	25.7	0.4	28.0	0.3
4	27.9	0.4	27.8	0.3	25.8	0.5	27.9	0.4
5	28.2	0.3	27.9	0.4	25.5	0.9	28.1	0.3
6	27.7	0.4	27.7	0.4	25.5	0.3	27.8	0.3
7	27.6	0.4	27.5	0.4	25.3	0.4	27.7	0.3
8	27.0	0.4	26.9	0.4	24.9	0.4	27.2	0.4
9	27.3	0.3	27.0	0.4	25.0	0.4	27.2	0.3
10	26.9	0.4	26.9	0.4	25.2	0.4	27.2	0.3
11	26.6	0.4	26.4	0.4	24.7	0.4	26.7	0.4
12	26.7	0.4	26.6	0.4	24.7	0.4	26.7	0.4
13	27.1	0.4	26.8	0.4	24.8	0.4	27.0	0.4
14	26.8	0.4	26.5	0.4	N/A	N/A	26.7	0.4

DTN: SN0307T0507803.001. Case 8 temp data Stations 2 thru 8 and WP temp data.xls and Case 8 temp data Stations 9 thru 15.xls.

Table 7.4.1-22. Case 8 Average Air Temperatures Inside Test Train, C

	Top		Right		Bottom		Left	
Station	**Temp**	**Std Dev.**	**Temp**	**Std Dev.**	**Temp**	**Std Dev.**	**Temp**	**Std Dev.**
2	28.6	0.3	28.0	0.3	28.5	0.3	28.1	0.2
3	29.0	0.3	28.8	0.3	30.5	0.2	28.8	0.3
4	29.0	0.4	28.9	0.4	28.1	0.4	28.8	0.4
5	29.1	0.3	29.0	0.3	31.3	0.3	29.0	0.3
6	29.0	0.2	28.8	0.2	29.8	0.2	28.9	0.2
7	28.9	0.3	28.7	0.3	29.4	0.3	28.7	0.3
8	28.3	0.3	28.2	0.2	29.7	0.2	28.2	0.2
9	28.4	0.2	28.2	0.3	30.6	0.3	28.3	0.3
10	28.2	0.3	28.1	0.3	29.6	0.2	28.2	0.3
11	28.2	0.3	28.0	0.3	29.1	0.3	28.1	0.3
12	27.8	0.3	27.8	0.3	28.8	0.3	27.8	0.3
13	28.2	0.3	28.0	0.3	30.8	0.3	28.0	0.3
14	27.9	0.3	27.8	0.3	28.5	0.3	27.8	0.4

DTN: SN0307T0507803.001. Case 8 temp data Stations 2 thru 8 and WP temp data.xls and Case 8 temp data Stations 9 thru 15.xls.

Table 7.4.1-23. Case 8 Average Invert Temperatures, C

	Right		Center		Left	
Station	**Temp**	**Std Dev.**	**Temp**	**Std Dev.**	**Temp**	**Std Dev.**
2	27.1	0.3	28.3	0.3	27.4	0.3
3	28.1	0.3	30.4	0.3	28.5	0.3
4	28.2	0.3	29.7	0.4	28.5	0.3
5	28.7	0.2	32.5	0.2	28.8	0.2
6	28.3	0.2	29.6	0.3	28.2	0.2
7	27.8	0.3	28.7	0.3	28.1	0.3
8	27.7	0.2	29.4	0.2	27.7	0.2
9	27.8	0.3	30.5	0.2	27.9	0.2
10	27.5	0.3	29.2	0.3	27.6	0.3
11	27.2	0.4	28.2	0.3	27.1	0.3
12	26.9	0.3	28.3	0.3	27.4	0.3
13	27.5	0.3	31.3	0.3	28.2	0.3
14	27.0	0.4	27.8	0.4	27.2	0.4

DTN: SN0307T0507803.001. Case 8 temp data Stations 2 thru 8 and WP temp data.xls and Case 8 temp data Stations 9 thru 15.xls.

Table 7.4.1-24. Case 8 Average Drip Shield Temperatures, C

	Top Sensor		Left Sensor		Right Sensor	
Station	Average Temp	Std. Dev.	Average Temp	Std. Dev.	Average Temp	Std. Dev.
3	29.9	0.2	28.9	0.2	28.7	0.3
4	29.5	0.2				
5	30.5	0.2	29.4	0.3	29.2	0.2
6	30.8	0.2				
7	29.6	0.2	28.8	0.3	28.6	0.3
8	29.5	0.3				
9	30.4	0.3	29.6	0.3	29.4	0.3
10	29.6	0.3				
11	29.2	0.4	28.4	0.3	28.2	0.3
12	29.1	0.3				
13	30.6	0.4	29.2	0.3	29.1	0.4

DTN: SN0307T0507803.001. Case 8 temp data Stations 2 thru 8 and WP temp data.xls and Case 8 temp data Stations 9 thru 15.xls.

Power

Review of the data shows that the power input was maintained at a reasonably constant value over the test duration as indicated by the standard deviations in Table 7.4.1-25. As a check to determine how steady the values were, simple statistics were performed on the data. Average values and standard deviations were calculated for a representative period of time using standard EXCEL functions (Appendix C). The time periods discussed previously were used for these calculations. Table 7.4.1-25 summarizes the results.

Table 7.4.1-25. Measured Power Input from Test Cases 4 and 8

	WP	Design Value, W	Average Measured Power, W	Standard Deviation, W
Case 4	1	50	52.2	3.18
	2	86.2	82.3	3.64
	3	0.12	0	0.00
	4	50	48.83	2.93
	5	1.9	2.77	0.59
	6	86.2	88.27	3.94
Case 8	1	154.9	153.35	7.96
	2	267.2	272.49	10.07
	3	0.39	0.00	0.00
	4	154.9	159.32	7.84
	5	6	7.37	1.99
	6	267.2	269.84	11.19

DTN: SN0307T0507803.001 Case 8 Power and drip shield temp data.xls; BSC 2002 [DIRS 158192], Table 5.

Velocity

Air velocity data for the annulus between the waste package (or drip shield, if present) and drift wall were collected after steady state was reached for each test. The air velocity profiles were measured by traversing selected locations in the test section with a velocity probe. Stations were selected based on the waste package layout and heat distribution of the tests. Velocity profiles along the length of the test were also measured for the cases. Data are presented in Tables 7.4.1-3 through 7.4.1-8. The position axis was adjusted to match the simulation coordinate system (Appendix C).

7.4.2 CFD Simulations

Simulation Description for the ¼-Scale Natural Convection Tests

CFD simulations for each of the experimental cases were developed to perform blind calculations. The analysis used anticipated boundary conditions. Because the actual boundary conditions varied from those used in the blind simulation calculations, a direct comparison to the experimental results was impractical. Upon completion of the tests, the blind simulations were adjusted to better reflect the operating conditions of the experiment.

Grid independence checks were performed using the blind simulation grids, while verification of the simulations was completed by comparing calculational results from the post-test simulations with experimental data. Because the blind and post-test simulation results are used to show confidence in the convection model, descriptions for both are discussed, including information about the physical models, grid specifications, thermal properties, boundary and operating conditions, and simulation settings and parameters. The validation results are presented in this section. The grid checks are presented in Appendix B.

Geometric Layout

Dimensions used while constructing the simulations were the nominal or planned values for the experiment. The overall layout for the two cases is identical with the exception of the scale and the space between the drip shield and the “cold” end of the test train. Figures 7.4.1-7 and 7.4.2-1 depict the dimensions for the concrete pipe, heat sources, insulation layer, and invert height for the 25% scale test (Case 4). Figures 7.4.1-9 and 7.4.2-2 show the same information for the 44% scale test (Case 8).

The concrete, insulation, waste packages and invert are simulated as solids, while the drip shield is simulated as a zero-thickness wall. The air is simulated as a non-participating incompressible ideal gas. Properties and boundary conditions are presented later in this section.

It is noted that neither the steel waste package pallets nor the steel rail system for emplacing the waste packages/pallets is included in the CFD simulations. The waste package pallets supported the waste packages at four discrete contact points (Figure 7.4.1-2), minimizing heat transfer from the packages to the pallets via conduction. Omission of this mode of heat transfer within the test train has a negligible impact on the calculational results. The end plates of the pallets were formed from ¼-inch thick steel plate, and the sides of the pallets were formed using two pieces of 1-inch steel bar stock (Howard 2002 [DIRS 161009], pp. 27-28). The small thickness of the

endplates and the gap between the edge pieces allowed the air to move freely around the waste package for those cases without a drip shield. Not including them in the simulations has little impact on the results. The drip shields were emplaced using the outer rails (Figure 7.4.1-2) after the waste packages were installed. When emplaced, the sides of the drip shield were close to the edges of the pallet. The pallet end plates filled a portion of the cross-sectional area between the drip shields, effectively restricting horizontal axial fluid flow (and thus, energy transfer) below the waste packages. Fluid could move freely vertically up around the waste packages, and once above the pallet endplates could move horizontally under the drip shield.

Omission of the support rails in the invert is considered to be the biggest deviation between the experimental set-up and the CFD simulations. The steel rails were on top of the invert material, allowing the highly conductive material to transfer energy directly into the invert. Effects from omitting this heat transfer mechanism from the simulations are discussed when the data are compared to the simulation results.

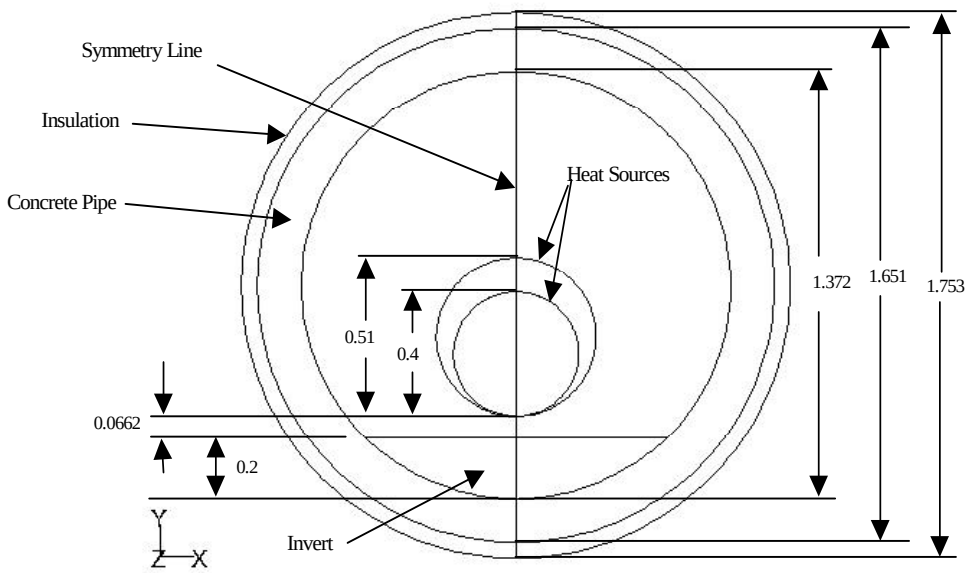

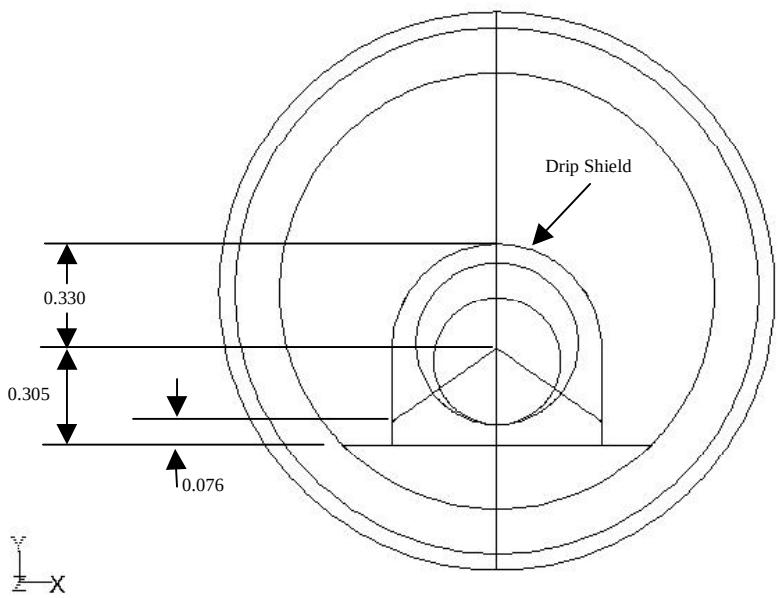

Source: Howard 2002 [DIRS 161009], pp. 27 and 34; BSC 2002 [DIRS 158192].

NOTE: All dimensions are in meters. Dimensions converted from inches.

Figure 7.4.2-1. Cross-Sectional Dimensions for Case 4 Simulations

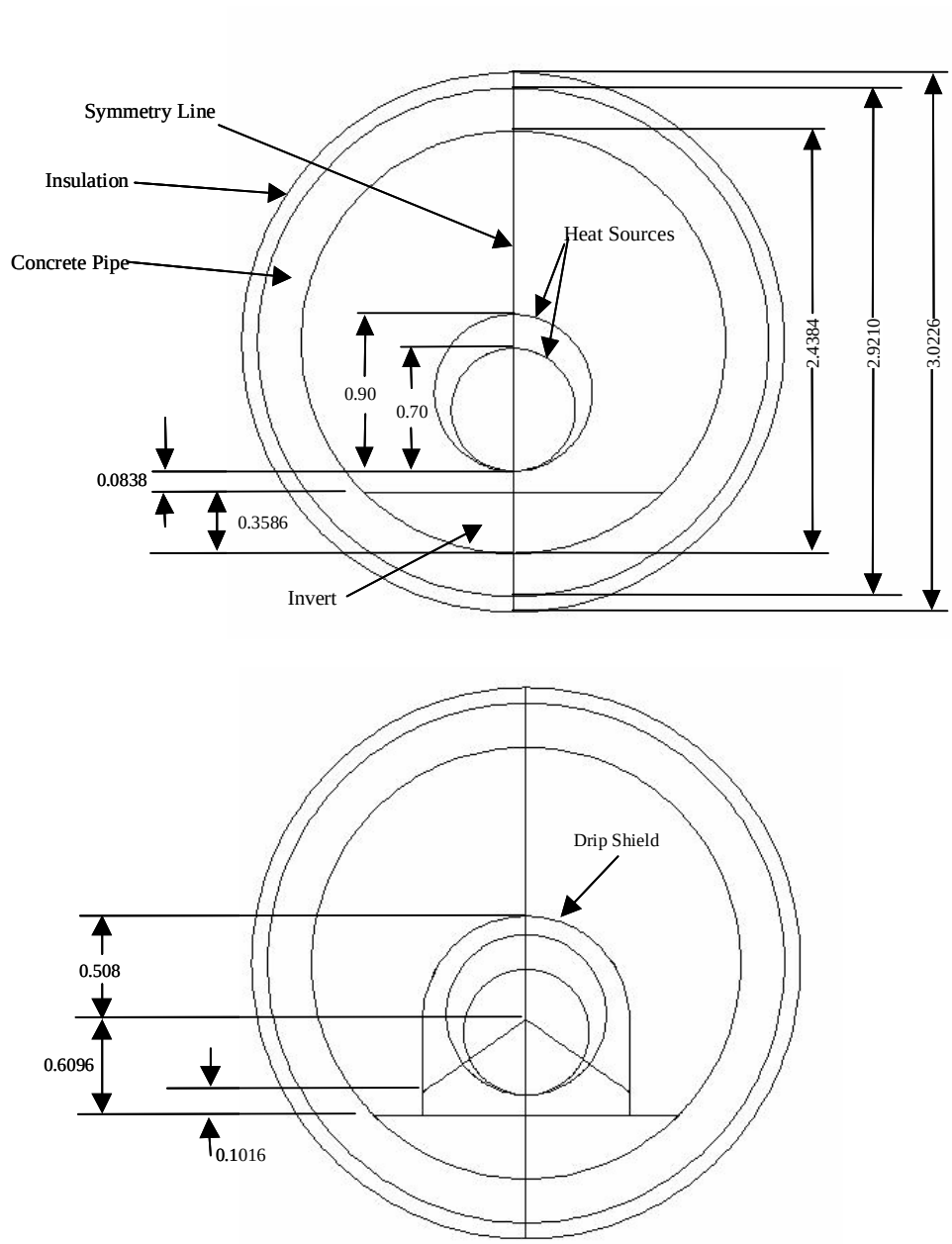

Source: Howard 2002 [DIRS 161009], pp. 27, 29, and 34; BSC 2002 [DIRS 158192].

NOTE: All dimensions are in meters. Dimensions converted from inches.

Figure 7.4.2-2. Cross-Sectional Dimensions for Case 8 Simulations

Physical Models

The simulations are run using the computer code FLUENT. Radiation, convection, conduction, and fluid flow processes are simulated.

Prior to setting up the blind simulation runs, it was determined that the fluid flow field would be in either a fully turbulent or transitional regime. As such, the RNG (renormalization group) k-ε model was chosen to simulate the air. This turbulence model was selected because of its unique ability to allow for variation in the turbulent Prandtl number as a function of flow conditions. Additionally, this turbulence model is capable of handling low-Reynolds number effects in the effective differential viscosity formulation, and it includes an extra strain rate term in the ε-equation to better simulate separated flows (Francis et al. 2002 [DIRS 164323], p. 16). Use of the differential formula for the effective viscosity requires an appropriate treatment of the near-wall region. Specifically, it requires that the viscous sublayer and the buffer layer (e.g., the near-wall region) are resolved (meshed) all the way to the wall (Francis et al. 2002 [DIRS 164323], p. 17). For a near-wall treatment of this type, wall y^+ values for turbulence should be small, on the order of 1. y^+ values for the meshes used in the simulations are presented in Appendix B. In addition to the chosen turbulence model, the differential viscosity model and full buoyancy model options were used.

Thermal radiation heat transfer is the dominant mode of heat transfer within the test train. For these analyses, the discrete ordinates (DO) model for thermal radiation was selected (Fluent, 2001 [DIRS 164453], Section 11.3.6). The DO model is capable of solving both surface-to-surface radiation and fluid participation radiation. Given the relatively low temperatures and low water vapor content of the fluid, the air is treated as a non-participating medium. This radiation submodel is restricted to either gray or non-gray thermal radiation using a banded gray model. In this analysis, diffuse, gray radiation is chosen. The DO thermal radiation model solves the radiative transfer equation (RTE) (Fluent 2001 [DIRS 164453], Equation 11.3.1). The DO model solves the RTE for a finite number of discrete solid angles (called control angles). Division of a domain occurs as $N_\theta \times N_\phi$ solid angles. In the three-dimensional calculations described in this report, eight octants are required making a total of $8N_\theta N_\phi$ directions solved, one RTE for each direction. Control angles are further subdivided into $N_{\theta p} \times N_{\phi p}$ pixels, in order to account for the possibility of incoming and outgoing radiation occurring within the same control angle. The RTE fully accounts for scattering, gas emission, and absorption, although the gas is considered a non-participating medium in these simulations.

The DO model settings used in these FLUENT simulations are theta divisions (=3), phi divisions (=3), theta pixels (=3), and phi pixels (=3). This results in the solution of 72 RTEs at each radiation iteration. The number of flow iterations per radiation iteration is maintained as the default value of 10 until a steady-state temperature field is achieved, after which the number of flow iterations per radiation iteration is increased to 100. The gray radiation model is applied as a constant emissivity over all wavelengths. Because the air in the test is non-participating, the absorption, scattering, and refractive index coefficients for thermal radiation are specified as 0 m^{-1}, 0 m^{-1}, and 1, respectively.

The heat sources, invert, concrete, and insulation layers are treated as conduction-only solids. Solids communicate thermally with each other or the fluid domain by the coupled thermal conditions feature in the CFD simulations.

Grid Specifications

Representative portions of the numerical grids developed for the two cases are shown in Figures 7.4.2-3 through 7.4.2-6. Figures 7.4.2-3 and 7.4.2-4 provide examples of cross-sectional gridding for Cases 4 and 8, respectively, while Figures 7.4.2-5 and 7.4.2-6 show the axial gridding. In order to achieve the desired y^+ values to properly calculate the flow and heat transfer at the walls, grid resolution is required all the way to the wall, e.g., the viscous sublayer is refined by the mesh rather than being bridged by standard wall functions. Because of this requirement, the number of computational cells required for the simulations is very large. The inner and outer surface of the drip shield, the inner surface of the concrete exposed to air, the top of the invert, and the surfaces of the waste package (including the end plates of the packages) are all finely gridded. These areas correspond to the plume and boundary layer regions. One way to reduce the number of cells required in the simulations is to take advantage of the geometric symmetry of the test train and simulate half of the problem as shown in Figures 7.4.2-3 and 7.4.2-4. It is noted that while the geometry is symmetrical, the actual ambient conditions, and thus the true boundary conditions, were not. Slight temperature differences were seen between the recorded temperatures on the two sides of the test train. These differences were typically small, often within the accuracy of the sensors. Ignoring the differences has minimal impact on the calculated temperatures of the test train. However, the calculated flow fields are forced to be steady, when in reality oscillating flows could occur. Table 7.4.2-1 lists the number of computational cells in each of the cases.

The same grids are used for both the blind and post-test runs, although in the post-test runs some of the cells are thermally decoupled from the grid. This is done primarily because of different applied boundary conditions between the runs. The blind runs assign a volumetric heat generation to the waste packages, thus the waste package volumes are included in the grid. In the post-test runs, a constant flux boundary condition is applied to the waste package surfaces. Cells internal to the waste packages are unnecessary, and are decoupled from the rest of the grid. Further, blind simulation calculations assign a constant temperature boundary to the entire exterior surface of the insulation. Measured data showed the temperature varied both circumferentially and axially along the test train. Only a minimal number of sensors (fourteen in total) were located on the exterior surface of the insulation, making it difficult to represent the measured temperature variation. Significantly more sensors (sixty-six in total) were located at the interface between the concrete and insulation, making this a more desirable outer boundary. Thus the insulation cells are decoupled from the thermal calculations inside the test train, and the concrete outer surface effectively becomes the outer boundary. The boundary conditions are described in more detail later in this section.

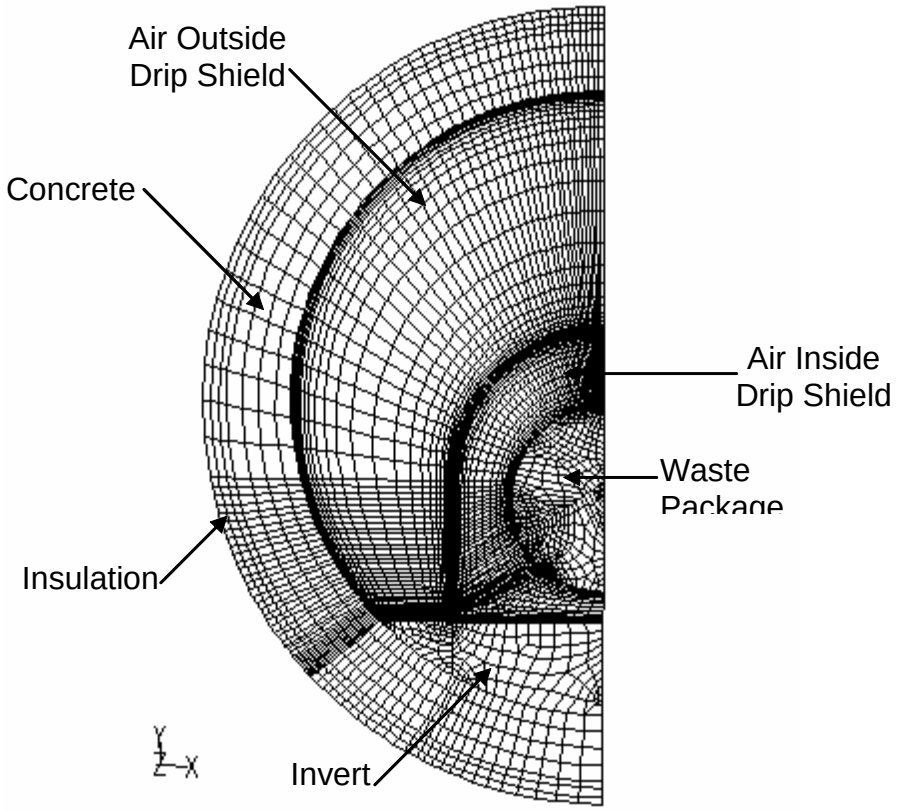

DTN: SN0308T0507803.004.

Figure 7.4.2-3. Gridding (XY) of a Cross-Section through One of the Smaller Waste Packages for Case 4 (25% Scale)

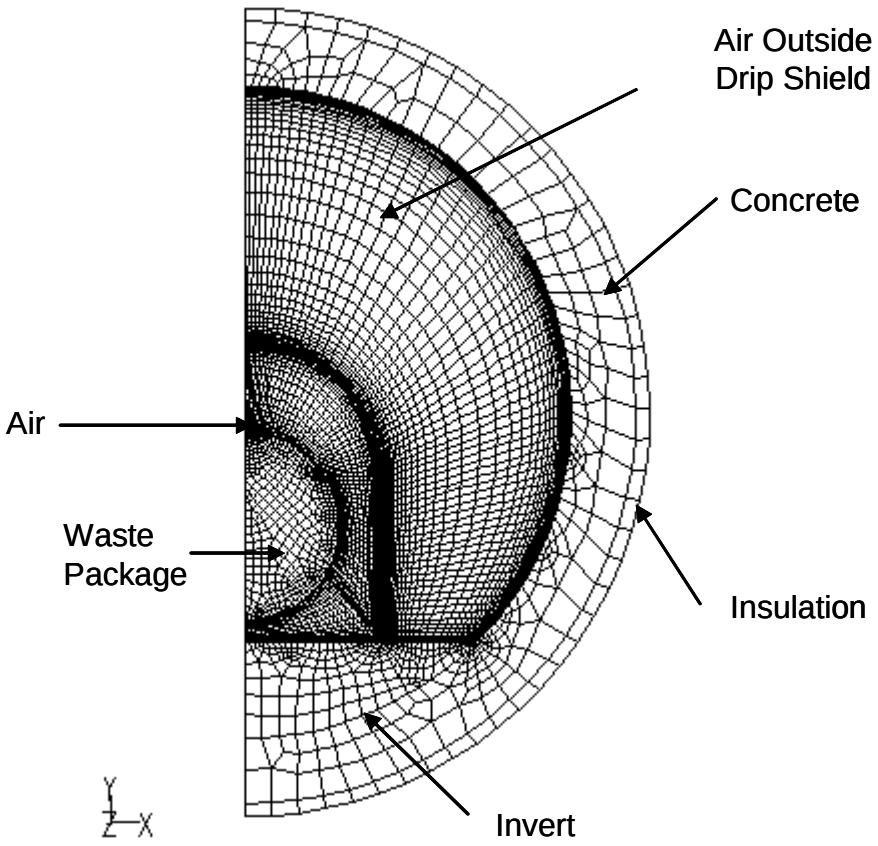

DTN: SN0308T0507803.004.

Figure 7.4.2-4. Gridding (XY) of a Cross-Section through One of the Smaller Waste Packages for Case 8 (44% Scale)

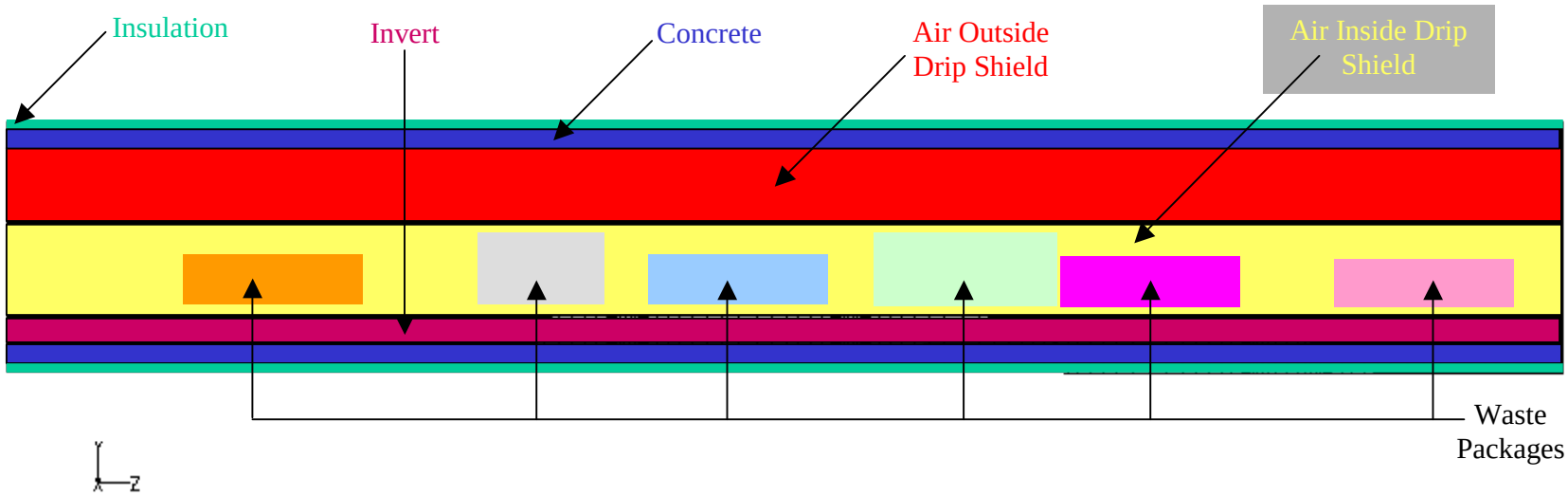

DTN: SN0308T0507803.004.

NOTE: Areas that appear solid are actually very finely meshed.

Figure 7.4.2-5. Axial Gridding for Case 4

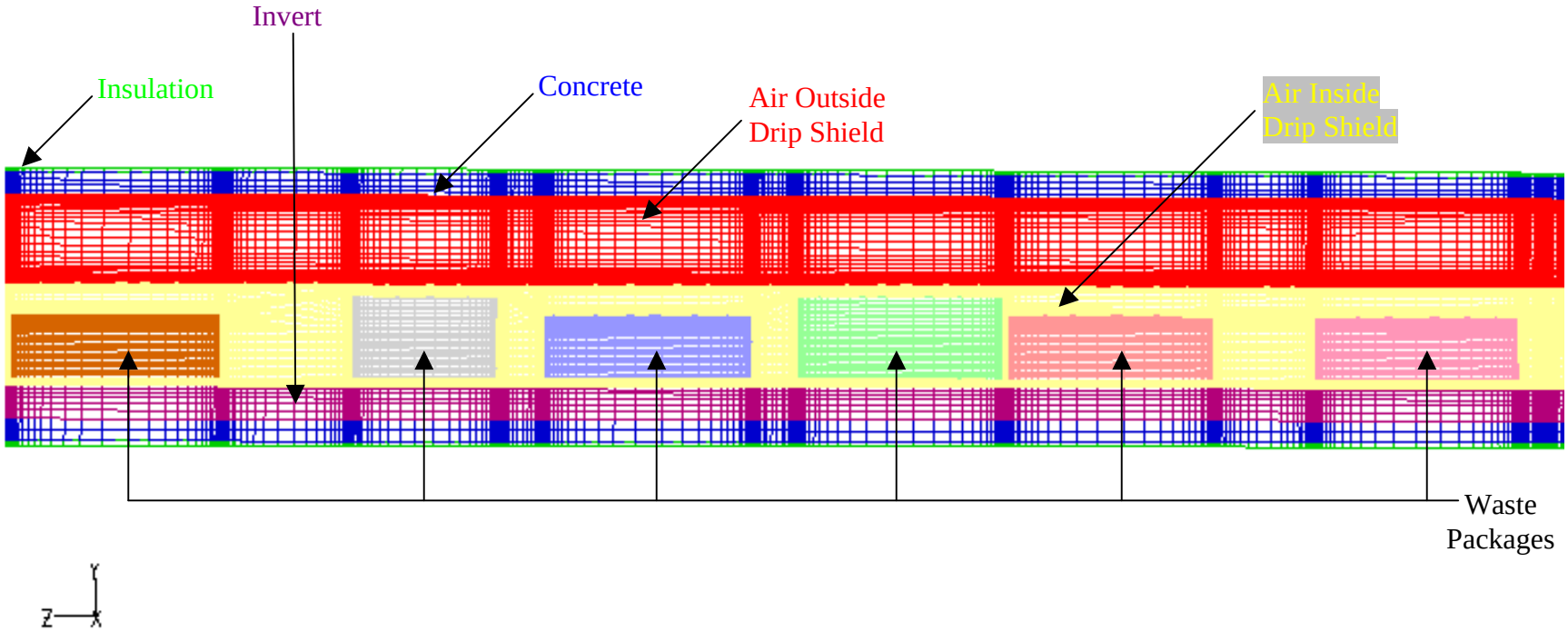

DTN: SN0308T0507803.004.

NOTE: Areas that appear solid are actually very finely meshed.

Figure 7.4.2-6. Axial Gridding for Case 8

Table 7.4.2-1. CFD Simulation Discretization

Simulation	Computational Cells
Case 4	2,325,444
Case 8	2,451,141

DTNs: SN0307T0507803.002 and SN0307T0507803.003.

Grid independence studies were performed using the blind simulation grids. It is found that once y^+ values on the order of 1 were achieved, refining the grid either by some form of adaptation or by re-gridding with a finer mesh does not significantly alter the calculational results. Appendix B provides summaries of the grid independence checks.

Thermal Properties

Numerical simulations require thermophysical properties of the introduced materials. FLUENT inputs include density, specific heat, thermal conductivity, and surface emissivity. Because the simulations provide steady-state solutions, only the thermal conductivities and the emissivities affect the results. Different values for the properties are used in the blind and post-test simulations due to either differences in the boundary conditions or to differences in the actual test conditions from those assumed prior to the tests. Values for both blind and post-test runs are described in detail below.

Concrete Properties

Emissivities of construction materials used in various EBS tests were measured. Data are provided in Table 7.4.2-3. Three to five measurements for a sample of the concrete pipe were made at each of five temperatures (ranging from 25 to 250ºC). Results showed no discernable variation as a function of temperature. The value cited in Table 7.4.2-2 is an average of all measurements below 50°C.

No measurements of thermal conductivity were made on the concrete pipe, and its conductivity probably varied depending on the type of concrete, moisture content, etc. In order to determine a realistic conductivity for the concrete, simple calculations using the experimental data were performed.

All of the power input to the waste package canisters must be conducted through the concrete walls/end plates of the test train. In turn, the energy must be conducted through the insulation/end plates to be dissipated into the test bay.

Conduction through a long, hollow cylinder with constant temperatures applied to the inner and outer walls is well understood. A one-dimensional, steady state analytical expression (Incropera and DeWitt 1990 [DIRS 156693], p. 98, Equation 3.27) is:

$$q_{cond} = \frac{2\pi k L(\Delta T)}{\ln\left(\frac{r_0}{r_i}\right)} \qquad \text{(Eq. 7.2-1)}$$

where q_{cond} is the conductive heat flux, k is the thermal conductivity of the cylinder, ΔT is the temperature change between the inner and outer surfaces of the cylinder, and r_o and r_i are the outer and inner radii of the cylinder, respectively.

While there was significant heat loss and thus end effects from the cool end of the test train, for measurement stations near the reflective boundary and the center of the heated region (for the uniform spacing/uniform line load case without a drip shield – Cases 1 and 5), Equation 7.2-1 can be used to estimate the thermal conductivity. For the experiment, the line load and surface temperatures were measured, and the radii are known constants, thus k for either the insulation or the concrete are calculated. Data from three stations (3, 9, and 11) were used. The calculations can be found in Appendix C. Results show the thermal conductivity to be 1.75 W/m-K.

Drip Shield Properties

FLUENT has the capability to allow a layer of cells with no associated mass, i.e., no volume, to be defined as a wall to simplify the mesh. The wall behaves as a solid in that mass cannot be transported through it and it can participate in radiation (e.g., an emissivity can be associated with it). However, because there is no thickness associated with it, there can be no temperature gradient from one side of the "wall" to the other. This feature can only be used for thin volumes having a high thermal conductivity, where anticipated temperature gradients across the material would be small. The drip shields are simulated with this feature to reduce the number of cells in the computational grid, eliminating the need to input a thermal conductivity for this material.

After the drip shields were manufactured they were painted with a paint of known emissivity (designated as "WP steel" in DTN: MO0109EBSAEQST.009 [DIRS 156696]); data are provided in Table 7.4.2-3. Three measurements for the sample were made at each of three temperatures (ranging from 30 to 100ºC). The emmisivity for the post-test simulations is an average of all measurements at 30°C and 50°C. When the blind simulations were constructed, it was unknown how the drip shield surface would be finished. Of the samples measured (DTN: MO0109EBSAEQST.009 [DIRS 156696], Table 7.4.2-3), the sample "stainless steel" seemed the most likely. Three measurements were made at each of three temperatures (ranging from 30 to 100ºC). The value cited in Table 7.4.1-17 for the blind simulations is an average of all measurements.

Insulation Properties

For the blind simulations, the thermal conductivity is taken from the specified manufacturer's literature. In these runs the exterior surface of the insulation is simulated as a constant temperature boundary condition. The interior surface of the insulation was in direct contact with the concrete. Thus, no emissivity for this material is used in the simulations.

The insulation is thermally decoupled from the rest of the grid in the post-test runs. The exterior boundary condition is defined at the interface between the concrete and insulation.

Invert Properties

Emissivities of the invert were measured (Table 7.4.2-3). Three measurements were made at each of five temperatures (ranging from 30 to 130ºC). Results showed no discernable variation as a function of temperature. The value cited in Table 7.4.2-2 is an average of all measurements.

For the blind simulations, the thermal conductivity of the invert is assumed to be that of dried crushed tuff, and was taken from DTN: MO0109EBSTCQST.011 [DIRS 156697] as a measured value between 25 and 50ºC. For the post-test simulations, the thermal conductivity of the invert material is taken from measured data for 4-10 crushed tuff (Table 7.4.2-4), which is the specific type of tuff used in the tests. Eleven measurements were taken at ambient temperature conditions. The value shown in Table 7.4.2-2 is the average of all measurements.

Waste Package Properties

The waste packages were painted with the same paint used on the drip shields (designated as "WP steel" in Table 7.4.2-3). Three measurements for the sample were made at each of three temperatures (ranging from 30 to 100°C). Results showed no discernable variation as a function of temperature. The value cited in Table 7.4.2-2 for the adjusted simulations is an average of all measurements.

In the blind simulations, energy is input into the waste packages as a constant volumetric heat generation. The waste packages are defined as volumes and are gridded accordingly. The nominal heat input values from the test plan are used (BSC 2002 [DIRS 158192], Table 5). The thermal conductivity of the material is 45 W/m-K.

Because the waste packages used in the test were specifically designed to maintain a constant flux, the post-test runs apply a constant heat flux to the exterior surface of the waste package. Doing so requires that the waste package volumes as defined in the blind simulations be thermally decoupled from the rest of the grid. Decoupling the interior waste package cells from the rest of the grid means that the defined thermal conductivity of the material has no influence on the simulation results.

Table 7.4.2-2 summarizes the pertinent properties for the waste packages, concrete pipe, insulation, drip shield and invert materials used in the simulations. Table 7.4.2-3 lists the measured emissivities of various materials used in the natural convection tests. Table 7.4.2-4 provides the measured thermal conductivity for 4-10 crushed tuff. Table 7.4.2-5 gives the thermophysical properties of air. These data were used in the validation simulations.

Table 7.4.2-2. Thermophysical Properties of Introduced Materials

Material	Post-Test Runs				Blind Simulation Runs			
	Thermal Conductivity		Emissivity		Thermal Conductivity		Emissivity	
	(W/m-K)				(W/m-K)			
Concrete	1.75	a	0.987	b	2.75	h	0.987	b
Drip Shield	NA	c	0.97	d	NA	c	0.828	l
Insulation	NA	c	NA	e	0.07	i	NA	e
Invert	0.16	f	0.996	g	0.03	j	0.996	g
WP Steel	NA	c	0.97	d	45	k	0.97	d

NOTE: (a) Calculated from measured experimental data for Case 1; (b) DTN: MO0109EBSAEQST.009 [DIRS 156696] (averaged for "concrete pipe"); (c) Values not needed based on simulation construction; (d) DTN: MO0109EBSAEQST.009 [DIRS 156696] (averaged for "waste package steel"); (e) Value not needed; insulation surfaces are not involved in radiative heat transport; (f) DTN: GS000483351030.003 [DIRS 152932] (averaged for "4-10 CWT); (g) DTN: MO0109EBSAEQST.009 [DIRS 156696] (averaged for "4-10 CWT"); (h) DTN MO0109EBSTCQST.011 [DIRS 156697] for concrete (averaged over 20 to 50°C); (i) Certain Teed 1996 [DIRS 153512] standard fiber glass duct wrap; (j) DTN: MO0109EBSTCQST.011 [DIRS 156697]; value for dry crushed tuff between 25 and 50°C; (k) DTN: MO0109EBSTCQST.011 [DIRS 156697]; linearly interpolated value for waste package steel at 28.7ºC; (l) DTN: MO0109EBSAEQST.009 [DIRS 156696] (averaged for "stainless steel" for 30 and 50°C).

Table 7.4.2-3. Emissivities of Materials

Concrete Pipe		Stainless Steel		4-10 CWT		WP Steel	
Sample Temp Deg C	E Sample at 8-14um	Sample Temp Deg C	E Sample at 8-14um	Sample Temp Deg C	E Sample at 8-14um	Sample Temp Deg C	E Sample at 8-14um
24.9	0.986	30.4	0.823	33.4	0.998	31.8	0.970
25.6	0.987	30.2	0.823	32.7	0.999	31.9	0.970
27.7	0.986	30.2	0.822	31.8	0.998	31.9	0.970
27.5	0.987	52.7	0.833	45.2	0.998	54.9	0.969
43.0	0.987	53.1	0.831	44.5	0.996	55.0	0.969
48.3	0.988	52.8	0.831	43.0	0.996	54.3	0.970
48.9	0.985	101.1	0.844	62.4	0.995	101.9	0.968
101.7	0.974	100.8	0.844	63.2	0.995	102.3	0.967
97.9	0.979	100.2	0.842	63.0	0.997	102	0.968
93.4	0.981	–	–	109	0.992	–	–
210	0.987	–	–	108.8	0.998	–	–
210	0.985	–	–	109.1	0.998	–	–
208.5	0.983	–	–	136.2	0.994	–	–
208.5	0.981	–	–	132.5	0.994	–	–
248.2	0.975	–	–	132.0	0.995	–	–
248.2	0.982	–	–	–	–	–	–
243.9	0.981	–	–	–	–	–	–
243.9	0.983	–	–	–	–	–	–
243.9	0.980	–	–	–	–	–	–

DTN: MO0109EBSAEQST.009 [DIRS 156696].

Table 7.4.2-4. Thermal Conductivity of 4-10 Crushed Tuff

Sample Type	Sample Number	Thermal Conductivity (W/m-C)	Temperature (C)
4-10 crushed tuff	TK-CT-01	0.17	16.2
4-10 crushed tuff	TK-CT-02	0.14	15.8
4-10 crushed tuff	TK-CT-03	0.17	16.1
4-10 crushed tuff	TK-CT-04	0.17	16.4
4-10 crushed tuff	TK-CT-05	0.17	17.1
4-10 crushed tuff	TK-CT-06	0.16	17.5
4-10 crushed tuff	TK-CT-07	0.17	17.6
4-10 crushed tuff	TK-CT-07a	0.15	18.9
4-10 crushed tuff	TK-CT-08	0.16	18.0
4-10 crushed tuff	TK-CT-09	0.17	18.1
4-10 crushed tuff	TK-CT-10	0.17	18.5

DTN: GS000483351030.003 [DIRS 152932].

Table 7.4.2-5. Thermophysical Properties of Air

Temperature (K)	Density (kg/m^3)	Specific Heat (J/kg-K)	Thermal Conductivity (W/m-K)	Viscosity (kg/s-m)
300	Incompressible-ideal-gas	1007	0.0263	1.846×10^{-5}
350	Incompressible-ideal-gas	1009	0.0300	2.082×10^{-5}

Source: Incropera and DeWitt 1990 [DIRS 156693], Table A.4.

NOTE: Density is described in Section 7.

Test Train End Plate Properties

The emissivity of the reflective boundary (e.g., the hot end of the test) shown in Figure 7.4.1-4 and Figure 7.4.1-5 was set to 0.1. This surface was covered with aluminum foil. The value is an approximation based on ranges provided in the literature (Incropera and Dewitt 1990 [DIRS 156693], Table A.11). The emissivity of the non-reflective boundary (e.g., the cold end of the test) is set to 0.97, the same as the drip shields and the waste packages (Table 7.4.2-3). This end was painted with the same grey paint as those surfaces.

Incompressible Ideal Gas

For all of the blind and post-test runs, the dynamic viscosity, thermal conductivity, and specific heat are inputs in the simulations are given in Table 7.4.2-5. These properties are evaluated in a piecewise-linear solution (in terms of the fluid temperature) directly in the CFD simulation.

The fluid density is computed by FLUENT using the incompressible-ideal-gas law (Fluent 2001 [DIRS 164453], Equation 7.2-5). The incompressible-ideal-gas law is annotated in Section 6 (Equation 6.1-17).

Internal natural convection occurs when a density variation (due to a temperature variation) exists in a gravitational field. The incompressible-ideal-gas law is applied (by FLUENT) in the

density calculation when pressure variations are small enough such that the overall internal flow conditions are essentially incompressible, but a relationship between density and temperature is required because this is the driving force for flow. The internal density variation is based on the input ambient operating pressure and the computed temperature.

Boundary Conditions

Boundary conditions for the blind and post-test runs differ. For the blind simulation runs, the temperature and heat input boundary conditions are specified for the surrounding air adjacent to the insulation layers and at the inner cylinder heat sources, respectively. The outer boundary is treated as a constant temperature boundary, specified as 26.9ºC (300K) for Case 4 and 27.0ºC (300.1K) for Case 8. Constant heat generation rates are input at the waste packages. These volumetric heat generation rates are computed from the design value heat generation (BSC 2002 [DIRS 158192], Table 6) for the blind runs and Table 7.4.1-25 for the post-test runs and geometries of individual heat sources (Figures 7.4.1-7 and 7.4.1-9). Calculated values are given in Tables 7.4.2-6 and 7.4.2-7.

For the post-test runs a spatially varying (both circumferentially and axially) temperature boundary based on measured data is applied to the exterior surface of the concrete. A constant heat flux boundary is applied to the exterior surface of the waste package. The fluxes are calculated using the measured heat input and geometries of the individual heat sources shown in Table 7.4.1-25 and the geometries of individual heat sources (Figures 7.4.1-7 and 7.4.1-9). Calculated values are given in Tables 7.4.2-6 and 7.4.2-7.

For both the blind and post-test runs the reflective boundary (hot end of the test) is treated as a no-flux (heat) boundary. All walls are treated as no-slip boundaries with constant (diffuse) surface emissivities. A vertical plane through the geometric center forms a symmetry boundary.

Table 7.4.2-6. Power Inputs for the Blind FLUENT Runs

	WP	Design Value (W)[a]	Diameter (m)[b]	Length (m)[c]	Volume (m^3)[d]	Heat Generation (W/m^3)[e]
Case 4	1	50	0.40	1.29	0.162	308.6
	2	86.2	0.40	1.29	0.162	532.1
	3	.12	0.51	1.29	0.264	.455
	4	50	0.40	1.29	0.162	308.6
	5	1.9	0.51	0.90	0.184	10.33
	6	86.2	0.40	1.29	0.162	532.1
Case 8	1	154.9	0.70	2.27	0.874	177.2
	2	267.2	0.70	2.27	0.874	305.7
	3	0.39	0.90	2.27	1.444	0.27
	4	154.9	0.70	2.27	0.874	177.2
	5	6	0.90	1.58	1.005	5.97
	6	267.2	0.70	2.27	0.874	305.7

[a] BSC 2002 [DIRS 158192], Table 5, waste package types found in Figures 7.4.1-7 and 7.4.1-9.
[b] Figures 7.4.1-7 and 7.4.1-9.
[c] Figures 7.4.1-7 and 7.4.1-9.
[d] Volume = pi*diameter^2*length/4.0.
[e] Volumetric heat generation used as boundary condition for these cases.

Table 7.4.2-7. Power Inputs for the Post-Test FLUENT Runs

	WP	Average Measured Power (W)[a]	Diameter (m)[b]	Length (m)[c]	Area of Each End (m^2)[d]	Area Cylinder[e]	Total Area (m^2)[f]	Flux (W/m^2)
Case 4	1	52.2	0.40	1.29	0.126	1.62	1.87	27.9
	2	82.3	0.40	1.29	0.126	1.62	1.87	44.0
	3	0	0.51	1.29	0.204	2.07	2.48	0.0
	4	48.83	0.40	1.29	0.126	1.62	1.87	26.1
	5	2.77	0.51	0.90	0.204	1.44	1.85	1.5
	6	88.27	0.40	1.29	0.126	1.62	1.87	47.1
Case 8	1	153.35	0.70	2.27	0.385	4.99	5.76	26.6
	2	272.49	0.70	2.27	0.385	4.99	5.76	47.3
	3	0.00	0.90	2.27	0.636	6.42	7.69	0.0
	4	159.32	0.70	2.27	0.385	4.99	5.76	27.6
	5	7.37	0.90	1.58	0.636	4.47	5.74	1.3
	6	269.84	0.70	2.27	0.385	4.99	5.76	46.8

[a] Table 7.4.1-25.
[b] Figures 7.4.1-7 and 7.4.1-9.
[c] Figures 7.4.1-7 and 7.4.1-9.
[d] Area end = pi*diameter^2/4.
[e] Area cylinder = pi*diameter*length.
[f] Flux applied to all surfaces of the waste package for these cases, total area includes the cylinder area plus the area of both ends.

Operating Conditions

The operating pressure for the three-dimensional Natural Convection Test Validation Simulations (Section 7.4) is found by calculating the standard atmospheric pressure at the approximate elevation of the Atlas test facility in North Las Vegas. Table 7.4.2-8 contains standard atmospheric pressure at two elevations that bound the elevation of the Atlas Test Facility, which is approximately 600 m above mean sea level (USGS 1969 [DIRS 149902]). The resulting ambient operating pressure interpolated from Table 7.4.2-8 is 94,400 Pa. The acceleration due to gravity applied in the simulations is taken to be 9.81 m/s^2 (Incropera and DeWitt 1990 [DIRS 156693], back cover).

Table 7.4.2-8. Standard Atmosphere

Elevation (m)	Pressure[a] (Pa)
500	95,480
1,000	89,889

[a] White 1986 [DIRS 111015], Table A.6.

CFD Simulation Settings and Parameters

The CFD numerical simulation settings and runtime monitoring for equation residuals, discretization, convergence, and steady-state energy balance are described in this section.

The steady-state segregated solver is used in this work. The segregated solver approach results in the governing equations being solved sequentially. An implicit linearization technique is applied in the segregated solution of the equations previously described. This results in a linear system of equations at each computational cell. The equations are coupled and non-linear; therefore, several iterations of the equation set are required to obtain a converged solution.

FLUENT uses a control-volume method to solve the governing equations. The equations are discrete for each computational cell. In applying this solution method the CFD simulation stores flow properties (e.g., dependent variables) at cell centers. However, face values are required for the convection terms in the discretized equations. Face values are obtained by interpolation from the cell centers using a second-order upwind scheme for both the momentum and energy equations and the turbulence equations. It is noted that the diffusion terms in the equations are central-differenced and are second-order accurate. The body-force-weighted pressure interpolation scheme is used to compute face pressure from cell center values. Pressure-velocity coupling is achieved through the SIMPLE algorithm. The SIMPLE algorithm uses the discrete continuity equation to determine a cell pressure correction equation. Once a solution to the cell pressure correction equation is obtained the cell pressure and face mass fluxes are then corrected using the cell pressure correction term.

Because the equation set being solved is linearized, it is necessary to control the rate of change of the flow/energy variables at each iteration step. Under-relaxation parameters are assigned to pressure, momentum, energy, turbulence kinetic energy, turbulence dissipation rate, and a variety of others that go unmodified from default settings (usually 1.0). For the buoyancy driven flow problems considered in this report, the default settings for the under-relaxation parameters for the flow equations are too high. Therefore, additional under-relaxation is necessary to obtain a

converged solution. For Rayleigh number cases (~10^7), the under-relaxation parameters for the flow equations are specified at about 0.1 (turbulence kinetic energy and dissipation rate are set about the same). Pressure is set to about 0.2. Typically, the under-relaxation for the energy equation is maintained at about 1.0.

The flow solution is given an arbitrary initial starting point for fluid velocity, temperature, and turbulence quantities. Additional iterations are required for solution convergence. A flow solution is considered to have converged after all equation residuals have been reduced by about 4 to 5 orders of magnitude. For the higher Rayleigh number flow cases, this may require about 10,000 or more iterations to achieve. A final convergence criteria specified in the CFD simulations is based on an overall steady-state energy balance. When the energy imbalance between the energy input into the grid and that leaving the grid is at or below about 1 percent, the flow simulation is assumed to be at steady-state.

7.4.3 Results

Validations of the FLUENT simulations are made by direct comparisons between the post-test CFD results and the measured experimental data. The two cases presented represent the most complex heat transfer modes of all of the experimental cases performed. The cases differ by scale (25% and 44% of full scale).

Comparison of Solid Temperatures

Data from sensors on the concrete, waste package, and drip shield surfaces and data from sensors embedded in the invert are presented below.

Interface between Concrete and Insulation

Figures 7.4.3-1 and 7.4.3-2 show the temperature boundary condition applied to the exterior surface of the concrete for the two cases. For both cases, the measured data are linearly interpolated along the length of the test train. The top and side sensors showed little difference in the measured temperatures (typically less than 0.5ºC). The greatest variation was seen near Station 15, the cool end of the test train. For Case 4, measured data from the bottom of the test train were on the order of 1 to 1.2ºC lower than the side/top sensors. For Case 8 this temperature difference was slightly greater, closer to 2ºC. The cool end of the test train (Station 15) is defined in the simulations to be a constant temperature over all end surfaces in Case 4 and all but the outer concrete surface for Case 8 (an artifact of how the grid was created, such that applying a spatially varying temperature over this surface is difficult), thus causing the temperature profile to have the same value for all of the sensors. The overall heat transfer through the end plate is small compared to that out the rest of the surfaces, so this deviation from the true condition causes relatively small differences in the calculated temperatures.

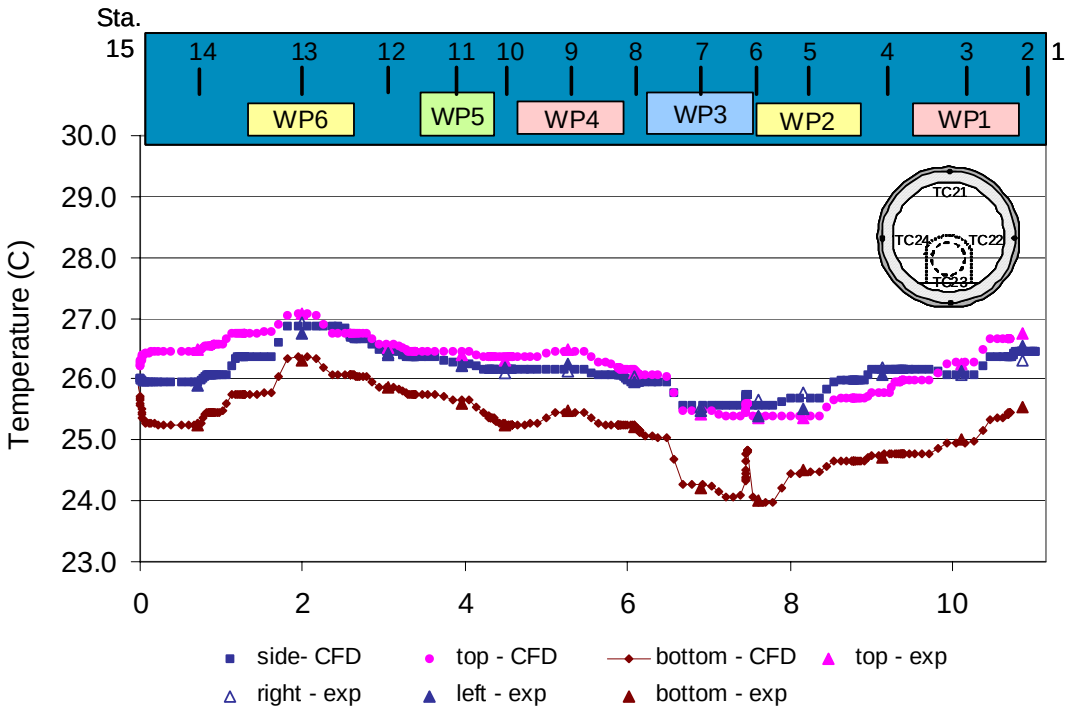

DTNs: SN0307T0507803.001[DIRS 164396] and SN0307T0507803.002.

Figure 7.4.3-1. Applied Temperature Boundary Condition to the Exterior Surface of the Concrete (Case 4)

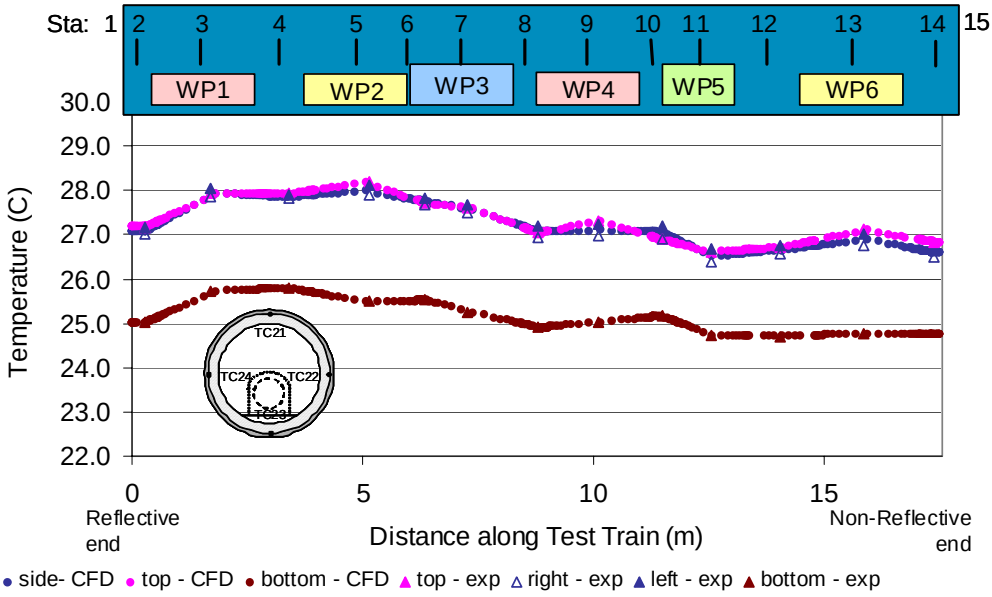

DTNs: SN0307T0507803.001 and SN0307T0507803.003.

Figure 7.4.3-2. Applied Temperature Boundary Condition to the Exterior Surface of the Concrete (Case 8)

Interior Surface of the Concrete

Agreement between the calculational and experimental results for the interior surface of the concrete is good, as seen in Figures 7.4.3-3 and 7.4.3-4. Side and top sensors typically agreed within 0.2°C, while the agreement for the bottom sensor position is even closer. The effect of the constant temperatures assigned to the cool end sections (Station 15) for each of the cases is evident.

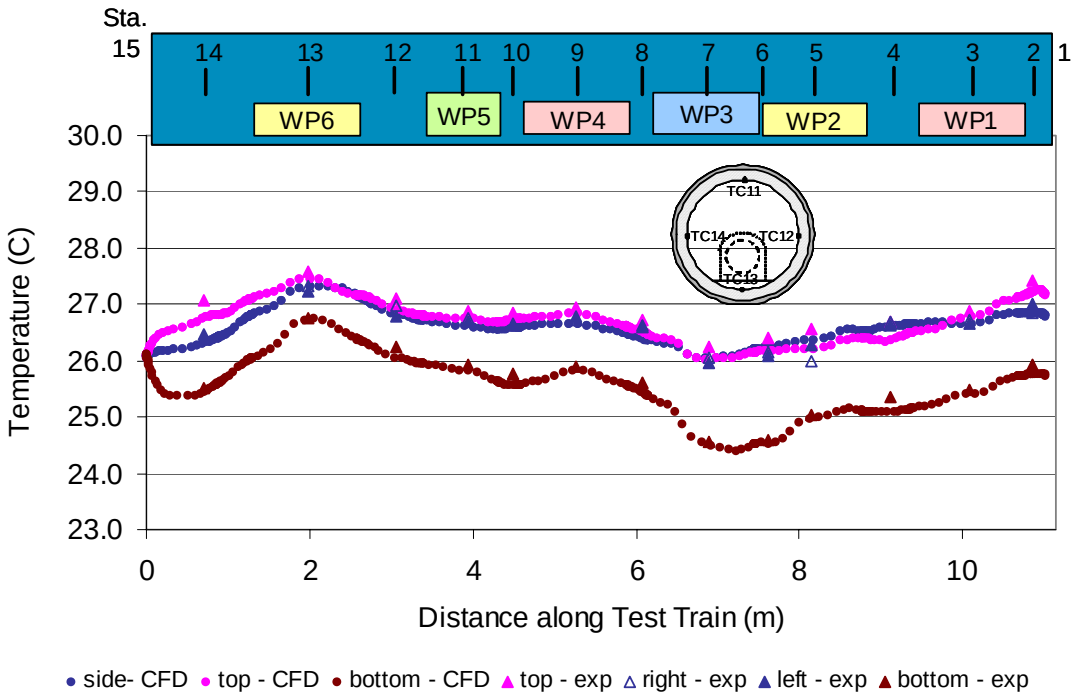

DTNs: SN0307T0507803.001 and SN0307T0507803.002.

Figure 7.4.3-3. Comparison of Experimentally Measured and Calculated Simulation Temperatures for the Interior Surface of the Concrete (Case 4)

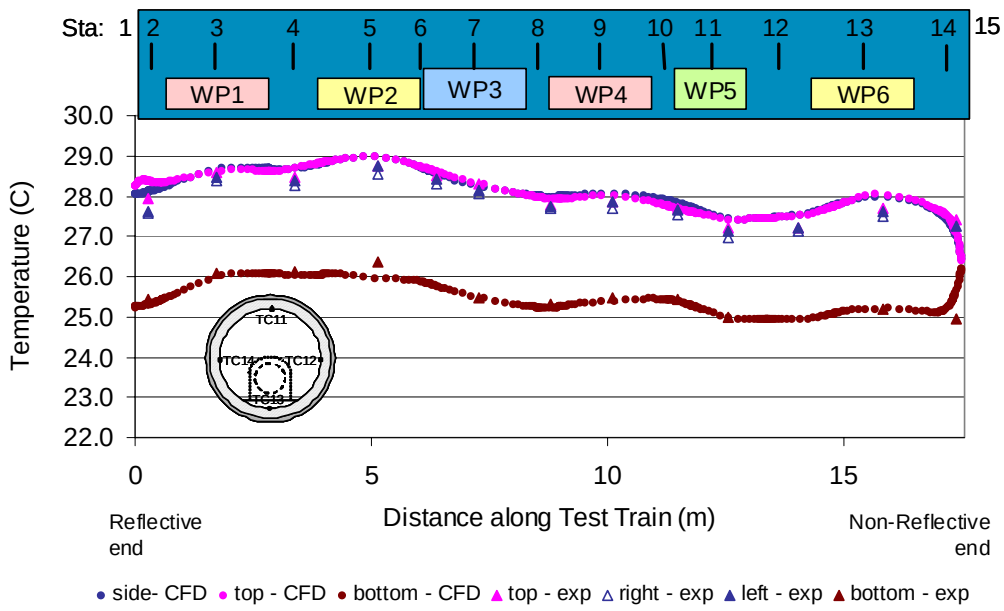

DTNs: SN0307T0507803.001 and SN0307T0507803.003[DIRS 164398].

Figure 7.4.3-4. Comparison of Experimentally Measured and Calculated Simulation Temperatures for the Interior Surface of the Concrete (Case 8)

Waste Packages

Figures 7.4.3-5 and 7.4.3-6 show the simulate predicted temperatures for all cells on the waste packages. Tables 7.4.3-1 through 7.4.3-4 compare predicted and measured temperatures for the waste package surfaces. The CFD simulations predict circumferential differences around the waste packages ranging from 0.2 to 2.2°C. Typical circumferential variations seen in the measured data are about 0.7°C. Absolute values for the two data sets typically compare within 1 to 2°C, with the FLUENT results being higher than the measured values.

Figures 7.4.3-5 and 7.4.3-6 show the influence of adjacent waste packages on one another. The two cold packages (packages 3 and 5) have their highest temperatures on their end plates. The small gap between waste packages 2 and 3 causes significant heat transfer between the end plates, resulting in high temperatures.

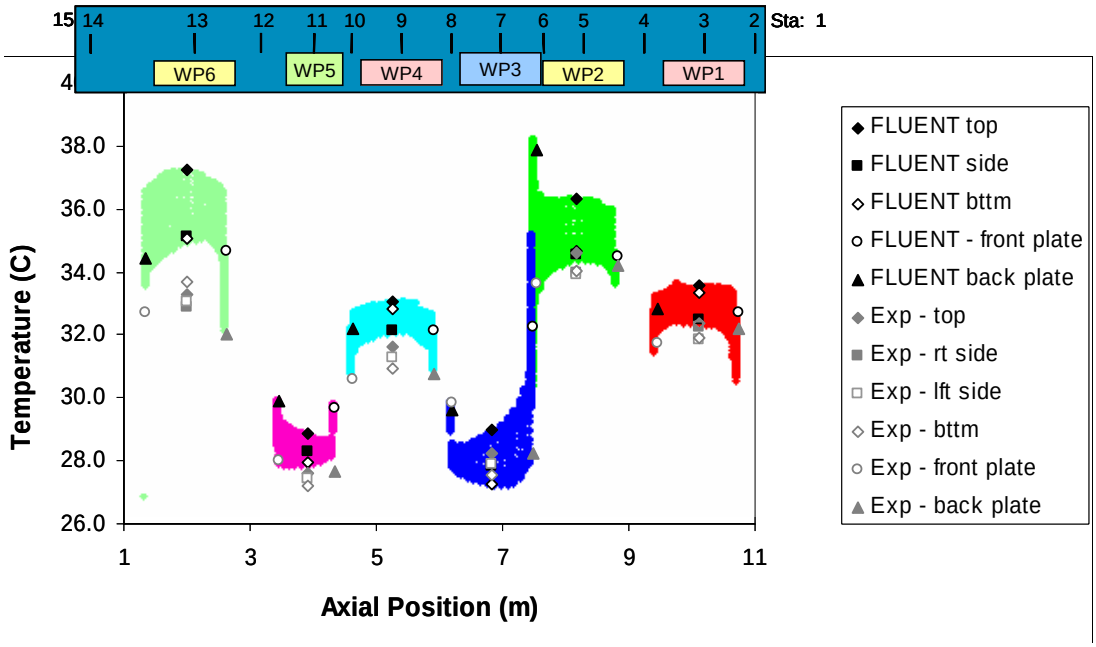

DTNs: SN0307T0507803.001 and SN0307T0507803.002.

Figure 7.4.3-5. Plot of Temperatures for All Cells on the Waste Packages (Case 4)

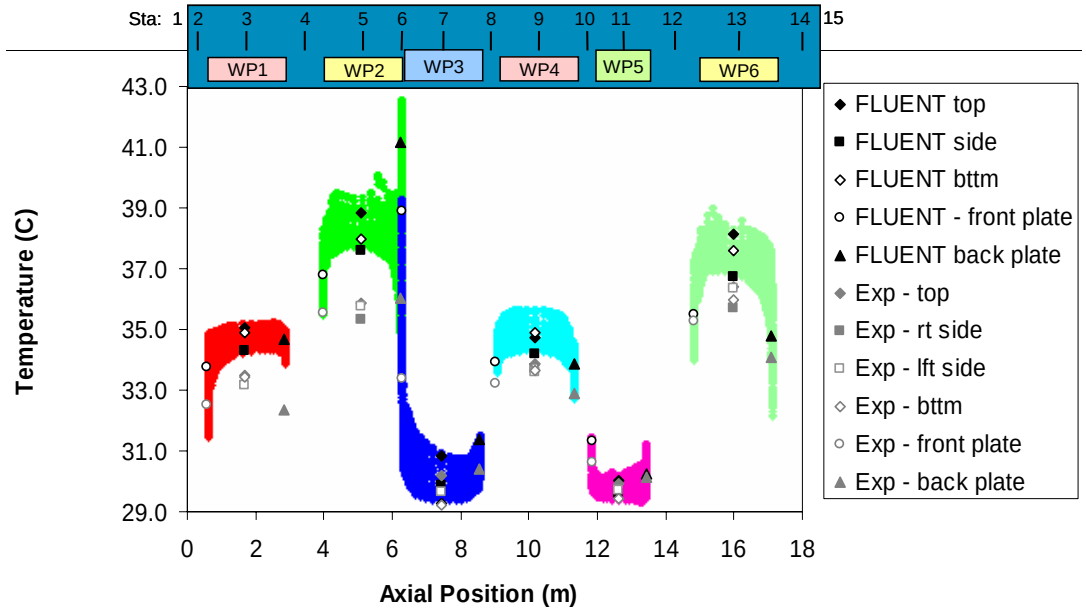

DTNs: SN0307T0507803.001 and SN0307T0507803.003.

Figure 7.4.3-6. Plot of Temperatures for All Cells on the Waste Packages (Case 8)

Table 7.4.3-1. Comparison of FLUENT and Experimental Temperature Data for the Waste Package Cylinders (Case 4)

	Top Center of Cylinder			Right Side of Cylinder				Bottom Center of Cylinder		
	FLUENT	EXP.	Difference	FLUENT	EXP. - Right	EXP. - Left	Difference (using avg. side temp for experimental data)	FLUENT	EXP.	Difference
Waste Package 1	33.6	32.3	1.2	32.5	32.3	31.9	0.4	33.3	31.9	1.4
Waste Package 2	36.4	34.6	1.8	34.5	34.0	33.9	0.6	34.6	34.0	0.6
Waste Package 3	29.0	28.2	0.8	27.9	27.9	27.9	0.0	27.2	27.5	-0.3
Waste Package 4	33.0	31.6	1.4	32.1	31.3	31.3	0.8	32.8	30.9	1.9
Waste Package 5	28.8	27.6	1.2	28.3	27.4	27.5	0.8	28.0	27.2	0.8
Waste Package 6	37.3	33.3	4.0	35.1	32.9	33.1	2.2	35.1	33.7	1.4

DTNs: SN0307T0507803.001 and SN0307T0507803.002.

Table 7.4.3-2. Comparison of FLUENT and Experimental Temperature Data for the Waste Package End Plates (Case 4)

	Center Front Plate			Center Back Plate		
	FLUENT	EXP.	Difference	FLUENT	EXP.	Difference
Waste Package 1	32.7	31.8	1.0	32.8	32.2	0.6
Waste Package 2	34.5	33.6	0.9	37.9	34.2	3.7
Waste Package 3	32.2	29.8	2.4	29.6	28.2	1.4
Waste Package 4	32.1	30.6	1.6	32.2	30.8	1.4
Waste Package 5	29.7	28.0	1.6	29.9	27.6	2.2
Waste Package 6	34.6	32.7	2.0	34.5	32.0	2.4

DTNs: SN0307T0507803.001 and SN0307T0507803.002.

Table 7.4.3-3. Comparison of FLUENT and Experimental Temperature Data for the Waste Package Cylinders (Case 8)

	Top Center of Cylinder			Right Side of Cylinder				Bottom Center of Cylinder		
	FLUENT	EXP.	Difference	FLUENT	EXP. - right	EXP. - left	Difference (using avg. side temp for experimental data)	FLUENT	EXP.	Difference
Waste Package 1	35.0	33.5	1.5	34.3	33.2	33.2	1.1	34.9	33.4	1.5
Waste Package 2	39.0	35.9	3.1	37.4	35.3	35.8	1.8	39.7	36.1	3.6
Waste Package 3	30.8	30.2	0.6	30.8	29.7	29.6	1.2	29.3	29.2	0.0
Waste Package 4	34.8	33.9	0.9	34.8	33.7	33.6	1.1	34.9	33.7	1.2
Waste Package 5	30.0	29.9	0.1	30.0	29.7	29.7	0.3	29.4	29.4	0.0
Waste Package 6	38.2	36.4	1.7	38.2	35.7	36.3	2.2	37.6	36.0	1.6

DTNs: SN0307T0507803.001 and SN0307T0507803.003.

Table 7.4.3-4. Comparison of FLUENT and Experimental Temperature Data for the Waste Package End Plates (Case 8)

	Center Front Plate			Center Back Plate		
	FLUENT	EXP.	Difference	FLUENT	EXP.	Difference
Waste Package 1	34.6	32.5	2.0	33.1	32.4	0.7
Waste Package 2	39.8	35.5	4.3	36.6	36.0	0.6
Waste Package 3	31.3	33.4	-2.0	36.6	30.4	6.2
Waste Package 4	33.7	33.2	0.5	33.8	32.9	0.9
Waste Package 5	30.1	30.6	-0.6	31.2	30.1	1.0
Waste Package 6	34.0	35.3	-1.3	35.3	34.1	1.2

DTNs: SN0307T0507803.001 and SN0307T0507803.003.

Invert

Figures 7.4.3-7 and 7.4.3-8 compare simulation and experimental data for the invert sensors. The side and center sensors show higher temperatures near the hot waste packages in both data sets. Data match well for the side sensors, typically being within 0.2ºC. For the center sensors the measured data was lower than the predicted values, particularly directly beneath the hot waste packages where differences as high as 2.5ºC are seen. While the absolute FLUENT temperatures are higher than the measured data, the temperature differences between the bottom of the waste package and the top (center) of the invert are very similar (comparing data from Tables 7.4.3-1 and 7.4.3-3 with Figures 7.4.3-6 and 7.4.3-8).

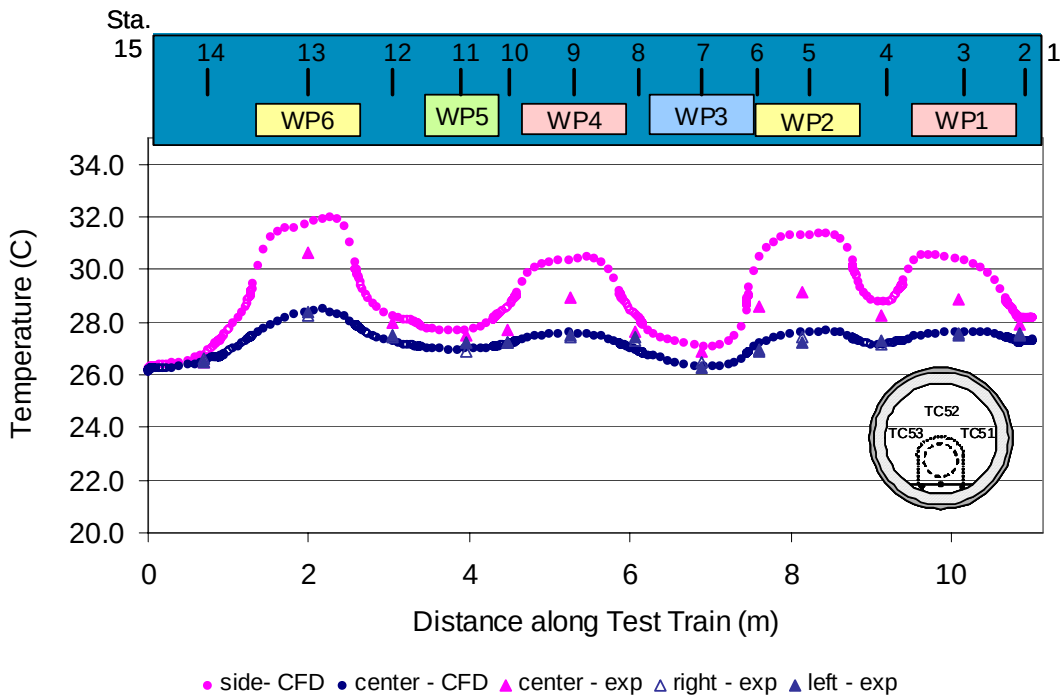

DTNs: SN0307T0507803.001 and SN0307T0507803.003.

Figure 7.4.3-7. Comparison of Experimentally Measured and Calculated Simulation Temperatures for the Invert (Case 4)

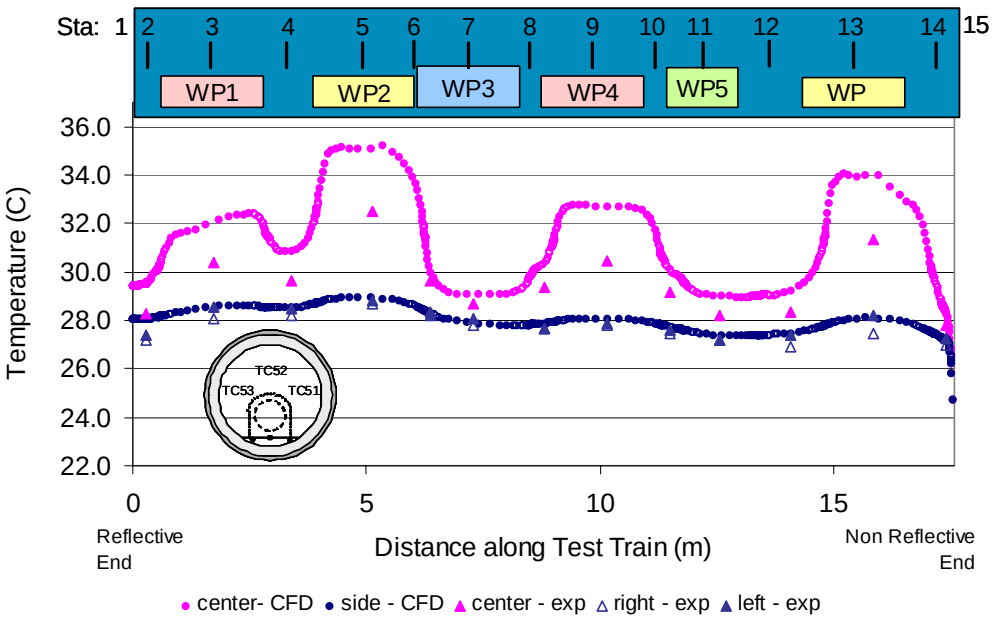

DTNs: SN0307T0507803.001 and SN0307T0507803.003.

Figure 7.4.3-8. Comparison of Experimentally Measured and Calculated Simulation Temperatures for the Invert (Case 8)

Drip Shield

Experimental and calculated data for the top and side positions on the drip shield are presented in Figures 7.4.3-9 and 7.4.3-10. CFD results for both cases show temperatures vary axially by as much as 3ºC along the length of the drip shield, with the higher temperatures corresponding to the areas nearest the hot waste packages. In both CFD cases and in the experimental data, the top of the drip shield is warmer than the sides (typically by about 1ºC). Comparison of the computational results with the experimental data shows that the data at the side position match the experimental data within 0.3ºC. Data at the top position differ slightly more, and are typically within 1ºC, with the FLUENT data generally being higher than the measured data. For Case 8, the computational data are higher than the measured data for both the top and side positions. Data sets differ by as much as 3ºC for the side position, and 2ºC for the top position.

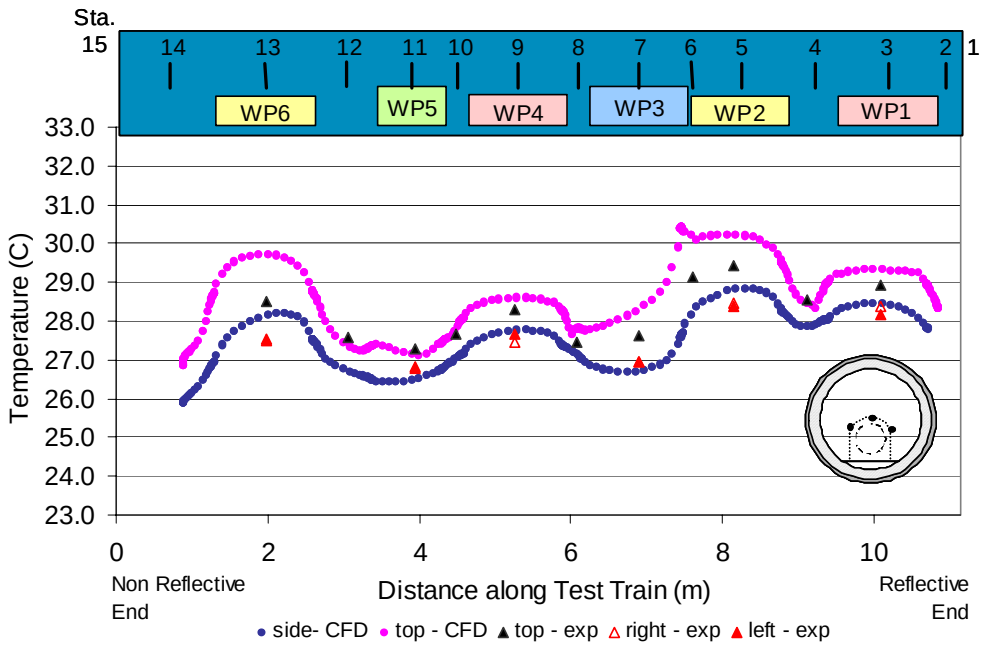

DTNs: SN0307T0507803.001 and SN0307T0507803.003.

Figure 7.4.3-9. Comparison of Experimentally Measured and Calculated Simulation Temperatures for the Drip Shield (Case 4)

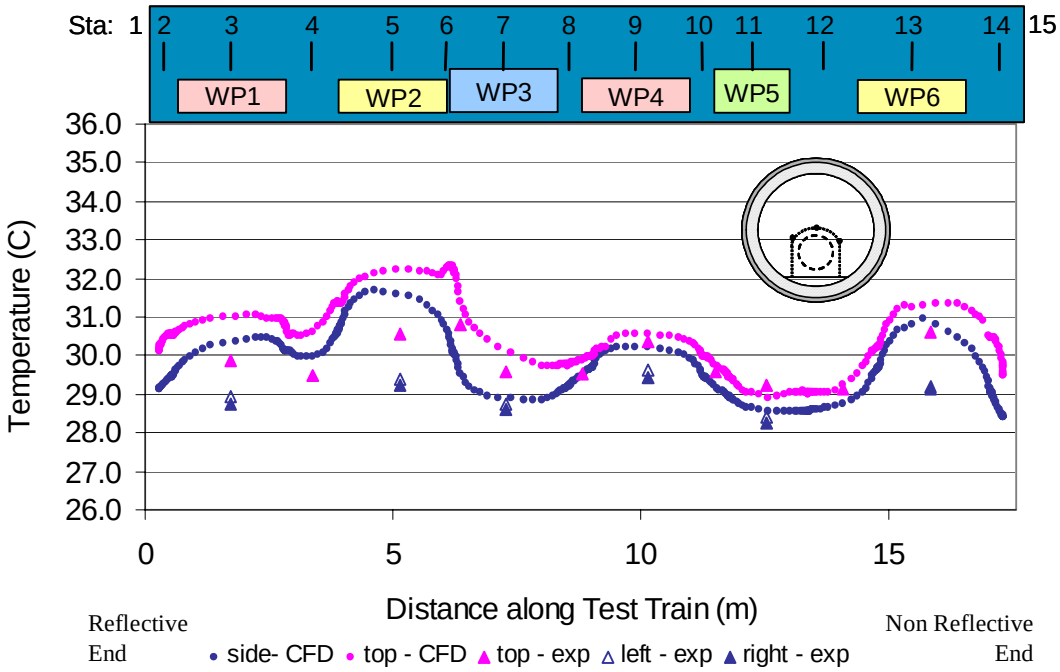

DTNs: SN0307T0507803.001 and SN0307T0507803.003.

Figure 7.4.3-10. Comparison of Experimentally Measured and Calculated Simulation Temperatures for the Drip Shield (Case 8)

Comparison of Fluid Temperatures

Figures 7.4.3-11 through 7.4.3-14 present experimental data collected from air sensors along with simulation predictions for top, side, and bottom sensor positions. Both the FLUENT and the measured data show fairly uniform temperatures (maximum variation < 2°C) along the length of the test train for the top and side positions. Temperatures along the bottom (under the drip shield where the drip shield is present) show slightly more variability. For Case 4, the temperatures drop by 1 to 1.5ºC at the end of the drip shield (Stations 2 and 14), show a slight change at the gap between hot and cold waste package pairs (packages 4 and 5, and packages 3 and 4), and show lower temperatures around the cold waste packages (packages 3 and 5). Data comparisons for this case typically agree within 0.5ºC for the top and side sensors, and within 1.5ºC for the bottom sensor. The measured data are typically slightly higher than the simulation results near waste package 6 and slightly lower than the simulation results near waste package 3. For Case 8, the computational results are typically higher than the measured data (typically about 1ºC). Again, the temperatures outside the drip shield (top and side positions) are fairly uniform along the length of the test train. Greater variability is seen at the "bottom" position. Temperatures under the drip shield are higher – by at least 1ºC (see drops at Stations 2 and 14). Peaks at the gaps near hot–cold waste packages are noticeable; however, for this case the greatest deviation under the drip shield is seen near the end of waste package 2.

Figures 7.4.3-15 and 7.4.3-16 are temperature contour plots from FLUENT. Side and cross-sections along the length of the test train are shown. For Case 4, fluid temperatures in the annulus between the drip shield and the waste package are fairly constant along the length of the test train in the top half (the area above the drip shield) and lower in the area to the side of the drip shield. Temperatures in the annulus between the waste package and the drip shield vary, with areas near the hotter waste packages (1, 2, 4 and 6) being higher than the areas near the cold waste packages or the large gaps between the packages. For Case 8 the fluid temperature in the annulus between the drip shield and the waste package is graded, with hotter air being near the reflective end of the boundary (Z=0). This is an artifact of the small gap between the end of the drip shield and the non-reflective boundary (Z=17.43). The temperature gradients under the drip shield are similar for the two cases.

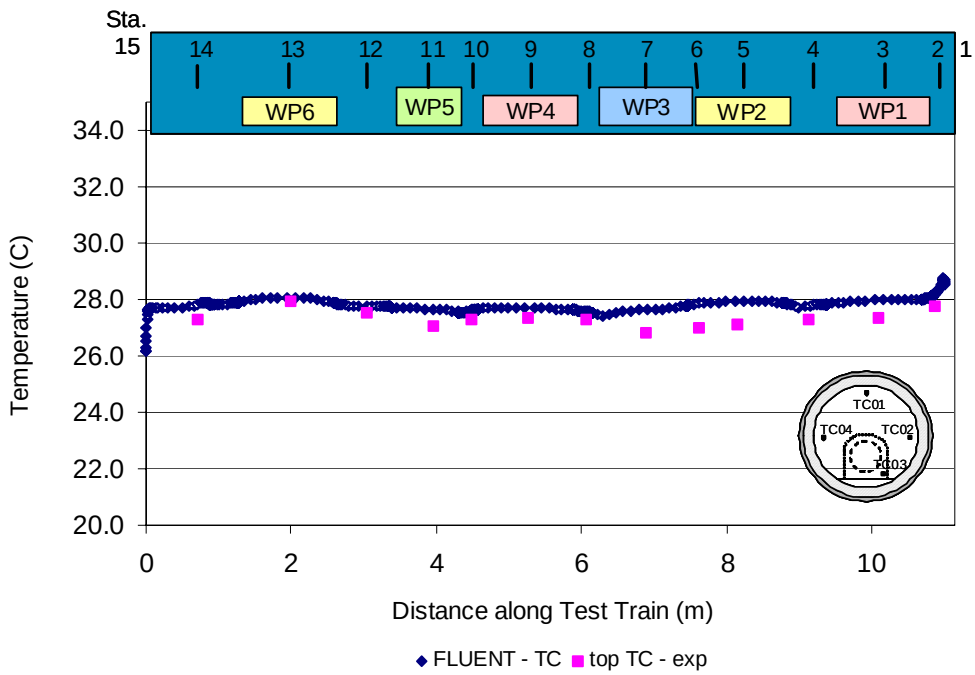

(a)

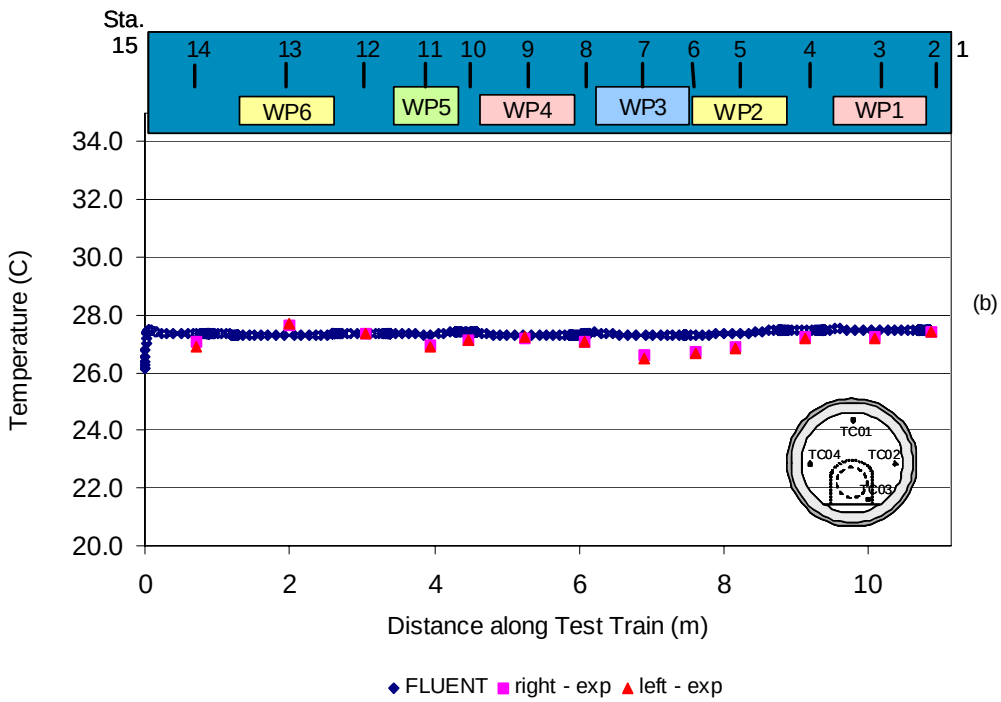

(b)

(b)

DTNs: SN0307T0507803.001 and SN0307T0507803.003.

Figure 7.4.3-11. Comparison of Simulation and Measured Fluid Temperatures for Position of (a) Top Sensor and (b) Side Sensor (Case 4)

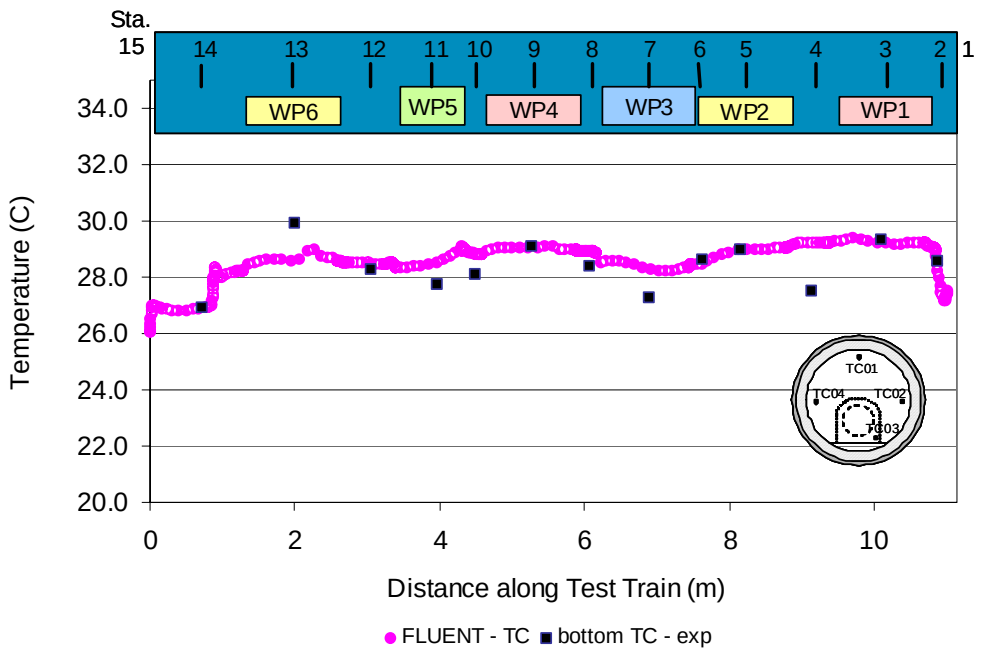

DTNs: SN0307T0507803.001 and SN0307T0507803.003.

Figure 7.4.3-12. Comparison of Simulation and Measured Fluid Temperatures for Positions of Bottom Sensors (Case 4)

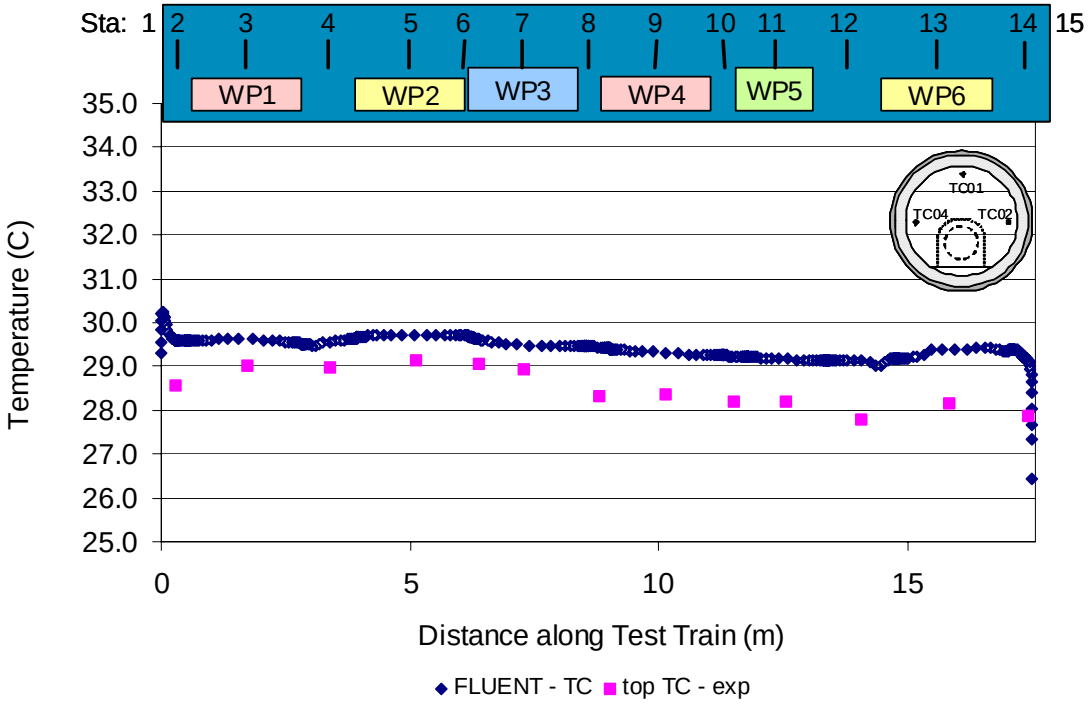

(a)

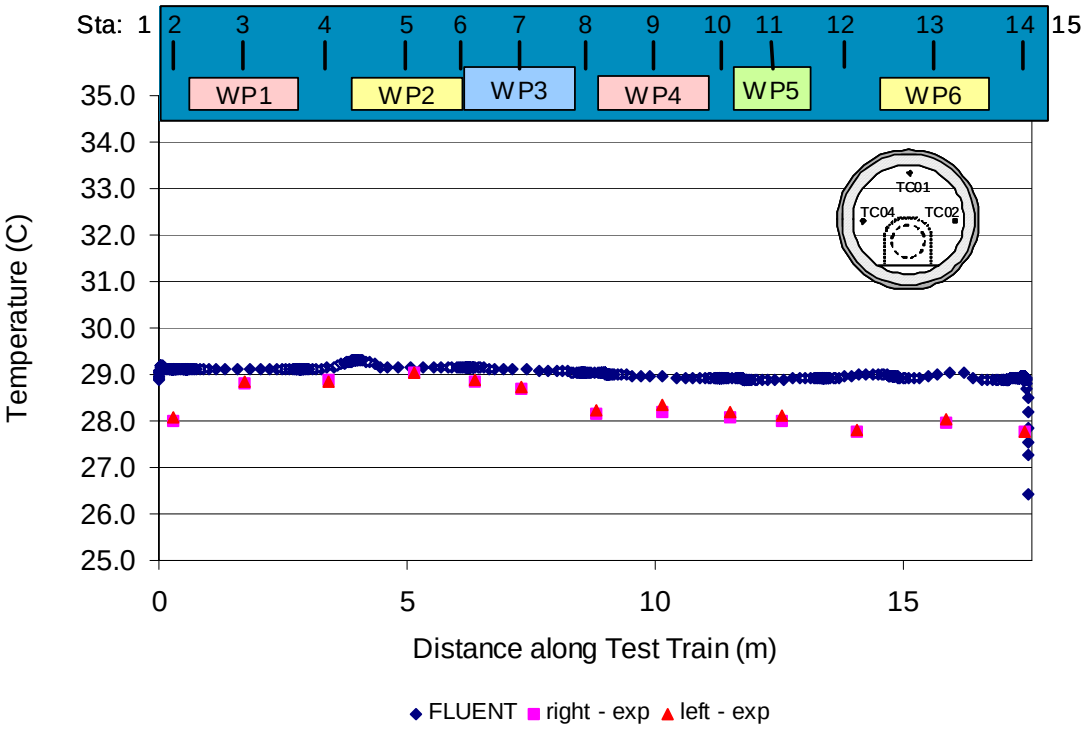

(b)

DTNs: SN0307T0507803.001 and SN0307T0507803.003.

Figure 7.4.3-13. Comparison of Simulation and Measured Fluid Temperatures for Position of (a) Top Sensor and (b) Side Sensor (Case 8)

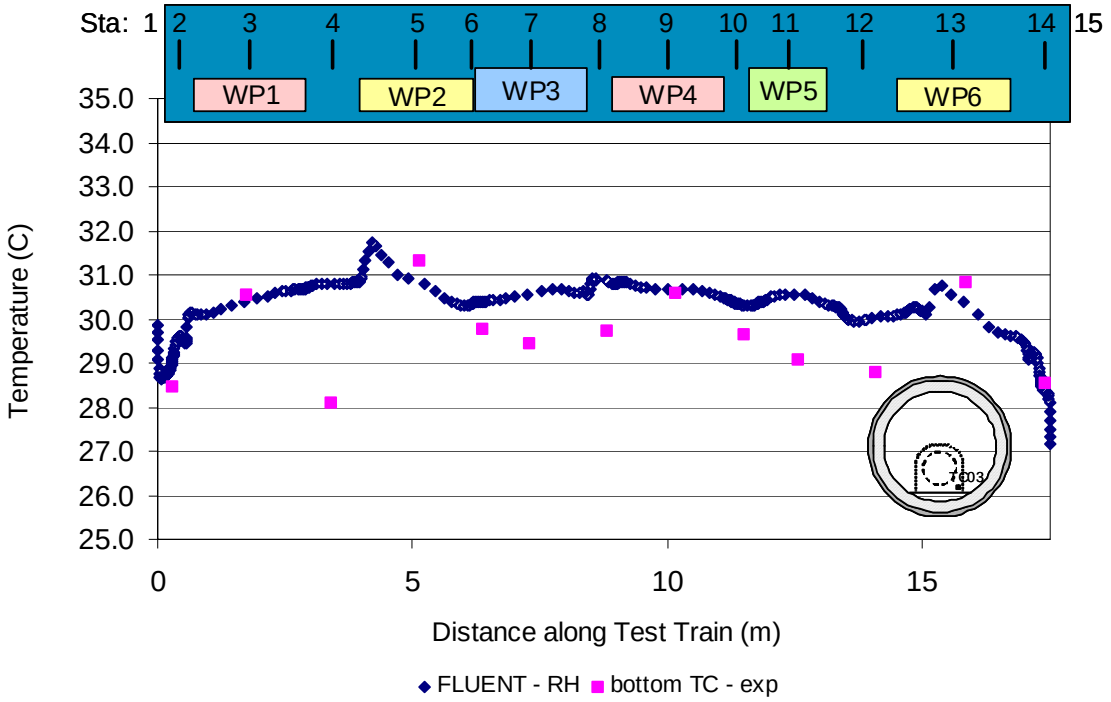

DTNs: SN0307T0507803.001 and SN0307T0507803.003.

Figure 7.4.3-14. Comparison of Simulation and Measured Fluid Temperatures for Positions of Bottom Sensors (Case 8)

INTENTIONALLY LEFT BLANK

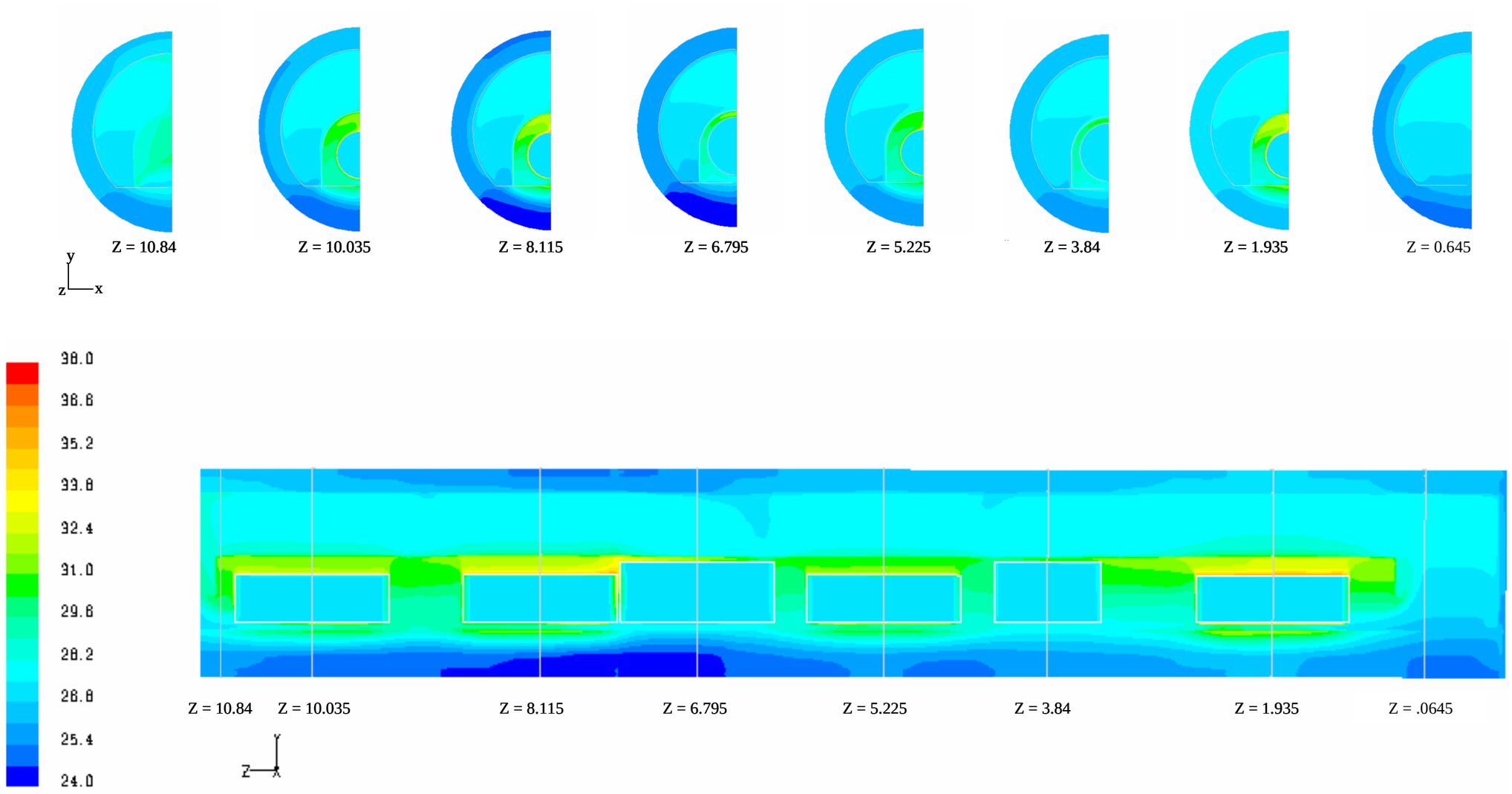

DTN: SN0307T0507803.002.

NOTE: Bottom figure shows temperature contours for each of the symmetry boundaries along the length of the test train. Top figures show temperature contours of a cross section at various z positions. Waste package temperatures have been set to an arbitrary constant value (300K). These cells are not thermally coupled to the rest of the simulation.

Figure 7.4.3-15. FLUENT Temperature Contours for Case 4

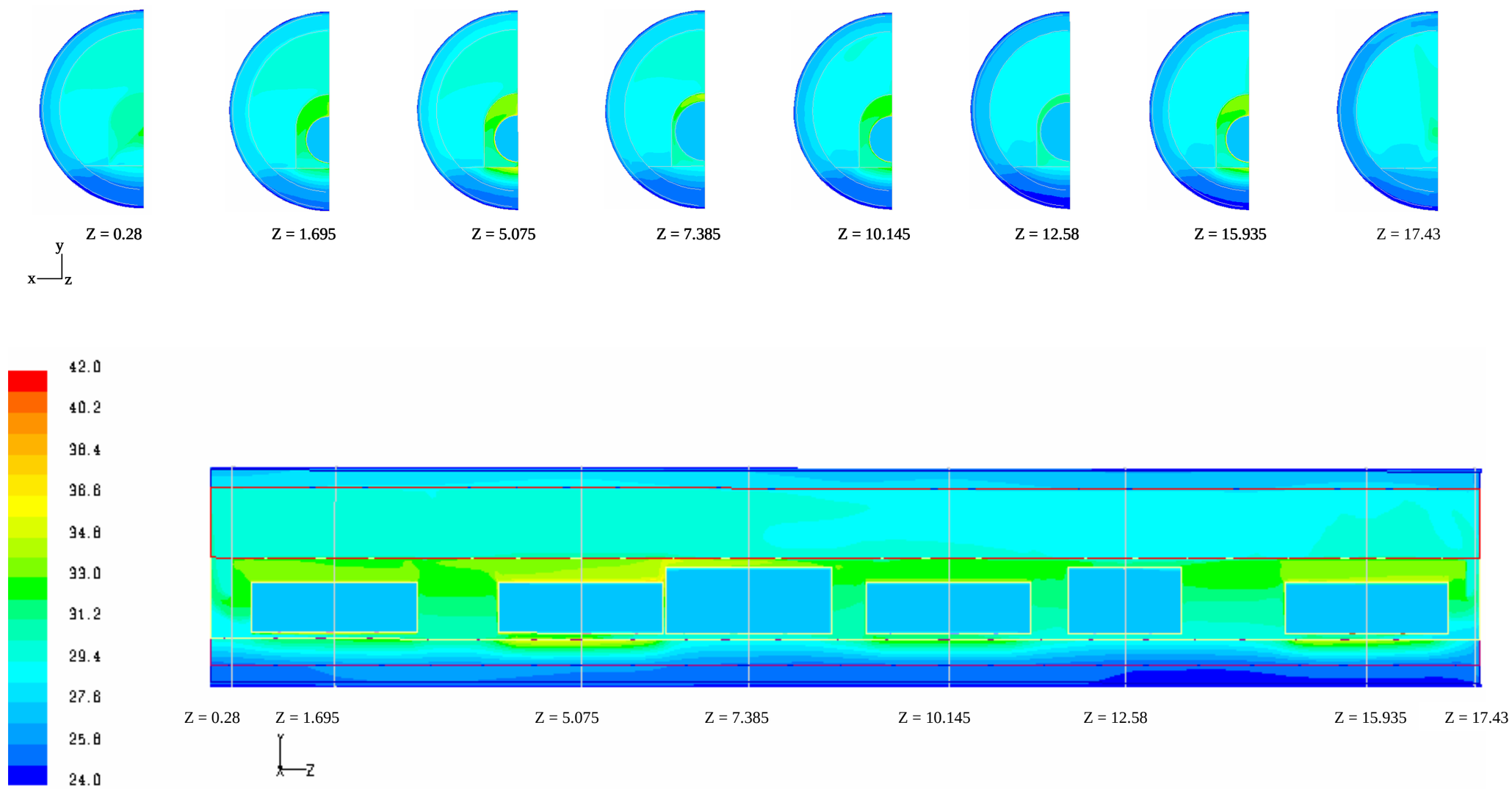

DTN: SN0307T0507803.002.

NOTE: Bottom figure shows temperature contours for each of the symmetry boundaries along the length of the test train. Top figures show temperature contours of a cross section at various z positions. Waste package temperatures have been set to an arbitrary constant value (300K). These cells are not thermally coupled to the rest of the simulation.

Figure 7.4.3-16. FLUENT Temperature Contours for Case 8

Comparison of Velocities

Figures 7.4.3-17 and 7.4.3-18 show side and cross sectional velocity vector plots from FLUENT. The highest velocities are seen at the hot end of the test train, in the gap between waste packages 2 and 3, and at the end of the drip shield closest to the cool end of the test train (Z=0). Flow above the drip shield over hot packages is predominantly in the y direction (air moves up from the top of the hot surfaces and then down along the opposite wall). Axial flow is significant above the cold packages and in the gaps between the packages. The same patterns are seen in the air annulus under the drip shield.

Velocity measurements (omni-directional) from the experiment are given in Tables 7.4.1-3 through 7.4.1-8. These measurements are compared to simulation results in Figures 7.4.3-19 through 7.4.3-22. Velocity data were obtained by inserting the probe to the desired location and observing the sensor output over a time period typically lasting more than a minute. Unlike the CFD simulations which is implicitly steady state flow (because of the use of symmetry), the indicated velocities were typically oscillatory. Because of this unsteady velocity, minimum and maximum velocities were reported at each measurement location. Both the maximum and minimum recorded values are provided in the plots. Data were collected in reference to the insertion depth of the probe from the end of the guide tube. Conversion between this datum and the coordinates used in the FLUENT simulations is presented in Appendix C.

Figure 7.4.3-19 shows measurements at Stations 5 and 11 (centered on hot and cold packages, respectively) for Case 4. Like the other cases, the velocity probe did not sense high velocities at the concrete wall. The fluid in the region between the concrete and the drip shield walls was fairly stagnant. Measured data agrees reasonably well for station 5. At station 11, the velocity probe did not sense any non-zero velocities. Figure 7.4.3-20 shows similar data for Case 8. Data matches reasonably well. One difference in the case figures is the absence of data through the center of the cross-section for Case 4. In the 25% scale tests, the top of the drip shield was in line with the access ports. The probe could only be inserted to the side of the drip shield. In the 44% scale tests, the top of the drip shield was slightly below the access ports, allowing for data to be collected across the entire test train. Both the experimental measurements and the FLUENT data show a stagnant zone immediately above the top of the drip shield. Figures 7.4.3-21 and 7.4.3-22 show velocity profiles along the length of the test train at two different positions above the drip shield. Velocities are higher for the data closer to the top of the drip shield ($y = 0.386$ and $y = 0.62$ m respectively for Cases 4 and 8). These velocities show considerable variation along the axis. The velocities in the more central region of the fluid ($y = 0.586$ and $y = 1.02$ m for Cases 4 and 8, respectively) show less variation. Experimental data follow the general shape of the FLUENT calculated values. However, the data are not adequate to validate the FLUENT simulations for the prediction of natural convection velocities.

INTENTIONALLY LEFT BLANK

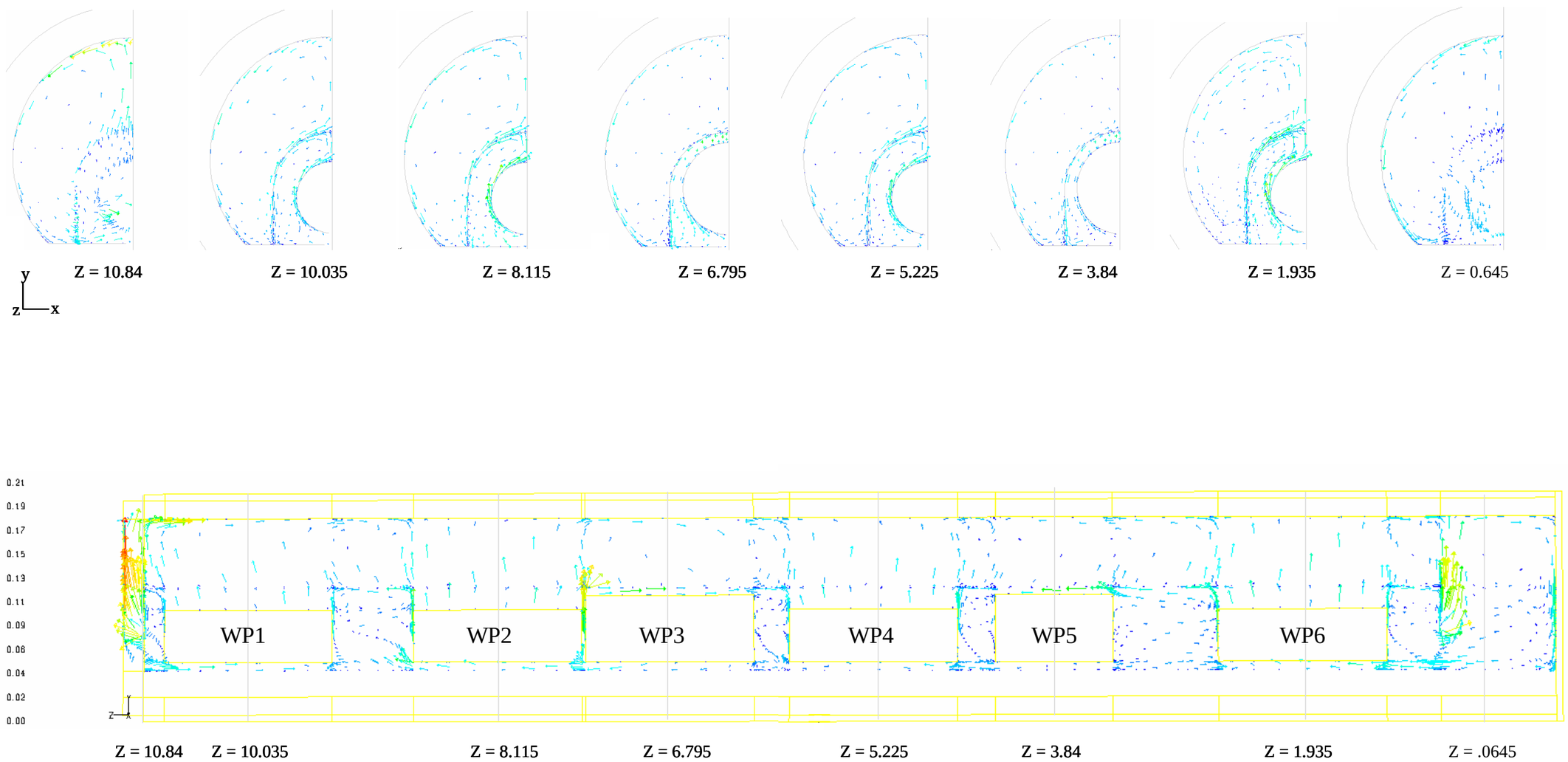

DTN: SN0307T0507803.002.

NOTE: Bottom figure shows velocity vectors for each of the symmetry boundaries along the length of the test train. Top figures show cross sectional vector plots at various z-positions.

Figure 7.4.3-17. FLUENT Velocity Vector Plots for Case 4

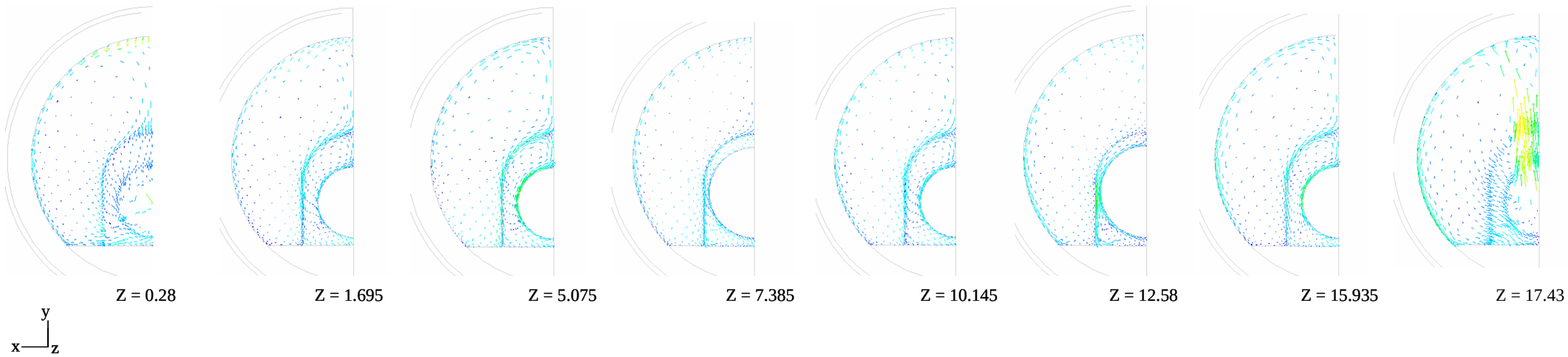

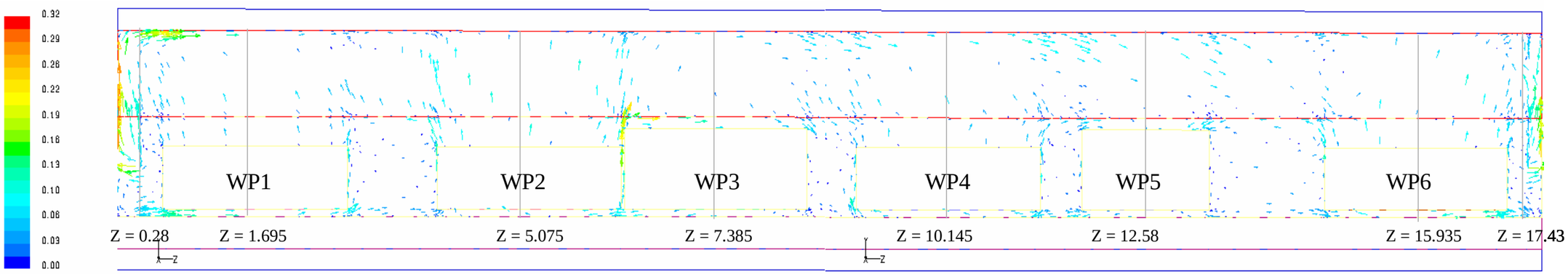

DTN: SN0307T0507803.002.

NOTE: Bottom figure shows velocity vectors for each of the symmetry boundaries along the length of the test train. Top figures show cross sectional vector plots at various z-positions.

Figure 7.4.3-18. FLUENT Velocity Vector Plots for Case 8

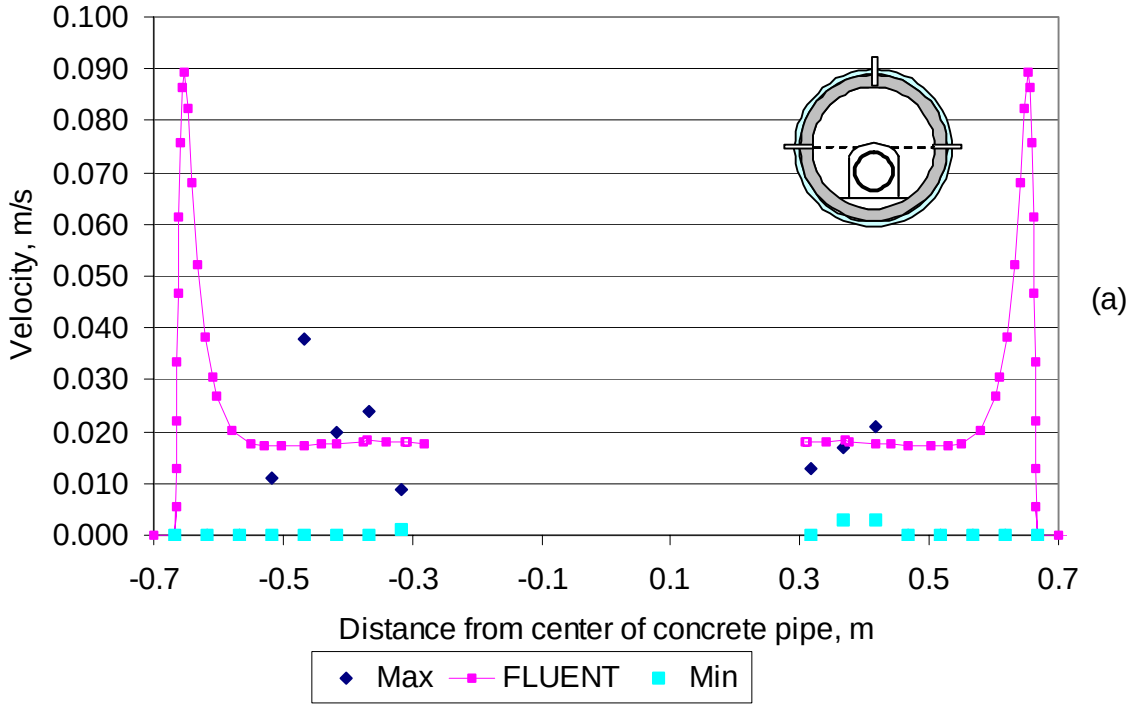

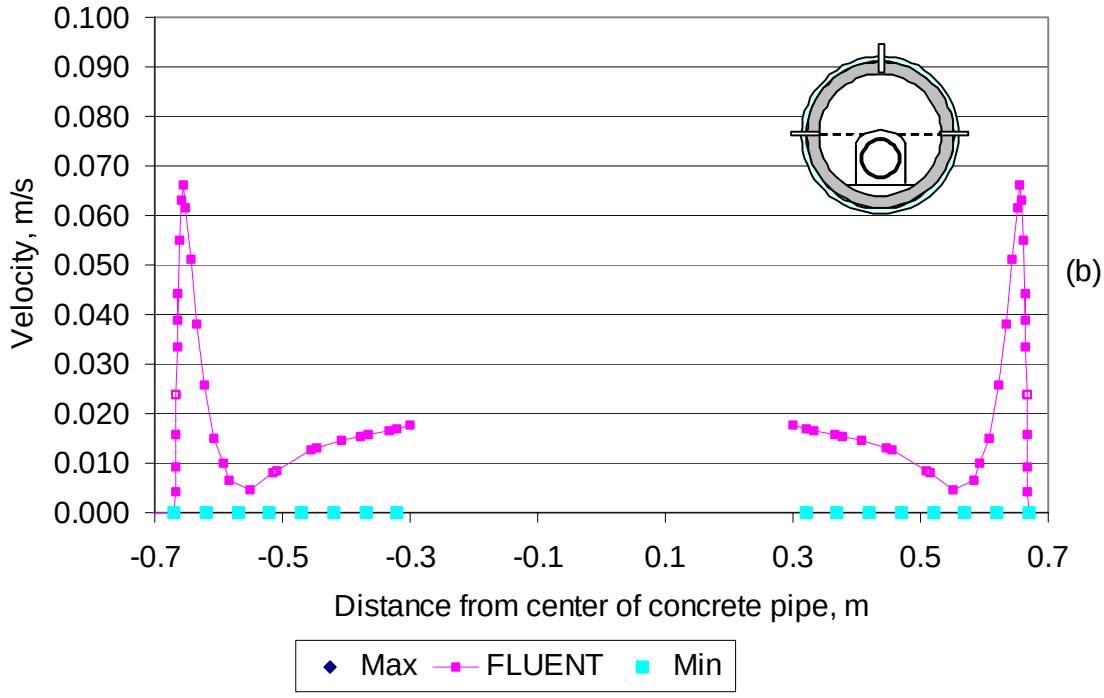

DTNs: SN0307T0507803.001 and SN0307T0507803.002.

NOTE: Measurements were omni-directional.

Figure 7.4.3-19. Comparison of Experimental and Calculated Velocities at (a) Station 5 and (b) Station 11 (Case 4)

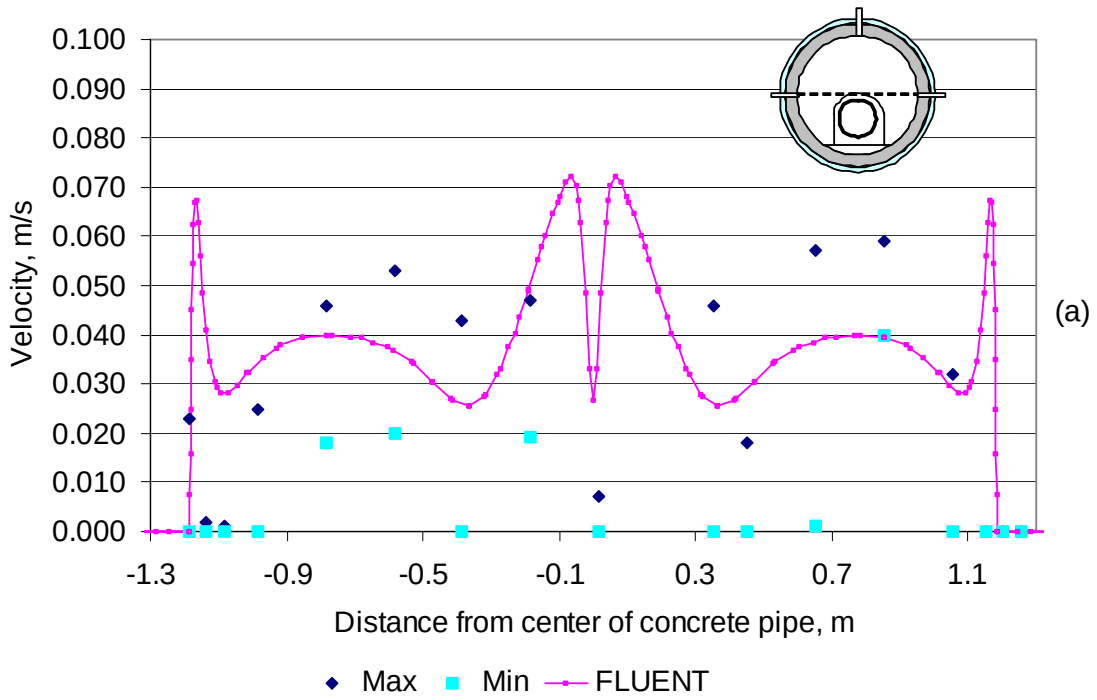

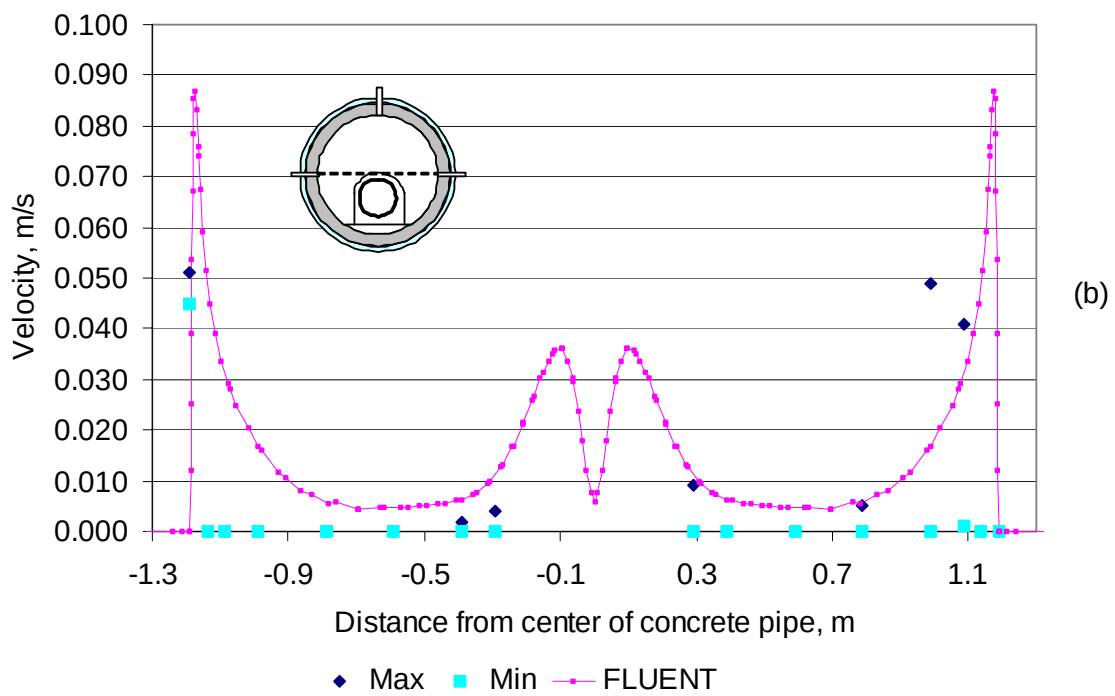

DTNs: SN0307T0507803.001 and SN0307T0507803.002.

NOTE: Measurements were omni-directional.

Figure 7.4.3-20. Comparison of Experimental and Calculated Velocities at (a) Station 5 and (b) Station 7 (Case 8)

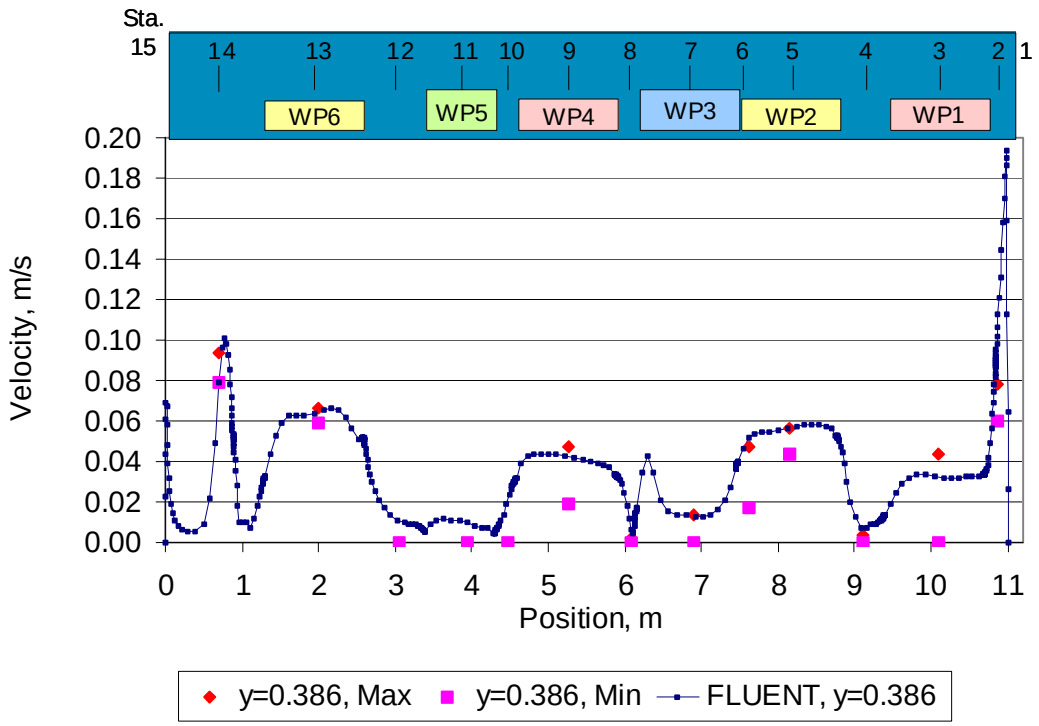

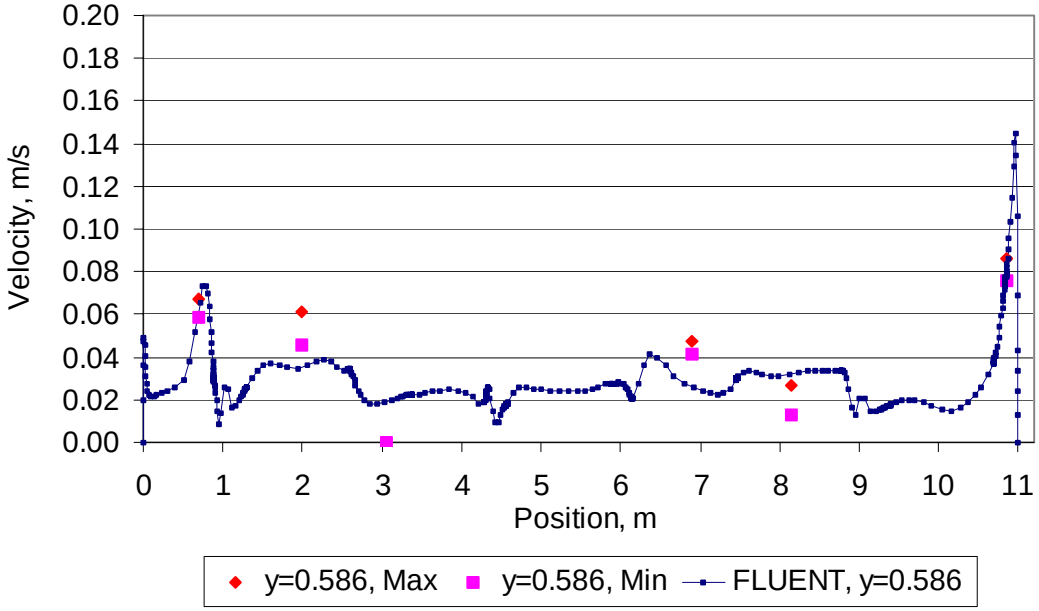

DTNs: SN0307T0507803.001 and SN0307T0507803.002.

NOTE: Measurements were omni-directional.

Figure 7.4.3-21. Comparison of Experimental and Calculated Velocities along the Length of the Test Train (Case 4)

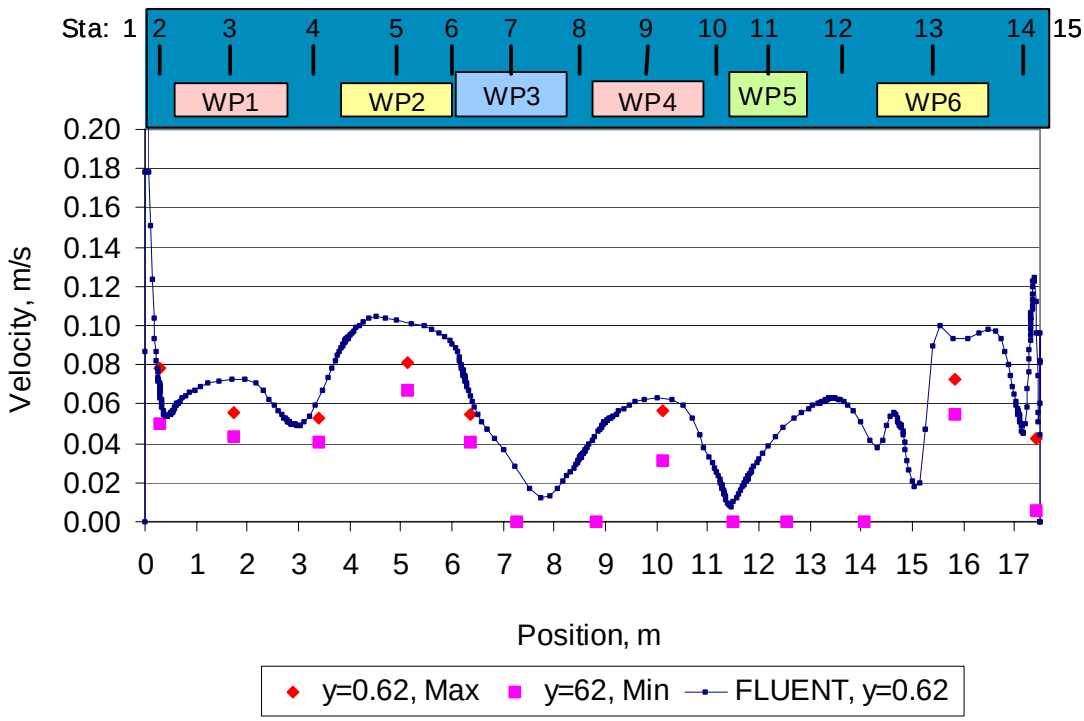

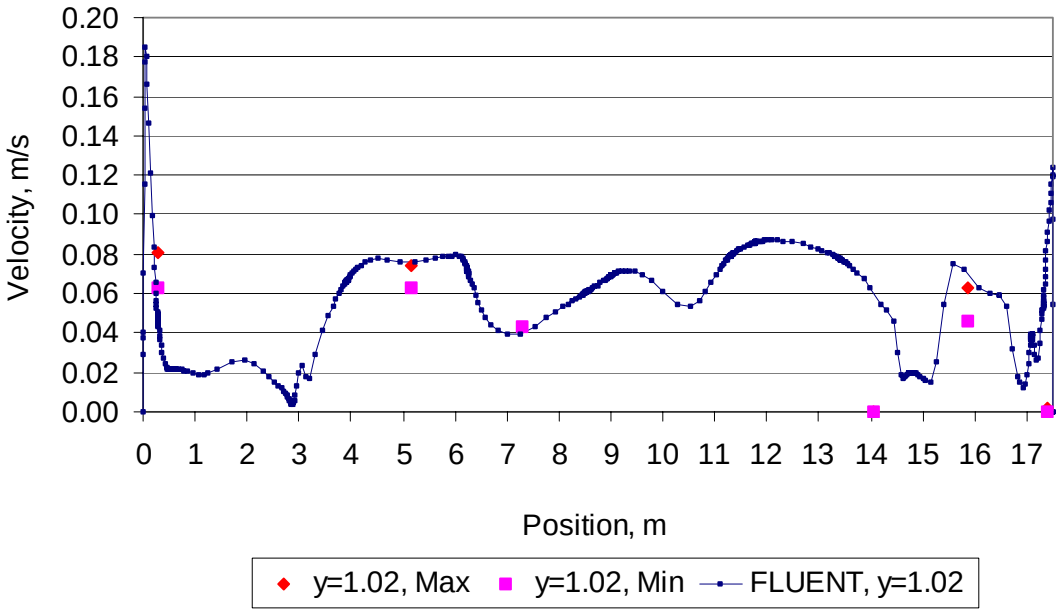

DTNs: SN0307T0507803.001 and SN0307T0507803.002.

NOTE: Measurements were omni-directional.

Figure 7.4.3-22. Comparison of Experimental and Calculated Velocities along the Length of the Test Train (Case 8)

7.4.4 Conclusions

Eight pilot-scale tests were executed at the Department of Energy's North Las Vegas Atlas Facility to evaluate the processes that govern thermal transport in an environment that scales to the proposed repository environment during the postclosure period. The tests were conducted at two geometric scales (25% and 44% of full scale), with and without drip shields, and under both uniform and distributed heat loads. The main purpose of the tests was to generate data that could be compared to predictions by computational fluid dynamics (CFD) codes to enable code validation. While all of the cases were simulated with FLUENT both prior to (blind predictions) and after (post-test comparisons) the execution of the test series, for brevity results from only two configurations are presented. These configurations most closely match the repository design (a configuration with a drip shield and non-uniform power loads). They had the most complex configuration, and hence the most complex heat transfer.

The computational fluids dynamics (CFD) computer code, FLUENT, is used to simulate the experimental tests. For these analyses, steady-state turbulent natural convection heat transfer, conduction, and thermal radiation were considered.

The CFD simulations included the major components of the experiment, including the waste packages (heated steel canisters), invert floor, and emplacement drift (insulated concrete pipe). The simulations do not incorporate details of the waste package supports. A separate CFD simulation is developed for each of the natural convection cases.

A grid independence study is described for both the 25% and 44% scale grids using the blind simulations. In each instance, the study uses a baseline case (Cases 1 and 5 for the 25% and 44% scale test series, respectively). Results from the baseline computational grids are compared with results from refined (or in one instance coarsened) meshes. Grids are adapted using both solution-based methods based on a reduction in y^+ values and by re-creating the mesh to be either more refined or coarse. Temperatures, velocities, and y+ values are compared; the number of cells in flow boundary layers are reviewed to ensure the boundary layers are adequately resolved. Grid independence studies show that confidence in the simulation results is gained by limiting y^+ to values under 5 and checking for adequate resolution of the boundary layers. A summary of the grid independence study can be found in Appendix B.

The blind simulation calculational meshes are used as a starting point to perform post-test calculations. Boundary conditions are altered to better match the experiment. This includes changing the exterior boundary from a constant to a spatially variable temperature boundary, and altering the energy input into the simulations from a constant volumetric heat generation to a constant flux boundary at the waste package surface. Calculated simulation temperatures of the surfaces, as well as the temperature and velocities of the fluid from the post-test runs, are compared with experimental data.

Temperature Comparisons

For both the 25% and 44% scale cases, the simulation temperature results are very similar to measured values. A summary of the temperature comparisons is given below.

25% Scale, Case 4

The calculated temperatures on the inner surface of the concrete match the experimental data very well. Differences between the two data sets are less than 0.2ºC.

Calculated air temperatures both above and within the drip shield match the experimental data within 1.5ºC.

Measurements taken along the side of the drip shield are within 0.3ºC of the simulation values. Measurements at the top of the drip shield show slightly greater differences, but are all within 1ºC of the calculational results.

Temperature sensors were located slightly below the surface of the invert both inside and outside the drip shield. The sensors inside the drip shield were located directly beneath the waste packages. The CFD results match the experimental data within 0.3ºC for the sensors outside the drip shield. The simulation results are consistently higher than the measured data for the sensors inside the drip shield. The greatest differences are seen for those sensors directly under a heated waste package, where FLUENT values are as much as 2.5ºC higher.

Finally, the simulations consistently predict higher temperatures on the exterior surface of the waste package than those measured, typically by 1 to 2ºC. FLUENT also shows greater spatial temperature differences on the package surfaces, with circumferential variations ranging between 0.2 and 2ºC. Differences from the measured data are typically about 0.7ºC.

44% Scale, Case 8

FLUENT results match the measured temperature data at the bottom position of the interior surface of the concrete within 0.1ºC. Comparison of the data sets for the top and side positions on this same surface show reasonable agreement (within 0.3ºC), with the FLUENT results being consistently higher than measured values.

Calculated air temperatures above the drip shield typically match the experimental data within 1ºC. Similar to the results on the interior surface of the concrete exposed to air, the computational results are always higher than the experimental values. Under the drip shield, comparison of the two data sets shows that simulation results are also generally higher than measured values, with most data points matching within 1ºC.

The greatest deviation between the simulations and measured data sets is seen on the drip shield. Values on the side of the shield differ by as much as 3ºC, while those on the top of the shield differ by as much as 2ºC. Simulated temperatures are always higher than measured values.

Invert and waste package temperature comparisons for the 44% test are similar to the 25% test.

While the temperature comparisons of both cases show FLUENT is able to accurately simulate the complex geometry, calculational results from Case 4 more closely match the experimental results. Comparing the trends seen in the data between the two cases, it is observed that both predict similar results for the waste packages and the air and invert under the drip shield. The Case 8 simulations predict higher temperatures on the interior surface of the concrete exposed to

the air, for the air above the drip shield, and for the drip shield surface than were observed in the test.

Velocity Comparisons

Fluid velocities were measured in the experiment using an omni-directional probe. Measurements indicated non-steady flow fields, and minimum and maximum values for a defined measuring period were recorded. The simulation is constructed taking advantage of the geometrical symmetry of the test train. Simulation data are compared to the measured values. The comparison shows consistency in the locations of high and low velocities, as well as in the overall peak values.

Evaluation of Acceptance Criteria

The temperature data-simulation comparisons in this section show that the FLUENT predictions are generally high, though in good qualitative agreement with the observed temperature trends. The predicted temperature values for the drip shield and waste packages are typically 2°C higher than the experimental data. The invert temperature under the drip shield is typically overpredicted by as much as 2.5°C. Based on an approximate temperature difference of 6 to 8°C between the inner surface of the concrete and the hotter waste packages, the difference is about 25 to 33 percent. These results are within the validation criteria of 35 percent. This comparison validates the use of FLUENT to predict component temperature differences.

The overprediction of temperatures is not related to the FLUENT code. The code includes all the relevant physics (Navier-Stokes equations, turbulence, thermal radiation) for an accurate calculation. FLUENT validation calculations for well-controlled laboratory experiments presented in Section 7.3 and validation test problems for natural convection, turbulence, and thermal radiation documented in the FLUENT Software Definition Report (SNL 2002 [DIRS 171415]) and Software Implementation Report (YMP 2003 [DIRS 166345]) confirm this capability. Rather, the overprediction is due to simplifications in the simulation geometry input to the FLUENT code.

The overprediction of the waste package, drip shield and invert temperatures in the simulations is related to the invert and the omission of the emplacement rail system and the waste package supports. As depicted in Figure 7.4.1-2, rails and steel I-beams are placed on top of the invert to support the waste package pallets. These structures, which are not simulated, would increase the effective thermal conductivity of the invert especially near the top of the invert, which would lead to reduced invert surface temperatures and corresponding waste package and drip shield temperatures that would be more in line with the experimental data. In addition, the waste package pallet is not simulated; its inclusion would also increase the heat transfer between the waste package and the invert leading to reduced waste package temperatures.

The FLUENT predictions for fluid velocities are not as good as the temperature predictions. There are also some concerns about the uncertainty associated with the velocity experimental data. The data are omni-directional, so the components of the measured velocity are not available. The result is that, while the predictions are qualitatively reasonable, significant quantitative differences are seen. Based on these comparisons with test data and the concerns

about the uncertainty of the data, FLUENT simulations are not validated for velocity predictions for the conditions similar to those expected in the repository. By extension, FLUENT calculations of mass dispersion coefficients, which are dependent on the detailed velocity field, are also not validated based on the test data. Accordingly, validation is supported by independent technical review as discussed in Section 7.6 and Appendix G.

7.5 DISPERSION COEFFICIENT VALIDATION

Validation of the dispersion coefficients obtained using the convection model is accomplished by independent technical review, in accordance with AP-SIII.10Q, *Models*. The technical reviewer is Professor Ivan Catton of UCLA, who holds a Ph.D. in mechanical engineering from UCLA. He has worked in the fields of heat and mass transport, fluid dynamics, numerical techniques, and nuclear reactor safety for 38 years, including being a member of the USNRC Advisory Committee on Reactor Safeguards. Professor Catton is independent of the development, checking, and interdisciplinary review of the dispersion calculations and of the convection model in general. Professor Catton's review is presented in Appendix G.

The review shows that the criteria for validation of the dispersion coefficients as a product of the convection model are met. Professor Catton states that "it is this reviewers [sic] opinion that, in spite of some open questions, the model as presently being used, is a valid tool for its intended use."

The FLUENT predictions for the gas velocities in the Natural Convection Tests given in this section are in qualitative agreement with the data, but significant quantitative differences in velocities exist. The calculated air2 concentration profiles shown in Figures 6.2.7-1 and 6.2.7-6 show significant "jumps" in the concentrations that may be an artifact of the turbulence submodel used in the convection model. In addition, the calculated influence of the temperature tilt on the dispersion coefficient is significant. Measurement of the dispersion coefficient in a well-controlled experiment would enable evaluation of these dispersion coefficient predictions.

7.6 CONDENSATION MODEL VALIDATION

Model validation is accomplished by a technical review, in accordance with AP-SIII.10Q. The technical reviewer is Dr. Michael F. Young, who holds a Ph.D. in nuclear engineering from the University of Illinois. He has worked in the fields of heat and mass transport, fluid dynamics, numerical techniques, and nuclear reactor safety for 27 years. Dr. Young is independent of the development, checking, and interdisciplinary review of the evaporation/condensation model. He is a permanent employee of Sandia National Laboratories. Dr. Young's review of the evaporation/condensation model is presented in Appendix G.

In addition to Dr. Young's review, Professor Ivan Catton of UCLA reviewed the condensation model. Professor Catton's credentials are summarized in Section 7.5. Professor Catton's review is also presented in Appendix G.

The review in Appendix G shows that the criteria for validation of the condensation model are met. Professor Catton states that "it is this reviewers [sic] opinion that, in spite of some open questions, the model as presently being used, is a valid tool for its intended use."

8. CONCLUSIONS

8.1 TWO-DIMENSIONAL IN-DRIFT CONVECTION

In-drift heat transfer is simulated through the use of a computational fluid dynamics (CFD) code, FLUENT, which solves the time-averaged Navier-Stokes equations including turbulence, and the energy equation including thermal radiation. In-drift heat transfer is thermally coupled to the surrounding rock.

The important physical features including the drip shield, waste packages, and invert are individually represented in three-dimensional simulations summarized in Section 8.2. The two-dimensional simulations use a line-averaged waste package and consider various submodels, such as radiation and turbulence, to evaluate the effect of different submodel assumptions. The uncertainty in the input parameters is evaluated based on the average waste package temperature. These results are used in the selection of various submodels for turbulence and thermal radiation for the three-dimensional convection simulations. The sensitivity study presented in this report shows that the uncertainty in properties used in the simulations will not result in large changes to the thermal environment inside the drift. In addition, the RNG k-ε turbulence model and thermal radiation with a nonparticipating medium are adequate for the three-dimensional simulation calculations.

The two-dimensional in-drift convection simulations are validated by comparison to small-scale literature data for natural convection in horizontal concentric cylinders, which is a geometrically similar configuration to the repository emplacement drifts. The overall heat transfer from the horizontal concentric cylinder geometry predicted by FLUENT compares within 10% of the available literature data over a wide range of Rayleigh numbers including laminar and turbulent flow conditions and within the experimental uncertainty of the data.

The uncertainty results from the two-dimensional in-drift convection simulations are used to justify some of the assumptions in the three-dimensional convection simulations; they are not used directly in TSPA-LA. Restrictions for subsequent use include evaluation against assumptions used in the analysis as documented in this report. The two-dimensional in-drift convection simulations are limited to post-closure conditions and do not include rock fall, repository-wide natural circulation, natural ventilation, or barometric pumping.

The product output DTNs for the two-dimensional in-drift convection simulations are listed in Table 8.1-1.

Table 8.1-1. Product Output DTNs for the Two-Dimensional Natural Convection Simulations

Description	DTN
Revised Fluent 6.0.12 Files for 2-d Natural Convection Sensitivity Study Simulations (submitted 04-Dec-2003).	SN0312T0507803.022
EVALUATION OF UNIFORMITY OF ROCK TEMPERATURES 5 METERS FROM THE DRIFT WALL (submitted 07-Jul-2004).	SN0406T0507803.023
CALCULATION OF 2-D IN-DRIFT TEMPERATURE DISTRIBUTIONS USING FLUENT 6.0.12 FOR COMPARISON TO CONDENSATION VALUES (submitted 07-Jul-2004).	SN0406T0507803.024

Table 8.1-2 lists the Output DTNs for the validation cases discussed in Section 7.3.

Table 8.1-2. Product Output DTNs for the Two-Dimensional Natural Convection Validation Simulations

Description	DTN
FLUENT 6.0.12 FILES FOR THE 2-D CONCENTRIC CYLINDER NATURAL CONVECTION SIMULATIONS (submitted 19-Aug-2003).	SN0308T0507803.014
FLUENT 6.0.12 FILES FOR THE 2-D KUEHN AND GOLDSTEIN NATURAL CONVECTION SIMULATIONS (submitted 19-Aug-2003).	SN0308T0507803.015

8.2 THREE-DIMENSIONAL IN-DRIFT CONVECTION

In-Drift Convection Simulations

In-drift heat transfer is simulated through the use of a computational fluid dynamics (CFD) code, FLUENT, which solves the time-averaged Navier-Stokes equations including turbulence, and the energy equation including thermal radiation. In-drift heat transfer is thermally coupled to the surrounding rock. The variation of the rock temperature along the drift, or the temperature tilt, is included and is a significant factor in the simulation results.

The important physical features including the drip shield, waste packages, and invert are individually represented in three-dimensional simulations. Natural convection and thermal radiation heat transfer are simulated in the air volumes located below and above the drip shield. Due to computational limitations, only a portion of a drift is simulated. The simulation is 71-m long encompassing 14 waste packages, or two 7-package sequences, while a full drift is approximately 600 m long. The spatial and temporal variation of the individual waste package power is included in the simulations.

The three-dimensional simulations use results from the two-dimensional simulations to justify the turbulence and thermal radiation submodels employed. The RNG k-ε turbulence model and thermal radiation with a nonparticipating medium are adequate in the present application. With these results, the three-dimensional simulations are constructed to produce detailed three-dimensional heat transfer and fluid flow velocities in the drift.

Axial mass transport in the drift environment is included in the three-dimensional convection simulations by specification of a trace gas. Cross-sectionally averaged trace gas concentrations can be used along with the flow rate of the tracer and the geometry to specify an effective one-dimensional axial dispersion coefficient down the drift. Axial dispersion coefficients are calculated for the regions inside and outside the drip shield, which are a strong function of temperature tilt. The magnitude of the coefficient is determined by the rate that air mixing occurs locally as well as the how fast air moves up and down the drift. The simulations are run at multiple heat loads (corresponding to times between 300 to 10,000 years after waste emplacement) with uniform and tilted boundary temperatures. These dispersion coefficients are used in the in-drift condensation model as described in this report.

Calculations show that the range in dispersion coefficients for the inner region under the drip shield is 0.006 m^2/s to 0.01 m^2/s and the range for the outer region outside the drip shield is

0.004 m^2/s to 0.1 m^2/s. The lower bound on the dispersion coefficients is found when the outer boundary temperature is uniform. A reasonable upper bound on the dispersion coefficients is found when the outer temperature boundary varies from one end of the simulation to the other. The effect of temperature tilt is substantial. The dispersion coefficient values increase slightly under the drip shield and orders of magnitude outside the drip shield when temperature tilt is included. The tilted boundary temperature is the condition expected for regions near the ends of the repository emplacement drifts. Because only one value can be used for each air volume in the in-drift condensation model, the bounding values presented in this report are reasonable bounds for high and low dispersion coefficients. Restrictions for subsequent use include evaluation against assumptions used in the analysis as documented in this report. The three-dimensional in-drift natural convection simulations and dispersion coefficient results are limited to post-closure conditions and do not include rock fall, repository-wide natural circulation, natural ventilation, or barometric pumping.

The three-dimensional convection simulations are validated by comparison to experimental data from the 25% and 44% Yucca Mountain Natural Convection Tests conducted in the DOE Atlas Facility in North Las Vegas. The predicted component temperatures are generally overpredicted for the waste package, drip shield, and invert under the drip shield due to simplifications in simulating the tests. These predictions are within the range of uncertainty of the experimental data, thereby validating FLUENT for the prediction of component temperatures. The FLUENT predictions for fluid velocities and FLUENT calculations of mass dispersion coefficients are validated by independent technical review. Professor Ivan Catton reviewed the convection and condensation models including the calculations of the dispersion coefficient presented in this report. His review is included in Appendix G.

The results from the in-drift convection simulations are not used directly in TSPA-LA. However, the dispersion coefficients are used in the condensation model (which does directly feed TSPA) and related sensitivity studies.

The product output DTNs for the three-dimensional in-drift convection simulations are listed in Table 8.2-1.

Table 8.2-1. Product Output DTNs for the Three-Dimensional Natural Convection Simulations

Description	DTN
Calculation of Dispersion Coefficients From Fluent 6.0.12 Results (submitted 07-Jul-2004)	SN0406T0507803.025

Table 8.2-2 lists the Output DTNs from the validation runs performed in Section 7.4.

Table 8.2-2. Product Output DTNs for the Three-Dimensional Natural Convection Validation Data-Simulation Comparisons

Description	DTN
Supporting Calculations of Natural Convection Test Data (submitted 23-Jul-2003).	SN0307T0507803.001
Fluent Natural Convection Test Case 4 Revised Boundary Model (submitted 23-Jul-2003).	SN0307T0507803.002
Fluent Natural Convection Test Case 8 Revised Boundary Model (submitted 23-Jul-2003).	SN0307T0507803.003
FLUENT NATURAL CONVECTION TEST, ORIGINAL CASES 1, 4, 5 AND 8 MODELS (submitted 07-Aug-2003).	SN0308T0507803.004
FLUENT 6.0.12 FILES FOR NATURAL VENTILATION TEST CASE 1 GRID INDEPENDENCE STUDY (COARSE GRID MODEL) (submitted 16-Oct-2003).	SN0310T0507803.017
FLUENT 6.0.12 FILES FOR NATURAL VENTILATION TEST CASE 1 GRID INDEPENDENCE STUDY (FIRST ADAPTION OF COARSE GRID BASED ON Y+) (submitted 16-Oct-2003).	SN0310T0507803.018
FLUENT 6.0.12 FILES FOR NATURAL VENTILATION TEST CASE 1 GRID INDEPENDENCE STUDY (SECOND ADAPTION OF COARSE GRID BASED ON Y+) (submitted 16-Oct-2003).	SN0310T0507803.019
FLUENT 6.0.12 FILES FOR NATURAL VENTILATION TEST CASE 1 GRID INDEPENDENCE STUDY (REFINED GRID MODEL) (submitted 16-Oct-2003).	SN0310T0507803.020.
FLUENT 6.0.12 FILES FOR NATURAL VENTILATION TEST CASE 5 GRID INDEPENDENCE STUDY (ADAPTION OF COARSE GRID BASED ON Y+) (submitted 16-Oct-2003).	SN0310T0507803.021.

8.3 IN-DRIFT CONDENSATION MODEL

The in-drift condensation model shows that condensation is a function of both the percolation rate and position in the individual drift. Water evaporated in one portion of the drift can condense 100 m or more away from the source.

Examination of the condensation model results (Section 6.3.7.2, Appendix E, calculation plots in DTN: SN0408T0509903.007) shows that, as time and the percolation rate increase, the condensation rates become more spatially uniform. The spatial variability occurs at earlier times and at lower percolation rates. The reason for this is the relative impact of axial transport of water. When the axial vapor transport is a small fraction of the available water, then the condensation rate on a given surface is primarily a function of local temperature differences and water availability and has a low spatial variability for the uniform percolation profile used in the analyses (Section 6.3.5.1.1).

This observation leads to the simplified abstraction of condensation described in the following sections. Condensation rates are correlated with percolation rate. When the percolation rate is high and the decay heats are small, the correlation has little scatter (example in Appendix H, Figure H.2-5). When the percolation rate is small and the decay heats are large, the correlation has substantial scatter (example in Appendix H, Figure H.2-1). This scatter reflects the relative importance of axial vapor transport.

The likelihood that a particular portion of the drift wall or a particular segment under the drip shield "sees" condensate is also correlated with percolation rate. At late times and high percolation rates, the fraction of the drift wall in the emplacement region where condensate forms correlates well with percolation rate (example in Appendix H, Figure H.2-6). At earlier times and low percolation rates, the correlation has substantial scatter (example in Appendix H, Figure H.2-2). The same trend holds with the likelihood of condensation in the immediate vicinity of waste packages under the drip shield (examples in Appendix I, Figures I.2-3, I.2-4, I.2-7, I.2-8).

The correlations presented in the following sections allow for a simple model of condensation to be implemented in a sampling scheme. First the correlation for the drift wall fraction and the correlation for waste package fraction are calculated from the appropriate fraction correlation. The appropriate correlation is checked for uncertainty if the scatter of the correlation is large. If the sample is determined to have condensate, the rate correlation is used to calculate the condensation rate. When the scatter in the rate correlation is large, the correlation is checked for the uncertainty in condensation rate.

Correlations are provided for permutations of invert transport (low and high) and axial dispersion coefficient (low and high). Low and high values for each of these parameters are sampled with equal frequency in order to reflect the underlying uncertainty in the physical model.

The correlations are to be applied to a selected region when the drift wall temperature of that region reaches the saturation temperature. The likelihood of realizing condensation and the rate of condensation are determined from the appropriate correlations for the time analyzed. If the scatter in the correlation reflects a significant influence of axial transport, the scatter in the correlation is to be sampled.

One consequence of this procedure is that the second stage of drift cooling (Section 6.3.03.1) is included in the use of the abstractions. In the second stage, part of the emplacement drift is above the saturation temperature and part is below. The supporting analyses do not explicitly address this earlier stage. However, the likelihood and rate of condensation is much lower at early times and the second stage of drift cooling is not expected to differ dramatically from the third. This is further supported by the three-dimensional, three-drift porous medium model calculations performed to support *Multiscale Thermohydrologic Model* (BSC 2004 [DIRS 169565], Section 7.5.3). The porous-medium model and the condensation model generate comparable results in terms of the temperature conditions for onset, location, and magnitude of condensation, although the porous-medium model predicts additional condensation to occur within the near-field host rock (Section 6.3.7.2.2; BSC 2004 [DIRS 169565, Section 7.5.3].

8.3.1 Condensation Model Abstraction Summary

The abstraction of the condensation model defines the condensation rate and the likelihood of condensation on the drift wall, under the drip shield, and on the waste packages, and the rate of condensation should it occur. The condensation abstraction includes algorithms used in the TSPA-LA for interpolating the condensation rates and probabilities, and specifies how parameters are used in the model and where they are obtained. In this discussion, negative

values represent condensation and positive values represent evaporation. Condensation can never be positive and the probability of condensation can never exceed unity or be less than zero.

The condensation model considers two types of condensation: wall condensation and drip shield condensation. The wall condensation represents the condensation that could form on the walls of the drifts. The drip shield condensation accounts for the condensation that could form under the drip shield and condensation that might form on the waste packages. These two types of condensation are analyzed with a ventilated and unventilated drip shield. In the ventilated drip shield cases, only wall condensation is produced. In the unventilated drip shield cases, wall and drip shield condensates are produced. Sections 8.3.1.1 and 8.3.1.2 describe the ventilated and unventilated analyses. The values produced by the analyses can be found in Appendices H and I.

8.3.1.1 Ventilated Drip Shield Drift Wall Condensation Model

The wall condensation for the ventilated drip shield conditions is determined through thirty-six different steady-state runs being conducted, with data for each of seven drifts being produced for each of the thirty-six runs:

- (2 dispersion coefficients) × (2 invert transport values) × (3 infiltration cases) × (3 simulation times)

In abstracting the condensation process model results, there are 12 distinct cases:

- (2 dispersion coefficients) × (2 invert transport values) × (3 simulation times)

because the three different infiltration cases are used to create functional relationships in which condensation flux and condensation fraction are dependent upon percolation flux. Some of the twelve distinct cases actually have no condensation at any simulation time. Whether or not the twelve distinct cases for the ventilated drip shield analysis had wall condensation is shown in Table 8.3.2.1-1.

The condensation fraction or probability of condensation on the wall, $P_w(\overline{p})$, for each percolation rate $\overline{p}$ is calculated using the following formula:

$$P_w(\overline{p}) = \frac{\sum L_i}{L_D} \qquad \text{(Eq. 8.3.1.1-1)}$$

Where L_i is the drift length at location i, L_D is the total drift length (not including the empty space at each end of a drift), and the sum ranges over all drift locations at which condensation occurred.

The mean wall condensation rate, $CW(\overline{p})$, in units of (kg/yr/m) for each percolation rate $\overline{p}$ is calculated using the following equation:

$$CW(\overline{p}) = f \times \frac{\sum C_i(\overline{p})}{\sum L_i} \qquad \text{(Eq. 8.3.1.1-2)}$$

where f is the form factor representing the portion of the drip shield under the drift wall; $C_i(\overline{p})$ is the amount of condensation on the wall (kg/yr) that occurs at package location i, integrated over the length of the waste package; L_i is the drift length at location i, and the sums range over all drift locations at which condensation occurs.

The form factor f is 0.36395 (Eq. 6.3-71) and is independent of the waste packages type. This form factor represents the fraction of the drift wall that is over the drip shield. If condensate formed on the wall in this portion of the wall perimeter it would be directly over the drip shield. The calculation length for all of the PWR and BWR waste packages is 5.265 m, the calculation length of the HLW short packages is 3.69 m, and the calculation length of the HLW long packages is 5.317 m. These lengths include the void space between packages (Table 4.1.3-8).

The fraction of the wall where condensate forms $P_w(\overline{p})$ is approximated by the following function:

$$\hat{P}_w = 1 - e^{a\ln(\overline{p})+b} \qquad \text{(Eq. 8.3.1.1-3)}$$

The regression is done by performing a linear regression between $\ln(\overline{p})$ and $\ln[1 - P_w(\overline{p})]$. In this equation, the quantity $\hat{P}_w$ estimates the likelihood of wall condensation $P_w(\overline{p})$. The parameters a and b are the slope and y-intercept of the linear regression, and are found in Appendix H.

The rate of condensation on the wall $CW(\overline{p})$ (in kg/yr/m-of-drift) is approximated by the following function:

$$CW = c\overline{p} + d \qquad \text{(Eq. 8.3.1.1-4)}$$

The regression is done by performing a linear regression between $\overline{p}$ and $CW(\overline{p})$. In this equation, the quantity CW estimates the rate of wall condensation $CW(\overline{p})$. The parameters c and d are the slope and y-intercept of the linear regression, and are found in Appendix H.

The R-squared values and standard errors for the regressions for probability of condensation on the wall are found in Appendix H (DTNs: SN0402T0809903.003 for the well-ventilated drip shield with low-invert transport and SN0402T0809903.004 for the well-ventilated drip shield with high-invert transport). The standard errors are used as uncertainty ranges around the slope and intercept parameters; uncertainty in the slope and intercept parameters is normally distributed about the computed value for parameters stated in Appendix H, with standard deviation equal to the standard error. Sampling for parameter values should be independent.

The data from the DTN are abstracted as follows:

- The four cases corresponding to the four combinations of the two dispersion coefficient values and two invert transport values are treated as four equally likely cases and given equal weight in the TSPA-LA model.

- Non-HLW (commercial spent nuclear fuel) and HLW (co-disposed) packages are treated the same as far as drift wall condensation is concerned, i.e., the abstraction for the fraction of packages hit by condensation and the corresponding condensation flux applies equally to commercial spent nuclear fuel (CSNF) or co-disposal packages.

- In the condensation model the average percolation flux, ($\overline{p}$ **),** represents the average of the MSTHM (BSC 2004 [DIRS 169565]) percolation fluxes along the length of each of the seven simulated drifts. In the TSPA model, $\overline{q}_{perc}$ will represent the average of the percolation flux over one of the five TSPA percolation subregions. The implicit assumption is that the $CW(\overline{p})$ abstraction derived on a drift basis, by using an average MSTHM percolation flux ($\overline{p}$ **)** over the drift length, can be applied at the subregion level in TSPA to the average representative package for that subregion, i.e., both $CW(\overline{q}_{perc})$ and $\hat{P}_w(\overline{q}_{perc})$ are valid functions.

Generally speaking, the correlation of condensation with percolation improves with increasing time and increasing percolation rate. This is because the influence of axial dispersion decreases with increasing time and increasing percolation rate. The limited number of times evaluated precludes a quantitative estimate of the influence of the power decay. However, it is known that the percolation rate increases substantially when the climate changes at 2,000 years. This is the basis of the interpolation scheme.

Additional details specific to each of the four alternative condensation models are listed below. The actual response surfaces and stochastic variables used for these four cases are described in Appendix H.

Low Invert Transport /Low Dispersion Case (Ventilated)

- The condensation rate on the drift wall will be set to zero at early times when the drift temperature is above the saturation (boiling) temperature.

- Between the time that the drift wall reaches the saturation (boiling) temperature and 2,000 years, the 1,000-year correlations will be used.

- After 2,000 years, the values for condensation rate and probability will be obtained by interpolating/extrapolating using the correlations for 3,000 and 10,000 years. If no condensate is predicted at either of these times, the wall condensation rate is zero after 2,000 years.

Low Invert Transport /High Dispersion Case (Ventilated Drip Shield)

- No condensate is predicted to form on the drift wall for the high dispersion case at any time (Section 6.3.7.2.2).

High Invert Transport /Low Dispersion Case (Ventilated Drip Shield)

- The condensation rate on the drift wall will be set to zero at early times when the drift temperature is above the saturation (boiling) temperature.

- Between the time that the drift wall reaches the saturation (boiling) temperature and 2,000 years, the 1,000 years correlations will be used.

- After 2,000 years, the values for condensation rate and probability will be obtained by interpolating/extrapolating using the correlations for 3,000 and 10,000 years.

High Invert Transport /High Dispersion Case (Ventilated Drip Shield)

- The condensation rate on the drift wall is calculated to be zero at 1,000 years. Therefore the condensation rate and probability of condensation will be set to zero through 2,000 years.

- After 2,000 years, the values for condensation rate and probability will be obtained by interpolating/extrapolating using the correlations for 3,000 and 10,000 years.

The following discussion pertains to the use of a form factor discussed above that decreases the amount of total drift-wall condensation that can affect engineered barrier system (EBS) transport. The form factor approach is not the same as that used in the seepage abstraction, but this is justified considering the differences between seepage and condensation as they may affect radionuclide transport in the EBS:

- Whereas the seepage abstraction applies all seepage directly to the drip shield (BSC 2004 [DIRS 169131]), the seepage process is different from condensation in that seepage generally occurs where fracture water accumulates above the opening, whereas condensation occurs on the full exposed perimeter of the drift wall.

- Condensate on the drift wall will tend to be imbibe into the host rock, away from the drift opening. Condensate that does not imbibe runs down the drift walls. Condensate that runs down the drift walls can flow only to the edges of the invert, where it is in contact with the host rock and proceeds to drain away from the drift.

- The condensation abstraction conservatively represents the amount of condensate that can fall onto the drip shield, and like seepage, can enter the invert either at the edge of the drip shield or underneath. The location of entry is closer to the invert center and not in contact with the host rock, hence this water is included in the invert transport part of the EBS transport model (BSC 2004 [DIRS 169868]).

- The EBS-UZ partitioning model is sensitive to the presence of seepage or condensate, and partitions all seepage and drift-wall condensate (as represented by the abstraction) to the fractures of the host rock (BSC 2004 [DIRS 169868]). The flux of liquid water in the invert resulting from condensation is generally much greater than the flux that is partitioned to the rock matrix, therefore when seepage and/or condensation conditions exist, most of the released radionuclide flux is partitioned to the fractures. Changes in the form factor, which control the amount of condensation used in the partitioning calculation, have a relatively small affect on the fraction partitioned to the host rock fractures.

8.3.1.2 Unventilated Drip Shield Condensation Model

The condensation abstraction to be used for TSPA-LA consists of the drift-wall condensation results for the ventilated drip shield cases discussed above. The unventilated drip shield cases are not used as discussed in Section 8.3.2. The results for the unventilated cases, including condensation under the drip shield, are fully described in the following sections for completeness and comparison.

Wall condensation for unventilated conditions is determined in the same manner as wall condensation for ventilated conditions, discussed in Section 8.3.1.1. Table 8.3.2.2-1 summarizes the results of the twelve cases with respect to whether drift wall condensation occurs or not for unventilated conditions.

The general abstraction methodology for wall condensation flux and wall condensation fraction discussed in Section 8.3.1.1 is applied in the same manner for unventilated conditions. The parameters *a*, *b*, *c*, and *d* along with the R-squared values and standard errors and how they are to be used for the unventilated conditions can be found in Appendix I.

Condensation under the drip shield for unventilated conditions is determined through seventy-two different steady-state runs being conducted, with data for each of seven drifts being produced for each of the seventy-two runs:

- (2 dispersion coefficients) × (2 invert transport values) × (3 infiltration cases) × (3 simulation times) × (2 waste types)

In abstracting the condensation process model results, there are twenty-four distinct cases:

- (2 dispersion coefficients) × (2 invert transport values) × (3 simulation times) × (2 waste types)

because the three different infiltration cases are used to create functional relationships in which condensation flux and condensation fraction are dependent upon percolation flux. Some of the twenty-four distinct cases actually have no condensation at any simulation time. Tables 8.3.2.2-2 and 8.3.2.2-3 summarize the results of the twenty-four cases with respect to whether drip shield condensation occurs or not for the HLW (co-disposal) waste packages and the non-HLW (CNSF) waste packages in unventilated conditions.

The likelihood that condensation will form under the drip shield $P_D(\overline{p})$ for each percolation rate $\overline{p}$ and each package type k (HLW, non-HLW) is calculated using the following formula:

$$P_D(\overline{p},k) = \frac{N(k)}{T(k)} \qquad \text{(Eq. 8.3.1.2-1)}$$

where *N(k)* is the number of packages of type k for which condensation under the drip shield occurs or condensation occurs directly on the package, and *T(k)* is the total number of packages of type k. Condensation only occurs directly on some packages where condensation underneath the drip shield also occurs.

The mean condensation rate under the drip shield $CD(\overline{p})$ (kg/yr/waste-package) for each percolation rate $\overline{p}$ is calculated using the following equation:

$$CD(\overline{p}) = \frac{\left(f \times \sum C_i(\overline{p})\right) + WP_i}{N(k)} \qquad \text{(Eq. 8.3.1.2-2)}$$

where *f* is the form factor representing the portion of the package under the drip shield, $\boldsymbol{C_i}(\overline{\boldsymbol{p}})$ is the amount of condensation under the drip shield (kg/yr) that occurs at package location *i*, WP_i is the amount of condensation that occurs on waste package *i*, ***N(k)*** is the number of packages of type k over which condensation occurs, and the sum ranges over all package locations at which condensation occurs under the drip shield. The form factor *f* is 0.34751 for HLW packages and is 0.25966 for non-HLW packages (Eq. 6.3-72). These form factors represent the portion of the package that is under the drip shield where condensation could form. If condensate forms on the drip shield in this area it would be directly over the package.

The likelihood of condensation under the drip shield for a particular waste package type $P_D(\overline{p})$ is approximated by one of the functional forms listed in Table 8.3.1.2-1. For each case, the functional form that best fits the data is chosen; the functional form for each model is presented in Appendix I. For power law and logarithmic functional forms, the data are transformed as indicated in Table 8.3.1.2-1 so that the model parameters are determined by linear regression. The parameters *a* and *b* are the slope and Y-intercept of the linear regression, and are found in Appendix I. In the case of the logarithmic with shift regression model, the parameter *m* is determined by the data, as the largest value of $\overline{\boldsymbol{p}}$ at which condensation does not occur on any package.

Table 8.3.1.2-1. Regression Models for Likelihood of Condensation Under the Drip Shield.

Regression Model	Model Equation	Transformed Equation for Linear Regression	Equation
Linear	$\overline{P}_D = b + a\overline{p}$	N/A	**8.3.1.2-3**
Linear with shift	$\overline{P}_D = \begin{cases} 0 & \overline{p} < m \\ b + a(\overline{p} - m) & \overline{p} \geq m \end{cases}$	Linear regression only on data for which $\overline{p} \geq m$	**8.3.1.2-4**
Logarithmic	$\overline{P}_D = b + a\log_{10}(\overline{p})$	N/A	**8.3.1.2-5**
Logarithmic with shift	$\overline{P}_D = \begin{cases} 0 & \overline{p} < m \\ b + a\log_{10}(\overline{p} - m) & \overline{p} \geq m \end{cases}$	N/A	**8.3.1.2-6**

The rate of condensation under the drip shield $\boldsymbol{CD}(\overline{\boldsymbol{p}})$ is approximated by the following function:

$$\overline{CD} = c\overline{p} + d \qquad \text{(Eq. 8.3.1.2-7)}$$

The regression is done by performing a linear regression between $\overline{p}$ and $CD(\overline{p})$. In this equation, the quantity $\overline{CD}$ estimates the rate of condensation under the drip shield $CD(\overline{p})$. The parameters c and d are the slope and Y-intercept of the linear regression, and are found in Appendix I.

The R-squared values and standard errors for the model parameters for each regression model are also found in Appendix I. The standard errors can be used as uncertainty ranges around the slope and intercept parameters; uncertainty in the slope and intercept parameters should be normally distributed about the computed value for parameters stated in Appendix H, with standard deviation equal to the standard error. Sampling for parameter values should be independent.

The data for condensation under the drip shield from the unventilated drip shield with high-invert transport (contained in DTN: SN0403T0809903.005) are abstracted as follows:

- The four scenarios corresponding to the four combinations of the two dispersion coefficient values and two invert transport values are treated as four equally likely models and are given equal weighting.

- Non-HLW (CSNF) and HLW (co-disposal) packages: are undifferentiated as far as drift wall condensation is concerned, *i.e.*, the abstraction for fraction of drift wall receiving condensate and for drift wall condensation rate is the same for both waste package types. Non-HLW and HLW packages are treated separately for drip shield condensation.

- In the condensation model the average percolation flux for the drift wall, ($\overline{p}$), represents the average of the MSTHM (BSC 2004 [DIRS 169565]) percolation fluxes along the

length of each of the seven simulated drifts. In the TSPA model, $\overline{q}_{perc}$ represents the average of the percolation flux over one of the five TSPA percolation subregions. The implicit assumption is that the $CW(\overline{p})$ abstraction derived on a drift basis, by using an average MSTHM percolation flux over the drift length, can be applied at the subregion level in TSPA to the average representative package for that subregion, i.e., both $CW(\overline{q}_{perc})$ and $\hat{P}_w(\overline{q}_{perc})$ are valid functions. In the condensation model the average percolation flux for the drip shield, $CD(\overline{p})$, represents the average of the MSTHM percolation fluxes along the seven simulated drifts for the given waste package type. Both $CD(\overline{q}_{perc})$ and $\overline{P}_D(\overline{q}_{perc})$ are reasonable estimates as well.

Generally speaking, the correlation of condensation with percolation improves with increasing time and increasing percolation rate. This is because the influence of axial dispersion decreases with increasing time and increasing percolation rate. The limited number of times evaluated precludes a quantitative estimate of the influence of the power decay. However, it is known that the percolation rate increases substantially when the climate changes at 2,000 years. This is the basis of the interpolation scheme.

Additional details specific to each of the four alternative condensation models are listed below. All actual response surfaces and stochastic variables used for these four cases are described in Appendix I.

Low Invert Transport/Low Dispersion Case (Unventilated Drip Shield)

- The condensation rate on the drift wall and drip shield is zero at early times when the drift temperature is above the saturation (boiling) temperature.
- Between the time that the drift wall reaches the saturation (boiling) temperature and 2,000 years, the 1,000-year correlations are used.
- After 2,000 years, the fraction of the drift wall upon which condensate forms and the condensation rate will be obtained by interpolating/extrapolating using the correlations for 3,000 and 10,000 years. Since no condensate is predicted at either of these times, the wall condensation rate is zero after 2,000 years.
- No condensate is predicted to form under the drip shield or on waste packages for the low-invert transport, low dispersion case at any time.

Low Invert Transport /High Dispersion Case (Unventilated Drip Shield)

- No condensate is predicted to form on the drift wall for the high dispersion case at any time.
- No condensate is predicted to form on the drip shield or waste packages for the low-invert transport, high dispersion case at any time.

High Invert Transport /Low Dispersion Case (Unventilated Drip Shield)

- The condensation rate on the drift wall and drip shield is zero at early times when the drift temperature is above the saturation (boiling) temperature.
- Between the time that the drift wall reaches the saturation (boiling) temperature and 2,000 years, the 1,000 years correlations are used.
- After 2,000 years, the values for drift wall condensation rate and probability are obtained by interpolating/extrapolating using the correlations for 3,000 and 10,000 years. Since no condensate is predicted at either of these times, the wall condensation rate is zero after 2,000 years.
- Between the time that the drip shield reaches the saturation (boiling) temperature and 2,000 years, the 1,000 years correlations are used. Since there is no drip shield condensate predicted to form for non-HLW packages at 1,000 years, the rate is zero for these packages.
- After 2,000 years, the values for drift shield condensation rate and probability are obtained by interpolating/extrapolating using the correlations for 3,000 and 10,000 years.

High Invert Transport /High Dispersion Case (Unventilated Drip Shield)

- No condensate is predicted to form on the drift wall for the high dispersion case at any time.
- The condensation rate on the drip shield is zero at early times when the drift temperature is above the saturation (boiling) temperature.
- Between the time that the drip shield reaches the saturation (boiling) temperature and 2,000 years, the 1,000 years correlations is used. Since there is no drip shield condensate predicted to form for non-HLW packages at 1,000 years the rate is zero for these packages.
- After 2,000 years, the values for drift shield condensation rate and probability are obtained by interpolating/extrapolating using the correlations for 3,000 and 10,000 years.

8.3.2 Model Outputs – Condensation Model Summary

The product output DTNs for the in-drift condensation model are listed in Table 8.3.2-1.

Table 8.3.2-1. Product Output DTNs for the In-Drift Condensation Model

Description	DTN
IN-DRIFT CONDENSATION: MATHCAD FILES USED FOR CALCULATION (submitted 07-Sep-2004)	SN0408T0509903.007
IN-DRIFT CONDENSATION: CORRECTED MATHCAD FILES USED FOR CALCULATION (submitted 07-Sep-2004)	SN0408T0509903.008
Excel Files for the Condensation Abstraction: Ventilated Drip Shield; Low Invert Transport (submitted 26-Feb-2004)	SN0402T0809903.003
Excel Files for the Condensation Abstraction: Ventilated Drip Shield; High Invert Transport (submitted 26-Feb-2004)	SN0402T0809903.004
Excel Files for the Condensation Abstraction: Unventilated Drip Shield; High Invert Transport (submitted 31-Mar-2004)	SN0403T0809903.005
Excel Files for the Condensation Abstraction: Unventilated Drip Shield; Low Invert Transport (submitted 31-Mar-2004)	SN0403T0809903.006

The TSPA-LA uses the ventilated drip shield abstraction for condensation on the drift wall (Section 8.3.1.1), and does not use the unventilated drip shield abstraction (Section 8.3.2.2). As stated previously, the unventilated drip shield abstraction is fully developed and presented in this report for completeness and comparison to the ventilated drip shield abstraction.

The ventilated drip shield abstraction is selected for use in TSPA-LA to ensure consistency of assumptions with *Multiscale Thermohydrologic Model* (BSC 2004 [DIRS 169565]), and as part of an integrated approach to screening of features, events, and processes (FEPs) detailed in *Engineered Barrier System Features, Events, and Processes* (BSC 2004 [DIRS 169898], Section 6.2.43). The selection basis is summarized in the following points:

- Condensation is included in the TSPA-LA to address the potential effects on EBS transport (Blair et al., 1998 [DIRS 133836], Section 8), which include: (1) enhanced advective transport from condensate dripping through breaches in the drip shield and waste package, as represented in the EBS Transport Model; (2) greater advective transport through the invert, also controlled by the EBS Transport Model; and (3) greater partitioning of invert transport to the fractures of the host rock, represented by the EBS-UZ Interface Model.

- The ventilated drip shield abstraction maximizes the incidence and rate of drift-wall condensation, because the water vapor that evolves from the invert can condense on the drift wall.

- The MSTHM uses the assumption that the mass fraction of water vapor is uniform in the gas-phase within the emplacement drifts, in order to calculate the relative humidity conditions at the drip shield and waste package surfaces, based on the averaged relative humidity at the drift wall.

- Whereas the condensation model shows that condensation under the drip shield is possible for certain bounding conditions (high-invert transport, unventilated), the consequences of such condensation under are excluded from TSPA-LA (FEP number 2.1.08.14.0A, Table 6.1.2-2) as justified in *Engineered Barrier System Features, Events, and Processes* (BSC 2004 [DIRS 169898]).

Finally, and as noted in Section 1, the terms "ventilated" and "unventilated" describe the limiting conditions for the extent of gas-phase mixing, which is uncertain. The terms do not imply reliance on any specific design features to facilitate mixing for the current drip shield design.

8.3.2.1 Ventilated Drip Shield Condensation Model Output Summary

Table 8.3.2.1-1 summarizes the results of the twelve cases with respect to whether drift wall condensation occurs or not for the ventilated drip shield (see DTN submittals SN0402T0809903.003 and SN0402T0809903.004). All actual response surfaces and stochastic variables used for these cases are described in Appendix H.

Table 8.3.2.1-1. Ventilated Drip Shield: Drift Wall Condensation

Transport	Time (yr)	Dispersion	Condensation on Wall
Mixed High Invert	1,000	High	No
Mixed High Invert	3,000	High	Yes (only at 3 percolation values)
Mixed High Invert	10,000	High	Yes
Mixed High Invert	1,000	Low	Yes
Mixed High Invert	3,000	Low	Yes
Mixed High Invert	10,000	Low	Yes
Mixed Low Invert	1,000	High	No
Mixed Low Invert	3,000	High	No
Mixed Low Invert	1,0000	High	No
Mixed Low Invert	1,000	Low	Yes
Mixed Low Invert	3,000	Low	No
Mixed Low Invert	10,000	Low	No

DTNs: SN0402T0809903.003 and SN0402T0809903.004.

8.3.2.2 Unventilated Drip Shield Condensation Model Output Summary

Table 8.3.2.2-1 summarizes the results of the twelve cases with respect to whether drift wall condensation occurs or not for the unventilated drip shield. All actual response surfaces and stochastic variables used for these cases are described in Appendix I.

Table 8.3.2.2-1. Unventilated Drip Shield: Drift Wall Condensation

Transport	Time (yr)	Dispersion	Condensation on Wall
Unmixed High Invert	1,000	High	No
Unmixed High Invert	3,000	High	No
Unmixed High Invert	10,000	High	No
Unmixed High Invert	1,000	Low	Yes
Unmixed High Invert	3,000	Low	No
Unmixed High Invert	10,000	Low	No
Unmixed Low Invert	1,000	High	No
Unmixed Low Invert	3,000	High	No
Unmixed Low Invert	10,000	High	No
Unmixed Low Invert	1,000	Low	Yes
Unmixed Low Invert	3,000	Low	No
Unmixed Low Invert	10,000	Low	No

DTNs: SN0403T0809903.005 and SN0403T0809903.006.

Tables 8.3.2.2-2 and 8.3.2.2-3 summarize the results of the twenty-four cases with respect to whether drip shield condensation occurs or not for the HLW (co-disposed) waste and the non-HLW (CNSF) waste in unventilated conditions. All actual response surfaces and stochastic variables used for these cases are described in Appendix I.

Table 8.3.2.2-2. Unventilated Drip Shield: Drip Shield Condensation, HLW Waste Packages

Transport	Time (yr)	Dispersion	Condensation under Drip Shield
Unmixed High Invert	1,000	High	Yes
Unmixed High Invert	3,000	High	Yes
Unmixed High Invert	10,000	High	Yes
Unmixed High Invert	1,000	Low	Yes
Unmixed High Invert	3,000	Low	Yes
Unmixed High Invert	10,000	Low	Yes
Unmixed Low Invert	1,000	High	No
Unmixed Low Invert	3,000	High	No
Unmixed Low Invert	1,0000	High	No
Unmixed Low Invert	1,000	Low	No
Unmixed Low Invert	3,000	Low	No
Unmixed Low Invert	10,000	Low	No

DTNs: SN0403T0809903.005 and SN0403T0809903.006.

Table 8.3.2.2-3. Unventilated Drip Shield: Drip Shield Condensation, Non-HLW Waste Packages

Transport	Time (yr)	Dispersion	Condensation under Drip Shield
Unmixed High Invert	1,000	High	No
Unmixed High Invert	3,000	High	Yes (1 occurrence)
Unmixed High Invert	10,000	High	Yes
Unmixed High Invert	1,000	Low	No
Unmixed High Invert	3,000	Low	Yes (3 occurrences)
Unmixed High Invert	10,000	Low	Yes
Unmixed Low Invert	1,000	High	No
Unmixed Low Invert	3,000	High	No
Unmixed Low Invert	1,0000	High	No
Unmixed Low Invert	1,000	Low	No
Unmixed Low Invert	3,000	Low	No
Unmixed Low Invert	10,000	Low	No

DTNs: SN0403T0809903.005 and SN0403T0809903.006.

8.3.3 Restrictions For Subsequent Use – Condensation Model

This abstraction is developed specifically for application in TSPA-LA (the ventilated drip shield, drift wall condensation abstract is used for TSPA-LA). Assumptions and approximations are made in order to integrate with and be consistent with other models and abstractions that are allowed in TSPA-LA. Therefore, individual submodels of this abstraction should not be used independently outside of the TSPA-LA framework, and this abstraction should be reevaluated if any information that feeds it is modified. The in-drift condensation model results are limited to post-closure conditions and do not include rock fall, repository-wide natural circulation, natural ventilation, or barometric pumping. Condensation for rock fall or seismic conditions is discussed in *Engineered Barrier System Features, Events, and Processes* (BSC 2004 [DIRS 169898]).

8.4 K_{EQ} ANALYSIS AND CORRELATIONS

Two-dimensional CFD simulations are run to determine the effective thermal conductivity for emplacement drift geometry under conditions of no fluid movement. The analysis includes the inner and outer drip shield air volumes. The boundary conditions consist of constant waste package, inner invert, outer invert, drip shield, and host rock surface temperatures. Because the purpose of this analysis is to quantify natural convection heat transfer, thermal radiation is not included in the k_{eq} analysis or in the correlation. The effective thermal conductivity is the ratio of the natural convection heat transfer divided by the heat transfer for conduction-only heat transfer.

These analyses are run at different Rayleigh numbers so that the correlation created can be used over a wide range of waste package diameters and waste package thermal output. Correlations are developed for both the inside and outside of the drip shield.

For the inside of the drip shield, the correlations were found to be (Eq. 6.4-5 and 6.4-10 in Chapter 6):

$$k_{eq} = 0.142 Ra_{Lc}^{0.257} \qquad \text{(Eq. 8.4-1)}$$

or

$$k_{eq} = 1450 \overline{T}^{-1.207} \left(\Delta T \, L_c^3 \, P^2 \right)^{0.257} \qquad \text{(Eq. 8.4-2)}$$

Equation 8.4-1 is the general relationship and Equation 8.4-2 is specific to the conditions in the repository drifts. The ranges of validity for these correlations are a characteristic length (see Equation 6.1-10) between 0.3 and 0.7 meters, ΔT between 0.0108°C and 27°C, average fluid temperatures between 20°C and 300°C, pressure between 0.0013 and 10 atmospheres, Rayleigh numbers in the range $4.55 \times 10^4 \leq Ra_{L_c} \leq 3.53 \times 10^8$, and it should only be used for the region inside of the drip shield.

A separate correlation equation is developed for the region outside of the drip shield. Because the region outside of the drip shield does not vary between simulations, the characteristic length does not change. The correlations found are (Eq. 6.4-13 and 6.4-15 in Chapter 6):

$$k_{eq} = 0.100 Ra_{Lc}^{0.263} \qquad \text{(Eq. 8.4-3)}$$

or

$$k_{eq} = 1267 \overline{T}^{-1.236} \left(\Delta T \, L_c^3 \, P^2 \right)^{0.263} \qquad \text{(Eq. 8.4-4)}$$

Equation 8.4-3 is the general relationship. Equation 8.4-4 is specific to the conditions in the repository drifts. The ranges of applicability for these correlations are a characteristic length of 1.5 m, ΔT between 0.0092ºC and 23ºC, average fluid temperatures between 20ºC and 300ºC, pressure between 0.0013 and 10 atmospheres, Rayleigh numbers in the range $1.32x10^6 \leq Ra_{L_c} \leq 4.05x10^9$, and it should only be used for the region outside of the drip shield.

The effective thermal conductivity of the porous media is the equivalent thermal conductivity, which is a ratio, times the molecular thermal conductivity, $k_a(\overline{T})$, or

$$k_{eff,th} = k_{eq} * k_a(\overline{T}) \qquad \text{(Eq. 8.4-5)}$$

Note that the average equivalent thermal conductivity (k_{eq}) is a dimensionless quantity, while the effective thermal conductivity, $k_{eff,th}$, includes the effects of natural convection and has units of thermal conductivity. The two terms should not be confused.

Equations 8.4-1 through 8.4-4 are developed to match the overall heat transfer of a natural convection system with that of a conduction-only system (no thermal radiation). A limitation for users of these equations is that heat transfer by convection and conduction is very different in these two modes. While the overall heat flux is matched in the two approaches, the local variation in temperature may not be as closely matched.

If these correlations are used in a porous media code, the permeability of the region should be zero or small enough in order to suppress fluid movement. If fluid movement is not suppressed, the effect of convection may be double-counted – once through the above correlation, and once through the simulated fluid movement.

The equivalent thermal conductivity correlations are limited to post-closure conditions and do not include rock fall, repository-wide natural circulation, natural ventilation, or barometric pumping. Parameter limits on the equivalent thermal conductivity correlations are explicitly listed in Table 6.4.7-3.

The product output DTN for the two-dimensional k_{eq} analysis and correlations is given in Table 8.4-1.

Table 8.4-1. Product Output DTN for the k_{eq} Analysis and Correlations

Description	DTN
Fluent 6.0.12 Files for the 2-D Natural Convection Simulations for Equivalent Thermal Conductivity Determination and Comparison to Kuehn and Goldstein Models and Data (submitted 15-jul-2004)	SN0407T0507803.026

8.5 EVALUATION OF YUCCA MOUNTAIN REVIEW PLAN CRITERIA

This model report predicts results that directly pertain to the abstraction of the quantity of condensate contacting engineered barriers and waste forms. This section summarizes the contents of this report as they apply to NRC criteria for a detailed review of that abstraction. These are the relevant criteria from *Yucca Mountain Review Plan, Final Report* (NRC 2003, Section 2.2.1.3.3.3 [DIRS 163274] which is from 10 CFR 63.114(a)-(c) and (e)-(g)).

This report provides predictions of the probability and rate of condensation on the drift walls, engineered barriers, and waste packages; it does not predict seepage rates or water chemistry. Abstractions of these condensation predictions are provided to the downstream process models for use in global calculations of in-drift coupled flow and transport processes. An acceptance criterion is not relevant to this report if it applies only to the chemistry of water, only to seepage, or to the model abstraction.

8.5.1 Acceptance Criterion 1: *System Description and Model Integration Are Adequate*.

1) *Total system performance assessment adequately incorporates important design features, physical phenomena, and couplings, and uses consistent and appropriate assumptions throughout the quantity and chemistry of water contacting engineered barriers and waste forms abstraction process.*

   Section 4.1 lists the sources of input for design features and physical features. Most of the design features that are inputs to the natural convection and condensation analyses are in accordance with Interface Exchange Design Drawings (IEDs). Appendix K discusses the effects of small changes to the IEDs subsequent to the calculations documented in this report. Supplementary properties of the planned components are inputs from ASME standards and other justified sources. These design features and couplings are adequately and appropriately incorporated into the natural convection and condensation models documented in this report. Simplifying assumptions about material properties are stated, justified, and appropriate. The ventilation efficiency as a function of drift location and time is input from *Ventilation Model and Analysis Report* (BSC 2004 [DIRS 169862]).

   Properties of the natural materials are taken from the Technical Data Management System (DTN numbers in Section 4.1), *Thermal Conductivity of the Potential Repository Horizon* (BSC 2004 [DIRS 169854]), and other justified sources. These sources assure consistency in the calculation of the quantity of water contacting engineered barriers and waste forms in the abstraction process.

2) *The abstraction of the quantity and chemistry of water contacting engineered barriers and waste forms uses assumptions, technical bases, data, and models, that are appropriate and consistent with other related U.S. Department of Energy abstractions. For example, the assumptions used for the quantity and chemistry of water contacting engineered barriers and waste forms are consistent with the abstractions of "Degradation of Engineered Barriers" (Section 2.2.1.3.1); "Mechanical Disruption of Engineered Barriers (Section 2.2.1.3.2); "Radionuclide Release Rates and Solubility Limits" (Section 2.2.1.3.4); "Climate and Infiltration" (Section 2.2.1.3.5); and "Flow Paths in the Unsaturated Zone" (Section 2.2.1.3.6). The descriptions and technical bases provide transparent and traceable support for the abstraction of quantity and chemistry of water contacting engineered barriers and waste forms;*

   The technical bases provide transparent and traceable support for the abstraction of quantity of water contacting engineered barriers and waste forms. The abstractions of the condensation rates (Section 8.3, Appendices H and I) are based upon models that include direct inputs (Section 4.1) from established sources (see item 1 above). The abstraction is clearly documented in this report as well as in the output DTNs (Table 8.3.2-1). The ventilated drip shield assumption used to select the abstraction of condensation for TSPA-LA is consistent with a similar assumption made in *Multiscale Thermohydrologic Model* (BSC 2004 [DIRS 169565]).

3) *Important design features, such as waste package design and material selection, backfill, drip shield, ground support, thermal loading strategy, and degradation processes, are adequate to determine the initial and boundary conditions for calculations of the quantity and chemistry of water contacting engineered barriers and waste forms;*

   The waste package design and materials, drip shield design, thermal loading strategy, and time-varying decay heats are used directly in both the natural convection and condensation analyses. The IEDs are the sources of these inputs (Section 4.1). These inputs are adequate for the determination of initial and boundary conditions used in this analysis.

4) *Spatial and temporal abstractions appropriately address physical couplings (thermal-hydrologic-mechanical-chemical). For example, the U.S. Department of Energy evaluates the potential for focusing of water flow into drifts, caused by coupled thermal-hydrologic-mechanical-chemical processes;*

   This report addresses the coupling of water vapor condensation on surfaces within the emplacement drifts to the gas natural convection within the drift and the axial temperature profiles on the drift wall surface. This is integrated into the abstraction for total system performance assessment in the form of correlations for condensation rates and probabilities as a function of percolation rate (Section 8.3, Appendices H and I). This allows the total system performance assessment to account for spatial variations based upon local percolation rates. The temporal abstraction of the condensation probability/rate accounts for the climate changes. The condensation abstractions therefore appropriately address physical couplings.

5) *Sufficient technical bases and justification are provided for total system performance assessment assumptions and approximations for modeling coupled thermal-hydrologic-mechanical-chemical effects on seepage and flow, the waste package chemical environment, and the chemical environment for radionuclide release. The effects of distribution of flow on the amount of water contacting the engineered barriers and waste forms are consistently addressed, in all relevant abstractions;*

   This report provides sufficient technical bases and justification about natural convection and condensation in the emplacement drift to the total system performance assessment (TSPA) for its assumptions and approximations. The effect of percolation on the calculation of condensation rate and fraction is integral to the condensation model (Section 6.3.5.1.1). Percolation fluxes are taken from the UZ flow models, including uncertainties. Hence, the effect of flow distribution on condensation is addressed in a manner consistent with the repository characterization in both the detailed models and in the condensation abstractions. Selection of the condensation abstraction for TSPA-LA is consistent with other models and is justified in *Engineered Barrier System Features, Events, and Processes* (BSC 2004 [DIRS 169898], Section 6.2.43) (see Section 8.3.2).

6) *The expected ranges of environmental conditions within the waste package emplacement drifts, inside of breached waste packages, and contacting the waste forms and their evolution with time are identified. These ranges may be developed to include: (i) the effects of the drip shield and backfill on the quantity and chemistry of water (e.g., the potential for condensate formation and dripping from the underside of the shield); (ii) conditions that promote corrosion of engineered barriers and degradation of waste forms; (iii) irregular wet and dry cycles; (iv) gamma-radiolysis; and (v) size and distribution of penetrations of engineered barriers;*

   The environmental conditions within the emplacement pertinent to evaporation and condensation are i) the drift wall temperature and axial temperature profile, and ii) the vapor pressure at the invert surface. The drift wall temperature and temperature profile are estimated from line source solutions for thermal conduction at various times after emplacement (Section 6.3.5.1.1). The vapor pressure at the invert surface is bounded by the equation of state of water. These estimates and bounds are sufficient for their intended purpose. The natural convection patterns (Section 6.2.7) and condensation rates are calculated for times of 300, 1,000, 3,000, and 10,000 years (Section 6.3.7). This provides the basis for the evolution of condensation with time.

7) *The model abstraction for quantity and chemistry of water contacting engineered barriers and waste forms is consistent with the detailed information on engineered barrier design and other engineered features. For example, consistency is demonstrated for: (i) dimensionality of the abstractions; (ii) various design features and site characteristics; and (iii) alternative conceptual approaches. Analyses are adequate to demonstrate that no deleterious effects are caused by design or site features that the U.S. Department of Energy does not take into account in this abstraction.*

   The natural convection and condensation models use the waste package design and materials, drip shield design, thermal loading strategy, and time-varying decay heat rate (Section 4.1). The IEDs are the sources of these inputs. Therefore the model abstraction for condensation fraction and rate (Section 8.3) is consistent with the detailed information on engineered barrier design and other engineered features.

8) *Adequate technical bases are provided, including activities such as independent modeling, laboratory or field data, or sensitivity studies, for inclusion of any thermal-hydrologic-mechanical-chemical couplings and features, events, and processes;*

   The technical basis for the two-dimensional and three-dimensional modeling of natural convection is based on experimental data. The in-drift convection simulations have been validated by comparison to small-scale literature data for natural convection in horizontal concentric cylinders, which is a geometrically similar configuration to that of Yucca Mountain (Section 7.3). The overall heat transfer from the horizontal concentric cylinder geometry predicted by FLUENT compares very well with the available literature data over a wide range of Rayleigh numbers, including laminar and turbulent flow conditions, and is well within the experimental uncertainty of the data.

The convection model has also been validated by comparison to experimental data from the 25% and 44% Yucca Mountain Natural Convection Tests conducted in Las Vegas (Section 7.4). The temperature data-simulation comparisons in this section show that the FLUENT predictions are generally high, though in good qualitative agreement with the observed temperature trends. The results are within the justified validation criteria thereby validating the use of FLUENT to predict component temperature differences.

Coupled processes that are not addressed in this report are considered, and their rationale for exclusion is presented in *Engineered Barrier System Features, Events, and Processes* (BSC 2004 [DIRS 169898]).

9) *Performance-affecting processes that have been observed in thermal-hydrologic tests and experiments are included into the performance assessment. For example, the U.S. Department of Energy either demonstrates that liquid water will not reflux into the underground facility or incorporates refluxing water into the performance assessment calculation, and bounds the potential adverse effects of alteration of the hydraulic pathway that result from refluxing water.*

   The three-dimensional natural convection simulations are validated against a series of scaled tests designed to observe natural convection flow patterns (Section 7.4). The tests were conducted at two geometric scales (25% and 44% scales based on the repository design), with and without drip shields, and under both uniform and distributed heat loads. Both cross-sectional and axial flow velocities were measured in these tests. The gas flow patterns are found to be directly responsible for the redistribution of moisture within the drift. Evidence of moisture migration is also observed in the ECRB Cross Drift (BSC 2004 [DIRS 170004] Section 6.10.2.2) and in the Drift-Scale Test (Blair et al., 1998 [DIRS 133836], Section 8). Hence the argument for vapor migration by natural convection is well grounded in experimental observation.

12) *Guidance in NUREG-1297 and NUREG-1298 (Altman, et. al., 1988 [DIRS 103597 and 103750]), or other acceptable approaches, is followed.*

   Inputs were selected and documented, and documents were checked and reviewed according to applicable BSC procedures, which comply with NUREG-1297 and 1298 (Section 2).

8.5.2 Acceptance Criterion 2: *Data Are Sufficient for Model Justification.*

1) *Geological, hydrological, and geochemical values used in the license application are adequately justified. Adequate description of how the data were used, interpreted, and appropriately synthesized into the parameters is provided;*

   Properties of the natural materials are taken from the Technical Data Management System (DTN numbers in Section 4.1), *Thermal Conductivity of the Potential Repository Horizon* (BSC 2004 [DIRS 169854]), and other appropriately justified sources. Descriptions of how the data were used, interpreted, and appropriately synthesized into the parameters are provided in those documents.

2) *Sufficient data were collected on the characteristics of the natural system and engineered materials to establish initial and boundary conditions for conceptual models of thermal-hydrologic-mechanical-chemical coupled processes, that affect seepage and flow and the engineered barrier chemical environment;*

   Initial and boundary conditions for the natural convection and condensation models are described for this report (Sections 6.1.5.1.3, 6.2.5.1.3, 6.3.5.1.1). They are appropriate for their intended purposes and are consistent with the other coupled process models.

3) *Thermo-hydrologic tests were designed and conducted with the explicit objectives of observing thermal-hydrologic processes for the temperature ranges expected for repository conditions and making measurements for mathematical models. Data are sufficient to verify that thermal-hydrologic conceptual models address important thermal-hydrologic phenomena;*

   The two-dimensional and three-dimensional natural convection simulations are validated against experimental data specific to the repository design as well as more generic data in the published literature. Validation against these measurements is documented in Section 7.

   The natural convection tests discussed in Section 7.4 were designed to evaluate fluid flow and heat transfer processes under conditions similar to repository post-closure conditions. These tests were designed to recreate these processes at a much smaller scale than the full-scale repository (Kalia 2001 [DIRS 156939]). Because it was not practical to maintain Rayleigh numbers between scaled test and full-scale repository, scaling was based on maintaining equal heat fluxes and direct geometric scaling. Tests at two different geometric scales (25% and 44%) are used to provide confidence in extrapolation to full-scale conditions. The Scientific Investigation Test Plan, *Atlas Natural Convection Test Plan* (BSC 2002 [DIRS 158192]), provides the complete scaling analysis.

The temperature ranges of this experiment are lower than those expected in the repository as shown in Section 7.4. The experiments were conducted to investigate the heat transfer processes important during post-closure conditions. The important heat transfer phenomena are operative in these experiments, even at the lower temperatures.

4) *Sufficient information to formulate the conceptual approach(es) for analyzing water contact with the drip shield, engineered barriers, and waste forms is provided;*

   The processes of natural convection and vapor transport are well known and adequately documented in the literature (Bird et al. (1960) [DIRS 103524]). This is sufficient information to formulate the conceptual approach used to analyze natural convection and vapor condensation.

8.5.3 Acceptance Criterion 3: *Data Uncertainty Is Characterized and Propagated Through the Model Abstraction.*

1) *Models use parameter values, assumed ranges, probability distributions, and bounding assumptions that are technically defensible, reasonably account for uncertainties and variabilities, and do not result in an under-representation of the risk estimate;*

   The model parameter values are selected based upon the characteristics of the input and are considered representative of the natural and engineered systems (Section 4.1). Design information is taken from Interface Exchange Drawings and qualified analyses. Boundary conditions and percolation fluxes are from UZ flow models, including uncertainties. Properties of the natural and engineered materials are based upon measurements taken and documented in accordance with DOE quality requirements (Section 4.1). Uncertainties in percolation rate (Section 6.3.5.2.3), the effects of water transport in the invert (6.3.3.2.1), and the rate of vapor axial dispersion (Section 6.2.7) are included in the abstraction and the underlying models. When modeling decisions were necessary, the choices were made to result in conservative outcomes that avoid dilution of overall risk.

2) *Parameter values, assumed ranges, probability distributions, and bounding assumptions used in the total system performance assessment calculations of quantity and chemistry of water contacting engineered barriers and waste forms are technically defensible and reasonable, based on data from the Yucca Mountain region (e.g., results from large block and drift-scale heater and niche tests), and a combination of techniques that may include laboratory experiments, field measurements, natural analog research, and process-level modeling studies*

   Parameter values identified in Section 4 are appropriate and justified. Bounding assumptions (Sections 6.1.3.2, 6.2.3.2, 6.3.3.2, 6.4.3.2) are based upon either approximations whose consequence has little sensitivity or physical limits. Both parameter values and bounding assumptions are technically defensible and reasonable.

3) *Input values used in the total system performance assessment calculations of quantity and chemistry of water contacting engineered barriers (e.g., drip shield and waste package) are consistent with the initial and boundary conditions and the assumptions of the conceptual models and design concepts for the Yucca Mountain site. Correlations between input values are appropriately established in the U.S. Department of Energy total system performance assessment. Parameters used to define initial conditions, boundary conditions, and computational domain in sensitivity analyses involving coupled thermal-hydrologic-mechanical-chemical effects on seepage and flow, the waste package chemical environment, and the chemical environment for radionuclide release, are consistent with available data. Reasonable or conservative ranges of parameters or functional relations are established.*

   The model parameter values are selected based upon the characteristics of the input and are considered representative of the natural and engineered systems (Section 4.1). Design information is taken from Interface Exchange Drawings and qualified analyses.

Boundary conditions and percolation fluxes (Section 6.3.5.2.3) are from UZ flow models, including uncertainties. Properties of the natural and engineered materials are based upon measurements taken and documented in accordance with DOE quality requirements (Section 4.1). When modeling decisions are necessary, the choices are made to result in conservative outcomes that avoid dilution of overall risk (Sections 6.1.3.2, 6.2.3.2, 6.3.3.2, 6.4.3.2). The input values used in the calculation of condensation probability and rate are consistent with the initial and boundary conditions and the assumptions of the conceptual models and design concepts for the Yucca Mountain site.

Note that certain design changes were implemented in the Interface Exchange Drawings during the development of this document. These changes and their impacts are documented in Appendix K. There are no impacts when this more current design information is considered.

4) *Adequate representation of uncertainties in the characteristics of the natural system and engineered materials is provided in parameter development for conceptual models, process-level models, and alternative conceptual models. The U.S. Department of Energy may constrain these uncertainties using sensitivity analyses or conservative limits. For example, the U.S. Department of Energy demonstrates how parameters used to describe flow through the engineered barrier system bound the effects of backfill and excavation-induced changes;*

The primary data uncertainty in the condensation model is the percolation flux. The uncertainty in percolation flux at the repository horizon is addressed by lower, mean, and upper bound cases, generated by the UZ flow model for each of three climate states: present-day, monsoonal, and glacial transition (Section 6.3.5.1.1). This uncertainty is propagated in the model abstraction (Section 8.3.2).

8.5.4 Acceptance Criterion 4: *Model Uncertainty Is Characterized and Propagated Through the Model Abstraction*.

2) *Alternative modeling approaches are considered and the selected modeling approach is consistent with available data and current scientific understanding. A description that includes a discussion of alternative modeling approaches not considered in the final analysis and the limitations and uncertainties of the chosen model is provided.*

There are no completely analogous alternative conceptual models for in-drift condensation. Some limited alternate conceptual models for in-drift condensation do exist. In particular, Danko and Bahrami (2004 [DIRS 171417 and 171418]) present an alternate conceptual model for repository condensation. However, their model is only appropriate for natural ventilation, not natural convection. In addition, their model does not include a drip shield, even for post-closure conditions. Therefore, the results for this alternate conceptual model cannot be compared to the results from this report because they are for different situations.

3) *Consideration of conceptual model uncertainty is consistent with available site characterization data, laboratory experiments, field measurements, natural analog information and process-level modeling studies; and the treatment of conceptual model uncertainty does not result in an under-representation of the risk estimate;*

The fundamentals of natural convection, vapor transport, and boundary layer transport are well established (Bird et al. 1960 [DIRS 103524]). Alternative conceptual models to these well established phenomena are not considered. However, within both the natural convection and the condensation models, decisions about modeling processes are made.

The three-dimensional natural convection simulations consider alternatives in the turbulence model. A discussion of turbulence models and the justification for selection is provided in Section 6.2.3.2.3 and Section 6.2.5.1.1.

The three-dimensional natural convection simulations produce an upper and lower estimate of axial dispersion coefficient that is used in the condensation model (Section 6.2.7). Condensation probabilities and rates are computed for both of these bounds and supplied in the abstractions for TSPA-LA (Section 8.3.2). The lower bound is a true phenomenological lower bound. The upper bound reflects the range of phenomena included in the natural convection simulations; barometric pumping and repository-scale natural ventilation are not included in the convection calculation. The uncertainty in the natural convection simulations does not lead to an under-representation of the risk estimate because higher axial vapor transport results in lower condensation rates in the emplacement drifts.

The condensation model does not describe water transport in the invert explicitly. It bounds the effects of water transport in the invert by applying upper and lower bounds to the vapor pressure at the invert surface. This captures the theoretical limits of invert flow uncertainty on condensation (Sections 6.3.3.2.4 and 6.3.5.1.3). Both limits are included in the abstraction of condensation rate and probability (Section 8.3.2). Since the bounds capture the full range of uncertainty for invert vapor pressure, the risk is not under-represented.

8.5.5 Acceptance Criterion 5: *Model Abstraction Output Is Supported by Objective Comparisons*.

1) *The models implemented in this total system performance assessment abstraction provide results consistent with output from detailed process-level models and/or empirical observations (laboratory and field testings and/or natural analogs);*

The abstraction of condensation probability and rate (Section 8.3.2) is derived directly from the detailed condensation model. Therefore the condensation abstractions are consistent with the detailed model as well as other models such as those presented in *Multiscale Thermohydrologic Model* (BSC 2004 [DIRS 169565]). The abstractions are also qualitatively consistent with the observations of apparent condensation described in Section 6.10.2.2.2 *In Situ Field Testing of Processes* (BSC 2004 [DIRS 170004]).

2) *Abstracted models for coupled thermal-hydrologic-mechanical-chemical effects on seepage and flow and the engineered barrier chemical environment, as well as on the chemical environment for radionuclide release, are based on the same assumptions and approximations demonstrated to be appropriate for process-level models or closely analogous natural or experimental systems. For example, abstractions of processes, such as thermally induced changes in hydrological properties, or estimated diversion of percolation away from the drifts, are adequately justified by comparison to results of process-level modeling, that are consistent with direct observations and field studies*

   The abstraction is created by correlating the condensation rate, which is calculated by the detailed process models, and the probability with the local percolation rate (Section 8.3.2). This correlation eliminates the dependence of condensation upon position within the specific emplacement drift and introduces additional scatter into the correlation. The positional dependence is recaptured in the abstraction by using standard deviations in the correlations for condensation rate and probability. This approximation is consistent with the structure of the total system performance assessment model.

   The correlation of condensation with proximity to the repository edges is eliminated from the abstraction, however, this is acceptable because every waste package type and thermal history is accounted for in correct proportion in the TSPA-LA, and because the effect of condensation on in-drift transport for each waste package is independent of condensation on nearby waste packages.

3) *Accepted and well-documented procedures are used to construct and test the numerical models that simulate coupled thermal-hydrologic-mechanical-chemical effects on seepage and flow, engineered barrier chemical environment, and the chemical environment for radionuclide release. Analytical and numerical models are appropriately supported. Abstracted model results are compared with different mathematical models, to judge robustness of results.*

   The present report uses two software packages. For the in-drift convection model, the FLUENT controlled and baselined software has been used. For the condensation model, the MATHCAD commercial off-the-shelf software package was used. Other exempt software was also employed. GAMBIT version 2.0.4 was used in this report to prepare input including the calculational mesh for the FLUENT simulations and visual examination of the graphical display. Ensight 7.4, a post-processing code to visualize CFD results, was used. Microsoft Excel was also used for graphical presentation and arithmetic manipulation. All software was used in accordance with LP-SI.11Q-BSC, *Software Management*.

   The numerical model for natural convection was validated against experimental measurements (Sections 7.3 and 7.4). The numerical model for dispersion and condensation was tested against analytic solutions (Appendix D). The condensation abstractions were compared against the values computed by the condensation model to ensure fidelity of the abstraction (Appendix H).

INTENTIONALLY LEFT BLANK

9. INPUTS AND REFERENCES

The following is a list of the references cited in this document. Column 2 represents the unique six-digit identifier (the Document Input Reference System (DIRS) number), which is placed in the text following the reference callout (e.g., BSC 2002 [DIRS 158192]). The purpose of these numbers is to assist the reader in locating a specific reference. Within the reference list, multiple sources by the same author (e.g., BSC 2003) are sorted alphabetically by title.

9.1 DOCUMENTS CITED

Abramowitz, M. and Stegun, I.A., eds. 1972. *Handbook of Mathematical Functions with Formulas, Graphs, and Mathematical Tables.* National Bureau of Standards, Applied Mathematics Series. 55, 1046. Washington, D.C.: U.S. Department of Commerce. TIC: 229060. 103280

Altman, W.D.; Donnelly, J.P.; and Kennedy, J.E. 1988. *Peer Review for High-Level Nuclear Waste Repositories: Generic Technical Position.* NUREG-1297. Washington, D.C.: U.S. Nuclear Regulatory Commission. TIC: 200651. 103597

Altman, W.D.; Donnelly, J.P.; and Kennedy, J.E. 1988. *Qualification of Existing Data for High-Level Nuclear Waste Repositories: Generic Technical Position.* NUREG-1298. Washington, D.C.: U.S. Nuclear Regulatory Commission. TIC: 200652. 103750

Bejan, A. 1995. *Convection Heat Transfer.* 2nd Edition. New York, New York: John Wiley & Sons. TIC: 241140. 152307

Bird, R.B.; Stewart, W.E.; and Lightfoot, E.N. 1960. *Transport Phenomena.* New York, New York: John Wiley & Sons. TIC: 208957. 103524

Bishop, E.H. 1988. "Heat Transfer by Natural Convection of Helium Between Horizontal Isothermal Concentric Cylinders at Cryogenic Temperature." *Journal of Heat Transfer, 110,* (1), 109-115. New York, New York: American Society of Mechanical Engineers. TIC: 251047. 156511

Bishop, E.H.; Carley, C.T.; and Powe, R.E. 1968. "Natural Convective Oscillatory Flow in Cylindrical Annuli." *International Journal of Heat and Mass Transfer, 11,* 1741-1752. New York, New York: Pergamon. TIC: 255229. 164423

Blair, S.C.; Buscheck, T.A.; Carlberg, E.; Carlson, R.; Costantino, M.; Daily, W.D.; DeLoach, L.D.; Lee, K.; Lin, W.; Pletcher, R.; Ramirez, A.L.; Roberts, J.; Rosenberg, N.D.; Ruddle, D.; and Wagoner, J. 1998. *Drift-Scale Test Status Report, Satisfying the Deliverables Second-Quarter Drift-Scale Test Report (SP2670M4) and Draft Drift-Scale Test Progress Report (SP2931M4).* UCRL-ID-131195. Livermore, California: Lawrence Livermore National Laboratory. ACC: MOL.19980831.0212. 133836

BSC (Bechtel SAIC Company) 2002. *Atlas Natural Convection Test Plan.* SITP-02-EBS-002 REV 00. Las Vegas, Nevada: Bechtel SAIC Company. ACC: MOL.20020128.0433. 158192

BSC 2003. *Design and Engineering, D&E/PA/C IED Typical Waste Package Components Assembly 1 of 9.* 800-IED-WIS0-00201-000-00C. Las Vegas, Nevada: Bechtel SAIC Company. ACC: ENG.20030917.0002. 165406

BSC 2003. *Interlocking Drip Shield.* 000-MW0-TED0-00102-000-00A. Las Vegas, Nevada: Bechtel SAIC Company. ACC: ENG.20030205.0002. 171024

BSC 2003. *Repository Design Project, RDP/PA IED Typical Waste Package Components Assembly 1 of 9.* 800-IED-WIS0-00201-000-00A. Las Vegas, Nevada: Bechtel SAIC Company. ACC: ENG.20030702.0001. 164053

BSC 2003. *Repository Design Project, Repository/PA IED Emplacement Drift Committed Materials (2).* 800-IED-WIS0-00302-000-00A. Las Vegas, Nevada: Bechtel SAIC Company. ACC: ENG.20030627.0004. 164101

BSC 2003. *Repository Design Project, Repository/PA IED Emplacement Drift Configuration 1 of 2.* 800-IED-EBS0-00201-000-00A. Las Vegas, Nevada: Bechtel SAIC Company. ACC: ENG.20030630.0002. 164069

BSC 2003. *Repository Design, Repository/PA IED Subsurface Facilities.* 800-IED-EBS0-00402-000-00B. Las Vegas, Nevada: Bechtel SAIC Company. ACC: MOL.20030109.0146. 161727

BSC 2003. *Repository Twelve Waste Package Segment Thermal Calculation.* 800-00C-WIS0-00100-000-00A. Las Vegas, Nevada: Bechtel SAIC Company. ACC: ENG.20030915.0003. 164726

BSC 2004. *Abstraction of Drift Seepage.* MDL-NBS-HS-000019, Rev. 01. Las Vegas, Nevada: Bechtel SAIC Company. 169131

BSC 2004. *D&E / PA/C IED Emplacement Drift Configuration and Environment.* 800-IED-MGR0-00201-000-00B. Las Vegas, Nevada: Bechtel SAIC Company. ACC: ENG.20040326.0001. 168489

BSC 2004. *D&E / PA/C IED Interlocking Drip Shield and Emplacement Pallet.* 800-IED-WIS0-00401-000-00D. Las Vegas, Nevada: Bechtel SAIC Company. ACC: ENG.20040503.0018. 169220

BSC 2004. *D&E / PA/C IED Subsurface Facilities.* 800-IED-WIS0-00101-000-00A. Las Vegas, Nevada: Bechtel SAIC Company. ACC: ENG.20040309.0026. 164519

BSC 2004. *D&E / PA/C IED Typical Waste Package Components Assembly.* 800-IED-WIS0-00203-000-00B. Las Vegas, Nevada: Bechtel SAIC Company. ACC: ENG.20040202.0011. 167754

BSC 2004. *D&E / PA/C IED Typical Waste Package Components Assembly.* 800-IED-WIS0-00205-000-00D. Las Vegas, Nevada: Bechtel SAIC Company. ACC: ENG.20040518.0001. 169990

BSC 2004. *D&E/PA/C IED Typical Waste Package Components Assembly.* 800-IED-WIS0-00202-000-00C. Las Vegas, Nevada: Bechtel SAIC Company. ACC: ENG.20040517.0008. 169472

BSC 2004. *Design and Engineering, Interlocking Drip Shield Configuration.* 000-M00-SSE0-00102-000-00B. Las Vegas, Nevada: Bechtel SAIC Company. ACC: ENG.20040305.0021. 168067

BSC 2004. *The Development of the Total System Performance Assessment License Application Features, Events, and Processes.* TDR-WIS-MD-000003, Rev. 01. Las Vegas, Nevada: Bechtel SAIC Company. 168706

BSC 2004. *Drift-Scale THC Seepage Model.* MDL-NBS-HS-000001, Rev. 03. Las Vegas, Nevada: Bechtel SAIC Company. 169856

BSC 2004. *EBS Radionuclide Transport Abstraction.* ANL-WIS-PA-000001, Rev. 01. Las Vegas, Nevada: Bechtel SAIC Company. 169868

BSC 2004. *Engineered Barrier System Features, Events, and Processes.* ANL-WIS-PA-000002, Rev. 03. Las Vegas, Nevada: Bechtel SAIC Company. 169898

BSC 2004. *In Situ Field Testing of Processes.* ANL-NBS-HS-000005, Rev. 03. Las Vegas, Nevada: Bechtel SAIC Company. 170004

BSC 2004. *Multiscale Thermohydrologic Model.* ANL-EBS-MD-000049 REV 02. Las Vegas, Nevada: Bechtel SAIC Company. ACC: DOC.20041014.0008. 169565

BSC 2004. *Q-List.* 000-30R-MGR0-00500-000-000 REV 00. Las Vegas, Nevada: Bechtel SAIC Company. ACC: ENG.20040721.0007. 168361

BSC 2004. *Repository Subsurface Emplacement Drift Panel 2 General Arrangement.* 800-KM0-SSE0-00901-000-00A. Las Vegas, Nevada: Bechtel SAIC Company. ACC: ENG.20040213.0001. 171424

BSC 2004. *Repository Subsurface Emplacement Drifts Steel Invert Structure Plan & Elevation.* 800-SS0-SSE0-00101-000-00B. Las Vegas, Nevada: Bechtel SAIC Company. ACC: ENG.20040520.0004. 169503

BSC 2004. *Repository Subsurface Turnout Drift 1-8 Interface.* 800-KMO-SSD0-00301-000-00A. Las Vegas, Nevada: Bechtel SAIC Company. ACC: ENG.20040220.0009. 171423

BSC 2004. *Technical Work Plan for: Near-Field Environment and Transport In-Drift Heat and Mass Transfer Model and Analysis Reports Integration.* TWP-MGR-PA-000018 REV 01. Las Vegas, Nevada: Bechtel SAIC Company. ACC: DOC.20040729.0006. 170950

BSC 2004. *Thermal Conductivity of the Potential Repository Horizon.* MDL-NBS-GS-000005 REV 01. Las Vegas, Nevada: Bechtel SAIC Company. ACC: DOC.20040928.0006. 169854

BSC 2004. *UZ Flow Models and Submodels.* MDL-NBS-HS-000006 REV 02. Las Vegas, Nevada: Bechtel SAIC Company. 169861

BSC 2004. *Ventilation Model and Analysis Report.* ANL-EBS-MD-000030, Rev. 04. Las Vegas, Nevada: Bechtel SAIC Company. 169862

Buscheck, T.A.; Rosenberg, N.D.; Gansemer, J.; and Sun, Y. 2002. "Thermohydrologic Behavior at an Underground Nuclear Waste Repository." *Water Resources Research, 38,* (3), 10-1 through 10-19. Washington, D.C.: American Geophysical Union. TIC: 253566. 160749

Canori, G.F. and Leitner, M.M. 2003. *Project Requirements Document.* TER-MGR-MD-000001 REV 02. Las Vegas, Nevada: Bechtel SAIC Company. ACC: DOC.20031222.0006. 166275

Carslaw, H.S. and Jaeger, J.C. 1959. *Conduction of Heat in Solids.* 2nd Edition. Oxford, Great Britain: Oxford University Press. TIC: 206085. 100968

CertainTeed 1996. Submittal Sheet, Standard Fiber Glass Duct Wrap. Valley Forge, Pennsylvania: CertainTeed Corporation. TIC: 249257. 153512

Char, M-I. and Hsu, Y-H. 1998. "Comparative Analysis of Linear and Nonlinear Low-Reynolds-Number Eddy Viscosity Models to Turbulent Natural Convection in Horizontal Cylindrical Annuli." *Numerical Heat Transfer, 33,* (2), 191-206. Washington, D.C.: Taylor & Francis. TIC: 251356. 156701

Choi, J.Y. and Kim, M-U. 1993. "Three-Dimensional Linear Stability of Natural Convective Flow Between Concentric Horizontal Cylinders." *International Journal of Heat and Mass Transfer, 36,* (17), 4173-4180. New York, New York: Pergamon. TIC: 255178. 164647

CRWMS (Civilian Radioactive Waste Management System) M&O (Management and Operating Contractor) 2000. *Total System Performance Assessment for the Site Recommendation.* TDR-WIS-PA-000001 REV 00 ICN 01. Las Vegas, Nevada: CRWMS M&O. ACC: MOL.20001220.0045. 153246

CRWMS M&O 2001. *Water Distribution and Removal Model.* ANL-EBS-MD-000032 REV 01. Las Vegas, Nevada: CRWMS M&O. ACC: MOL.20010214.0031. 152016

Danko, G. and Bahrami, D. 2004. "Coupled, Multiscale Thermohydrologic-Ventilation Modeling with Multiflux." *2004 SME Annual Meeting and Exhibit, February 23-25, Denver, Colorado.* Preprint 04-144. Littleton, Colorado: Society of Mining, Metallurgy, and Exploration. TIC: 256396. 171418

Danko, G. and Bahrami, D. 2004. "Heat and Moisture Flow Simulation with Multiflux." *2004 ASME, Proceedings of ASME Heat Transfer/Fluid Engineering Summer Conference, July 11-15, 2004, Charlotte, North Carolina, USA.* HT-FED2004-56048. New York, New York: American Society of Mechanical Engineers. TIC: 256451. 171417

Desai, C.P. and Vefai, K. 1994. "An Investigation and Comparative Analysis of Two- and Three-Dimensional Turbulent Natural Convection in a Horizontal Annulus." *International Journal of Heat and Mass Transfer, 37,* (16), 2475-2504. Tarrytown, New York: Elsevier. TIC: 251357. 156702

DOE (U.S. Department of Energy) 2002. *Yucca Mountain Site Suitability Evaluation.* DOE/RW-0549. Washington, D.C.: U.S. Department of Energy, Office of Civilian Radioactive Waste Management. ACC: MOL.20020404.0043. 156958

Farouk, B. and Guceri, S.I. 1982. "Laminar and Turbulent Natural Convection in the Annulus Between Horizontal Concentric Cylinders." *Journal of Heat Transfer, 104,* 631-636. New York, New York: American Society of Mechanical Engineers. TIC: 251358. 156715

Fluent 2001. *Fluent 6.0 User's Guide, Nomenclature, Bibliography & Index.* Five volumes. Lebanon, New Hampshire: Fluent. TIC: 254880. 164453

Francis, N.D., Jr.; Itamura, M.T.; Webb, S.W.; and James, D.L. 2002. *CFD Calculation of Internal Natural Convection in the Annulus Between Horizontal Concentric Cylinders.* SAND2002-3132. Albuquerque, New Mexico: Sandia National Laboratories. ACC: MOL.20021224.0115. 164323

Francis, N.D., Jr.; Webb, S.W.; Itamura, M.T.; and James, D.L. 2003. *CFD Modeling of Natural Convection Heat Transfer and Fluid Flow in Yucca Mountain Project (YMP) Enclosures.* SAND2002-4179. Albuquerque, New Mexico: Sandia National Laboratories. ACC: MOL.20030906.0165. 164602

Freeze, G.A.; Brodsky, N.S.; and Swift, P.N. 2001. *The Development of Information Catalogued in REV00 of the YMP FEP Database.* TDR-WIS-MD-000003 REV 00 ICN 01. Las Vegas, Nevada: Bechtel SAIC Company. ACC: MOL.20010301.0237. 154365

Fusegi, T. and Farouk, B. 1986. "A Three-Dimensional Study of Natural Convection in the Annulus Between Horizontal Concentric Cylinders." *Heat Transfer, 1986. Volume 4, General Papers, Proceedings of the Eighth International Heat Transfer Conference, San Francisco, California, USA, August 17-22, 1986.* Tien, C.L.; Carey, V.P.; and Ferrell, J.K., eds. Pages 1575-1580. Washington, D.C.: Hemisphere Publishing Corporation. TIC: 251367. 156719

Haar, L.; Gallagher, J.S.; and Kell, G.S. 1984. *NBS/NRC Steam Tables: Thermodynamic and Transport Properties and Computer Programs for Vapor and Liquid States of Water in SI Units.* New York, New York: Hemisphere Publishing Corporation. TIC: 241793. 105175

Ho, C.K. 1997. "Evaporation of Pendant Water Droplets in Fractures." *Water Resources Research, 33,* (12), 2665-2671. Washington, D.C.: American Geophysical Union. TIC: 246969. 141521

Howard, C. 2002. Natural Convection Testing Scientific Notebook, Testing Performed by Engineered Barrier Systems Testing. Scientific Notebook SN-SNL-SCI-025-V1. ACC: MOL.20020710.0554. 161009

Howell, J.R. 1982. *A Catalog of Radiation Configuration Factors.* Klas, R.H., ed. New York, New York: McGraw-Hill. TIC: 255176. 164711

Incropera, F.P. and DeWitt, D.P. 1990. *Fundamentals of Heat and Mass Transfer.* 3rd Edition. New York, New York: John Wiley & Sons. TIC: 250415. 156693

Incropera, F.P. and DeWitt, D.P. 1996. *Fundamentals of Heat and Mass Transfer.* 4th Edition. New York, New York: John Wiley & Sons. TIC: 243950. 108184

Incropera, F.P. and DeWitt, D.P. 2002. *Fundamentals of Heat and Mass Transfer.* 5th Edition. New York, New York: John Wiley & Sons. TIC: 254280. 163337

Kalia, H.N. 2001. "Guidance for the Implementation of Convection Test." Memorandum from H.N. Kalia (BSC) to Distribution, June 22, 2001, PROJ.06/01.053, with enclosure. ACC: MOL.20010719.0155. 156939

Kuehn, T.H. 1976. *Natural Convection Heat Transfer From a Horizontal Circular Cylinder to a Surrounding Cylindrical Enclosure.* Ph.D. thesis. Minneapolis, Minnesota: University of Minnesota. TIC: 252167. 156720

Kuehn, T.H. and Goldstein, R.J. 1976. "An Experimental and Theoretical Study of Natural Convection in the Annulus Between Horizontal Concentric Cylinders." *Journal of Fluid Mechanics, 74,* (4), 695-719. New York, New York: Cambridge University Press. TIC: 251359. 156722

Kuehn, T.H. and Goldstein, R.J. 1976. "Correlating Equations for Natural Convection Heat Transfer Between Horizontal Circular Cylinders." *International Journal of Heat and Mass Transfer, 19,* (10), 1127-1134. New York, New York: Pergamon Press. TIC: 238411. 100675

Kuehn, T.H. and Goldstein, R.J. 1978. "An Experimental Study of Natural Convection Heat Transfer in Concentric and Eccentric Horizontal Cylindrical Annuli." *Journal of Heat Transfer, 100,* (4), 635-640. New York, New York: American Society of Mechanical Engineers. TIC: 244433. 130084

Lide, D.R., ed. 1995. *CRC Handbook of Chemistry and Physics.* 76th Edition. Boca Raton, Florida: CRC Press. TIC: 216194. 101876

Lis, J. 1966. "Experimental Investigation of Natural Convection Heat Transfer in Simple and Obstructed Horizontal Annuli." *Proceedings of the Third International Heat Transfer Conference.* Volume 2. Pages 196-204. New York, New York: American Institute of Chemical Engineers. TIC: 251371. 156513

McLeod, A.E. and Bishop, E.H. 1989. "Turbulent Natural Convection of Gases in Horizontal Cylindrical Annuli at Cryogenic Temperatures." *International Journal of Heat and Mass Transfer, 32,* (10), 1967-1978. Elmsford, New York: Pergamon Press. TIC: 251360. 156725

NRC (U.S. Nuclear Regulatory Commission) 2003. *Yucca Mountain Review Plan, Final Report.* NUREG-1804, Rev. 2. Washington, D.C.: U.S. Nuclear Regulatory Commission, Office of Nuclear Material Safety and Safeguards. TIC: 254568. 163274

Perry, R.H.; Green, D.W.; and Maloney, J.O., eds. 1984. *Perry's Chemical Engineers' Handbook.* 6th Edition. New York, New York: McGraw-Hill. TIC: 246473. 125806

Press, W.H.; Teukolsky, S.A.; Vetterling, W.T.; and Flannery, B.P. 1992. *Numerical Recipes in Fortran 77, The Art of Scientific Computing.* Volume 1 of *Fortran Numerical Recipes.* 2nd Edition. Cambridge, United Kingdom: Cambridge University Press. TIC: 243606. 103316

Pruess, K. 1987. *TOUGH User's Guide.* NUREG/CR-4645. Washington, D.C.: U.S. Nuclear Regulatory Commission. TIC: 217275. 100684

Raithby, G.D. and Hollands, K.G.T. 1985. "Natural Convection." Chapter 6 of *Handbook of Heat Transfer Fundamentals.* 2nd Edition. Rohsenow, W.M.; Hartnett, J.P.; and Ganic, E.N., eds. New York, New York: McGraw-Hill. TIC: 255177. 164700

Raithby, G.D. and Hollands, K.G.T. 1975. "A General Method of Obtaining Approximate Solutions to Laminar and Turbulent Free Convection Problems." *Advances in Heat Transfer.* Irvine, T.F., Jr. and Hartnett, J.P., eds. 11. 265-315. New York, New York: Academic Press. TIC: 251361. 156726

Reid, R.C.; Prausnitz, J.M.; and Sherwood, T.K. 1977. *The Properties of Liquids and Gases.* New York, New York: McGraw-Hill Book Company. TIC: 240958. 130310

Reynolds, W.C. 1979. *Thermodynamic Properties in SI. Graphs, Tables, and Computational Equations for Forty Substances.* Stanford, California: Stanford University, Department of Mechanical Engineering. TIC: 242560. 158410

Rohsenow, W.M.; Hartnett, J.P.; and Cho, Y.I. 1998. *Handbook of Heat Transfer.* 3rd Edition. New York, New York: McGraw-Hill. TIC: 253612. 169241

Sánchez, A. 2002. Natural Convection Testing, Scientific Notebook Attachment Volume 10, Data Preparation for TDMS Submittal of Natural Convection Test Case #7, Test Dates: May 2, 2002 to May 19, 2002. Supporting Scientific Notebook SN-SNL-SCI-025-V1. ACC: MOL.20021114.0049. 166237

Sánchez, A. 2002. Natural Convection Testing, Scientific Notebook Attachment Volume 11, Data Preparation for TDMS Submittal of Natural Convection Test Case #8, Test Dates: March 20, 2002 to April 17, 2002. Supporting Scientific Notebook SN-SNL-SCI-025-V1. ACC: MOL.20021114.0053. 166238

Sánchez, A. 2002. Natural Convection Testing, Scientific Notebook Attachment Volume 4, Data Preparation for TDMS Submittal of Natural Convection Test Case #1, Test Dates: January 15, 2002 to January 31, 2002. Supporting Scientific Notebook SN-SNL-SCI-025-V1. ACC: MOL.20021114.0024. 166231

Sánchez, A. 2002. Natural Convection Testing, Scientific Notebook Attachment Volume 5, Data Preparation for TDMS Submittal of Natural Convection Test Case #2, Test Dates: February 13, 2002 to March 3, 2002. Supporting Scientific Notebook SN-SNL-SCI-025-V1. ACC: MOL.20021114.0028. 166232

Sánchez, A. 2002. Natural Convection Testing, Scientific Notebook Attachment Volume 6, Data Preparation for TDMS Submittal of Natural Convection Test Case #3, Test Dates: May 2, 2002 to May 19, 2002. Supporting Scientific Notebook SN-SNL-SCI-025-V1. ACC: MOL.20021114.0033. 166233

Sánchez, A. 2002. Natural Convection Testing, Scientific Notebook Attachment Volume 7, Data Preparation for TDMS Submittal of Natural Convection Test Case #4, Test Dates: March 12, 2002 to April 17, 2002. Supporting Scientific Notebook SN-SNL-SCI-025-V1. ACC: MOL.20021114.0037. 166234

Sánchez, A. 2002. Natural Convection Testing, Scientific Notebook Attachment Volume 8, Data Preparation for TDMS Submittal of Natural Convection Test Case #5, Test Dates: January 14, 2002 to January 31, 2002. Supporting Scientific Notebook SN-SNL-SCI-025-V1. ACC: MOL.20021114.0041. 166235

Sánchez, A. 2002. Natural Convection Testing, Scientific Notebook Attachment Volume 9, Data Preparation for TDMS Submittal of Natural Convection Test Case #6, Test Dates: February 13, 2002 to March 6, 2002. Supporting Scientific Notebook SN-SNL-SCI-025-V1. ACC: MOL.20021114.0045. 166236

SNL (Sandia National Laboratories) 2002. *FLUENT Version 6.0.12, Software Definition Report.* Software Baseline Documentation Number: 10550-SDR-6.0.12-01. Albuquerque, New Mexico: Sandia National Laboratories. 171415

Siegel, R. and Howell, J.R. 1992. *Thermal Radiation Heat Transfer.* 3rd Edition. Washington, D.C.: Taylor & Francis. TIC: 236759. 100687

Stuckless, J.S. and Toomey, R.S., III 2003. "A Case for Long-Term Passive Ventilation of the Proposed Repository at Yucca Mountain, Nevada - Evidence from Natural Analogues." *Proceedings of the 10th International High-Level Radioactive Waste Management Conference (IHLRWM), March 30-April 2, 2003, Las Vegas, Nevada.* Pages 267-278. La Grange Park, Illinois: American Nuclear Society. TIC: 254559. 171855

USGS (U.S. Geological Survey) 1969. *Topographic Map of Las Vegas, Nevada; Arizona; California. Grid Zone Designation 11S.* Quadrangle NJ 11-12. Denver, Colorado: U.S. Geological Survey. TIC: 241810. 149902

Vafai, K.; Desai, C.P.; Iyer, S.V.; and Dyko, M.P. 1997. "Buoyancy Induced Convection in a Narrow Open-Ended Annulus." *Journal of Heat Transfer, 119,* (3), 483-494. New York, New York: American Society of Mechanical Engineers. TIC: 251362. 156727

Van Wylen, G.J. and Sonntag, R.E. 1986. *Fundamentals of Classical Thermodynamics.* New York, New York: John Wiley & Sons. TIC: 245655. 108881

Webb, S.W. 2001. "Modeling of Open Space Natural Convection in Porous Media Codes." *"Back to the Future - Managing the Back End of the Nuclear Fuel Cycle to Create a More Secure Energy Future," Proceedings of the 9th International High-Level Radioactive Waste Management Conference (IHLRWM), Las Vegas, Nevada, April 29-May 3, 2001.* La Grange Park, Illinois: American Nuclear Society. TIC: 247873. 156409

Webb, S.W.; Francis, N.D.; Dunn, S.D.; Itamura, M.T.; and James, D.L. 2003. "Thermally Induced Natural Convection Effects in Yucca Mountain Drifts." *Journal of Contaminant Hydrology, 62-63,* 713-730. New York, New York: Elsevier. TIC: 254205. 164366

White, F.M. 1986. *Fluid Mechanics.* 2nd Edition. New York, New York: McGraw-Hill. TIC: 243415. 111015

Wood, W.D.; Deem, H.W.; and Lucks, C.F. 1964. *Thermal Radiative Properties.* Plenum Press Handbooks of High-Temperature Materials No. 3. New York, New York: Plenum Press. TIC: 255156. 164664

YMP (Yucca Mountain Site Characterization Project) 2003. *FLUENT Version 6.0.12 Software Implementation Report.* 10550-SIR-6.0.12-01. Las Vegas, Nevada: Yucca Mountain Site Characterization Office. 166345

9.2 CODES, STANDARDS, REGULATIONS, AND PROCEDURES

10 CFR 63. Energy: Disposal of High-Level Radioactive Wastes in a Geologic Repository at Yucca Mountain, Nevada. Readily available. 156605

AP-2.14Q, Rev. 3, ICN 0. *Document Review.* Washington, D.C.: U.S. Department of Energy, Office of Civilian Radioactive Waste Management. ACC: DOC.20030827.0018.

AP-2.22Q, Rev. 1, ICN 1. *Classification Analyses and Maintenance of the Q-List.* Washington, D.C.: U.S. Department of Energy, Office of Civilian Radioactive Waste Management. ACC: DOC.20040714.0002.

AP-3.15Q, Rev. 4, ICN 5. *Managing Technical Product Inputs.* Washington, D.C.: U.S. Department of Energy, Office of Civilian Radioactive Waste Management. ACC: DOC.20040812.0004.

AP-SIII.10Q, Rev. 2, ICN 7. *Models.* Washington, D.C.: U.S. Department of Energy, Office of Civilian Radioactive Waste Management. ACC: DOC.20040920.0002.

ASME (American Society of Mechanical Engineers) 1995. "Materials." Section II of *1995 ASME Boiler and Pressure Vessel Code*. New York, New York: American Society of Mechanical Engineers. TIC: 245287. 108417

LP-SI.11Q-BSC, Rev. 0, ICN 1. *Software Management.* Washington, D.C.: U.S. Department of Energy, Office of Civilian Radioactive Waste Management. ACC: DOC.20041005.0008.

9.3 SOURCE DATA, LISTED BY DATA TRACKING NUMBER

GS000483351030.003. Thermal Properties Measured 12/01/99 to 12/02/99 Using the Thermolink Soil Multimeter and Thermal Properties Sensor on Selected Potential Candidate Backfill Materials Used in the Engineered Barrier System. Submittal date: 11/09/2000.	152932
GS020183351030.001. Uncompacted Bulk Density for Analyses Performed 02/02/00 to 05/23/00 on Potential Backfill Materials Used in the Engineered Barrier System. Submittal date: 01/22/2002.	163107
LB0208UZDSCPMI.002. Drift-Scale Calibrated Property Sets: Mean Infiltration Data Summary. Submittal date: 08/26/2002.	161243
LL030602723122.027. Multiscale Thermohydrologic Model Output to TSPA and WAPDEG for the Upper Infiltration Case. Submittal date: 06/25/2003.	164514
LL030608723122.028. Multiscale Thermohydrologic Model Output to TSPA and WAPDEG for the Lower Infiltration Case. Submittal date: 06/27/2003.	164510
LL030610323122.029. Multiscale Thermohydrologic Model Output to TSPA and WAPDEG for the Mean Infiltration Case. Submittal date: 06/27/2003.	164513
MO0003RIB00071.000. Physical and Chemical Characteristics of Alloy 22. Submittal date: 03/13/2000.	148850
MO0109EBSAEQST.009. Engineered Barrier System Average Emissivity/Reflectivity Measurements of Materials Used at Different Temperatures in Quarter Scale Tests. Submittal date: 09/19/2001.	156696
MO0109EBSTCQST.011. Engineered Barrier System Thermal Conductivity, Thermal Diffusivity, and Specific Heat Capacity Measurements of Materials Used in Quarter Scale Tests. Submittal date: 10/15/2001.	156697
MO0307MWDAC8MV.000. Analytical-La-Coarse-800M Ventilation. Submittal date: 07/15/2003.	165395
MO0308SPACO2GL.001. EBS Environment In-Drift CO_2 Gas Lookup Tables for TSPA-LA. Submittal date: 08/08/2003.	168096
MO0407SEPFEPLA.000. LA FEP List. Submittal date: 07/20/2004.	170760
SN0208F3407102.002. Natural Convection Test, Case #1 (Test Dates: January 15, 2002 through January 31, 2002). Submittal date: 08/02/2002.	161053
SN0208F3407102.004. Natural Convection Test, Case #4 (Test Dates: March 12, 2002 through April 17, 2002). Submittal date: 08/02/2002.	161056

SN0208F3407102.008. Natural Convection Test, Case #8 (Test Dates: March 20, 2002 through April 17, 2002). Submittal date: 08/02/2002. 161062

SN0208F3407102.009. Natural Convection Test Air Velocities (Test Dates: January 14, 2002 through May 19, 2002). Submittal date: 08/07/2002. 161063

SN0307T0510902.003. Updated Heat Capacity of Yucca Mountain Stratigraphic Units. Submittal date: 07/15/2003. 164196

SN0404T0503102.011. Thermal Conductivity of the Potential Repository Horizon Rev 3. Submittal date: 04/27/2004. 169129

9.4 OUTPUT DATA, LISTED BY DATA TRACKING NUMBER

SN0307T0507803.001. Supporting Calculations of Natural Convection Test Data. Submittal date: 07/23/2003.

SN0307T0507803.002. Fluent Natural Convection Test Case 4 Revised Boundary Model. Submittal date: 07/23/2003.

SN0307T0507803.003. Fluent Natural Convection Test Case 8 Revised Boundary Model. Submittal date: 07/23/2003.

SN0308T0507803.004. Fluent Natural Convection Test, Original Cases 1, 4, 5 and 8 Models. Submittal date: 08/07/2003.

SN0308T0507803.014. FLUENT 6.0.12 Files For the 2-D Concentric Cylinder Natural Convection Simulations. Submittal date: 08/19/2003.

SN0308T0507803.015. FLUENT 6.0.12 Files for the 2-D Kuehn and Goldstein Natural Convection Simulations. Submittal date: 08/19/2003.

SN0407T0507803.026. FLUENT 6.0.12 Files for 2-D Natural Convection Simulations for Equivalent Thermal Conductivity Determination. Submittal date: 07/15/2004.

SN0310T0507803.017. FLUENT 6.0.12 Files for Natural Ventilation Test Case 1 Grid Independence Study (Coarse Grid Model). Submittal date: 10/16/2003.

SN0310T0507803.018. FLUENT 6.0.12 Files for Natural Ventilation Test Case 1 Grid Independence Study (First Adaption of Coarse Grid Based on Y+). Submittal date: 10/16/2003.

SN0310T0507803.019. FLUENT 6.0.12 Files for Natural Ventilation Test Case 1 Grid Independence Study (Second Adaption of Coarse Grid Based on Y+). Submittal date: 10/16/2003.

SN0310T0507803.020. FLUENT 6.0.12 Files for Natural Ventilation Test Case 1 Grid Independence Study (Refined Grid Model). Submittal date: 10/16/2003.

SN0310T0507803.021. FLUENT 6.0.12 Files for Natural Ventilation Test Case 5 Grid Independence Study (Adaption of Coarse Grid Based on Y+). Submittal date: 10/16/2003.

SN0312T0507803.022. REVISED FLUENT 6.0.12 Files for 2-D Natural Convection Sensitivity Study Simulations. Submittal date: 12/04/2003.

SN0402T0809903.003. Condensation Abstraction: Well-Ventilated Drip Shield; Low Invert Transport. Submittal date: 2/26/2004.

SN0402T0809903.004. Condensation Abstraction: Well-Ventilated Drip Shield; High Invert Transport. Submittal date: 2/26/2004.

SN0403T0809903.005. Condensation Abstraction: Unventilated Drip Shield; High Invert Transport. Submittal date: 3/31/2004.

SN0403T0809903.006. Condensation Abstraction: Unventilated Drip Shield; Low Invert Transport. Submittal date: 3/31/2004.

SN0406T0507803.023. Evaluation of Uniformity of Rock Temperatures 5 Meters from the Drift Wall. Submittal date: 7/7/2004.

SN0406T0507803.024. Calculation of 2-D In-Drift Temperature Distributions Using FLUENT 6.0.12 for Comparison to Condensation Values. Submittal date: 7/7/2004.

SN0406T0507803.025. Calculation of Dispersion Coefficients from FLUENT 6.0.12 Results. Submittal date: 7/7/2004.

SN0408T0509903.007. In-Drift Condensation: MATHCAD Files Used for Calculation. Submittal date: 09/07/2004.

SN0408T0509903.008. In-Drift Condensation: Corrected MATHCAD Files Used for Calculation. Submittal date: 09/07/2004.

9.5 SOFTWARE CODES

FLUENT V6.0.12. PC, Redhat Linux V7.3. 10550-6.0.12-01. 164315

INTENTIONALLY LEFT BLANK

APPENDIX A

KUEHN AND GOLDSTEIN CORRELATIONS

A.1 KUEHN AND GOLDSTEIN CORRELATION EQUATIONS FOR NATURAL CONVECTION HEAT TRANSFER BETWEEN HORIZONTAL CIRCULAR CYLINDERS

Kuehn and Goldstein (1976 [DIRS 100675]) produced correlation equations for natural convection heat transfer in concentric and eccentric horizontal cylinders applicable to conduction, laminar, and turbulent flow heat transfer. The correlation equations are:

The overall equivalent conductivity (Kuehn and Goldstein 1976 [DIRS 100675], Equation 27):

$$\bar{k}_{eq} = \frac{\overline{Nu'}_{Di}}{\overline{Nu'}_{Di_{cond}}} \qquad \text{(Eq. A.1-1)}$$

The overall Nusselt number valid at any Rayleigh number (Kuehn and Goldstein 1976 [DIRS 100675], Equation 26):

$$\overline{Nu'}_{Di} = [(\overline{Nu'}_{Di_{cond}})^{15} + (\overline{Nu'}_{Di_{conv}})^{15}]^{1/15} \qquad \text{(Eq. A.1-2)}$$

The Nusselt number for conduction between an inner and outer horizontal cylinder (Kuehn and Goldstein 1976 [DIRS 100675], Equation 25):

$$\overline{Nu'}_{Di_{cond}} = \frac{2}{\cosh^{-1}[(Di^2 + Do^2 - 4\varepsilon^2)/2DiDo]} \qquad \text{(Eq. A.1-3)}$$

where *Di* and *Do* are the diameters of the inner and outer cylinders respectively, and ε is the eccentricity of the inner cylinder (distance moved from its concentric position).

The overall Nusselt number for heat transfer by natural convection between an inner and outer horizontal cylinder (Kuehn and Goldstein 1976 [DIRS 100675], Equations 23a and 23b):

$$\overline{Nu'}_{Di_{conv}} = \frac{2}{\ln[X]} \qquad \text{(Eq. A.1-4)}$$

where X is given by:

$$X = \frac{Y}{Z} \qquad \text{(Eq. A.1-5)}$$

$$Y = 1 + \frac{2}{\left[\left(0.518 Ra_{Di}^{1/4}\left[1 + \left(\frac{0.559}{\Pr}\right)^{3/5}\right]^{-5/12}\right)^{15} + \left(0.1 Ra_{Di}^{1/3}\right)^{15}\right]^{1/15}} \qquad \text{(Eq. A.1-6)}$$

$$Z = 1 - \frac{2}{\left\{\left(\left[\left(\frac{2}{1-e^{-0.25}}\right)^{5/3} + \left(0.587 G Ra_{Do}^{1/4}\right)^{5/3}\right]^{3/5}\right)^{15} + \left(0.1 Ra_{Do}^{1/3}\right)^{15}\right\}^{1/15}} \quad \text{(Eq. A.1-7)}$$

$$G = \left[\left(1 + \frac{0.6}{\Pr^{0.7}}\right)^{-5} + \left(0.4 + 2.6 \Pr^{0.7}\right)^{-5}\right]^{-1/5} \quad \text{(Eq. A.1-8)}$$

Where Ra_{Di} and Ra_{Do} are Rayleigh numbers based on length scales *Di* and *Do*, respectively, as indicated in Kuehn and Goldstein 1976 [DIRS 100675] in the text after Equations 8 and 16, respectively, or:

$$Ra_{Di} = \frac{g\beta\left(T_i - \overline{T}_b\right)D_i^3}{\nu\alpha} \quad \text{(Eq. A.1-9)}$$

$$Ra_{Do} = \frac{g\beta\left(\overline{T}_b - T_o\right)D_o^3}{\nu\alpha} \quad \text{(Eq. A.1-10)}$$

T_i, T_o and $\overline{T_b}$ are the inner surface, outer surface, and bulk temperatures, respectively. The fluid Prandtl number, Pr, is defined by (Bejan 1995 [DIRS 152307], p. xxiii).

$$\Pr = \frac{\nu}{\alpha} \quad \text{(Eq. A.1-11)}$$

The fluid properties in Equation A.1-9 and Equation A.1-10 are evaluated at the film temperature written as a function of the bulk temperature. For the inner cylinder, $T_{film_i} = (\overline{T}_b + T_i)/2$, and for the outer cylinder, $T_{film_o} = (\overline{T}_b + T_o)/2$ (Incropera and DeWitt 2002 [DIRS 163337], Equation 7.2). The average bulk temperature is found by equating the heat transfer at each cylinder, which reduces to (Kuehn and Goldstein 1976 [DIRS 100675], Equation 24):

$$\frac{\overline{T}_b - T_o}{T_i - \overline{T}_b} = \frac{\overline{Nu}_{Di_{conv}}}{\overline{Nu}_{Do_{conv}}} \quad \text{(Eq. A.1-12)}$$

where (Kuehn and Goldstein 1976 [DIRS 100675], Equation 12),

$$\overline{Nu}_{Di_{conv}} = \frac{2}{\ln[Y]} \quad \text{(Eq. A.1-13)}$$

and (Kuehn and Goldstein 1976 [DIRS 100675], Equation 22):

$$\overline{Nu}_{Do_{conv}} = \frac{2}{-\ln[Z]} \qquad \text{(Eq. A.1-14)}$$

An iterative method is used to evaluate the average bulk temperature using Equations A.1-12 through A.1-14. An initial guess was taken to be the average of the inner and outer cylinder temperatures and a new calculated average bulk temperature was calculated. For the next iteration, the initial guess was replaced by the new calculated average bulk temperature. The process is repeated a few times until the difference between the guessed and calculated average bulk temperature values is very small. This procedure, repeated at different Rayleigh numbers, generates the data needed to make a plot of equivalent thermal conductivity versus Rayleigh number.

The purpose of this work is to develop an equivalent thermal conductivity relationship for use in the YMP models for all times. At early times, the temperature difference is large while at later times temperature difference is small. Non-dimensional numbers, like *Ra*, can be used to describe the parameters that can change without affecting the flow. For example, the flow is similar for any combination of α, β, g, ΔT, L that gives the same *Ra*. The Rayleigh number based on gap width, Ra_L, is calculated using Equation 6.1-8 shown below as Equation A.1-15. A number of different Rayleigh numbers were obtained by using different acceleration due to gravity (g) values.

$$Ra_L = \frac{\beta g \Delta T L^3}{\nu \alpha} \qquad \text{(Eq. A.1-15)}$$

In order to make comparisons with other correlations and with output of FLUENT, the Kuehn and Goldstein correlations were used to evaluate equivalent thermal conductivity for large-scale concentric cylinders (YMP-type) geometry at elevated temperatures using air as the working fluid. The inner cylinder diameter (D_i) and outer cylinder diameter (D_o) were 1.71 m and 5.5 m, respectively (shown in Table 7.3.2-1). The inner and outer cylinder temperatures were 100°C and 80°C, respectively, and air properties used were as shown in Table 7.3.3-1. These input values were used to evaluate the average bulk temperature. Table A.1-1 shows calculated values of parameters from the iteration process for evaluating the average bulk temperature. The values shown were obtained at the end of the iteration cycle. In the table, Ra_L is the Rayleigh number based on gap width (i.e., L = D_o/2 - D_i/2) as a length scale. The Rayleigh number is calculated similar to the procedure in Section 7.3.2. The symbol T_b is the initial value of the bulk temperature, while $T_{b,new}$ is the value derived at the end of the iteration cycle. When these two numbers agree with each other, the process has converged.

Table A.1-1. Iteration Procedure to Evaluate Average Bulk Temperature for Kuehn and Goldstein Correlations: Average Bulk Temperature Values at the End of the Iteration Cycle

g m/s^2	Ra_L	T_b °C	T_{film-i} °C	T_{film-o} °C	ν_I m^2/s	α_I m^2/s	ν_o m^2/s	α_o m^2/s
46.2737700	2.50E+10	85.300	92.650	82.650	2.264E-5	3.253E-5	2.154E-5	3.085E-5
12.1791150	6.58E+9	84.991	92.496	82.496	2.262E-5	3.250E-5	2.152E-5	3.082E-5
9.8100000	5.30E+9	84.941	92.470	82.470	2.262E-5	3.250E-5	2.152E-5	3.082E-5
0.9810000	5.30E+8	84.430	92.215	82.215	2.259E-5	3.246E-5	2.149E-5	3.078E-5
0.0981000	5.30E+7	84.028	92.014	82.014	2.257E-5	3.242E-5	2.147E-5	3.074E-5
0.0098100	5.30E+6	83.907	91.954	81.954	2.256E-5	3.241E-5	2.146E-5	3.073E-5
0.0009810	5.30E+5	83.948	91.974	81.974	2.256E-5	3.242E-5	2.147E-5	3.074E-5
0.0000981	5.30E+4	83.987	91.994	81.994	2.257E-5	3.242E-5	2.147E-5	3.074E-5

Ra_{Di}	Ra_{Do}	$\overline{Nu}_{Di}$	$\overline{Nu}_{Do}$	T_{bnew} °C
1.265E+10	1.727E+11	234.03	649.08	85.300
3.407E+9	4.288E+10	151.48	455.52	84.991
2.754E+9	3.420E+10	141.19	430.33	84.941
2.857E+8	3.077E+9	66.98	235.40	84.430
2.939E+7	2.805E+8	32.65	129.47	84.028
2.963E+6	2.724E+7	17.64	72.66	83.907
2.955E+5	2.752E+6	10.26	41.72	83.948
2.947E+4	2.778E+5	6.17	24.77	83.987

DTN: SN0308T0507803.015.

Once the average bulk temperature is known, Equations A.1-3 and A.1-4 are used to calculate the Nusselt numbers for the conduction and natural convection. The equivalent thermal conductivities shown in Table A.1-2 are then evaluated using Equation A.1-1. The procedure and data are included in DTN: SN0308T0507803.015.

Table A.1-2. Rayleigh Number, Nusselt Numbers, and Equivalent Thermal Conductivity for Kuehn and Goldstein Correlations

Ra_L	$\overline{Nu}'_{Dicond}$	$\overline{Nu}'_{Di}$	k_{eq}
2.50E+10	1.71	172.5	100.7
6.58E+9	1.71	114.2	66.7
5.30E+9	1.71	106.8	62.4
5.30E+8	1.71	52.7	30.8
5.30E+7	1.71	26.7	15.6
5.30E+6	1.71	14.8	8.63
5.30E+5	1.71	8.80	5.14
5.30E+4	1.71	5.48	3.20

DTN: SN0308T0507803.015.

A.2 MODIFIED KUEHN AND GOLDSTEIN CORRELATION EQUATIONS FOR NATURAL CONVECTION HEAT TRANSFER BETWEEN HORIZONTAL CIRCULAR CYLINDERS

Kuehn and Goldstein (1978 [DIRS 130084]) modified their earlier correlating equations for natural convection heat transfer in concentric and eccentric horizontal cylinders (Kuehn and Goldstein (1976 [DIRS 100675]), which are discussed in Appendix A.1. The modified correlating equations are discussed below.

The average equivalent conductivity (Kuehn and Goldstein 1978 [DIRS 130084], Equation 1g):

$$\bar{k}_{eq} = \frac{Nu}{Nu_{cond}} \qquad \text{(Eq. A.2-1)}$$

The overall Nusselt number valid at any Rayleigh number (Kuehn and Goldstein 1978 [DIRS 130084], Equation 1f):

$$Nu = [(Nu_{cond})^{15} + (Nu_{conv})^{15}]^{1/15} \qquad \text{(Eq. A.2-2)}$$

Nusselt number for conduction between cylinders (Kuehn and Goldstein 1978 [DIRS 130084], Equation 1e):

$$Nu_{cond} = 2/\ln(D_o / D_i) \qquad \text{(Eq. A.2-3)}$$

Nusselt number for convection between cylinders (Kuehn and Goldstein 1978 [DIRS 130084], Equation 1d):

$$Nu_{conv} = \left[\frac{1}{Nu_i'} + \frac{1}{Nu_o'}\right]^{-1} \qquad \text{(Eq. A.2-4)}$$

The equation for average bulk temperature (Kuehn and Goldstein 1978 [DIRS 130084], Equation 1c):

$$\frac{\bar{T}_b - T_o}{T_i - T_o} = \frac{Nu_i'}{Nu_i' + Nu_o'} \qquad \text{(Eq. A.2-5)}$$

Where, Nu_i', the Nusselt number for natural convection from a horizontal cylinder in an infinite fluid, is given by (Kuehn and Goldstein 1978 [DIRS 130084], Equation 1a):

$$Nu_i' = \frac{2}{\ln\left[1 + \frac{2}{\left[\left(0.5 Ra_{Di}^{1/4}\right)^{15} + \left(0.12 Ra_{Di}^{1/3}\right)^{15}\right]^{1/15}}\right]} \qquad \text{(Eq. A.2-6)}$$

And Nu_o', the Nusselt number for quasi-steady natural convection to a fluid contained within a horizontal cylinder is given by (Kuehn and Goldstein 1978 [DIRS 130084], Equation 1b):

$$Nu_o' = \frac{-2}{\ln\left[1 - \frac{2}{\left[\left(Ra_{Do}^{1/4}\right)^{15} + \left(0.12 Ra_{Do}^{1/3}\right)^{15}\right]^{1/15}}\right]} \qquad \text{(Eq. A.2-7)}$$

The same iterative method described in Appendix A.1 for the earlier Kuehn and Goldstein correlations was used to evaluate the average bulk temperature ($\overline{T}_b$) using Equations A.2-5 through A.2-7.

In this study, the modified Kuehn and Goldstein correlations were evaluated for two different geometries and operating conditions. The first set used geometry and other input given in the modified Kuehn and Goldstein correlations. The second set of calculations used the same YMP geometry and input as used to evaluate the earlier Kuehn and Goldstein correlations above (Section A.1).

For the modified Kuehn and Goldstein configuration, the inner and outer cylinder diameters used are 0.0356 m and 0.0925 m, respectively (Table 7.3.1-2). The inner and outer cylinder temperatures are 28.155°C and 27.245°C, respectively, and nitrogen properties (the working fluid) are shown in Table 7.3.1-3. These input values were used to evaluate the average bulk temperature. The Rayleigh number is calculated similar to the procedure in Section 7.3.1. Table A.2-1 shows the values found in the iteration process to find the average bulk temperature. $T_{film\text{-}i}$ and $T_{film\text{-}o}$ are mean temperatures used to evaluate fluid properties for the inner and outer cylinders respectively. In Table A.2-1 the kinematic viscosities and thermal diffusivities were evaluated using the relationships $\nu = \mu/\rho$ and $\alpha = k/(c_p\ \rho)$, respectively. Here μ and c_p are the dynamic viscosity and specific heat of nitrogen given in Table 7.3.1-3. The density ρ for nitrogen was calculated from the gas law equation $\rho = P/(R\ T)$, using pressure (P) =34.6 atmospheres and nitrogen gas constant (R) of 297 J/kg K. R was calculated using the universal gas constant divided by the molecular weight of nitrogen, both given in Table 7.3.1-3. The symbol T_b in Table A.2-1 is the initial value of the bulk temperature, while $T_{b,new}$ is the value derived at the end of the iteration cycle. When these two numbers agree with each other, the process has converged.

Table A.2-1. Iteration Procedure to Evaluate Average Bulk Temperature for Modified Kuehn and Goldstein Correlations Using Original Geometry and Temperatures with Nitrogen as the Working Fluid: Average Bulk Temperature Values for the Final Iteration Cycle

g m/s^2	Ra_L	T_b °C	T_{film-i} °C	T_{film-o} °C	ν_I m^2/s	α_I m^2/s	ν_o m^2/s
9.81000	2.51E+6	27.476	27.816	27.361	4.658E-7	6.369E-7	4.646E-7
0.98100	2.51E+5	27.482	27.818	27.363	4.658E-7	6.369E-7	4.646E-7
0.09810	2.51E+4	27.493	27.824	27.369	4.658E-7	6.369E-7	4.646E-7
0.00981	2.51E+3	27.511	27.833	27.378	4.658E-7	6.370E-7	4.646E-7

α_o m^2/s	Ra_{Di}	Ra_{Do}	$N'u_i$	$N'u_o$	T_{bnew} °C
6.352E-7	3.37E+6	2.02E+7	22.50	66.08	27.476
6.352E-7	3.34E+5	2.07E+6	13.00	36.94	27.482
6.352E-7	3.29E+4	2.17E+5	7.69	20.56	27.493
6.352E-7	3.19E+3	2.33E+4	4.69	11.33	27.511

DTN: SN0308T0507803.015.

Once the average bulk temperature is known, Equation A.2-2 and Equation A.2-3 were used to calculate the Nusselt numbers for conduction and natural convection. The procedure was applied at different Rayleigh numbers (by varying g) and corresponding equivalent thermal conductivities were calculated. Table A.2-2 shows the results. The procedure and data are included in DTN: SN0308T0507803.015.

Table A.2-2. Rayleigh Number, Nusselt Numbers, and Equivalent Thermal Conductivity for Modified Kuehn and Goldstein Correlations Using Original Geometry and Temperatures, with Nitrogen as the Working Fluid

Ra_L	Nu_{conv}	Nu_{cond}	Nu	k_{eq}
2.51E+6	16.79	2.09	16.79	8.01
2.51E+5	9.61	2.09	9.61	4.59
2.51E+4	5.60	2.09	5.60	2.67
2.51E+3	3.32	2.09	3.32	1.58

DTN: SN0308T0507803.015.

The modified Kuehn and Goldstein correlations were also applied to large-scale geometry (YMP) at elevated temperatures. The inner cylinder diameter (*Di*) and outer cylinder diameter (*Do*) were 1.71 m and 5.5 m, respectively (shown in Table 7.3.2-1). The inner and outer cylinder temperatures were 100°C and 80°C, respectively, and air properties used were as shown in Table 7.3.3-1. The same data used for the earlier Kuehn and Goldstein calculations in Section A.1 was employed. The same iterative method was also used to evaluate the average bulk temperature ($\overline{T}_b$) using Equations A.2-5 through A.2-7. Table A.2-3 shows the values found in the iteration process to find the average bulk temperature and Table A.2-4 shows calculated equivalent thermal conductivity values for the YMP geometry.

Table A.2-3. Iteration Procedure to Evaluate Average Bulk Temperature for Modified Kuehn and Goldstein Correlations Using Large-Scale Geometry and Elevated Temperatures with Air as the Working Fluid: Average Bulk Temperature Values for the Final Iteration Cycle

g m/s^2	Ra_L	Tavgb °C	T_{film-i} °C	T_{film-o} °C	ν_I m^2/s	α_I m^2/s	ν_o m^2/s
9.81000	5.30E+09	85.7456	92.8728	82.8728	2.2663E-05	3.2567E-05	2.1565E-05
0.98100	5.30E+08	85.2326	92.6163	82.6163	2.2635E-05	3.2524E-05	2.1537E-05
0.09810	5.30E+07	84.8547	92.4273	82.4273	2.2614E-05	3.2492E-05	2.1516E-05
0.00981	5.30E+06	84.8119	92.4059	82.4059	2.2612E-05	3.2488E-05	2.1514E-05

α_o m^2/s	Ra_{Di}	Ra_{Do}	Nu_i	Nu_o	Tavgbnew °C
3.0887E-05	2.5939E+09	3.9562E+10	165.9141	452.1908	85.74556
3.0844E-05	2.6960E+08	3.6153E+09	78.80618	244.4297	85.23256
3.0812E-05	2.7717E+07	3.3627E+08	39.0057	134.4206	84.85467
3.0808E-05	2.7803E+06	3.3340E+07	21.47753	74.9832	84.81187

DTN: SN0308T0507803.015.

Table A.2-4. Rayleigh Number, Nusselt Numbers, and Equivalent Thermal Conductivity for Modified Kuehn and Goldstein Correlations Using Large-Scale Geometry and Elevated Temperatures with Air as the Working Fluid

Ra_L	Nu_{conv}	Nu_{cond}	Nu	k_{eq}
5.30E+09	121.4	1.71	121.4	70.9
5.30E+08	59.6	1.71	59.6	34.8
5.30E+07	30.2	1.71	30.2	17.7
5.30E+06	16.7	1.71	16.7	9.75

DTN: SN0308T0507803.015.

APPENDIX B

BLIND ANALYSES OF THE EBS NATURAL CONVECTION TESTS

CFD simulations were developed to perform blind analyses of the EBS natural convection experiments. Extensive grid checks were performed with these simulations, showing that the chosen grids were fine enough to accurately capture the viscous boundary layers and to have the calculation results be grid independent. These simulations were developed without recourse to the experimental data, and some assumptions such as the appropriate waste package boundary condition (heat generation vs. heat flux) were not available. These assumptions were reevaluated in view of the experimental data, and new simulations were performed. These new simulations are presented in Chapter 7. The simulations in this Appendix, while not having some of the appropriate parameters, are nonetheless useful. Nodalization sensitivity results were performed on the simulations presented in this Appendix as well as other quality checks. These evaluations can be directly applied to the simulations discussed in Chapter 7.

The geometric layout, physical models, grid specifications, thermal properties, boundary conditions, operating conditions, and CFD simulation settings and parameters used for these runs are described in detail in Section 7, and are not duplicated in this Appendix. The ability of the grids to adequately capture the viscous boundary layer is based on reviewing near-wall meshing and temperatures. Adequacy of the near-wall meshing may be determined using y^+, which measures the distance from the wall over which the log-law is valid ($y^+ \equiv \rho u y/\mu$, where ρ, u and μ are fluid density, velocity and dynamic viscosity, respectively, and y is distance from the wall). For the natural convection simulations described in this report, the near-wall method, where refined meshing is applied up to the wall, has been used. The method is further improved using the enhanced wall treatment approach that is useful when, due to computational restrictions, the mesh is not refined enough. When the near-wall method with enhanced wall treatment is used, the FLUENT-recommended y^+ values for cells or regions adjacent to the wall are of order 1, and that approximately 10 elements are inside the boundary layer (Fluent 2001 [DIRS 164453], Section 10.9.2). However values as high as $y^+ = 5$ are acceptable because the elements near the wall are inside the viscous sublayer.

The simulation results are presented below for the 25% and 44% scale cases. The results from the case in question are presented first, followed by an overall assessment of grid independence using a baseline case.

B.1 25% SCALE NATURAL CONVECTION TEST CFD SIMULATION RESULTS SHOWING GRID ACCEPTABILITY

The numerical simulation results illustrated in this section correspond to the natural convection test cell shown in Figure 7.4.1-6. The hot boundary corresponds to the reflective boundary shown in the figure and the cold boundary corresponds to the non-reflective boundary. Case 4 has been selected for this analysis. Case 4 is shown in Figure 7.4.1-7. Operationally, Case 4 was a 25% scale test having non-uniform spacing of the waste packages, non-uniform power input to the packages, and a drip shield encompassing the entire length of the heat sources. The numerical simulation for the case contains 2,325,444 control volumes.

The y^+ values for this test case are illustrated on the heat sources (including cylindrical shell and both ends), invert floor, and concrete walls in Figures B.1-1 through B.1-3. The x-axis on Figures B.1-1 though B.1-5 is the distance from the non-reflective boundary (see Figure 7.4.1-6). The families of data points represent all of the elements of each surface.

From Figure B.1-1 it is noted that all of the y^+ values on the heat sources are in the acceptable range ($y^+ < 5$). As in previous cases, the y^+ values on the end of the heat sources are the largest values reported. Figures B.1-2 and B.1-3 illustrate y^+ values on the concrete and invert, respectively.

Figures B.1-4 and B.1-5 illustrate y^+ values on the drip shield inside and outside surfaces, respectively. The y^+ values are small and acceptable for this analysis.

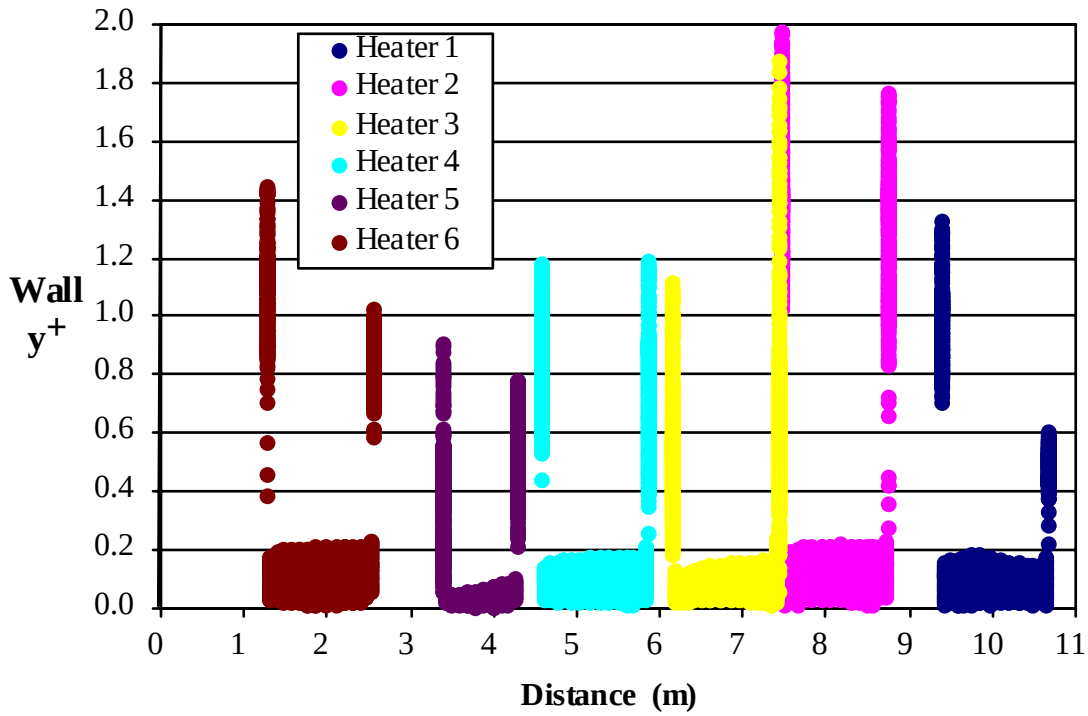

DTN: SN0308T0507803.004.

Figure B.1-1. Wall y^+ Distribution on the Heat Sources for Case 4

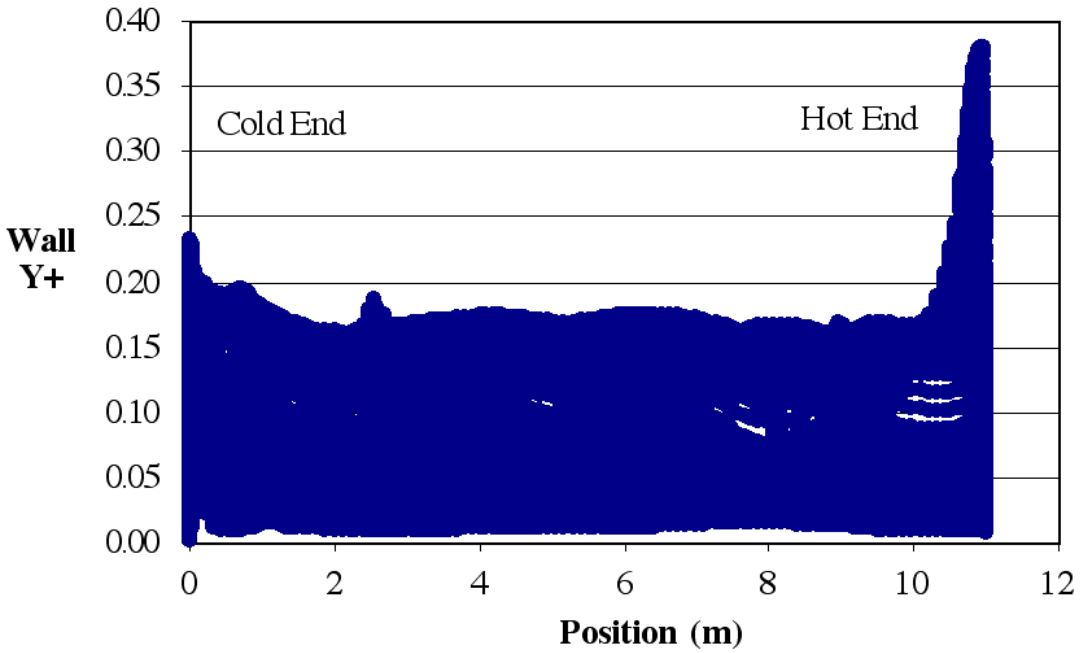

DTN: SN0308T0507803.004.

Figure B.1-2. Wall y^+ Distribution on the Concrete for Case 4

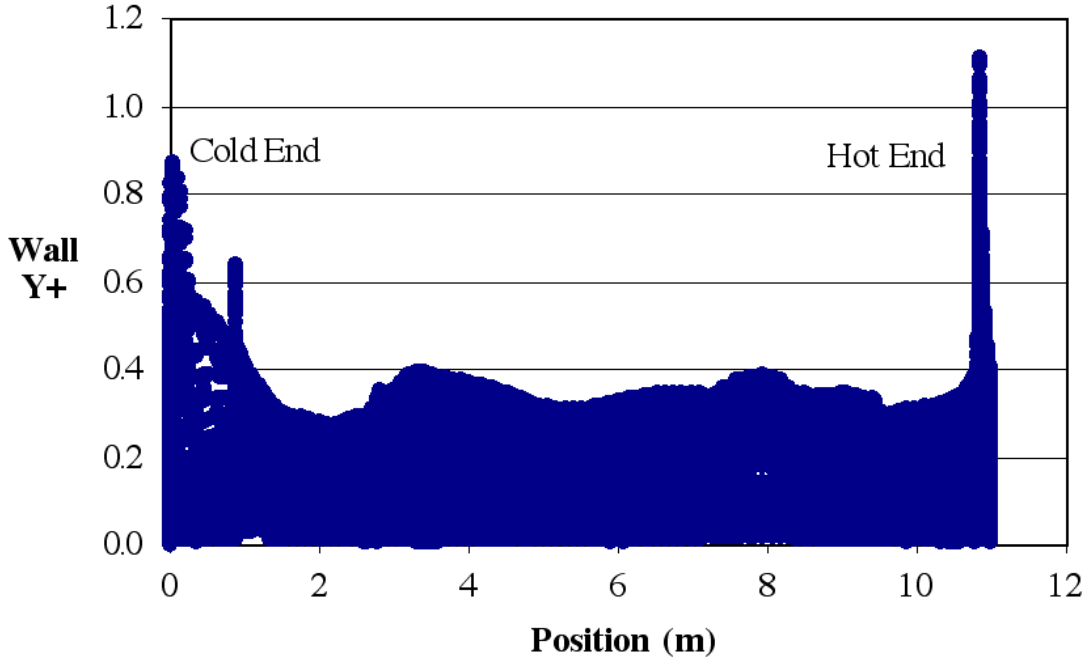

DTN: SN0308T0507803.004.

Figure B.1-3. Wall y^+ Distribution on the Invert Floor for Case 4

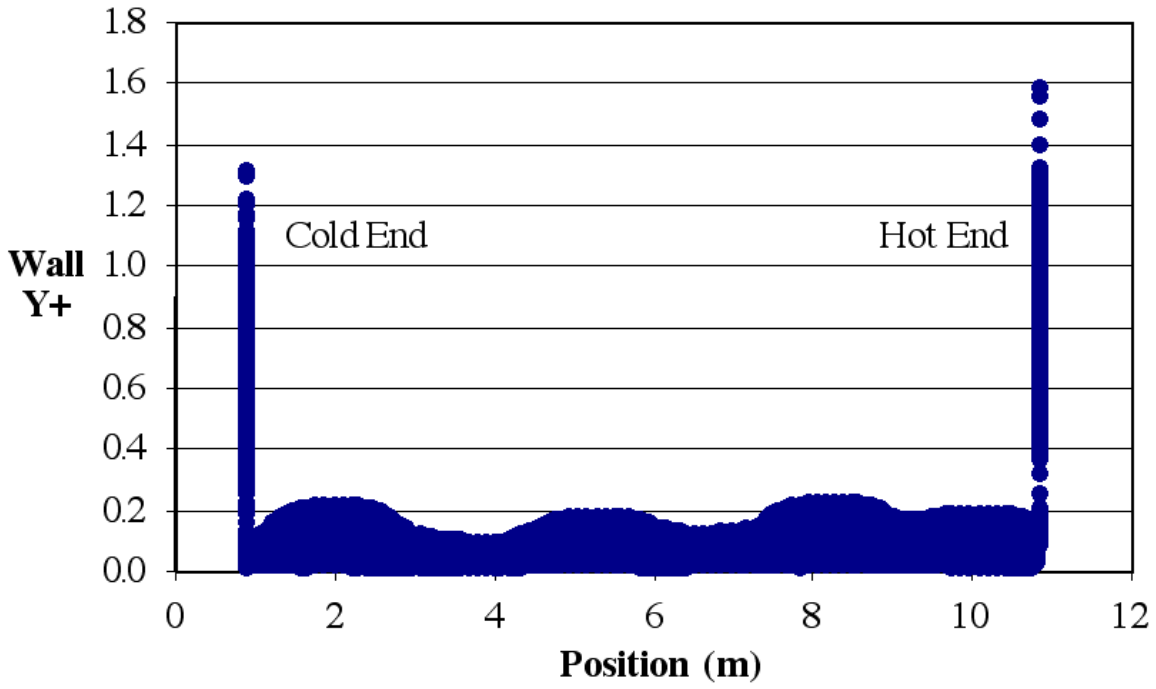

DTN: SN0308T0507803.004.

Figure B.1-4. Wall y^+ Distribution on the Inside of the Drip Shield for Case 4

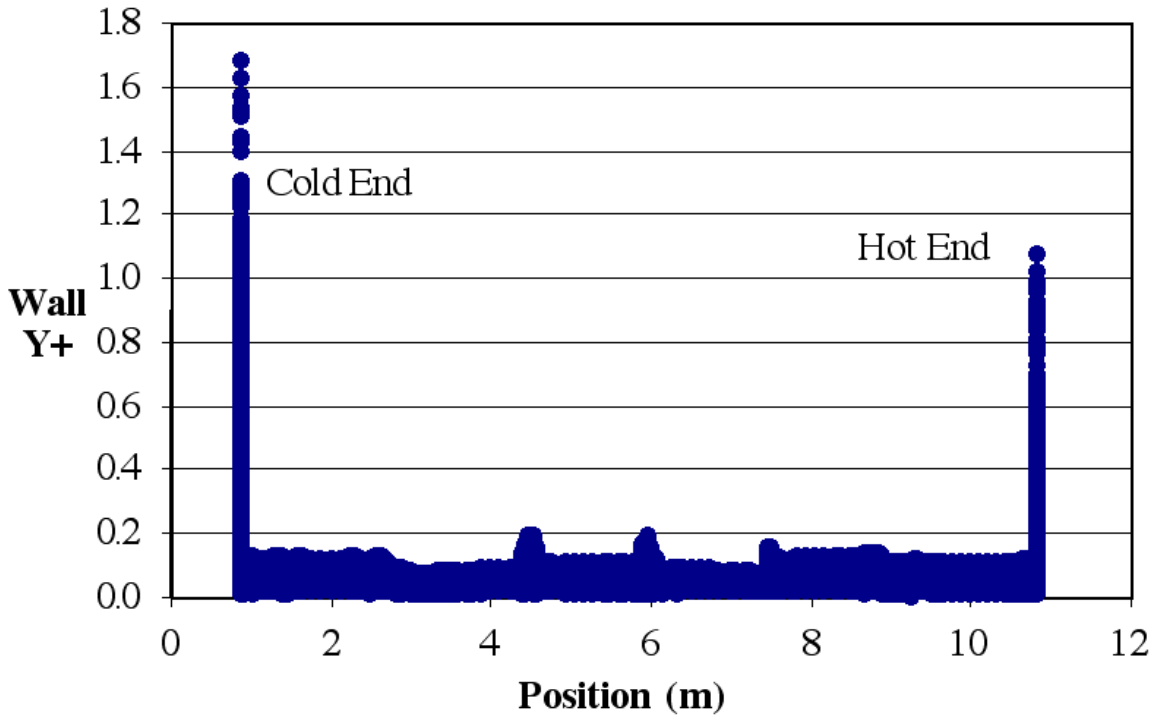

DTN: SN0308T0507803.004.

Figure B.1-5. Wall y^+ Distribution on the Outside of the Drip Shield for Case 4

The next section illustrates temperatures along specific lines in the cross-sections that contain both large and small diameter heat sources.

Two cross-sections are considered in the analysis for Case 4 (refer to the layout of Figure 7.4.1-7). The first is at location z = 8.115 m. where z is the distance from the non-reflective boundary (Figure 7.4.1-7). This cross-section corresponds to a slice through the center of hot heat source NC4-WP2. The second cross-section is at location z = 6.795 m. This cross-section corresponds to a slice through the center of heat source NC4-WP3. The first cross-section is through a small heat source diameter; the second cross-section is through a large heat source diameter. NC4-WP2 is one of the highest power output heat sources in the test cell. NC4-WP3 is the lowest power output heat source. In each cross-section, temperature data are plotted along a horizontal line located at the heater centerline, through the heat source, fluid domain, concrete, and insulation. This horizontal line is called the "eccentric line." Figure B.1-6 represents the temperature distribution on the eccentric line for NC4-WP2; Figure B.1-7 represents the temperature distribution on this line for NC4-WP3.

Figure B.1-6 indicates that most of the temperature drop at this particular location occurs through the boundary layers on the inner surfaces of the enclosure (when viewed in cross-section). Inside the drip shield the primary temperature drop occurs through the boundary layer adjacent to the heat source. The heat source temperature is about 41°C and the core fluid temperature inside the drip shield is fairly uniform at approximately 35 to 36°C. Outside the drip shield the primary temperature drop occurs through the boundary layer adjacent to the drip shield. The drip shield temperature is approximately between 34 and 35°C. The core fluid temperature outside the drip shield is about 32°C.

Figure B.1-7 indicates that the temperature of the surrounding fluid inside the drip shield near the cool heat source (NC4-WP3) is actually warmer than the cool heat source itself. The surrounding air temperature is elevated due to the nearby hot heat source (NC4-WP2). A temperature drop from the fluid to the cool heat source occurs across the boundary layer near that heat source. Although the heat source is cooler than the surrounding fluid, it is warmer than the surrounding drip shield. The temperature drop adjacent to the concrete wall is greater at this location because this region of the test (adjacent to NC4-WP3) is locally cooler than the region surrounding heat source NC4-WP2 (high heat output).

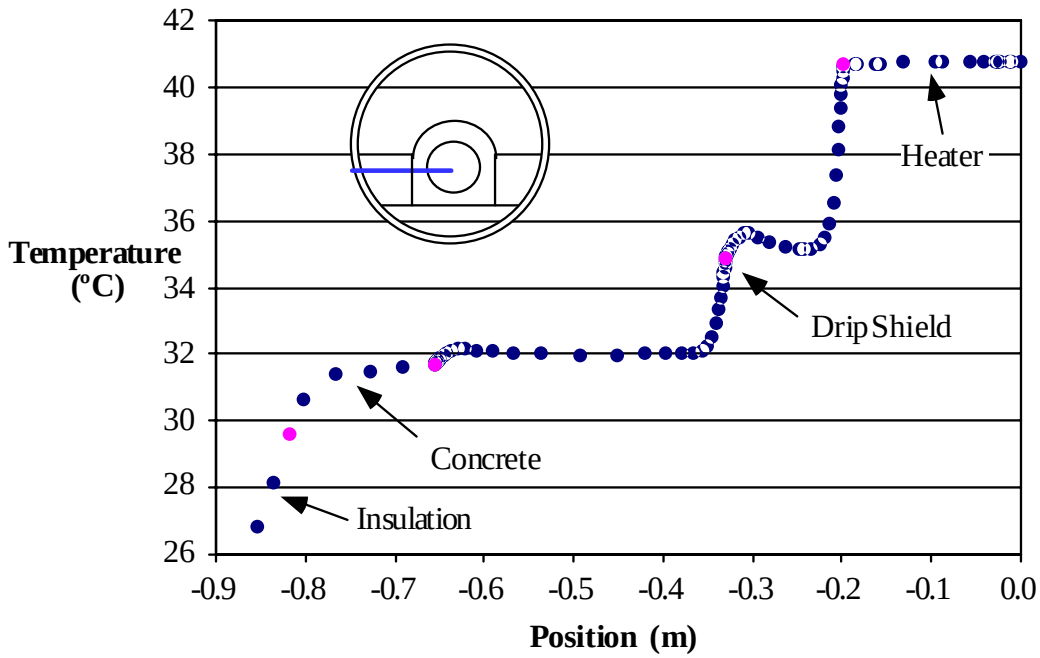

DTN: SN0308T0507803.004.

NOTE: Blue dots = simulation temperatures; red dots = surfaces.

Figure B.1-6. Temperature Distribution at Eccentric Line through the Center of NC4-WP2 (Hot Heater) for Case 4

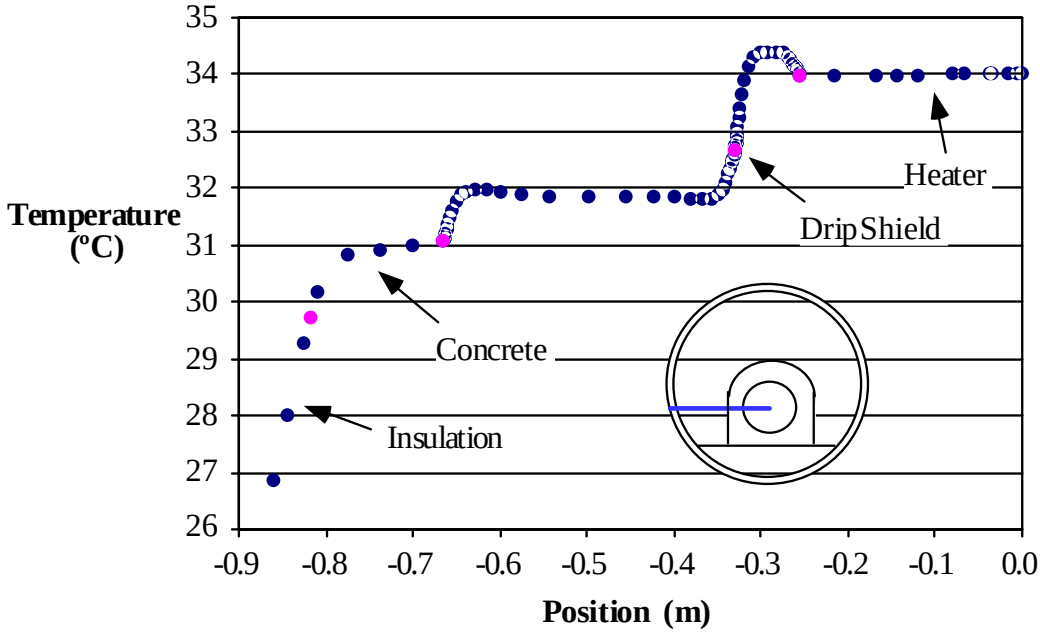

DTN: SN0308T0507803.004.

NOTE: Blue dots = simulation temperatures; red dots = surfaces.

Figure B.1-7. Temperature Distribution at Eccentric Line through the Center of NC4-WP3 (Cool Heater) for Case 4

Using the same cross-sections and eccentric lines, vertical (or Y) velocity distributions are illustrated in a manner similar to the temperature profiles. Figure B.1-8 represents the vertical velocity distribution on the eccentric line through NC4-WP2 (hot source, small diameter); Figure B.1-9 represents the vertical velocity distribution on the eccentric horizontal line through NC4-WP3 (cold source, large diameter).

The vertical (Y) velocity profiles are not at all similar in the fluid spaces between the large and small diameter heat sources (e.g., NC4-WP2 and NC4-WP3), drip shield, and concrete wall. For a uniform heating case the velocity profiles from source-to-source would be similar (that is, typical upward directed flow on the heat source, downward on the inside of the drip shield, upward directed flow on the outside of the drip shield and downward on the concrete wall). This flow pattern is not generally true of all heat sources in the non-uniform heating case due to the cold heat sources. From Figure B.1-8 it is noted that at this location the upward component of vertical velocity on the heat source is larger than the downward components on the inside drip shield or concrete wall. This is due to the velocity in the z-direction in the lower portion of the annulus near the floor of the hot heat source. The maximum upward component of velocity at this location near the heat source is about 0.12 m/s. The higher heat output sources (NC4 –WP1, –WP2, –WP4, and –WP6) follow this typical flow pattern. Figure B.1-9 indicates that *both* vertical velocity components inside the drip shield are directed downward. That is, the velocity of the fluid adjacent to the concrete wall and heat source are both directed downward (expected for buoyancy flow on a cold wall). Recall from Figure B.1-7 that the fluid surrounding NC4–WP3 is warmer than the heat source itself. The flow pattern near the cold sources (NC4–WP3, –WP5) is indicative of a strong, recirculating, z-component velocity (inside the drip shield) of warm air movement above the cool sources from surrounding hot heat sources.

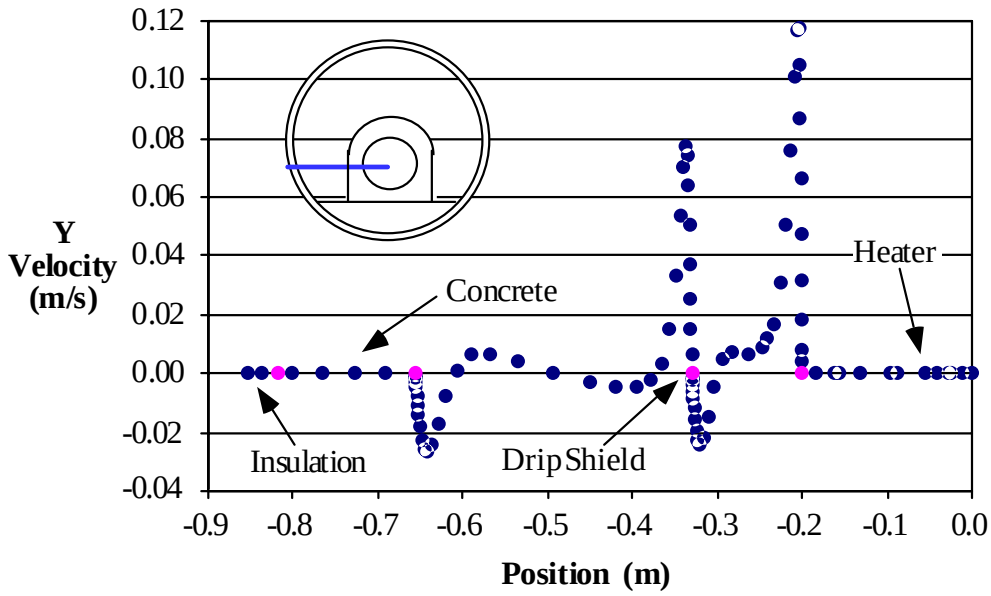

DTN: SN0308T0507803.004.

NOTE: Blue dots = simulation temperatures; red dots = surfaces.

Figure B.1-8. Vertical Velocity Distribution at Eccentric Line through the Center of NC4-WP2 (Hot Heater) for Case 4

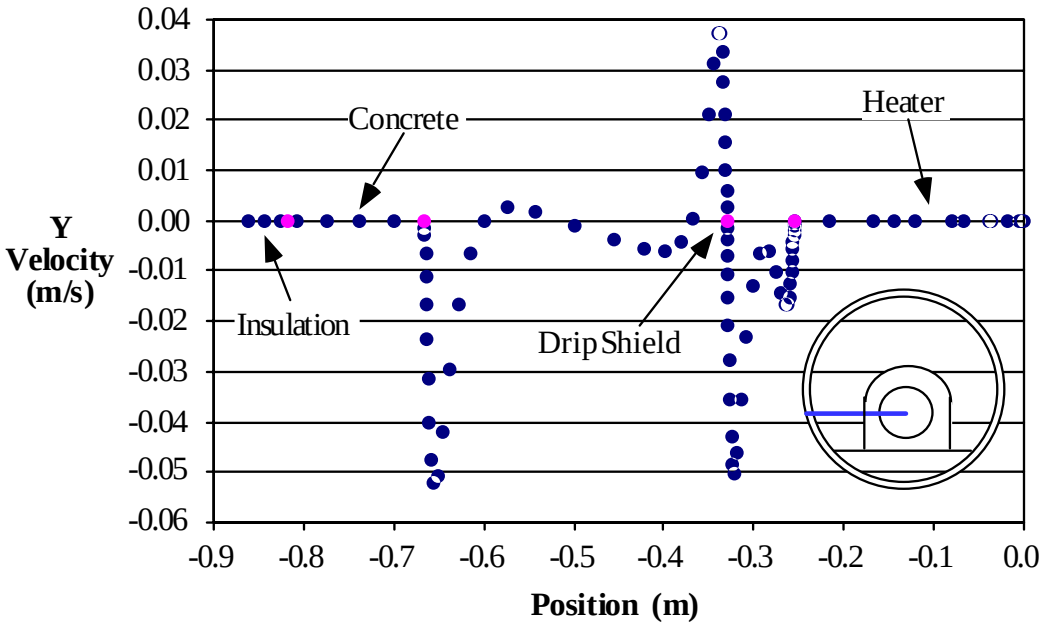

DTN: SN0308T0507803.004.

NOTE: Blue dots = simulation temperatures; red dots = surfaces.

Figure B.1-9. Vertical Velocity Distribution at Eccentric Line through the Center of NC4-WP3 (Cool Heater) for Case 4

B.2 25% SCALE GRID INDEPENDENCE STUDY

A grid independence study was performed using a baseline simulation for the 25% scale runs. The baseline was chosen to be the grid associated with Case 1, a uniform spacing, uniform power case without a drip shield; see Figure 7.4.1-6. In addition to the base case (original, unrevised) working computational grid (1,277,088 computational cells), four additional grids were considered. Table B.2-1 indicates the cell statistics for the computational grids used in the grid independence study.

Table B.2-1. Grid Independence Study for Case 1

Number of Computational Cells	Grid Description	YMP Data Tracking Number (DTN)
1,277,088	Base case grid (Original, Unrevised)	SN0308T0507803.004
1,090,344	Coarse grid	SN0310T0507803.017
1,168,632	First adaption on coarse grid based on y+	SN0310T0507803.018
1,373,472	Refined grid	SN0310T0507803.020
1,409,334	Second adaption on coarse grid based on y+	SN0310T0507803.019

Axial (z-direction) temperatures and heat source temperatures are investigated in this study. Specifically, the fluid-solid interface temperatures from the base simulation will be compared to temperatures at the same locations obtained from the computational grids described in Table B.2-1. Axial temperatures are selected because grid refinements or grid adaptations occurred in the z -direction of the simulations. That is, the cross-sectional mesh near heat sources remained unaltered in all cases. This is reasonable because y+ values were shown to be adequate on the cylindrical shells for all of the 25% scale cases (see Figures B.1-1 through B.1-5 for examples), and the boundary layers were appropriately resolved (e.g., by 10 or more cells). Figures B.2-1 through B.2-3 illustrate temperature comparisons between CFD simulations at top, side, and bottom locations described in a previous section.

Based on the small differences in the solid-fluid interface temperatures at these locations, a grid independent solution has been achieved with the working computational grid (1,277,088 cells). One additional comparison is used to investigate the influence of y^+.

Review of the y^+ values for the baseline case (Figure B.2-4) indicated a potential issue with the working grid with respect to y+ values on the end heat source number seven ($y^+ > 5$ at position ≈ -9.2 m). In order to investigate this, a temperature comparison for heat source number seven is performed using the 1,277,088 and 1,373,472 computational cell simulations. The y^+ values from the heat sources in the 1,373,472 computational cell simulation are shown in Figure B.2-5. It is noted that all y^+ values are less than the recommended five. The temperature comparison is illustrated in Figure B.2-6. This figure indicates that a reduction in y+ at the walls of heat source seven resulted in very minor changes in heat source surface temperatures.

Based on this analysis and the y+ results of each case, it was determined that the working computational grids for the 25% scale tests were reasonably grid independent.

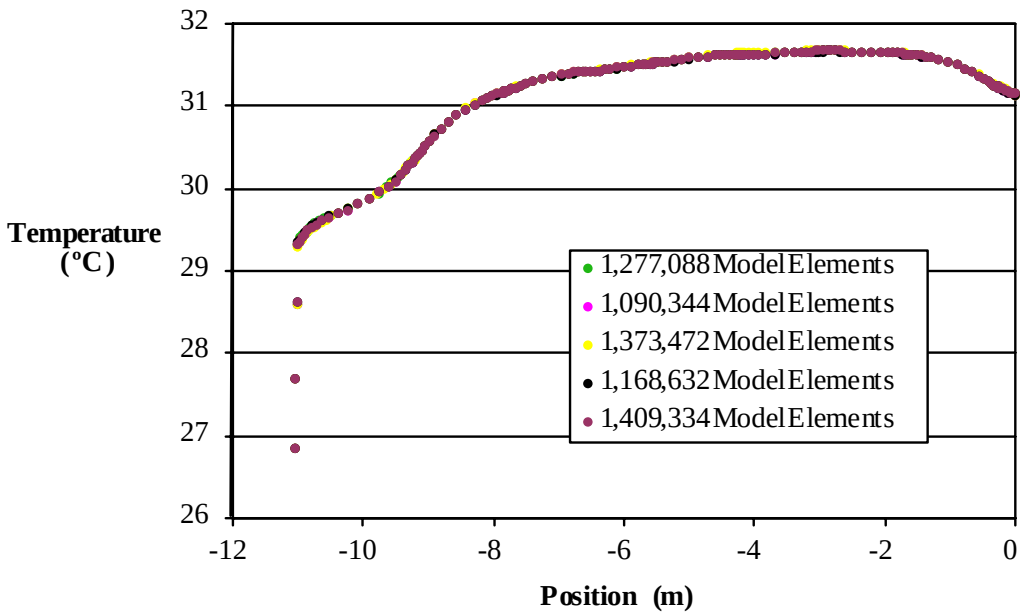

NOTE: See Table B.2-1 for DTNs.

Figure B.2-1. Axial Temperature Distribution at the Top of the Concrete Pipe Adjacent to the Fluid for Different Grids: Case 1

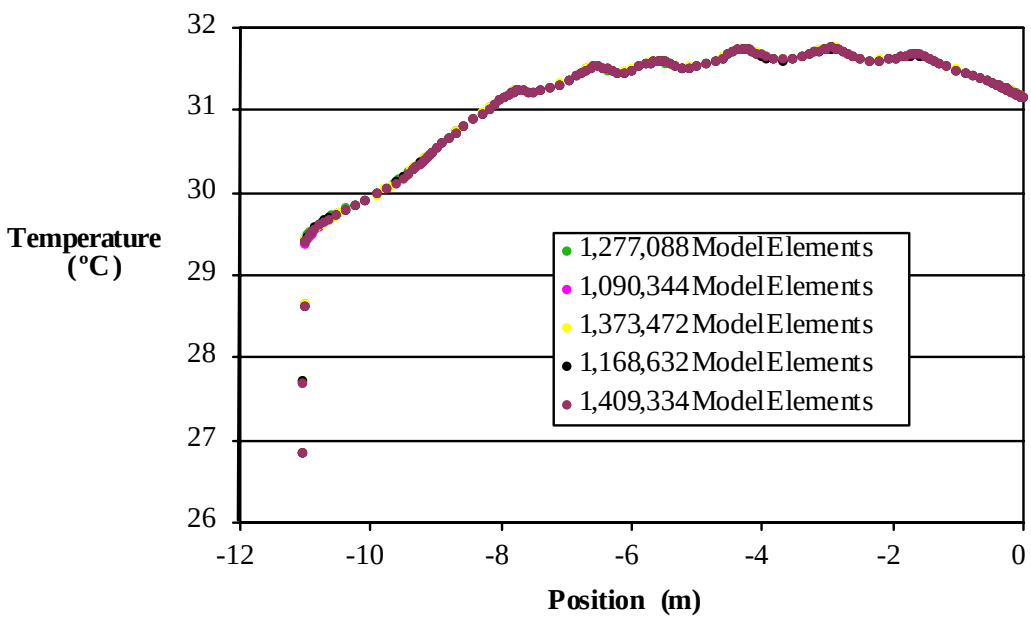

NOTE: See Table B.2-1 for DTNs.

Figure B.2-2. Axial Temperature Distribution at the Side of the Concrete Pipe Adjacent to the Fluid for Different Grids: Case 1

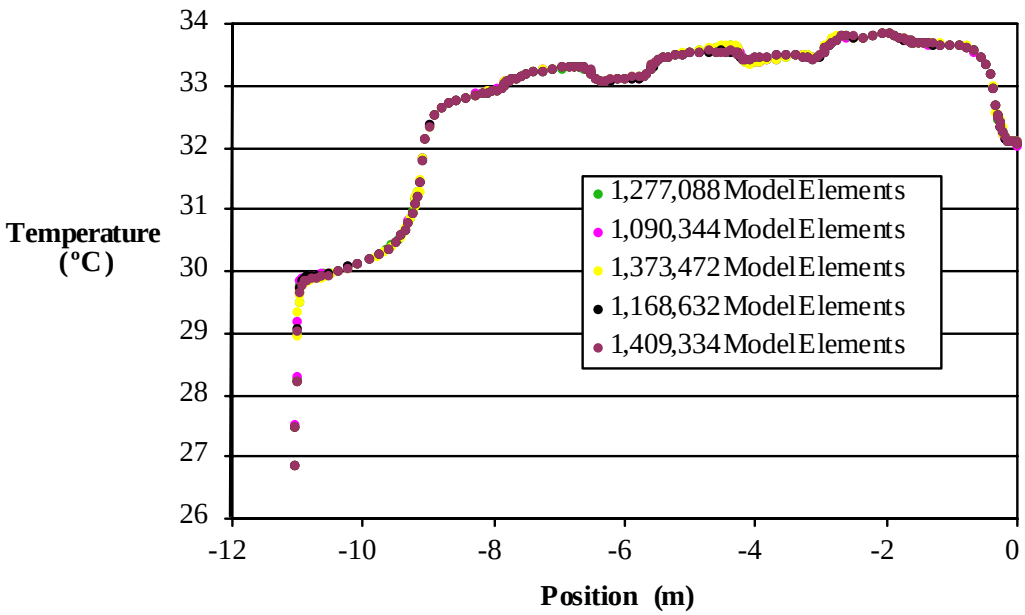

NOTE: See Table B.2-1 for DTNs.

Figure B.2-3. Axial Temperature Distribution Directly Below the Heat Sources and Above the Invert Floor Adjacent to the Fluid for Different Grids: Case 1

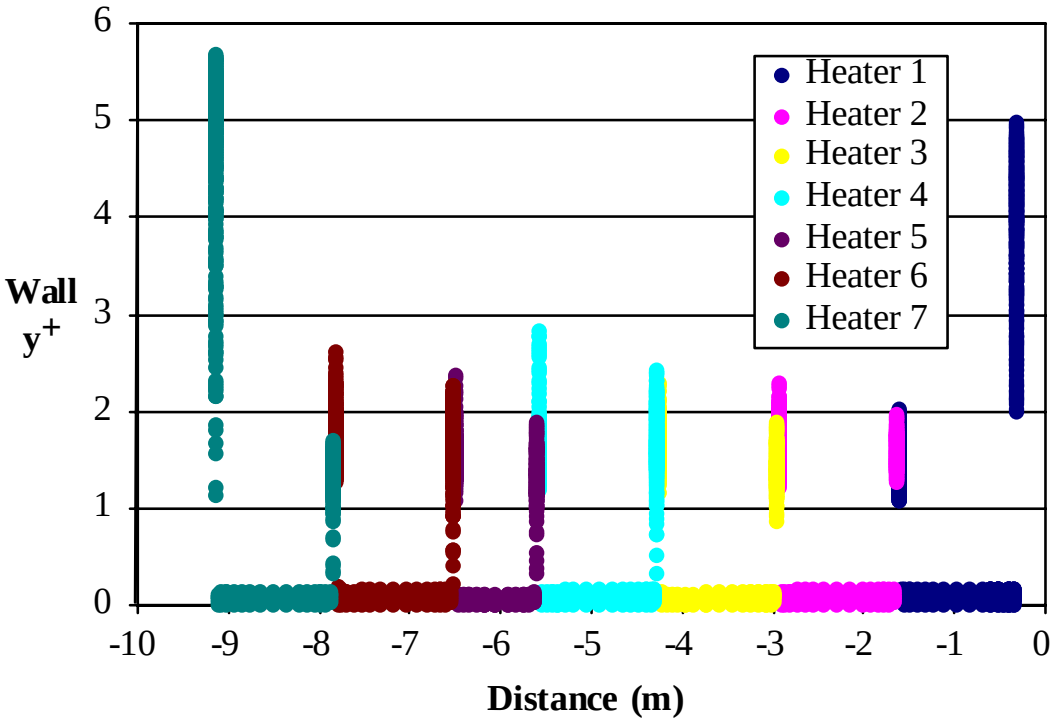

DTN: SN0308T0507803.004.

Figure B.2-4. Wall y^+ Distribution on the Heat Sources (Baseline): Case 1

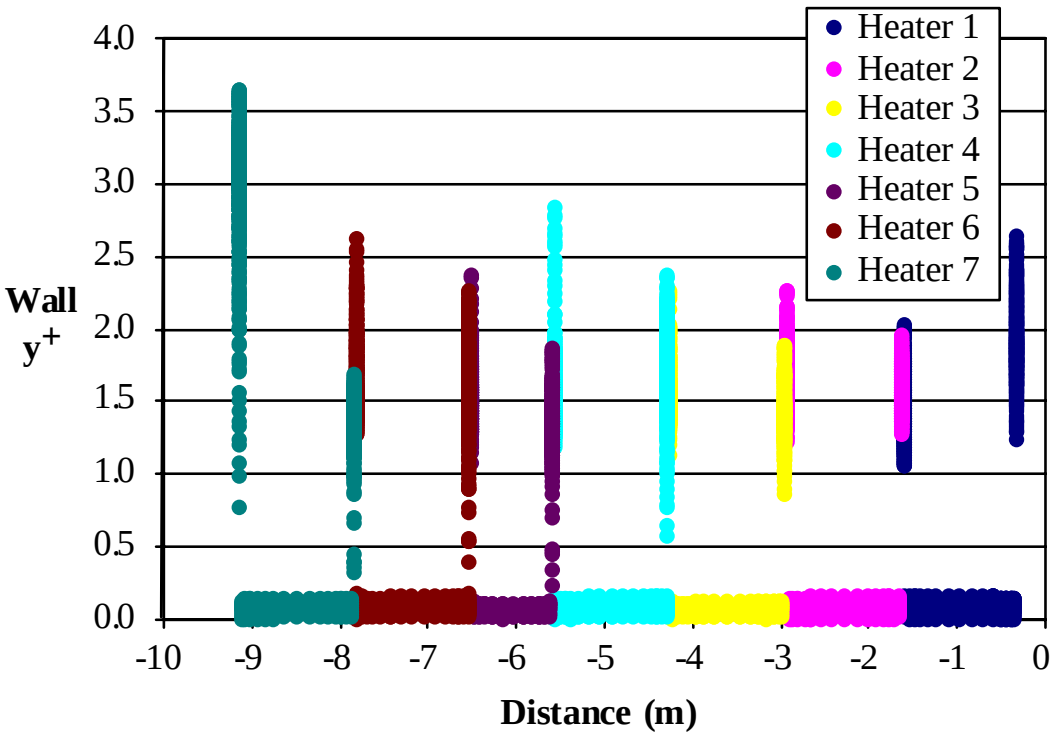

DTN: SN0310T0507803.020.

Figure B.2-5. Wall y+ Distribution on the Heat Sources (Refined): Case 1

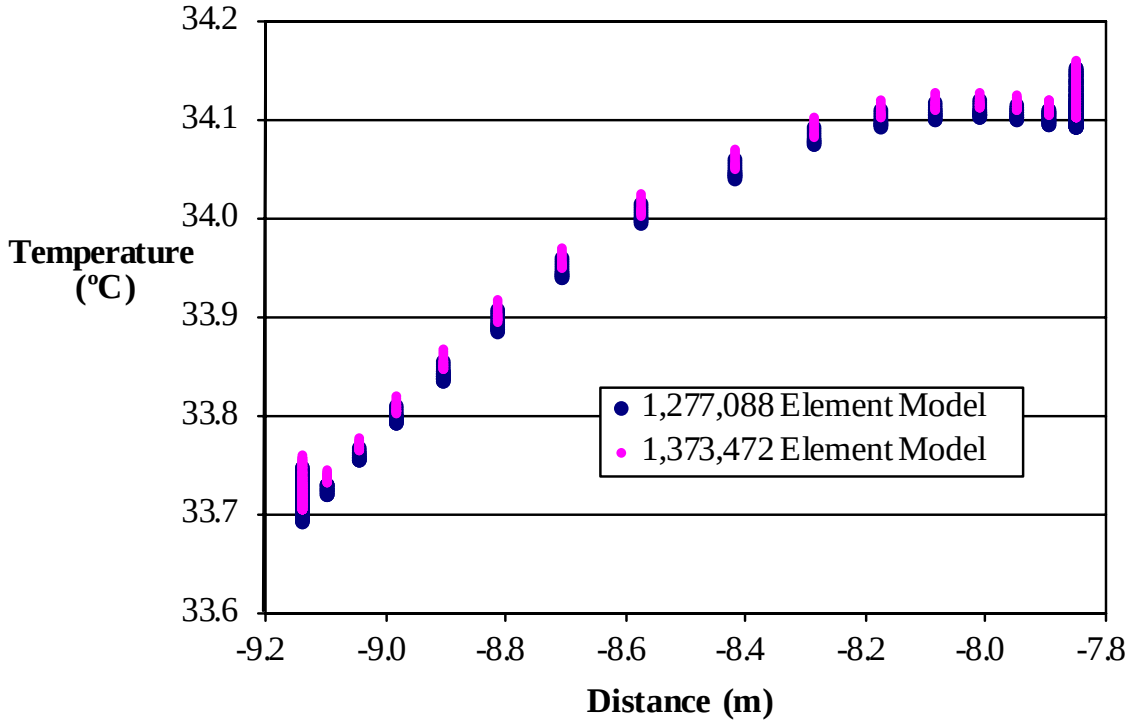

NOTE: See Table B.2-1 for DTNs.

Figure B.2-6. Temperature Comparison for Surface Elements Along Heat Source Seven: Case 1

B.3 44% SCALE NATURAL CONVECTION TEST CFD SIMULATION RESULTS SHOWING GRID ACCEPTABILITY

The numerical simulation results illustrated in this section correspond to the natural convection test cell shown in Figure 7.4.1-7. The hot boundary corresponds to the reflective boundary shown in the figure and the cold boundary corresponds to the non-reflective boundary. Case 8 was selected for this analysis; see Figure 7.4.1-9. Operationally, Case 8 was a 44% scale test having non-uniform spacing of the waste packages, non-uniform power input to the packages, and a drip shield encompassing the entire length of the heat sources.

B.3.1 Temperature

Figure B.3-1 represents the temperature distribution on the eccentric line for the heat source NC8-WP3. As in Figure B.1-7, the temperature distribution indicates that the temperature of the air inside the drip shield near the cool heat source (NC8-WP3) is warmer than the cool heat source itself. The air temperature is elevated due to the nearby hot heat source (NC8-WP2). A temperature drop from the fluid to the cool heat source occurs across the boundary layer near that heat source. Although the heat source is cooler than the surrounding air, it is warmer than the surrounding drip shield. The temperature drop adjacent to the concrete wall is greater at this location than at NC8-WP2 because this region of the test (adjacent to NC8-WP3) is locally cooler than the region surrounding heat source NC8-WP2.

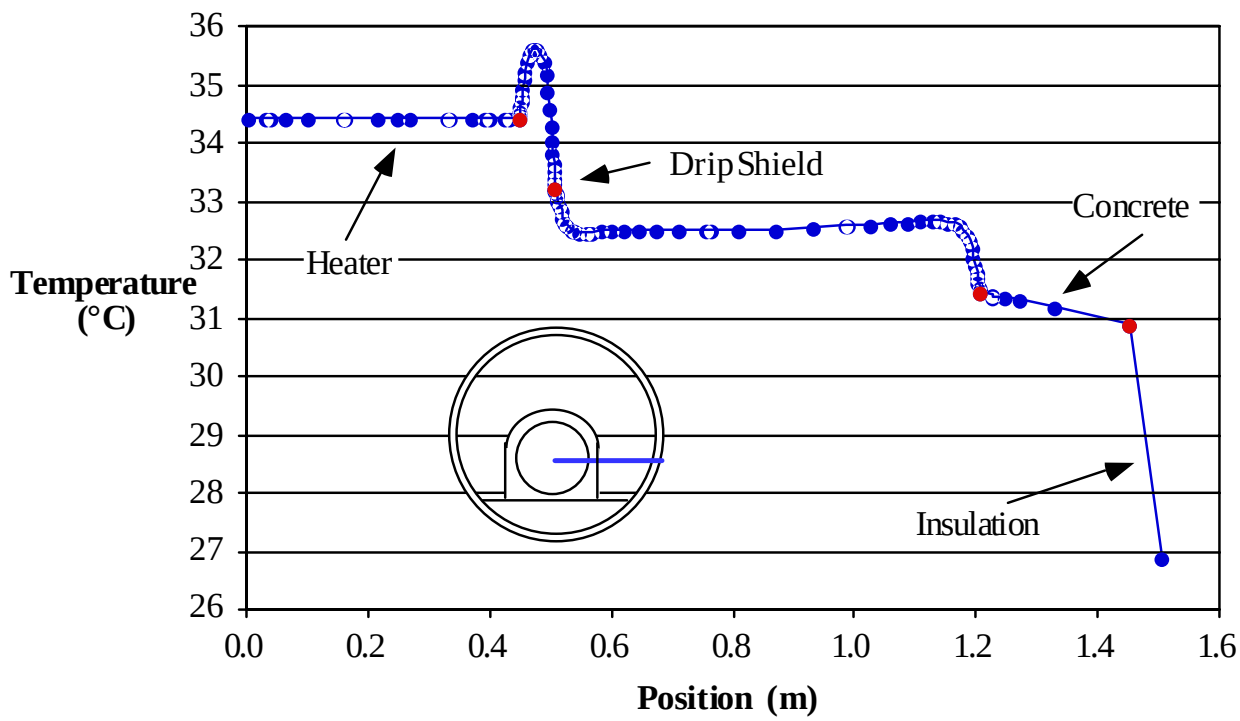

DTN: SN0308T0507803.004.

NOTE: Blue dots = simulation temperatures; red dots = surfaces.

Figure B.3-1. Temperature Distribution at Eccentric Line through the Center of NC8-WP3 (Cool Heater) for Case 8

Figure B.3-2 contains the temperatures for every element on the surface of all six heaters and the drip shield for Case 8. The relative temperatures of the two hot PWR, the two medium BWR, and the two cold HLW heaters can be easily seen in the figure. The temperature variation over any single heater was less than 1°C. The distance is from the reflective end – see Figure 7.4.1-7.

The variation in drip shield temperatures at locations down the drift was less than 1°C everywhere except for the ends. The temperature of the drip shield adjacent to the PWR heaters was approximately 6°C less than the PWR heater temperature and the temperature of the drip shield adjacent to the HLW heaters was approximately 1°C less than the HLW heater temperature.

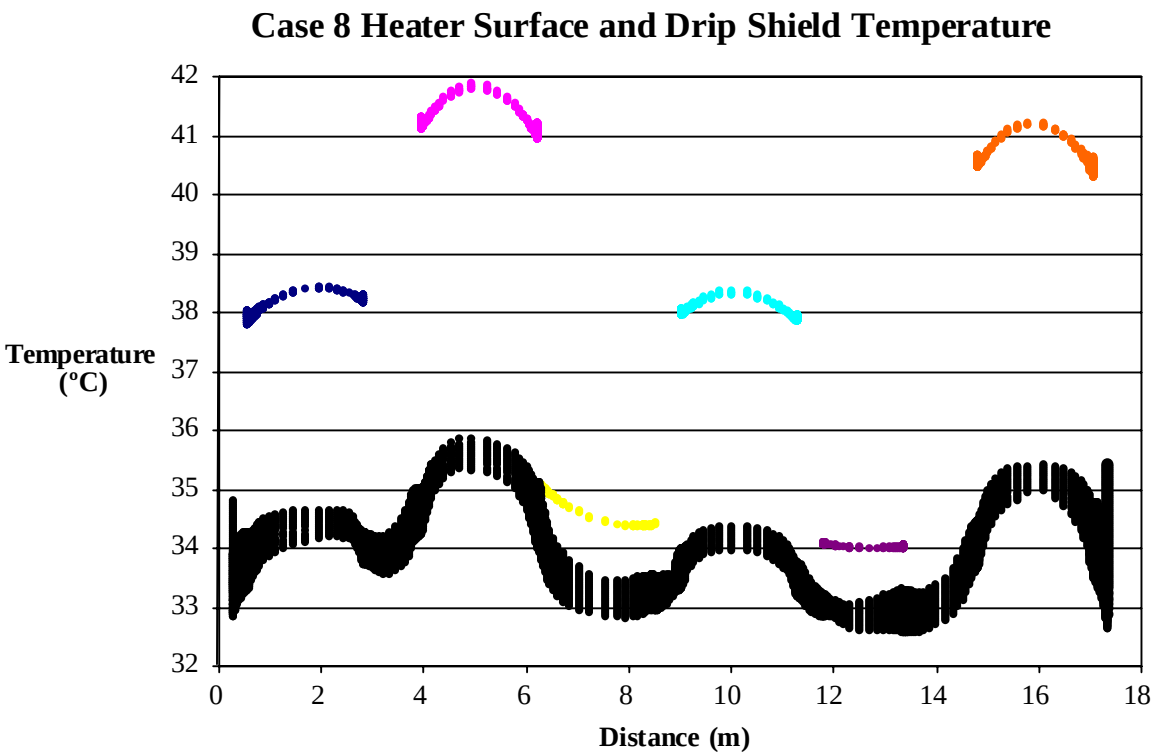

DTN: SN0308T0507803.004.

NOTE: From left to right, the heaters in the simulation represent a 44-BWR, 21-PWR, 5-DHLW Long, 44-BWR, 5-DHLW Short, and a 21-PWR. The drip shield is represented by the continuous black dots.

Figure B.3-2. Heater and Drip Shield Surface Temperatures (Case 8)

The temperature on the inner (under drip shield) and outer (outside drip shield) invert, insulation, and concrete surfaces are shown in Figure B.3-3. The locations of the two hot PWR heaters and the two medium BWR heaters can be easily seen in the inner invert temperature profiles. The peak inner invert temperatures are 1 to 2°C lower than the adjacent heater surface temperatures.

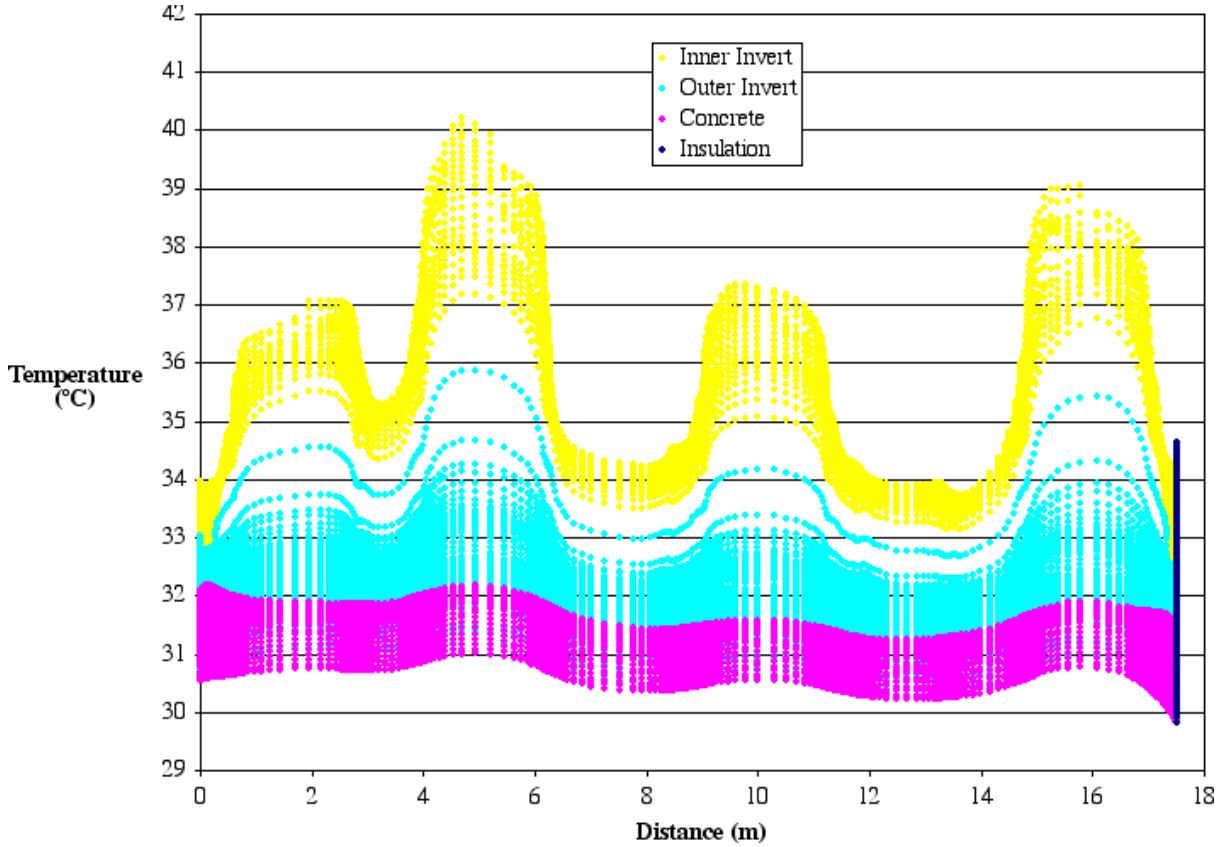

DTN: SN0308T0507803.004.

NOTE: From left to right, the heaters in the simulation represent a 44-BWR, 21-PWR, 5-DHLW Long, 44-BWR, 5-DHLW Short, and a 21-PWR.

Figure B.3-3. Inner Invert, Outer Invert, Insulation, and Concrete Surface Temperatures (Case 8)

Figure B.3-4 shows the wall y+ values for all six heaters in the Case 8 simulations. All of the wall y+ values are of order 1.

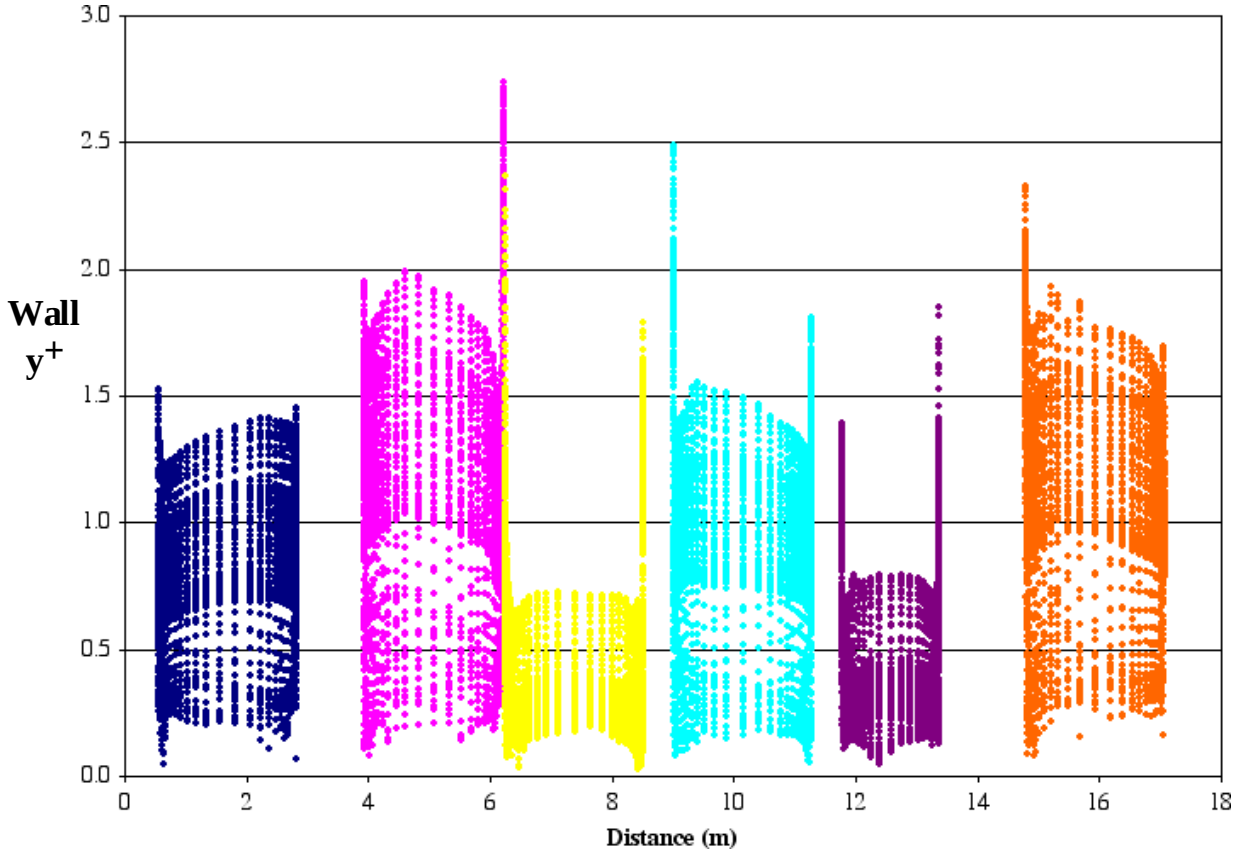

DTN: SN0308T0507803.004.

NOTE: From left to right, the heaters in the simulation represent a 44-BWR, 21-PWR, 5-DHLW Long, 44-BWR, 5-DHLW Short, and a 21-PWR.

Figure B.3-4. Wall y^+ Values on Heater Surfaces (Case 8)

Figure B.3-5 shows the wall y^+ values for both sides of the drip shield surface. Only three surface elements on the drip shield had wall y+ values over 2.5 with most of the wall y+ values on the side of the drip shield being 1.0 or lower.

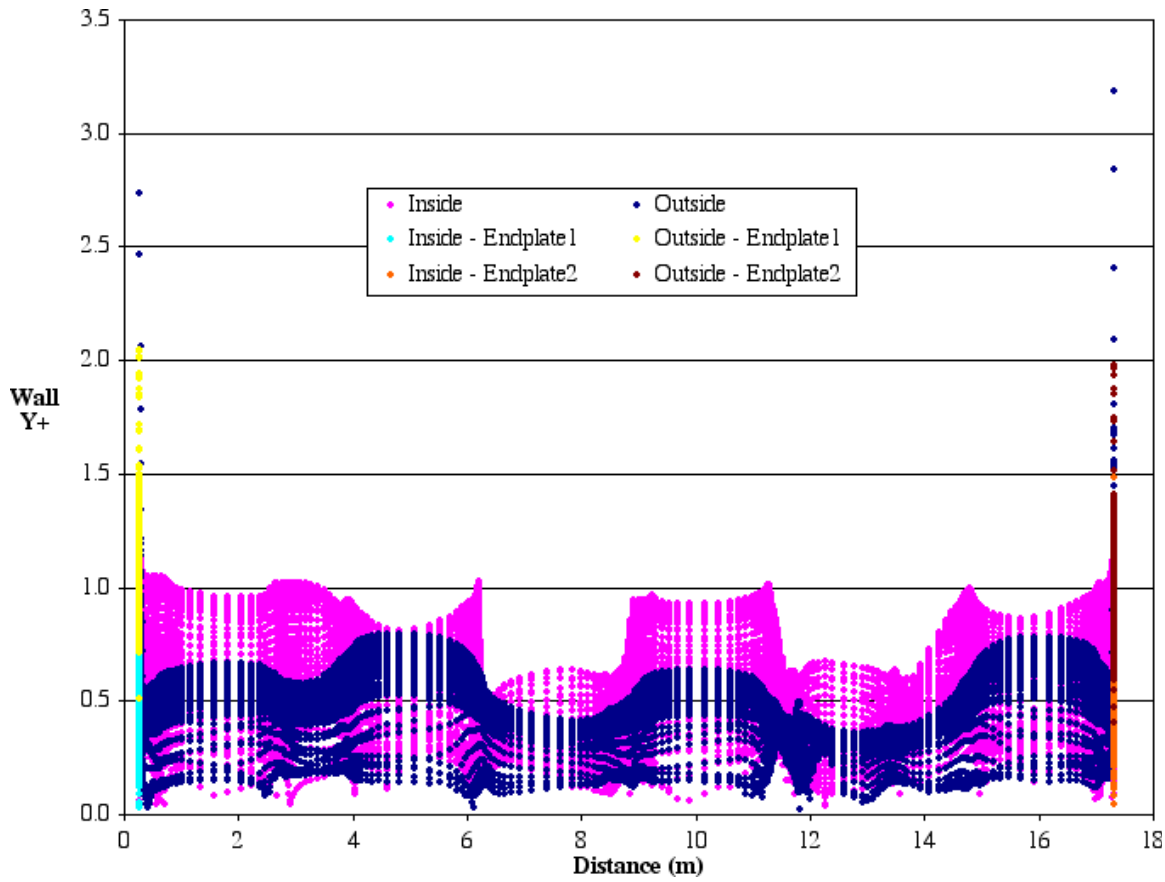

DTN: SN0308T0507803.004.

NOTE: From left to right, the heaters in the simulation represent a 44-BWR, 21-PWR, 5-DHLW Long, 44-BWR, 5-DHLW Short, and a 21-PWR.

Figure B.3-5. Wall y^+ Values on Both Sides of the Drip Shield (Case 8)

The wall y^+ values on the insulation, inner (or inside) and outer (or outside) invert, and concrete surfaces are presented in Figure B.3-6. The wall y^+ values on the concrete are all less than 1.0. They are also almost all less than 1 on the entire inner invert (e.g., the invert inside the drip shield) except for an area near the ends of the experiment. The wall y^+ values on the outer invert (e.g., the invert surface outside the drip shield) were typically below 2.5, with the exception of some isolated areas at the end and near one of the heater gaps, which had values greater than 3.5. These areas are not expected to have high local convection heat fluxes making it less critical to resolve the boundary layer. Nevertheless, all of the wall y^+ values are less than 5.

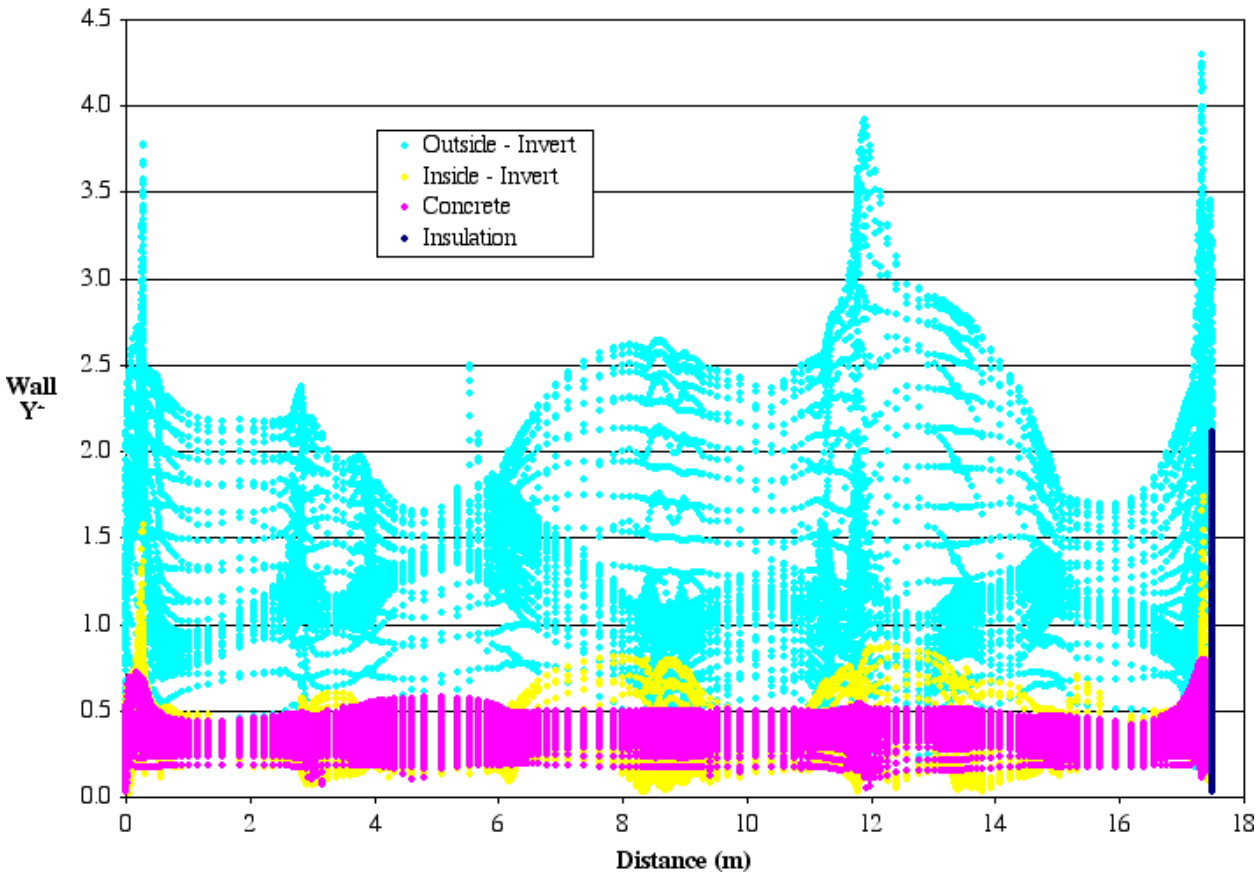

DTN: SN0308T0507803.004.

NOTE: From left to right, the heaters in the simulation represent a 44-BWR, 21-PWR, 5-DHLW Long, 44-BWR, 5-DHLW Short, and a 21-PWR.

Figure B.3-6. Wall y^+ Values on Invert, End Insulation, and Concrete Surfaces (Case 8)

Figure B.3-7 shows the convective heat flux from the surfaces of the six heaters. The convective heat flux for the PWR and the BWR heaters is positive, thus heat is moving from the surface into the fluid. The two HLW heaters have a negative convective heat flux and are being heated by the air and radiation from adjacent heaters.

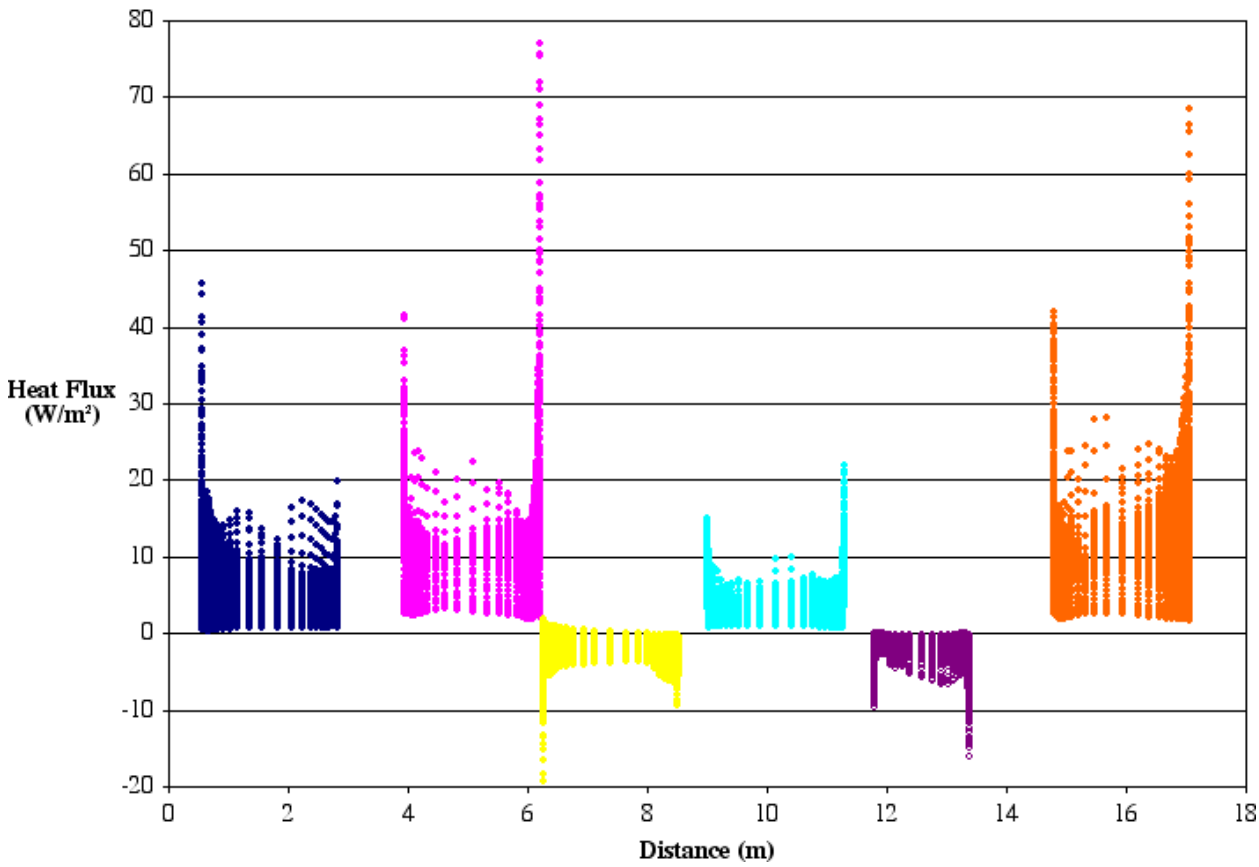

DTN: SN0308T0507803.004.

NOTE: From left to right, the heaters in the simulation represent a 44-BWR, 21-PWR, 5-DHLW Long, 44-BWR, 5-DHLW Short, and a 21-PWR.

Figure B.3-7. Convective Heat Flux from Heater Surfaces (Case 8)

Figure B.3-8 displays the convective heat flux on both the inner and outer surfaces of the drip shield. The hot and cold heaters can be clearly seen in the shape of the data. The location of the gaps can be clearly seen on the inside surface of the drip shield.

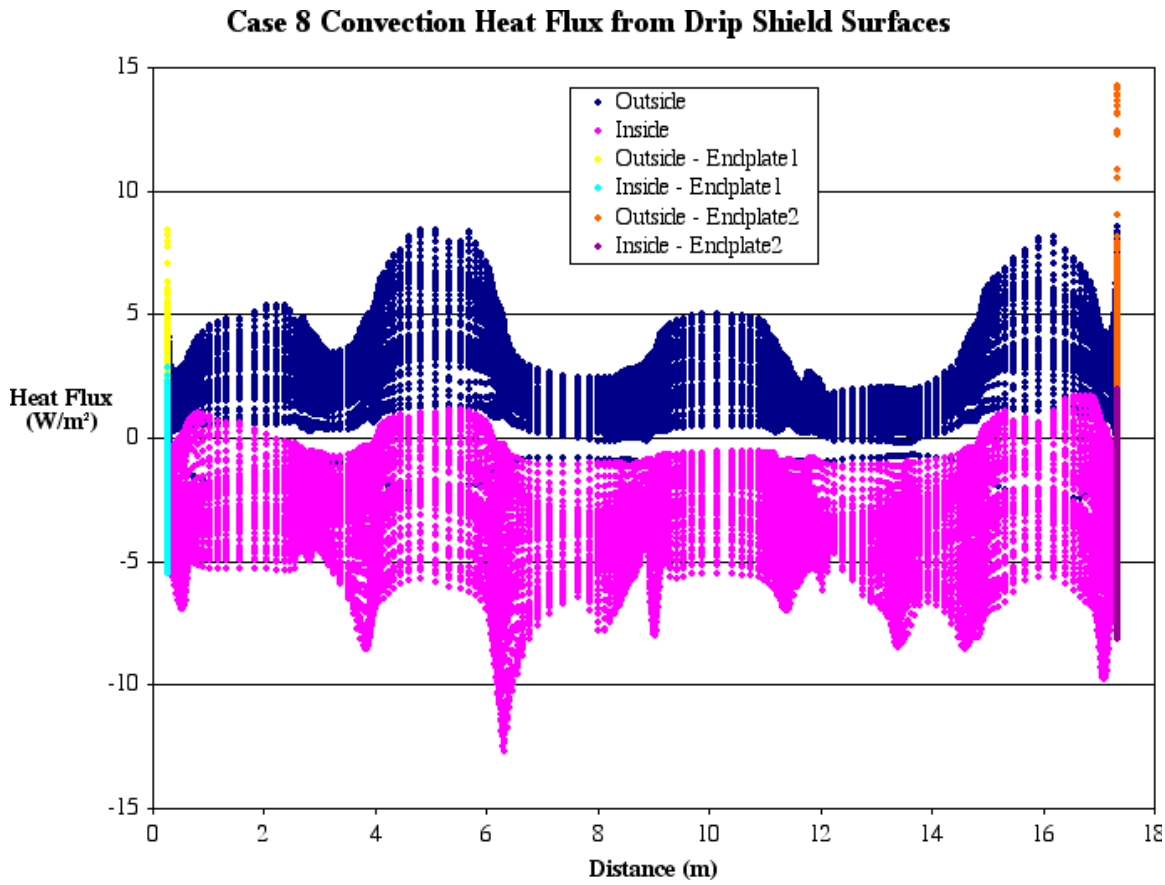

DTN: SN0308T0507803.004.

NOTE: From left to right, the heaters in the simulation represent a 44-BWR, 21-PWR, 5-DHLW Long, 44-BWR, 5-DHLW Short, and a 21-PWR.

Figure B.3-8. Convective Heat Flux from Both Sides of the Drip Shield (Case 8)

The convective heat flux off the invert, insulation, and concrete surfaces are shown in Figure B.3-9. The convection heat flux is highest on the concrete at the ends of the simulation. This is a result of the strong convective flow coming off of the ends of the drip shield. The variation over the outside invert is small but the variation around the inside of the invert is quite large. The convection is less than 2 W/m^2 near the cold heaters but went up to 17 W/m^2 near one of the hot heaters.

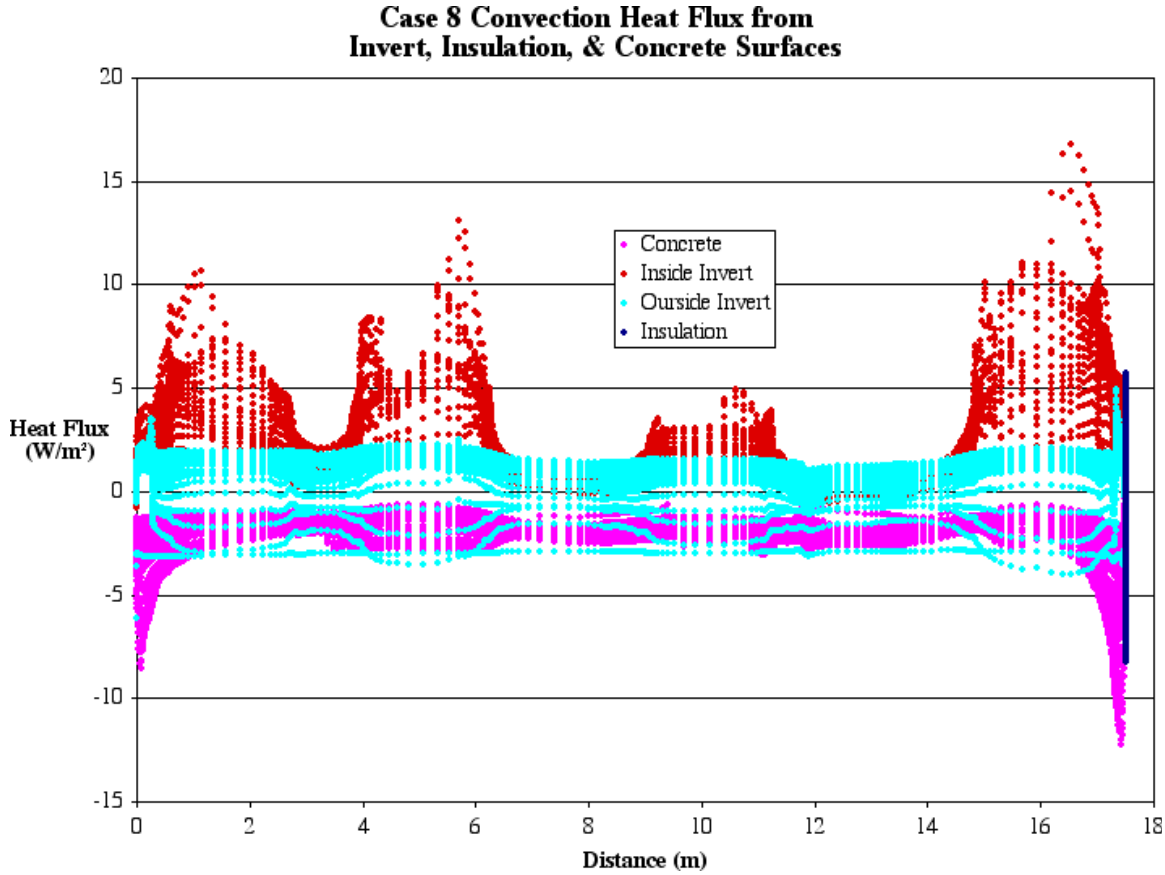

DTN: SN0308T0507803.004.

NOTE: From left to right, the heaters in the simulation represent a 44-BWR, 21-PWR, 5-DHLW Long, 44-BWR, 5-DHLW Short, and a 21-PWR.

Figure B.3-9. Convective Heat Flux from Invert, End Insulation, and Concrete Surfaces (Case 8)

The radiative heat flux from the heaters is shown in Figure B.3-10. The largest fluxes are on the hottest packages and the lowest radiant heat fluxes are from the coldest packages. The cold packages show a negative flux (e.g., energy is radiating into the package) at the ends facing hot packages. Unlike the calculated convective heat transfer, the radiant fluxes on the ends of the PWR and BWR packages are not higher than those on the package surfaces.

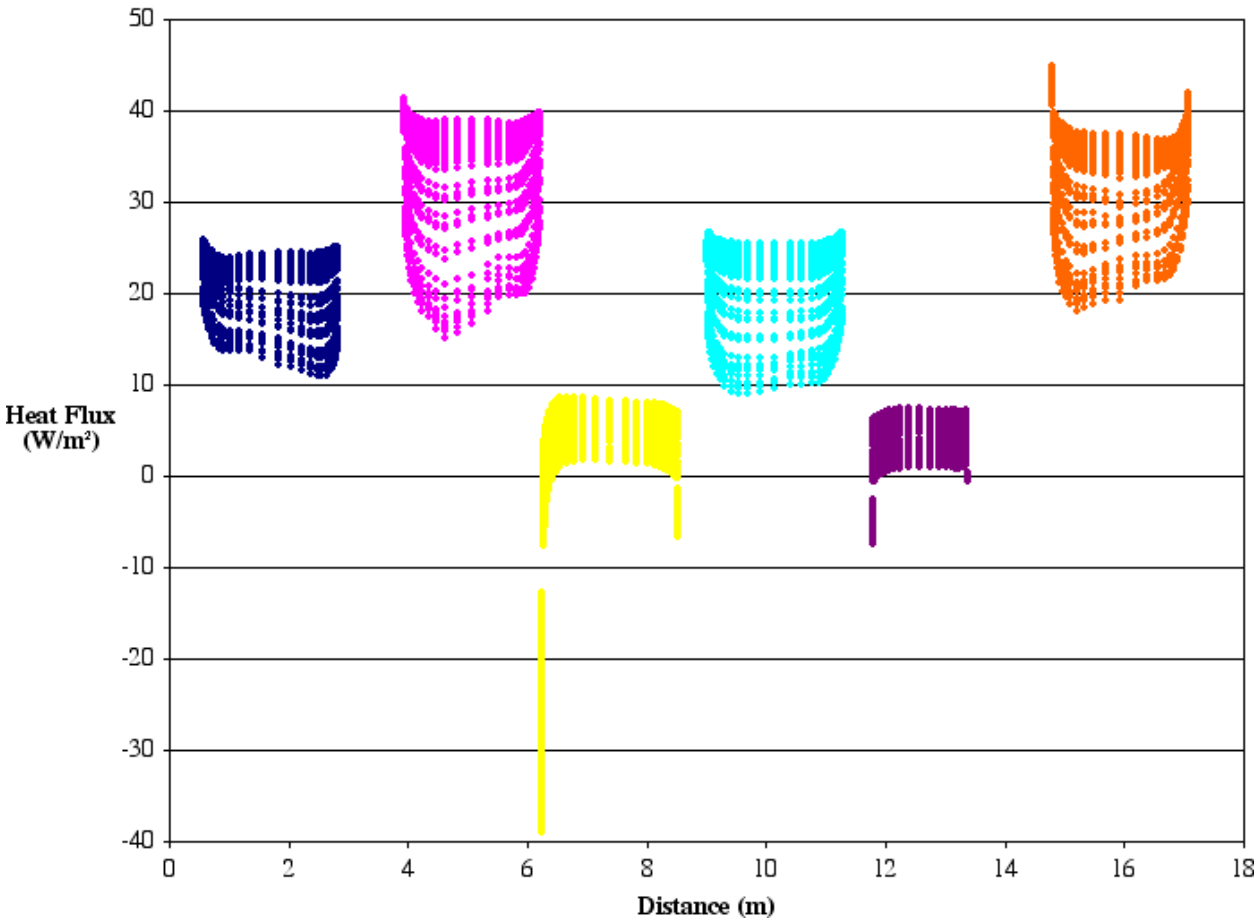

DTN: SN0308T0507803.004.

NOTE: From left to right, the heaters in the simulation represent a 44-BWR, 21-PWR, 5-DHLW Long, 44-BWR, 5-DHLW Short, and a 21-PWR.

Figure B.3-10. Radiative Heat Flux from Heater Surfaces (Case 8)

Figure B.3-11 shows the radiative heat flux off both sides of the drip shield. The variation resulting from the non-uniform heater power and spacing can be clearly seen in the plot. The stray dark blue series of data corresponds to elements closest to the invert drip shield intersection.

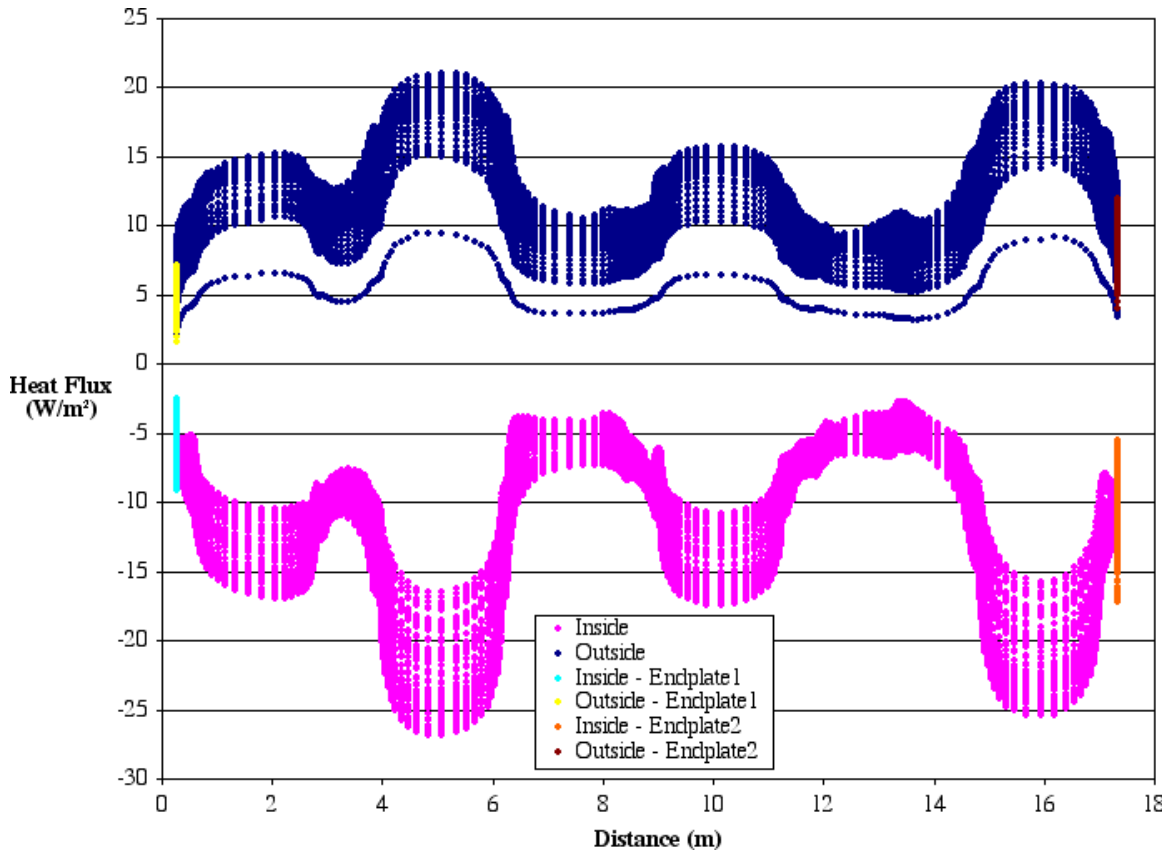

DTN: SN0308T0507803.004.

NOTE: From left to right, the heaters in the simulation represent a 44-BWR, 21-PWR, 5-DHLW Long, 44-BWR, 5-DHLW Short, and a 21-PWR.

Figure B.3-11. Radiative Heat Flux from Both Sides of the Drip Shield (Case 8)

Figure B.3-12 shows the radiative heat flux from the concrete, invert, and end insulation surfaces. The radiation variation on the inside invert surface is a result of the variations of surface temperatures caused by the local convective flows. The radiation flux on the invert and concrete clearly shows the location of hot heaters, cold heaters, and large gaps.

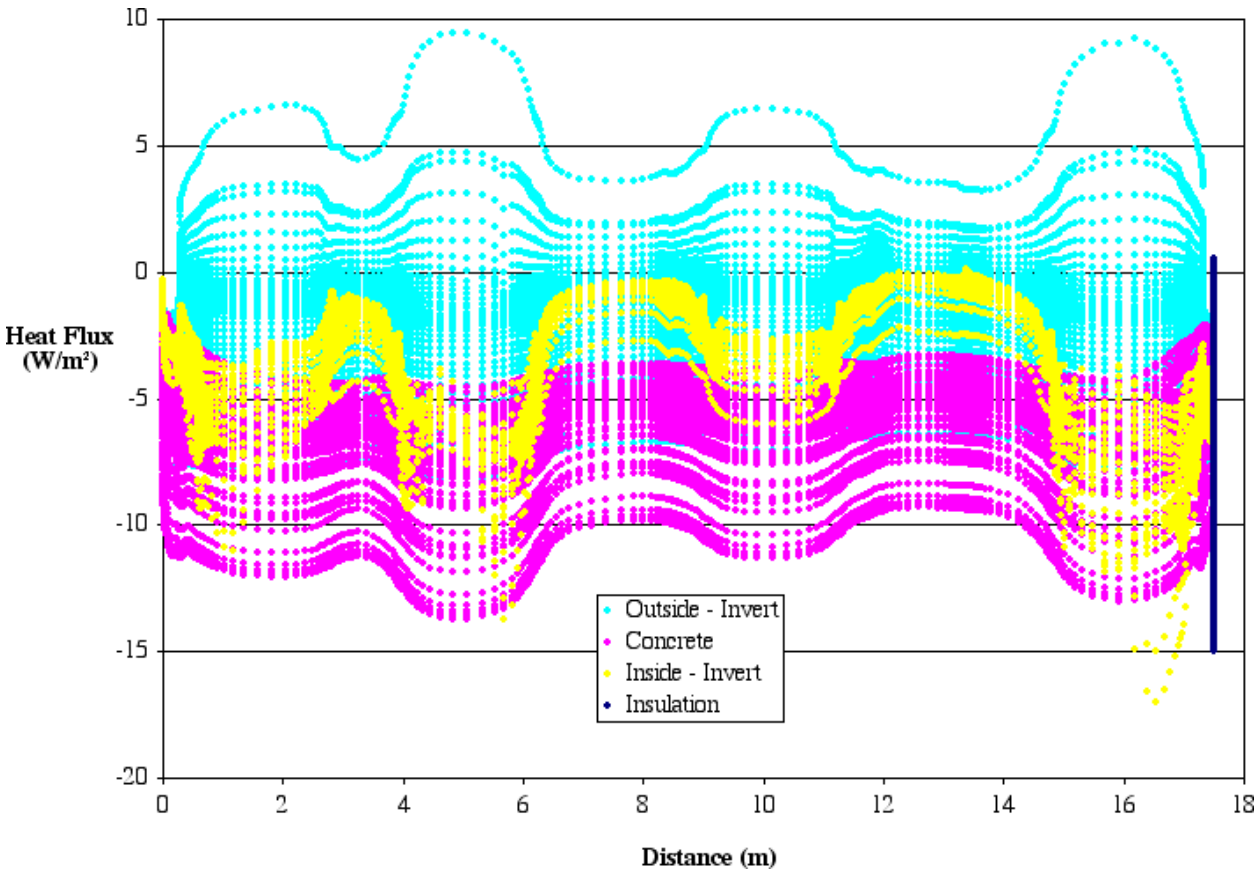

DTN: SN0308T0507803.004.

NOTE: From left to right, the heaters in the simulation represent a 44-BWR, 21-PWR, 5-DHLW Long, 44-BWR, 5-DHLW Short, and a 21-PWR.

Figure B.3-12. Radiative Heat Flux from Invert, End Insulation, and Concrete Surfaces (Case 8)

The total heat flux from the six heaters in the Case 8 simulation is shown in Figure B.3-13. The four hot heaters have higher heat fluxes on the ends than on the sides. For the cold heaters, there is a loss of heat on the sides of the heaters but a gain of energy through the ends.

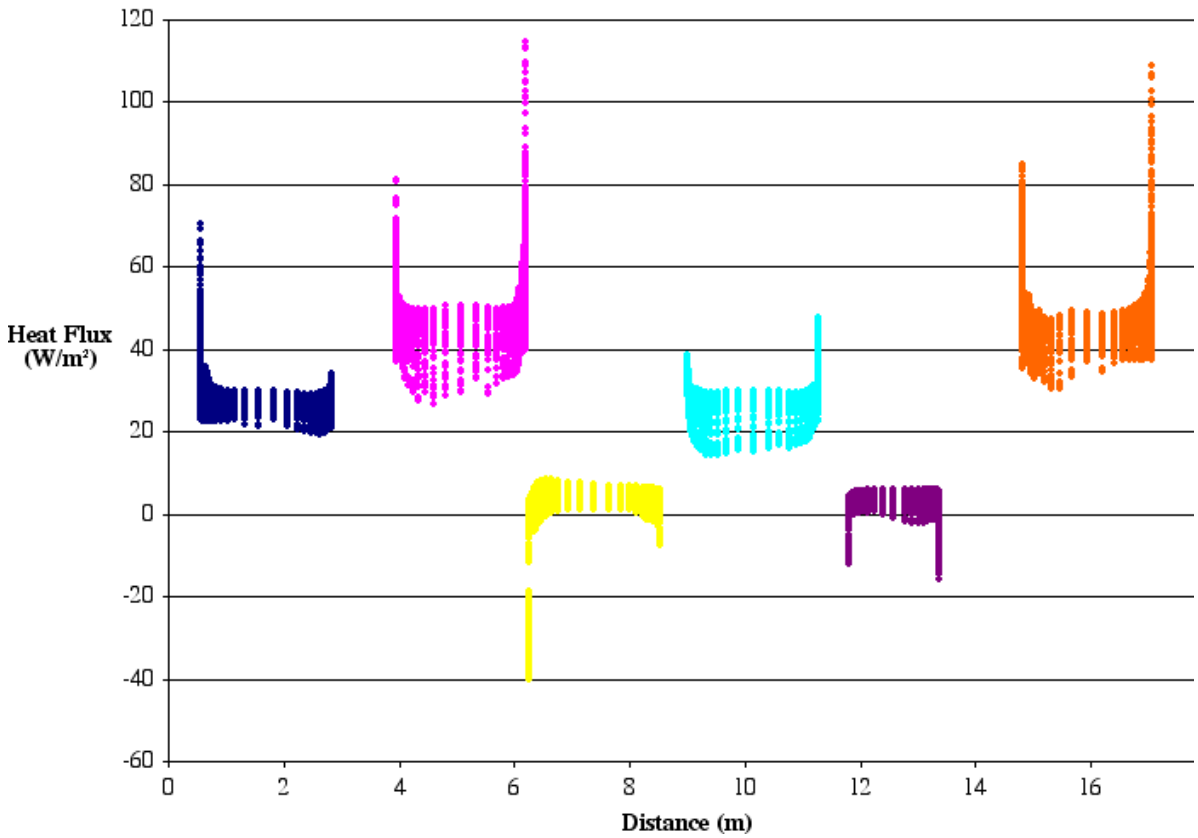

DTN: SN0308T0507803.004.

NOTE: From left to right, the heaters in the simulation represent a 44-BWR, 21-PWR, 5-DHLW Long, 44-BWR, 5-DHLW Short, and a 21-PWR.

Figure B.3-13. Total Heat Flux from Heater Surfaces (Case 8)

The total heat flux through the drip shield for the Case 8 simulation is shown in Figure B.3-14. The location of the hot and cold heaters can be easily seen. The stray blue line of data corresponds to the intersection of the drip shield and the invert.

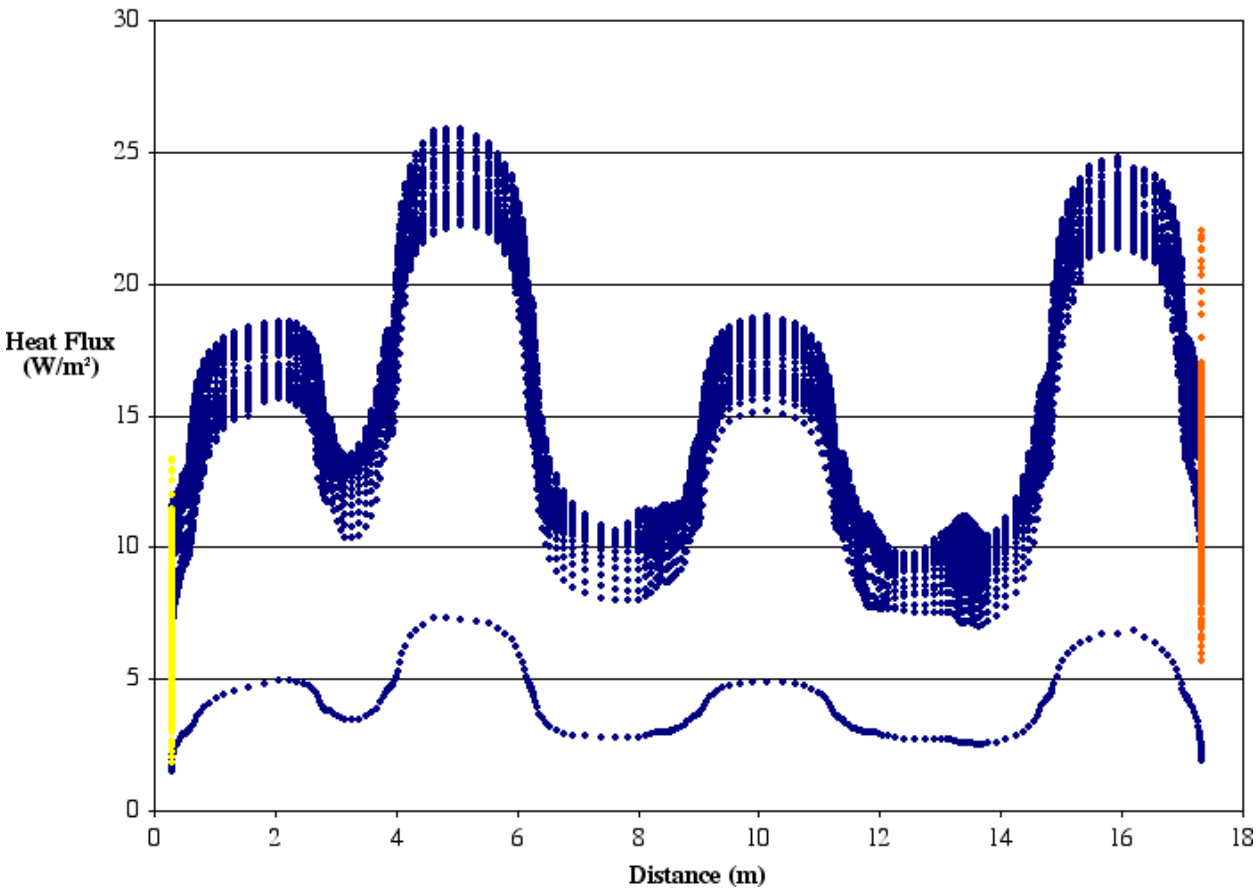

DTN: SN0308T0507803.004.

NOTE: From left to right, the heaters in the simulation represent a 44-BWR, 21-PWR, 5-DHLW Long, 44-BWR, 5-DHLW Short, and a 21-PWR

Figure B.3-14. Total Heat Flux from Drip Shield Surface (Case 8)

Figure B.3-15 shows the total heat flux through the invert, end insulation and the concrete surfaces for the Case 8 simulation.

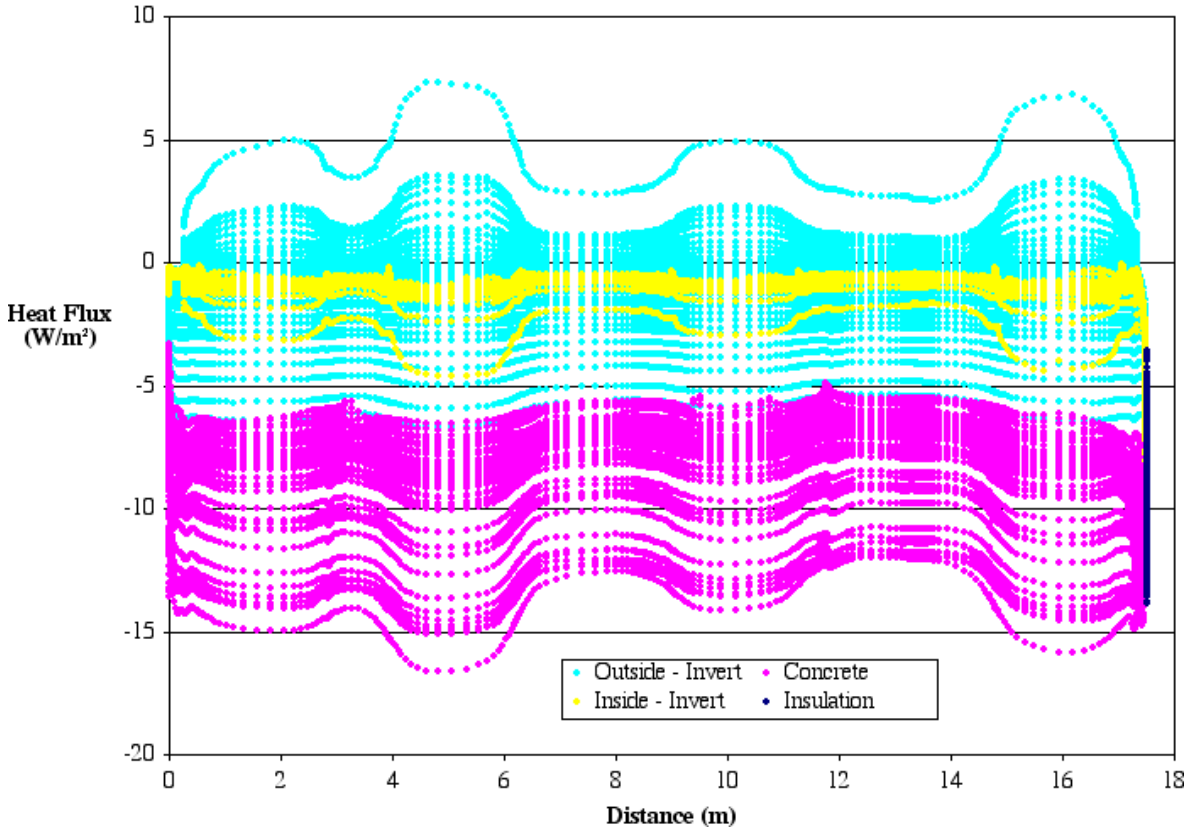

DTN: SN0308T0507803.004.

NOTE: From left to right, the heaters in the simulation represent a 44-BWR, 21-PWR, 5-DHLW Long, 44-BWR, 5-DHLW Short, and a 21-PWR.

Figure B.3-15. Total Heat Flux from Invert, End Insulation, and Concrete Surfaces (Case 8)

Figure B.3-16 shows the convective and radiative heat fluxes from the sides of all six heaters for Case 8. The numbers under each waste package is the heat generated in each package. Note that only half of the packages are simulated (symmetry). The convective and radiative heat fluxes are all positive for the four hottest packages and only the radiative component on the side of the HLW packages are positive. The convective heat flux for the two HLW packages is negative, indicating that the HLW package temperatures are less than the surrounding air. The fraction of total heat flux from the four hot heaters that is convected into the air ranges between 18 and 27 percent. The remainder of the energy is transferred via radiation.

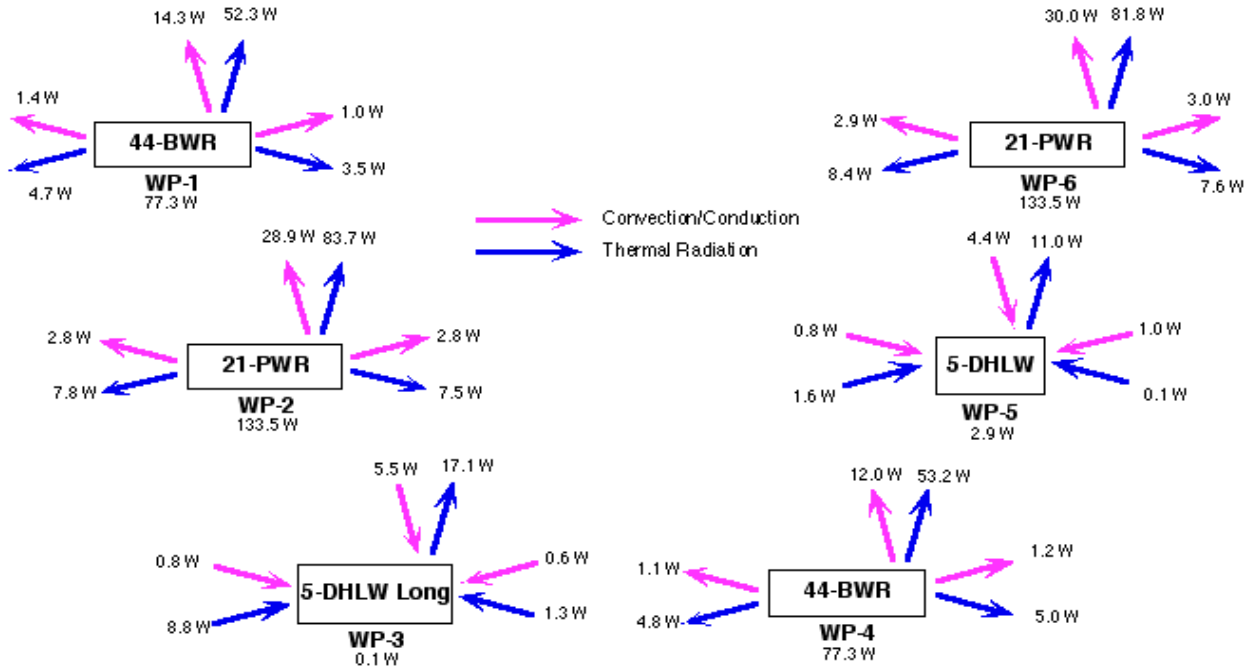

DTN: SN0308T0507803.004.

Figure B.3-16. Heat Transfer Modes on Sides and Ends of Individual Surfaces (Case 8)

Figure B.3-17 shows the velocity vectors near that side of the concrete near the fourth heater. The peak velocity in the boundary layer is 0.13 m/s.

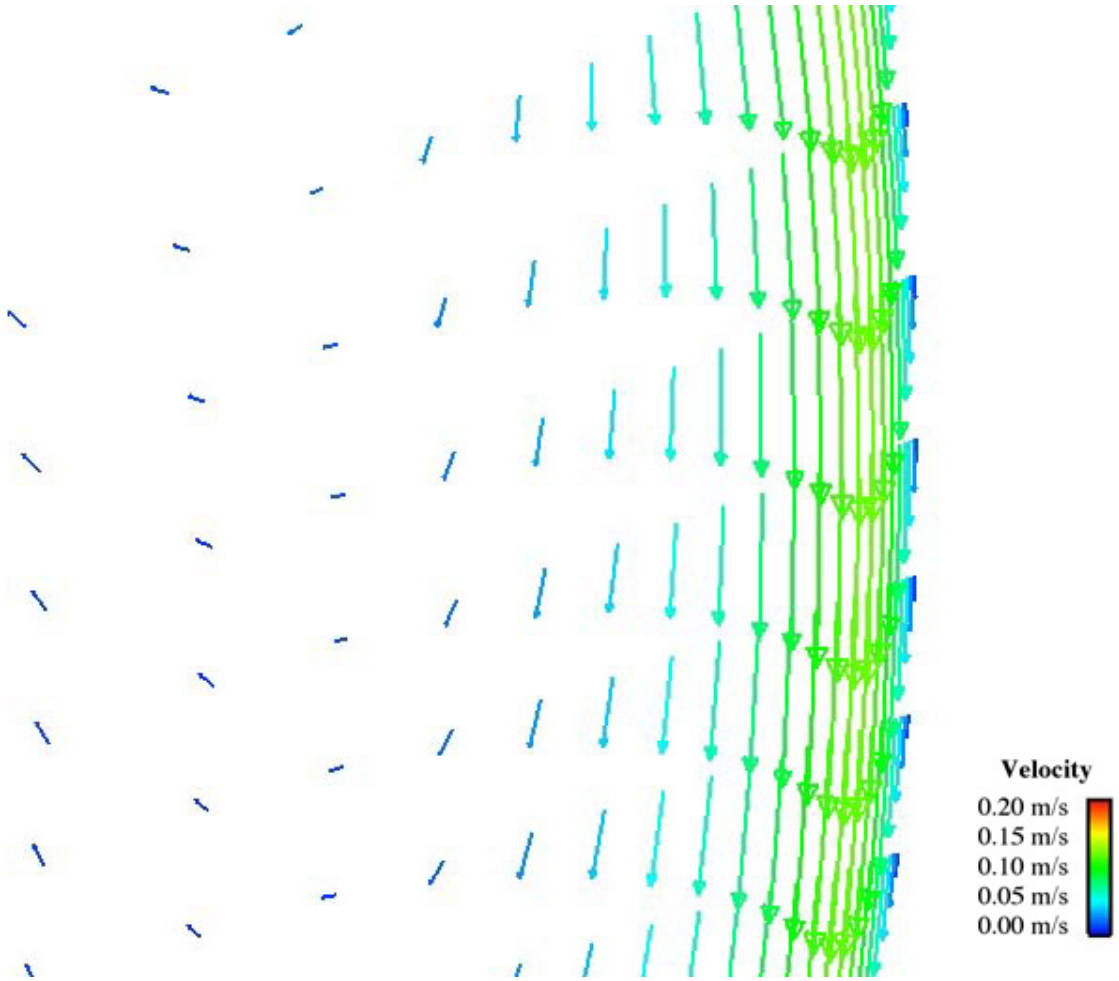

DTN: SN0308T0507803.004.

NOTE: This is near the mid-point of the fourth heater, a medium powered small radius 44-BWR.

Figure B.3-17. Velocity Vectors for Elements Located Near the Middle of the Air-Rock Interface 10.145 Meters Down the Drift (Case 8)

Figure B.3-18 shows the boundary layer flow near the concrete-air-invert interface 10.145 meters down the experiment. The peak velocity in the boundary layer is 0.06 m/s.

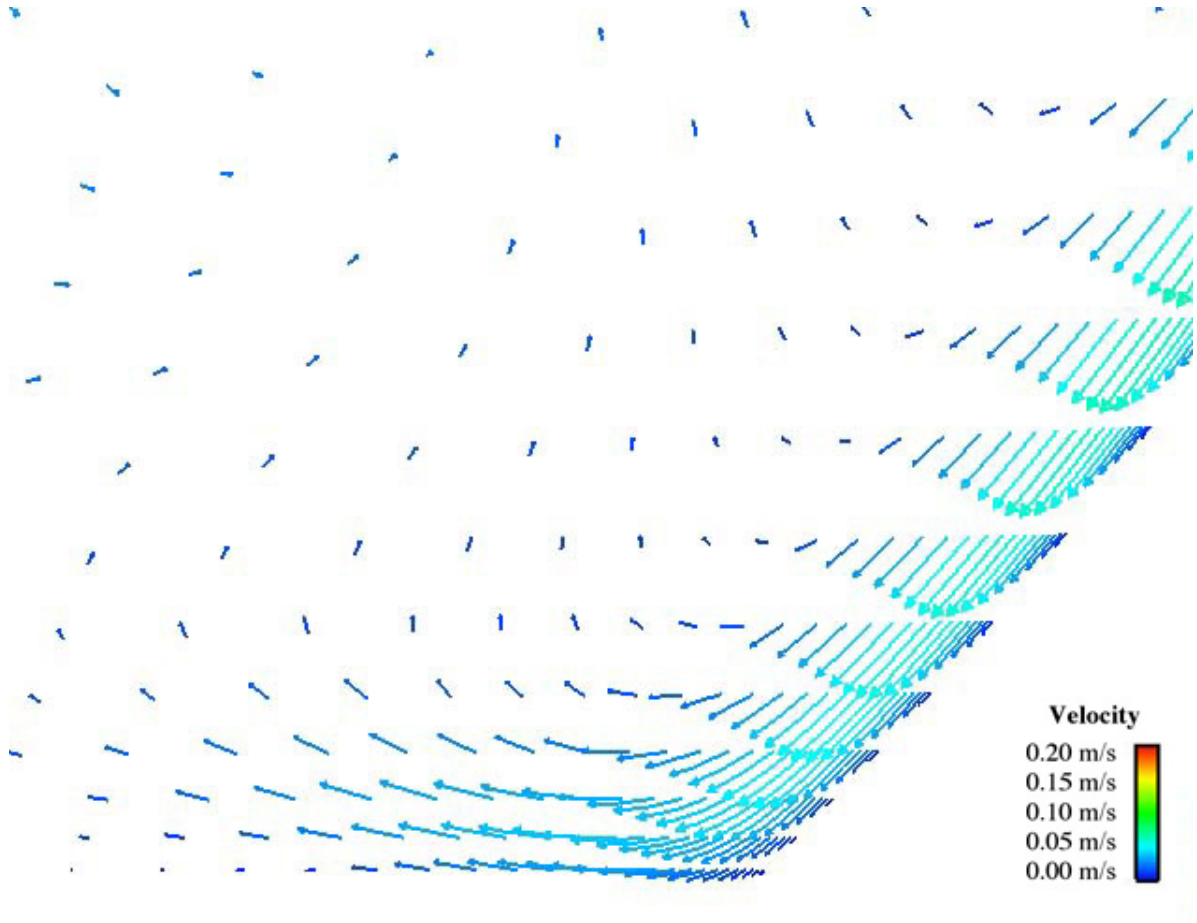

DTN: SN0308T0507803.004.

NOTE: This is near the mid-point of the fourth heater, a medium powered small radius 44-BWR.

Figure B.3-18. Velocity Vectors for Elements Located Near the Air-Invert-Concrete Interface 10.145 Meters Down the Drift (Case 8)

Figure B.3-19 shows the velocity vectors near the drip shield and the side of the fourth 44-BWR heater. The peak velocity in the boundary layer next to the heater is 0.13 m/s, while the peak velocity of the boundary layer on both sides of the drip shield is 0.09 m/s.

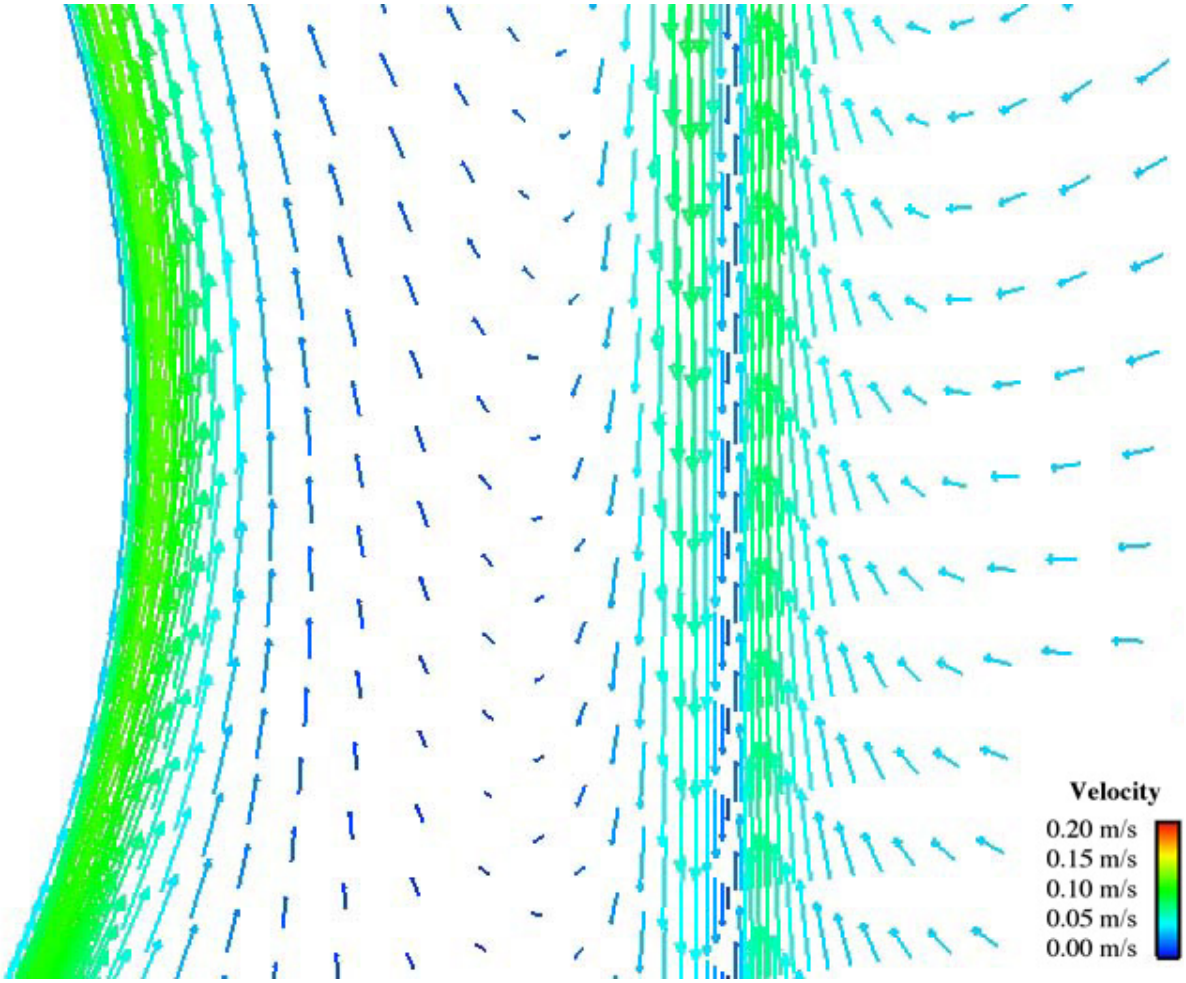

DTN: SN0308T0507803.004.

NOTE: This is near the mid-point of the fourth heater, a medium powered small radius 44-BWR.

Figure B.3-19. Velocity Vectors for Elements Located on the Side of the Heater and Part of the Adjacent Drip Shield 10.145 Meters Down the Drift (Case 8)

Figure B.3-20 shows the velocity vectors on the surface of the heater and drip shield near the third 5-DHLW heater. The flow next to the heater is downward since the air is heating up the cooler heater. The peak vertical velocity at this location for the boundary layer on the inside of the drip shield is 0.11 m/s while the peak vertical velocity on the outside of the drip shield was 0.05 m/s. Table B.3-1 shows the maximum calculated velocities for the case.

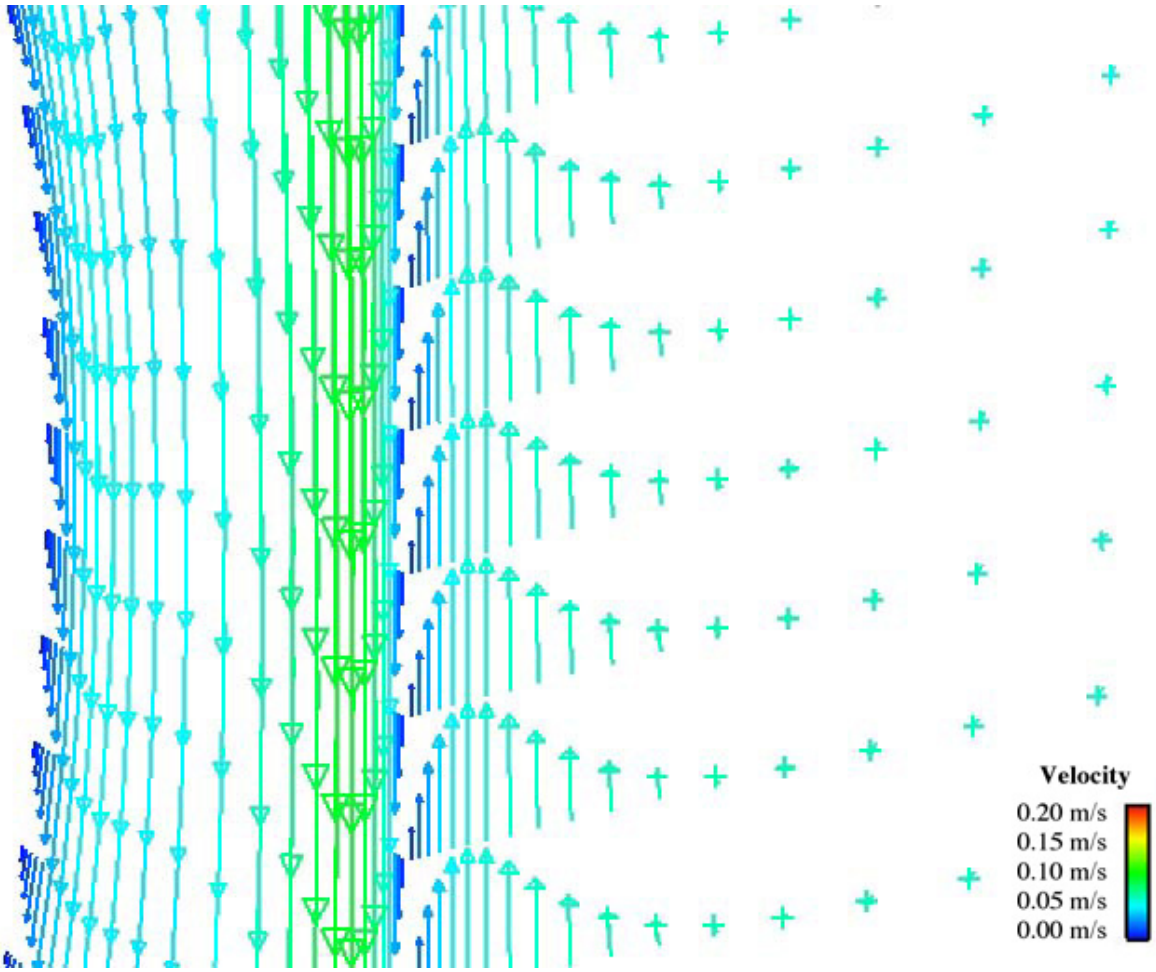

DTN: SN0308T0507803.004.

NOTE: This is near the mid-point of the third heater, a low powered large radius long 5-DHLW.

Figure B.3-20. Velocity Vectors for Elements Located on the Side of the Heater and Part of the Adjacent Drip Shield 7.385 Meters Down the Drift (Case 8)

Table B.3-1. Maximum Calculated Velocities (Case 8)

Maximum Velocity Magnitude	0.330 m/s
Maximum X-Velocity Magnitude (horizontal)	0.177 m/s
Maximum Y-Velocity Magnitude (vertical)	0.323 m/s
Maximum Z-Velocity Magnitude (axial -down drift)	0.229 m/s

DTN: SN0308T0507803.004.

B.4 44% SCALE GRID INDEPENDENCE STUDY

A grid independence study was performed using a baseline simulation for the 44% scale runs. The baseline was chosen to be the grid associated with Case 5, a uniform spacing, uniform power case without a drip shield; see Figure 7.4.1-8. In addition to the baseline computational grid (having 1,660,854 cells), a refined grid based on y+ adaptation was tested. The adapted grid had 1,734,592 cells. Results from the baseline run showed highest y+ values to be close to 5.2. The highest post-adaption wall y+ value was 3.2.

The following two sections describe simulation results for the original and adapted grids. Similar simulation results imply that grid independence was achieved.

The heater surface temperatures down the test cell for the baseline grid are presented in Figure B.4-1. The overall temperature variation is 1.4°C down the length of the test cell. The largest variation along a single heater was 0.7°C over the last heater while several of the heaters had an overall temperature variation of 0.2°C. The third and fifth heaters are the larger radius heaters that represent HLW waste packages. The input powers for the heaters were selected to give a uniform lineal heat generation so the larger radius heaters are expected to be cooler since the heat generation is distributed over 34 percent larger surface area. The large radius heaters are 0.8°C cooler than their neighboring packages.

There is 0.56 meters of air to the left of the first heater and 1.53 meters of air to the right of the seventh heater. This extra volume of the air causes the larger temperature drop on the right side of the experiment.

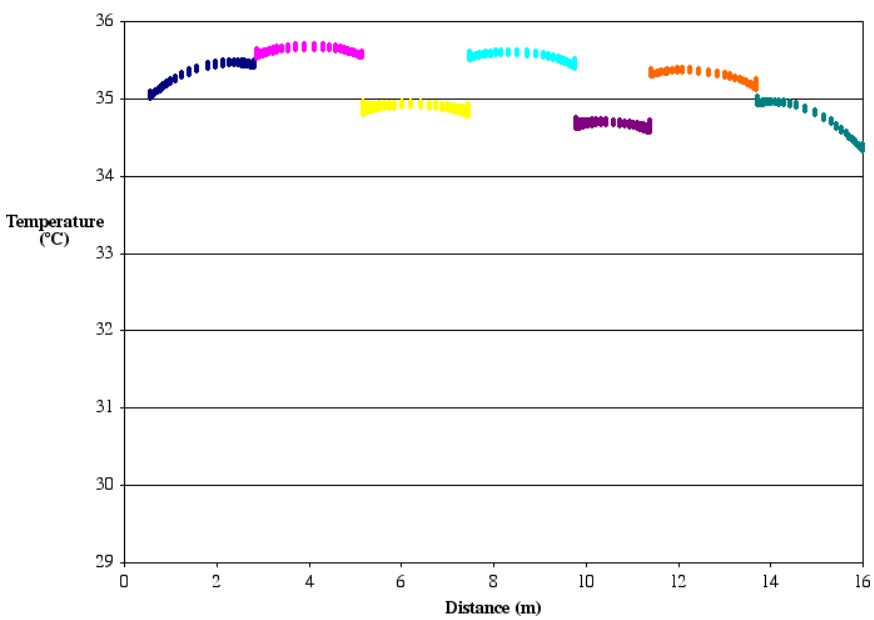

DTN: SN0308T0507803.004.

NOTE: From left to right, the heaters in the simulation represent a 44-BWR, 21-PWR, 5-DHLW Long, 44-BWR, 5-DHLW Short, 21-PWR, and a generic package.

Figure B.4-1. Heater Surface Temperatures for the Baseline Grid (Case 5)

The baseline grid was adapted based on wall y^+ to make these values be near 1 in order to correctly resolve the boundary layer. A total of 5,267 surface elements were selected for adaption based on having a y^+ of 2.5 or higher. The adapted elements were located on the ends of the heaters and on the internal insulation boundary. The surface temperatures on the heaters, the insulation, invert, and the concrete surfaces were similar for the two cases. The average surface temperatures for the seven heaters in the adapted and original (baseline) Case 5 are shown in Table B.4-1. This table shows that the average surface temperatures changed by less than 0.001°C between the two simulation runs.

Table B.4-1. Comparison of Average Surface Temperatures for Case 5 Original and Adapted Grids

	Original (˚C) [a]	**Adapted (˚C)** [b]
NC5-WP-1	35.3235	35.3235
NC5-WP-2	35.6198	35.6198
NC5-WP-3	34.8778	34.8779
NC5-WP-4	35.5413	35.5410
NC5-WP-5	34.6571	34.6570
NC5-WP-6	35.2980	35.2980
NC5-WP-7	34.7550	34.7550

[a]DTN: SN0308T0507803.004.
[b]DTN: SN0310T0507803.021.

The invert, insulation, and concrete surface temperatures from the baseline Case 5 simulation are shown in Figure B.4-2. The concrete temperature has small temperature peaks that correspond to the locations of the air gaps between the individual heaters. The highest temperatures on the concrete occur at the roof of the test train and the lowest temperatures near the invert-concrete interface. The largest concrete temperature gradients occur closest to the invert-concrete interface. The temperature difference from top to bottom of the concrete at any particular location down the experiment was only 1°C. The invert surface temperature has a much larger variation down the drift with the coolest temperatures at the invert-concrete interface and the hottest temperatures directly under the heaters. These peak invert temperatures are between 0.5 and 1.0˚C lower than the nearest heaters. The invert surface temperature variation is as much as 3˚C at any location down the test cell.

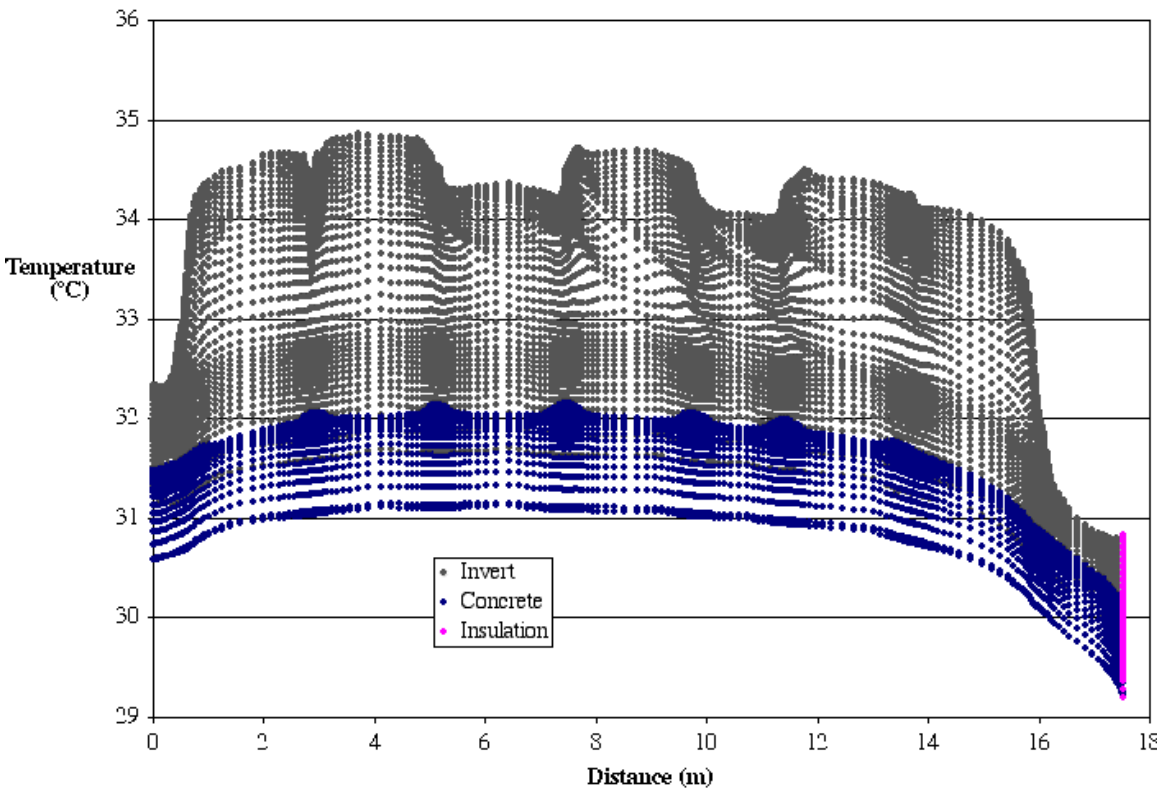

DTN: SN0308T0507803.004.

NOTE: From left to right, the heaters in the simulation represent a 44-BWR, 21-PWR, 5-DHLW Long, 44-BWR, 5-DHLW Short, 21-PWR, and a generic package.

Figure B.4-2. Invert, End Insulation, and Concrete Surface Temperatures for the Baseline Grid (Case 5)

The heater wall y^+ for the baseline grid is shown in Figure B.4-3. As can be seen, most of the y^+ values on the side of the heaters are less than 2.2. The peak wall y^+ values on the end of the heaters ranged from 2.7 to 4.7. The adaption on elements with high wall y^+ values occurred on the sides of the heaters where the wall y^+ values were greater than 2.5.

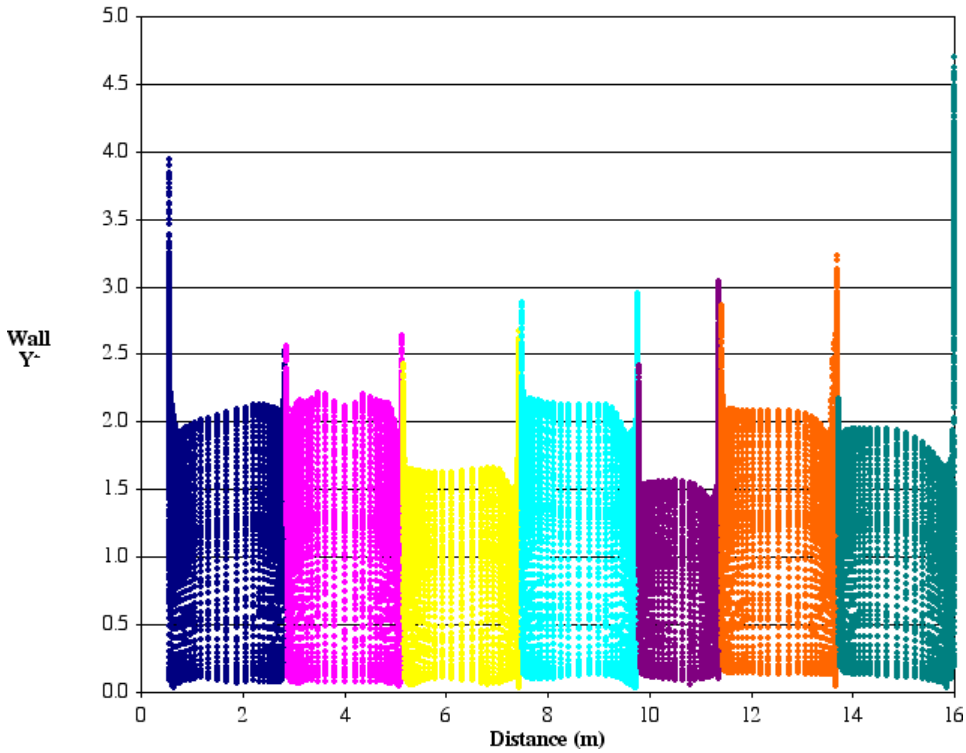

DTN: SN0308T0507803.004.

NOTE: From left to right, the heaters in the simulation represent a 44-BWR, 21-PWR, 5-DHLW Long, 44-BWR, 5-DHLW Short, 21-PWR, and a generic package.

Figure B.4-3. Wall y^+ Values on Heater Surfaces for the Baseline Grid (Case 5)

Figure B.4-4 shows the wall y^+ values for the heaters after adaption. The peak y^+ dropped from a high of 4.7 down to a peak of 3.2. The peak did not drop down to half of the unadapted peak value since the y^+ does not necessarily scale linearly with y. Figure B.4-5 shows the baseline grid wall y^+ for the concrete, invert, and insulation. Adaption was only applied on the insulation end and peak y^+ values dropped from 5.2 to 2.7 (Figure B.4-6).

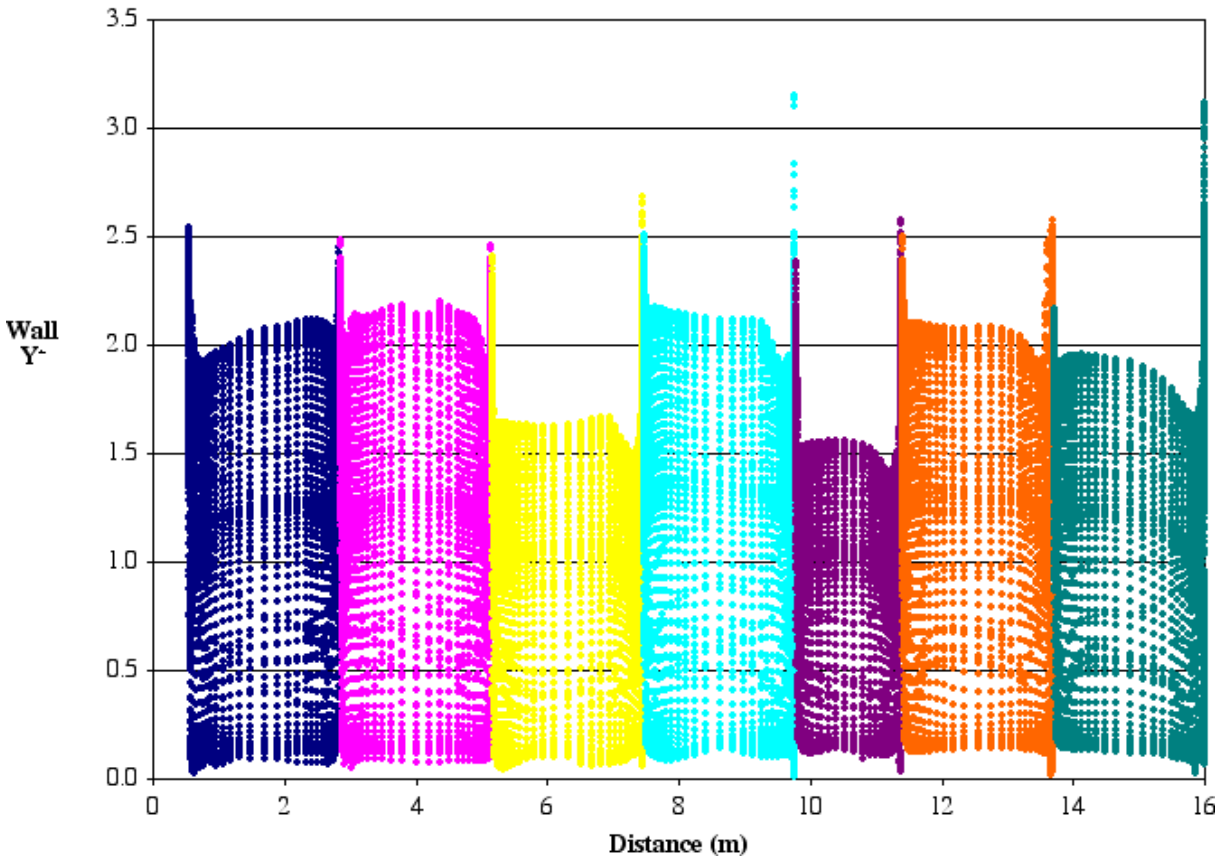

DTN: SN0310T0507803.021.

NOTE: From left to right, the heaters in the simulation represent a 44-BWR, 21-PWR, 5-DHLW Long, 44-BWR, 5-DHLW Short, 21-PWR, and a generic package.

Figure B.4-4. Wall y^+ Values on Heater Surfaces for the Adapted Grid (Case 5)

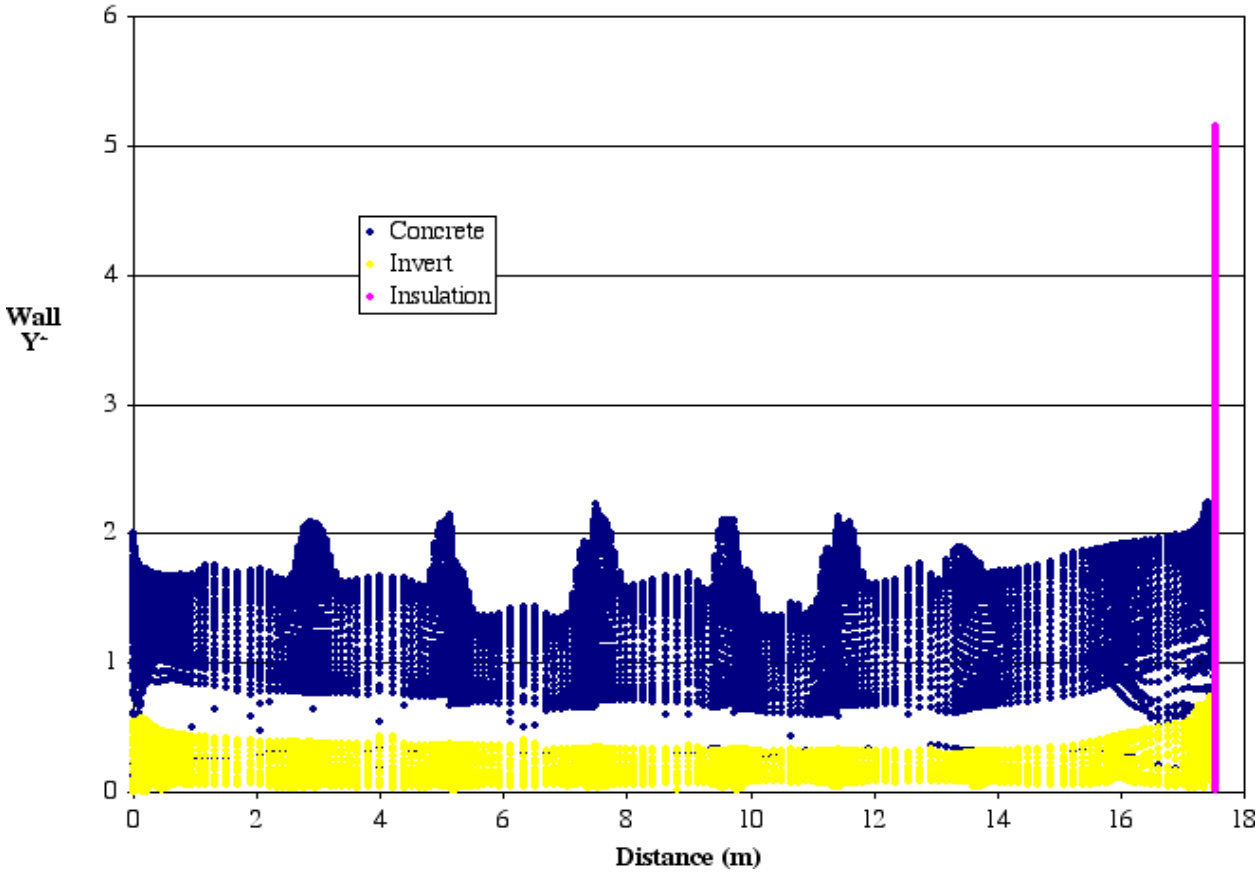

DTN: SN0308T0507803.004.

NOTE: From left to right, the heaters in the simulation represent a 44-BWR, 21-PWR, 5-DHLW Long, 44-BWR, 5-DHLW Short, 21-PWR, and a generic package.

Figure B.4-5. Wall y^+ Values on Invert, End Insulation, and Concrete Surfaces for the Baseline Grid (Case 5)

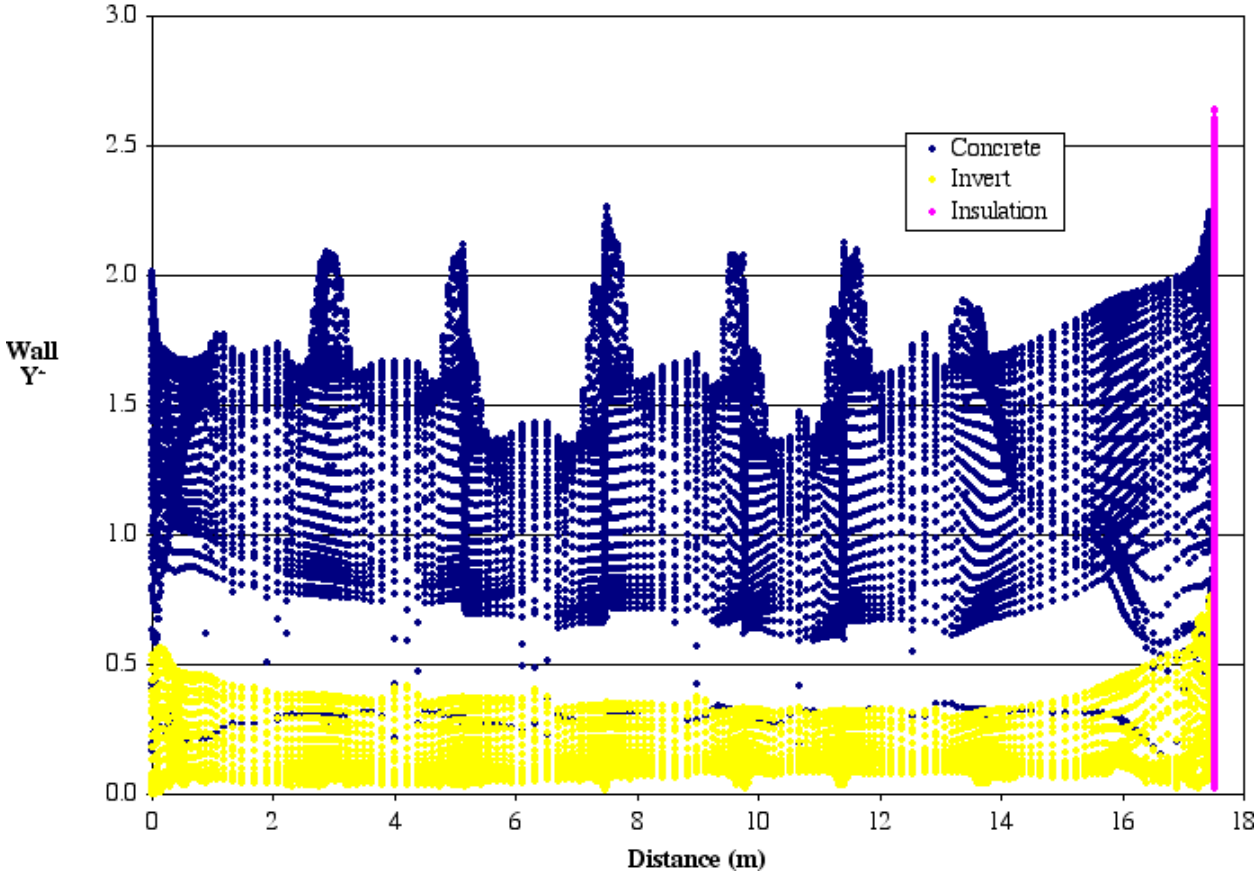

DTN: SN0310T0507803.021.

NOTE: From left to right, the heaters in the simulation represent a 44-BWR, 21-PWR, 5-DHLW Long, 44-BWR, 5-DHLW Short, 21-PWR, and a generic package.

Figure B.4-6. Wall y^+ Values on Invert, End Insulation, and Concrete Surfaces for the Adapted Grid (Case 5)

Figure B.4-7 shows the convective heat flux off of the seven heaters for the baseline Case 5 simulation. The highest convective heat flux occurred on the ends of the heaters. In this region, there is a strong vertical flow in the gap between heaters resulting in high convection rates. The convective heat flux on the side of the heaters varied mostly between 0 and 10 W/m^2 while the convective heat flux on the end of the heaters ranged from 0 to 37 W/m^2. The third and fifth heaters are cooler heaters so the convective heat flux is lower on those two heaters than on the other five.

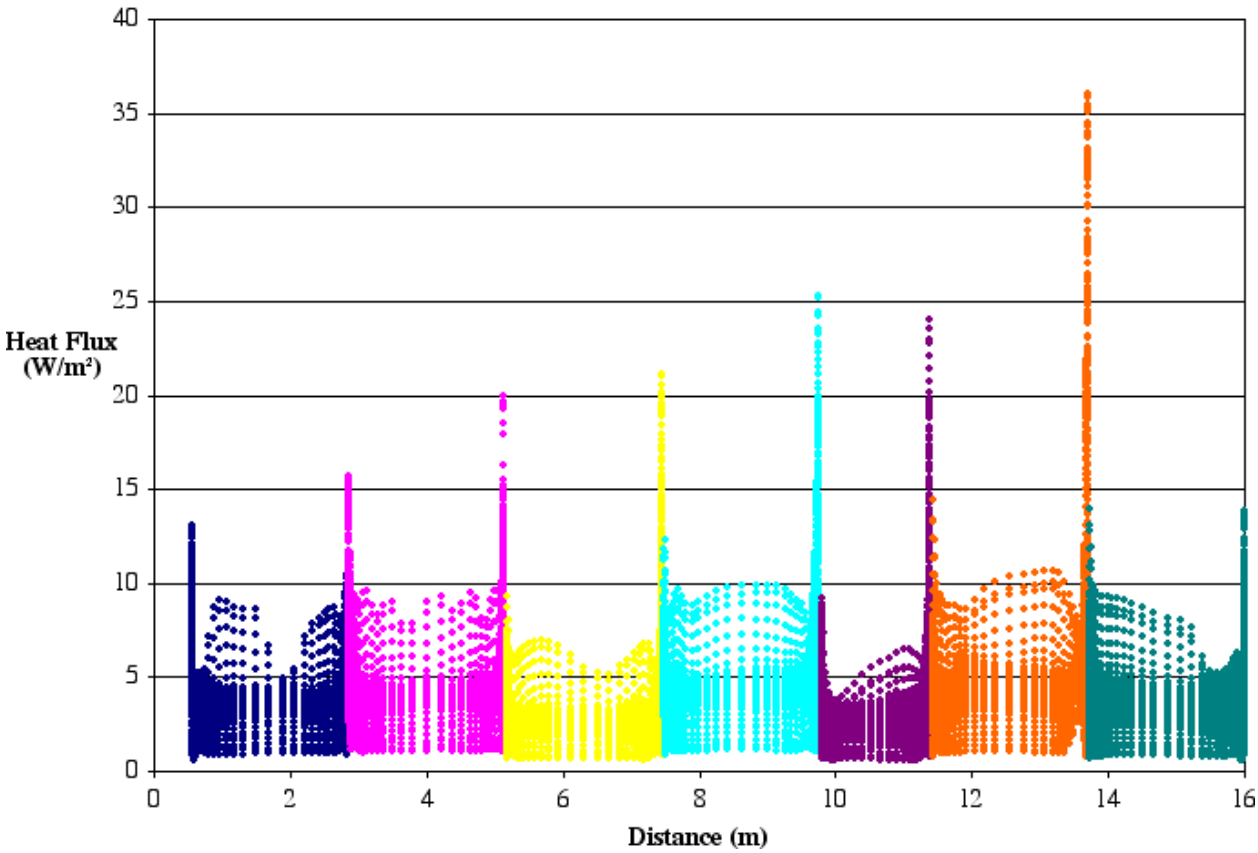

DTN: SN0308T0507803.004.

NOTE: From left to right, the heaters in the simulation represent a 44-BWR, 21-PWR, 5-DHLW Long, 44-BWR, 5-DHLW Short, 21-PWR, and a generic package.

Figure B.4-7. Convective Heat Flux from Heater Surfaces for Baseline Grid (Case 5)

The convective heat flux on the heaters for the adapted grid Case 5 are shown in Figure B.4-8. Since adaption did not occur on the cylindrical surfaces of the heater, convective heat transfer is not expected to change much between the two simulations. Comparison of the figures shows this to be true. Grid adaption did occur on a few elements on the majority of the ends of the heaters making it more likely for the flow and heat transfer to change there. The range of convection on the ends of several heaters was higher for the adapted case.

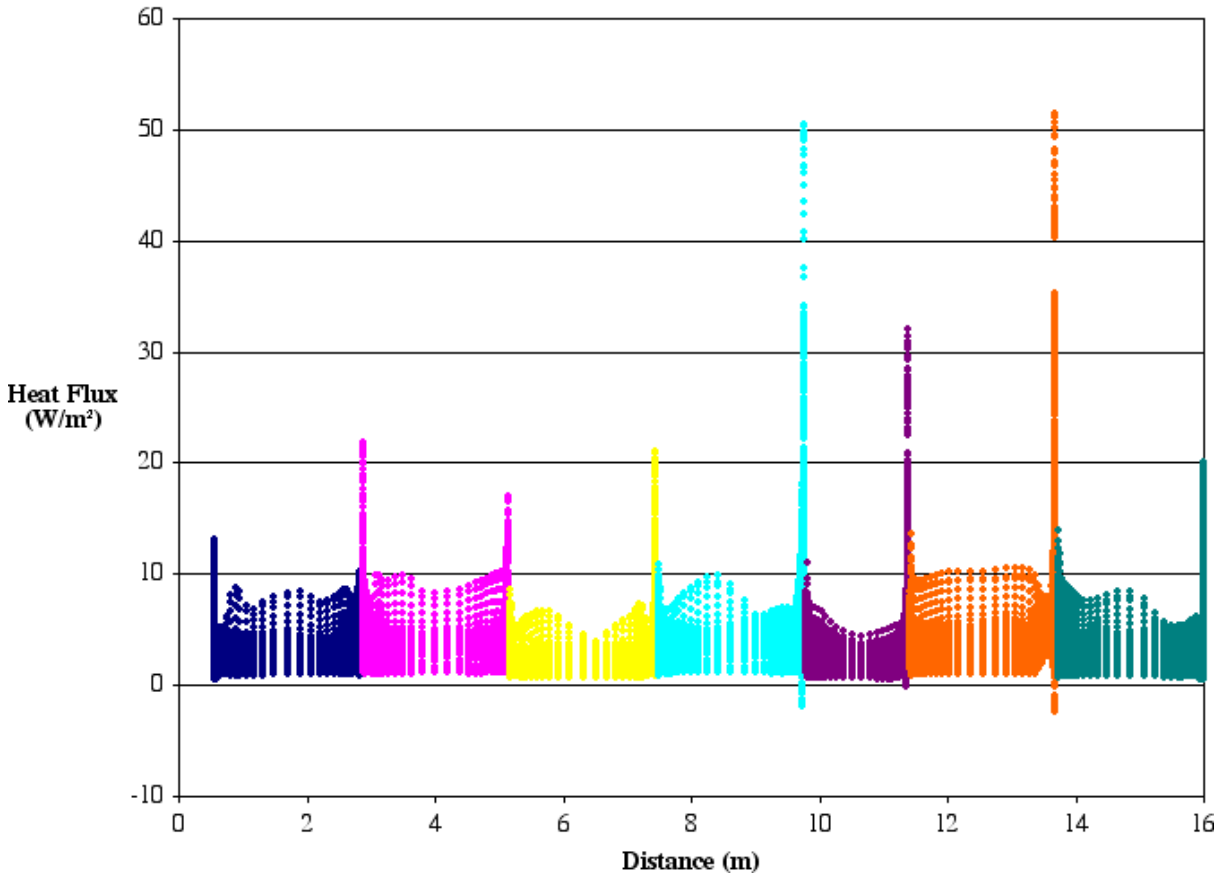

DTN: SN0310T0507803.021.

NOTE: From left to right, the heaters in the simulation represent a 44-BWR, 21-PWR, 5-DHLW Long, 44-BWR, 5-DHLW Short, 21-PWR, and a generic package.

Figure B.4-8. Convective Heat Flux from Heater Surfaces for Adapted Grid (Case 5)

Figure B.4-9 shows the convective flux off of the concrete, invert, and insulation for the baseline simulation. The convective heat flux on the concrete is negative, meaning that the heat is going into the concrete from the air. A positive convective heat flux on much of the invert implies that heat is moving from the invert surface into the air by convection. Although there is no heat being generated in the invert, the source of the energy on the invert surface is the energy radiated from the heater surfaces. The location of the heaters can be clearly seen in the convection on the concrete surface. Local high convection at the top of the concrete occurs at the end of the first and last heaters at 0.6 and 16 meters as well as the heater gaps at 2.8, 5.2, 7.5, 9.8, 11.4, and 13.7 meters. High local heat convection on the invert is not as pronounced near the gaps as it is on the concrete surface.

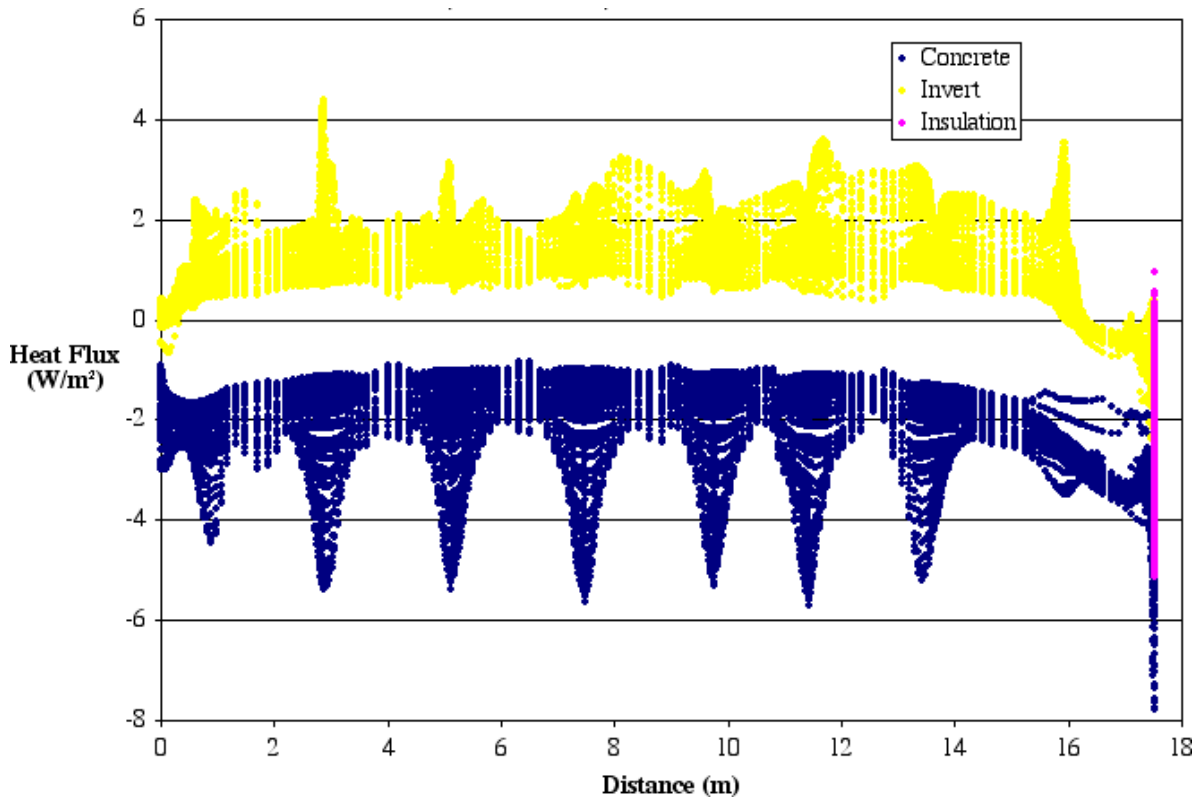

DTN: SN0308T0507803.004.

NOTE: From left to right, the heaters in the simulation represent a 44-BWR, 21-PWR, 5-DHLW Long, 44-BWR, 5-DHLW Short, 21-PWR, and a generic package.

Figure B.4-9. Convective Heat Flux from Invert, End Insulation, and Concrete Surfaces for the Baseline Grid (Case 5)

Figure B.4-10 shows the convective heat flux from the invert, end insulation, and concrete surfaces for the adapted grid. Just as it was for the baseline simulation, there is a high convective heat flux rate on the concrete in the gap regions. The convective heat flux on the invert is similar but the magnitude of the local maxima are slightly different.

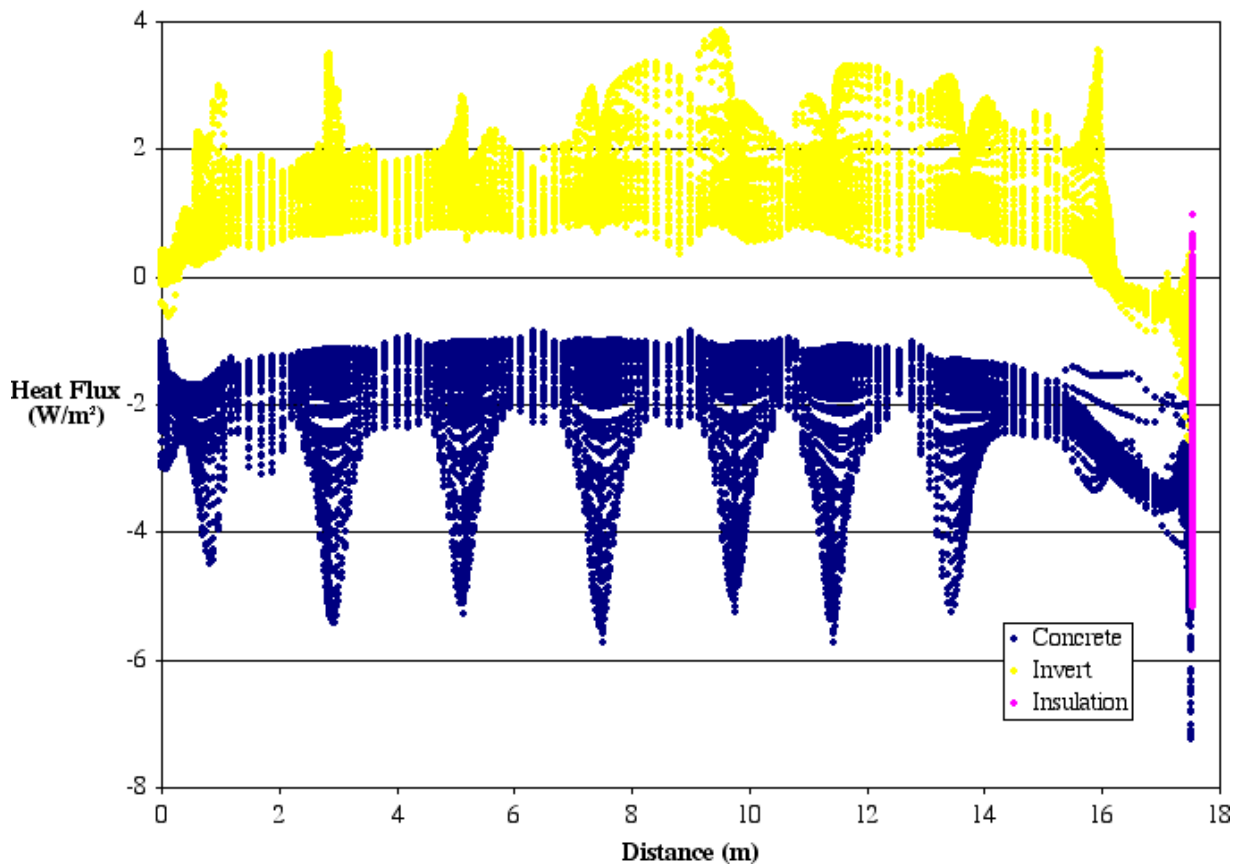

DTN: SN0310T0507803.021.

NOTE: From left to right, the heaters in the simulation represent a 44-BWR, 21-PWR, 5-DHLW Long, 44-BWR, 5-DHLW Short, 21-PWR, and a generic package.

Figure B.4-10. Convective Heat Flux from Invert, End Insulation, and Concrete Surfaces for the Adapted Grid (Case 5)

Figure B.4-11 shows the net radiation heat flux from the heater surfaces for the baseline simulation. The radiative heat flux from the sides of the heaters ranged from 5 to 25 W/m^2. The radiative heat flux on the ends of the heaters tended to be lower than on the sides of the heaters with some of the sides absorbing 5 W/m^2. This behavior is expected since high convection inside of the gaps would result in smaller temperature variations within a gap. The colder packages had some areas where the net radiation flux was negative or where there was a net input of energy by radiation on that part of the surface. The two HLW packages were 0.8˚C cooler than the adjacent packages, which resulted in lower overall radiation fluxes from those heaters. The radiative heat flux for the adapted simulation on the heaters was similar to that for the original simulation and is not presented.

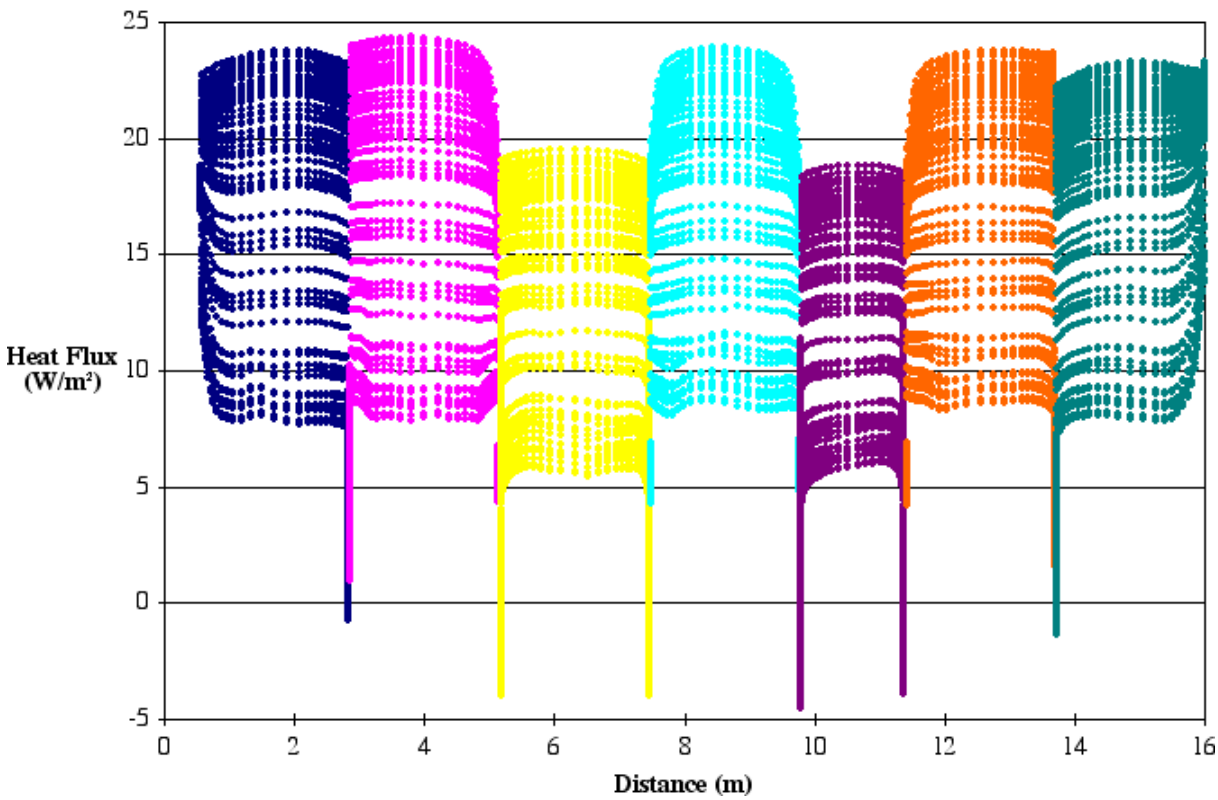

DTN: SN0308T0507803.004.

NOTE: From left to right, the heaters in the simulation represent a 44-BWR, 21-PWR, 5-DHLW Long, 44-BWR, 5-DHLW Short, 21-PWR, and a generic package.

Figure B.4-11. Radiative Heat Flux from Heater Surfaces for the Baseline Grid (Case 5)

Figure B.4-12 shows the net radiation heat flux for the invert, insulation, and concrete surfaces. There is a small area on one side of the simulation where the net radiation flux on the invert surface is positive. On the rest of the surfaces, the net radiation flux is negative or there is a net absorption of radiative thermal energy over those surfaces. The gaps between the individual heaters can be clearly seen near the ceiling of the concrete. The variability resulting from the gaps is 1.2 W/m^2 at the crown of the concrete. The radiative flux plot for the adapted case was similar to the baseline case and is not presented.

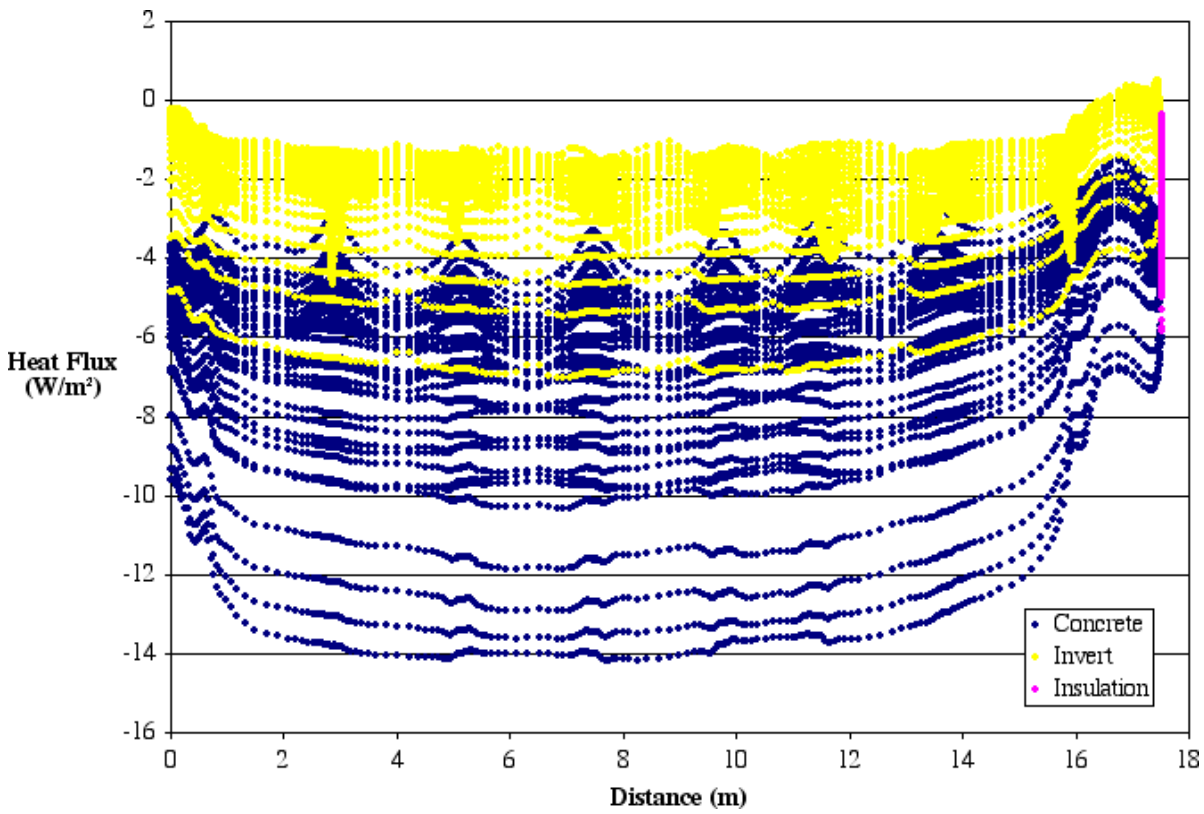

DTN: SN0308T0507803.004.

NOTE: From left to right, the heaters in the simulation represent a 44-BWR, 21-PWR, 5-DHLW Long, 44-BWR, 5-DHLW Short, 21-PWR, and a generic package.

Figure B.4-12. Radiative Heat Flux from Invert, End Insulation, and Concrete Surfaces for the Baseline Grid (Case 5)

The total heat flux from the heaters is shown in Figure B.4-13 for the baseline grid. The variation in heat flux on the end of the heaters is higher than that on the sides of the heaters. Net heat flux ranged from 42 W/m^2 out of a surface to 2 W/m^2 into the surface. The variation of the total heat flux on the side of the heaters was 15 W/m^2 or nearly the same as the variation when only the radiation heat flux is considered.

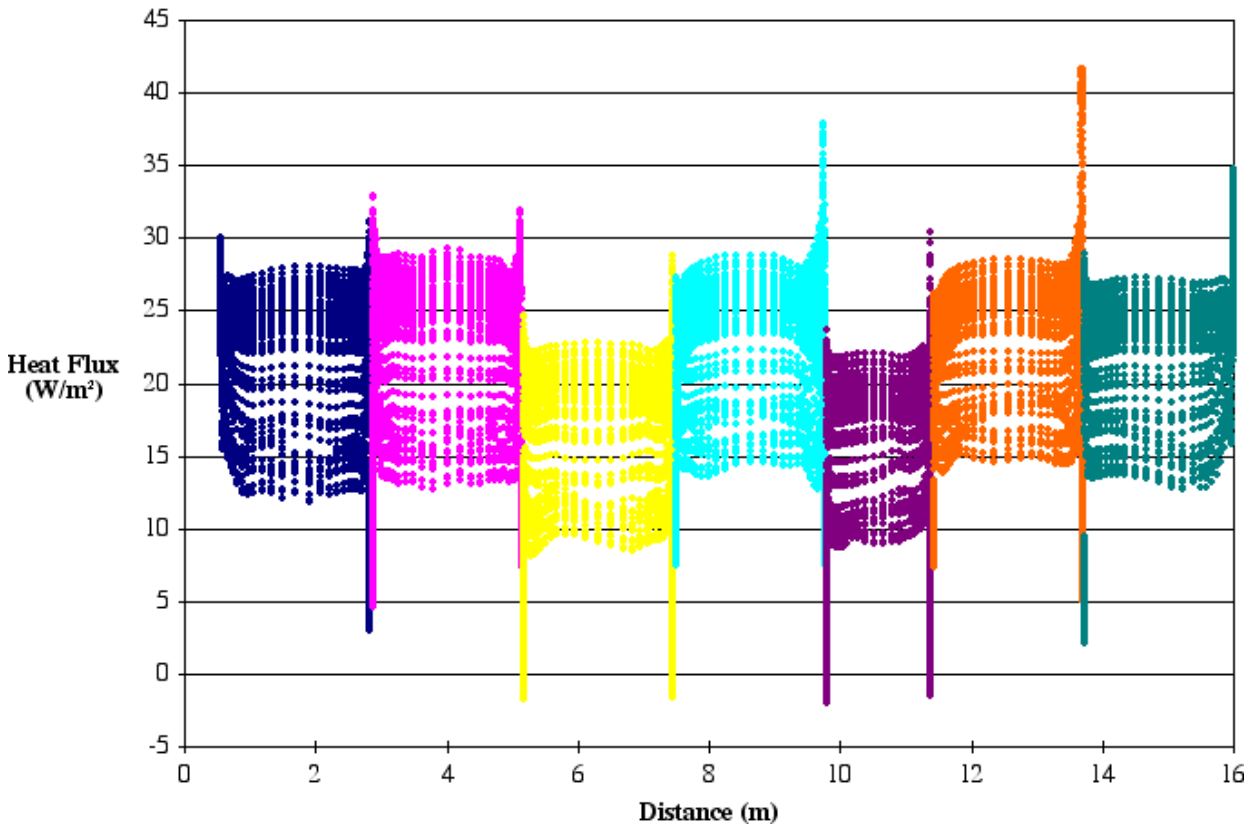

DTN: SN0308T0507803.004.

NOTE: From left to right, the heaters in the simulation represent a 44-BWR, 21-PWR, 5-DHLW Long, 44-BWR, 5-DHLW Short, 21-PWR, and a generic package.

Figure B.4-13. Total Heat Flux from Heater Surfaces for the Baseline Grid (Case 5)

The total heat flux off of the heaters for the adapted mesh for the Case 5 simulation is presented in Figure B.4-14. Since the convective heat flux on the ends of the heaters was different for the two cases, the magnitude of the total heat flux is also different. The peak flux on the ends of the heater is 58 W/m^2 which is 16 W/m^2 higher than for the baseline grid. The variation in local heat flux was not great enough over a large enough area to make a substantial change in the temperatures between the two simulations.

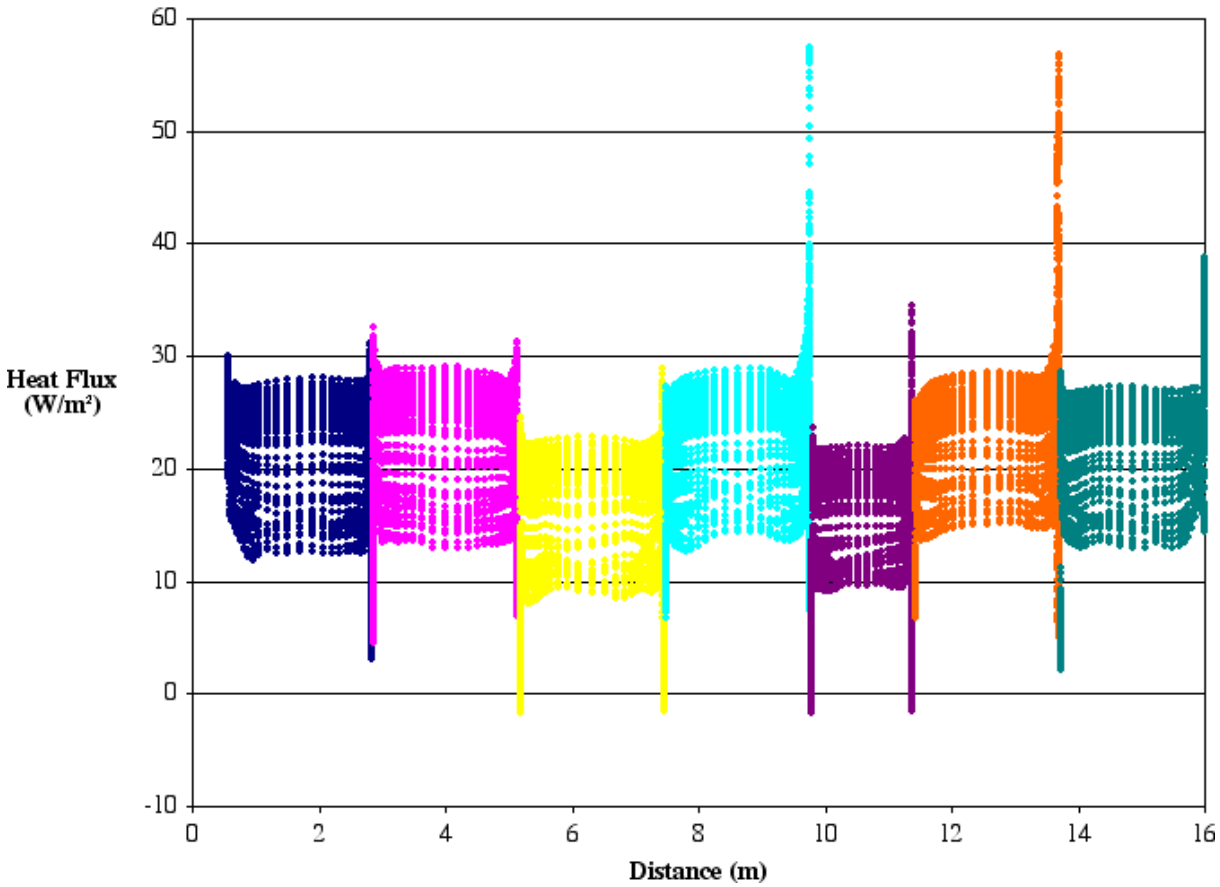

DTN: SN0310T0507803.021.

NOTE: From left to right, the heaters in the simulation represent a 44-BWR, 21-PWR, 5-DHLW Long, 44-BWR, 5-DHLW Short, 21-PWR, and a generic package.

Figure B.4-14. Total Heat Flux from Heater Surfaces for the Adapted Grid (Case 5)

The total heat flux from the invert, insulation, and concrete for the baseline grid Case 5 simulation is presented in Figure B.4-15. This plot indicates that more heat is lost to the environment directly through the concrete than the heat that moves first through the invert. The heat flux onto the invert was mostly less than 6 W/m^2 while the heat flux directly onto the concrete tube ranged mostly between 6 and 16 W/m^2. Regions of local high heat flux on the concrete correspond to the high local convective heat flux in the area directly above the heater gaps. The total heat flux plot on the same surfaces for the adapted simulation is similar and is not presented.

These plots show that the grid adaption mainly impacts convective heat flux on the ends of the waste package. The temperatures were unaffected.

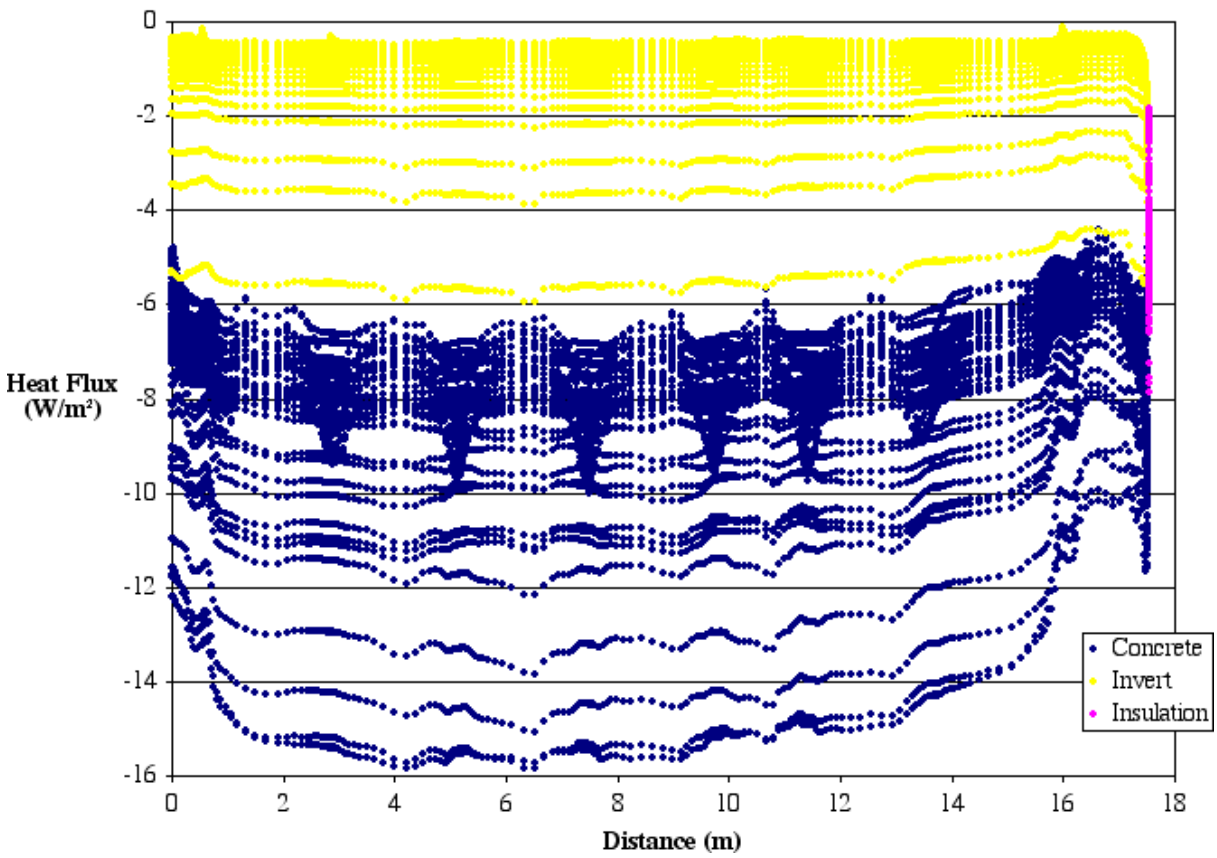

DTN: SN0308T0507803.004.

NOTE: From left to right, the heaters in the simulation represent a 44-BWR, 21-PWR, 5-DHLW Long, 44-BWR, 5-DHLW Short, 21-PWR, and a generic package.

Figure B.4-15. Total Heat Flux from Invert, End Insulation, and Concrete Surfaces for the Baseline Grid (Case 5)

Figure B.4-16 above shows the amount of energy leaving the surface by convection and by radiation. The fraction of total energy leaving each heater by convective heat transfer varies between 18 and 22 percent. The numbers under each waste package is the heat generated in each package. Note that only half of the packages are simulated (symmetry).

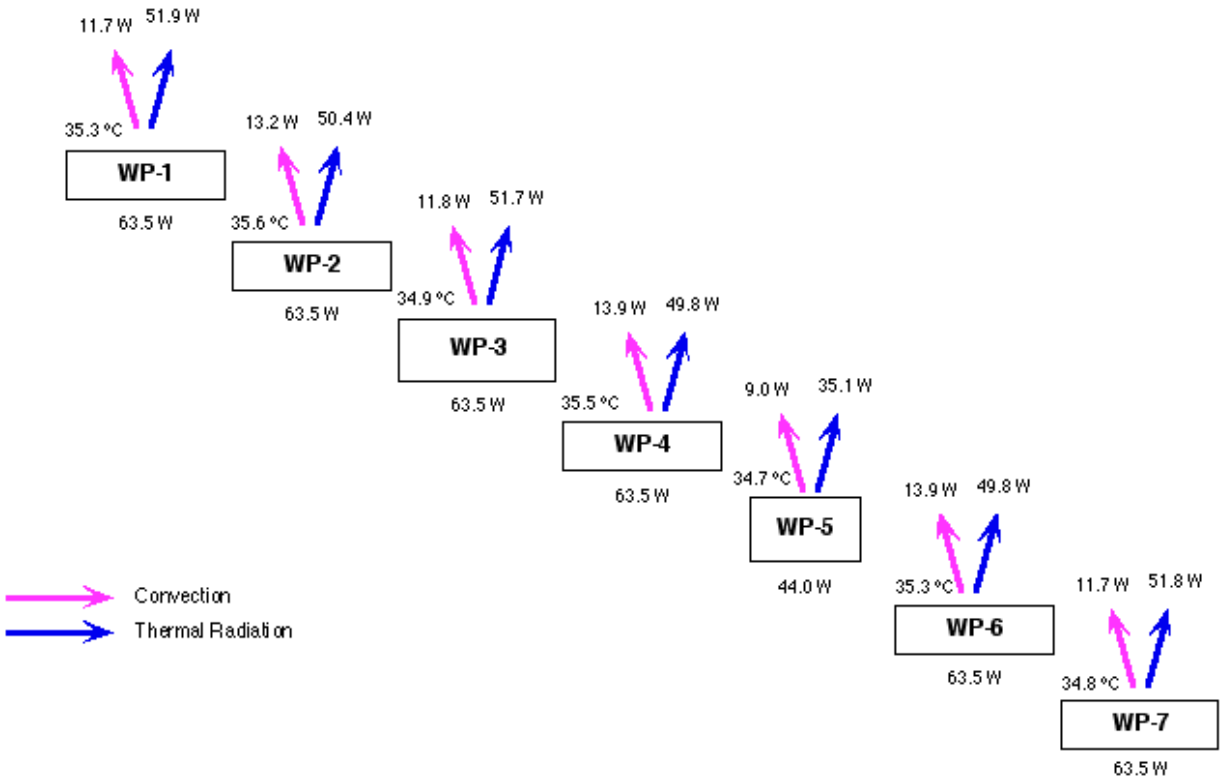

DTN: SN0308T0507803.004.

Figure B.4-16. Heat Transfer Modes on the Cylindrical and end Surfaces of the Waste Packages for the Baseline Grid (Case 5)

The peak air velocities seen in the baseline and the adapted Case 5 runs are shown in Table B.4-2. Peak velocities occurred near the top ends of the gaps next to the cool heaters. The flow is mostly vertical there so this is where the peak y (vertical) velocities occur. The peak z (down drift) velocities occur under the waste packages in the gap between the packages. The peak x (horizontal) velocities occur at the top of the cool end of the drift.

Table B.4-2. Peak Velocity and Component Velocity for Case 5 Simulations

	Original Grid [a]	**Adapted Grid [b]**
Maximum Velocity Magnitude	0.213 m/s	0.215 m/s
Maximum X-Velocity Magnitude (horizontal)	0.154 m/s	0.159 m/s
Maximum Y-Velocity Magnitude (vertical)	0.213 m/s	0.214 m/s
Maximum Z-Velocity Magnitude (down drift)	0.139 m/s	0.147 m/s

[a] DTN: SN0308T0507803.004.

[b] DTN: SN0310T0507803.021.

The next three figures show flow fields at different locations for the adapted mesh simulations for Case 5. Figure B.4-17 shows the flow vectors for the elements near the side of the concrete wall at a location down the experiment at the mid-point of the fourth heater. In addition to having the wall y^+ of order one, there should be at least 10 elements in the boundary layer. This figure shows that the boundary layer has been resolved. At this location, the peak boundary layer velocity is 0.13 m/s. The boundary layer profile is typical for that of natural convection with a sharp rise in flow velocity and then a slow drop in flow velocity away from the wall. The thickness of the boundary layer is the distance from the wall to the point where the velocity returns to free stream value, which in Figure B.4-17 is about the combined thickness of 15 cells.

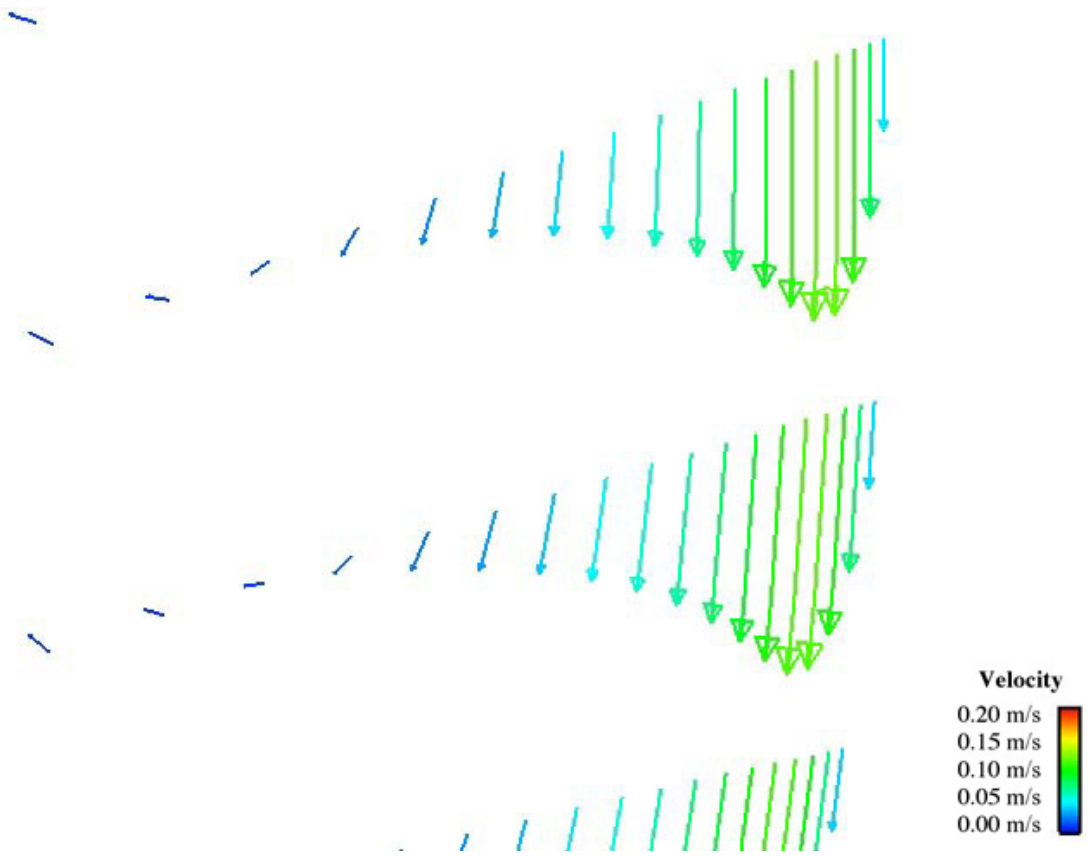

DTN: SN0310T0507803.021.

NOTE: This is near the mid-point of the fourth heater, a medium powered small radius 44-BWR.

Figure B.4-17. Velocity Vectors for Elements Located Near the Middle of the Air-Rock Interface 8.625 Meters Down the Drift for the Adapted Grid (Case 5)

Figure B.4-18 shows the velocity vectors at the intersection of the invert, air, and concrete at the same location down the drift in the experiment as Figure B.4-17. The peak velocity in the boundary layer in this part of the simulation is 0.05 m/s or half of what it was near the side of the drift. The boundary layer is more than 10 elements thick so the boundary layer has been resolved.

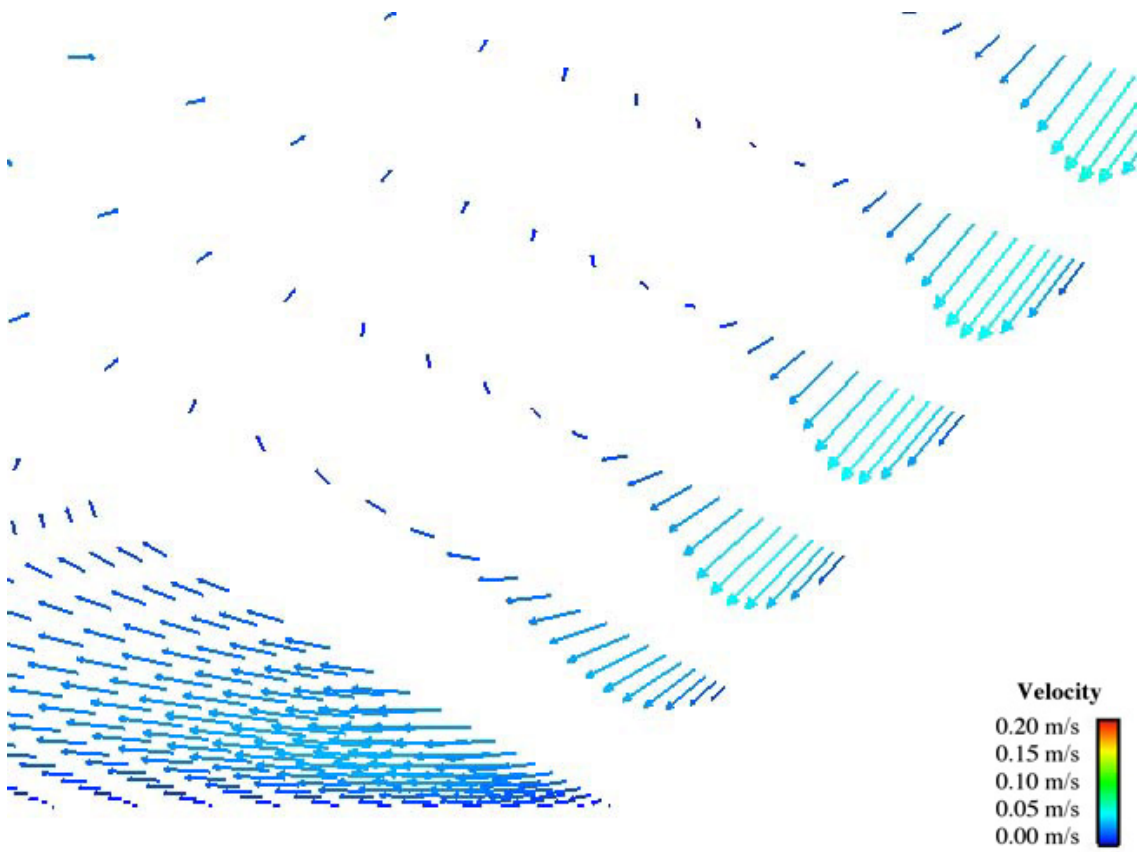

DTN: SN0310T0507803.021.

NOTE: This is near the mid-point of the fourth heater, a medium powered small radius 44-BWR.

Figure B.4-18. Velocity Vectors for Elements Located Near the Air-Invert-Rock Interface 8.625 Meters Down the Drift for the Adapted Grid (Case 5)

Figure B.4-19 shows the flow vectors on the middle of the side of the fourth heater. The flow velocity profile is again typical for natural convection flow. The peak flow velocity in the boundary layer is 0.13 m/s. There are more than 10 elements in the boundary layer meaning that it has been resolved.

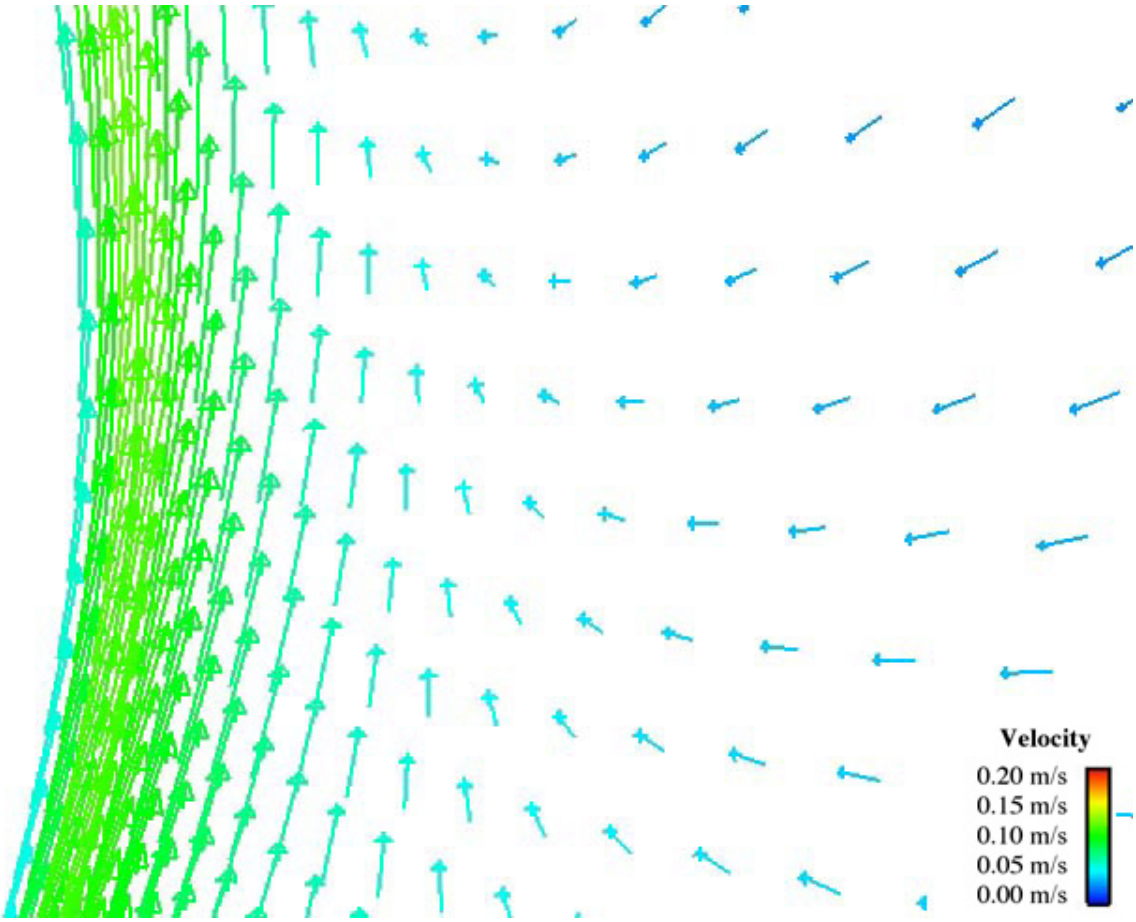

DTN: SN0310T0507803.021.

NOTE: This is near the mid-point of the fourth heater, a medium powered small radius 44-BWR.

Figure B.4-19. Velocity Vectors for Elements Located Near the Air-Heater Interface 8.625 Meters Down the Drift for the Adapted Grid (Case 5)

INTENTIONALLY LEFT BLANK

APPENDIX C

NATURAL CONVECTION TEST DATA INFORMATION

The volume of the test data automatically collected during the natural convection test series prohibited it from being presented in tabular format in Section 7. The data is provided electronically in the workbooks outlined in Table C-1 and may be found in DTN: SN0307T0507803.001. These workbooks also contain minimal calculations. Averages and standard deviations for the three-day period chosen as representative of the test (the data presented in Section 7) are included for all of the Case 4 and Case 8 data. These calculations were performed with standard EXCEL functions. Additionally, Case 1 data were used to determine the thermal conductivity of the concrete test pipe. This data and the associated calculations are provided in "Case 1 Data (for figs and calcs in report).xls." DTNs associated with the data are included in the workbooks and are listed in Table C-2.

Note that these data are used for validation purposes only in Chapter 7 and are not direct input.

Table C-1. Spreadsheets Containing Natural Convection Test Data

File Name (.xls)	Contents
Case 4 Power and Drip Shield Temp Data	Case 4 power input and drip shield temperature data for the three-day period used to determine average values. Averages are calculated in the workbook.
Case 4 Temp Data Stations 2 thru 8 and WP Temp Data	Case 4 temperature data measured at Stations 2 through 8 as well as temperature data for the waste packages for the three-day period used to determine average values. Averages are calculated in the workbook.
Case 4 Temp Data Stations 9 thru 15	Case 4 temperature data measured at Stations 9 through 15 for the three-day period used to determine average values. Averages are calculated in the workbook.
Case 8 Power and Drip Shield Temp Data	Case 8 power input and drip shield temperature data for the three-day period used to determine average values. Averages are calculated in the workbook.
Case 8 Temp Data Stations 2 thru 8 and WP Temp Data	Case 8 temperature data measured at Stations 2 through 8 as well as temperature data for the waste packages for the three-day period used to determine average values. Averages are calculated in the workbook.
Case 8 Temp Data Stations 9 thru 15	Case 8 temperature data measured at Stations 9 through 15 for the three-day period used to determine average values. Averages are calculated in the workbook.
Case 1 Data (for figs and calcs in report)	Case 1 ambient temperature and relative humidity data used in figures in Section 7. Case 1 temperature data at discreet stations used to determine the thermal conductivity of the concrete.

DTN: SN0307T0507803.001.

Prior to using the manually measured velocity data, the measurement coordinate system had to be transposed to the simulation coordinate system. The velocity data are presented in Tables 7.4.1-3 though 7.4.1-8. Supporting calculations are provided in workbook "N C Measured Velocities.xls."

Table C-2. Data Sources for Natural Convection Test Data

Data	YMP Data Tracking Number (DTN)
Case 1	SN0208F3407102.002 [DIRS 161053]
Case 4	SN0208F3407102.004 [DIRS 161056]
Case 8	SN0208F3407102.008 [DIRS 161062]

APPENDIX D

SOLUTION TO THE DISPERSION EQUATIONS

The steady state equations for axial dispersion of water vapor and energy are solved with a one-dimensional finite difference solution technique. The axial length of each cell in the occupied portion of the storage drift contains one waste package. The inter-package distance is specified as 10 cm. The exhaust standoff is set to 15 m for all drifts and is divided into 3 cells of 5 m length. The turnout length is set to 60 m for all drifts and is approximated as a straight extension of the drift; it is divided into 12 cells of 5-m length. Only cells in the exhaust standoff and the turnout have lengths that are precisely 5 m; cells within the storage drift have lengths that reflect the individual waste package dimensions (Section 6.3.5.2.6).

D.1 VAPOR DISPERSION EQUATIONS: UNVENTILATED DRIP SHIELD

Figure D.1-1 shows the control volumes at location n inside and outside of the drip shield. Cell n is bounded by cell n–1 on the left and cell n+1 on the right. The vapor flux entering cell n from cell n–1 is m_{left}; the vapor flux entering cell n+1 from cell n is m_{right}. Outside the drip shield, evaporation and condensation on the drift wall ($m_{wall,n}$) are possible; only condensation is possible on the drip shield ($m_{ds_out,n}$). Inside the drip shield, evaporation and condensation on the invert surface ($m_{invert,n}$) are possible; only condensation is possible on the drip shield ($m_{ds_in,n}$) and the waste package ($m_{wp,n}$).

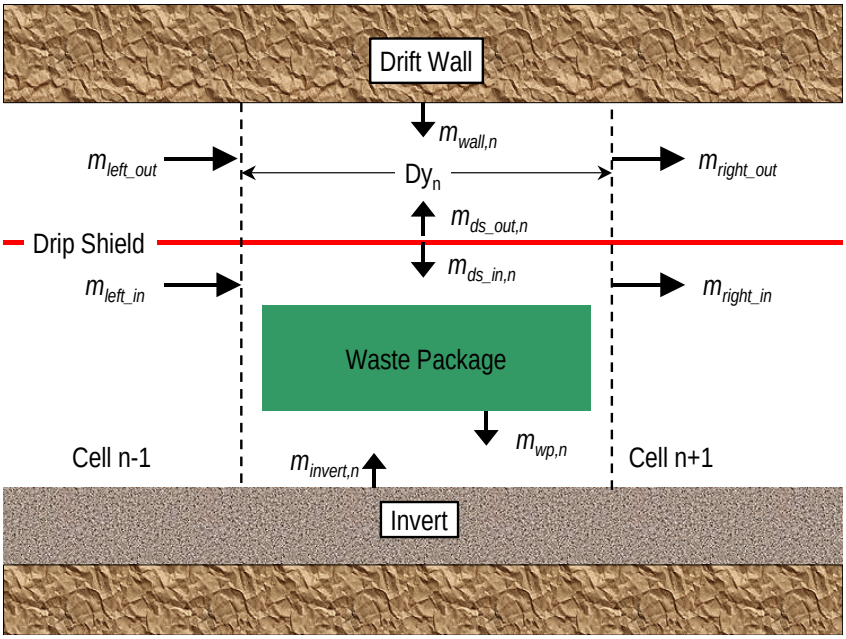

Figure D.1-1. Discretization of Vapor Dispersion Equations

The drip shield terminates with the last waste package in the drift, but the drift extends into drift standoff and the turnout. The ends of the drip shield are open; vapor that migrates to the end under the drip shield will diffuse/convect into the larger cavity undivided by the drip shield.

For simplicity, the structure of a drip shield is maintained in the calculation throughout the domain (Figure D.1-2). To mimic the blending of the two air streams in the end regions without

the drip shield, a mass diffusion term connecting the inner and outer gas regions (M_{inout}) is added and the mass transport terms to the invert, waste package, and drip shield are set to zero.

The inter-region mass transport term is formulated as:

$$M_{inout} = Km_{inout}\left(Xst_{in\,n} - Xst_{out\,n}\right)$$

(Eq. D-1)

where Xst is the vapor mass fraction of the gas and Km_{inout} is a constant. This forces the gas composition on either side of the "phantom" drip shield to equilibrate producing a calculation that adequately mimics the physical case. By trial and error, it has been found that an adequate value for Km_{inout} is

$$Km_{inout} = \frac{2mdot_{\max} P_{inv} \sum_n DY_n \left(D_{wp_n} \neq 0m\right)}{\sum_n DY_n \left(DY_n = 5m\right)}$$

(Eq. D.1-2)

The expressions ($D_{wp,n}=5m$) and ($DY_n \neq 5m$) are Boolean functions that equal unity when the enclosed statement is true and equal zero when the enclosed statement is false. The summation in the numerator adds up the lengths of the cells that contain a waste package. The summation in the denominator adds up the cell lengths in the exhaust standoff and the turnout.

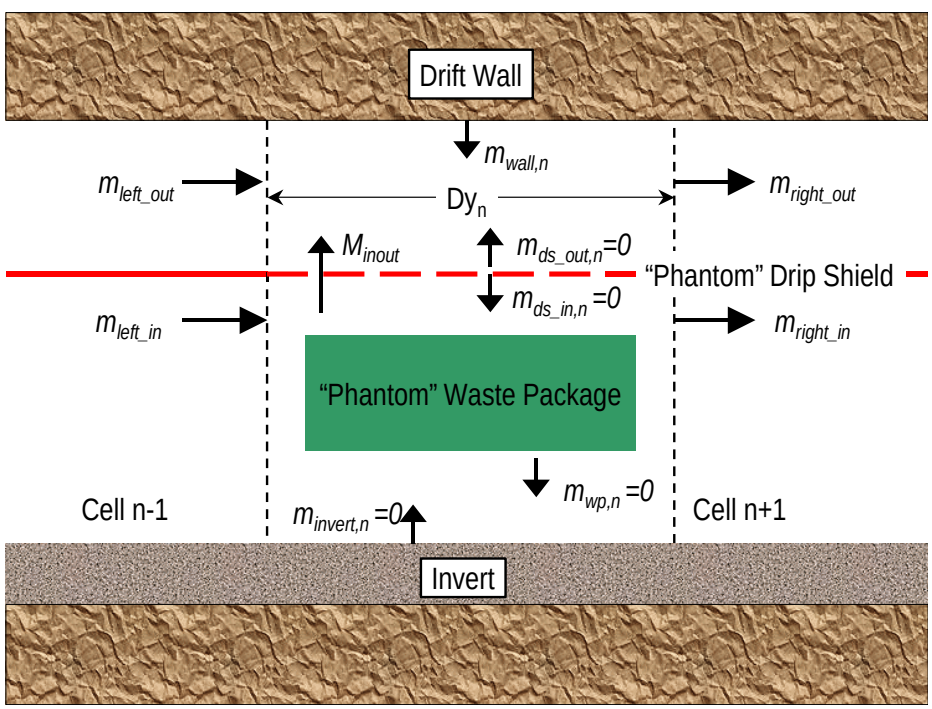

Figure D.1-2. "Phantom" Structure in the Exhaust Standoff and Access Turnout

Conservation of mass is applied to cell n

$$0 = \begin{bmatrix} \left(m_{left_in} - m_{right_in}\right)Ac_{in} - M_{inout}DY_n\left(DY_n = 5m\right) + \\ \left(m_{ds_in,n}P_{ds} + m_{wp,n}P_{wp,n} + m_{invert,n}P_{invert}\right)DY_n\left(DY_n \neq 5m\right) \end{bmatrix} \quad \text{Inside Drip Shield}$$

$$0 = \begin{bmatrix} \left(m_{left_out} - m_{right_out}\right)Ac_{out} + M_{inout}DY_n\left(DY_n = 5m\right) + \\ \left[m_{ds_out,n}P_{ds}\left(DY_n \neq 5m\right) + m_{wall,n}P_{wall}\right]DY_n \end{bmatrix} \quad \text{Outside Drip Shield}$$

(Eq. D.1-3)

where Ac_{in} and Ac_{out} are the cross-sectional areas inside and outside of the drip shield, and P_{ds}, P_{wall}, and $P_{wp,n}$ are the cross-sectional perimeters of the drip shield, drift wall, and waste package. The waste package perimeter is indexed to the cell to account for different diameters. The expressions ($DY_n=5m$) and ($DY_n \neq 5m$) are Boolean functions that equal unity when the enclosed statement is true and equal zero when the enclosed statement is false. These Boolean functions are used to "turn on" the M_{inout} term and turn off the appropriate surface fluxes (m_{ds_in}, m_{wp}, m_{invert}, m_{ds_out}) when the cell length is 5 m. This makes use of the computational artifact that the regions on either end of the drip shield have cell lengths of 5 m, and none of the cells in the storage region have 5-m-long cells.

The entering and leaving fluxes are calculated from Equation 6.3-16 using harmonic averaging:

$$m_{left} = \frac{-\left(\rho_{gas}D_{eff}\right)_{n-1}}{\frac{DY_{n-1}}{2}\left(1 - Xst_{n-1}\right)}\left(XstInt_{n-1,n} - Xst_{n-1}\right) = \frac{-\left(\rho_{gas}D_{eff}\right)_{n}}{\frac{DY_{n}}{2}\left(1 - Xst_{n}\right)}\left(Xst_{n} - XstInt_{n-1,n}\right)$$

$$m_{right} = \frac{-\left(\rho_{gas}D_{eff}\right)_{n}}{\frac{DY_{n}}{2}\left(1 - Xst_{n}\right)}\left(XstInt_{n,n+1} - Xst_{n}\right) = \frac{-\left(\rho_{gas}D_{eff}\right)_{n+1}}{\frac{DY_{n+1}}{2}\left(1 - Xst_{n+1}\right)}\left(Xst_{n+1} - XstInt_{n,n+1}\right)$$

(Eq. D.1-4)

where XstInt is the value of the vapor mass fraction at the interface between adjoining cells. The two pairs of equations are first solved for the interface mass fractions ($XstInt_{n-1,n}$ and $XstInt_{n,n+1}$). The interface mass fractions are then substituted into the equations for the mass fluxes (m_{left}, m_{right}):

$$m_{left} = \begin{cases} 0\dfrac{kg}{m^2 s} & \text{if } n = 1 \\ \dfrac{2\left(Xst_{n-1} - Xst_n\right)}{\dfrac{\left(1 - Xst_n\right) DY_n}{\left(\rho_{gas} D_{eff}\right)_n} + \dfrac{\left(1 - Xst_{n-1}\right) DY_{n-1}}{\left(\rho_{gas} D_{eff}\right)_{n-1}}} & \text{otherwise} \end{cases}$$

$$m_{right} = \begin{cases} 0\dfrac{kg}{m^2 s} & \text{if } n = NTOT \\ \dfrac{2\left(Xst_n - Xst_{n+1}\right)}{\dfrac{\left(1 - Xst_n\right) DY_n}{\left(\rho_{gas} D_{eff}\right)_n} + \dfrac{\left(1 - Xst_{n+1}\right) DY_{n+1}}{\left(\rho_{gas} D_{eff}\right)_{n+1}}} & \text{otherwise} \end{cases}$$

(Eq. D.1-5)

The logic in the equation accounts for the end nodes (1 and NTOT); there is no flux from the left side for node 1 and there is no flux moving out of the right side of node NTOT.

The vapor mass conservation equations (Eq. D.1-4) for all the cells are coupled and transcendental. In principle, these matrix equations for vapor mass could be formulated as:

$$\begin{aligned} Ac_{in}\,\mathbf{M_{in}} \bullet \mathbf{Xst_{in}} &= -\mathbf{S_{in}} \\ Ac_{out}\,\mathbf{M_{out}} \bullet \mathbf{Xst_{out}} &= -\mathbf{S_{out}} \end{aligned} \qquad \text{(Eq. D.1-6)}$$

where **M** is the tri-diagonal matrix describing the axial transport, **Xst** is the vapor mass fraction vector, and **S** is the source vector.

$$\mathbf{M}_{\mathbf{in}_{n,n-1}} = \frac{mst_{left_in_n}}{Xst_{in_{n-1}} - Xst_{in_n}} \quad \mathbf{M}_{\mathbf{in}_{n,n+1}} = \frac{mst_{right_in_n}}{Xst_{in_n} - Xst_{in_{n+1}}}$$

$$\mathbf{M}_{\mathbf{in}_{n,n}} = -\left(\mathbf{M}_{\mathbf{in}_{n,n-1}} + \mathbf{M}_{\mathbf{in}_{n,n+1}}\right)$$

$$\mathbf{S}_{\mathbf{in}_n} = \begin{bmatrix} \left(m_{ds_in,n}P_{ds} + m_{wp,n}P_{wp,n} + m_{invert,n}P_{wall}\right)\left(DY_n \neq 5m\right)DY_n \\ -M_{inout}\left(DY_n = 5m\right) \end{bmatrix}$$

$$\mathbf{M}_{\mathbf{out}_{n,n-1}} = \frac{mst_{left_out_n}}{Xst_{out_{n-1}} - Xst_{out_n}} \quad \mathbf{M}_{\mathbf{out}_{n,n+1}} = \frac{mst_{right_out_n}}{Xst_{out_n} - Xst_{out_{n+1}}}$$

$$\mathbf{M}_{\mathbf{out}_{n,n}} = -\left(\mathbf{M}_{out_{n,n-1}} + \mathbf{M}_{out_{n,n+1}}\right)$$

$$\mathbf{S}_{\mathbf{out}_n} = \begin{bmatrix} \left(m_{ds_out,n}P_{ds}\left(DY_n \neq 5m\right) + m_{wall,n}P_{wall}\right)DY_n \\ +M_{inout}\left(DY_n = 5m\right) \end{bmatrix}$$

(Eq. D.1-7)

If this equation is solved for $\boldsymbol{Xst_{in}}$ and $\boldsymbol{Xst_{out}}$ as part of an over/under relaxation technique, the method tends to be unstable. This is because the sources ($\mathbf{S_{in}}$, $\mathbf{S_{out}}$) are functions of the gas vapor fractions. To overcome this problem, the source vectors are written as:

$$\mathbf{S}_{\mathbf{in}_n} = \begin{bmatrix} \left(\begin{array}{l} \dfrac{m_{ds_in,n}P_{ds}}{\left(\mathrm{Xst}_{\mathrm{eq}}\left(Tds_n\right) - Xst_{in,n}\right)}\left(\mathrm{Xst}_{\mathrm{eq}}\left(Tds_n\right) - Xst_{in,n}\right) + \\ \dfrac{m_{wp,n}P_{wp,n}}{\left(\mathrm{Xst}_{\mathrm{eq}}\left(Twp_n\right) - Xst_{in,n}\right)}\left(\mathrm{Xst}_{\mathrm{eq}}\left(Twp_n\right) - Xst_{in,n}\right) + \\ \dfrac{m_{invert,n}P_{wall}}{\left(\mathrm{Xst}_{invert,n} - Xst_{in,n}\right)}\left(\mathrm{Xst}_{invert,n} - Xst_{in,n}\right) \end{array} \right) DY_n \ \left(DY_n \neq 5m\right) \\ -Km_{inout}\left(Xst_{in,n} - Xst_{out,n}\right)\left(DY_n = 5m\right) \end{bmatrix}$$

$$\mathbf{S}_{\mathbf{out}_n} = \begin{bmatrix} \left(\begin{array}{l} \dfrac{m_{ds_out,n}P_{ds}}{\left(\mathrm{Xst}_{\mathrm{eq}}\left(Tds_n\right) - Xst_{out,n}\right)}\left(\mathrm{Xst}_{\mathrm{eq}}\left(Tds_n\right) - Xst_{out,n}\right)\left(DY_n \neq 5m\right) + \\ \dfrac{m_{wall,n}P_{wall}}{\left(\mathrm{Xst}_{\mathrm{eq}}\left(Twall_n\right) - Xst_{out\,n}\right)}\left(\mathrm{Xst}_{\mathrm{eq}}\left(Twall_n\right) - Xst_{out,n}\right) \end{array} \right) DY_n \\ +Km_{inout}\left(Xst_{in,n} - Xst_{out,n}\right)\left(DY_n = 5m\right) \end{bmatrix}$$

(Eq. D.1-8)

where $\mathrm{Xst}_{\mathrm{eq}}(\mathrm{T})$ is the equilibrium vapor mass fraction at temperature T. A portion of the source vector is carried to the left side of the axial transport equation, which becomes:

$$\mathbf{M}'_{\mathbf{in}} \cdot \mathbf{Xst}_{\mathbf{in}} = \mathbf{S}'_{\mathbf{in}}$$
$$\mathbf{M}'_{\mathbf{out}} \cdot \mathbf{Xst}_{\mathbf{out}} = \mathbf{S}'_{\mathbf{out}}$$

(Eq. D.1-9)

where

$$\mathbf{M'_{in}}_{n,n-1} = \frac{Ac_{in}\ mst_{left_in,n}}{Xst_{in,n-1} - Xst_{in,n}} \quad \mathbf{M'_{in}}_{n,n+1} = \frac{Ac_{in}\ mst_{right_in,n}}{Xst_{in,n} - Xst_{in,n+1}}$$

$$\mathbf{M'_{in}}_{n,n} = \left\{ \begin{array}{l} -\left(\mathbf{M'_{in}}_{n,n-1} + \mathbf{M'_{in}}_{n,n+1}\right) - Km_{inout} DY_n \left(DY_n = 5m\right) - \\ \left[\begin{array}{l} \dfrac{m_{ds_in,n} P_{ds}}{\left(\mathrm{Xst}_{\mathrm{eq}}\left(Tds_n\right) - Xst_{in,n}\right)} + \\ \dfrac{m_{wp,n} P_{wp,n}}{\left(\mathrm{Xst}_{\mathrm{eq}}\left(Twp_n\right) - Xst_{in,n}\right)} + \dfrac{m_{invert,n} P_{invert}}{\left(\mathrm{Xst}_{invert,n} - Xst_{in,n}\right)} \end{array} \right] DY_n \left(DY_n \neq 5m\right) \end{array} \right\}$$

$$\mathbf{S'_{in}} = \left\{ \begin{array}{l} -\left[\begin{array}{l} \dfrac{m_{ds_in,n} P_{ds}\ \mathrm{Xst}_{\mathrm{eq}}\left(Tds_n\right)}{\left(\mathrm{Xst}_{\mathrm{eq}}\left(Tds_n\right) - Xst_{in,n}\right)} + \dfrac{m_{wp,n} P_{wp,n}\ \mathrm{Xst}_{\mathrm{eq}}\left(Twp_n\right)}{\left(\mathrm{Xst}_{\mathrm{eq}}\left(Twp_n\right) - Xst_{in,n}\right)} \\ + \dfrac{m_{invert,n} P_{wall}\ \mathrm{Xst}_{invert,n}}{\left(\mathrm{Xst}_{invert,n} - Xst_{in,n}\right)} \end{array} \right] DY_n \left(DY_n \neq 5m\right) \\ -Km_{inout} Xst_{out,n} DY_n \left(DY_n = 5m\right) \end{array} \right\}$$

$$\mathbf{M'_{out}}_{n,n-1} = \frac{Ac_{out}\ mst_{left_out,n}}{Xst_{out,n-1} - Xst_{out,n}} \quad \mathbf{M'_{out}}_{n,n+1} = \frac{Ac_{out}\ mst_{right_out,n}}{Xst_{out,n} - Xst_{out,n+1}}$$

$$\mathbf{M'_{out}}_{n,n} = \left\{ \begin{array}{l} -\left(\mathbf{M'_{out}}_{n,n-1} + \mathbf{M'_{out}}_{n,n+1}\right) - Km_{inout} DY_n \left(DY_n = 5m\right) \\ -\left[\begin{array}{l} \dfrac{m_{ds_out,n} P_{ds}}{\left(\mathrm{Xst}_{\mathrm{eq}}\left(Tds_n\right) - Xst_{out,n}\right)} \left(DY_n \neq 5m\right) \\ + \dfrac{m_{wall,n} P_{wall}}{\left(\mathrm{Xst}_{\mathrm{eq}}\left(Twall_n\right) - Xst_{out,n}\right)} \end{array} \right] DY_n \end{array} \right\}$$

$$\mathbf{S'_{out}}_{n} = \left\{ \begin{array}{l} -\left[\begin{array}{l} \dfrac{m_{ds_out,n} P_{ds}\ \mathrm{Xst}_{\mathrm{eq}}\left(Tds_n\right)}{\left(\mathrm{Xst}_{\mathrm{eq}}\left(Tds_n\right) - Xst_{out,n}\right)} \left(DY_n \neq 5m\right) \\ + \dfrac{m_{wall,n} P_{wall}\ \mathrm{Xst}_{\mathrm{eq}}\left(Twall_n\right)}{\left(\mathrm{Xst}_{\mathrm{eq}}\left(Twall_n\right) - Xst_{out,n}\right)} \end{array} \right] DY_n \\ -Km_{inout} Xst_{in,n} \left(DY_n = 5m\right) \end{array} \right\}$$

(Eq. D.1-10)

D.2 VAPOR DISPERSION EQUATIONS: VENTILATED DRIP SHIELD

Perfect mixing between the gases inside and outside the drip shield is applied to the ventilated drip shield case. Axial dispersion for this case is approximated by keeping the dispersion coefficient inside and outside the drip shield the same as for the unventilated drip shield. Since there is no longer a distinction between the two gas zones, the gas temperature and composition are characterized by the unsubscripted variables Tgas and Xst. The mass conservation equation becomes:

$$0 = \begin{bmatrix} \left(m_{left_in} - m_{right_in}\right) Ac_{in} + \left(m_{left_out} - m_{right_out}\right) Ac_{out} \\ \begin{bmatrix} \left(m_{ds_in,n} + m_{ds_out,n}\right) P_{ds} \\ m_{wp,n} P_{wp,n} + m_{invert,n} P_{invert} \end{bmatrix} DY_n \left(DY_n \neq 5m\right) \\ + m_{wall,n} P_{wall} DY_n \end{bmatrix}$$

(Eq. D.2-1)

The vector equation now becomes:

$$\mathbf{M}' \cdot \mathbf{Xst} = \mathbf{S}'$$

(Eq. D.2-2)

where

$$\mathbf{M}'_{n,n-1} = \begin{bmatrix} \dfrac{Ac_{in}\ mst_{left_in,n}}{Xst_{n-1} - Xst_n} + \\ \dfrac{Ac_{out}\ mst_{left_out,n}}{Xst_{n-1} - Xst_n} \end{bmatrix} \quad \mathbf{M}'_{n,n+1} = \begin{bmatrix} \dfrac{Ac_{in}\ mst_{right_in,n}}{Xst_n - Xst_{n+1}} + \\ \dfrac{Ac_{out}\ mst_{right_out,n}}{Xst_n - Xst_{n+1}} \end{bmatrix}$$

$$\mathbf{M}'_{n,n} = \left\{ \begin{matrix} -\left(\mathbf{M}'_{n,n-1} + \mathbf{M}'_{n,n+1}\right) - \dfrac{m_{wall,n} P_{wall}}{\left(\mathrm{Xst}_{\mathrm{eq}}\left(Twall_n\right) - Xst_{out,n}\right)} DY_n - \\ \begin{bmatrix} \dfrac{\left(m_{ds_in,n} + m_{ds_out,n}\right) P_{ds}}{\left(\mathrm{Xst}_{\mathrm{eq}}\left(Tds_n\right) - Xst_n\right)} + \\ \dfrac{m_{wp,n} P_{wp,n}}{\left(\mathrm{Xst}_{\mathrm{eq}}\left(Twp_n\right) - Xst_n\right)} + \dfrac{m_{invert,n} P_{invert}}{\left(\mathrm{Xst}_{invert,n} - Xst_n\right)} \end{bmatrix} DY_n \left(DY_n \neq 5m\right) \end{matrix} \right\}$$

$$\mathbf{S}'_{\mathbf{in}} = \left\{ \begin{matrix} -\dfrac{m_{wall,n} P_{wall}\ \mathrm{Xst}_{\mathrm{eq}}\left(Twall_n\right)}{\left(\mathrm{Xst}_{\mathrm{eq}}\left(Twall_n\right) - Xst_{out,n}\right)} DY_n - \\ \begin{bmatrix} \dfrac{\left(m_{ds_in,n} + m_{ds_out,n}\right) P_{ds}\ \mathrm{Xst}_{\mathrm{eq}}\left(Tds_n\right)}{\left(\mathrm{Xst}_{\mathrm{eq}}\left(Tds_n\right) - Xst_n\right)} + \\ \dfrac{m_{wp,n} P_{wp,n}\ \mathrm{Xst}_{\mathrm{eq}}\left(Twp_n\right)}{\left(\mathrm{Xst}_{\mathrm{eq}}\left(Twp_n\right) - Xst_n\right)} + \dfrac{m_{invert,n} P_{wall}\ \mathrm{Xst}_{invert,n}}{\left(\mathrm{Xst}_{invert,n} - Xst_n\right)} \end{bmatrix} DY_n \left(DY_n \neq 5m\right) \end{matrix} \right\}$$

(Eq. D.2-3)

D.3 ENERGY DISPERSION EQUATIONS: UNVENTILATED DRIP SHIELD

Figure D.3-1 shows the energy fluxes in the gas at the boundaries of cells n. Each boundary has two energy flux components. The first is a thermal conduction/dispersion term that accounts for thermal conduction enhanced by convection. The heat that diffuses/advects axially into and out of the cell are q_{left} and q_{right}. Outside the drip shield, heat is convected from the drift wall (q_{wall}) and from the drip shield (q_{ds_out}) into the gas. Inside the drip shield, heat is convected into the gas from the invert (q_{invert}), the waste package (q_{wp}), and the drip shield (q_{ds_in}). Note that the wall temperature is a computed boundary condition for the cell (Section 6.3.5.1.1).

The second component of the energy flux is the enthalpy flux associated with the vapor transport. The water vapor entering and leaving the cell by gas axial diffusion have enthalpy fluxes qst_{left} and qst_{right} associated with them. Outside the drip shield, condensation/evaporation from the drift wall and the drip shield have associated enthalpy fluxes of qst_{wall} and qst_{ds_out}, respectively. Inside the drip shield, condensation/evaporation from the invert, waste package, and drip shield have associated enthalpy fluxes of qst_{wp}, qst_{invert}, and qst_{ds_in}, respectively.

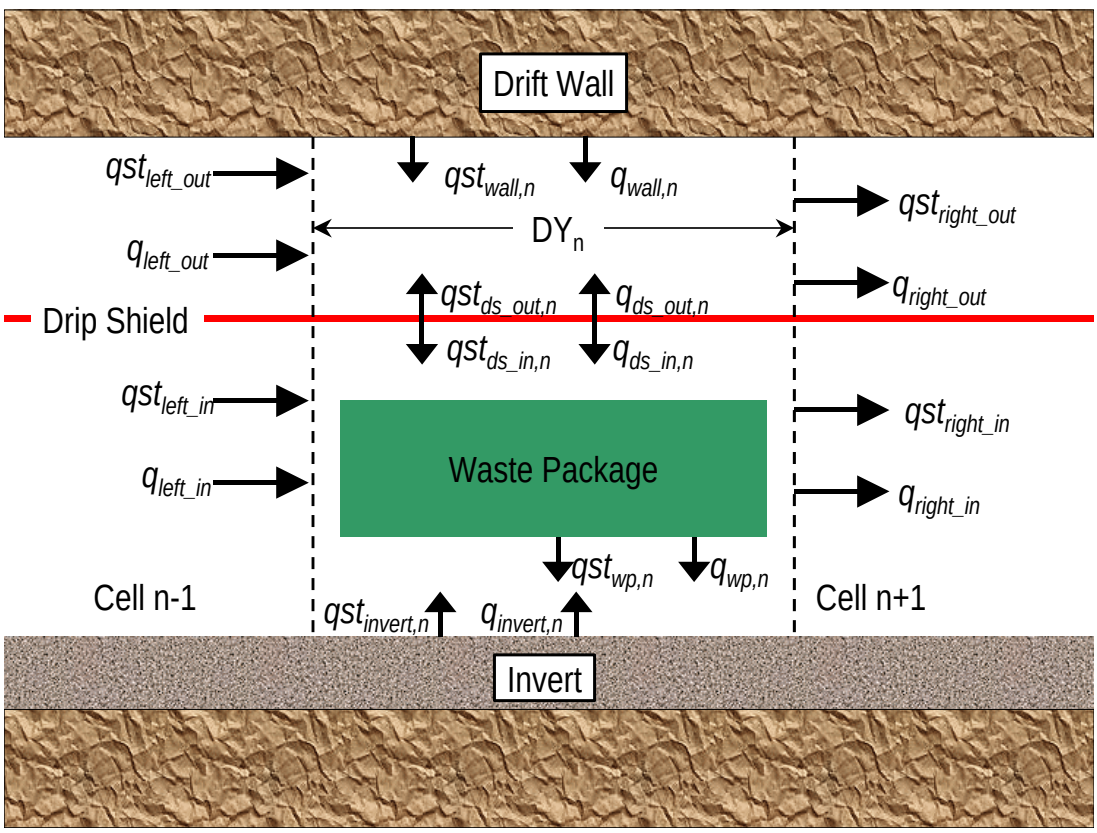

Figure D.3-1. Discretization of Gas Energy Dispersion Equations

The "phantom" drip shield at either end of the storage region is handled in the same way as for the vapor mass equations. An inter-region heat transfer term (q_{inout}) is formulated as:

$$q_{inout} = Kq_{inout}\left(Tgas_{in\,n} - Tgas_{out\,n}\right)$$

(Eq. D.3-1)

and applied to the zones without a drip shield. Heat fluxes to the invert, waste package, and drip shield are set to zero in these zones. This forces the gas temperature on either side of the "phantom" drip shield to equilibrate, producing a calculation that adequately mimics the physical case. By trial and error, it has been found that an adequate value for Kq_{inout} can be related to Km_{inout}.

$$Kq_{inout} = Km_{inout}Cp_{steam}$$

(Eq. D.3-2)

An additional inter-region enthalpy transfer accounts for the inter-region mass transfer between these two regions

$$qst_{inout} = M_{inout}Cp_{steam}\left\lfloor\left(Xst_{in_n} > Xst_{out_n}\right)Tgas_{in\,n} + \left(Xst_{out_n} > Xst_{in_n}\right)Tgas_{out\,n}\right\rfloor$$

(Eq. D.3-3)

The Boolean logic functions ($Xst_{in}>Xst_{out}$) and ($Xst_{out}>Xst_{in}$) "upwind" the inter-region energy transport.

Conservation of energy is applied to cell n

$$0 = \left\{\begin{array}{l}\begin{pmatrix} q_{left_in} - q_{right_in} + \\ qst_{left_in} - qst_{right_in}\end{pmatrix} Ac_{in} - Q_{inout}\left(DY_n = 5m\right) + \\ \begin{pmatrix} q_{ds_in_n}P_{ds} + q_{wp_n}P_{wp,n} + q_{invert_n}P_{invert} + \\ qst_{ds_in_n}P_{ds} + qst_{wp_n}P_{wp,n} + qst_{invert_n}P_{invert}\end{pmatrix}\left(DY_n \neq 5m\right)DY_n\end{array}\right\}$$

$$0 = \left\{\begin{array}{l}\begin{pmatrix} q_{left_out} - q_{right_out} + \\ qst_{left_out} - qst_{right_out}\end{pmatrix} Ac_{out} + Q_{inout}\left(DY_n = 5m\right) + \\ \left[\begin{array}{l}\left(q_{ds_out_n} + qst_{ds_out_n}\right)P_{ds}\left(DY_n \neq 5m\right) + \\ \left(q_{wall_n} + qst_{wall_n}\right)P_{wall}\end{array}\right]DY_n\end{array}\right\}$$

(Eq. D.3-4)

The entering and leaving axial energy fluxes are calculated using harmonic averaging in a manner similar to Eq. D.1-4:

$$q_{left} = \begin{cases} 0\dfrac{W}{m^2} & \text{if } n = 1 \\ \dfrac{2k_{eff}\left(Tgas_{n-1} - Tgas_n\right)}{DY_n + DY_{n-1}} & \text{otherwise} \end{cases}$$

$$q_{right} = \begin{cases} 0\dfrac{W}{m^2} & \text{if } n = NTOT \\ \dfrac{2k_{eff}\left(Tgas_n - Tgas_{n+1}\right)}{DY_n + DY_{n+1}} & \text{otherwise} \end{cases}$$

(Eq. D.3-5)

The convective heat fluxes from the solid surfaces are computed using the appropriate heat transfer coefficients:

$$\begin{aligned} q_{ds_in_n} &= hc_{ds}\left(Tds_n - Tgas_{in_n}\right) \\ q_{wp_n} &= hc_{wp}\left(Twp_n - Tgas_{in_n}\right) \\ q_{invert_n} &= hc_{invert}\left(Tinv_n - Tgas_{in_n}\right) \\ q_{ds_out_n} &= hc_{ds}\left(Tds_n - Tgas_{out_n}\right) \\ q_{wall_n} &= hc_{wall}\left(Twall_n - Tgas_{out_n}\right) \end{aligned}$$

(Eq. D.3-6)

The enthalpy fluxes due to axial steam diffusion are calculated using the average temperature of the upwind and downwind cells. This is used instead of upwinding to stabilize the iteration.

$$qst_{left} = \begin{cases} 0\dfrac{W}{m^2} & \text{if } n = 1 \\ m_{left}\dfrac{Tgas_{n-1} + Tgas_n}{2}Cp_{steam} & \text{otherwise} \end{cases}$$

$$qst_{right} = \begin{cases} 0\dfrac{W}{m^2} & \text{if } n = NTOT \\ m_{right}\dfrac{Tgas_{n+1} + Tgas_n}{2}Cp_{steam} & \text{otherwise} \end{cases}$$

(Eq. D.3-7)

The enthalpy fluxes associated with condensation and evaporation at surfaces are based upon the temperature of the gas. The energy associated with the latent heat is assigned to the solid surface.

$$
\begin{aligned}
qst_{ds_in_n} &= m_{ds_in_n} Tgas_{in_n} Cp_{steam} \\
qst_{wp_n} &= m_{wp_n} Tgas_{in_n} Cp_{steam} \\
qst_{invert_n} &= m_{invert_n} Tgas_{in_n} Cp_{steam} \\
qst_{ds_out_n} &= m_{ds_out_n} Tgas_{out_n} Cp_{steam} \\
qst_{wall_n} &= m_{wall_n} Tgas_{out_n} Cp_{steam}
\end{aligned}
$$

(Eq. D.3-8)

D.4 ENERGY DISPERSION EQUATIONS: UNVENTILATED DRIP SHIELD

Perfect mixing between the gases inside and outside the drip shield is applied to the ventilated drip shield case. The energy equation for the ventilated drip shield case reduces to a single equation.

$$
0 = \left\{ \begin{array}{l}
\begin{pmatrix} q_{left_in} - q_{right_in} + \\ qst_{left_in} - qst_{right_in} \end{pmatrix} Ac_{in} + \begin{pmatrix} q_{left_out} - q_{right_out} + \\ qst_{left_out} - qst_{right_out} \end{pmatrix} Ac_{out} \\
+ \left(q_{wall_n} + qst_{wall_n} \right) P_{wall} \\
\begin{pmatrix} \left(q_{ds_in,n} + q_{ds_out,n} \right) P_{ds} + q_{wp_n} P_{wp,n} + q_{invert_n} P_{invert} + \\ \left(qst_{ds_in,n} + qst_{ds_out,n} \right) P_{ds} + qst_{wp_n} P_{wp,n} + qst_{invert_n} P_{invert} \end{pmatrix} \left(DY_n \neq 5m \right) DY_n
\end{array} \right\}
$$

(Eq. D.4-1)

All the flux equations (Equations D.3-5 through D.3-8) remain the same with the exception that the gas temperatures are replaced by T_{gas}.

D.5 SOLUTION PROCEDURE

For the unventilated drip shield, the surface energy equations (Equations 6.3-20, 6.3-21, and 6.3-22) (3), gas energy equations (Equation D.1-4) (2), and gas vapor equations (Equation D.1-9) (2), form a set of seven (7) coupled equations for each axial location in the drift. The number of cells in the drift is dependent upon the length of the drift. A typical drift is represented by about 150 axial locations. Hence the total number of coupled equations to be solved is about 1,050. For the ventilated drip shield, there are five (5) coupled for each location and the total number of coupled equations to be solved is about 750.

Since the conservation equations are transcendental functions of the unknowns, a direct solution technique is not possible. Instead, the method of successive substitution with over and under relaxation factors is used (Press et al. 1992 [DIRS 103316], p. 857). The change in value of a particular unknown needed to satisfy the appropriate equation is calculated. The new value of the unknown is calculated as the sum of the old value and the product of the computed change

and the relaxation factor (*fctT*, *fctX*). This procedure is executed for every unknown value. The cycle is repeated until a relative error criterion of 10^{-7} is realized. A schematic of the procedure is shown in Figure D.5-1.

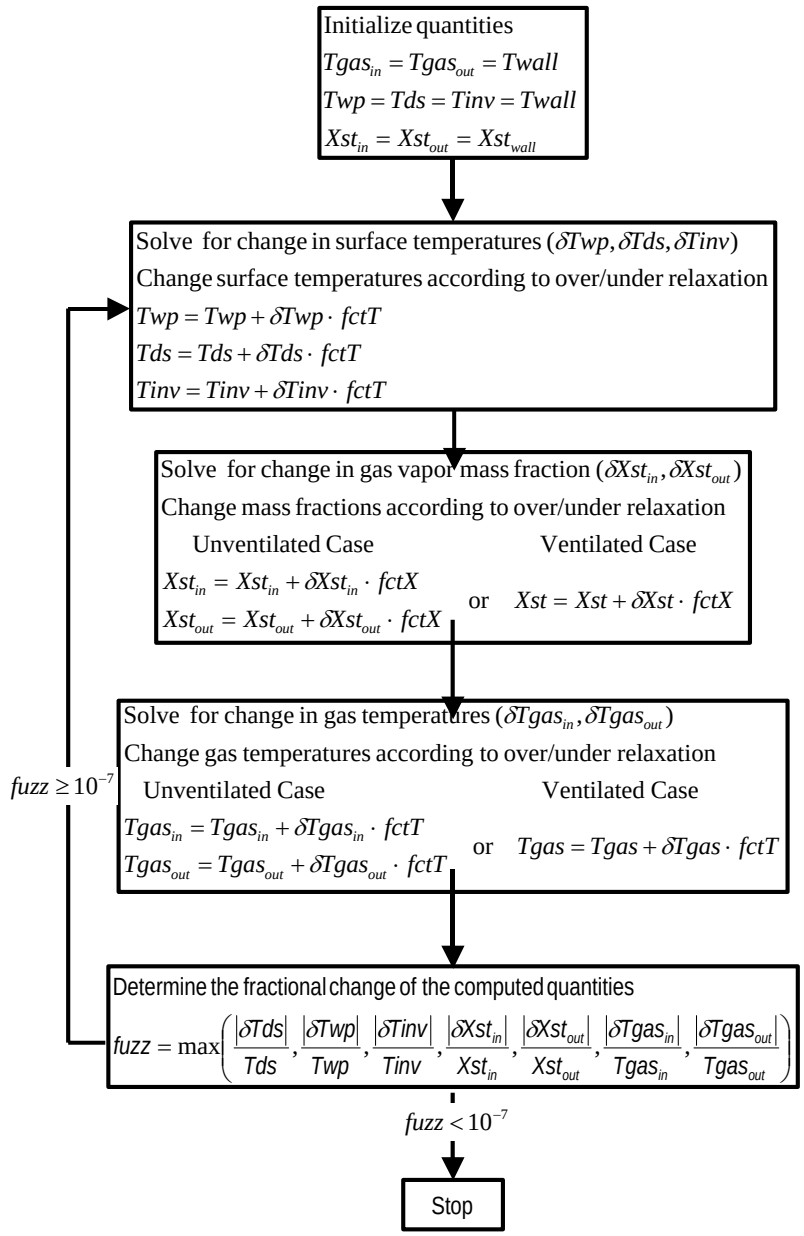

Figure D.5-1. Flow Chart of Solution Procedure

Step 1: Initialize the Unknowns

The unknown temperatures for each of the cells ($Tgas_{in}$, $Tgas_{out}$, T_{wp}, T_{ds}, T_{inv}) are set equal to the drift wall temperature of that cell (T_{wall}). The unknown vapor mass fractions (Xst_{in}, Xst_{out}) are set equal to the equilibrium vapor mass fraction of the wall (Xst_{wall}).

Step 2: Compute the Changes in the Surface Temperatures

The energy equations for the surfaces (waste package, drip shield, invert) are rewritten so that the net thermal radiation fluxes from the surfaces (qr_{wp}, qr_{ds}, qr_{inv}) are calculated as functions of the surface temperatures.

$$qr_{wp} = \frac{Q_{wp}}{P_{wp}} - \left[q_{wp} + m_{wp} h_{fg}\right]$$

where $q_{wp} = hc_{wp}\left(T_{wp} - T_{gas_in}\right)$

$$qr_{ds} = -\left[\begin{array}{l} q_{ds_in} + q_{ds_out} + \\ \dfrac{\sigma\left(T_{ds}{}^{4} - T_{wall}{}^{4}\right)}{\dfrac{1}{\varepsilon_{ds}} + \dfrac{P_{ds}}{P_{wall}}\left(\dfrac{1}{\varepsilon_{wall}} - 1\right)} + \left(m_{ds_in} + m_{ds_out}\right) h_{fg} \end{array}\right]$$

where $q_{ds_in} = hc_{ds_in}\left(T_{ds} - T_{gas_in}\right)$ $\quad q_{ds_out} = hc_{ds_out}\left(T_{ds} - T_{gas_out}\right)$

$$qr_{invert} = -\left[q_{inv} + m_{invert} h_{fg}\right]$$

where $q_{inv} = hc_{invert}\left(T_{invert} - T_{gas_in}\right)$

$$qst_{ds_in_n} = m_{ds_in_n} Tgas_{in_n} Cp_{steam}$$
$$qst_{wp_n} = m_{wp_n} Tgas_{in_n} Cp_{steam}$$
$$qst_{invert_n} = m_{invert_n} Tgas_{in_n} Cp_{steam}$$
$$qst_{ds_out_n} = m_{ds_out_n} Tgas_{out_n} Cp_{steam}$$
$$qst_{wall_n} = m_{wall_n} Tgas_{out_n} Cp_{steam}$$

(Eq. D.5-1)

Then three functions (GT_{wp}, GT_{ds}, GT_{inv}) are written from the surface radiation equations as functions of the changes in surfaces temperatures (δT_{wp}, δT_{ds}, δT_{inv}). The roots of these functions are found sequentially using the Mathcad solver **root** at each cell. These computed temperature changes are multiplied by the temperature relaxation factor, *fctT*, and added to the old value to produce updated values of surface temperatures.

$$GT_{wp}\left(\delta T_{wp}\right)=\sigma\begin{bmatrix}\left(T_{wp}+\delta T_{wp}\right)^4\\ +\left(-F_{wp-ds}\ T_{ds}{}^4\right)\\ +\left(-F_{wp-invert}\ T_{inv}{}^4\right)\end{bmatrix}-\begin{bmatrix}\left(\dfrac{1}{\varepsilon_{wp}}\right)qr_{wp}\left(\delta T_{wp}\right)\\ +\left(-F_{wp-ds}\dfrac{1-\varepsilon_{ds}}{\varepsilon_{ds}}\right)qr_{ds}\\ +\left(-F_{wp-invert}\dfrac{1-\varepsilon_{invert}}{\varepsilon_{invert}}\right)qr_{invert}\end{bmatrix}$$

$$GT_{ds}\left(\delta T_{ds}\right)=\sigma\begin{bmatrix}\left(-F_{ds-wp}\right)T_{wp}{}^4+\\ \left(1-F_{ds-ds}\right)\left(T_{ds}+\delta T_{ds}\right)^4\\ +\left(-F_{ds-invert}\ T_{inv}{}^4\right)\end{bmatrix}-\begin{bmatrix}\left(-F_{ds-wp}\dfrac{1-\varepsilon_{wp}}{\varepsilon_{wp}}\right)qr_{wp}\\ +\left(\dfrac{1}{\varepsilon_{ds}}-F_{ds-ds}\dfrac{1-\varepsilon_{ds}}{\varepsilon_{ds}}\right)qr_{ds}\left(\delta T_{ds}\right)\\ +\left(-F_{ds-invert}\dfrac{1-\varepsilon_{invert}}{\varepsilon_{invert}}\right)qr_{invert}\end{bmatrix}$$

$$GT_{inv}\left(\delta T_{inv}\right)=\sigma\begin{bmatrix}\left(-F_{invert-wp}\right)T_{wp}{}^4\\ +\left(-F_{invert-ds}\right)T_{ds}{}^4+\\ \left(T_{inv}+\delta T_{inv}\right)^4\end{bmatrix}-\begin{bmatrix}\left(-F_{invert-wp}\dfrac{1-\varepsilon_{wp}}{\varepsilon_{wp}}\right)qr_{wp}\\ +\left(-F_{invert-ds}\dfrac{1-\varepsilon_{ds}}{\varepsilon_{ds}}\right)qr_{ds}\\ +\left(\dfrac{1}{\varepsilon_{invert}}\right)qr_{invert}\left(\delta T_{inv}\right)\end{bmatrix}$$

(Eq. D.5-2)

Step 3: Compute Changes in the Vapor Mass Fractions

In the equation for vapor mass fraction, the values of the matrices (**M'$_{in}$**, **M'$_{out}$** or **M'**) and the forcing vectors (**S'$_{in}$**, **S'$_{out}$** or **S'**) are computed using old values of vapor mass fraction. The change in the vapor mass fraction values is calculated by solving the equation for the mass fraction vectors (**Xst$_{in}$**, **Xst$_{out}$** or **Xst**) using Mathcad's linear solver, **lsolve,** and then subtracting the old values of these vectors. These computed mass fraction changes are multiplied by the mass fraction relaxation factor, fctX and added to the old value to produce updated values of vapor mass fraction.

Step 4: Compute Changes in the Gas Temperatures

Functions (GT_{in}, GT_{out} or GT) are written from the gas energy equations as functions of the changes in the gas temperatures (δT_{in}, δT_{out} *or* δT). The dispersive heat fluxes (q_{left_in}, q_{right_in}, q_{left_out}, q_{right_out}) and the convective heat fluxes from the surfaces (q_{wall_in}, q_{ds_out}, q_{ds_in}, q_{ds_inv}, q_{ds_wp}) are calculated using the temperature changes ($T+\delta T$). Only the sensible heat for the surface enthalpy fluxes (qst_{wall_in}, qst_{ds_out}, qst_{ds_in}, qst_{ds_inv}, qst_{ds_wp}) is changed by δT (i.e., the product $m(T) \times Cp_{steam} \times (T+\delta T)$). The roots of these functions are found sequentially using the Mathcad solver root at each cell. These computed temperature changes are multiplied by the temperature relaxation factor, fctT, and added to the old value to produce updated values of gas temperatures.

For the unventilated drip shield case, the gas energy functions (GT_{in}, GT_{out}) are:

$$
\begin{aligned}
GT_{in}(\delta Tgas_{in}) = & \begin{pmatrix} q_{left_in}(\delta T_{gas_in}) - q_{right_in}(\delta T_{gas_in}) + \\ qst_{left_in}(\delta T_{gas_in}) - qst_{right_in}(\delta T_{gas_in}) \end{pmatrix} Ac_{in} \\
& - (q_{inout} + qst_{inout})(DY_n = 5m) \\
& + \begin{bmatrix} [q_{ds_in_n}(\delta T_{gas_in}) + qst_{ds_in_n}(\delta T_{gas_in})] P_{ds} \\ + [q_{wp_n}(\delta T_{gas_in}) + qst_{wp_n}(\delta T_{gas_in})] P_{wp,n} \\ + [q_{invert_n}(\delta T_{gas_in}) + qst_{invert_n}(\delta T_{gas_in})] P_{invert} \end{bmatrix} DY_n (DY_n \neq 5m)
\end{aligned}
$$

$$
\begin{aligned}
GT_{out}(\delta Tgas_{out}) = & \begin{pmatrix} q_{left_out}(\delta T_{gas_out}) - q_{right_out}(\delta T_{gas_out}) + \\ qst_{left_out}(\delta T_{gas_out}) - qst_{right_out}(\delta T_{gas_out}) \end{pmatrix} Ac_{out} \\
& + Q_{inout}(DY_n = 5m) \\
& + \begin{pmatrix} \begin{bmatrix} q_{ds_out_n}(\delta T_{gas_out}) + \\ qst_{ds_out_n}(\delta T_{gas_out}) \end{bmatrix} P_{ds}(DY_n \neq 5m) \\ + [q_{wall_n}(\delta T_{gas_out}) + qst_{wall_n}(\delta T_{gas_out})] P_{wall} \end{pmatrix} DY_n
\end{aligned}
$$

(Eq. D.5-3)

For the ventilated drip shield case, the gas energy function (*GT*) is:

$$
\begin{aligned}
GT(\delta Tgas) = & \begin{pmatrix} q_{left_in}(\delta T_{gas}) - q_{right_in}(\delta T_{gas}) + \\ qst_{left_in}(\delta T_{gas}) - qst_{right_in}(\delta T_{gas}) \end{pmatrix} Ac_{in} + \\
& \begin{pmatrix} q_{left_out}(\delta T_{gas}) - q_{right_out}(\delta T_{gas}) + \\ qst_{left_out}(\delta T_{gas}) - qst_{right_out}(\delta T_{gas}) \end{pmatrix} Ac_{out} \\
& + \left[q_{wall_n}(\delta T_{gas_out}) + qst_{wall_n}(\delta T_{gas_out}) \right] P_{wall} DY_n \\
& + \begin{bmatrix} \begin{bmatrix} q_{ds_in,n}(\delta T_{gas}) + qst_{ds_in,n}(\delta T_{gas}) \\ + q_{ds_out,n}(\delta T_{gas}) + qst_{ds_out,n}(\delta T_{gas}) \end{bmatrix} P_{ds} \\ + \left[q_{wp,n}(\delta T_{gas}) + qst_{wp,n}(\delta T_{gas}) \right] P_{wp,n} \\ + \left[q_{invert,n}(\delta T_{gas}) + qst_{invert,n}(\delta T_{gas}) \right] P_{invert} \\ \\ \end{bmatrix} DY_n (DY_n \neq 5m)
\end{aligned}
$$

(Eq. D.5-4)

D.6 VERIFICATION OF DIFFERENCING TECHNIQUE

The differencing technique used to calculate the axial temperature and vapor mass fraction profiles is verified by comparing its predictions to the analytic solution to a simplified problem. The energy dispersion equations solved in the full problem are (Equation 6.3-19):

$$
\begin{aligned}
Ac_{in} \frac{d}{dy} \left[q_{cond} + h_{st}(T_{gas_in}) m_{y_in} \right] = & P_{wp}\ hc_{wp}(T_{wp} - T_{gas_in}) + P_{ds}\ hc_{ds}(T_{ds} - T_{gas_in}) \\
& + P_{invert}\ hc_{invert}(T_{invert} - T_{gas_in}) \\
& + P_{wp}\ m_{wp} h_{st}(T_{gas_in}) + P_{ds}\ m_{ds_in} h_{st}(T_{gas_in}) \\
& + P_{invert}\ m_{invert} h_{st}(T_{gas_in}) \\
Ac_{out} \frac{d}{dy} \left[q_{cond} + h_{st}(T_{gas_out}) m_{y_out} \right] = & P_{wall}\ hc_{wall}(T_{wall} - T_{gas_out}) + P_{ds}\ hc_{ds}(T_{ds} - T_{gas_out}) \\
& + P_{wall}\ m_{wall} h_{st}(T_{gas_out}) + P_{ds}\ m_{ds_out} h_{st}(T_{gas_out})
\end{aligned}
$$

(Eq. D.6-1)

In the benchmark problem, the convective heat transport coefficients to the waste package and drip shield (hc_{wp}, hc_{ds}) are set to zero. Additionally, the steam enthalpy (h_{st}) is set to zero by setting the steam heat capacity (Cp_{steam}) to zero. Substituting in Fourier's law (constant thermal conductivity, k) for the heat conduction (q_{cond}), the simplified energy dispersion equations become:

$$\frac{d^2}{dy^2}\left[T_{gas_in}\right] = -\frac{P_{invert}\ hc_{invert}}{k_{eff}\ Ac_{in}}\left(T_{invert} - T_{gas_in}\right)$$
$$\frac{d^2}{dy^2}\left[T_{gas_out}\right] = -\frac{P_{wall}\ hc_{wall}}{k_{eff}\ Ac_{out}}\left(T_{wall} - T_{gas_out}\right)$$

(Eq. D.6-2)

The “zero flux” boundary conditions at either end of the domain are unchanged for the full problem.

$$\left[\frac{d}{dy}T_{gas_in}\right]_{y=0} = \left[\frac{d}{dy}T_{gas_in}\right]_{y=L} = 0$$
$$\left[\frac{d}{dy}T_{gas_out}\right]_{y=0} = \left[\frac{d}{dy}T_{gas_out}\right]_{y=L} = 0$$

(Eq. D.6-3)

The simplified energy dispersion equations have an analytic solution for the case where the heat transfer coefficients (hc_{invert}, hc_{wall}) are spatially constant and the invert and wall temperatures are linear in space. Rewriting the two independent simplified dispersion equations for this case without distinguishing between the inner and outer regions:

$$\frac{d^2}{dy^2}\left[T_{gas}\right] = -\frac{P_{surface}\ hc_{surface}}{k_{eff}\ Ac}\left[\left(T0_{surface} + BT_{surface}y\right) - T_{gas}\right] \qquad \text{(Eq. D.6-4)}$$

Using operator notation, the equation is rewritten as:

$$\left(D^2 - \frac{P_{surface}\ hc_{surface}}{k_{eff}\ Ac}\right)T_{gas} = -\frac{P_{surface}\ hc_{surface}}{k_{eff}\ Ac}\left(T0_{surface} + \Delta T_{surface}\frac{y}{L}\right) \qquad \text{(Eq. D.6-5)}$$

Differentiating this equation produces:

$$\left[D\left(D^2 - \frac{P_{surface}\ hc_{surface}}{k_{eff}\ Ac}\right)\right]T_{gas} = -\frac{P_{surface}\ hc_{surface}}{k_{eff}\ Ac}\frac{\Delta T_{surface}}{L} \qquad \text{(Eq. D.6-6)}$$

Differentiating again produces:

$$\left[D^2 \left(D^2 - \frac{P_{surface}\ hc_{surface}}{k_{eff}\ Ac} \right) \right] T_{gas} = 0 \qquad \text{(Eq. D.6-7)}$$

The solution to this fourth order differential equation can now be written by inspection:

$$T_{gas} = C_1 + C_2 \frac{y}{L} + C_3 \sinh\left(\beta \frac{y}{L} \right) + C_4 \cosh\left(\beta \frac{y}{L} \right)$$

$$\text{where} \quad \beta = L \sqrt{\frac{P_{surface}\ hc_{surface}}{k_{eff}\ Ac}}$$

(Eq. D.6-8)

The solution is now differentiated

$$\frac{d}{dy} T_{gas} = \frac{C_2}{L} + \frac{C_3\ \beta}{L} \cosh\left(\beta \frac{y}{L} \right) + \frac{C_4\ \beta}{L} \sinh\left(\beta \frac{y}{L} \right)$$

$$\frac{d^2}{dy^2} T_{gas} = \frac{C_3\ \beta^2}{L^2} \sinh\left(\beta \frac{y}{L} \right) + \frac{C_4\ \beta^2}{L^2} \cosh\left(\beta \frac{y}{L} \right)$$

(Eq. D.6-9)

The derivatives are substituted into the original differential equation:

$$\left[\begin{array}{l} \dfrac{C_3\ \beta^2}{L^2} \sinh\left(\beta \dfrac{y}{L} \right) + \dfrac{C_4\ \beta^2}{L^2} \cosh\left(\beta \dfrac{y}{L} \right) \\ - \dfrac{\beta^2}{L^2} \left[\begin{array}{l} C_1 + C_2 \dfrac{y}{L} + C_3 \sinh\left(\beta \dfrac{y}{L} \right) \\ + C_4 \cosh\left(\beta \dfrac{y}{L} \right) \end{array} \right] \end{array} \right] = -\beta^2 \left(T0_{surface} + \Delta T_{surface} \frac{y}{L} \right)$$

(Eq. D.6-10)

Matching coefficients produces:

$$C_1 = T0_{surface} \quad C_2 = \Delta T_{surface} \qquad \text{(Eq. D.6-11)}$$

The derivative boundary conditions are enforced to find the other two coefficients:

$$\left[\frac{d}{dy}T_{gas}\right]_{y=0} = 0 = \frac{\Delta T_{surface}}{L} + \frac{C_3\ \beta}{L}$$

$$\left[\frac{d}{dy}T_{gas}\right]_{y=L} = 0 = \frac{\Delta T_{surface}}{L} + \frac{C_3\ \beta}{L}\cosh(\beta) + \frac{C_4\ \beta}{L}\sinh(\beta)$$

(Eq. D.6-12)

This produces:

$$C_3 = \frac{-\Delta T_{surface}}{\beta}$$

$$C_4 = \frac{\Delta T_{surface}\left[\cosh(\beta)-1\right]}{\beta\sinh(\beta)}$$

(Eq. D.6-13)

The complete solution is now written as:

$$T_{gas} = T_{surface}(y) + \frac{\Delta T_{surface}}{\beta}\left[\frac{\left[\cosh(\beta)-1\right]}{\sinh(\beta)}\cosh\left(\beta\,\frac{y}{L}\right) - \sinh\left(\beta\,\frac{y}{L}\right)\right]$$

$$\text{where}\quad T_{surface}(y) = T0_{surface} + \Delta T_{surface}\,\frac{y}{L};\quad \beta = L\sqrt{\frac{P_{surface}\ hc_{surface}}{k_{eff}\ Ac}}$$

(Eq. D.6-14

An analytic solution for a simplification of the vapor dispersion equations is found in a similar manner. The mass dispersion equations solved in the full problem are (Equation 6.3-16):

$$Ac_{in}\,\frac{d}{dy}m_{y_in} = P_{wp}\ m_{wp} + P_{ds}\ m_{ds_in} + P_{invert}\ m_{invert}$$

$$Ac_{out}\,\frac{d}{dy}m_{y_out} = P_{wall}\ m_{wall} + P_{ds}\ m_{ds_out}$$

where

$Ac = \text{cross} - \text{sectional area}$

$P = \text{Perimeter}$

$m_y = \text{mass flux in the y direction}$

(Eq. D.6-15)

In the simplified problem, the condensation fluxes to the waste package and the drip shield (m_{wp}, m_{ds_in}, m_{ds_out}) are set to zero, and the mass transfer coefficients at the drift wall surface and the invert surface are set to a constant (hm_{wall}, hm_{invert}). Substituting in the transport equations (Equation 6.3-18) for the axial mass flux, the simplified dispersion equations become:

$$Ac_{in}\frac{d}{dy}\left[-\rho_{total}\frac{D_{eff}}{1-X_{st_in}}\frac{d}{dy}X_{st_out}\right]=P_{invert}\ hm_{invert}\frac{\left(X_{st_invert}-X_{st_in}\right)}{1-X_{st_in}}$$

$$Ac_{out}\frac{d}{dy}\left[-\rho_{total}\frac{D_{eff}}{1-X_{st_out}}\frac{d}{dy}X_{st_out}\right]=P_{wall}\ hm_{wall}\frac{\left(X_{st_wall}-X_{st_out}\right)}{1-X_{st_out}}$$

(Eq. D.6-16)

Here, the mass fluxes at the walls (m_{invert}, m_{wall}) are written in terms of mass transfer coefficients (hm_{invert}, hm_{wall}).

For small values of the vapor mass fractions, these equations reduce to:

$$\frac{d^2}{dy^2}X_{st_out}=\frac{P_{invert}\ hm_{invert}}{Ac_{in}\ \rho_{total}D_{eff}}\left(X_{st_invert}-X_{st_in}\right)$$

$$\frac{d^2}{dy^2}X_{st_out}=\frac{P_{wall}\ hm_{wall}}{Ac_{out}\ \rho_{total}D_{eff}}\left(X_{st_wall}-X_{st_out}\right)$$

(Eq. D.6-17)

These simplified mass dispersion equations are of the same form as the simplified energy dispersion equations (Equation D.4-2). The solution is the same when the surface vapor mass fraction varies linearly in y.

$$X_{st}=X_{surface}(y)+\Delta X_{surface}\left[\left(\frac{\beta\cosh(\beta)-1}{\beta\sinh(\beta)}\right)\cosh\left(\beta\frac{y}{L}\right)-\sinh\left(\beta\frac{y}{L}\right)\right]$$

where $X_{surface}(y)=X0_{surface}+\Delta X_{surface}\frac{y}{L}$; $\beta=L\sqrt{\frac{P_{surface}\ hm_{surface}}{\rho_{total}\ Ac\ D_{eff}}}$

(Eq. D.6-18)

The simplified problem is implemented in the Mathcad calculation (DTN : SN0408T0509903.007) by performing the following steps:

1. The Mathcad file containing the heat and mass transfer correlations (**Correlations2.mcd**) is replaced by a file that contains constant heat and mass transfer coefficients (**Test Correlations.mcd**). In this file, the heat and mass transfer coefficients for the drip shield and the waste package are set to zero. Heat and mass transfer coefficients to the invert and drift wall are set to a constant value. The correlations Mathcad file (**Correlations2.mcd**) is an inserted reference in **Solution Algorithm.mcd**. For the current test calculation, this inserted reference was replaced with the **Test Correlations.mcd** file and saved as **Solution Algorithm Test Version.mcd**.

2. The specific heat of steam is set to zero in **Test Correlations.mcd**.

3. The simplified mass dispersion equation requires that the steam mass fraction be small. This is achieved by setting T0surface to 279.9 K.

4. The simplified mass dispersion equation requires that the steam mass fraction at the surface (invert, drift wall) be linear. The relationship between the steam mass fraction and the temperature is nonlinear. The requirement is met by setting the end-to-end temperature difference along the wall (ΔTsurface) to 0.2 K. Over this temperature range, the vapor mass fraction profile at the wall will be nearly linear.

5. The node spacing from Drift Choice #5 is used in the test problem. Because a node length of 5.00 m is used as an indicator of a region without drip shields, all of the node lengths in Drift Choice #5 are lengthened by 10^{-6}m

6. The waste package powers are set to zero.

7. The heat transfer coefficient to the drift wall and the invert is chosen so that the convective heat loss from the invert is small. As a result, the invert temperature profile computed by the differencing technique will be nearly identical to the specified wall temperature profile.

The finite difference calculations are compared to the analytic solutions in Figure D6-1. There is no distinguishable difference between the two. The finite difference calculation is verified.

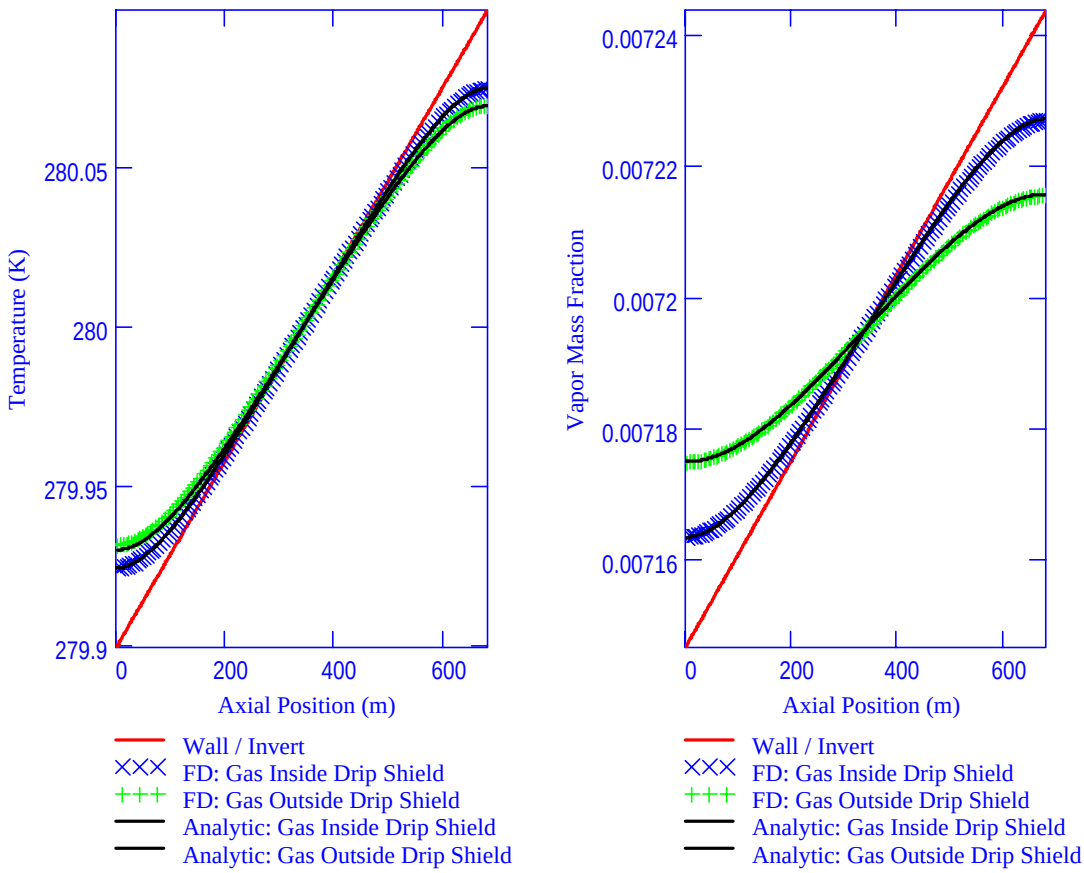

DTN : SN0408T0509903.007; file TOC.mcd; hyperlink 6.4.5, Verification of the Solution Algorithm.

NOTE: Left: temperature; Right: vapor mass fraction.

Figure D.6-1. Comparison of Analytic and Finite Difference Solutions

D.7 CALCULATION FILES

The files containing the calculations for the in-drift condensation model (Appendix E) are listed in the following tables. Table D.7-1 lists the calculation and documentation files that are common to all of the calculations documented in this report. The table of contents file (TOC.mcd) contains hyperlinks to the other files. Each file contains documentation describing the component of the calculation contained by that file. The linked Mathcad files serve as a descriptive document as well as a set of calculations files.

When the Mathcad files are cited as the source of specific figures and tables in this document, the descriptive location utilizes the hyperlink. First the DTN number of the Mathcad files is cited (DTN : SN0408T0509903.007). Then the table of contents file is cited (file TOC.mcd). Finally the appropriate hyperlink number and title is cited (for example hyperlink 7.1.7 Calculated Results for Drift Choice #7). "Clicking" on the cited hyperlink in TOC.mcd will take the reader to the appropriate Mathcad file containing the desired calculation, figure, or table.

Table D.7-1. Common Documentation and Calculation Files

	Size (KB)	Date	Sections of Report
1. MS WORD FILES			
References.doc	68	8/9/2004	text
2. MATHCAD FILES			
Beginnings.mcd	2307	8/9/2004	text
Calculation Plots.mcd	16	8/9/2004	text
Calculation Results2.mcd	1909	8/9/2004	6.3.7
Correlations2.mcd	1015	8/9/2004	6.3.5.1.3
Differencing Test.mcd	503	8/9/2004	Appendix D.6
Dispersion Formulation.mcd	740	8/9/2004	6.3.5.1.2
Evaporation Limits.mcd	915	8/9/2004	6.3.5.1.4
FLUENT Results.mcd	41	8/9/2004	6.3.5.1.2
Fluid Properties.mcd	322	8/9/2004	4.1.3 & 6.3.5.2.8 & 6.3.5.2.9
Repository Description LA 2.mcd	3194	8/9/2004	4.1.3 & 6.3.5.2
Repository Temperature Field 3.mcd	884	8/9/2004	6.3.5.1.1
Solution Algorithm Test Version.mcd	2072	8/9/2004	Appendix D.6
Solution Algorithm.mcd	2071	8/9/2004	Appendix D.5
Test Corelations.mcd	23	8/9/2004	Appendix D.6
TOC.mcd	374	8/9/2004	table of contents (hyperlinked)
2D Comparison.mcd	732	8/9/2004	Appendix J

Tables D.7-2 through D.7-5 list the files that contain the calculation results for four parameter variations addressed by the analysis:

- Table D.7-2: Ventilated drip shield with high invert transport
- Table D.7-3: Ventilated drip shield with low invert transport
- Table D.7-4: Unventilated drip shield with high invert transport
- Table D.7-5: Unventilated drip shield with low invert transport

Each parameter variation is located in the subdirectory identified in the table.

Each subdirectory contains seven calculation files having file names of the form "Choice#X.mcd," where "X" is the number of the drift choice. These files are linked to the "driver" files listed in Table D.7-1. Time, percolation rates, and axial dispersion are varied in each of these files. The results of the calculations are contained in embedded Excel workbooks. The results can be verified by the viewer by "enabling" the equation that was used to generate the results. Verification is performed by comparing the results of the calculation to the numbers contained in the Excel spreadsheet. Additionally, the graph of the convergence progression that appears at the end of the calculation can be compared to the picture of this graph that was stored at the time of the original calculation.

Each subdirectory also contains seven calculation files having file names of the form "Choice#Figures.mcd," where # is the number of the drift choice. These files contain plots of the results that are stored in the "Choice#Figures.mcd" files. In addition, the "Choice#Figures.mcd" files contain summary tables of condensation rates for individual drifts at individual times. These tables are saved as MS Excel files to the subdirectory "DIRs." The names of these Excel files contain the drift choice and the time (e.g., Choice#1_1000yrs.xls, etc.).

The Mathcad files named "Summary Tables.mcd" are linked to all of the Excel files in the underlying subdirectory. These four "Summary Tables" files assemble composite tables for condensation on the drift walls, condensation under the drip shield, and axial transport of energy. These composite tables are presented in Section 6.3.7 of this report.

Table D.7-2. Calculation Files: Well Ventilated Drip Shield; High Invert Transport

Subdirectory: Mixed_HighInvertTransport	**Size (KB)**	**Date**	**Sections of Report**
Choice 1.mcd	1483	8/9/2004	electronic file only
Choice 1Figures.mcd	1578	8/9/2004	electronic file only
Choice 2.mcd	1518	8/9/2004	electronic file only
Choice 2Figures.mcd	1582	8/9/2004	electronic file only
Choice 3.mcd	1813	8/9/2004	electronic file only
Choice 3Figures.mcd	2019	8/9/2004	electronic file only
Choice 4.mcd	1501	8/9/2004	electronic file only
Choice 4Figures.mcd	1582	8/9/2004	electronic file only
Choice 5.mcd	1508	8/9/2004	electronic file only
Choice 5Figures.mcd	1589	8/9/2004	electronic file only
Choice 6.mcd	1355	8/9/2004	electronic file only
Choice 6Figures.mcd	1508	8/9/2004	electronic file only
Choice 7.mcd	1663	8/9/2004	electronic file only
Choice 7Figures.mcd	1726	8/9/2004	6.3.7.2; Appendix E.1
Summary Tables.mcd	702	8/9/2004	Table 6.3.7-2, Table 6.3.7-3, Table 6.3.7-10, Table 6.3.7-11
Subdirectory: Mixed_HighInvertTransport\DTNs			
Choice#1_1000yrs.xls	240	8/9/2004	electronic file only
Choice#1_3000yrs.xls	243	8/9/2004	electronic file only
Choice#1_10000yrs.xls	243	8/9/2004	electronic file only
Choice#2_1000yrs.xls	243	8/9/2004	electronic file only
Choice#2_3000yrs.xls	244	8/9/2004	electronic file only
Choice#2_10000yrs.xls	243	8/9/2004	electronic file only
Choice#3_300yrs.xls	203	8/9/2004	electronic file only
Choice#3_1000yrs.xls	201	8/9/2004	electronic file only
Choice#3_3000yrs.xls	201	8/9/2004	electronic file only
Choice#3_10000yrs.xls	203	8/9/2004	electronic file only
Choice#4_1000yrs.xls	243	8/9/2004	electronic file only
Choice#4_3000yrs.xls	243	8/9/2004	electronic file only
Choice#4_10000yrs.xls	243	8/9/2004	electronic file only
Choice#5_1000yrs.xls	248	8/9/2004	electronic file only
Choice#5_3000yrs.xls	247	8/9/2004	electronic file only
Choice#5_10000yrs.xls	247	8/9/2004	electronic file only
Choice#6_1000yrs.xls	198	8/9/2004	electronic file only
Choice#6_3000yrs.xls	198	8/9/2004	electronic file only
Choice#6_10000yrs.xls	198	8/9/2004	electronic file only
Choice#7_1000yrs.xls	290	8/9/2004	electronic file only
Choice#7_3000yrs.xls	292	8/9/2004	electronic file only
Choice#7_10000yrs.xls	290	8/9/2004	electronic file only

Table D.7-3. Calculation Files: Well Ventilated Drip Shield; Low Invert Transport

Subdirectory: Mixed_LowInvertTransport	Size (KB)	Date	Sections of Report
Choice 1.mcd	1642	8/9/2004	electronic file only
Choice 1Figures.mcd	1578	8/9/2004	electronic file only
Choice 2.mcd	1549	8/9/2004	electronic file only
Choice 2Figures.mcd	1582	8/9/2004	electronic file only
Choice 3.mcd	2016	8/9/2004	electronic file only
Choice 3Figures.mcd	2019	8/9/2004	electronic file only
Choice 4.mcd	1503	8/9/2004	electronic file only
Choice 4Figures.mcd	1582	8/9/2004	electronic file only
Choice 5.mcd	1503	8/9/2004	electronic file only
Choice 5Figures.mcd	1590	8/9/2004	electronic file only
Choice 6.mcd	1453	8/9/2004	electronic file only
Choice 6Figures.mcd	1508	8/9/2004	electronic file only
Choice 7.mcd	1711	8/9/2004	electronic file only
Choice 7Figures.mcd	1731	8/9/2004	6.3.7.2; Appendix E.2
Summary Tables.mcd	701	8/9/2004	Table 6.3.7-1, Table 6.3.7-8, Table 6.3.7-9
Subdirectory: Mixed_LowInvertTransport\DTNs			
Choice#1_1000yrs.xls	240	8/9/2004	electronic file only
Choice#1_3000yrs.xls	243	8/9/2004	electronic file only
Choice#1_10000yrs.xls	243	8/9/2004	electronic file only
Choice#2_1000yrs.xls	243	8/9/2004	electronic file only
Choice#2_3000yrs.xls	245	8/9/2004	electronic file only
Choice#2_10000yrs.xls	243	8/9/2004	electronic file only
Choice#3_300yrs.xls	203	8/9/2004	electronic file only
Choice#3_1000yrs.xls	201	8/9/2004	electronic file only
Choice#3_3000yrs.xls	201	8/9/2004	electronic file only
Choice#3_10000yrs.xls	203	8/9/2004	electronic file only
Choice#4_1000yrs.xls	243	8/9/2004	electronic file only
Choice#4_3000yrs.xls	243	8/9/2004	electronic file only
Choice#4_10000yrs.xls	243	8/9/2004	electronic file only
Choice#5_1000yrs.xls	248	8/9/2004	electronic file only
Choice#5_3000yrs.xls	247	8/9/2004	electronic file only
Choice#5_10000yrs.xls	247	8/9/2004	electronic file only
Choice#6_1000yrs.xls	198	8/9/2004	electronic file only
Choice#6_3000yrs.xls	198	8/9/2004	electronic file only
Choice#6_10000yrs.xls	198	8/9/2004	electronic file only
Choice#7_1000yrs.xls	290	8/9/2004	electronic file only
Choice#7_3000yrs.xls	292	8/9/2004	electronic file only
Choice#7_10000yrs.xls	290	8/9/2004	electronic file only

Table D.7-4. Calculation Files: Unventilated Drip Shield; High Invert Transport

Subdirectory: Unmixed_HighInvertTransport	Size (KB)	Date	Sections of Report
Choice 1.mcd	1578	8/9/2004	electronic file only
Choice 1Figures.mcd	1580	8/9/2004	electronic file only
Choice 2.mcd	1546	8/9/2004	electronic file only
Choice 2Figures.mcd	1583	8/9/2004	electronic file only
Choice 3.mcd	1831	8/9/2004	electronic file only
Choice 3Figures.mcd	2019	8/9/2004	electronic file only
Choice 4.mcd	1541	8/9/2004	electronic file only
Choice 4Figures.mcd	1583	8/9/2004	electronic file only
Choice 5.mcd	1529	8/9/2004	electronic file only
Choice 5Figures.mcd	1591	8/9/2004	electronic file only
Choice 6.mcd	1468	8/9/2004	electronic file only
Choice 6Figures.mcd	1510	8/9/2004	electronic file only
Choice 7.mcd	1770	8/9/2004	electronic file only
Choice 7Figures.mcd	1735	8/9/2004	6.3.7.2; Appendix E.3
Summary Tables.mcd	702	8/9/2004	Table 6.3.7-2, Table 6.3.7-3, Table 6.3.7-6, Table 6.3.7-7, Table 6.3.7-14, Table 6.3.7-15
Subdirectory: Unmixed_HighInvertTransport\DTNs			
Choice#1_1000yrs.xls	241	8/9/2004	electronic file only
Choice#1_3000yrs.xls	247	8/9/2004	electronic file only
Choice#1_10000yrs.xls	250	8/9/2004	electronic file only
Choice#2_1000yrs.xls	244	8/9/2004	electronic file only
Choice#2_3000yrs.xls	248	8/9/2004	electronic file only
Choice#2_10000yrs.xls	250	8/9/2004	electronic file only
Choice#3_300yrs.xls	203	8/9/2004	electronic file only
Choice#3_1000yrs.xls	203	8/9/2004	electronic file only
Choice#3_3000yrs.xls	205	8/9/2004	electronic file only
Choice#3_10000yrs.xls	209	8/9/2004	electronic file only
Choice#4_1000yrs.xls	244	8/9/2004	electronic file only
Choice#4_3000yrs.xls	247	8/9/2004	electronic file only
Choice#4_10000yrs.xls	251	8/9/2004	electronic file only
Choice#5_1000yrs.xls	248	8/9/2004	electronic file only
Choice#5_3000yrs.xls	249	8/9/2004	electronic file only
Choice#5_10000yrs.xls	253	8/9/2004	electronic file only
Choice#6_1000yrs.xls	198	8/9/2004	electronic file only
Choice#6_3000yrs.xls	201	8/9/2004	electronic file only
Choice#6_10000yrs.xls	203	8/9/2004	electronic file only
Choice#7_1000yrs.xls	291	8/9/2004	electronic file only
Choice#7_3000yrs.xls	296	8/9/2004	electronic file only
Choice#7_10000yrs.xls	299	8/9/2004	electronic file only

Table D.7-5 Calculation Files: Unventilated Drip Shield; Low Invert Transport

Subdirectory: Unmixed_LowInvertTransport	Size (KB)	Date	Sections of Report
Choice 1.mcd	1581	8/9/2004	electronic file only
Choice 1Figures.mcd	1578	8/9/2004	electronic file only
Choice 2.mcd	1553	8/9/2004	electronic file only
Choice 2Figures.mcd	1582	8/9/2004	electronic file only
Choice 3.mcd	1851	8/9/2004	electronic file only
Choice 3Figures.mcd	2017	8/9/2004	electronic file only
Choice 4.mcd	1530	8/9/2004	electronic file only
Choice 4Figures.mcd	1582	8/9/2004	electronic file only
Choice 5.mcd	1685	8/9/2004	electronic file only
Choice 5Figures.mcd	1590	8/9/2004	electronic file only
Choice 6.mcd	1386	8/9/2004	electronic file only
Choice 6Figures.mcd	1508	8/9/2004	electronic file only
Choice 7.mcd	1657	8/9/2004	electronic file only
Choice 7Figures.mcd	1726	8/9/2004	6.3.7.2; Appendix E.4
Summary Tables.mcd	699	8/9/2004	Table 6.3.7-4, Table 6.3.7-12, Table 6.3.7-13
Subdirectory: Unmixed_LowInvertTransport\DTNs			
Choice#1_1000yrs.xls	240	8/9/2004	electronic file only
Choice#1_3000yrs.xls	243	8/9/2004	electronic file only
Choice#1_10000yrs.xls	243	8/9/2004	electronic file only
Choice#2_1000yrs.xls	243	8/9/2004	electronic file only
Choice#2_3000yrs.xls	245	8/9/2004	electronic file only
Choice#2_10000yrs.xls	243	8/9/2004	electronic file only
Choice#3_300yrs.xls	203	8/9/2004	electronic file only
Choice#3_1000yrs.xls	201	8/9/2004	electronic file only
Choice#3_3000yrs.xls	201	8/9/2004	electronic file only
Choice#3_10000yrs.xls	203	8/9/2004	electronic file only
Choice#4_1000yrs.xls	243	8/9/2004	electronic file only
Choice#4_3000yrs.xls	243	8/9/2004	electronic file only
Choice#4_10000yrs.xls	243	8/9/2004	electronic file only
Choice#5_1000yrs.xls	248	8/9/2004	electronic file only
Choice#5_3000yrs.xls	247	8/9/2004	electronic file only
Choice#5_10000yrs.xls	247	8/9/2004	electronic file only
Choice#6_1000yrs.xls	198	8/9/2004	electronic file only
Choice#6_3000yrs.xls	198	8/9/2004	electronic file only
Choice#6_10000yrs.xls	198	8/9/2004	electronic file only
Choice#7_1000yrs.xls	290	8/9/2004	electronic file only
Choice#7_3000yrs.xls	292	8/9/2004	electronic file only
Choice#7_10000yrs.xls	290	8/9/2004	electronic file only

APPENDIX E

CALCULATION PLOTS FOR DRIFT CHOICE #7

Calculated condensation rates and locations are graphed in this Appendix, Sections E.1 through E.4. Each section contains a permutation of drip shield ventilation and invert transport level:

Section E.1:	ventilated drip shield; low invert transport (Figures E.1-1 through E.1-7; Tables E.1-1 thru E.1-3)
Section E.2:	ventilated drip shield; high invert transport (Figures E.2-1 through E.2-10; Tables E.2-1 thru E.2-3)
Section E.3:	unventilated drip shield; low invert transport (Figures E.3-1 through E.3-7; Tables E.3-1 thru E.3-3)
Section E.4:	unventilated drip shield; high invert transport (Figures E.4-1 through E.4-16; Tables E.4-1 thru E.4-3)

Each of these sections contains seven subsections that contain all the calculations for a particular drift choice. All of these sections contain the same sequence of plots. The plots contained in Section E.4 are described here to guide the reader through the information that all four of the following sections contain.

Figure E.4-1 shows the vapor mass fraction of the air in the drift for the three percolation rates at 1,000 years for the low axial dispersion bound of the unventilated drip shield high invert transport case. The top plot is the air under the drip shield; the bottom plot is the air outside the drip shield. The red dashed lines correspond to the mean percolation rate. The top and bottom of the range bars correspond to the upper and lower values of percolation, respectively. The solid blue line in the top plot is the equilibrium vapor mass fraction associated with the drip shield; the solid blue line in bottom plot is the vapor mass fraction at the wall. Vertical dashed lines indicate the limits of the waste storage region. The access turnout and the exhaust standoff lie outside these dashed lines. The stepped variation in the equilibrium vapor mass fraction of the drip shield (solid blue line in the top plot) reflects the local variation in drip shield temperature. Drip shield sections above hotter waste packages are hotter than those above cooler waste packages.

Condensation on a surface is possible only when the vapor pressure in the gas is greater than the equilibrium vapor pressure on the condensing surface. In the top plot of Figure E.4-1, no condensation on the underside of the drip shield is possible in the center of the storage drift. However, on either side of the center region, the equilibrium vapor pressure of the drip shield above colder waste packages dips to the vapor pressure in the gas for the high percolation rate. It is in this region where condensation on the underside of the drip shield takes place.

The same observations hold for the drift wall on the outside of the drip shield (bottom plot). The vapor pressure in the gas outside the drip shield is lower than the vapor pressure at the drift surface in the center; in this region water is evaporating from the drift wall. On either side of the center, the vapor pressure in the gas is very close to that at the drift wall. Water is evaporating in a part of this region and condensing in a different part; this plot lacks sufficient resolution to distinguish between these two parts.

Figure E.4-2 shows the locations and magnitude of condensation on the drift wall within the waste storage region at 1,000 years for the low dispersion case. Condensation in the access turnout and exhaust standoff has been eliminated from these plots in order to highlight the condensation inside of the storage region. The top plot corresponds to the low percolation rate;

the middle corresponds to the mean percolation rate; the bottom corresponds to the upper percolation rate. The plots indicate that, for this case, condensation on the drift wall is confined to a region near, but not contiguous to, the access turnout and the exhaust standoff.

Figure E.4-3 shows the condensation rate on the underside of the drip shield at 1,000 years for the high dispersion bound. Each node in the calculation corresponds to a particular waste package at a particular location. Hence, the condensation rates computed in this calculation are specific to individual waste packages. The condensation rate plotted is not a flux, but the integral amount that each package, or section of drip shield corresponding to a package, experiences (in kg/yr).

The plot contains the condensation rates in the form of range bars with symbols that correspond to the waste package types indicated in the legend. The three markers on each range bar correspond to the low, mean, and high percolation rates. The lowest marked value on the range bar corresponds to the lower percolation limit, the middle marked value on the range bar corresponds to the mean percolation rate, and the highest marked value on the range bar corresponds to the upper percolation rate.

In many locations, the condensation rate is zero for all percolation rates. In these locations, the range bar collapses to a single point on the axis. The **left-most** range bar of nonzero size in Figure E.4-3 (at about –300 m) displays two solid blue circles corresponding to a 5-HLW Long waste package. The top marker indicates that the condensation rate corresponding to the upper percolation bound is about 200 kg/yr. The marker below it (connected by the solid vertical line) indicates that the condensation rate corresponding to the mean percolation rate is about 39 kg/yr. The third marker lies on the zero line, indicating that no condensation takes place at this waste package for the low percolation bound.

The calculation allows condensate to form directly on the waste packages. In cases where this occurs, it is graphed on a plots labeled “Condensation on Waste Packages.” In this particular case (unventilated drip shield, high invert transport, 1,000 years, low axial dispersion bound), the rates of condensation directly on the waste packages are all zero. Whenever the condensation rates are uniformly zero for all waste packages at all percolation rates, the graph is not shown.

The next pair of graphs display the vapor mass fraction profiles (Figure E.4-4) and the condensation rate on the underside of the drip shield (Figure E.4-5) for the high axial dispersion bound at the same time (1,000 years). Neither the plot of condensation on the outside of the drip shield nor the plot of condensation directly on the waste package are shown because both rates are uniformly zero for all percolation rates.

At the end of the plots for 1,000 years is a summary table (Table E.4-1) for this time. The first three columns of the table sort the calculated results according to axial dispersion bound (low, high), percolation level (low, mean, upper), and location (underside of the drip shield, directly on the waste packages). The number of waste packages that experience condensation and the average rate of condensation are tabulated for each waste package type. The plots for low and high axial dispersion along with the summary table are then repeated for the analyzed times of 3,000 years and 10,000 years.

E.1 VENTILATED DRIP SHIELD; LOW INVERT TRANSPORT

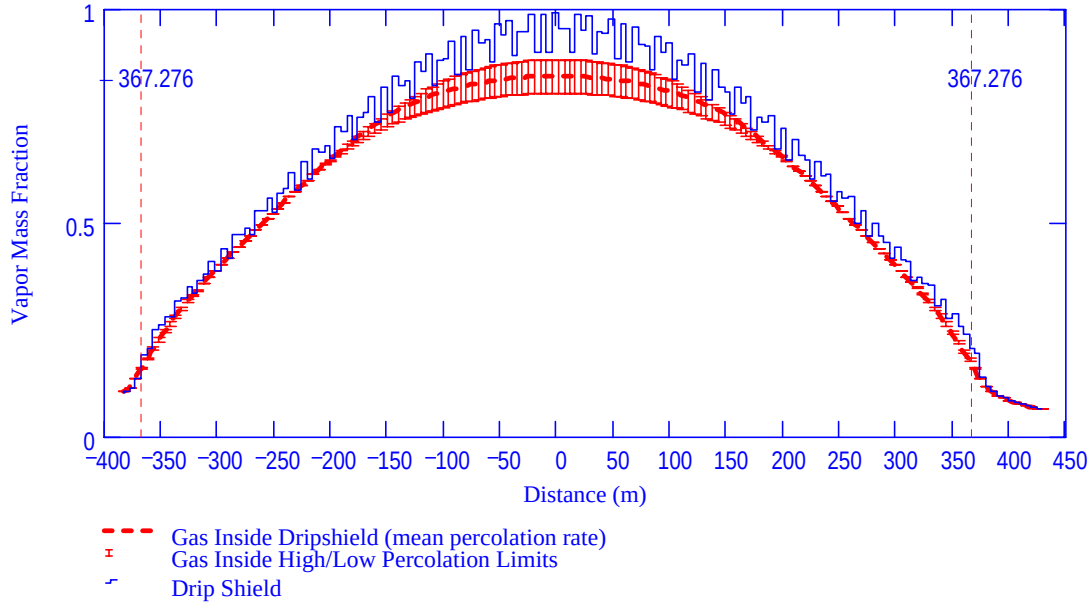

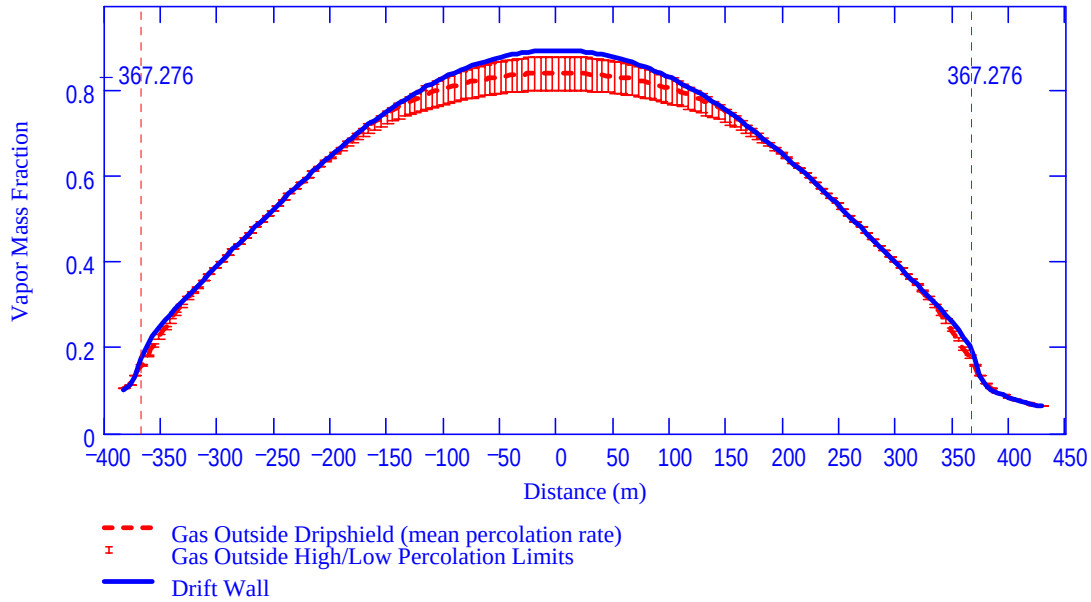

DTN: SN0408T0509903.007; file TOC.mcd; hyperlink 7.1.7, Calculated Results for Drift Choice #7.

NOTE: Top: inside drip shield; Bottom: outside drip shield.

Figure E.1-1. Vapor Mass Fractions in Gas: Choice #7, 1,000 Years, Low Dispersion Bound

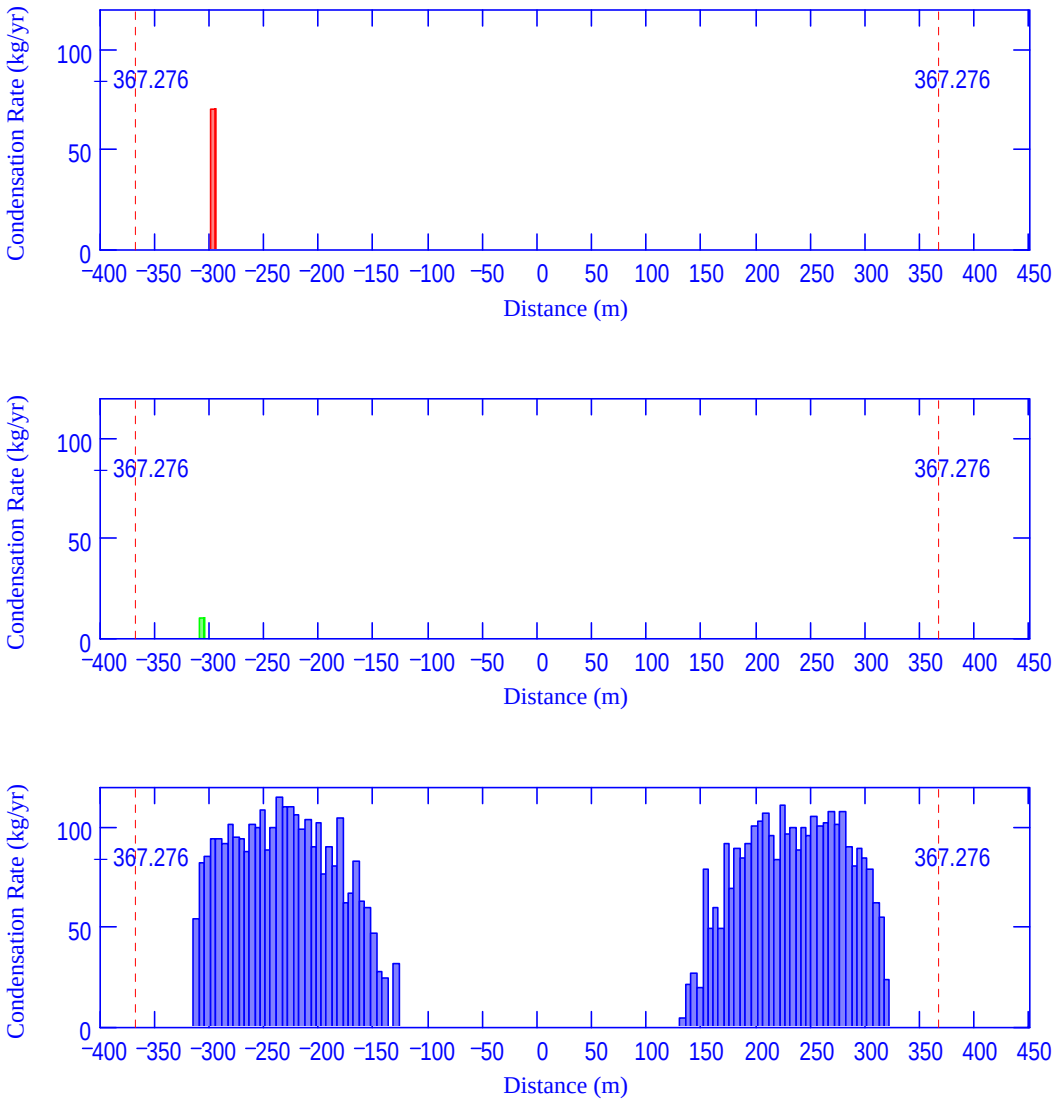

DTN: SN0408T0509903.007; file TOC.mcd; hyperlink 7.1.7, Calculated Results for Drift Choice #7.

NOTE: Low (top), Mean (middle), Upper (bottom).

Figure E.1-2. Condensation Rate on Drift Wall: Choice #7, 1,000 Years, Low Dispersion Bound Percolation Levels

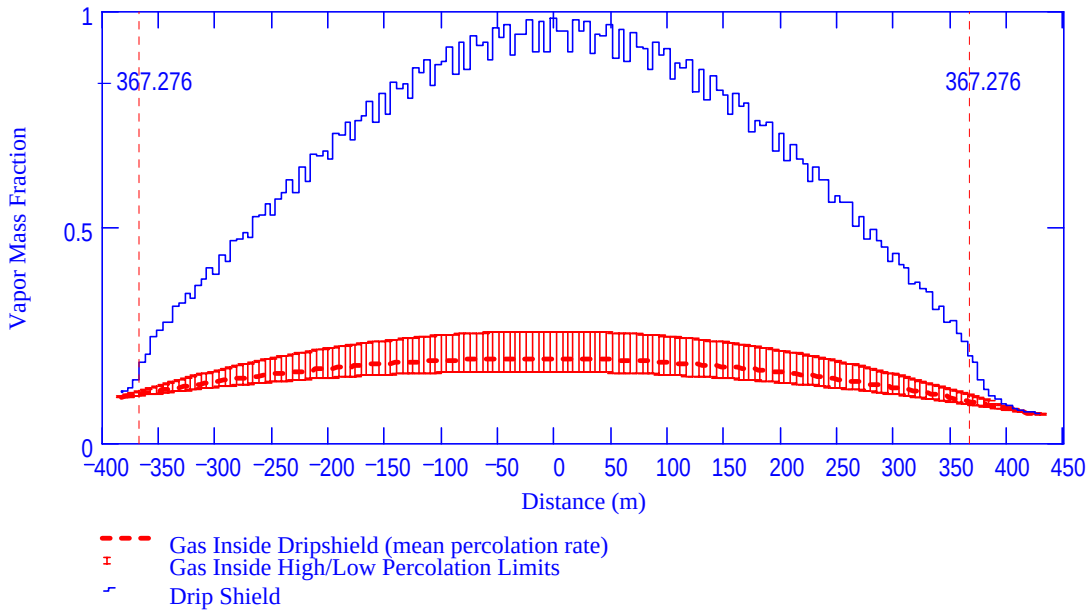

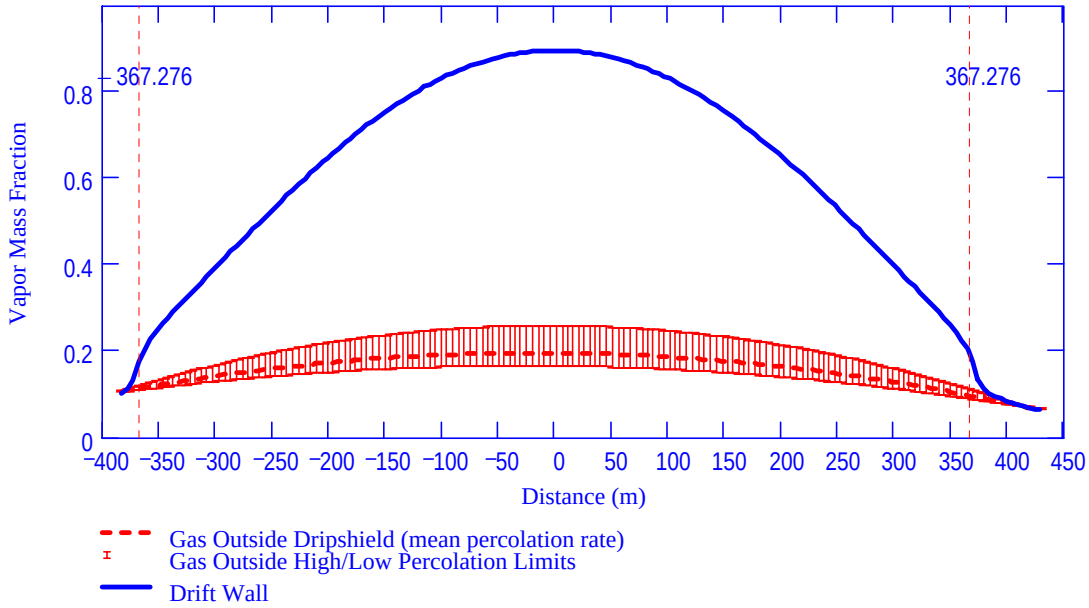

DTN: SN0408T0509903.007; file TOC.mcd; hyperlink 7.1.7, Calculated Results for Drift Choice #7.

NOTE: Top: inside drip shield; Bottom: outside drip shield.

Figure E.1-3. Vapor Mass Fractions in Gas: Choice #7, 1,000 Years, High Dispersion Bound

Table E.1-1 Summary of Condensation Rates: Choice #7, 1,000 Years

Dispersion Bound	Percolation Level	Condensation Location		21-PWR AP	5-HLW Long	21-PWR AP (Hot)	4-BWR AP	4-BWR AP (Adjusted)	5-HLW Short
	Low	Underside of	# WP's	0	0	0	0	0	0
		Drip Shield	Avg. Rate	0	0	0	0	0	0
		On Waste	# WP's	0	0	0	0	0	0
		Package	Avg. Rate	0	0	0	0	0	0
	Mean	Underside of	# WP's	0	0	0	0	0	0
Low		Drip Shield	Avg. Rate	0	0.0	0	0	0	0.0
		On Waste	# WP's	0	0	0	0	0	0
		Package	Avg. Rate	0	0	0	0	0	0
	Upper	Underside of	# WP's	0	0	0	0	0	0
		Drip Shield	Avg. Rate	0	0.0	0	0	0	0.0
		On Waste	# WP's	0	0	0	0	0	0
		Package	Avg. Rate	0	0	0	0	0	0
	Low	Underside of	# WP's	0	0	0	0	0	0
		Drip Shield	Avg. Rate	0	0	0	0	0	0
		On Waste	# WP's	0	0	0	0	0	0
		Package	Avg. Rate	0	0	0	0	0	0
	Mean	Underside of	# WP's	0	0	0	0	0	0
High		Drip Shield	Avg. Rate	0	0	0	0	0	0
		On Waste	# WP's	0	0	0	0	0	0
		Package	Avg. Rate	0	0	0	0	0	0
	Upper	Underside of	# WP's	0	0	0	0	0	0
		Drip Shield	Avg. Rate	0	0.0	0	0	0	0.0
		OnWaste	# WP's	0	0	0	0	0	0
		Package	Avg. Rate	0	0	0	0	0	0

DTN : SN0408T0509903.007; file TOC.mcd; hyperlink 7.1.7 Calculated Results for Drift Choice #7

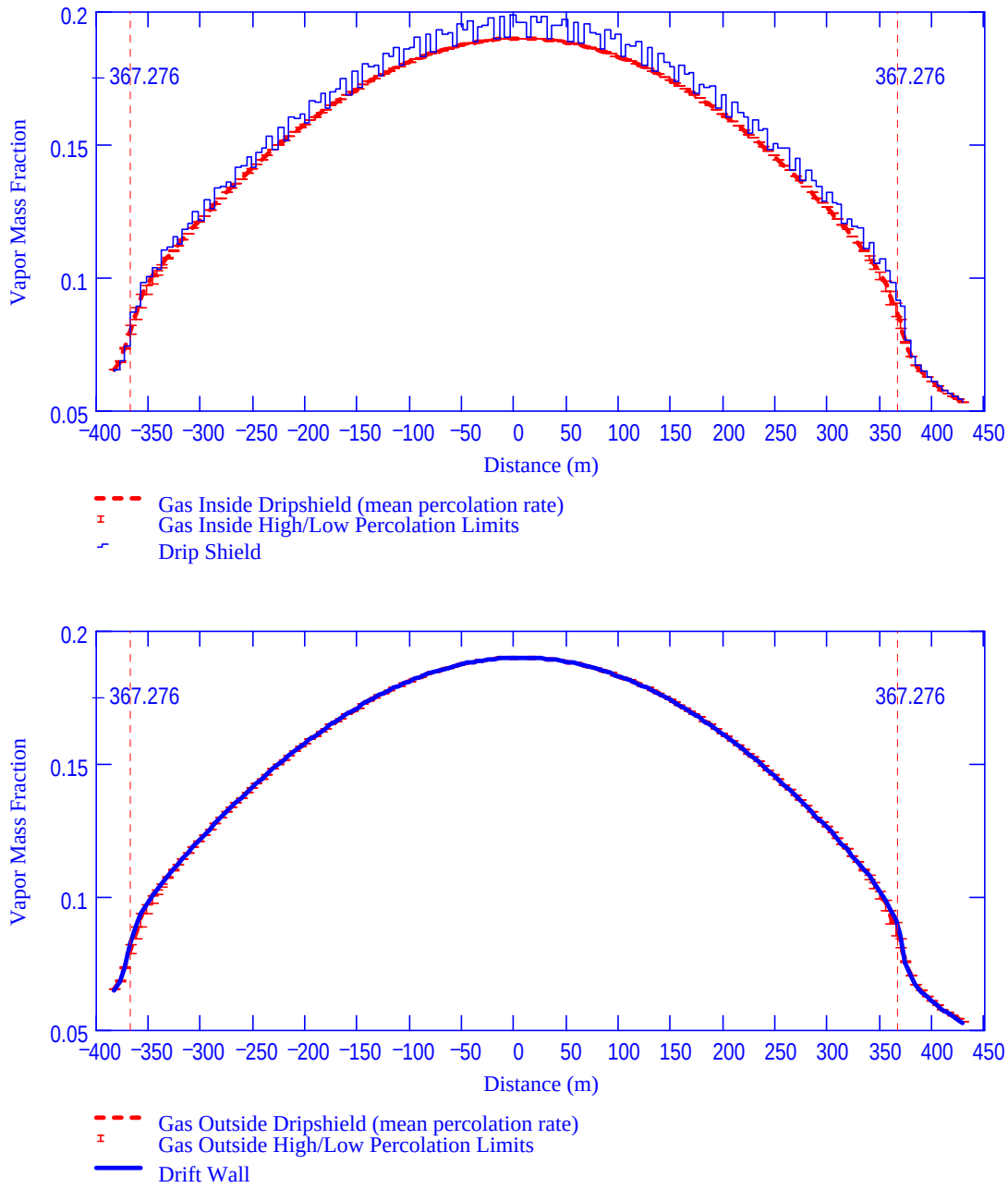

DTN: SN0408T0509903.007; file TOC.mcd; hyperlink 7.1.7, Calculated Results for Drift Choice #7.

NOTE: Top: inside drip shield; Bottom: outside drip shield.

Figure E.1-4. Vapor Mass Fractions in Gas: Choice #7, 3,000 Years, Low Dispersion Bound

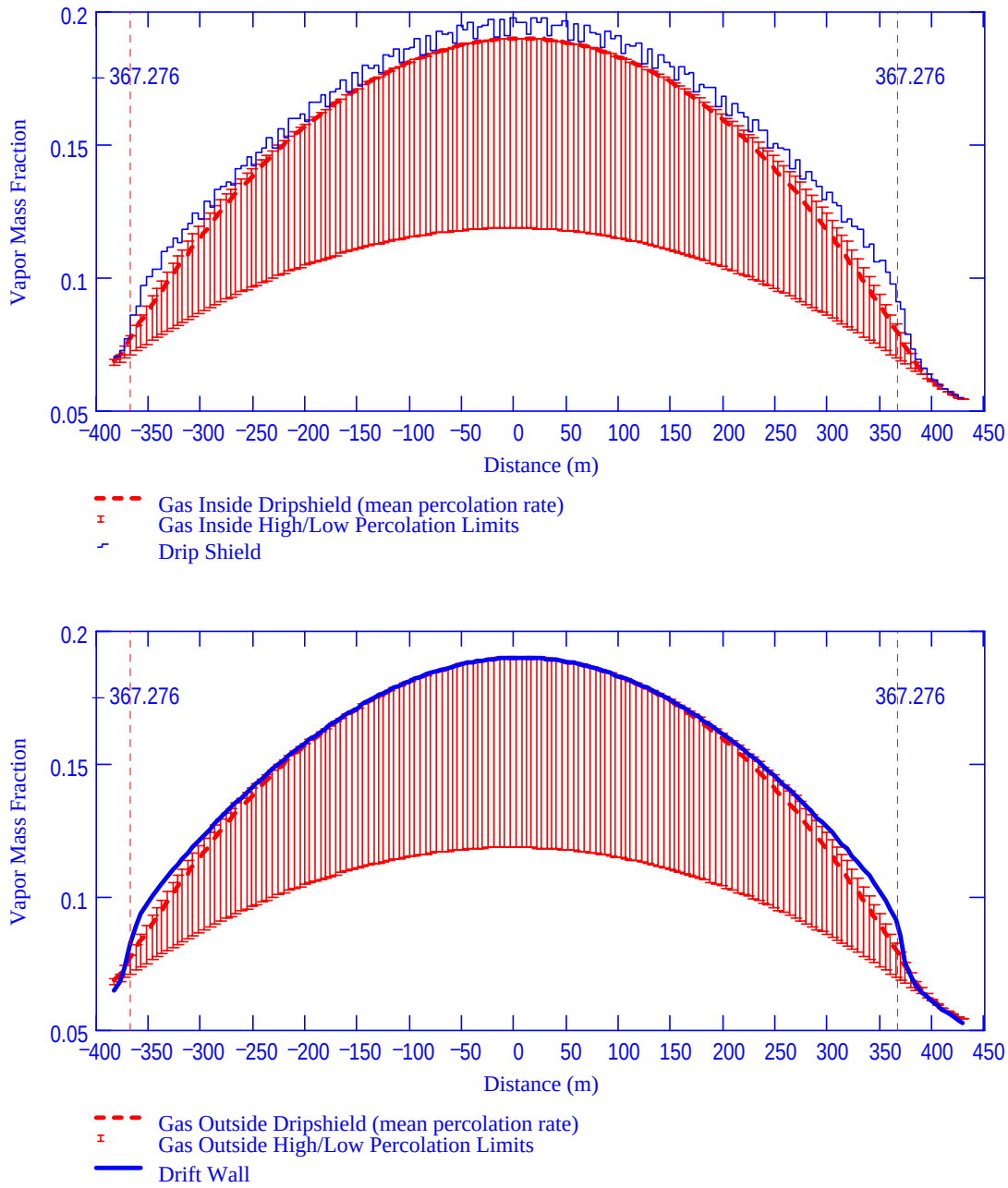

DTN: SN0408T0509903.007; file TOC.mcd; hyperlink 7.1.7, Calculated Results for Drift Choice #7.

NOTE: Top: inside drip shield; Bottom: outside drip shield.

Figure E.1-5. Vapor Mass Fractions in Gas: Choice #7, 3,000 Years, High Dispersion Bound

Table E.1-2. Summary of Condensation Rates: Choice #7, 3,000 Years

Dispersion Bound	Percolation Level	Condensation Location		21-PWR AP	5-HLW Long	21-PWR AP (Hot)	4-BWR AP	4-BWR AP (Adjusted)	5-HLW Short
	Low	Underside of	# WP's	0	0	0	0	0	0
		Drip Shield	Avg. Rate	0	0.0	0	0	0	0.0
		On Waste	# WP's	0	0	0	0	0	0
		Package	Avg. Rate	0	0	0	0	0	0
	Mean	Underside of	# WP's	0	0	0	0	0	0
Low		Drip Shield	Avg. Rate	0	0.0	0	0	0	0.0
		On Waste	# WP's	0	0	0	0	0	0
		Package	Avg. Rate	0	0	0	0	0	0
	Upper	Underside of	# WP's	0	0	0	0	0	0
		Drip Shield	Avg. Rate	0	0.0	0	0	0	0.0
		On Waste	# WP's	0	0	0	0	0	0
		Package	Avg. Rate	0	0	0	0	0	0.0
	Low	Underside of	# WP's	0	0	0	0	0	0
		Drip Shield	Avg. Rate	0	0.0	0	0	0	0.0
		On Waste	# WP's	0	0	0	0	0	0
		Package	Avg. Rate	0	0	0	0	0	0
	Mean	Underside of	# WP's	0	0	0	0	0	0
High		Drip Shield	Avg. Rate	0	0.0	0	0	0	0.0
		On Waste	# WP's	0	0	0	0	0	0
		Package	Avg. Rate	0	0	0	0	0	0
	Upper	Underside of	# WP's	0	0	0	0	0	0
		Drip Shield	Avg. Rate	0	0.0	0	0	0	0.0
		On Waste	# WP's	0	0	0	0	0	0
		Package	Avg. Rate	0	0	0	0	0	0

DTN: SN0408T0509903.007; file TOC.mcd; hyperlink 7.1.7, Calculated Results for Drift Choice #7

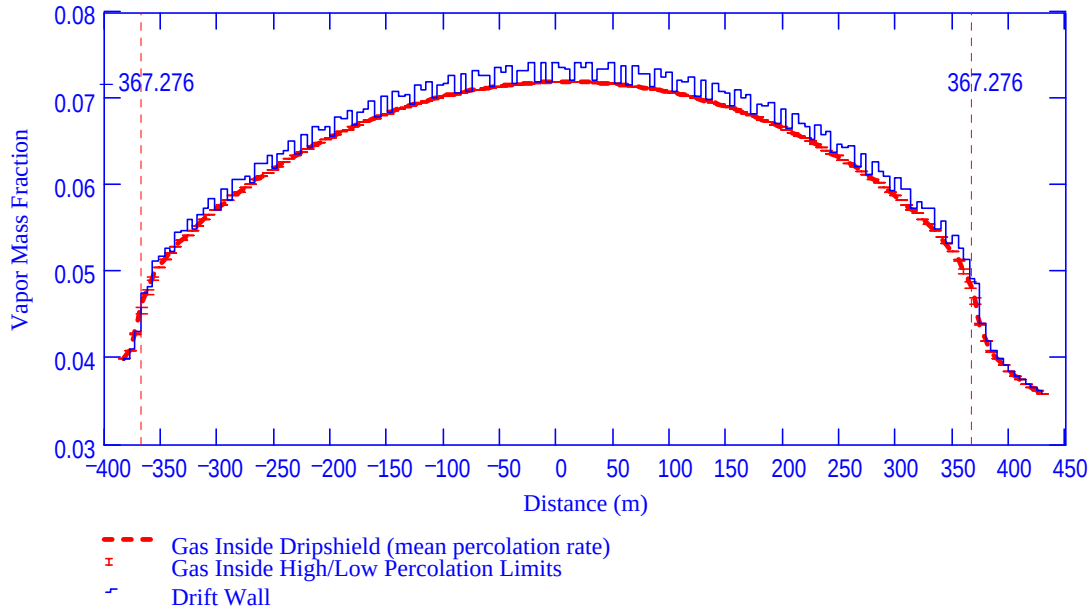

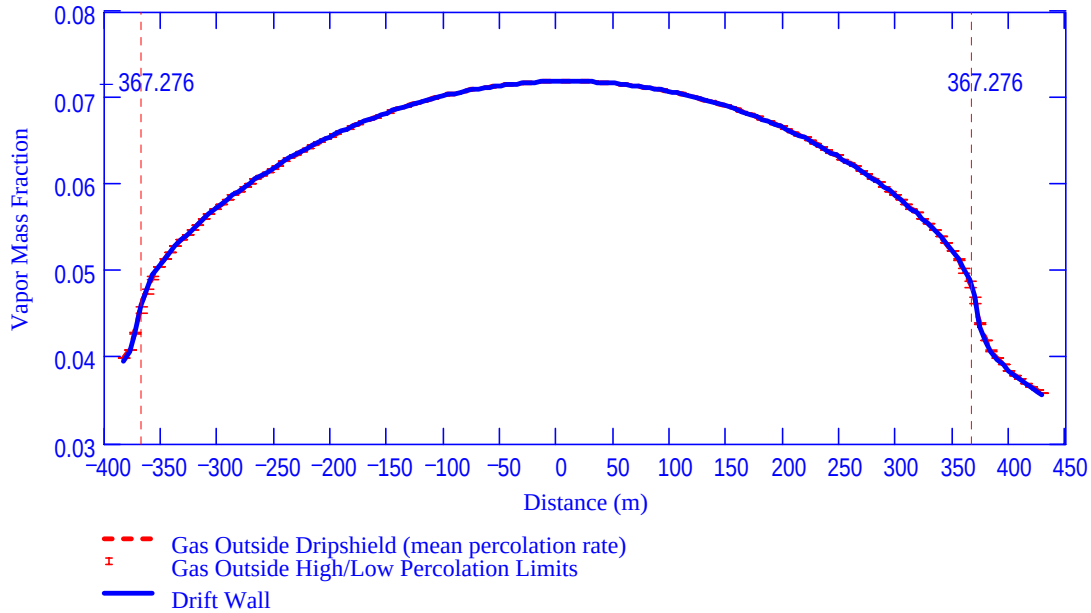

DTN : SN0408T0509903.007; file TOC.mcd; hyperlink 7.1.7, Calculated Results for Drift Choice #7.

NOTE: Top: inside drip shield; Bottom: outside drip shield.

Figure E.1-6. Vapor Mass Fractions in Gas: Choice #7, 10,000 Years, Low Dispersion Bound

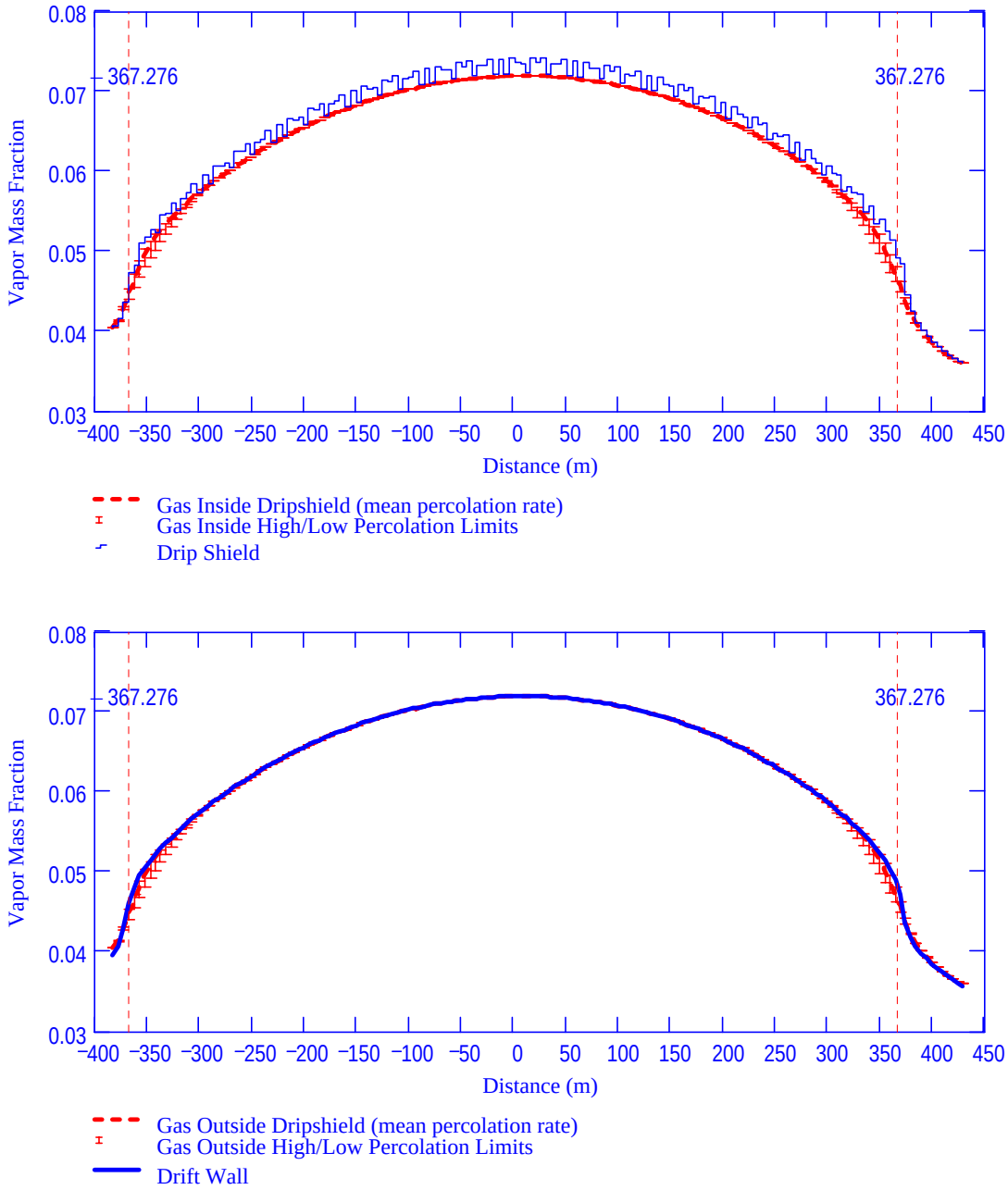

DTN: SN0408T0509903.007; file TOC.mcd; hyperlink 7.1.7, Calculated Results for Drift Choice #7.

NOTE: Top: inside drip shield; Bottom: outside drip shield.

Figure E.1-7. Vapor Mass Fractions in Gas: Choice #7, 10,000 Years, High Dispersion Bound

Table E.1-3. Summary of Condensation Rates: Choice #7, 10,000 Years

Dispersion Bound	Percolation Level	Condensation Location		21-PWR AP	5-HLW Long	21-PWR AP (Hot)	4-BWR AP	4-BWR AP (Adjusted)	5-HLW Short
	Low	Underside of	# WP's	0	0	0	0	0	0
		Drip Shield	Avg. Rate	0	0.0	0	0	0	0.0
		On Waste	# WP's	0	0	0	0	0	0
		Package	Avg. Rate	0	0	0	0	0	0
	Mean	Underside of	# WP's	0	0	0	0	0	0
Low		Drip Shield	Avg. Rate	0	0.0	0	0	0	0.0
		On Waste	# WP's	0	0	0	0	0	0
		Package	Avg. Rate	0	0	0	0	0	0
	Upper	Underside of	# WP's	0	0	0	0	0	0
		Drip Shield	Avg. Rate	0	0.0	0	0	0	0.0
		On Waste	# WP's	0	0	0	0	0	0
		Package	Avg. Rate	0	0	0	0	0	0.0
	Low	Underside of	# WP's	0	0	0	0	0	0
		Drip Shield	Avg. Rate	0	0.0	0	0	0	0.0
		On Waste	# WP's	0	0	0	0	0	0
		Package	Avg. Rate	0	0	0	0	0	0
	Mean	Underside of	# WP's	0	0	0	0	0	0
High		Drip Shield	Avg. Rate	0	0.0	0	0	0	0.0
		On Waste	# WP's	0	0	0	0	0	0
		Package	Avg. Rate	0	0	0	0	0	0
	Upper	Underside of	# WP's	0	0	0	0	0	0
		Drip Shield	Avg. Rate	0	0.0	0	0	0	0.0
		On Waste	# WP's	0	0	0	0	0	0
		Package	Avg. Rate	0	0	0	0	0	0

DTN: SN0408T0509903.007; file TOC.mcd; hyperlink 7.1.7, Calculated Results for Drift Choice #7.

E.2 VENTILATED DRIP SHIELD; HIGH INVERT TRANSPORT

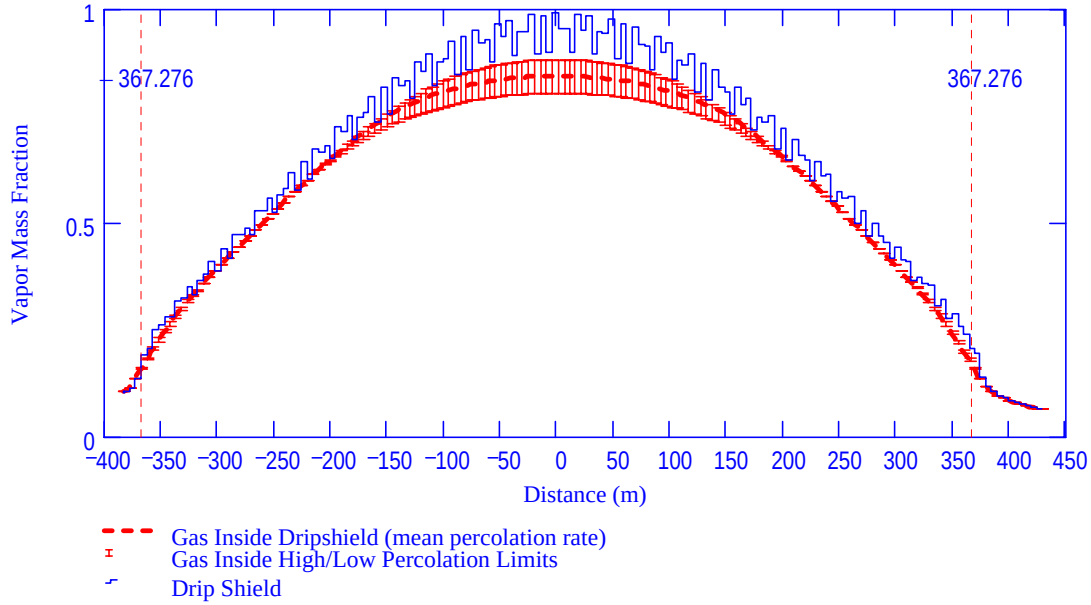

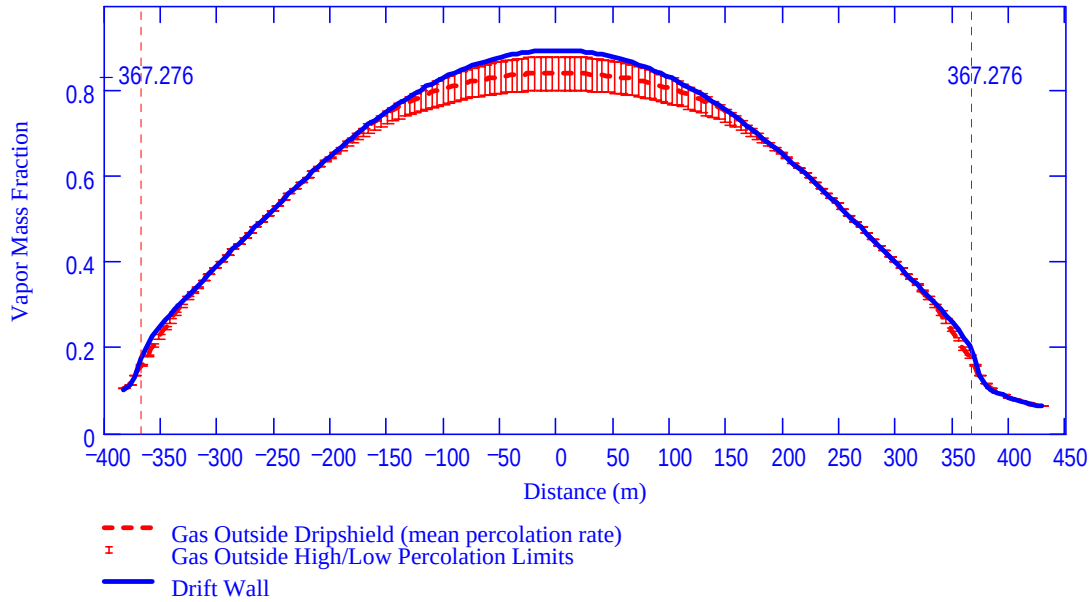

DTN: SN0408T0509903.007; file TOC.mcd; hyperlink 7.2.7, Calculated Results for Drift Choice #7.

NOTE: Top: inside drip shield; Bottom: outside drip shield.

Figure E.2-1. Vapor Mass Fractions in Gas: Choice #7, 1,000 Years, Low Dispersion Bound

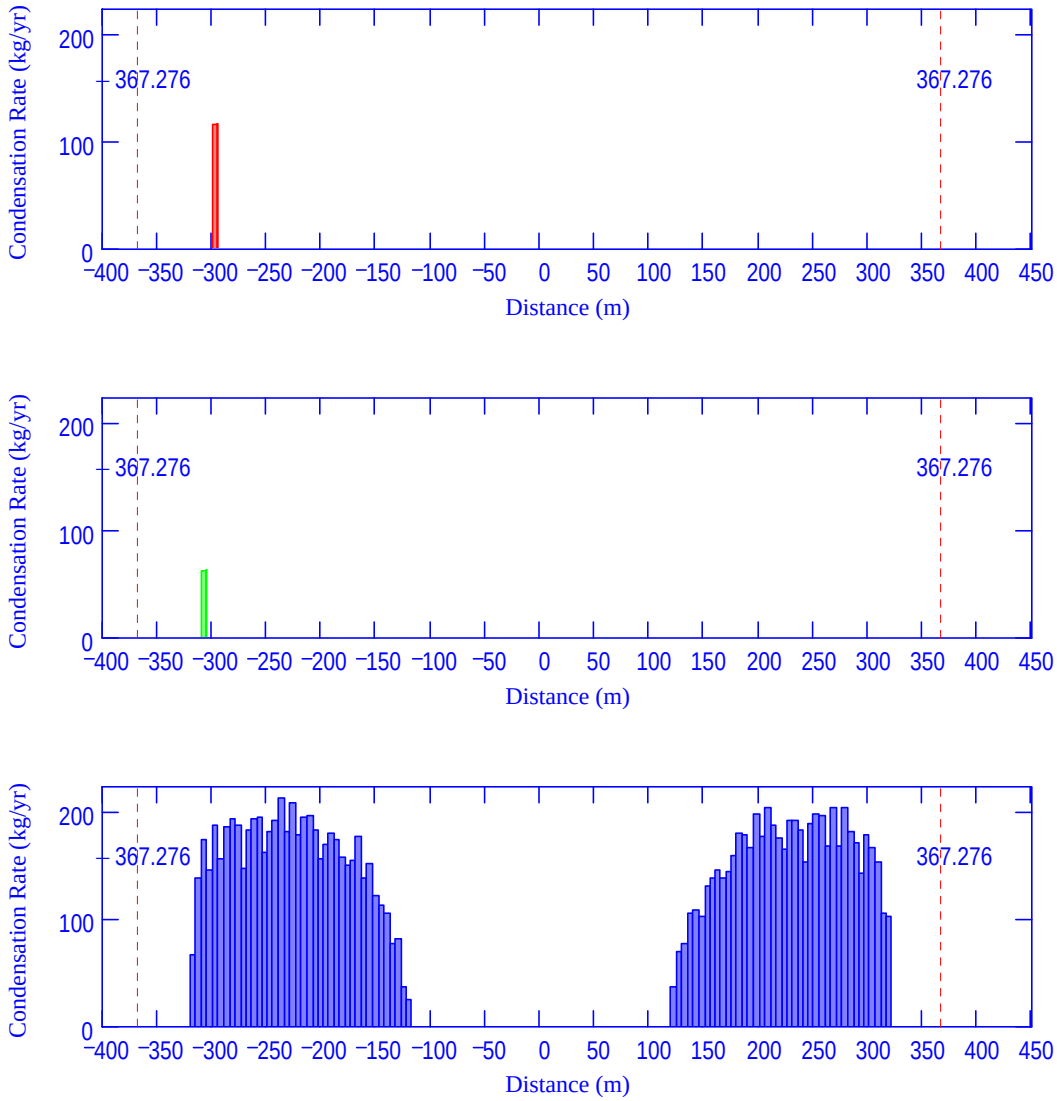

DTN: SN0408T0509903.007; file TOC.mcd; hyperlink 7.2.7, Calculated Results for Drift Choice #7.

NOTE: Low (top), Mean (middle), Upper (bottom).

Figure E.2-2. Condensation Rate on Drift Wall: Choice #7, 1,000 Years, Low Dispersion Bound Percolation Levels

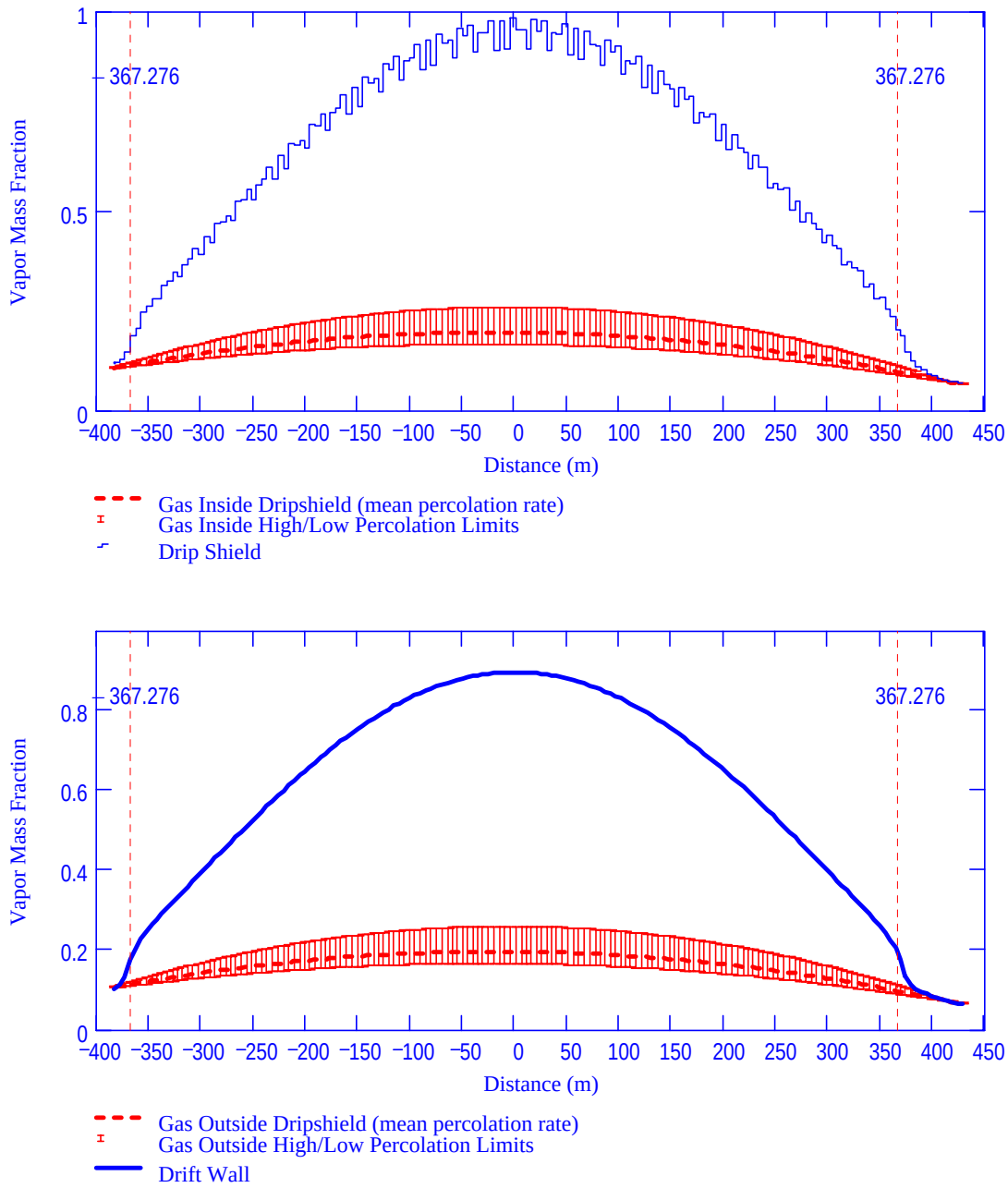

DTN: SN0408T0509903.007; file TOC.mcd; hyperlink 7.2.7, Calculated Results for Drift Choice #7.

NOTE: Top: inside drip shield; Bottom: outside drip shield.

Figure E.2-3. Vapor Mass Fractions in Gas: Choice #7, 1,000 Years, High Dispersion Bound

Table E.2-1 Summary of Condensation Rates: Choice #7, 1,000 Years

Dispersion Bound	Percolation Level	Condensation Location		21-PWR AP	5-HLW Long	21-PWR AP (Hot)	4-BWR AP	4-BWR AP (Adjusted)	5-HLW Short
	Low	Underside of	# WP's	0	0	0	0	0	0
		Drip Shield	Avg. Rate	0	0.0	0	0	0	0.0
		On Waste	# WP's	0	0	0	0	0	0
		Package	Avg. Rate	0	0	0	0	0	0
	Mean	Underside of	# WP's	0	0	0	0	0	0
Low		Drip Shield	Avg. Rate	0	0.0	0	0	0	0.0
		On Waste	# WP's	0	0	0	0	0	0
		Package	Avg. Rate	0	0	0	0	0	0
	Upper	Underside of	# WP's	0	0	0	0	0	0
		Drip Shield	Avg. Rate	0	0.0	0	0	0	0.0
		On Waste	# WP's	0	0	0	0	0	0
		Package	Avg. Rate	0	0	0	0	0	0.0
	Low	Underside of	# WP's	0	0	0	0	0	0
		Drip Shield	Avg. Rate	0	0.0	0	0	0	0.0
		On Waste	# WP's	0	0	0	0	0	0
		Package	Avg. Rate	0	0	0	0	0	0
	Mean	Underside of	# WP's	0	0	0	0	0	0
High		Drip Shield	Avg. Rate	0	0.0	0	0	0	0.0
		On Waste	# WP's	0	0	0	0	0	0
		Package	Avg. Rate	0	0	0	0	0	0
	Upper	Underside of	# WP's	0	0	0	0	0	0
		Drip Shield	Avg. Rate	0	0.0	0	0	0	0.0
		On Waste	# WP's	0	0	0	0	0	0
		Package	Avg. Rate	0	0	0	0	0	0

DTN: SN0408T0509903.007; file TOC.mcd; hyperlink 7.2.7, Calculated Results for Drift Choice #7.

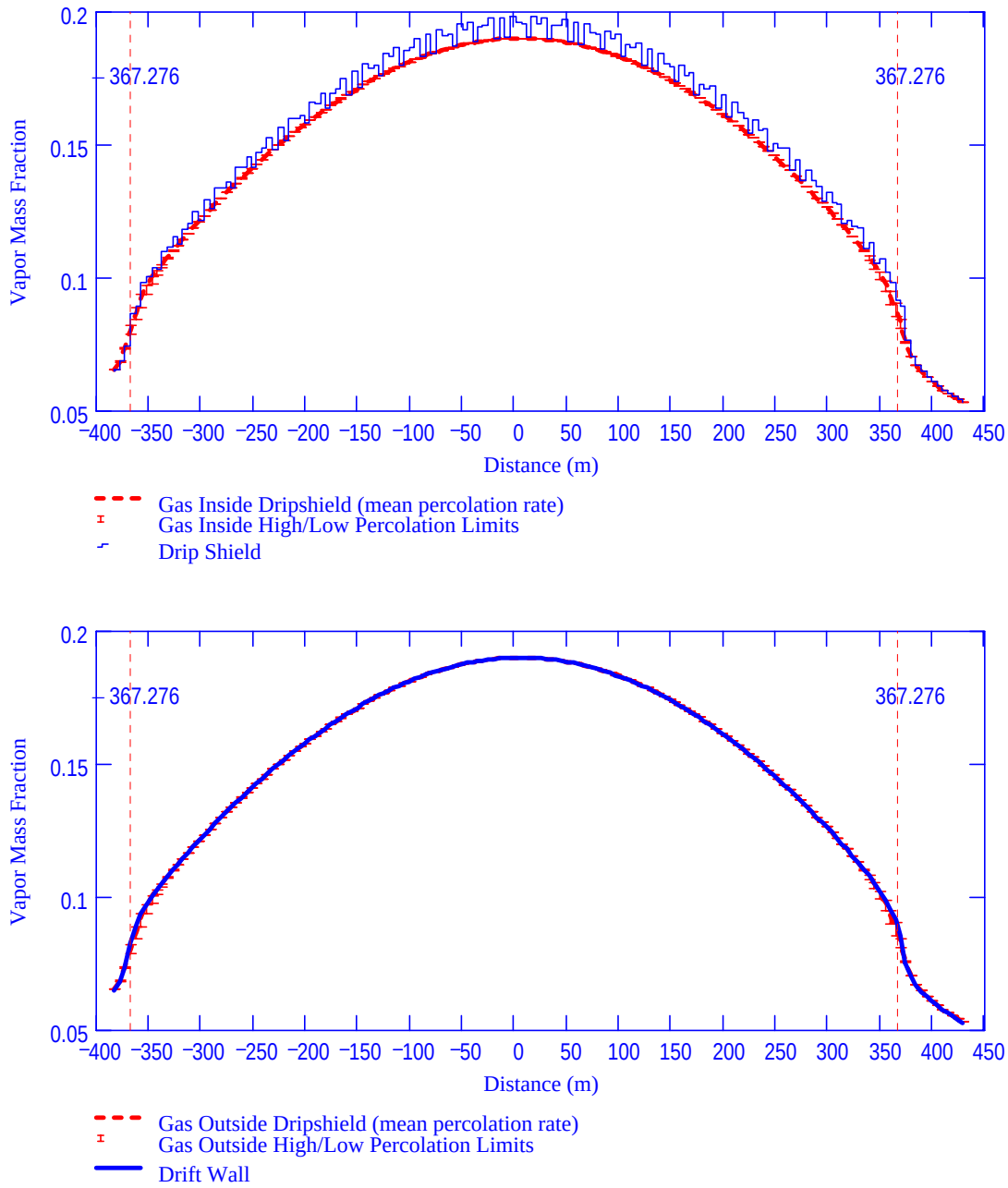

DTN: SN0408T0509903.007; file TOC.mcd; hyperlink 7.2.7, Calculated Results for Drift Choice #7.

NOTE: Top: inside drip shield; Bottom: outside drip shield.

Figure E.2-4. Vapor Mass Fractions in Gas: Choice #7, 3,000 Years, Low Dispersion Bound

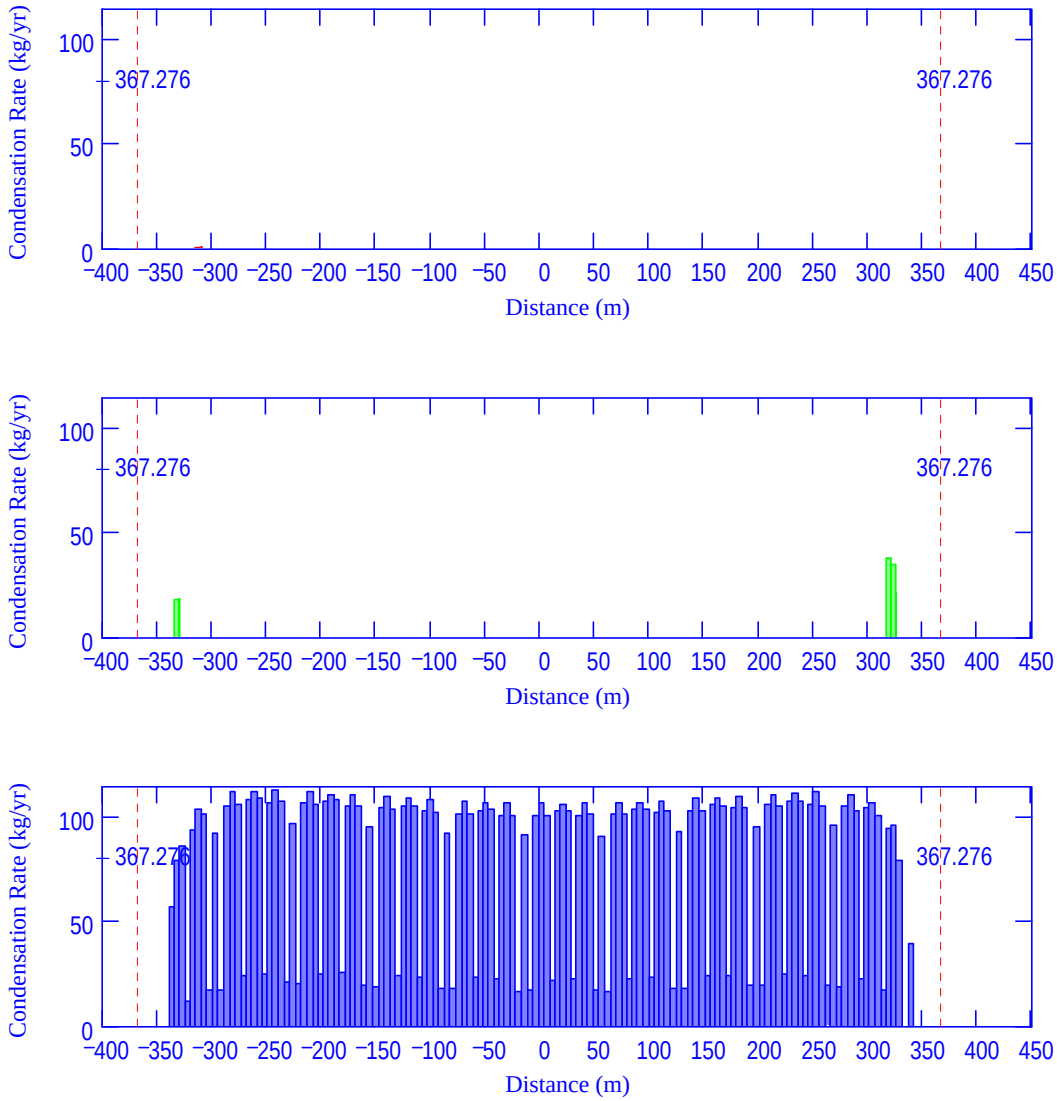

DTN: SN0408T0509903.007; file TOC.mcd; hyperlink 7.2.7, Calculated Results for Drift Choice #7.

NOTE: Low (top), Mean (middle), Upper (bottom).

Figure E.2-5. Condensation Rate on Drift Wall: Choice #7, 3,000 Years, Low Dispersion Bound Percolation Levels

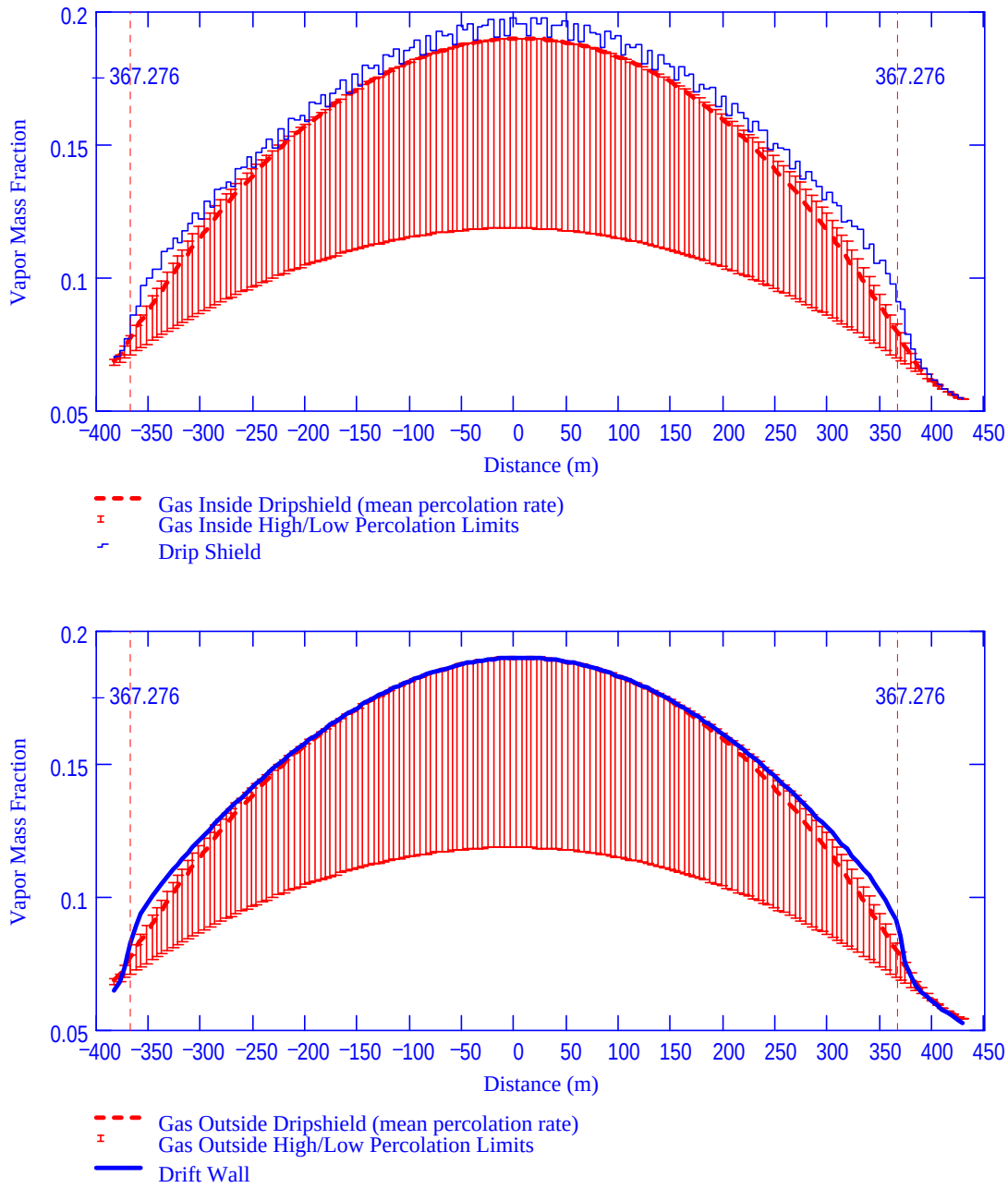

DTN: SN0408T0509903.007; file TOC.mcd; hyperlink 7.2.7, Calculated Results for Drift Choice #7.

NOTE: Top: inside drip shield, Bottom: outside drip shield.

Figure E.2-6. Vapor Mass Fractions in Gas: Choice #7, 3,000 Years, High Dispersion Bound

Table E.2-2 Summary of Condensation Rates: Choice #7, 3,000 Years

Dispersion Bound	Percolation Level	Condensation Location		21-PWR AP	5-HLW Long	21-PWR AP (Hot)	4-BWR AP	4-BWR AP (Adjusted)	5-HLW Short
	Low	Underside of	# WP's	0	0	0	0	0	0
		Drip Shield	Avg. Rate	0	0.0	0	0	0	0.0
		On Waste	# WP's	0	0	0	0	0	0
		Package	Avg. Rate	0	0	0	0	0	0
	Mean	Underside of	# WP's	0	0	0	0	0	0
Low		Drip Shield	Avg. Rate	0	0.0	0	0	0	0.0
		On Waste	# WP's	0	0	0	0	0	0
		Package	Avg. Rate	0	0	0	0	0	0
	Upper	Underside of	# WP's	0	0	0	0	0	0
		Drip Shield	Avg. Rate	0	0.0	0	0	0	0.0
		On Waste	# WP's	0	0	0	0	0	0
		Package	Avg. Rate	0	0	0	0	0	0.0
	Low	Underside of	# WP's	0	0	0	0	0	0
		Drip Shield	Avg. Rate	0	0.0	0	0	0	0.0
		On Waste	# WP's	0	0	0	0	0	0
		Package	Avg. Rate	0	0	0	0	0	0
	Mean	Underside of	# WP's	0	0	0	0	0	0
High		Drip Shield	Avg. Rate	0	0.0	0	0	0	0.0
		On Waste	# WP's	0	0	0	0	0	0
		Package	Avg. Rate	0	0	0	0	0	0
	Upper	Underside of	# WP's	0	0	0	0	0	0
		Drip Shield	Avg. Rate	0	0.0	0	0	0	0.0
		On Waste	# WP's	0	0	0	0	0	0
		Package	Avg. Rate	0	0	0	0	0	0

DTN: SN0408T0509903.007; file TOC.mcd; hyperlink 7.2.7, Calculated Results for Drift Choice #7.

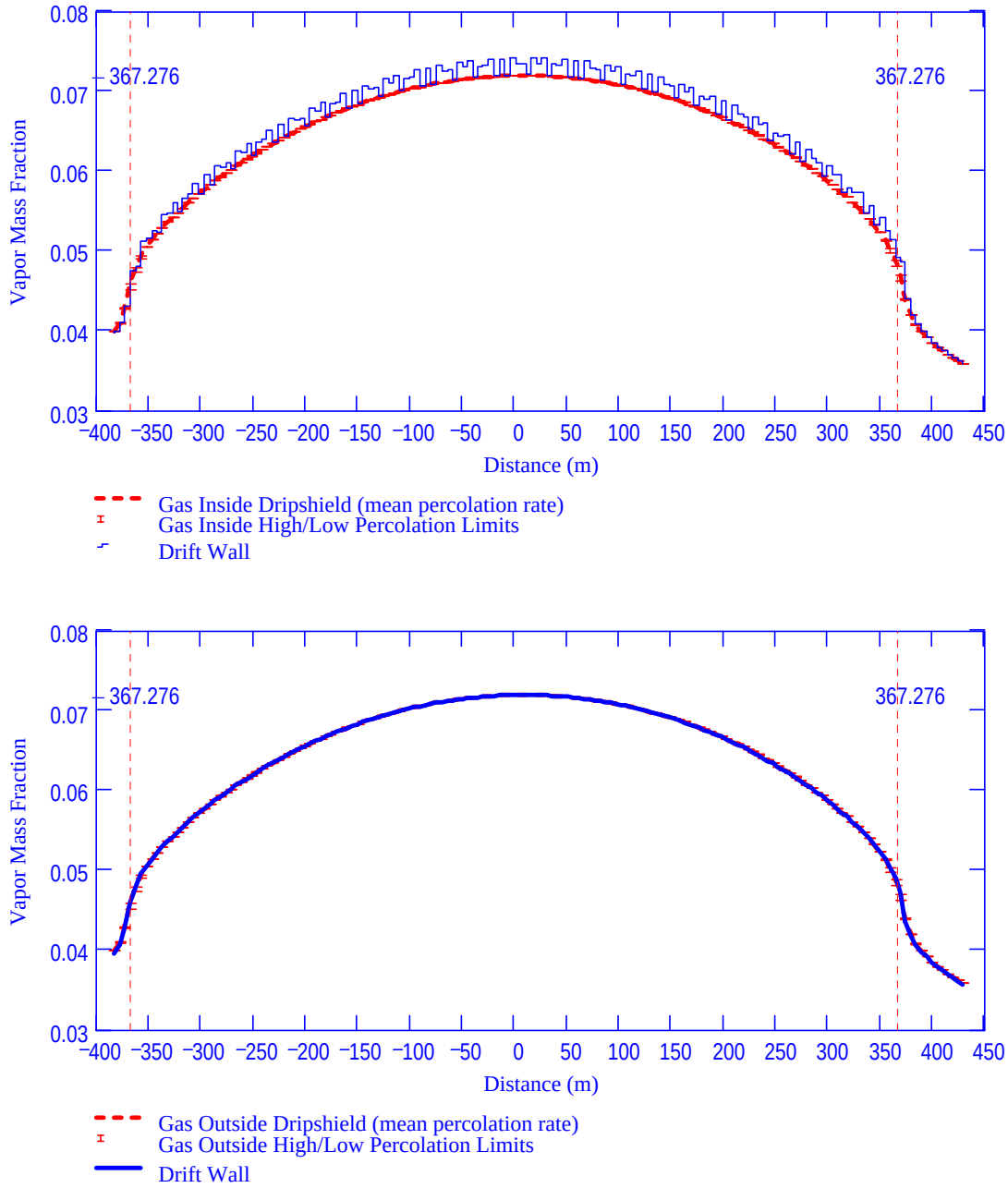

DTN: SN0408T0509903.007; file TOC.mcd; hyperlink 7.2.7, Calculated Results for Drift Choice #7.

NOTE: Top: inside drip shield; Bottom: outside drip shield.

Figure E.2-7. Vapor Mass Fractions in Gas: Choice #7, 10,000 Years, Low Dispersion Bound

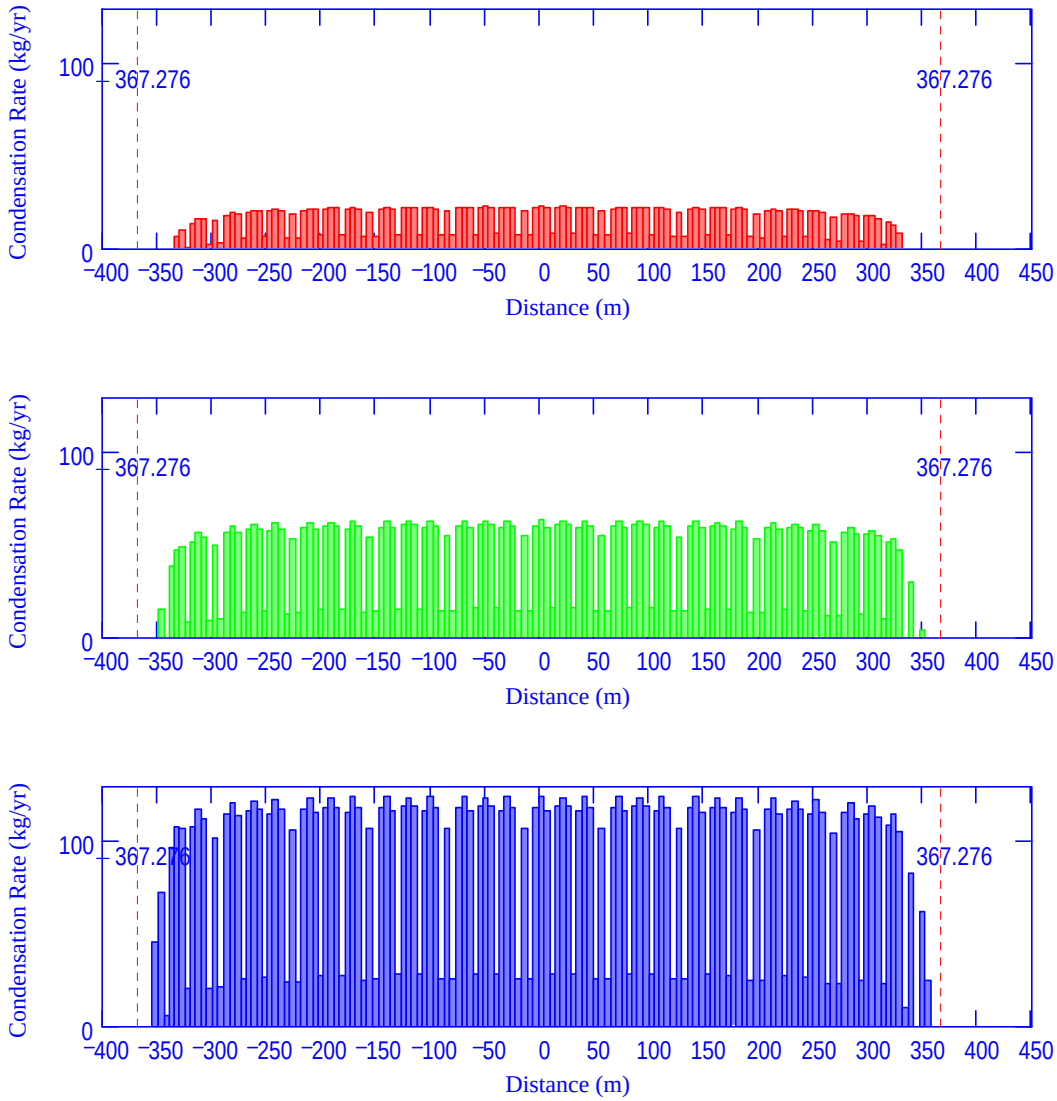

DTN: SN0408T0509903.007; file TOC.mcd; hyperlink 7.2.7, Calculated Results for Drift Choice #7.

NOTE: Low (top), Mean (middle), Upper (bottom).

Figure E.2-8. Condensation Rate on Drift Wall: Choice #7, 10,000 Years, Low Dispersion Bound Percolation Levels

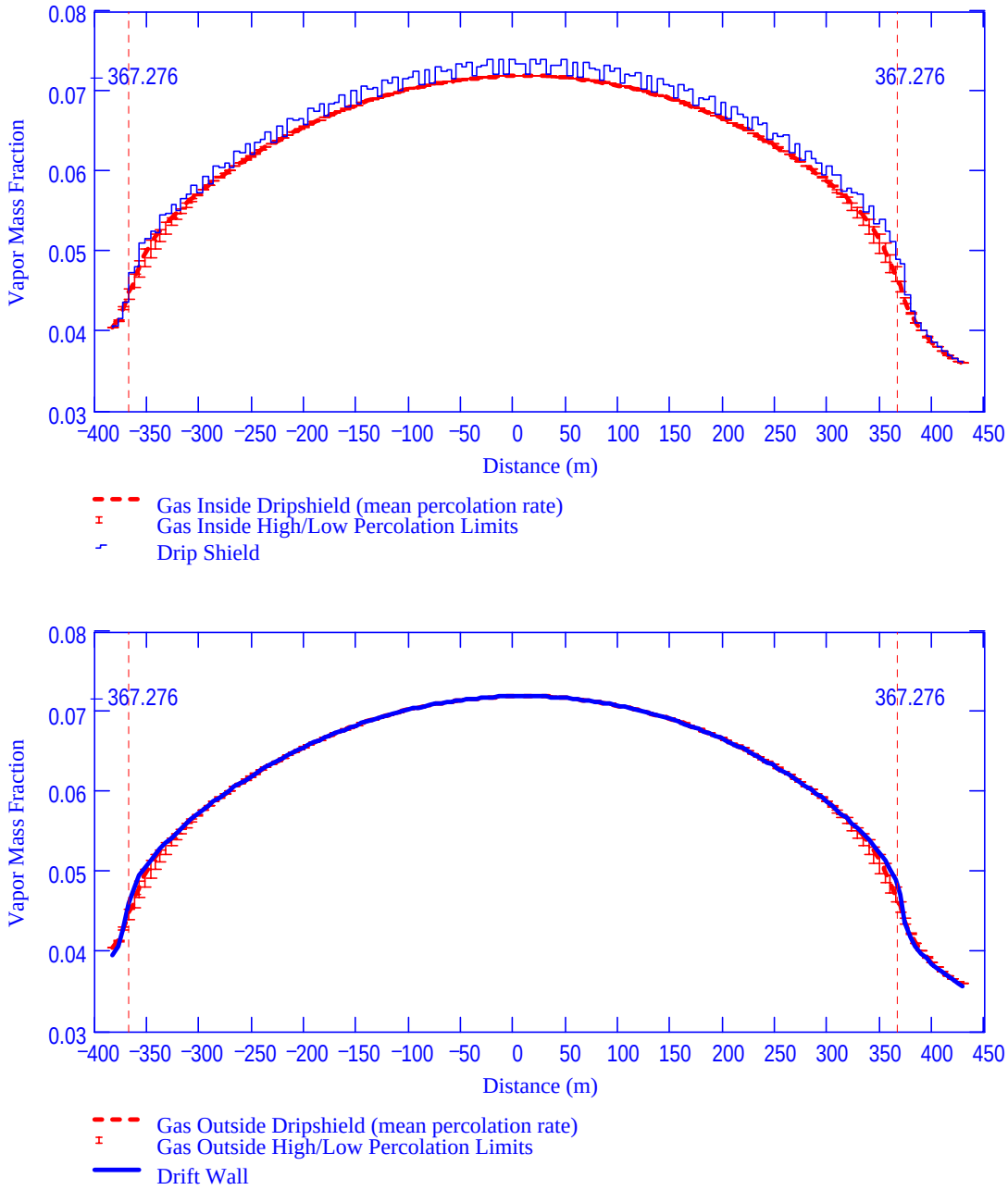

DTN: SN0408T0509903.007; file TOC.mcd; hyperlink 7.2.7, Calculated Results for Drift Choice #7.

NOTE: Top: inside drip shield; Bottom: outside drip shield.

Figure E.2-9. Vapor Mass Fractions in Gas: Choice #7, 10,000 Years, High Dispersion Bound

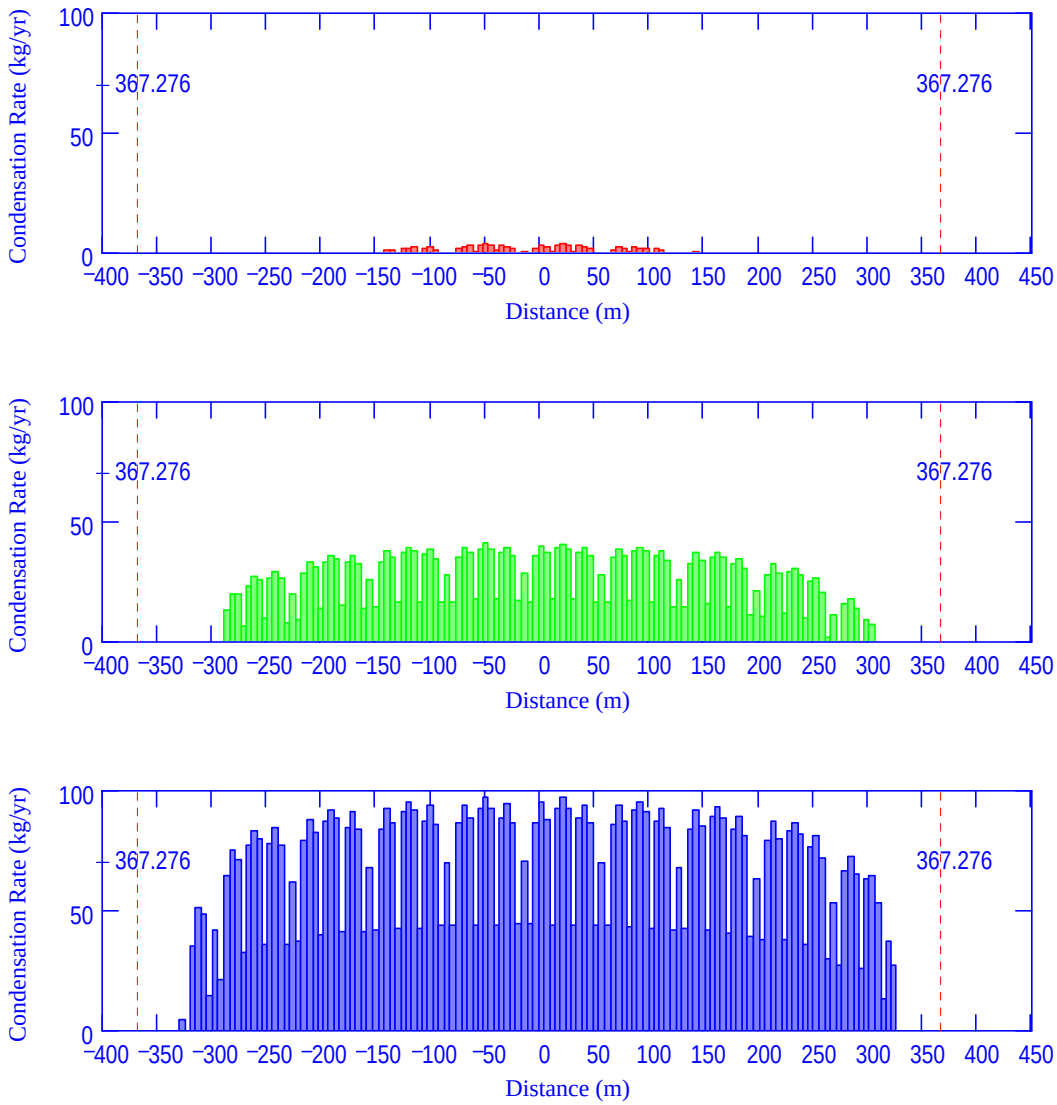

DTN: SN0408T0509903.007; file TOC.mcd; hyperlink 7.2.7, Calculated Results for Drift Choice #7.

NOTE: Low (top), Mean (middle), Upper (bottom).

Figure E.2-10. Condensation Rate on Drift Wall: Choice #7, 10,000 Years, High Dispersion Bound Percolation Levels

Table E.2-3. Summary of Condensation Rates: Choice #7, 10,000 Years

Dispersion Bound	Percolation Level	Condensation Location		21-PWR AP	5-HLW Long	21-PWR AP (Hot)	4-BWR AP	4-BWR AP (Adjusted)	5-HLW Short
	Low	Underside of	# WP's	0	0	0	0	0	0
		Drip Shield	Avg. Rate	0	0.0	0	0	0	0.0
		On Waste	# WP's	0	0	0	0	0	0
		Package	Avg. Rate	0	0	0	0	0	0
	Mean	Underside of	# WP's	0	0	0	0	0	0
Low		Drip Shield	Avg. Rate	0	0.0	0	0	0	0.0
		On Waste	# WP's	0	0	0	0	0	0
		Package	Avg. Rate	0	0	0	0	0	0
	Upper	Underside of	# WP's	0	0	0	0	0	0
		Drip Shield	Avg. Rate	0	0.0	0	0	0	0.0
		On Waste	# WP's	0	0	0	0	0	0
		Package	Avg. Rate	0	0	0	0	0	0.0
	Low	Underside of	# WP's	0	0	0	0	0	0
		Drip Shield	Avg. Rate	0	0.0	0	0	0	0.0
		On Waste	# WP's	0	0	0	0	0	0
		Package	Avg. Rate	0	0	0	0	0	0
	Mean	Underside of	# WP's	0	0	0	0	0	0
High		Drip Shield	Avg. Rate	0	0.0	0	0	0	0.0
		On Waste	# WP's	0	0	0	0	0	0
		Package	Avg. Rate	0	0	0	0	0	0
	Upper	Underside of	# WP's	0	0	0	0	0	0
		Drip Shield	Avg. Rate	0	0.0	0	0	0	0.0
		On Waste	# WP's	0	0	0	0	0	0
		Package	Avg. Rate	0	0	0	0	0	0

DTN: SN0408T0509903.007; file TOC.mcd; hyperlink 7.2.7, Calculated Results for Drift Choice #7.

E.3 UNVENTILATED DRIP SHIELD; LOW INVERT TRANSPORT

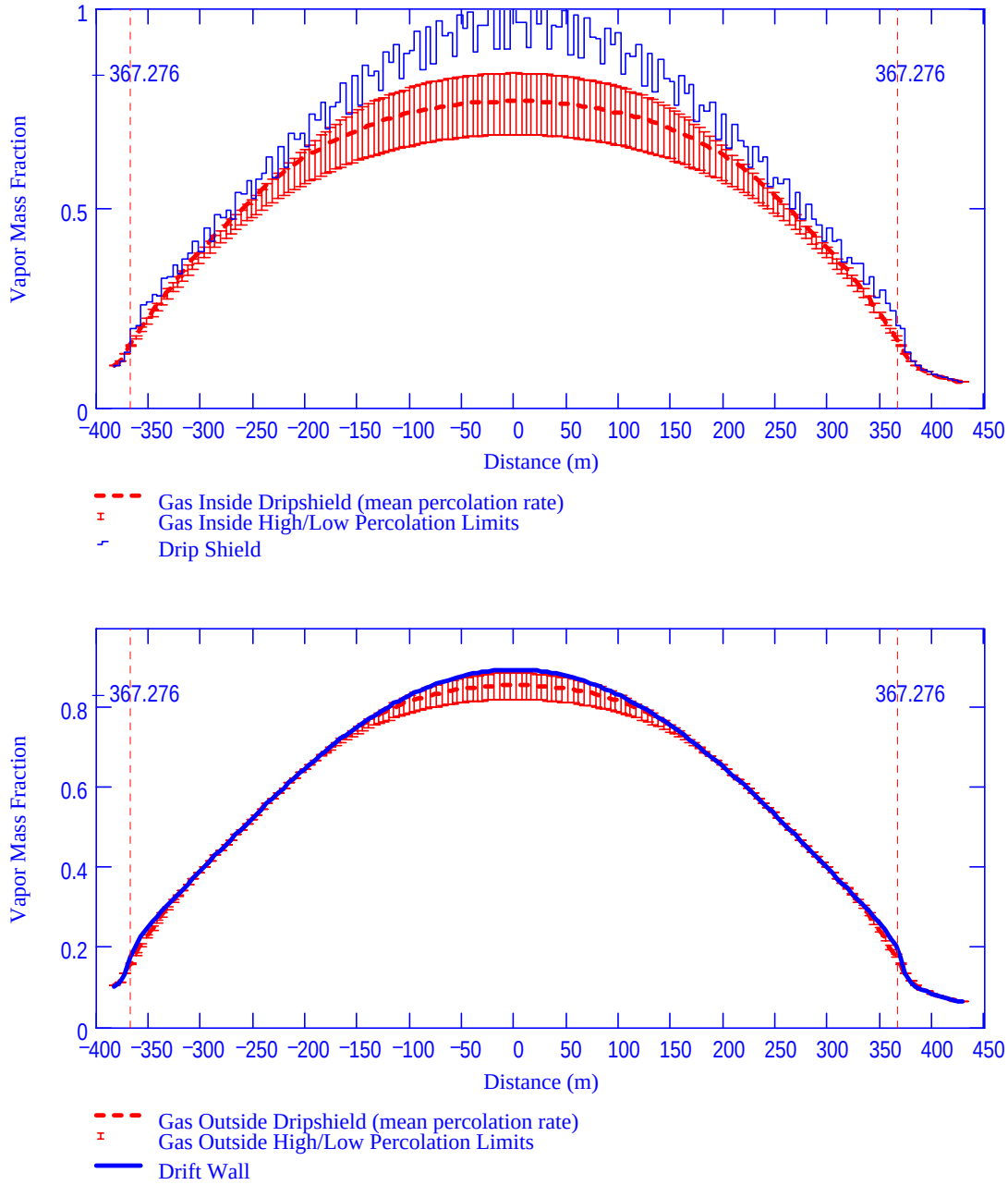

DTN: SN0408T0509903.007; file TOC.mcd; hyperlink 7.3.7, Calculated Results for Drift Choice #7.

NOTE: Top: inside drip shield; Bottom: outside drip shield.

Figure E.3-1. Vapor Mass Fractions in Gas: Choice #7, 1,000 Years, Low Dispersion Bound

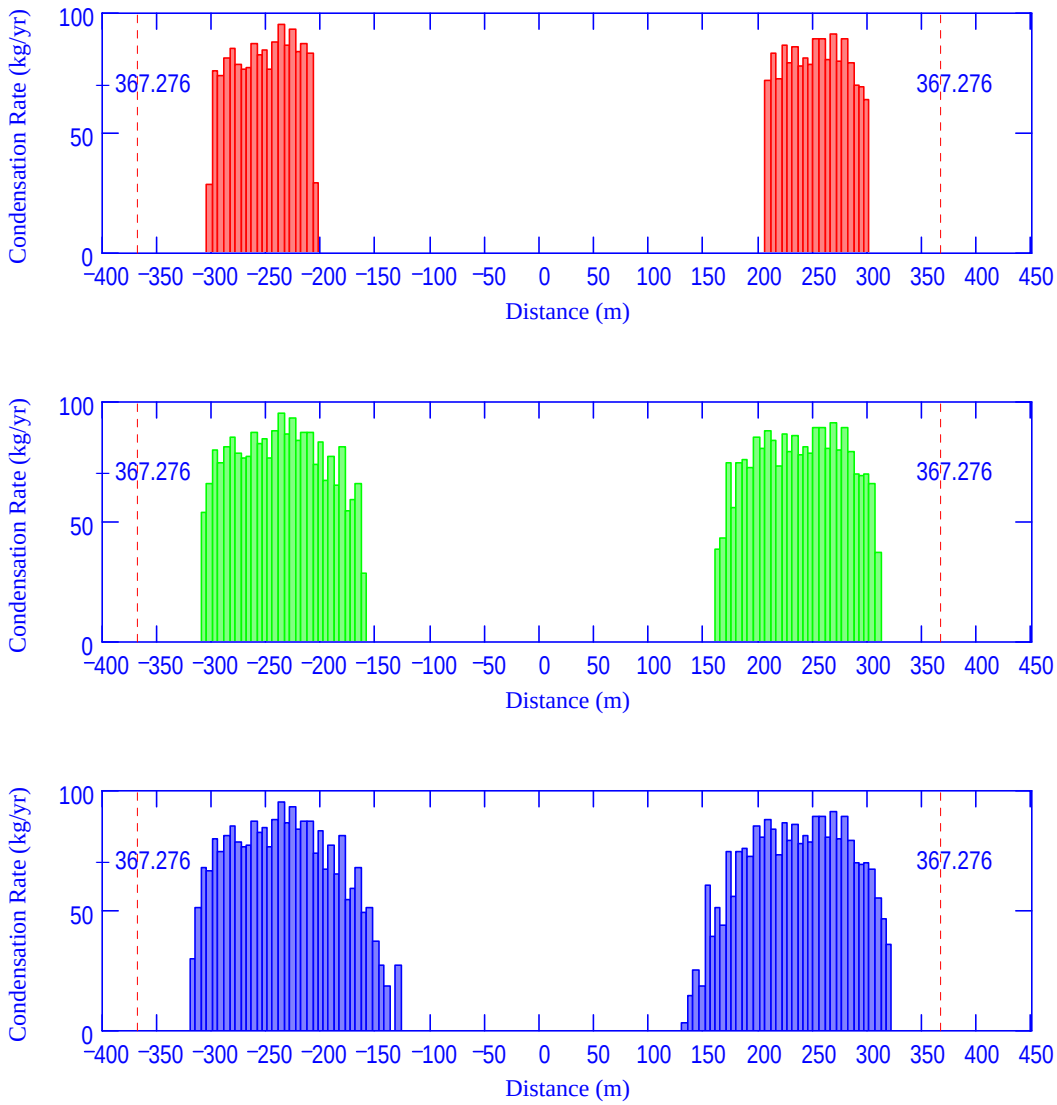

DTN: SN0408T0509903.007; file TOC.mcd; hyperlink 7.3.7, Calculated Results for Drift Choice #7.

NOTE: Low (top), Mean (middle), Upper (bottom).

Figure E.3-2. Condensation Rate on Drift Wall Choice #7, 1,000 Years, Low Dispersion Bound Percolation Levels

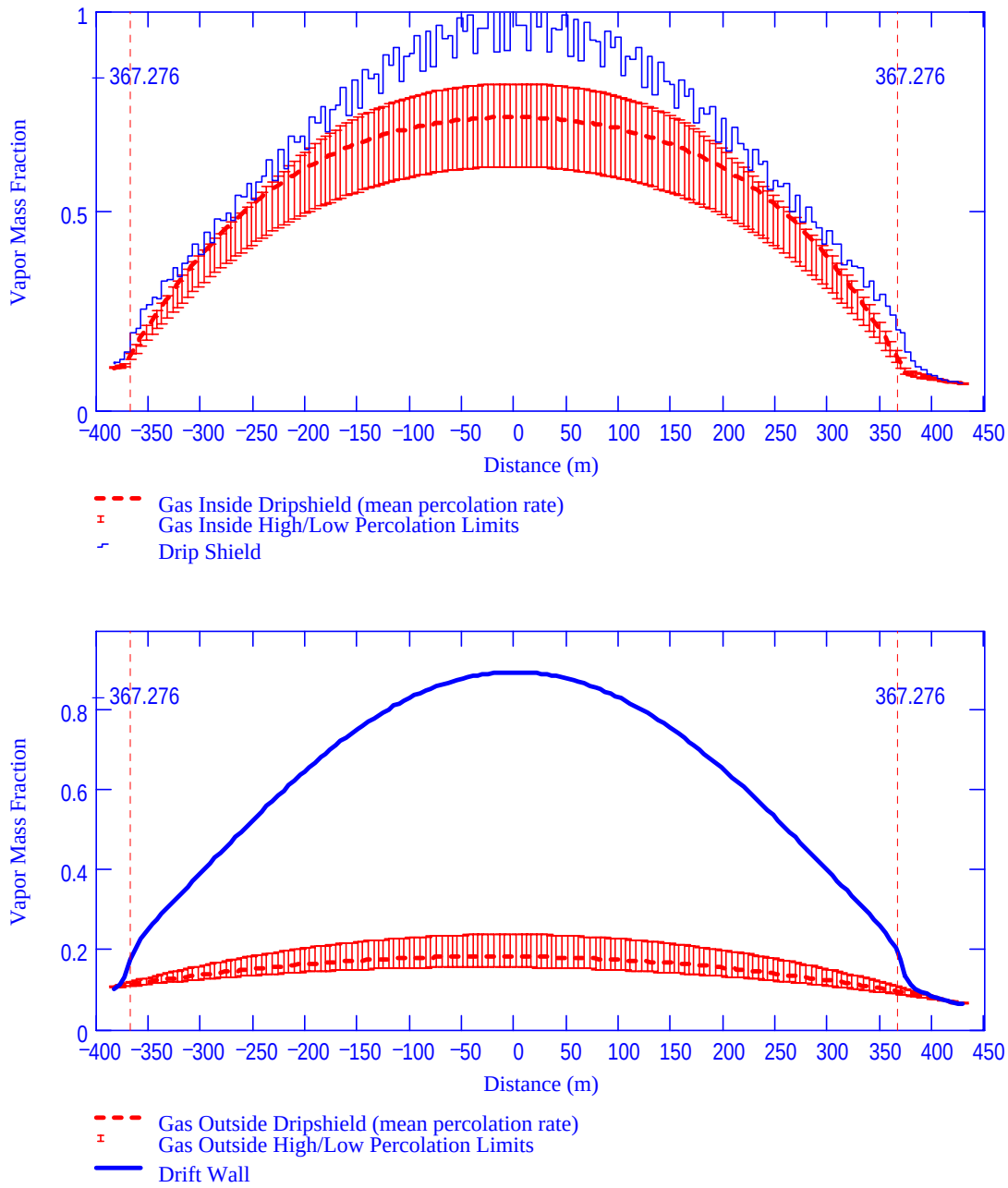

DTN: SN0408T0509903.007; file TOC.mcd; hyperlink 7.3.7, Calculated Results for Drift Choice #7.

NOTE: Top: inside drip shield; Bottom: outside drip shield.

Figure E.3-3. Vapor Mass Fractions in Gas: Choice #7, 1,000 Years, High Dispersion Bound

Table E.3-1 Summary of Condensation Rates: Choice #7, 1,000 Years

Dispersion Bound	Percolation Level	Condensation Location		21-PWR AP	5-HLW Long	21-PWR AP (Hot)	4-BWR AP	4-BWR AP (Adjusted)	5-HLW Short
	Low	Underside of	# WP's	0	0	0	0	0	0
		Drip Shield	Avg. Rate	0	0.0	0	0	0	0.0
		On Waste	# WP's	0	0	0	0	0	0
		Package	Avg. Rate	0	0	0	0	0	0
	Mean	Underside of	# WP's	0	0	0	0	0	0
Low		Drip Shield	Avg. Rate	0	0.0	0	0	0	0.0
		On Waste	# WP's	0	0	0	0	0	0
		Package	Avg. Rate	0	0	0	0	0	0
	Upper	Underside of	# WP's	0	0	0	0	0	0
		Drip Shield	Avg. Rate	0	0.0	0	0	0	0.0
		On Waste	# WP's	0	0	0	0	0	0
		Package	Avg. Rate	0	0	0	0	0	0.0
	Low	Underside of	# WP's	0	0	0	0	0	0
		Drip Shield	Avg. Rate	0	0.0	0	0	0	0.0
		On Waste	# WP's	0	0	0	0	0	0
		Package	Avg. Rate	0	0	0	0	0	0
	Mean	Underside of	# WP's	0	0	0	0	0	0
High		Drip Shield	Avg. Rate	0	0.0	0	0	0	0.0
		On Waste	# WP's	0	0	0	0	0	0
		Package	Avg. Rate	0	0	0	0	0	0
	Upper	Underside of	# WP's	0	0	0	0	0	0
		Drip Shield	Avg. Rate	0	0.0	0	0	0	0.0
		On Waste	# WP's	0	0	0	0	0	0
		Package	Avg. Rate	0	0	0	0	0	0

DTN: SN0408T0509903.007; file TOC.mcd; hyperlink 7.3.7, Calculated Results for Drift Choice #7.

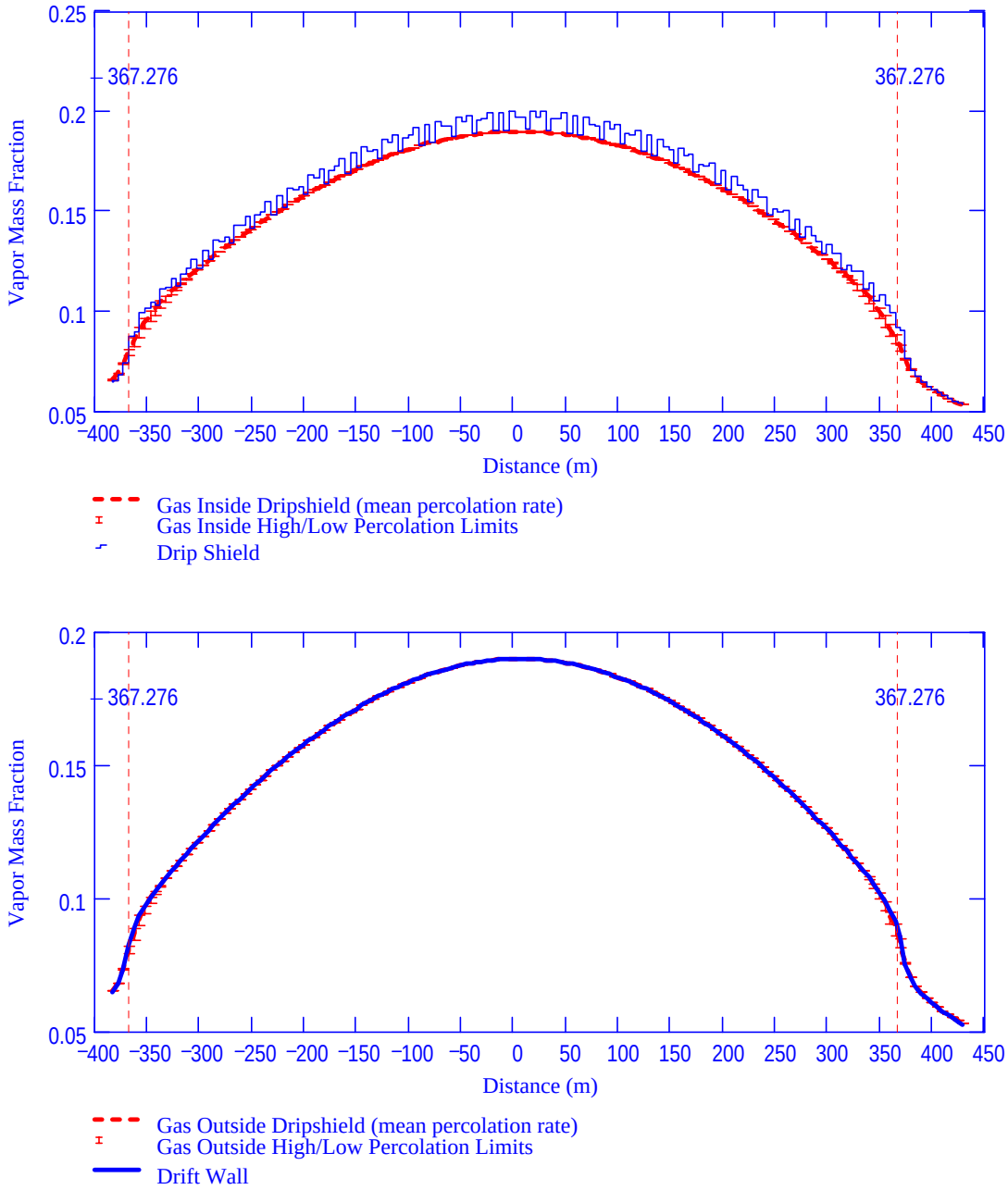

DTN: SN0408T0509903.007; file TOC.mcd; hyperlink 7.3.7, Calculated Results for Drift Choice #7.

NOTE: Top: inside drip shield; Bottom: outside drip shield.

Figure E.3-4. Vapor Mass Fractions in Gas: Choice #7, 3,000 Years, Low Dispersion Bound

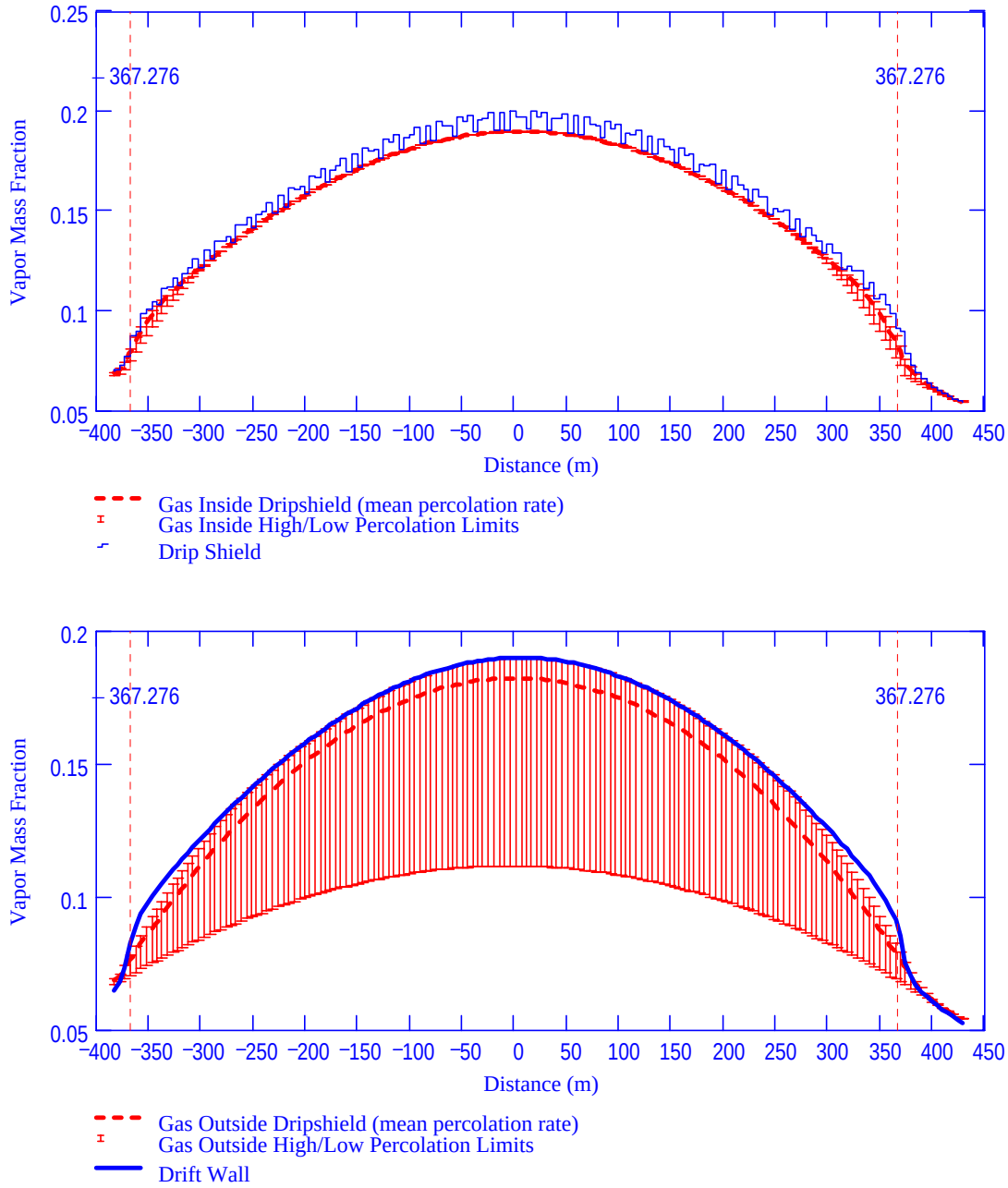

DTN: SN0408T0509903.007; file TOC.mcd; hyperlink 7.3.7, Calculated Results for Drift Choice #7.

NOTE: Top: inside drip shield; Bottom: outside drip shield.

Figure E.3-5. Vapor Mass Fractions in Gas: Choice #7, 3,000 Years, High Dispersion Bound

Table E.3-2. Summary of Condensation Rates: Choice #7, 3,000 Years

Dispersion Bound	Percolation Level	Condensation Location		21-PWR AP	5-HLW Long	21-PWR AP (Hot)	4-BWR AP	4-BWR AP (Adjusted)	5-HLW Short
	Low	Underside of	# WP's	0	0	0	0	0	0
		Drip Shield	Avg. Rate	0	0.0	0	0	0	0.0
		On Waste	# WP's	0	0	0	0	0	0
		Package	Avg. Rate	0	0	0	0	0	0
	Mean	Underside of	# WP's	0	0	0	0	0	0
Low		Drip Shield	Avg. Rate	0	0.0	0	0	0	0.0
		On Waste	# WP's	0	0	0	0	0	0
		Package	Avg. Rate	0	0	0	0	0	0
	Upper	Underside of	# WP's	0	0	0	0	0	0
		Drip Shield	Avg. Rate	0	0.0	0	0	0	0.0
		On Waste	# WP's	0	0	0	0	0	0
		Package	Avg. Rate	0	0	0	0	0	0.0
	Low	Underside of	# WP's	0	0	0	0	0	0
		Drip Shield	Avg. Rate	0	0.0	0	0	0	0.0
		On Waste	# WP's	0	0	0	0	0	0
		Package	Avg. Rate	0	0	0	0	0	0
	Mean	Underside of	# WP's	0	0	0	0	0	0
High		Drip Shield	Avg. Rate	0	0.0	0	0	0	0.0
		On Waste	# WP's	0	0	0	0	0	0
		Package	Avg. Rate	0	0	0	0	0	0
	Upper	Underside of	# WP's	0	0	0	0	0	0
		Drip Shield	Avg. Rate	0	0.0	0	0	0	0.0
		On Waste	# WP's	0	0	0	0	0	0
		Package	Avg. Rate	0	0	0	0	0	0

DTN: SN0408T0509903.007; file TOC.mcd; hyperlink 7.3.7, Calculated Results for Drift Choice #7.

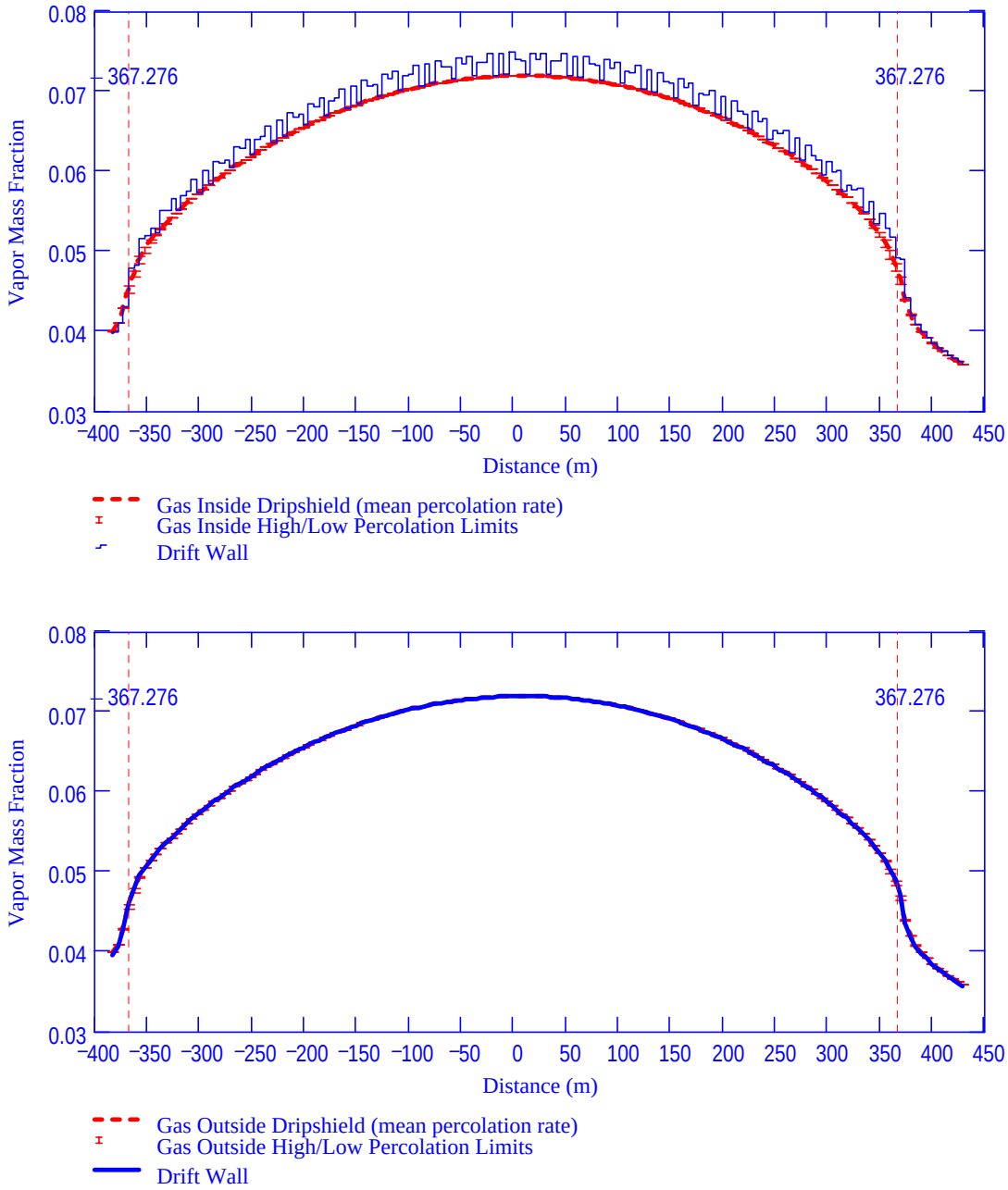

DTN: SN0408T0509903.007; file TOC.mcd; hyperlink 7.3.7, Calculated Results for Drift Choice #7.

NOTE: Top: inside drip shield; Bottom: outside drip shield.

Figure E.3-6. Vapor Mass Fractions in Gas: Choice #7, 10,000 Years, Low Dispersion Bound

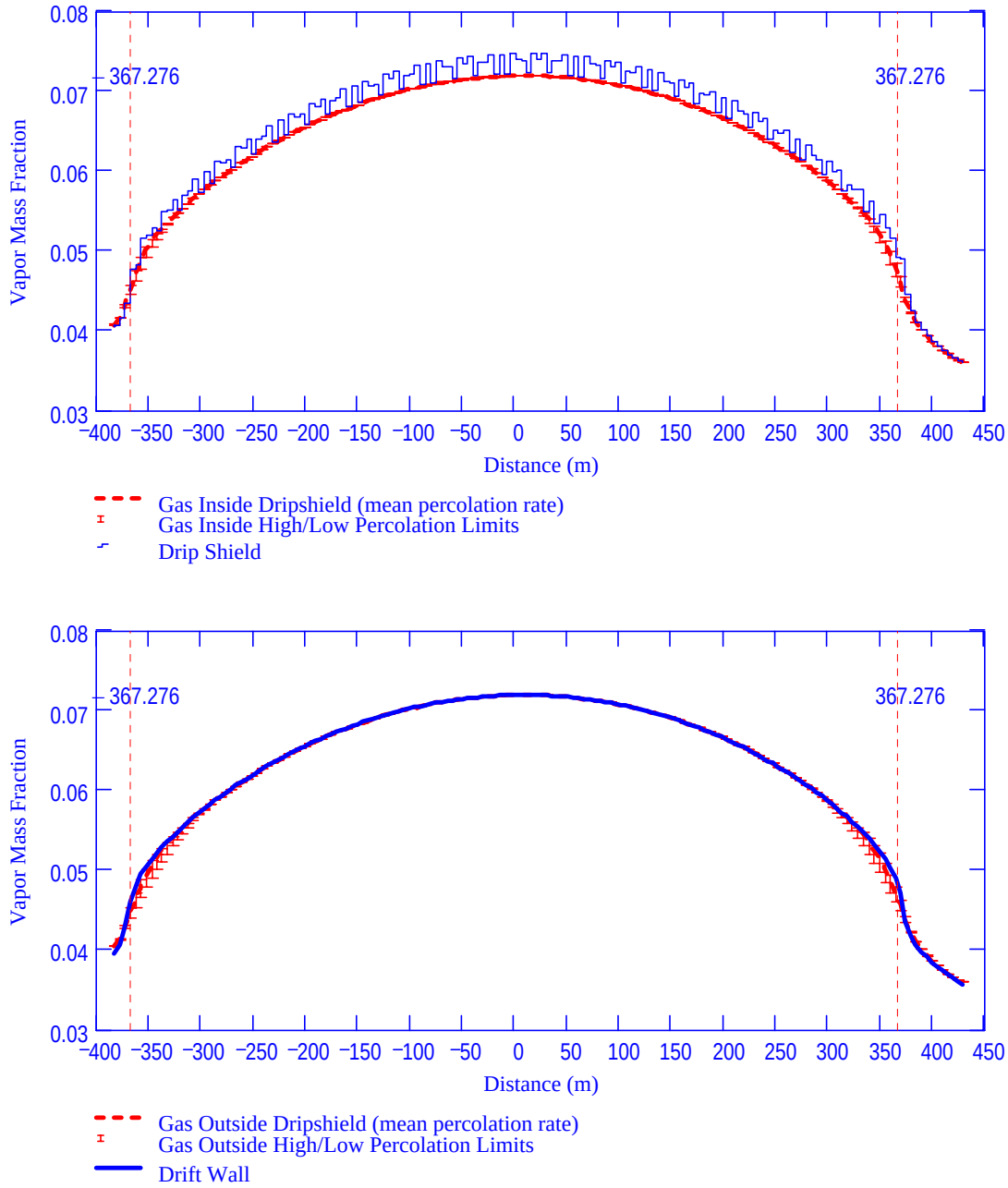

DTN: SN0408T0509903.007; file TOC.mcd; hyperlink 7.3.7, Calculated Results for Drift Choice #7.

NOTE: Top: inside drip shield; Bottom: outside drip shield.

Figure E.3-7. Vapor Mass Fractions in Gas: Choice #7, 10,000 Years, High Dispersion Bound

Table E.3-3. Summary of Condensation Rates: Choice #7, 10,000 Years

Dispersion Bound	Percolation Level	Condensation Location		21-PWR AP	5-HLW Long	21-PWR AP (Hot)	4-BWR AP	4-BWR AP (Adjusted)	5-HLW Short
	Low	Underside of	# WP's	0	0	0	0	0	0
		Drip Shield	Avg. Rate	0	0.0	0	0	0	0.0
		On Waste	# WP's	0	0	0	0	0	0
		Package	Avg. Rate	0	0	0	0	0	0
	Mean	Underside of	# WP's	0	0	0	0	0	0
Low		Drip Shield	Avg. Rate	0	0.0	0	0	0	0.0
		On Waste	# WP's	0	0	0	0	0	0
		Package	Avg. Rate	0	0	0	0	0	0
	Upper	Underside of	# WP's	0	0	0	0	0	0
		Drip Shield	Avg. Rate	0	0.0	0	0	0	0.0
		On Waste	# WP's	0	0	0	0	0	0
		Package	Avg. Rate	0	0	0	0	0	0.0
	Low	Underside of	# WP's	0	0	0	0	0	0
		Drip Shield	Avg. Rate	0	0.0	0	0	0	0.0
		On Waste	# WP's	0	0	0	0	0	0
		Package	Avg. Rate	0	0	0	0	0	0
	Mean	Underside of	# WP's	0	0	0	0	0	0
High		Drip Shield	Avg. Rate	0	0.0	0	0	0	0.0
		On Waste	# WP's	0	0	0	0	0	0
		Package	Avg. Rate	0	0	0	0	0	0
	Upper	Underside of	# WP's	0	0	0	0	0	0
		Drip Shield	Avg. Rate	0	0.0	0	0	0	0.0
		On Waste	# WP's	0	0	0	0	0	0
		Package	Avg. Rate	0	0	0	0	0	0

DTN: SN0408T0509903.007; file TOC.mcd; hyperlink 7.3.7, Calculated Results for Drift Choice #7.

E.4 UNVENTILATED DRIP SHIELD; HIGH INVERT TRANSPORT

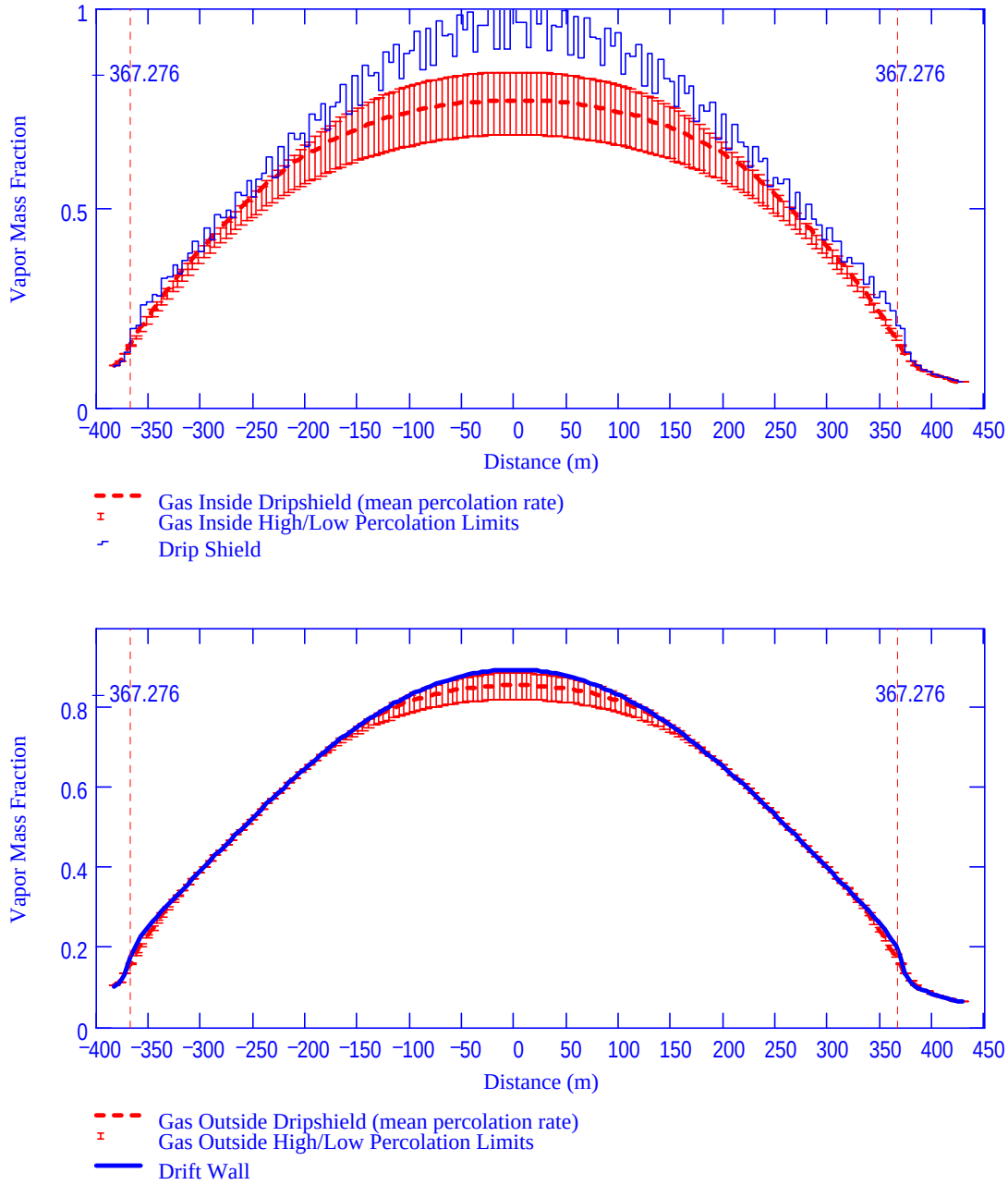

DTN: SN0408T0509903.007; file TOC.mcd; hyperlink 7.4.7, Calculated Results for Drift Choice #7.

NOTE: Top: inside drip shield; Bottom: outside drip shield.

Figure E.4-1. Vapor Mass Fractions in Gas: Choice #7, 1,000 Years, Low Dispersion Bound

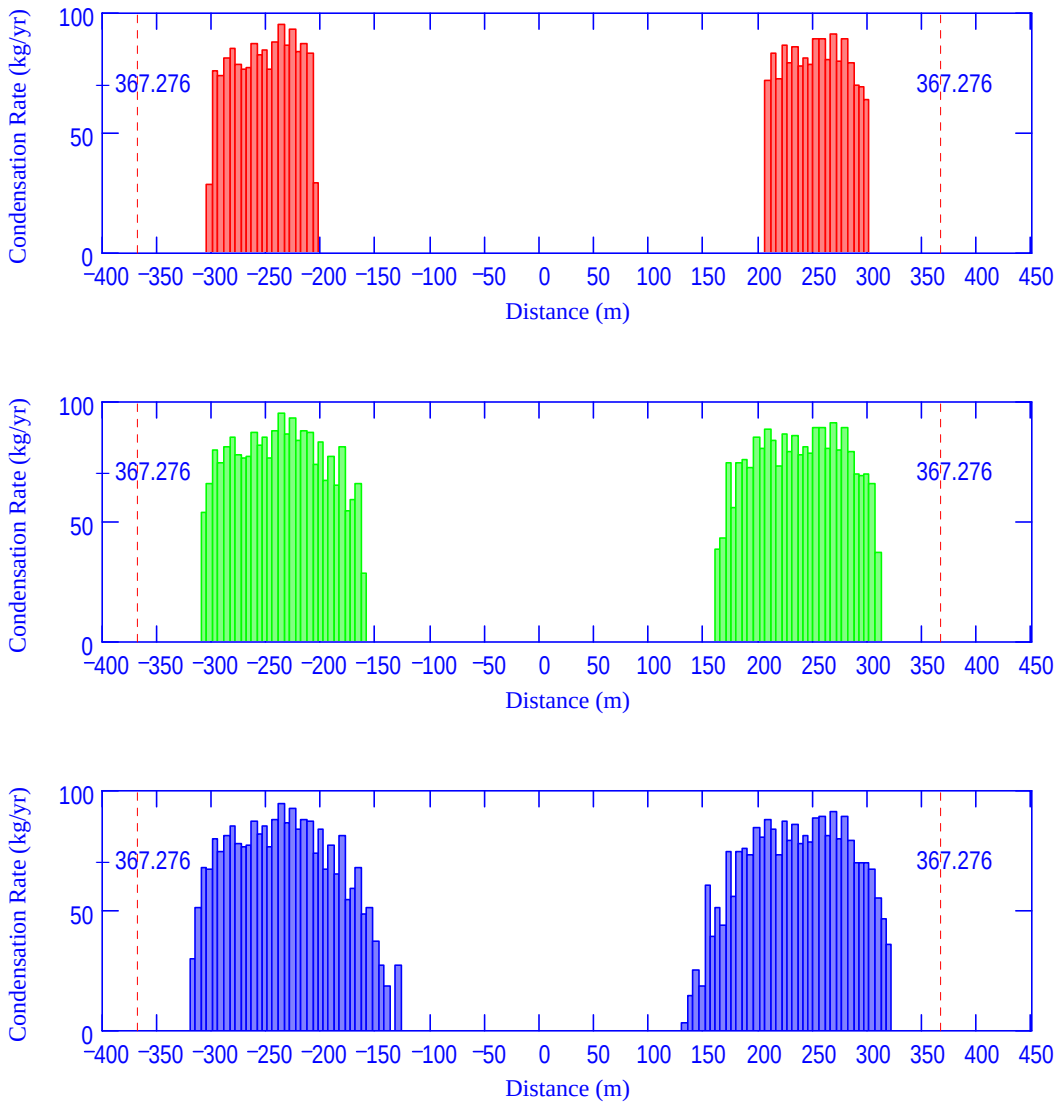

DTN: SN0408T0509903.007; file TOC.mcd; hyperlink 7.4.7, Calculated Results for Drift Choice #7.

NOTE: Low (top), Mean (middle), Upper (bottom).

Figure E.4-2. Condensation Rate on Drift Wall: Choice #7, 1,000 Years, Low Dispersion Bound Percolation Levels

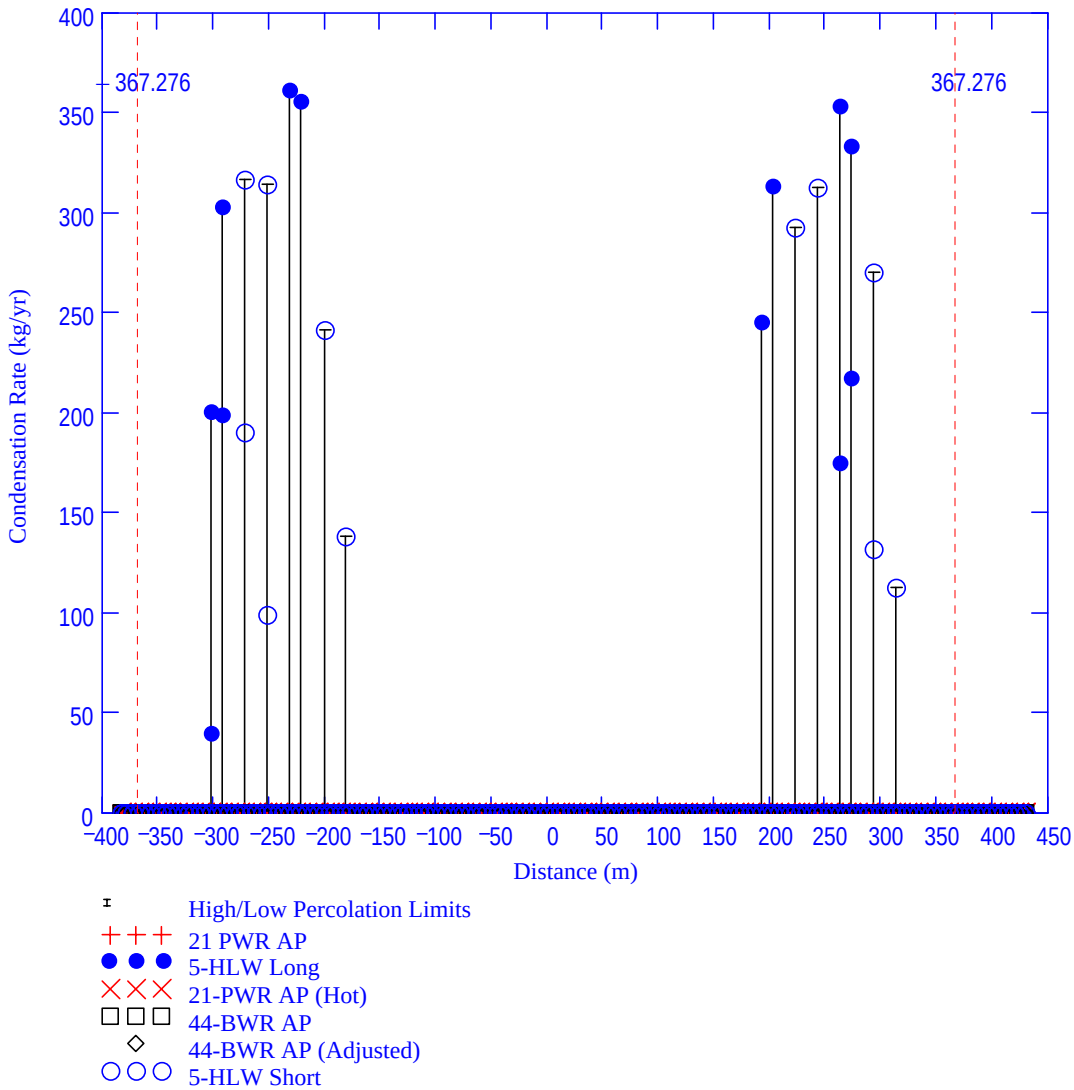

DTN: SN0408T0509903.007; file TOC.mcd; hyperlink 7.4.7, Calculated Results for Drift Choice #7.

Figure E.4-3. Condensation Rate on the Underside of the Drip Shield: Choice #7, 1,000 Years, Low Dispersion Bound

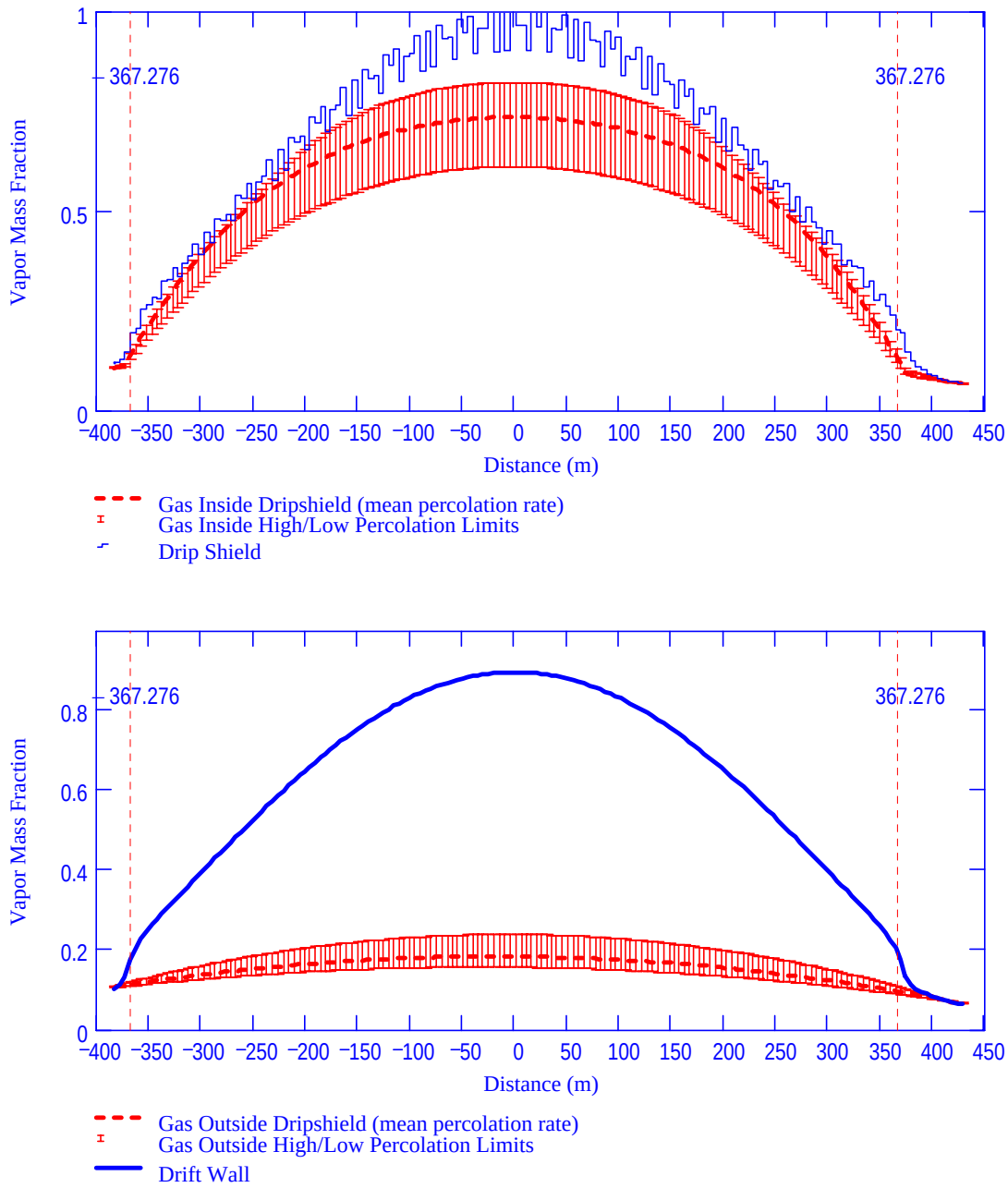

DTN: SN0408T0509903.007; file TOC.mcd; hyperlink 7.4.7, Calculated Results for Drift Choice #7.

NOTE: Top: inside drip shield; Bottom: outside drip shield.

Figure E.4-4. Vapor Mass Fractions in Gas: Choice #7, 1,000 Years, High Dispersion Bound

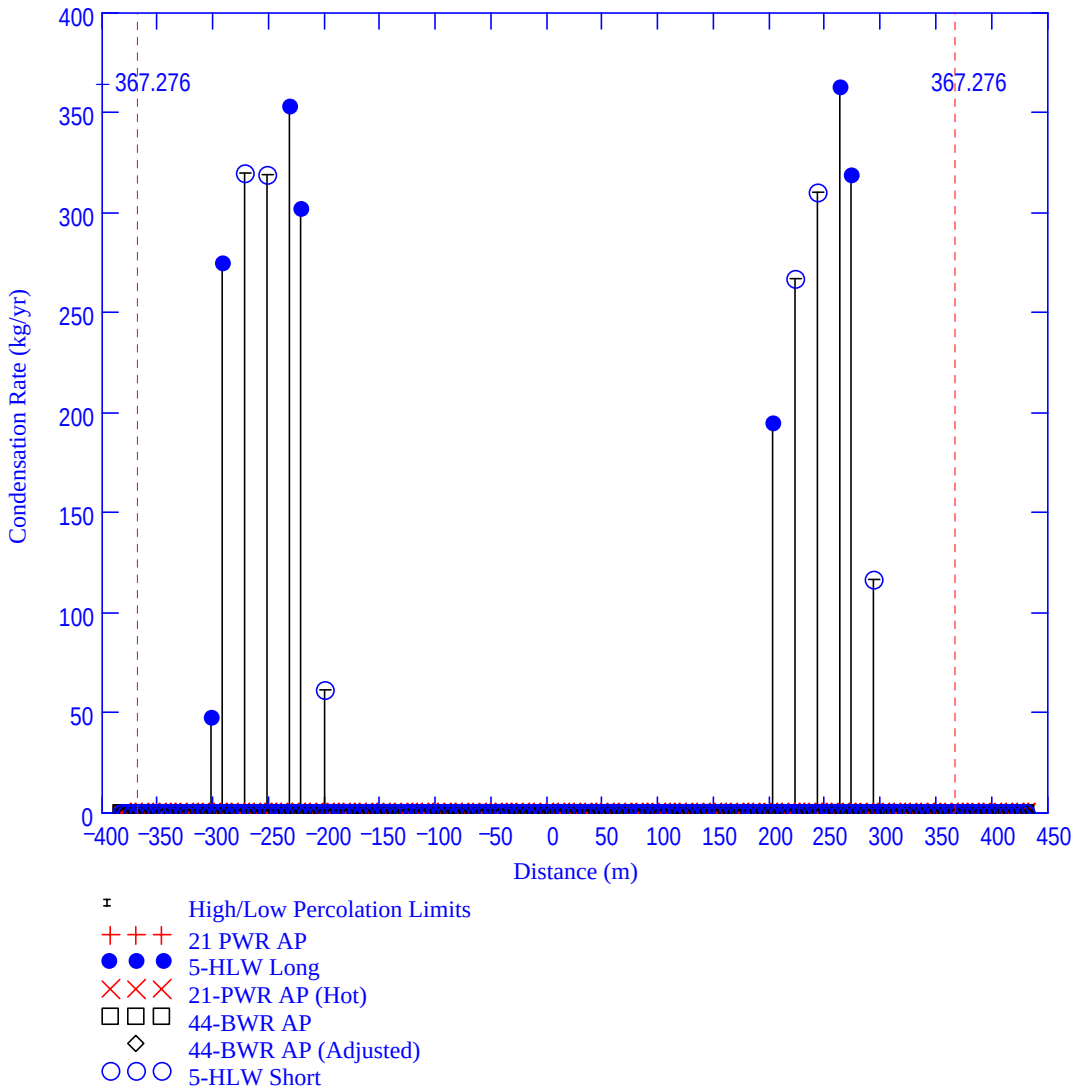

DTN: SN0408T0509903.007; file TOC.mcd; hyperlink 7.4.7, Calculated Results for Drift Choice #7.

Figure E.4-5. Condensation Rate on the Underside of the Drip Shield: Choice #7, 1,000 Years, High Dispersion Bound

Table E.4-1. Summary of Condensation Rates: Choice #7, 1,000 Years

Dispersion Bound	Percolation Level	Condensation Location		21-PWR AP	5-HLW Long	21-PWR AP (Hot)	4-BWR AP	4-BWR AP (Adjusted)	5-HLW Short
	Low	Underside of	# WP's	0	0	0	0	0	0
		Drip Shield	Avg. Rate	0	0	0	0	0	0
		On Waste	# WP's	0	0	0	0	0	0
		Package	Avg. Rate	0	0	0	0	0	0
	Mean	Underside of	# WP's	0	4	0	0	0	3
Low		Drip Shield	Avg. Rate	0	157.4	0	0	0	140.1
		On Waste	# WP's	0	0	0	0	0	0
		Package	Avg. Rate	0	0	0	0	0	0
	Upper	Underside of	# WP's	0	8	0	0	0	8
		Drip Shield	Avg. Rate	0	308.0	0	0	0	249.7
		On Waste	# WP's	0	0	0	0	0	0
		Package	Avg. Rate	0	0	0	0	0	0
	Low	Underside of	# WP's	0	0	0	0	0	0
		Drip Shield	Avg. Rate	0	0	0	0	0	0
		On Waste	# WP's	0	0	0	0	0	0
		Package	Avg. Rate	0	0	0	0	0	0
	Mean	Underside of	# WP's	0	0	0	0	0	0
High		Drip Shield	Avg. Rate	0	0	0	0	0	0
		On Waste	# WP's	0	0	0	0	0	0
		Package	Avg. Rate	0	0	0	0	0	0
	Upper	Underside of	# WP's	0	7	0	0	0	6
		Drip Shield	Avg. Rate	0	264.8	0	0	0	232.1
		On Waste	# WP's	0	0	0	0	0	0
		Package	Avg. Rate	0	0	0	0	0	0

DTN: SN0408T0509903.007; file TOC.mcd; hyperlink 7.4.7, Calculated Results for Drift Choice #7.

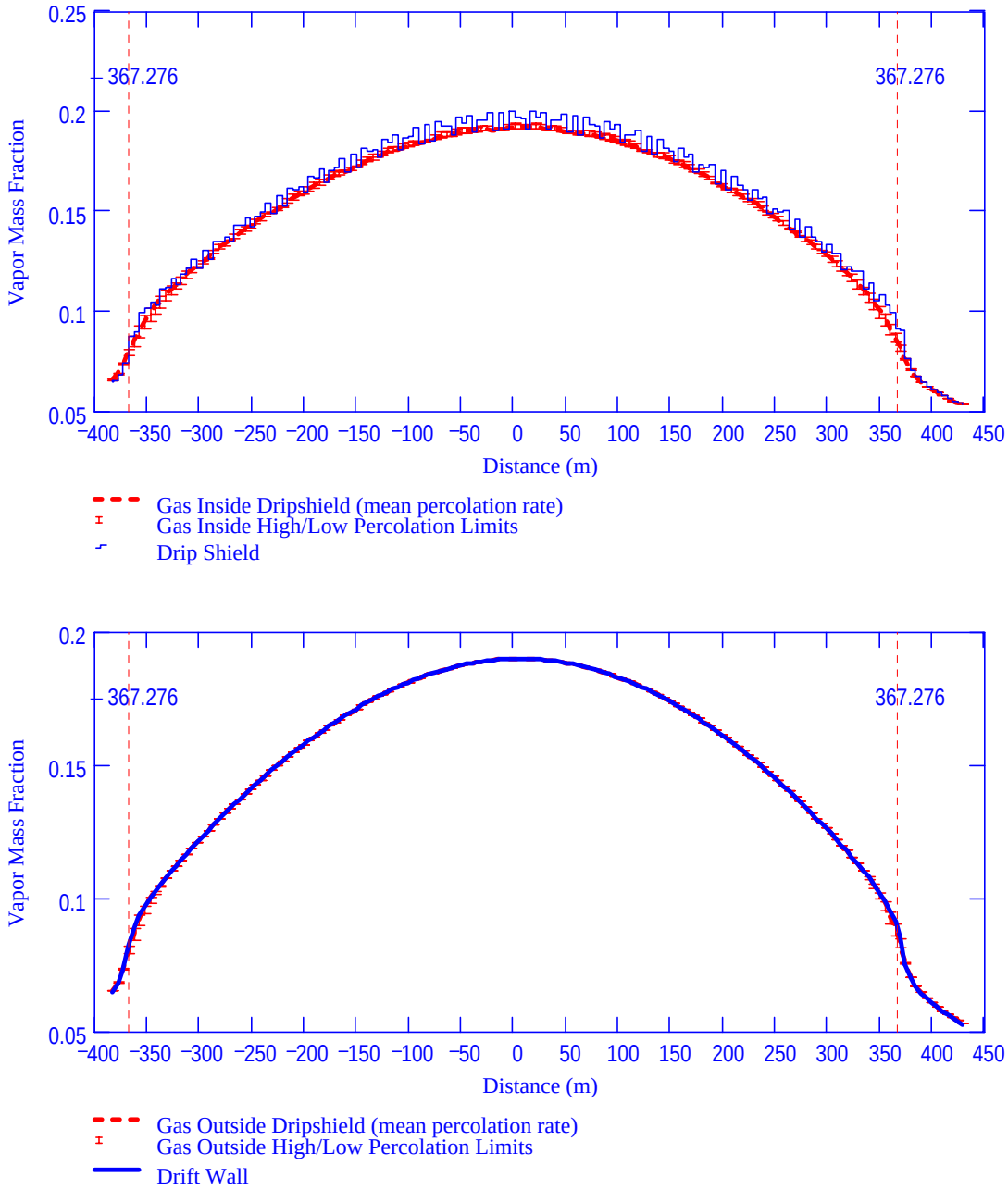

DTN: SN0408T0509903.007; file TOC.mcd; hyperlink 7.4.7, Calculated Results for Drift Choice #7.

NOTE: Top: inside drip shield; Bottom: outside drip shield.

Figure E.4-6. Vapor Mass Fractions in Gas: Choice #7, 3,000 Years, Low Dispersion Bound

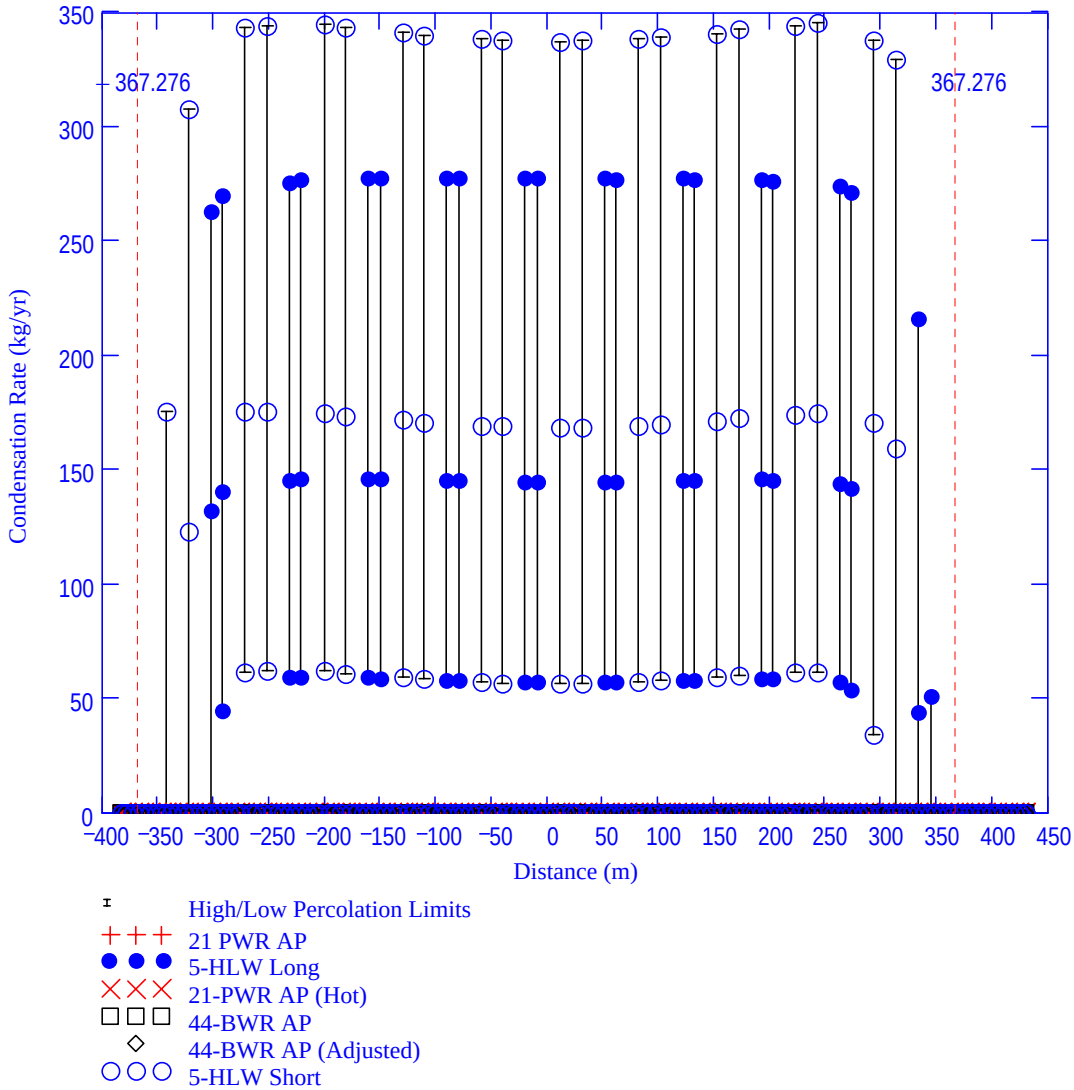

DTN: SN0408T0509903.007; file TOC.mcd; hyperlink 7.4.7, Calculated Results for Drift Choice #7.

Figure E.4-7. Condensation Rate on the Underside of the Drip Shield: Choice #7, 3,000 Years, Low Dispersion Bound

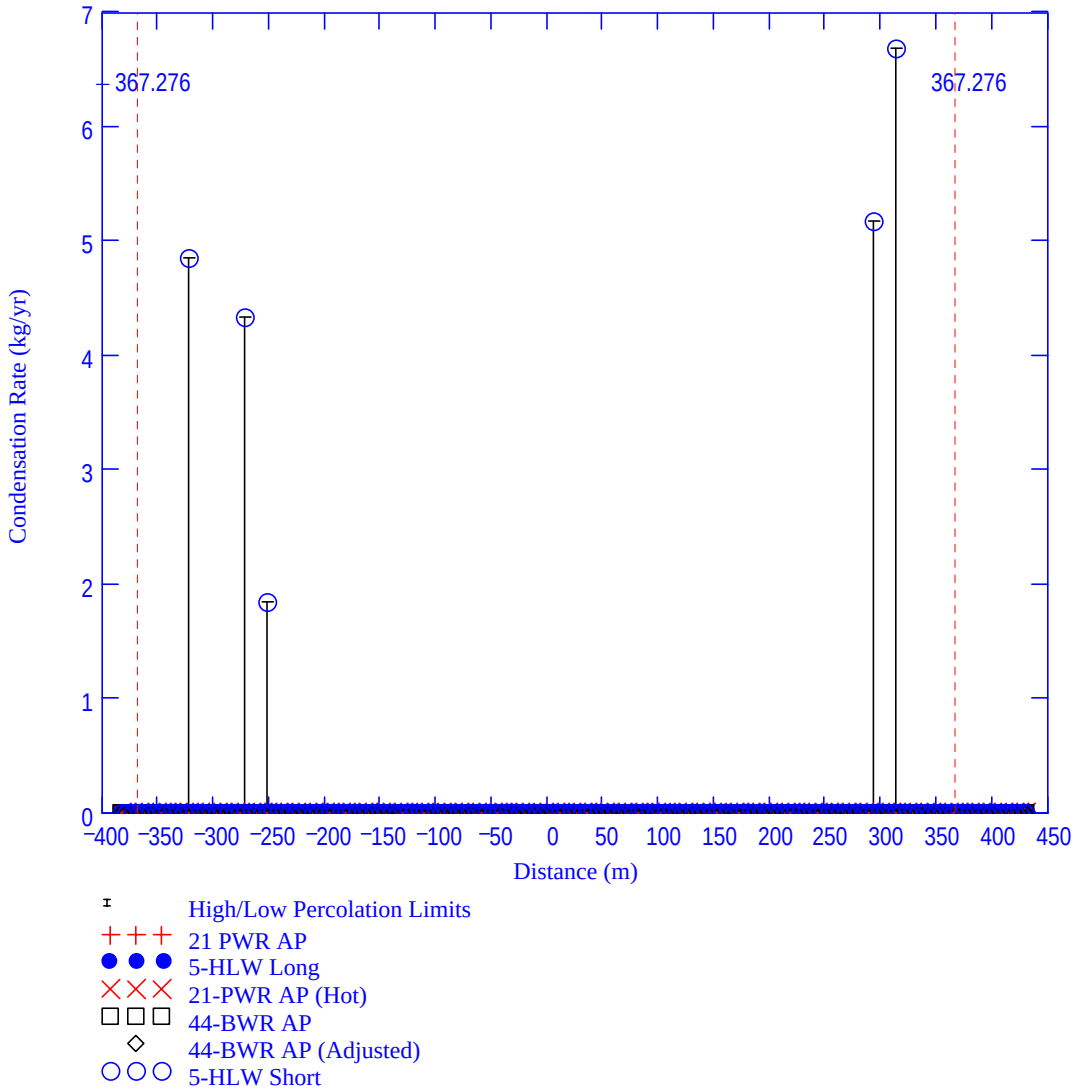

DTN: SN0408T0509903.007; file TOC.mcd; hyperlink 7.4.7, Calculated Results for Drift Choice #7.

Figure E.4-8. Condensation Rate on Waste Packages: Choice #7, 3,000 Years, Low Dispersion Bound

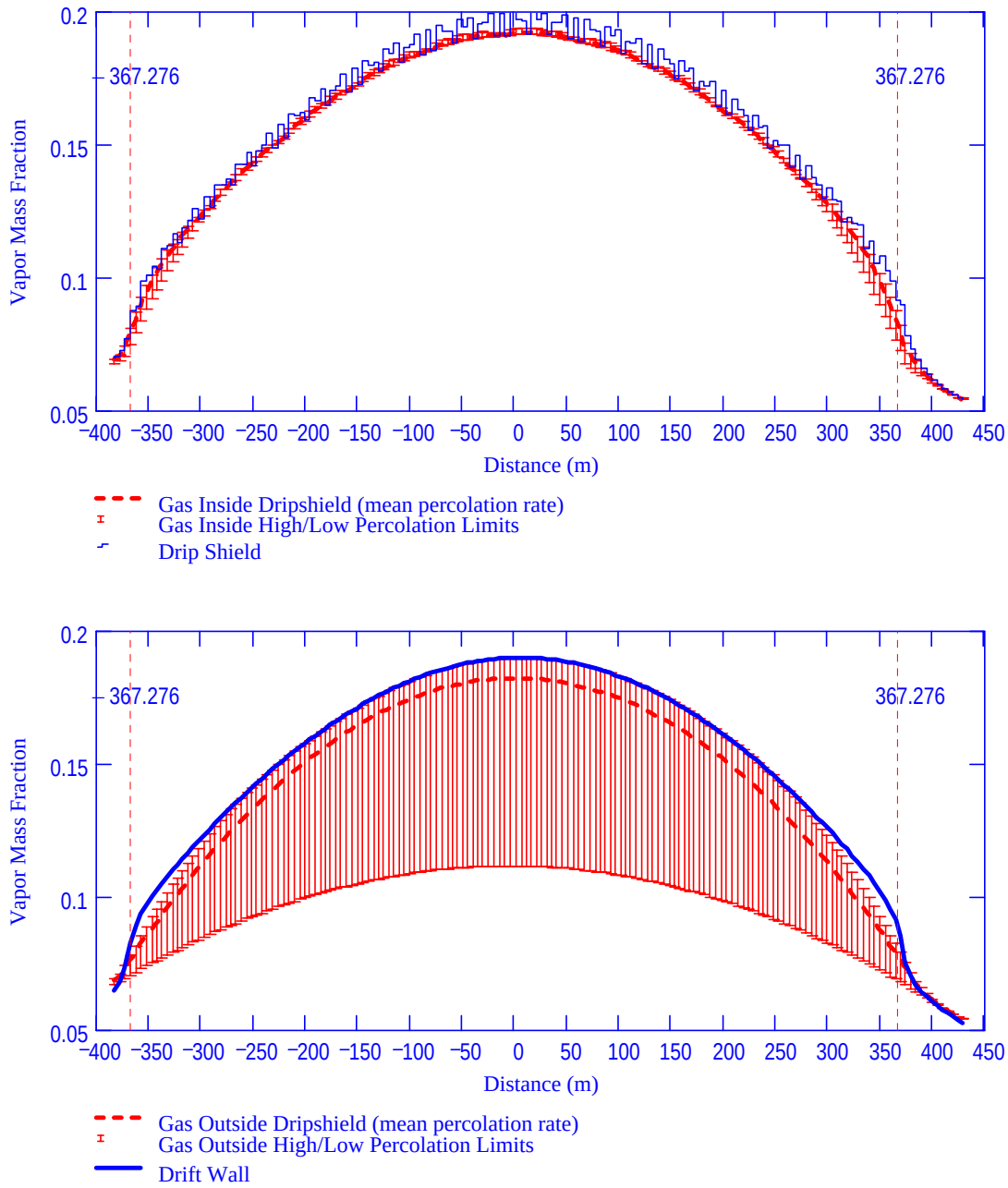

DTN: SN0408T0509903.007; file TOC.mcd; hyperlink 7.4.7, Calculated Results for Drift Choice #7.

NOTE: Top: inside drip shield; Bottom: outside drip shield.

Figure E.4-9. Vapor Mass Fractions in Gas: Choice #7, 3,000 Years, High Dispersion Bound

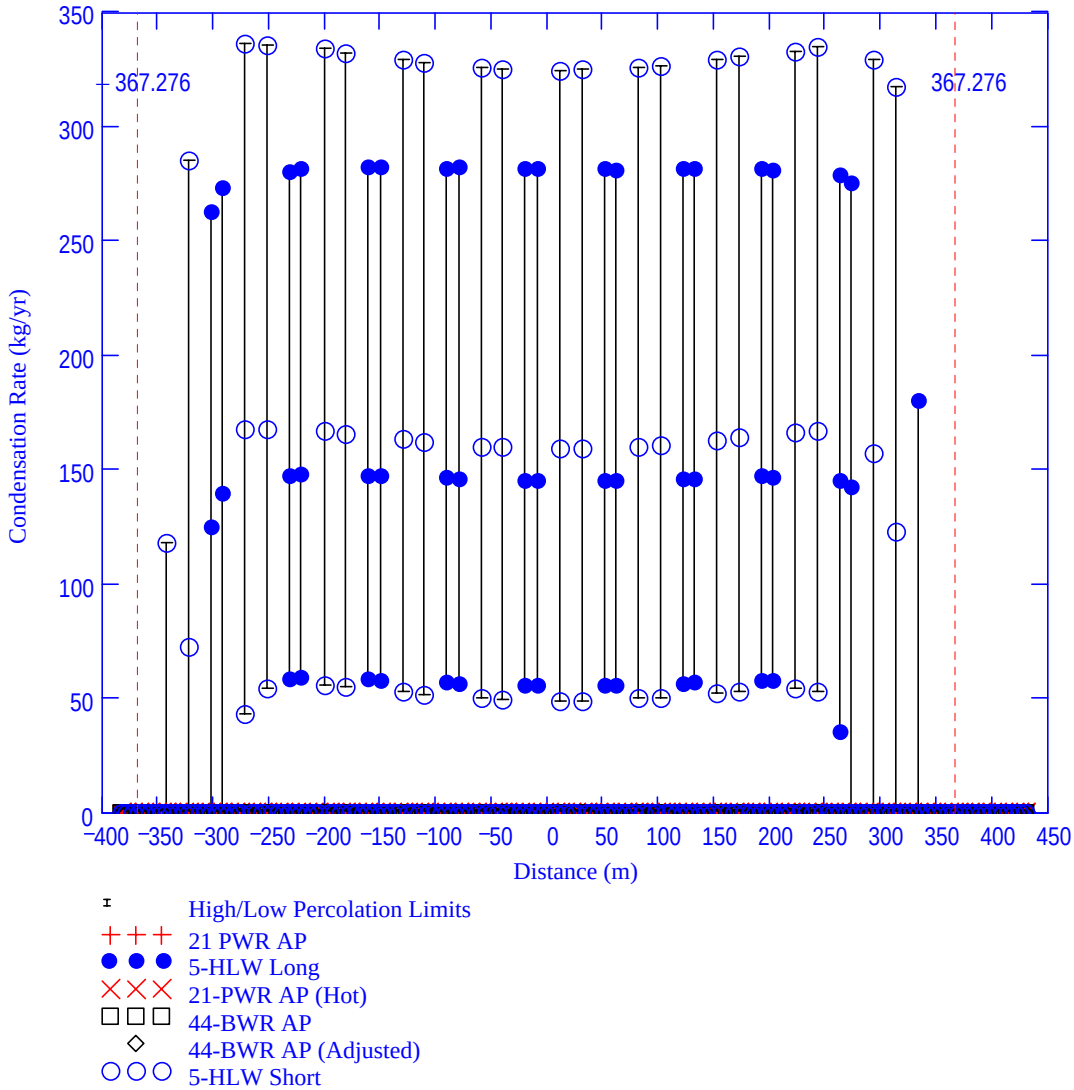

DTN: SN0408T0509903.007; file TOC.mcd; hyperlink 7.4.7, Calculated Results for Drift Choice #7.

Figure E.4-10. Condensation Rate on the Underside of the Drip Shield: Choice #7, 3,000 Years, High Dispersion Bound

Table E.4-2. Summary of Condensation Rates: Choice #7, 3,000 Years

Dispersion Bound	Percolation Level	Condensation Location		21-PWR AP	5-HLW Long	21-PWR AP (Hot)	4-BWR AP	4-BWR AP (Adjusted)	5-HLW Short
	Low	Underside of	# WP's	0	17	0	0	0	17
		Drip Shield	Avg. Rate	0	56.9	0	0	0	57.5
		On Waste	# WP's	0	0	0	0	0	0
		Package	Avg. Rate	0	0	0	0	0	0
	Mean	Underside of	# WP's	0	19	0	0	0	19
Low		Drip Shield	Avg. Rate	0	138.8	0	0	0	168.5
		On Waste	# WP's	0	0	0	0	0	0
		Package	Avg. Rate	0	0	0	0	0	0
	Upper	Underside of	# WP's	0	20	0	0	0	20
		Drip Shield	Avg. Rate	0	261.2	0	0	0	330.4
		On Waste	# WP's	0	0	0	0	0	5
		Package	Avg. Rate	0	0	0	0	0	4.6
	Low	Underside of	# WP's	0	15	0	0	0	16
		Drip Shield	Avg. Rate	0	55.6	0	0	0	51.4
		On Waste	# WP's	0	0	0	0	0	0
		Package	Avg. Rate	0	0	0	0	0	0
	Mean	Underside of	# WP's	0	18	0	0	0	19
High		Drip Shield	Avg. Rate	0	144.6	0	0	0	156.1
		On Waste	# WP's	0	0	0	0	0	0
		Package	Avg. Rate	0	0	0	0	0	0
	Upper	Underside of	# WP's	0	19	0	0	0	20
		Drip Shield	Avg. Rate	0	274.4	0	0	0	316.3
		On Waste	# WP's	0	0	0	0	0	0
		Package	Avg. Rate	0	0	0	0	0	0

DTN: SN0408T0509903.007; file TOC.mcd; hyperlink 7.4.7, Calculated Results for Drift Choice #7.

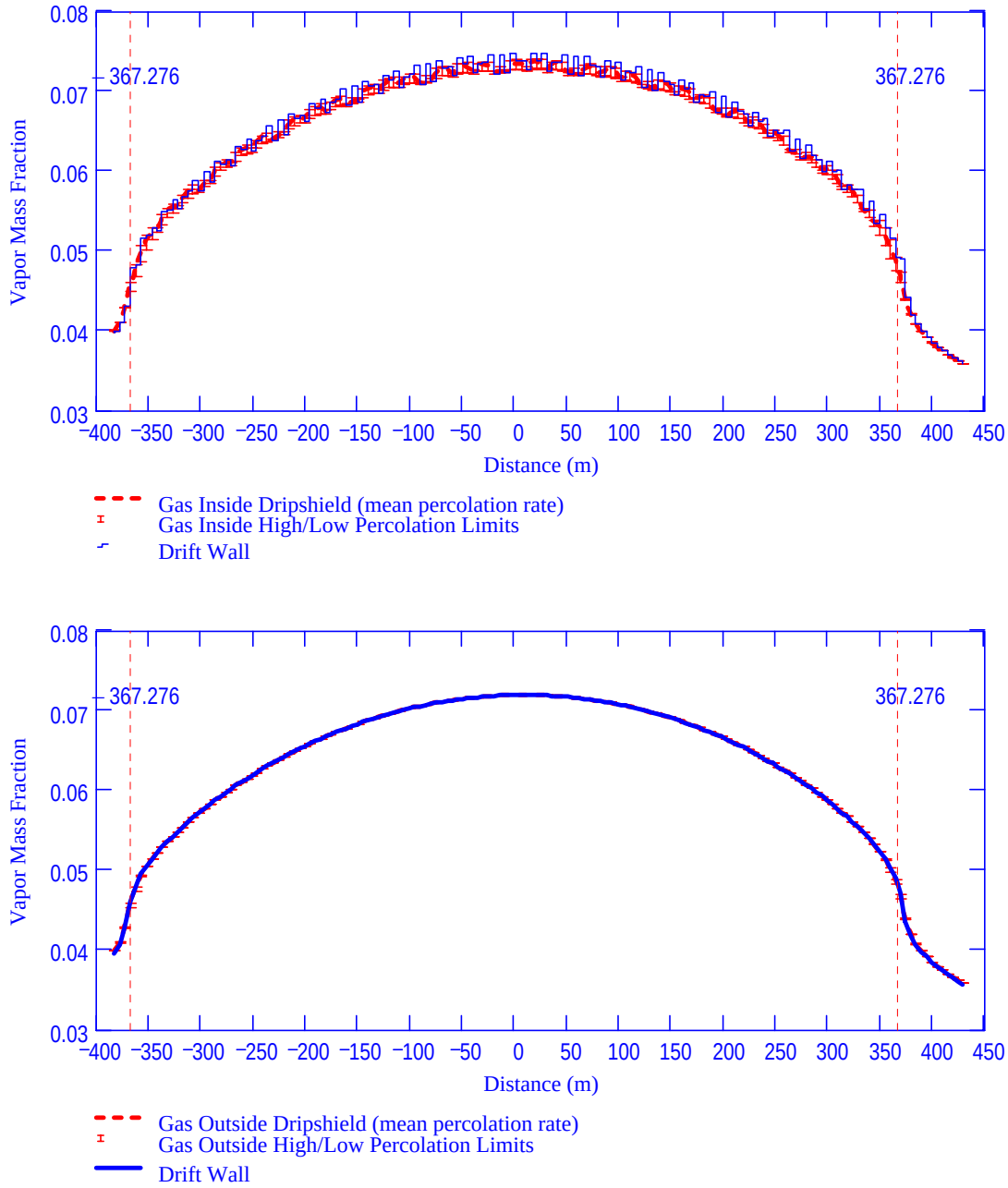

DTN: SN0408T0509903.007; file TOC.mcd; hyperlink 7.4.7, Calculated Results for Drift Choice #7.

NOTE: Top: inside drip shield; Bottom: outside drip shield.

Figure E.4-11. Vapor Mass Fractions in Gas: Choice #7, 10,000 Years, Low Dispersion Bound

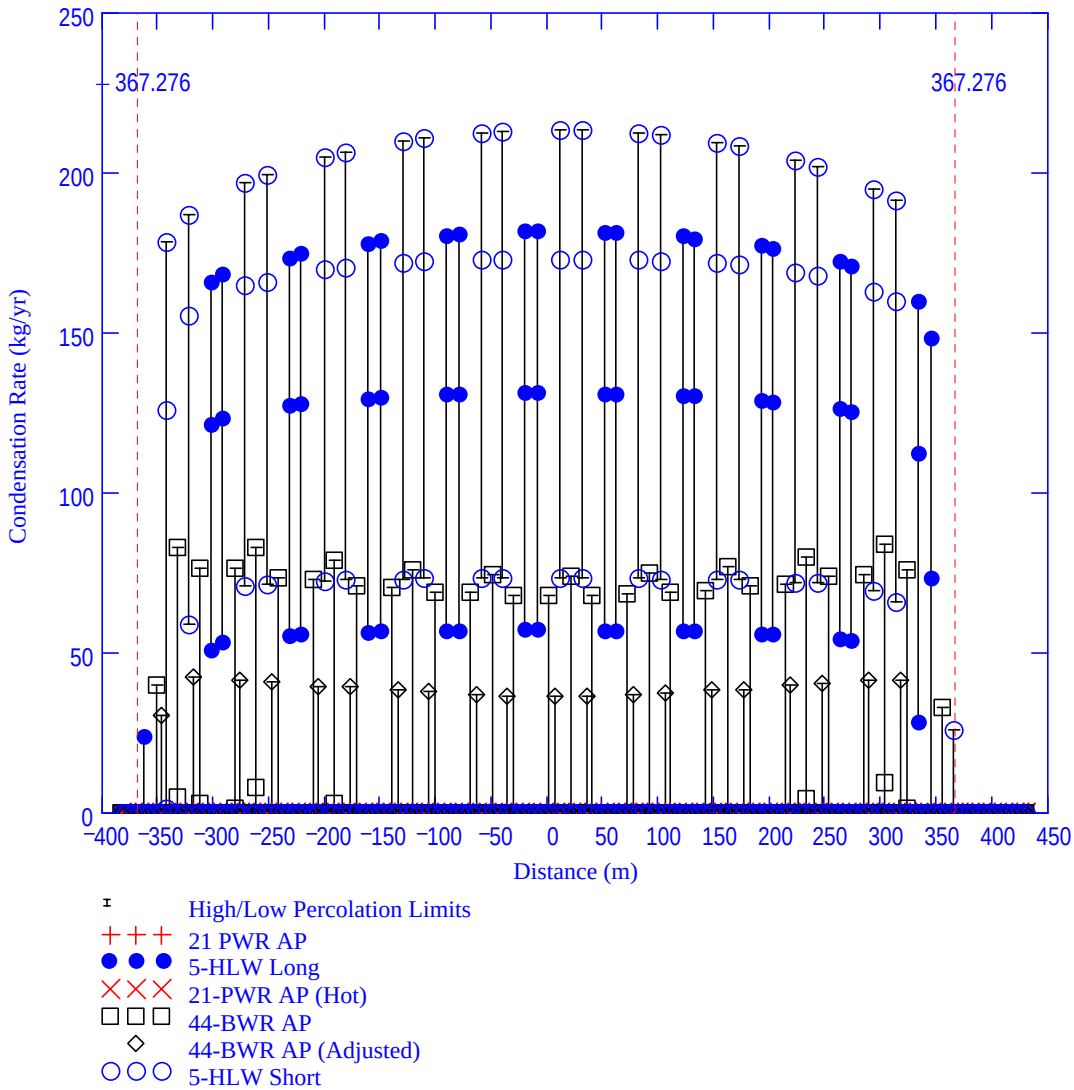

DTN: SN0408T0509903.007; file TOC.mcd; hyperlink 7.4.7, Calculated Results for Drift Choice #7.

Figure E.4-12. Condensation Rate on the Underside of the Drip Shield: Choice #7, 10,000 Years, Low Dispersion Bound

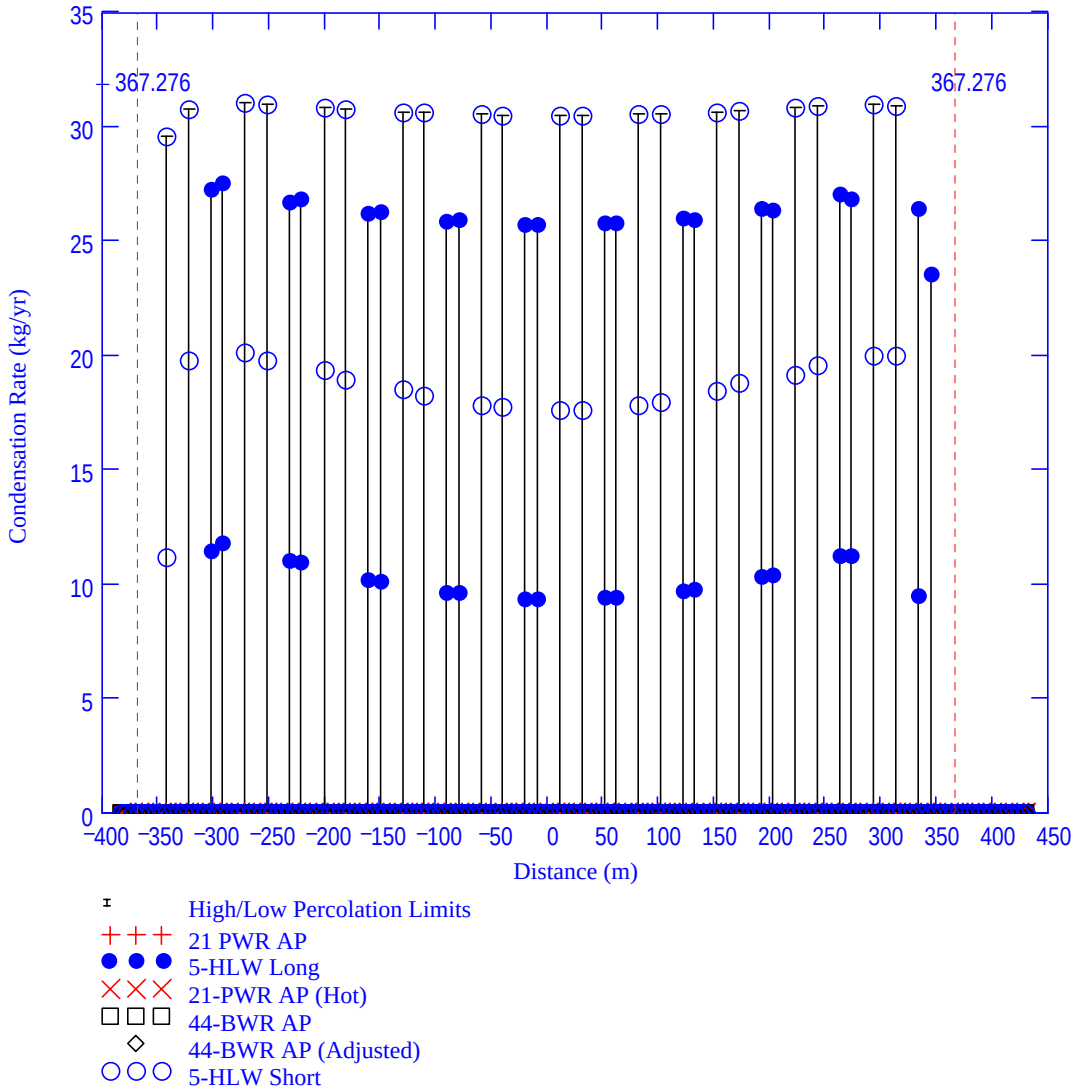

DTN: SN0408T0509903.007; file TOC.mcd; hyperlink 7.4.7, Calculated Results for Drift Choice #7.

Figure E.4-13. Condensation Rate on Waste Packages: Choice #7, 10,000 Years, Low Dispersion Bound

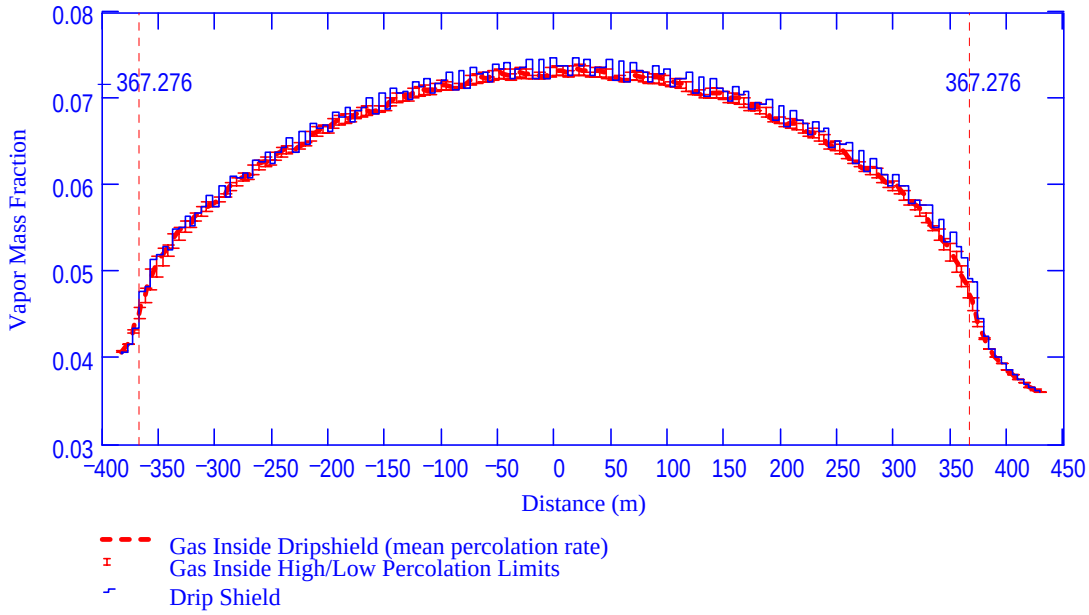

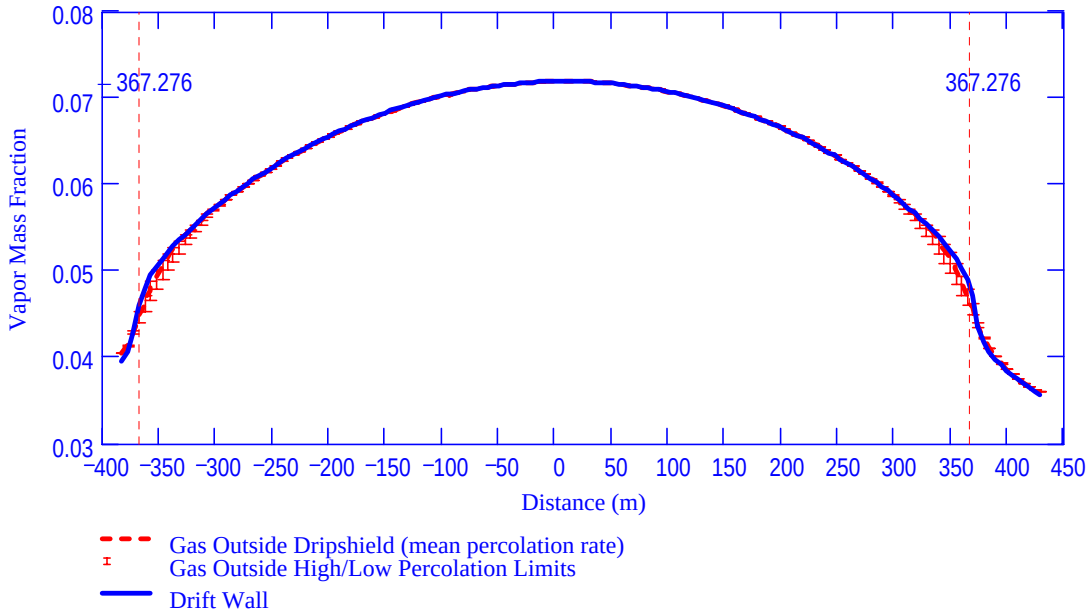

DTN: SN0408T0509903.007; file TOC.mcd; hyperlink 7.4.7, Calculated Results for Drift Choice #7.

NOTE: Top: inside drip shield; Bottom: outside drip shield.

Figure E.4-14. Vapor Mass Fractions in Gas: Choice #7, 10,000 Years, High Dispersion Bound

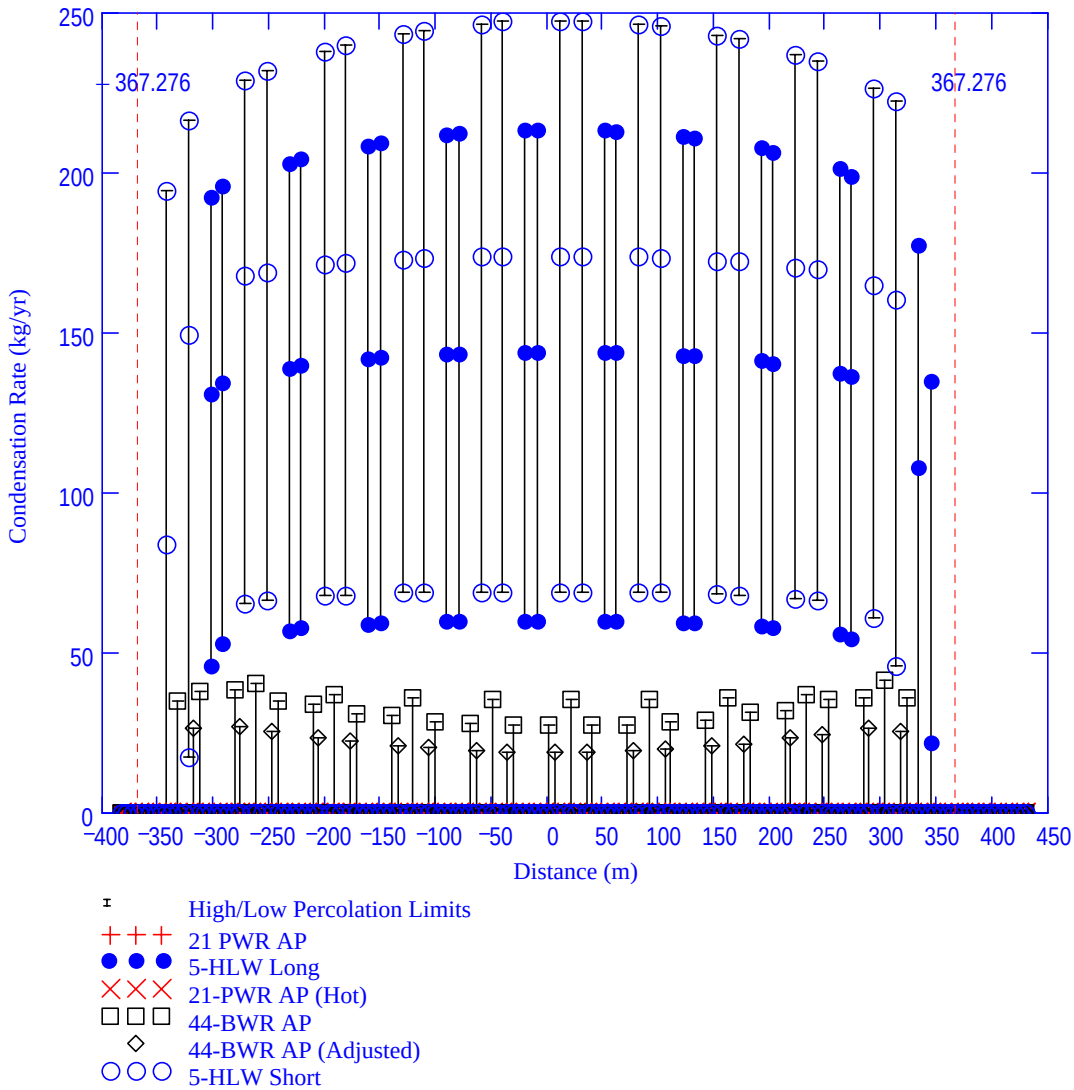

DTN: SN0408T0509903.007; file TOC.mcd; hyperlink 7.4.7, Calculated Results for Drift Choice #7.

Figure E.4-15. Condensation Rate on the Underside of the Drip Shield: Choice #7, 10,000 Years, High Dispersion Bound

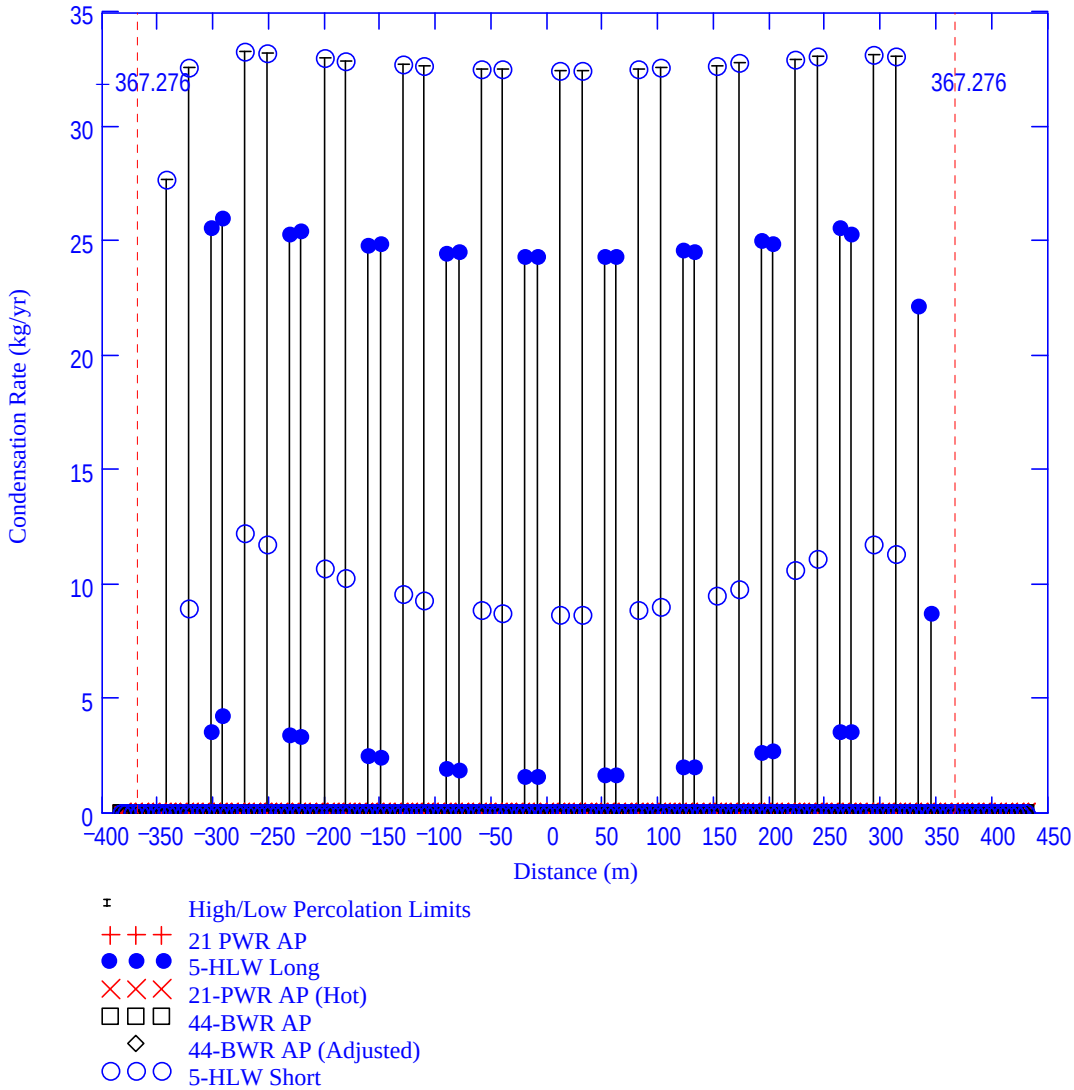

DTN: SN0408T0509903.007; file TOC.mcd; hyperlink 7.4.7, Calculated Results for Drift Choice #7.

Figure E.4-16. Condensation Rate on Waste Packages: Choice #7, 10,000 Years, High Dispersion Bound

Table E.4-3. Summary of Condensation Rates: Choice #7, 10,000 Years

Dispersion Bound	Percolation Level	Condensation Location		21-PWR AP	5-HLW Long	21-PWR AP (Hot)	4-BWR AP	4-BWR AP (Adjusted)	5-HLW Short
	Low	Underside of	# WP's	0	19	0	0	0	20
		Drip Shield	Avg. Rate	0	54.2	0	0	0	67.7
		On Waste	# WP's	0	0	0	0	0	0
		Package	Avg. Rate	0	0	0	0	0	0
	Mean	Underside of	# WP's	0	20	0	8	0	20
Low		Drip Shield	Avg. Rate	0	124.9	0	4.4	0	166.7
		On Waste	# WP's	0	19	0	0	0	20
		Package	Avg. Rate	0	10.2	0	0	0	18.4
	Upper	Underside of	# WP's	0	21	0	31	20	21
		Drip Shield	Avg. Rate	0	167.2	0	71.3	38.3	195.3
		On Waste	# WP's	0	20	0	0	0	20
		Package	Avg. Rate	0	26.2	0	0	0	30.7
	Low	Underside of	# WP's	0	18	0	0	0	19
		Drip Shield	Avg. Rate	0	57.4	0	0	0	63.7
		On Waste	# WP's	0	0	0	0	0	0
		Package	Avg. Rate	0	0	0	0	0	0
	Mean	Underside of	# WP's	0	20	0	0	0	20
High		Drip Shield	Avg. Rate	0	132.9	0	0	0	165.5
		On Waste	# WP's	0	18	0	0	0	19
		Package	Avg. Rate	0	2.6	0	0	0	10.0
	Upper	Underside of	# WP's	0	20	0	29	19	20
		Drip Shield	Avg. Rate	0	201.8	0	33.3	22.1	236.0
		On Waste	# WP's	0	20	0	0	0	20
		Package	Avg. Rate	0	24.0	0	0	0	32.5

DTN: SN0408T0509903.007; file TOC.mcd; hyperlink 7.4.7, Calculated Results for Drift Choice #7.

APPENDIX F

COMPARISON OF SOLUTIONS: LINE SOURCE VS. CYLINDER WITH PRESCRIBED WALL FLUX

The drift wall temperatures were approximated using the superposition of line sources in a homogeneous rock domain. In reality, the domain in the near field is not homogenous. The only mass within the drift itself is that of the waste packages, the drip shield, and the gas. In order to test the efficacy of the line source solution, it is compared to the solution for an infinite hollow cylinder with a prescribed heat flux at the surface.

The temperature field about an infinitely long cylinder (T_{cyl} in Eq. F-1) in an infinite domain is (Carslaw and Jaeger 1959 [DIRS 100968], p. 338, Eq. 17):

$$T_{cyl} = \frac{-2Q}{\pi\, k} \int_0^{\infty} \left(1 - e^{-\alpha u^2 t}\right) \frac{J_0(u\, r) Y_1(u\, R_{drift}) - Y_0(u\, r) J_1(u\, R_{drift})}{u^2 \left[J_1^2(u\, R_{drift}) + Y_1^2(u\, R_{drift})\right]} du \qquad \text{(Eq. F-1)}$$

where k is the thermal conductivity, α is the thermal diffusivity, and Q is the heat flux (W/m^2) at the wall surface which has a radius of R_{drift}. The heat flux at the drift wall (Q) is related to the line source (qL) strength by Equation F-2.

$$Q = \frac{qL}{\pi\, D_{drift}} \qquad \text{(Eq. F-2)}$$

The resulting equation for the temperature at the cylinder wall (r=R_{drift}) is:

$$T_{cyl} = \frac{-2\, qL}{\pi^2 D_{drift}\, k} \int_0^{\infty} \left(1 - e^{-\alpha u^2 t}\right) \frac{J_0(u\, R_{drift}) Y_1(u\, R_{drift}) - Y_0(u\, R_{drift}) J_1(u\, R_{drift})}{u^2 \left[J_1^2(u\, R_{drift}) + Y_1^2(u\, R_{drift})\right]} du \qquad \text{(Eq. F-3)}$$

Equation F-3 is non-dimensionalized. The non-dimensional temperature (Tnd_{cyl}) is written in terms of the non-dimensional time (τ) in Equation F-4.

$$Tnd_{cyl} = \frac{-2}{\pi} \int_0^{\infty} \left(1 - e^{-\upsilon^2 t}\right) \frac{J_0(\upsilon) Y_1(\upsilon) - Y_0(\upsilon) J_1(\upsilon)}{\upsilon^2 \left[J_1^2(\upsilon) + Y_1^2(\upsilon)\right]} d\upsilon$$

where (Eq. F-4)

$$\tau = \frac{\alpha\, t}{R_{drift}^2} \qquad Tnd_{cyl} = \frac{2\pi\, k}{qL} T_{cyl}$$

The temperature field about an infinitely long continuous line source in an infinite domain is (Carslaw and Jaeger 1959 [DIRS 100968], p. 261, Eq. F-4):

$$T_{line} = \frac{qL / \rho\, Cp}{4\pi\, \alpha} \int_{r^2/4\alpha t}^{\infty} \frac{e^{-u}}{u} du \qquad \text{(Eq. F-5)}$$

where qL is the line strength (W/m) and r is the radial distance from the line source. This equation is evaluated at the drift wall (R_{drift}) and non-dimensionalized to produce:

$$Tnd_{line} = \frac{1}{2}\int_{1/4\tau}^{\infty} \frac{e^{-u}}{u} du$$

where (Eq. F-6)

$$\tau = \frac{\alpha\, t}{R_{drift}^2} \quad Tnd_{line} = \frac{2\,\pi\, k}{qL} T_{line}$$

The integral in Equation F-6 is recognized as the exponential integral (Abramowitz and Stegun 1972 [DIRS 103280], p. 228, Eq. 5.1.1). Better computational accuracy is obtained by expanding the integral into a series (Abramowitz and Stegun 1972 [DIRS 103280], p. 228, Eq. 5.1.11):

$$Tnd_{line} = \frac{1}{2} E_1\left(\frac{1}{4\,\tau}\right)$$

where (Eq. F-7)

$$E_1(z) = -\gamma - \ln(z) - \sum_{n=1}^{\infty} \frac{(-1)^n z^n}{n\, n!}$$

The line source and cylindrical source solutions are compared in Figure F-1. The non-dimensional temperature increase is plotted as a function of dimensional time. The figure clearly shows that the two solutions converge with increasing time. At ten years, the solutions are functionally the same.

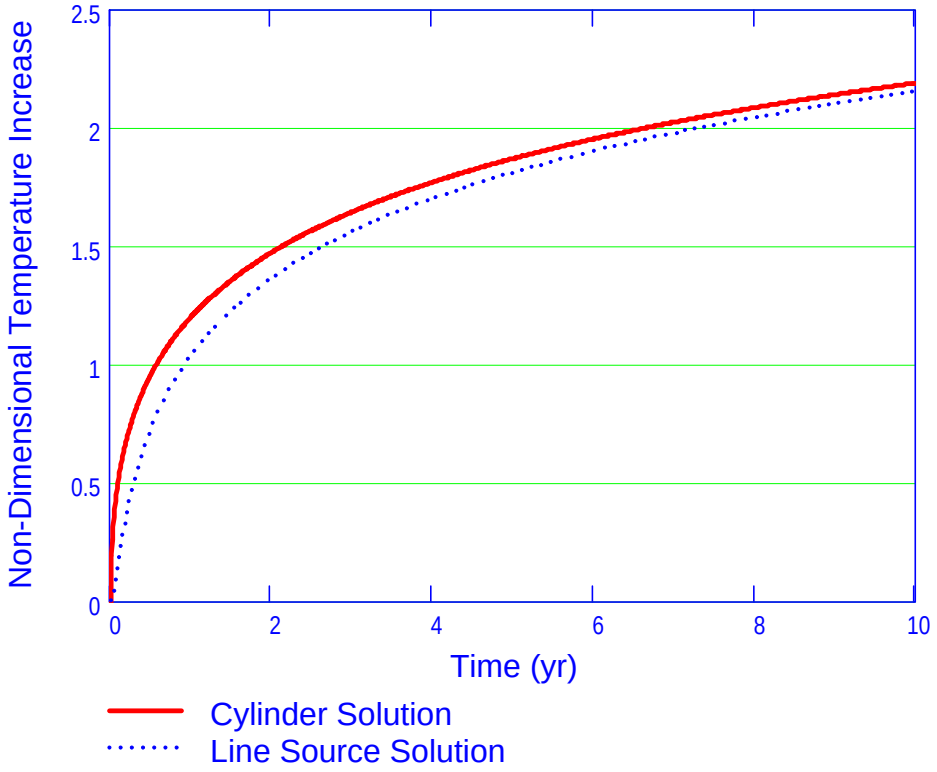

DTN: SN0408T0509903.008; file Cyl_vs_Line.mcd.

Figure F-1. Comparison of Solutions for Cylinder and Line Sources

INTENTIONALLY LEFT BLANK

APPENDIX G

TECHNICAL REVIEWS

Two independent technical reviews have been conducted.

The first technical review was performed by Dr. Michael F. Young of Sandia National Laboratories for the condensation model. His review comments are given in Section G.1. This review was performed on an earlier version of the report and only considered a subset of the criteria for independent technical review given in Section 7.2.2. His review is included here for information only.

The second technical review was performed on the convection and condensation models, including calculation of the dispersion coefficients. This technical review has been performed by Professor Ivan Catton of UCLA and is given in Section G.2. Professor Catton's technical review is based on the earlier version of the report dated June 28, 2004 as noted in his review. There are no significant technical differences between that version and the present revision of the report.

G.1 – REWIEW COMMENTS OF MICHAEL F. YOUNG

Technical Review of the
Condensation Model
September, 2003

Question #1: Is the model based upon generally accepted transport phenomena concepts that pertain to heat and mass trans, including mass transfer induced by temperature differences in the rock?

The model is based on the use of concepts and heat transfer correlations that have been validated and used in the engineering/industrial/scientific world for over 50 years. This is evident by reading the report and noting that the concepts are documented in commonly available handbooks such as: *Transport Phenomena*, by Bird, Stewart and Lightfoot (1960) [103524]. Mass transfer induced by temperature differences in rock is a version of the concept of a temperature difference inducing mass flow by natural convection. This concept is well validated in the open literature and can be found in handbooks such as the one already mentioned here.

Question #2: Does the model pertain specifically to the length scale for the repository design concept of Yucca Mountain?

The model pertains exactly to the length scale of the current repository design, as detailed in the report. The drift diameter, heat source lengths, ratio of heat source length to drift length, and dimensions of the drip shield, and invert depth are all pertinent.

Question #3: The calculation is based upon a steady-state model for natural convection and heat transfer. Is this appropriate?

The time scale for mass transfer by dispersion along the drift axis is minutes to hours over the entire length. Since this is much shorter than the time scale of interest (100-1000 years) the time-dependent nature of the waste-package power and heat transfer does not need to be considered and the steady-state model is appropriate. Similarly, the large thermal response time and heat capacitance of the rock means it is not necessary to consider the change in rock temperature over the time frames of interest.

Question #4: Are the mathematical solution techniques appropriate and adequate to solve the problem of interest?

The use of FLUENT and MathCad are completely appropriate.

General Reviewer Comments:

The reviewer concludes that the model described in this report is valid for the intended application. The transport phenomena concepts described and solved are found and documented in the open literature, as in the one example noted.

24 Mar 03

G.2 REVIEW COMMENTS OF PROFESSOR IVAN CATTON

Memorandum

To: Stephen W. Webb
Dangerous Materials Mitigation and Disposition
Sandia National Laboratories
P.O. Box 5800 MS-0719
Albuquerque, NM 87185-0719

From: Ivan Catton
1702 Crater Lane
Los Angeles, CA 90077

Date: 29 July 2004

Re: Review of "In-Drift Natural Convection and Condensation MDL-EBS-MD-000001 Rev 00x, BACKCHECK COPY, 28 June, 2004

General Comments

The referenced report describes an approach to the development of a model for prediction of condensation within a drift in Yucca Mountain. The computations needed to meet the stated objectives are challenging. Although the temptation to use a CFD code to model the complete drift is strong, it has been resisted. The present combination of CFD and modeling is a sensible approach to accomplishing the objectives of the work; evaluation of the possibility of condensation. The problem is just too big for CFD alone. To be able to make a substantive statement about the certainty of the predictions, many contributors to uncertainty will have to be evaluated and their distributions propagated through the computational process. This was done for the LBLOCA using the CSAU methodology by Westinghouse and can be done for the present problem. The process will require a large number of complete analyses be made. To do this entirely based on CFD would be a monumental task.

To overcome this problem, the authors have developed a multi-tiered approach:

1. Top Level; line heat sources are used to represent the many drifts. The line source reflects the power of the waste packages and enables temperatures of the rock structure to be calculated with all the drifts contributing. The results of this analysis yield the boundary conditions needed for a specific drift computation.
2. Bottom Level; 2D and 3D CFD natural convection computations are carried out. The temperature boundary conditions are far enough away from the drift rock interface to allow conjugate effects to be incorporated into the thermal response of the drift itself. The capability of the CFD code is demonstrated by comparing 2D natural convection results with experimental results found in the literature. The 3D results are used to determine mass dispersion coefficients for use in the midlevel solution.

3. Middle Level; The middle level is a lumped parameter solution allowing a complete drift to be treated. The drift atmosphere is divided into two parts; 1) under the drip shield and 2) between the drip shield and the tunnel wall. All surfaces are coupled to the volumes using heat and mass transfer coefficients. Dispersion coefficients from the bottom level 3D CFD natural convection computations are used to allow one to calculate drift axial migration of water vapor.

Some closure is still needed to validate that the process works. Computations based on the condensation model need to be compared with the 3D CFD results to show that what is distilled from the 3D results will reproduce its original values. These kinds of questions can easily be addressed by showing the details of some of the 3D or 2D results. To clearly demonstrate that the use of calculated dispersion coefficients in a model is a valid approach, the problem could be limited to strictly heat transfer by using the 3D heat transfer results to generate thermal dispersion coefficients and then determining whether or not the resulting heat fluxes compare well with the values calculated with the 3D code. If they do, the only remaining question would be the impact of vapor concentration on convective processes.

An interesting result is the existence of convection cells in the drift. These cells will have an essentially uniform vapor concentration and a step change at the cell to cell interface when no axial temperature gradient exists. This leads to an overall dispersion coefficient that may be artificially low when drift axial velocity exists because of the general tilt in temperature along the drift axis. Questions about how the dispersion coefficient is calculated also arise when one considers the drift re-circulation. This should receive enough attention to determine how conservative the result is.

Another aspect of the drift thermo-physical behavior is the existence of barometric pumping. There are arguments about the beneficial effects that deserve some attention. How this could be done is not clear.

Primary Issues and Their Resolution

As a part of the previous report, eight issues thought to be important issues were raised and their resolution, although incomplete, helps a great deal in developing confidence in the modeling strategy and results. The remaining issues are the following:

1. The length of the computational zone and temperature tilt need to be evaluated and shown to be sufficient. In that it is argued that temperature tilt reduces the potential for condensation, this only needs to be done for the case where there is no tilt.
   Resolution: This issue is not dealt with.

2. Ignoring buoyancy effects due to vapor content needs to be evaluated and an estimate of the uncertainty needs to be made.
   Resolution: The arguments given on pages 41 and 47 do not fully address this issue.

3. Heat release where there is condensation and where there is evaporation and its impact needs to be justified.
   Resolution: This issue is not dealt with and at some point some simple calculations need to be done to determine the impact its neglect should be carried out.

4. Close the loop by making comparisons of the condensation model results and the 3D results to at least see if the input is the same as the output. Condensation becomes less of a problem when the dispersion is high meaning that its under-prediction is conservative.
   Resolution: A great deal on this issue for 2D modeling is found in Appendix X of the report. The results are reasonable for the type of modeling done. Full resolution will require that similar calculations be made to allow comparison with 3D FLUENT predictions.

Specific Criteria for Model Acceptance

Unfortunately, a problem this complex requires a great deal of effort to quantitatively evaluate the output and its certainty or uncertainty. Note that best estimate predictions of the large break LOCA are still approximate with a difficult to define amount of uncertainty in the peak clad temperature. There is much that can be done in this regard but when done there will still be uncertainties. This is compounded by a time scale of 10,000 years. Six specific questions were asked and are addressed. In what follows, condensation model refers to the multi-level process described above.

1. Is the condensation model based on generally accepted transport phenomena concepts that pertain to heat and mass transfer in the drift? Are the transport equations appropriate for the purpose of the condensation model, which is to provide bounding calculations?
   Response: The condensation model is based on the conservation equations and modeling approaches that have been in common use by engineers for many years. The transport equations, see response to question 5, are appropriate for obtaining bounding results.
2. Does the model pertain specifically to the length and time scales for heat and mass transfer within the drifts in the repository design concept at Yucca Mountain? This question may be difficult to address in that few experimental data used in formulating the heat and mass transfer correlations are expected to be available. In the absence of such data, the review shall consider if the appropriate scaling parameters have been used (Rayleigh number, etc.) and if the proper flow regime (laminar, turbulent) has been employed.
   Response: Heat and mass transfer coefficients used in the analysis are quasi-steady and depend only on conditions within the drift at a given instant in time. As a result the time scale is adequately dealt with. The length scale used in the analysis is incorporated into the value of the Rayleigh number and is the primary variable for scaling. At present the lack of density change due to vapor concentrations within the drift is not properly dealt with although arguments are given for the result being conservative.
3. Are the mathematical solution techniques appropriate and adequate to solve the

problem of interest?

Response: The process is complex and a mathematical solution technique to address it is not easy to develop. To overcome this problem, the authors have developed a multi-tiered approach:

Top Level; line heat sources are used to represent the many drifts. The line source reflects the power of the waste packages and enables temperatures of the rock structure to be calculated with all the drifts contributing. The results of this analysis yield the boundary conditions needed for a specific drift computation.

Bottom Level; 2D and 3D CFD computations are carried out. The temperature boundary conditions are far enough away from the drift rock interface to allow conjugate effects to be incorporated into the thermal response of the drift itself. The capability of the CFD code is demonstrated by comparing 2D results with experimental results found in the literature. The 3D results are used to determine mass dispersion coefficients for use in the midlevel solution.

Middle Level; The middle level is a lumped parameter solution allowing a complete drift to be treated. The drift atmosphere is divided into two parts; 1) under the drip shield and 2) between the drip shield and the tunnel wall. All surfaces are coupled to the volumes using heat and mass transfer coefficients. Dispersion coefficients from the bottom level computations are used to allow one to calculate drift axial migration of water vapor.

The mathematical solution technique is appropriate for the problem being addressed.

4. Are the problem formulation and the resulting calculations reasonable?

Response: The problem formulation is discussed in my response to question 5. The resulting calculations are reasonable but with an unknown amount of conservatism.

5. Are the scope and purpose (intended use) for the model defined, and is the model a valid representation of repository performance given this scope and purpose?

Response: The scope and purpose for the model are defined and the model is a conservative representation of the repository performance. It is a valid tool for its intended purpose.

6. Are the uncertainties in the model, and their impact on the model output, adequately described?

Response: The report leads the reader to the conclusion that the model predictions are conservative. Unfortunately, it is not possible to ascertain how conservative the results are. A quantitative evaluation of the uncertainties is not made and would be a very difficult task if pursued. For the most part, the uncertainties and impact on the model output are adequately described.

To summarize, it is this reviewers opinion that, in spite of some open questions, the model as presently being used, is a valid tool for its intended use.

INTENTIONALLY LEFT BLANK

APPENDIX H

CORRELATION SUMMARY OF VENTILATED CONDENSATION MODEL ABSTRACTION

(DTNS: SN0402T0809903.003 AND SN0402T0809903.004)

This attachment summarizes the output DTNs produced by the condensation model for the ventilated drip shield case (DTN'S: SN0402T0809903.003 AND SN0402T0809903.004). It is included here for the convenience of the reader. The description of the calculations used to produce these correlations is contained in Section 8.3.

The regression for the drift-wall condensation rate is a straight line given by equation 8.3.1.1-4. The equation for the fraction is given by equation 8.3.1.1-3. The slope and y-intercept parameters are defined in Section 8.3.

H.1 VENTILATED, LOW INVERT TRANSPORT CORRELATION SUMMARY

Table H.1-1. Drift Wall Condensation: 1,000 Years; Low Dispersion Coefficient – Low Invert Transport

LowD	Slope	Y-intercept
Rate	–0.018889532	–2.340873005
Rate R-Squared	0.002608106	
Std. Error on Rate Slope	0.102451843	
Std. Error on Rate Intercept	1.476074119	
	Slope	**Y-intercept**
Fraction	–0.105987488	0.102214733
Fraction R-Squared	0.169198769	
Max Fraction	0.50	
Std. Error on Fraction Slope	0.053880022	
Std. Error on Fraction Intercept	0.124624717	

DTN: SN0402T0809903.003; file: Mixed_Low_Invert_1000_analysis.xls

The condensation rate at 1,000 years for the low dispersion coefficient does not correlate well with percolation rate (Table H.1-1, Figures H.1-1 and H.1-2). This is because the axial dispersion of water vapor is important at this time. Condensation on the drift wall is determined more by the location within the drift rather than the local percolation rate. It is important to sample the standard errors for condensation rate and fraction of condensation at this time. (Note: percolation units are mm/yr; wall condensation rates are kg/m/yr where evaporation is positive in Table H.1-1 and Figure H.1-1.)

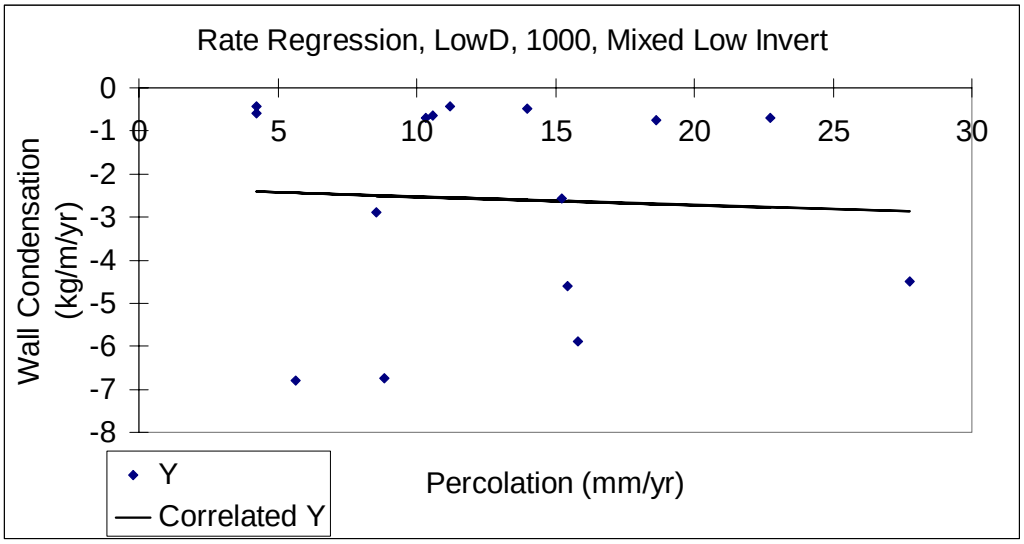

DTN: SN0402T0809903.003; file: Mixed_Low_Invert_1000_analysis.xls.

Figure H.1-1. Wall Rate Regression, Low D, 1,000 Years, Mixed Low Invert Transport

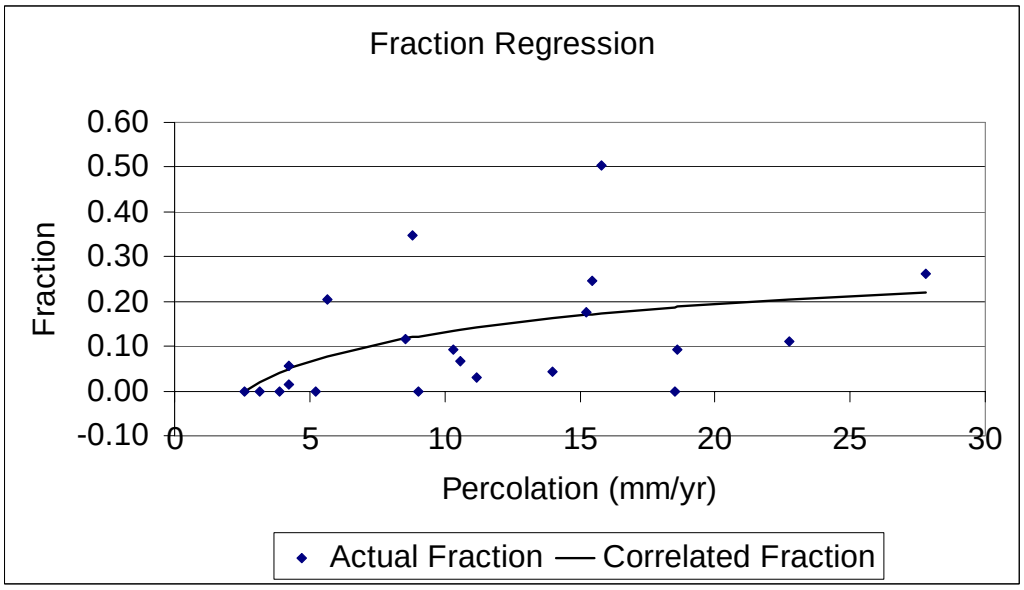

DTN: SN0402T0809903.003; file: Mixed_Low_Invert_1000_analysis.xls

Figure H.1-2. Wall Fraction Regression, Low D, 1,000 Years, Mixed Low Invert Transport

No drift wall condensate forms at 3,000 years for the low dispersion coefficient case.

No drift wall condensate forms at 10,000 years for the low dispersion coefficient case.

No drift wall condensate forms at 1,000 years for the high dispersion coefficient case.

No drift wall condensate forms at 3,000 years for the high dispersion coefficient case.

No drift wall condensate forms at 10,000 years for the high dispersion coefficient case

H.2 VENTILATED, HIGH INVERT TRANSPORT CORRELATION SUMMARY

Table H.2-1. Drift Wall Condensation: 1,000 Years; Low Dispersion Coefficient – High Invert Transport

LowD	Slope	Y-intercept
Rate	–0.224681495	–2.33951287
Rate R-Squared	0.159389496	
Std. Error on Rate Slope	0.128995593	
Std. Error on Rate Intercept	1.815489667	
	Slope	**Y-intercept**
Fraction	–0.271489322	0.283039007
Fraction R-Squared	0.432849545	
Max Fraction	0.67	
Std. Error on Fraction Slope	0.071294596	
Std. Error on Fraction Intercept	0.1649047	

DTN: SN0402T0809903.004; file: Mixed_High_Invert_1000_analysis.xls.

The condensation rate at 1,000 years for the low dispersion coefficient does not correlate well with percolation rate (Table H.2-1, Figures H.2-1 and H.2-2). This is because the axial dispersion of water vapor is important at this time. Condensation on the drift wall is determined more by the location within the drift rather than the local percolation rate. It is important to sample the standard errors for condensation rate and fraction of condensation at this time. (Note: percolation units are mm/yr; wall condensation rates are kg/m/yr where evaporation is positive in Table H.2-1 and Figure H.2-1).

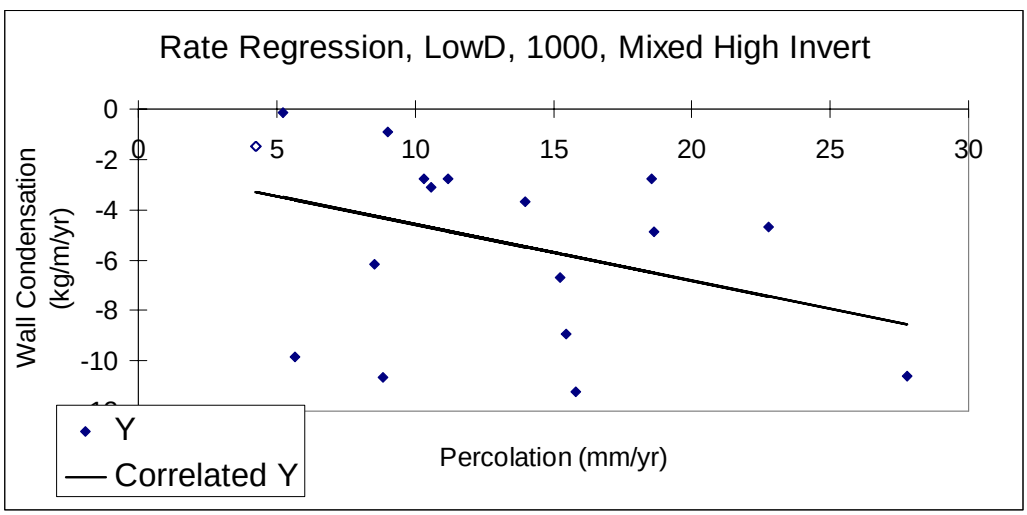

DTN: SN0402T0809903.004; file: Mixed_High_Invert_1000 _analysis.xls.

Figure H.2-1. Wall Rate Regression, Low D, 1,000 Years, Mixed High Invert Transport

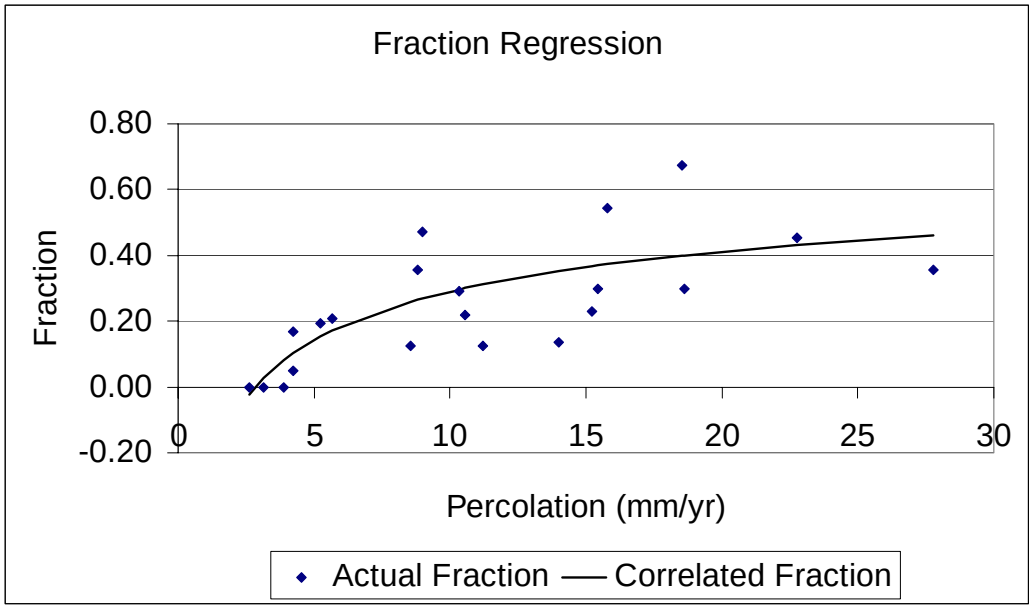

DTN: SN0402T0809903.004; file: Mixed_High_Invert_1000_analysis.xls.

Figure H.2-2 Wall Fraction Regression, Low D, 1,000 Years, Mixed High Invert Transport

Table H.2-2. Drift Wall Condensation: 3,000 Years; Low Dispersion Coefficient – High Invert Transport

LowD	Slope	Y-intercept
Rate	–0.213740042	0.060204846
Rate R-Squared	0.992409776	
Std. Error on Rate Slope	0.004288356	
Std. Error on Rate Intercept	0.09511343	
	Slope	**Y-intercept**
Fraction	–0.454010728	–0.62810343
Fraction R-Squared	0.849763511	
Max Fraction	0.91	
Std. Error on Fraction Slope	0.043795349	
Std. Error on Fraction Intercept	0.114220186	

DTN: SN0402T0809903.004; file: Mixed_High_Invert_3000_analysis.xls

The condensation rate at 3,000 years for the low dispersion coefficient correlates well with percolation rate (Table H.2-2, Figures H.2-3 and H.2-4). This is because the axial dispersion of water vapor has only marginal effect on the local condensation rate. The standard deviations of the condensation rate and the condensation fraction are not important at this time because they are so small. (Note: percolation units are mm/yr; wall condensation rates are kg/m/yr where evaporation is positive in Table H.2-2 and Figure H.2-3).

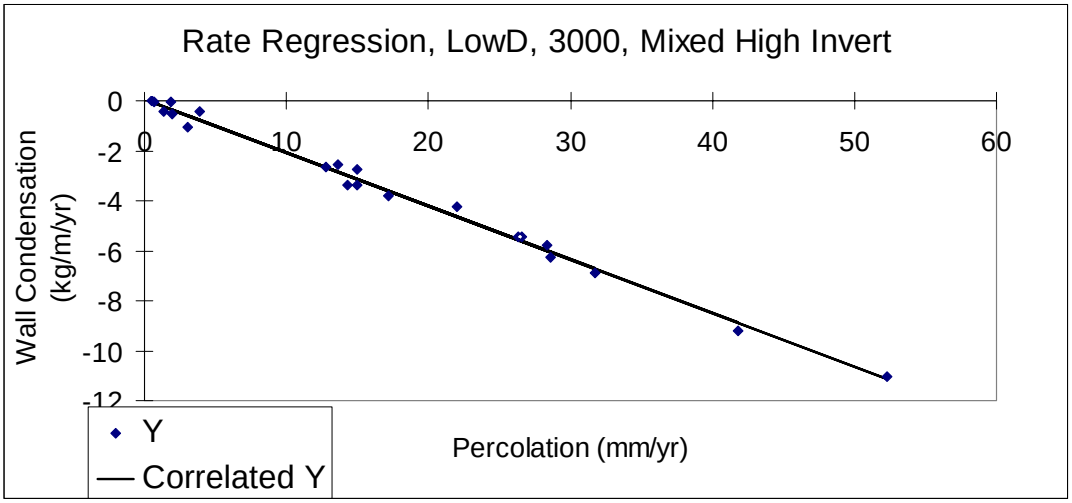

DTN: SN0402T0809903.004; file: Mixed_High_Invert_3000_analysis.xls.

Figure H.2-3. Wall Rate Regression, Low D, 3,000 Years, Mixed High Invert Transport

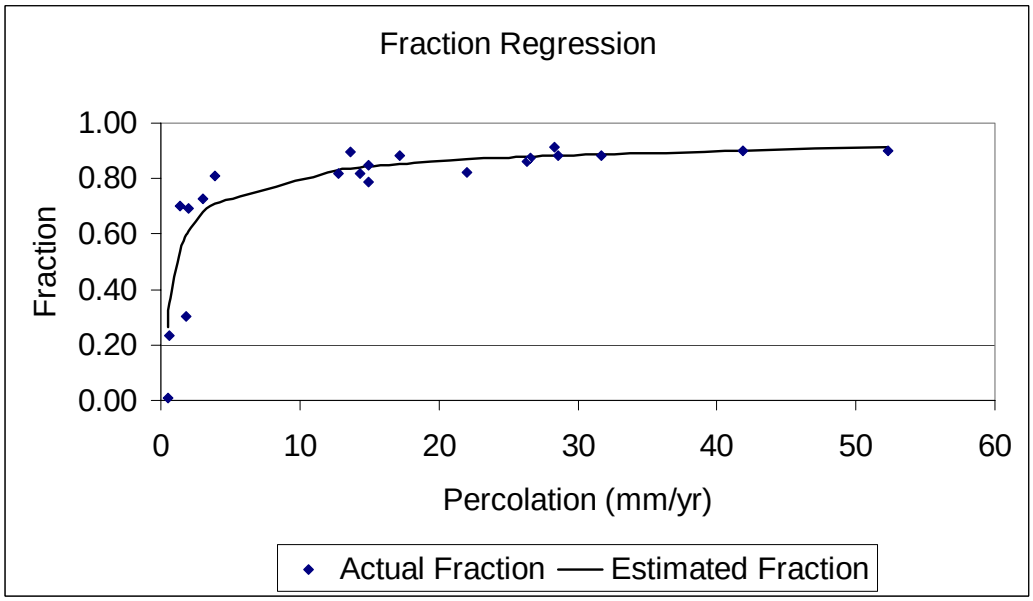

DTN: SN0402T0809903.004; file: Mixed_High_Invert_3000_analysis.xls.

Figure H.2-4. Wall Fraction Regression, Low D, 3,000 Years, Mixed High Invert Transport

Table H.2-3. Drift Wall Condensation: 10,000 Years; Low Dispersion Coefficient – High Invert Transport

LowD	Slope	Y-intercept
Rate	–0.213602098	–0.409597669
Rate R-Squared	0.99942241	
Std. Error on Rate Slope	0.00117805	
Std. Error on Rate Intercept	0.026128521	
	Slope	**Y-intercept**
Fraction	–0.280728115	–1.663883577
Fraction R-Squared	0.774907239	
Max Fraction	0.95	
Std. Error on Fraction Slope	0.034710831	
Std. Error on Fraction Intercept	0.090527367	

DTN: SN0402T0809903.004; file: Mixed_High_Invert_10000_analysis.xls.

The condensation rate at 10,000 years for the low dispersion coefficient correlates well with percolation rate (Table H.2-3, Figures H.2-5 and H.2-6). This is because the axial dispersion of water vapor has only marginal effect on the local condensation rate. The standard deviations of the condensation rate and the condensation fraction are not important at this time because they are so small. (Note: percolation units are mm/yr; wall condensation rates are kg/m/yr where evaporation is positive in Table H.2-5 and Figure H.2-5).

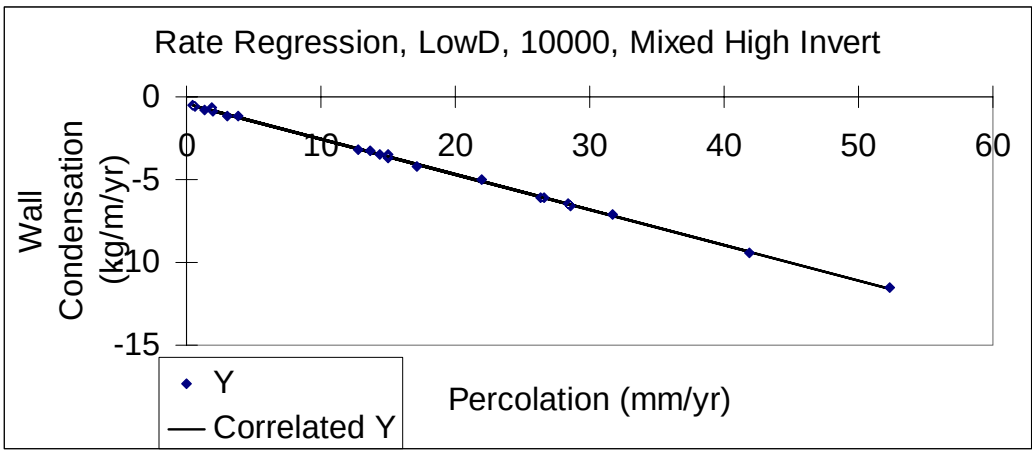

DTN: SN0402T0809903.004; file: Mixed_High_Invert_10000_analysis.xls.

Figure H.2-5. Wall Rate Regression, Low D, 10,000 Years, Mixed High Invert Transport

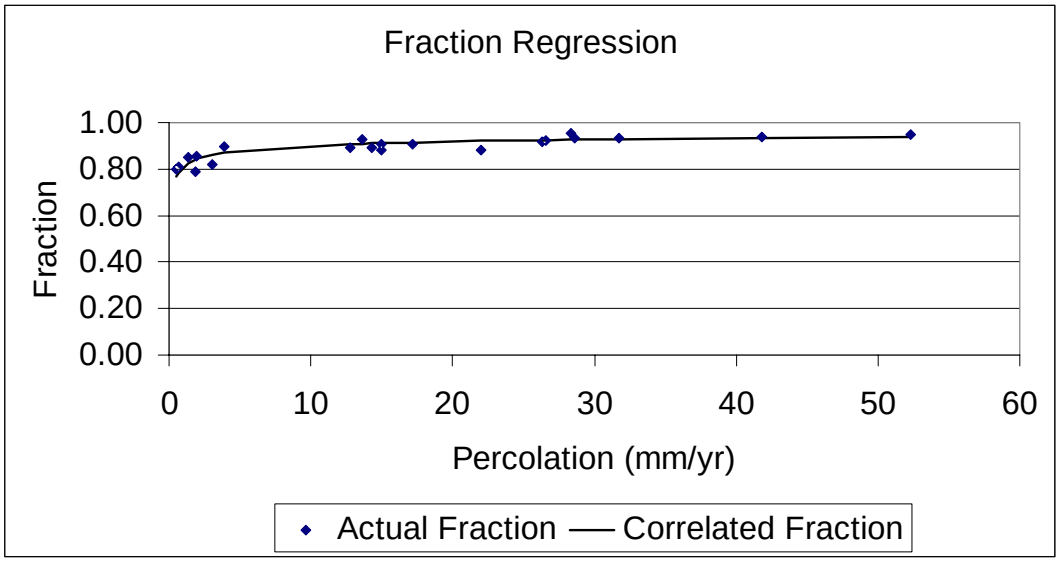

DTN: SN0402T0809903.004; file: Mixed_High_Invert_10000_analysis.xls.

Figure H.2-6. Wall Fraction Regression, Low D, 10,000 Years, Mixed High Invert Transport

No condensate forms at 1,000 years for the high dispersion coefficient case.

Table H.2-5. Drift Wall Condensation: 3,000 Years; High Dispersion Coefficient – High Invert Transport

HighD	Slope	Y-intercept
Rate	–0.018655423	–1.00881135
Rate R-Squared	0.022704542	
Std. Error on Rate Slope	0.122394433	
Std. Error on Rate Intercept	3.845147424	
	Slope	**Y-intercept**
Fraction	–0.026311983	0.016390613
Fraction R-Squared	0.085831531	
Max Fraction	0.42	
Std. Error on Fraction Slope	0.019700011	
Std. Error on Fraction Intercept	0.051378491	

DTN: SN0402T0809903.004; file: Mixed_High_Invert_3000_analysis.xls.

The condensation rate at 3,000 years for the low dispersion coefficient does not correlate well with percolation rate (Table H.2-5, Figures H.2-7 and H.2-8). This is because the axial dispersion of water vapor is important at this time. Only chosen drifts 1 and 3 are predicted to have any wall condensation. Chosen drift 1 manifests wall condensate only at the high percolation rate; chosen drift 3 manifests wall condensate only at the medium and high percolation rates. The balance of the chosen drifts has no wall condensate. The low fraction of wall condensation reflects the regional nature of wall condensation at this time. It is important to sample the standard errors for condensation rate and fraction of condensation at this time. (Note: percolation units are mm/yr; wall condensation rates are kg/m/yr where evaporation is positive in Table H.2-5 and Figure H.2-7).

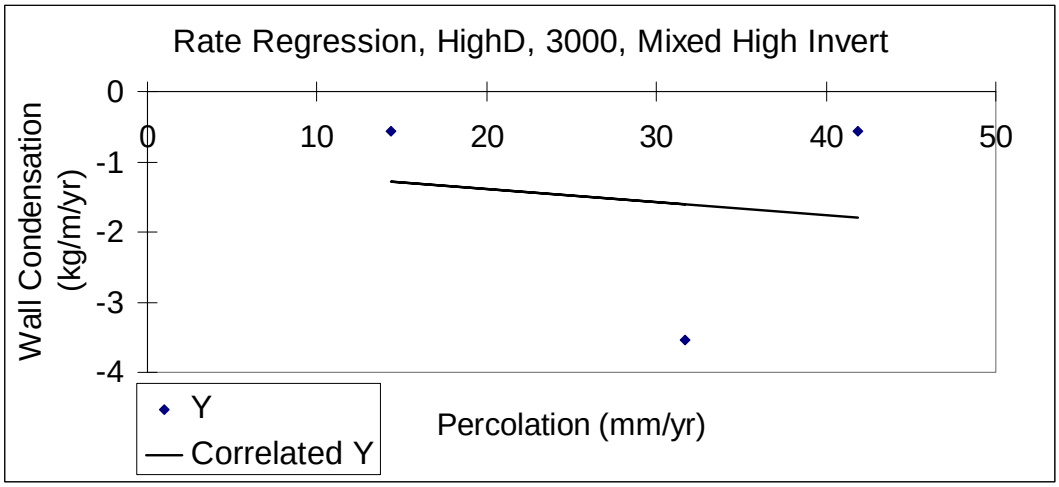

DTN: SN0402T0809903.004; file: Mixed_High_Invert_3000_analysis.xls.

Figure H.2-7. Wall Rate Regression, HighD, 3,000 Years, Mixed High Invert Transport

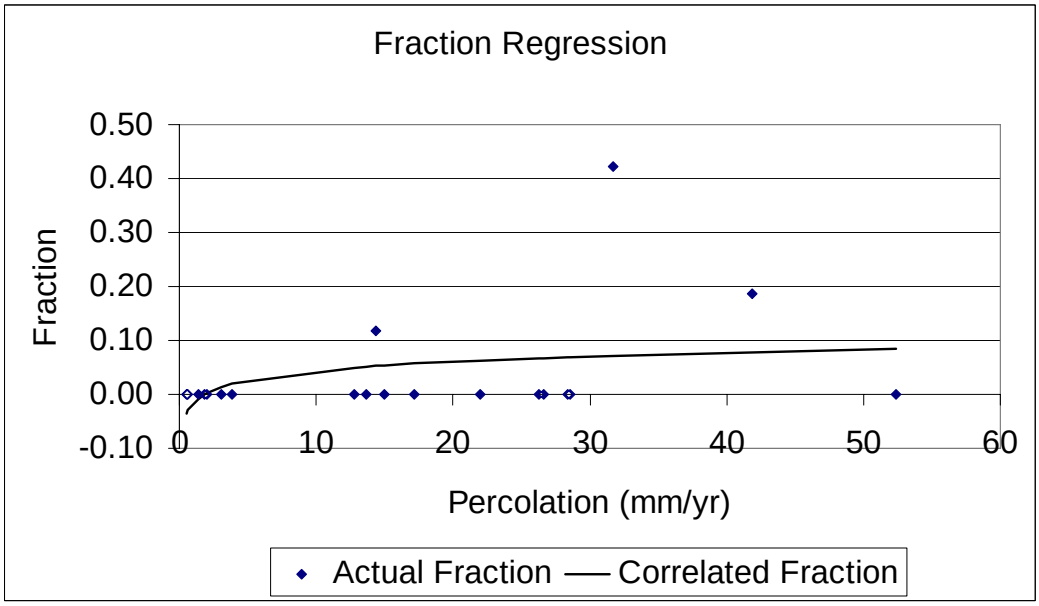

DTN: SN0402T0809903.004; file: Mixed_High_Invert_3000_analysis.xls

Figure H.2-8. Wall Fraction Regression, HighD, 3,000 Years, Mixed High Invert Transport

Table H.2-6. Drift Wall Condensation: 10,000 Years; High Dispersion Coefficient – High Invert Transport

HighD	Slope	Y-intercept
Rate	–0.198540265	0.346506228
Rate R-Squared	0.97490726	
Std. Error on Rate Slope	0.007963079	
Std. Error on Rate Intercept	0.190730641	
	Slope	**Y-intercept**
Fraction	–0.483119688	–0.158188361
Fraction R-Squared	0.910930245	
Max Fraction	0.88	
Std. Error on Fraction Slope	0.034657761	
Std. Error on Fraction Intercept	0.090388959	

DTN: SN0402T0809903.004; file: Mixed_High_Invert_10000_analysis.xls.

The condensation rate at 10,000 years for the high dispersion coefficient and high invert transport correlates well with percolation rate (Table H.2-6, Figures H.2-9 and H.2-10). This is because the axial dispersion of water vapor has only marginal effect on the local condensation rate. The standard deviations of the condensation rate and the condensation fraction are not important at this time because they are so small. (Note: percolation units are mm/yr; wall condensation rates are kg/m/yr where evaporation is positive in Table H.2-6 and Figure H.2-9).

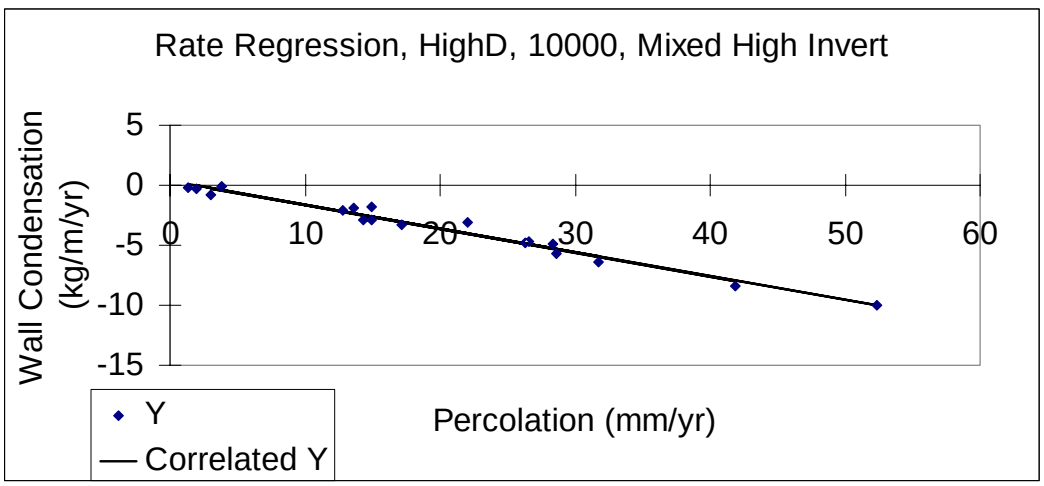

DTN: SN0402T0809903.004; file: Mixed_High_Invert_10000_analysis.xls.

Figure H.2-9. Wall Rate Regression, High D, 10,000 Years, Mixed High Invert Transport

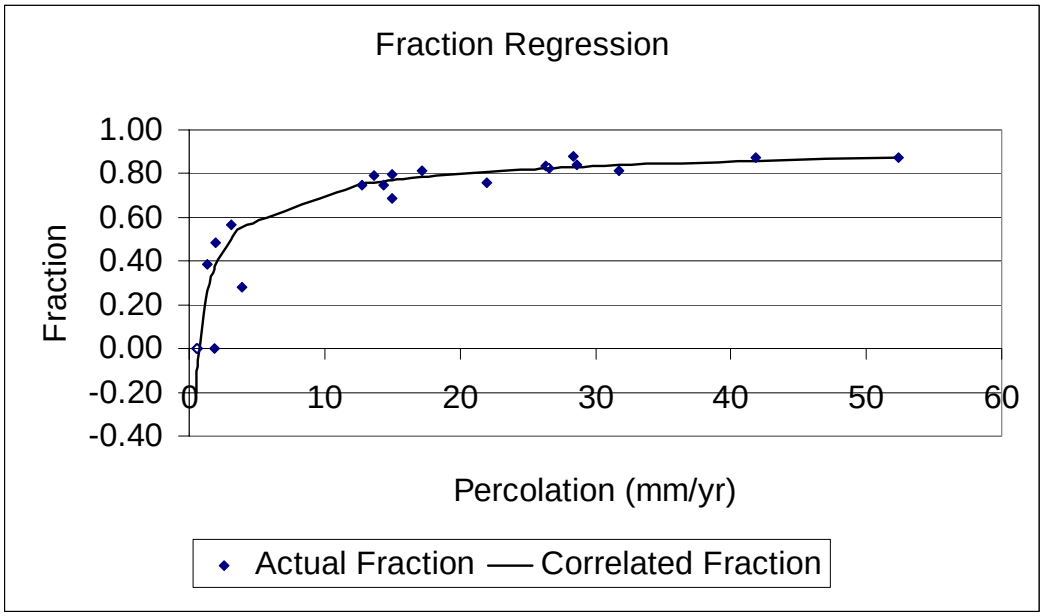

DTN: SN0402T0809903.004; file: Mixed_High_Invert_10000_analysis.xls.

Figure H.2-10. Wall Fraction Regression, High D, 10,000 Years, Mixed High Invert Transport

APPENDIX I

CORRELATION SUMMARY OF UNVENTILATED CONDENSATION MODEL ABSTRACTION

(DTNS: SN0403T0809903.005 AND SN0403T0809903.006)

This attachment summarizes the output DTNs produced by the condensation model for the unventilated drip shield case (DTNs: SN0403T0809903.005 and SN0403T0809903.006). It is included here for the convenience of the reader. The description of the calculations used to produce these correlations is contained in Section 8.3.

The regression for the drift wall condensation rate is a straight line given by equation 8.3.1.1-4. The equation for the fraction is given by equation 8.3.1.1-3. The slope and y-intercept parameters are defined in Section 8.3.

The equations for condensation under the drip shield are slightly different. The regression for the condensation rate is a straight line given by equation 8.3.1.2-7. The equation for the fraction has various functional forms that are summarized in Table 8.3.1.2-1. The appropriate equation is given in each table below. The slope and y-intercept parameters are defined in Section 8.3.

I.1 UNVENTILATED, LOW INVERT TRANSPORT CORRELATION SUMMARY

Drift Wall Condensation

Table I.1-1. Wall Condensation: 1,000 Years; Low Dispersion Coefficient – Low Invert Transport

LowD	Slope	Y-intercept
Rate	–0.001121607	–2.168012078
Rate R-Squared	1.53969E-05	
Std. Error on Rate Slope	0.076393616	
Std. Error on Rate Intercept	1.067376469	
	Slope	**Y-intercept**
Fraction	–0.10234547	0.079720705
Fraction R-Squared	0.136305086	
Max Fraction	0.51	
Std. Error on Fraction Slope	0.059103878	
Std. Error on Fraction Intercept	0.136707517	

DTN: SN0403T0809903.006; file: Unmixed_Low_Invert_1000_analysis.xls.

The condensation rate at 1,000 years for the low dispersion coefficient does not correlate well with the percolation rate (Table I.1-1, Figures I.1-1 and I.1-2). This is because the axial dispersion of water vapor is important at this time. Condensation on the drift wall is determined more by the location within the drift rather than the local percolation rate. It is important to sample the standard errors for condensation rate and fraction of condensation at this time. (Note: percolation units are mm/yr; wall condensation rates are kg/m/yr where evaporation is positive in Table I.1-1 and Figure I.1-1).

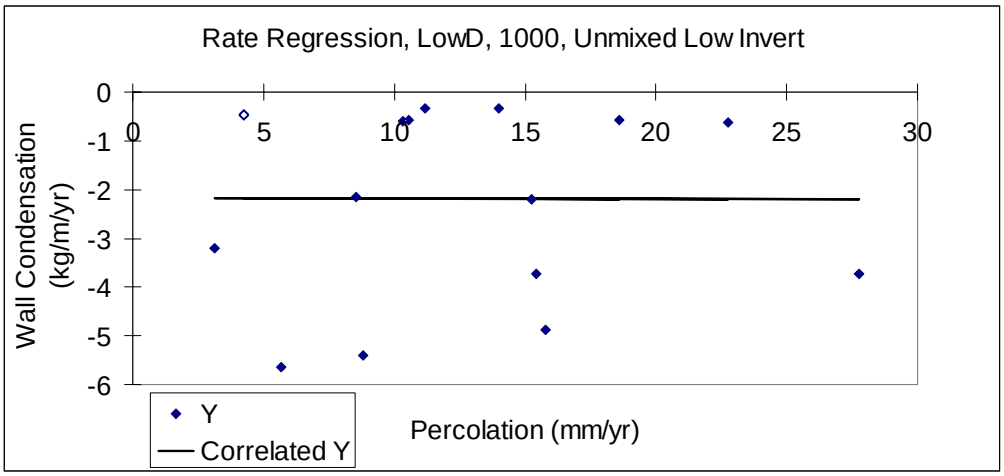

DTN: SN0403T0809903.006; file: Unmixed_Low_Invert_1000_analysis.xls.

Figure I.1-1. Wall Rate Regression, Low D, 1,000 Years, Unmixed Low Invert Transport

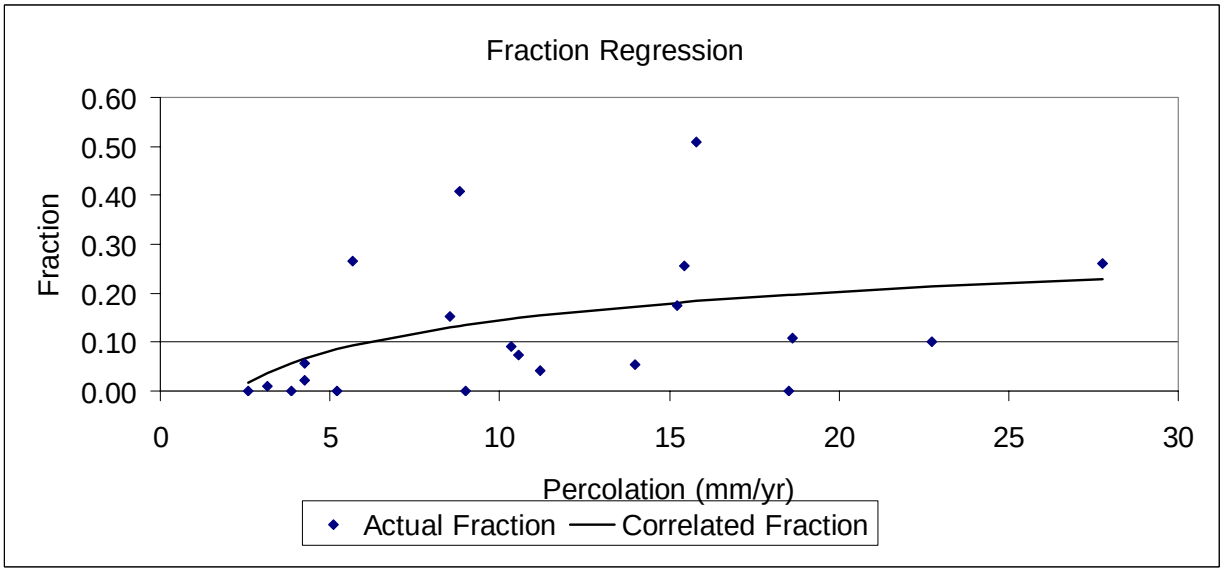

DTN: SN0403T0809903.006; file: Unmixed_Low_Invert_1000_analysis.xls.

Figure I.1-2. Wall Fraction Regression, Low D, 1,000 Years, Unmixed Low Invert Transport

No drift wall condensate forms at 3,000 years for the low dispersion coefficient case.

No drift wall condensate forms at 10,000 years for the low dispersion coefficient case.

No drift wall condensate forms at 1,000 years for the high dispersion coefficient case.

No drift wall condensate forms at 3,000 years for the high dispersion coefficient case.

No drift wall condensate forms at 10,000 years for the high dispersion coefficient case.

Drip Shield Condensation

In the low invert case, no condensation occurred under the drip shield or on the waste packages. Consequently, the fraction of condensation under the drip shield is estimated to be 0.0 and the rate of condensation is estimated to be 0.0 for all cases and times.

I.2 UNVENTILATED, HIGH INVERT TRANSPORT CORRELATION SUMMARY

Drift Wall Condensation

Table I.2-1. Wall Condensation: 1,000 Years; Low Dispersion Coefficient – High Invert Transport

LowD	Slope	Y-intercept
Rate	–0.001137781	–2.167548219
Rate R-Squared	1.58428E-05	
Std. Error on Rate Slope	0.076396714	
Std. Error on Rate Intercept	1.067419754	
	Slope	**Y-intercept**
Fraction	–0.10234547	0.079720705
Fraction R-Squared	0.136305086	
Max Fraction	0.51	
Std. Error on Fraction Slope	0.059103878	
Std. Error on Fraction Intercept	0.136707517	

DTN: SN0403T0809903.005; file: Unmixed_High_Invert_1000_analysis.xls.

The condensation rate at 1,000 years for the low dispersion coefficient does not correlate well with percolation rate (Table I.2-1, Figures I.2-1 and I.2-2). This is because the axial dispersion of water vapor is important at this time. Condensation on the drift wall is determined more by the location within the drift rather than the local percolation rate. It is important to sample the standard errors for condensation rate and fraction of condensation at this time. (Note: percolation units are mm/yr; wall condensation rates are kg/m/yr where evaporation is positive in Table I.2-1 and Figure I.2-1).

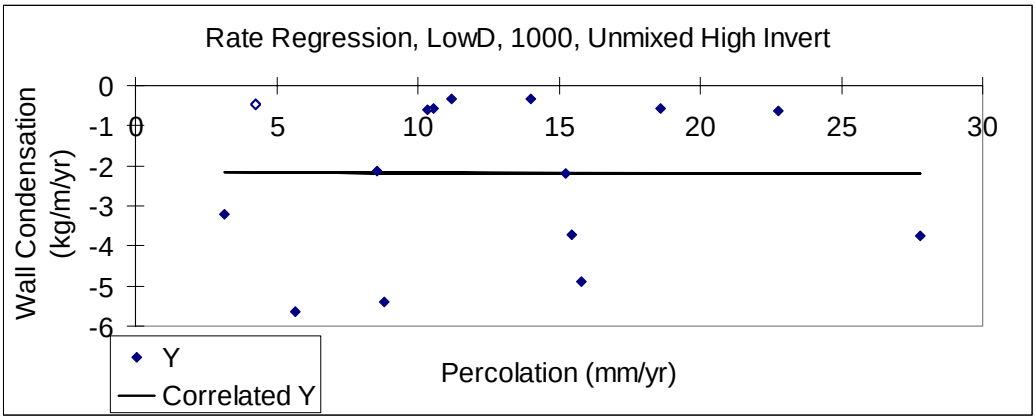

DTN: SN0403T0809903.005; file: Unmixed_High_Invert_1000_analysis.xls.

Figure I.2-1. Wall Rate Regression, Low D, 1,000 Years, Unmixed High Invert Transport

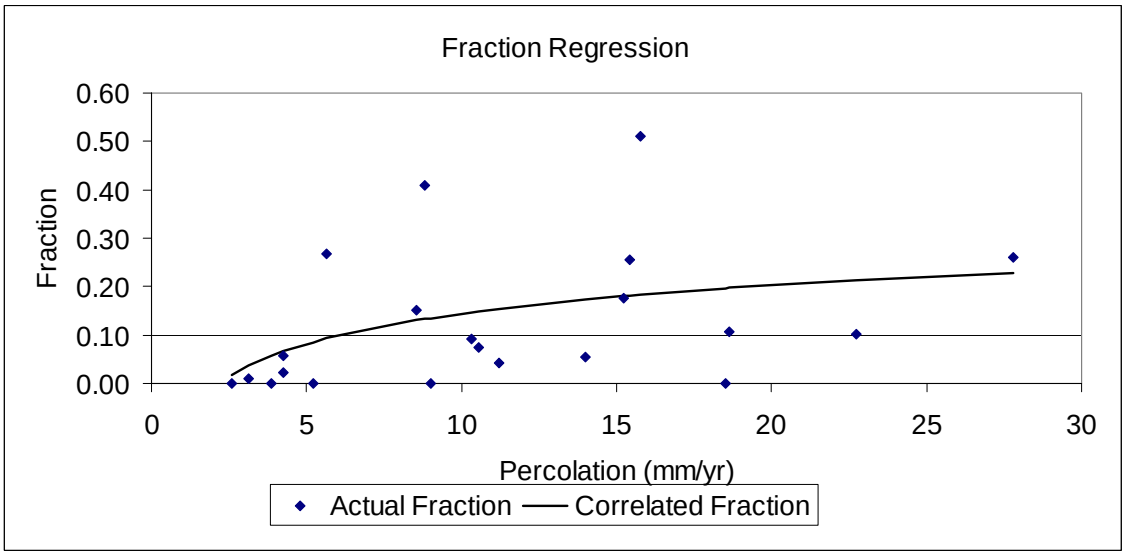

DTN: SN0403T0809903.005; file: Unmixed_High_Invert_1000_analysis.xls.

Figure I.2-2. Wall Fraction Regression, Low D, 1,000 Years, Unmixed High Invert Transport

No drift wall condensate forms at 3,000 years for the low dispersion coefficient case.

No drift wall condensate forms at 10,000 years for the low dispersion coefficient case.

No drift wall condensate forms at 1,000 years for the high dispersion coefficient case.

No drift wall condensate forms at 3,000 years for the high dispersion coefficient case.

No drift wall condensate forms at 10,000 years for the high dispersion coefficient case.

Condensation Under the Drip Shield: HLW Packages

Table I.2-2. Drip Shield Condensation: 1,000 Years, Low Dispersion Coefficient, HLW package – High Invert Transport

HLW, LowD	Slope	Y-intercept
Rate	–3.185910497	–10.87757015
Rate R-Squared	0.573558029	
Std. Error on Rate Slope	0.793020176	
Std. Error on Rate Intercept	12.40294408	
	Slope	**Y-intercept**
Fraction	0.025164149	–0.060758101
Fraction R-Squared	0.593147324	
Max Fraction	0.69	
Std. Error on Fraction Slope	0.004781264	
Std. Error on Fraction Intercept	0.062575685	
Fraction Regression Model	Linear	
Fraction Model Equation	P = b + ap	

DTN: SN0403T0809903.005; file: Unmixed_High_Invert_1000_analysis.xls.

The condensation rate under the drip shield over the HLW packages at 1,000 years for the low dispersion coefficient correlates reasonably well with percolation rate (Table I.2-2, Figures I.2-3 and I.2-4). However, the fraction of condensation under the drip shield does not correlate well with percolation rate. It is important to sample the standard errors for fraction of condensation at this time due to the lack of correlation. Although the condensation rate is reasonably correlated with percolation, sampling of the standard error for the rate parameters is recommended, because the magnitude of the standard error on the rate intercept parameter is large. (Note: percolation units are mm/yr; wall condensation rates are kg/yr where evaporation is positive in Table I.2-2 and Figure I.2-3).

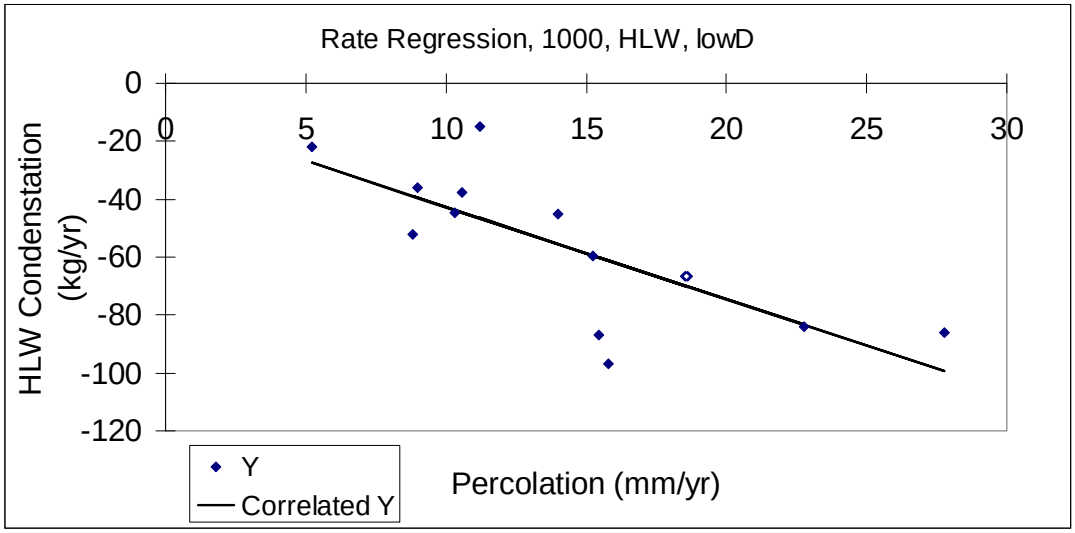

DTN: SN0403T0809903.005; file: Unmixed_High_Invert_1000_analysis.xls.

Figure I.2-3. HLW Rate Regression, Low D, 1,000 Years, Unmixed High Invert Transport

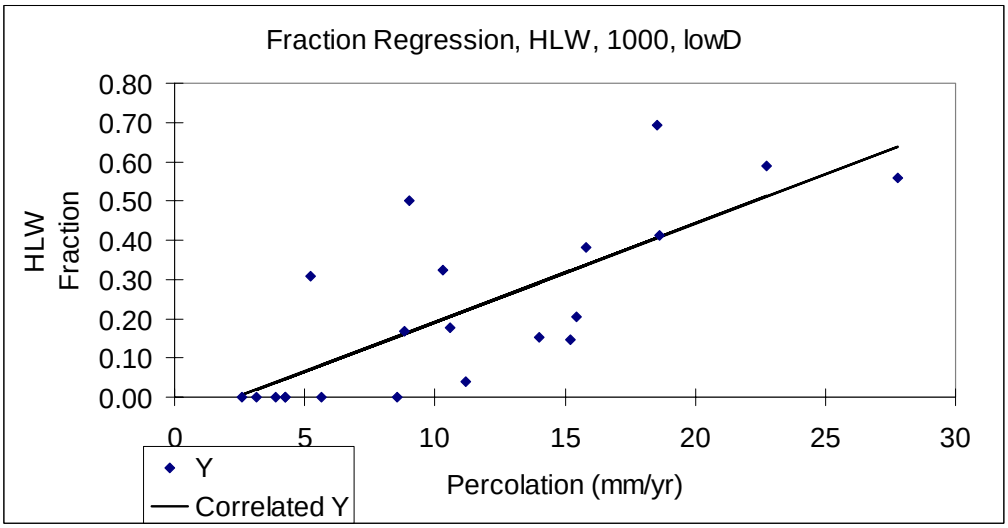

DTN: SN0403T0809903.005; file: Unmixed_High_Invert_1000_analysis.xls.

Figure I.2-4. HLW Fraction Regression, Low D, 1,000 Years, Unmixed High Invert Transport

Table I.2-3 Drip Shield Condensation: 3,000 Years, Low Dispersion Coefficient, HLW package – High Invert Transport

HLW, LowD	Slope	Y-intercept
Rate	–3.638993712	–5.285493604
Rate R-Squared	0.995323133	
Std. Error on Rate Slope	0.057226863	
Std. Error on Rate Intercept	1.26926092	
	Slope	**Y-intercept**
Fraction	0.264357377	0.52437173
Fraction R-Squared	0.901204932	
Max Fraction	0.95	
Std. Error on Fraction Slope	0.020080313	
Std. Error on Fraction Intercept	0.022744148	
Fraction Regression Model	Logarithmic	
Fraction Model Equation	$P = b + a \log_{10}(p)$	

DTN: SN0403T0809903.005; file: Unmixed_High_Invert_3000_analysis.xls.

The condensation rate under the drip shield over the HLW packages at 3,000 years for the low dispersion coefficient correlates strongly with percolation rate (Table I.2-3, Figures I.2-5 and I.2-6). The fraction of condensation under the drip shield correlates well with percolation rate, using the logarithmic model. It is not necessary to sample the standard errors for the regression parameters at this time. (Note: percolation units are mm/yr; wall condensation rates are kg/yr where evaporation is positive in Table I.2-3 and Figure I.2-5).

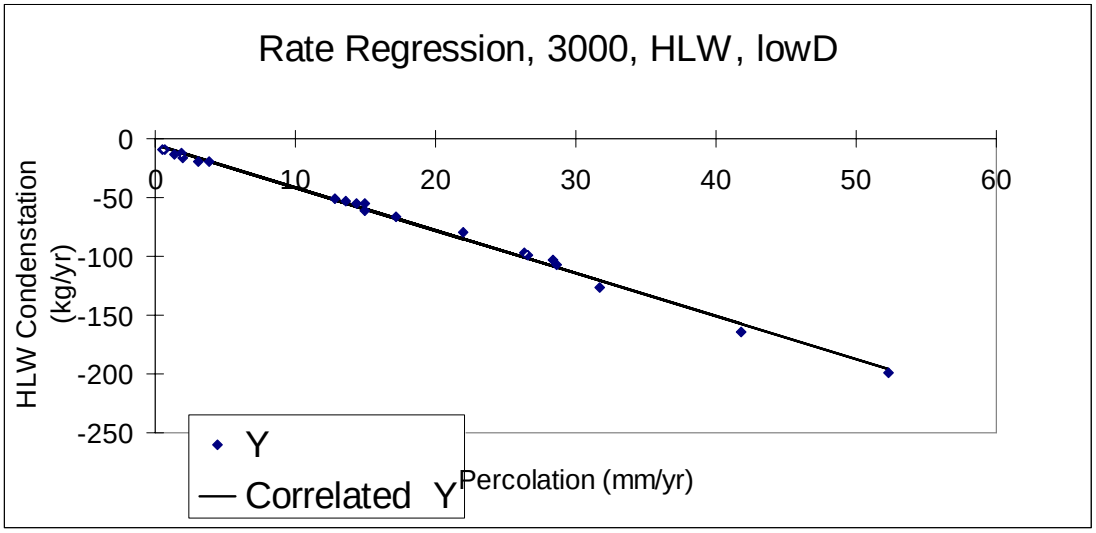

DTN: SN0403T0809903.005; file: Unmixed_High_Invert_3000_analysis.xls.

Figure I.2-5. HLW Rate Regression, Low D, 3,000 Years, Unmixed High Invert Transport

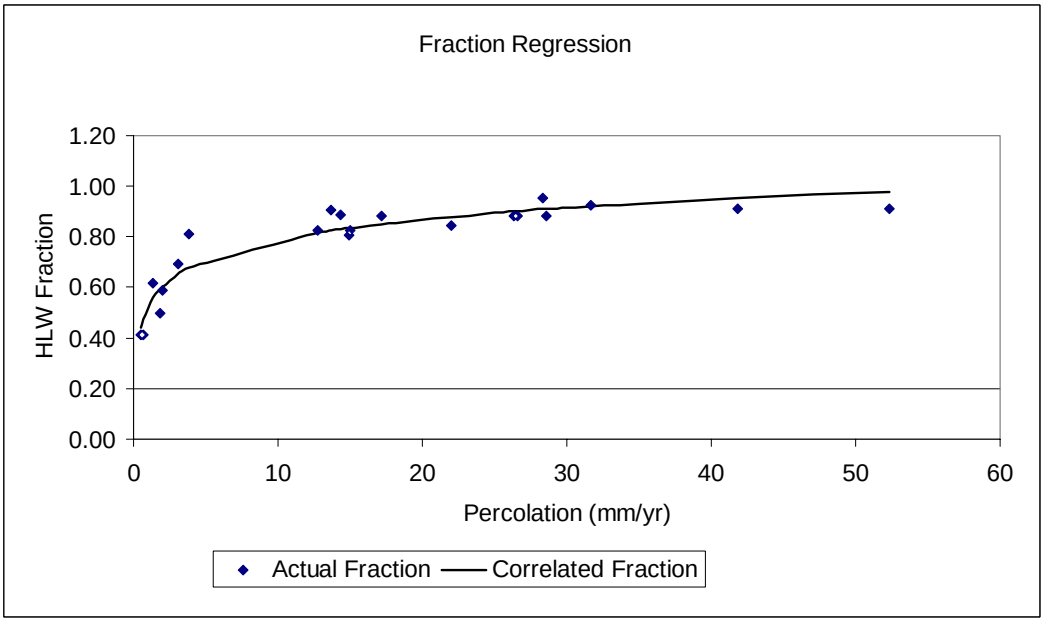

DTN: SN0403T0809903.005; file: Unmixed_High_Invert_3000_analysis.xls.

Figure I.2-6. HLW Fraction Regression, Low D, 3,000 Years, Unmixed High Invert Transport

Table I.2-4. Drip Shield Condensation: 10,000 Years, Low Dispersion Coefficient, HLW package – High Invert Transport

HLW, LowD	Slope	Y-intercept
Rate	–2.448326047	–19.20138434
Rate R-Squared	0.918415822	
Std. Error on Rate Slope	0.167407822	
Std. Error on Rate Intercept	3.713015062	
	Slope	**Y-intercept**
Fraction	0.106504424	0.812627163
Fraction R-Squared	0.846247459	
Max Fraction	1.00	
Std. Error on Fraction Slope	0.010414857	
Std. Error on Fraction Intercept	0.011796482	
Fraction Regression Model	Logarithmic	
Fraction Model Equation	$P = b + a \log_{10}(p)$	

DTN: SN0403T0809903.005; file: Unmixed_High_Invert_10000_analysis.xls.

The condensation rate under the drip shield over the HLW packages at 10,000 years for the low dispersion coefficient correlates reasonably well with percolation rate (Table I.2-4, Figures I.2-15 and I.2-16). The fraction of condensation under the drip shield correlates well with percolation rate, using the logarithmic model. It is not necessary to sample the standard errors for the regression parameters at this time. (Note: percolation units are mm/yr; wall condensation rates are kg/yr where evaporation is positive in Table I.2-4 and Figure I.2-15).

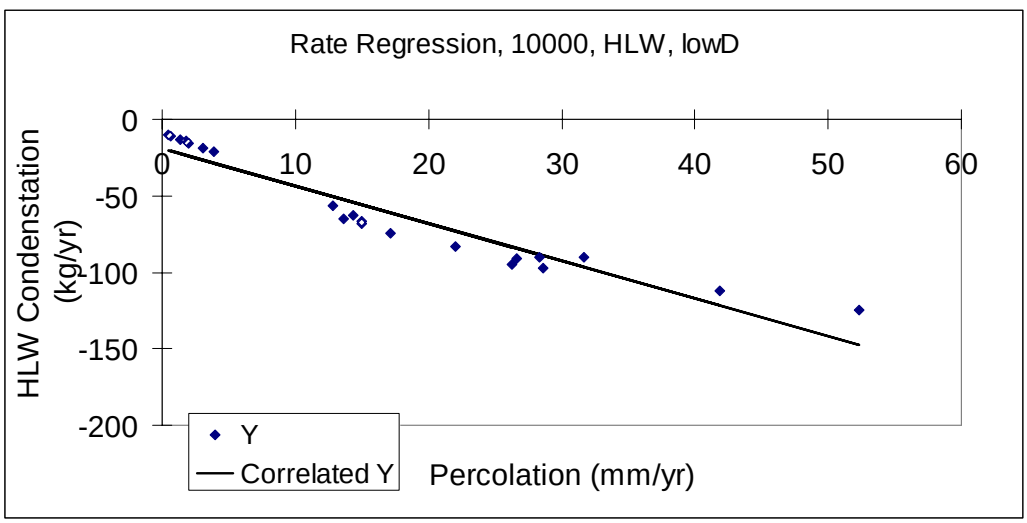

DTN: SN0403T0809903.005; file: Unmixed_High_Invert_10000_analysis.xls.

Figure I.2-7. HLW Rate Regression, Low D, 10,000 Years, Unmixed High Invert Transport

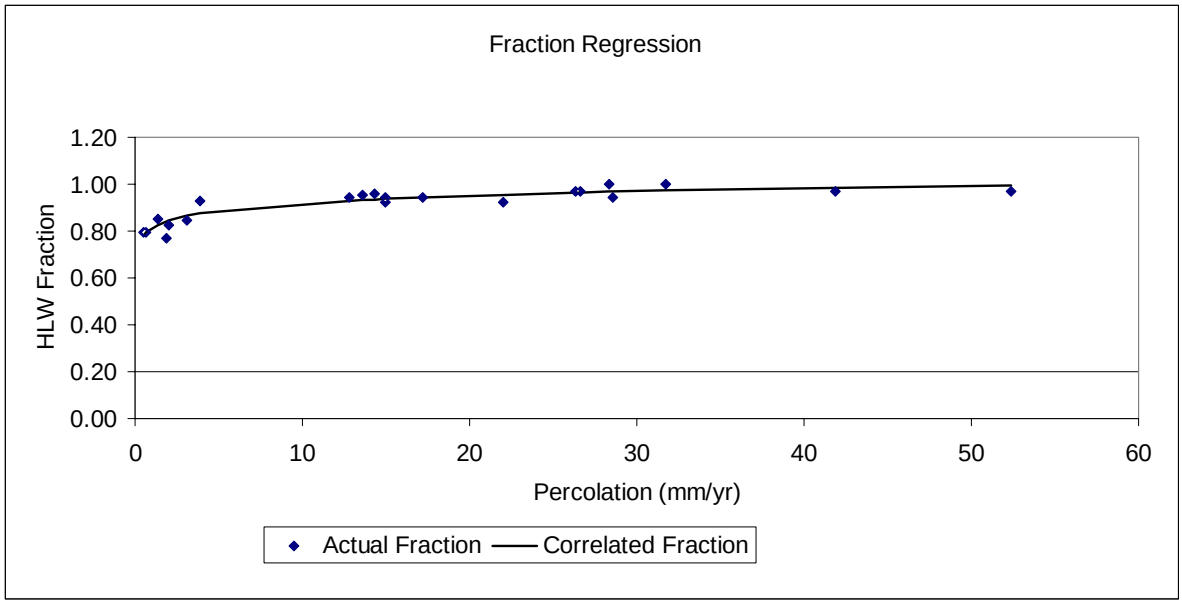

DTN: SN0403T0809903.005; file: Unmixed_High_Invert_10000_analysis.xls.

Figure I.2-8. HLW Fraction Regression, Low D, 10,000 Years, Unmixed High Invert Transport

Table I.2-5. Drip Shield Condensation: 1,000 Years, High Dispersion Coefficient, HLW package – High Invert Transport

HLW, HighD	Slope	Y-intercept
Rate	–4.408497866	4.347556684
Rate R-Squared	0.891866024	
Std. Error on Rate Slope	0.580193542	
Std. Error on Rate Intercept	10.01566432	
	Slope	**Y-intercept**
Fraction	0.01856291	–0.070340077
Fraction R-Squared	0.456916831	
Max Fraction	0.58	
Std. Error on Fraction Slope	0.004642841	
Std. Error on Fraction Intercept	0.060764051	
Fraction Regression Model	Linear	
Fraction Model Equation	P = b + ap	

DTN: SN0403T0809903.005; file: Unmixed_High_Invert_1000_analysis.xls.

The condensation rate under the drip shield over the HLW packages at 1,000 years for the high dispersion coefficient correlates reasonably well with percolation rate (Table I.2-5, Figures I.2-9 and I.2-10). However, the fraction of condensation under the drip shield does not correlate well with percolation rate. It is important to sample the standard errors for fraction of condensation at this time due to the lack of correlation. Although the condensation rate is reasonably correlated with percolation, sampling of the standard error for the rate parameters is recommended, because the magnitude of the standard error on the rate intercept parameter is large. (Note: percolation

units are mm/yr; wall condensation rates are kg/yr where evaporation is positive in Table I.2-5 and Figure I.2-9).

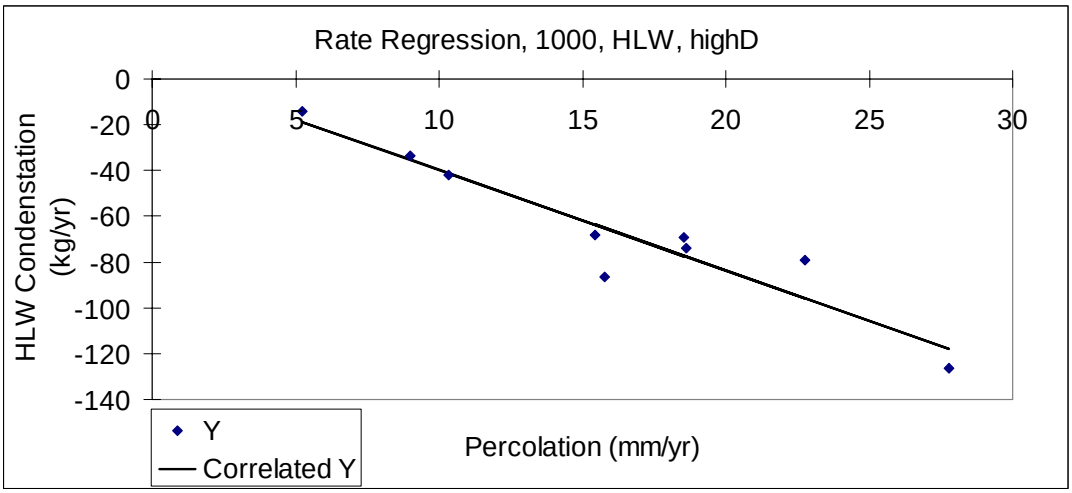

DTN: SN0403T0809903.005; file: Unmixed_High_Invert_1000_analysis.xls.

Figure I.2-9. HLW Rate Regression, High D, 1,000Years, Unmixed High Invert Transport

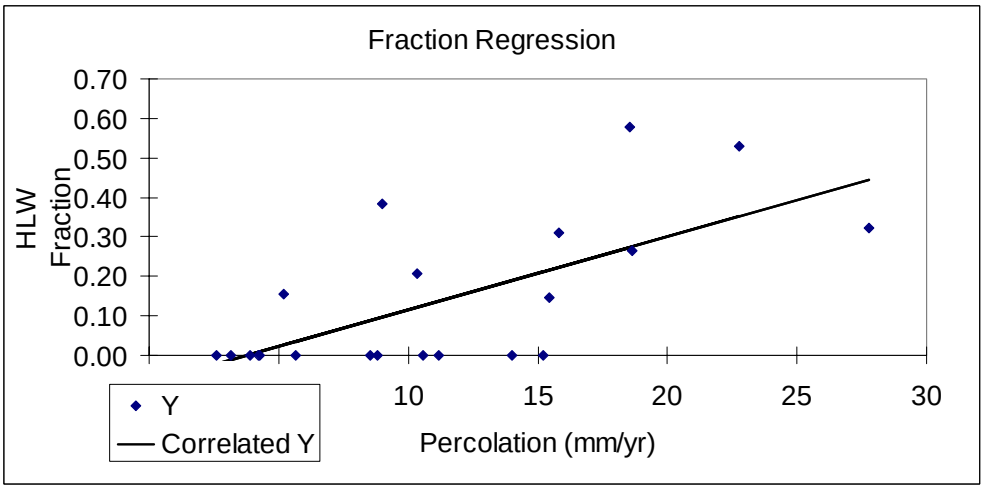

DTN: SN0403T0809903.005; file: Unmixed_High_Invert_1000_analysis.xls.

Figure I.2-10. HLW Fraction Regression, High D, 1,000 Years, Unmixed High Invert Transport

Table I.2-6. Drip Shield Condensation: 3,000 Years, High Dispersion Coefficient, HLW package – High Invert Transport

HLW, HighD	Slope	Y-intercept
Rate	–3.547687837	–5.214050337
Rate R-Squared	0.996518849	
Std. Error on Rate Slope	0.048104676	
Std. Error on Rate Intercept	1.066935733	
	Slope	**Y-intercept**
Fraction	0.401570431	0.309302132
Fraction R-Squared	0.902967789	
Max Fraction	0.93	
Std. Error on Fraction Slope	0.030199987	
Std. Error on Fraction Intercept	0.034206288	
Fraction Regression Model	Logarithmic	
Fraction Model Equation	$P = b + a \log_{10}(p)$	

DTN: SN0403T0809903.005; file: Unmixed_High_Invert_3000_analysis.xls.

The condensation rate under the drip shield over the HLW packages at 3,000 years for the high dispersion coefficient correlates strongly with percolation rate (Table I.2-6, Figures I.2-11 and I.2-12). The fraction of condensation under the drip shield correlates well with percolation rate, using the logarithmic model. It is not necessary to sample the standard errors for the regression parameters at this time. (Note: percolation units are mm/yr; wall condensation rates are kg/yr where evaporation is positive in Table I.2-11 and Figure I.2-7).

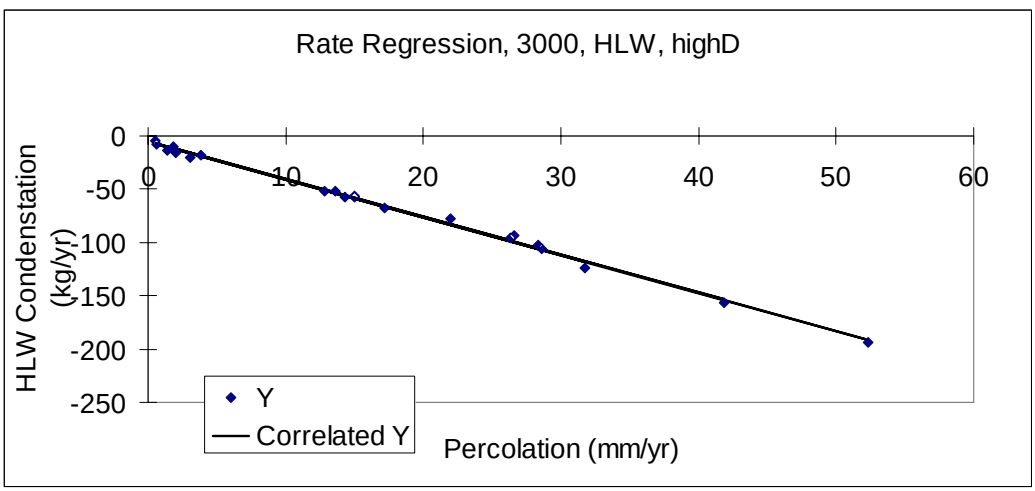

DTN: SN0403T0809903.005; file: Unmixed_High_Invert_3000_analysis.xls.

Figure I.2-11. HLW Rate Regression, High D, 3,000 Years, Unmixed High Invert Transport

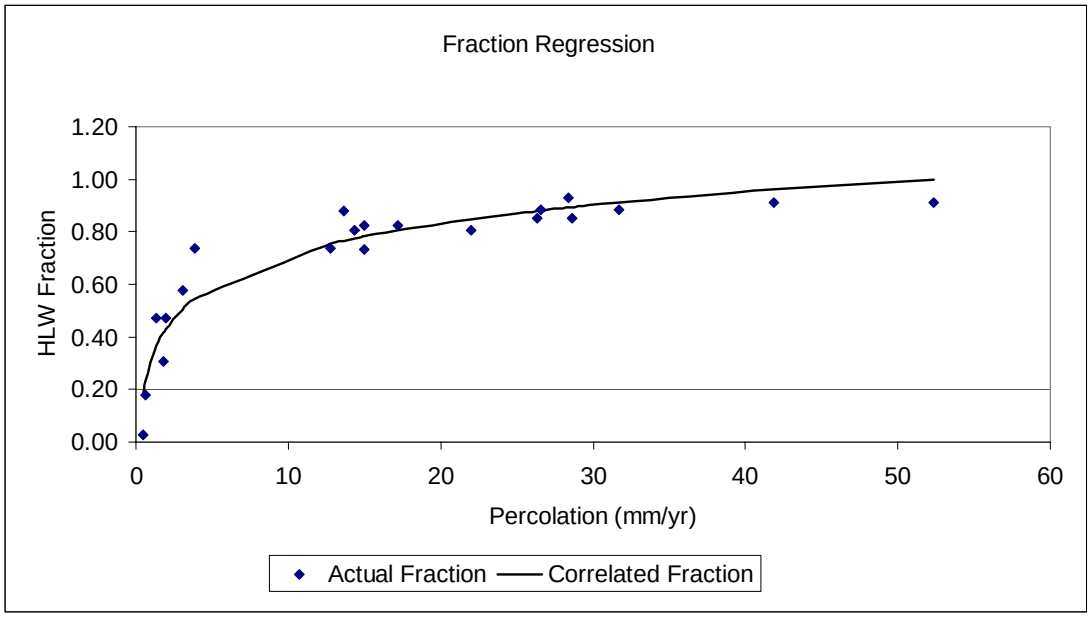

DTN: SN0403T0809903.005; file: Unmixed_High_Invert_3000_analysis.xls.

Figure I.2-12. HLW Fraction Regression, High D, 3,000 Years, Unmixed High Invert Transport

Table I.2-7. Drip Shield Condensation: 10,000 Years, High Dispersion Coefficient, HLW package – High Invert Transport

HLW, HighD	Slope	Y-intercept
Rate	-2.786933398	-16.67427327
Rate R-Squared	0.936093823	
Std. Error on Rate Slope	0.167055785	
Std. Error on Rate Intercept	3.705207082	
	Slope	**Y-intercept**
Fraction	0.153486754	0.723915359
Fraction R-Squared	0.91988595	
Max Fraction	0.97	
Std. Error on Fraction Slope	0.010391577	
Std. Error on Fraction Intercept	0.011770113	
Fraction Regression Model	Logarithmic	
Fraction Model Equation	$P = b + a \log_{10}(p)$	

DTN: SN0403T0809903.005; file: Unmixed_High_Invert_10000_analysis.xls.

The condensation rate under the drip shield over the HLW packages at 10,000 years for the high dispersion coefficient correlates reasonably well with percolation rate (Table I.2-7, Figures I.2-13 and I.2-14). The fraction of condensation under the drip shield correlates well with percolation rate, using the logarithmic model. It is not necessary to sample the standard errors for the regression parameters at this time. (Note: percolation units are mm/yr; wall condensation rates are kg/yr where evaporation is positive in Table I.2-7 and Figure I.2-13).

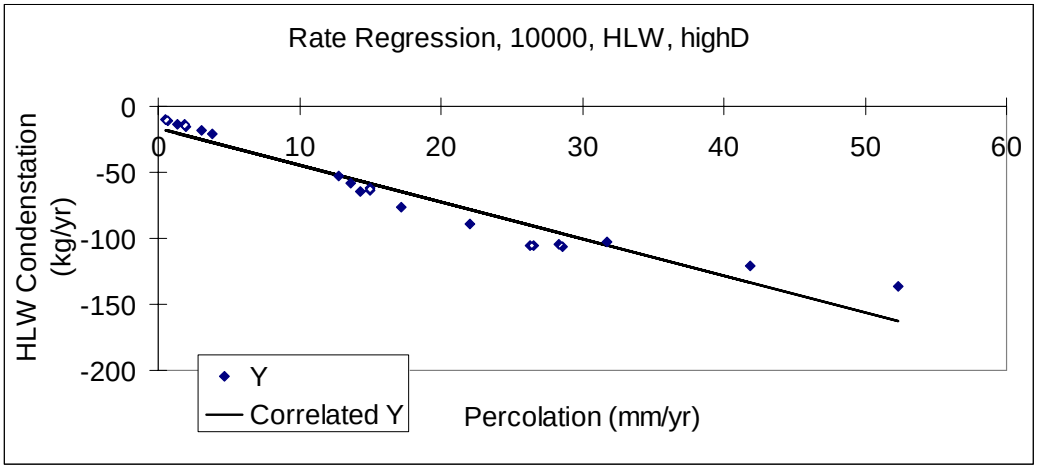

DTN: SN0403T0809903.005; file: Unmixed_High_Invert_10000_analysis.xls.

Figure I.2-13. HLW Rate Regression, High D, 10,000 Years, Unmixed High Invert Transport

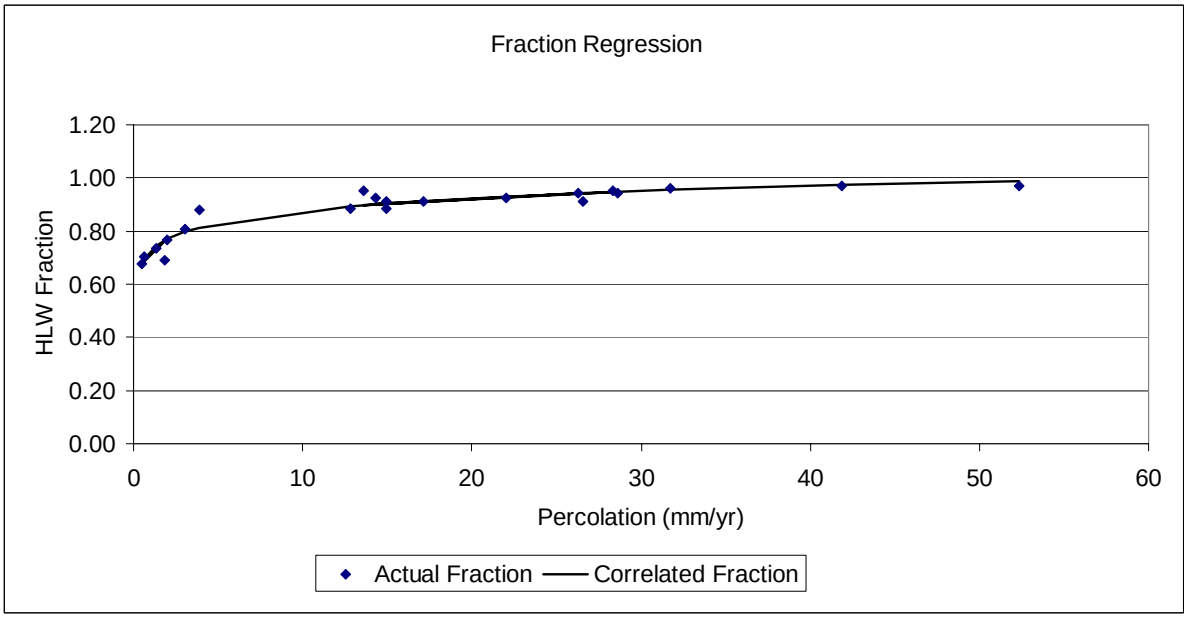

DTN: SN0403T0809903.005; file: Unmixed_High_Invert_10000_analysis.xls.

Figure I.2-14. HLW Fraction Regression, High D, 10,000 Years, Unmixed High Invert Transport

Condensation Under the Drip Shield: Non-HLW Packages

No condensate forms under the drip shield over non-HLW packages at 1,000 years for the low dispersion coefficient case.

Table I.2-8. Drip Shield Condensation: 3,000 Years, Low Dispersion Coefficient, non-HLW package – High Invert Transport

non-HLW, LowD	Slope	Y-intercept
Rate	-0.4072527	12.28769181
Rate R-Squared	0.830216059	
Std. Error on Rate Slope	0.184169077	
Std. Error on Rate Intercept	7.882001336	
	Slope	**Y-intercept**
Fraction	0.004696825	-0.000309124
Fraction R-Squared	0.982312923	
Max Fraction	0.12	
Std. Error on Fraction Slope	0.000144587	
Std. Error on Fraction Intercept	0.000863338	
Max perc. With zero Fraction (m)	28.596	
Fraction Regression Model	Linear with shift	
Fraction Model Equation	$\overline{P}_D = \begin{cases} 0 & \overline{p} < m \\ b + a(\overline{p} - m) & \overline{p} \geq m \end{cases}$	

DTN: SN0403T0809903.005; file: Unmixed_High_Invert_3000_analysis.xls.

The condensation rate under the drip shield over the non-HLW packages at 3,000 years for the low dispersion coefficient correlates reasonably well with percolation rate (Table I.2-8, Figures I.2-15 and I.2-16). The fraction of condensation under the drip shield correlates well with percolation rate, using the linear with shift model. It is not necessary to sample the standard errors for the regression parameters at this time. (Note: percolation units are mm/yr; wall condensation rates are kg/yr where evaporation is positive in Table I.2-8 and Figure I.2-15).

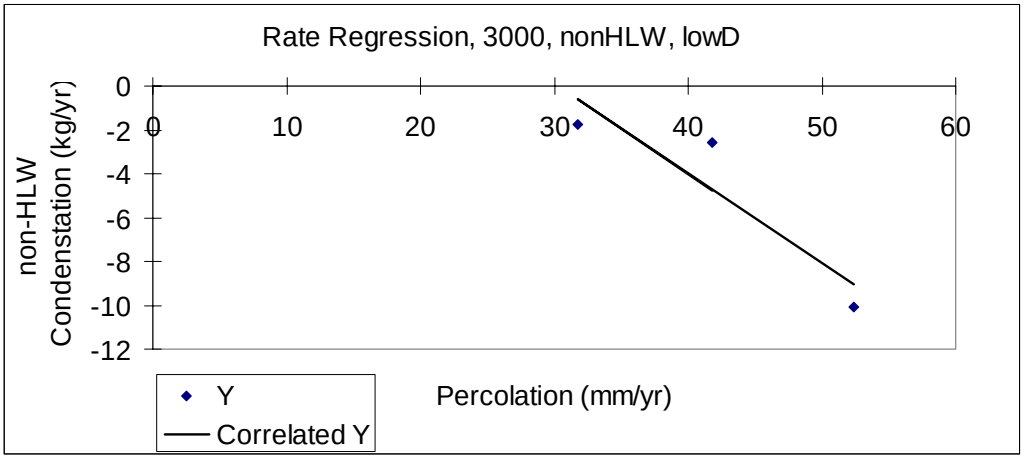

DTN: SN0403T0809903.005; file: Unmixed_High_Invert_3000_analysis.xls.

Figure I.2-15. Non-HLW Rate Regression, Low D, 3,000 Years, Unmixed High Invert Transport

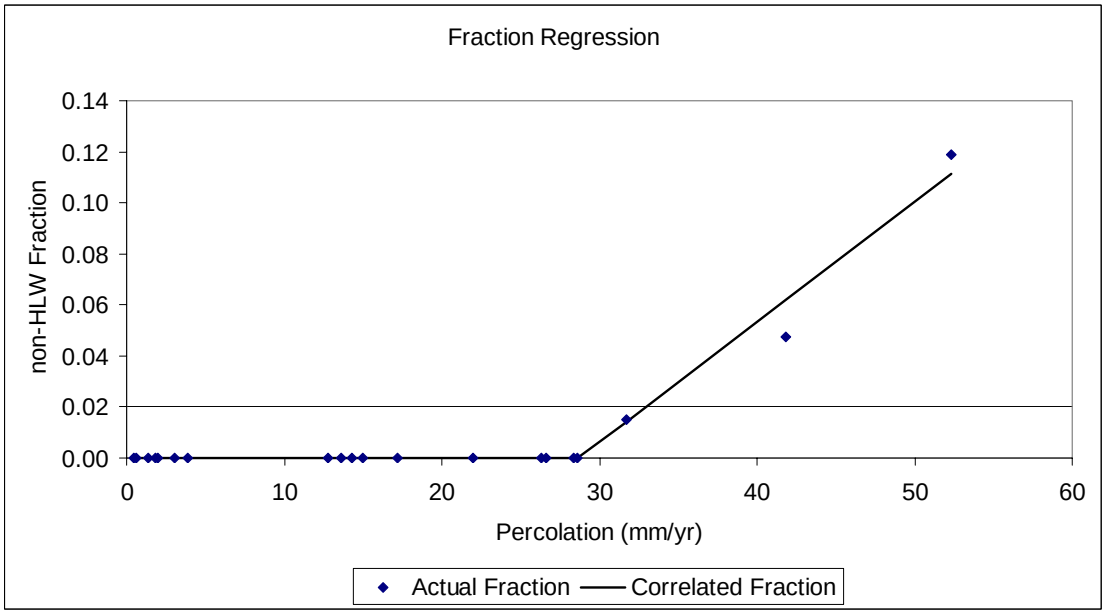

DTN: SN0403T0809903.005; file: Unmixed_High_Invert_3000_analysis.xls.

Figure I.2-16. Non-HLW Fraction Regression, Low D, 3,000 Years, Unmixed High Invert Transport

Table I.2-9. Drip Shield Condensation: 10,000 Years, Low Dispersion Coefficient, non-HLW package – High Invert Transport

nonHLW, LowD	Slope	Y-intercept
Rate	-0.626323922	5.632620647
Rate R-Squared	0.917323422	
Std. Error on Rate Slope	0.056693421	
Std. Error on Rate Intercept	1.582792841	
	Slope	**Y-intercept**
Fraction	0.348097952	0.027929979
Fraction R-Squared	0.920042392	
Max Fraction	0.49	
Std. Error on Fraction Slope	0.023542395	
Std. Error on Fraction Intercept	0.018781658	
Max perc. With zero Fraction (m)	12.791	
Fraction Regression Model	Logarithmic with shift	
Fraction Model Equation	$\bar{P}_D = \begin{cases} 0 & \bar{p} < m \\ b + a\log_{10}(\bar{p} - m) & \bar{p} \geq m \end{cases}$	

DTN: SN0403T0809903.005; file: Unmixed_High_Invert_10000_analysis.xls.

The condensation rate under the drip shield over the non-HLW packages at 10,000 years for the low dispersion coefficient correlates reasonably well with percolation rate(Table I.2-10, Figures I.2-17 and I.2-18). The fraction of condensation under the drip shield correlates well with percolation rate, using the logarithmic with shift model. It is not necessary to sample the standard errors for the regression parameters at this time. (Note: percolation units are mm/yr; wall condensation rates are kg/yr where evaporation is positive in Table I.2-9 and Figure I.2-17).

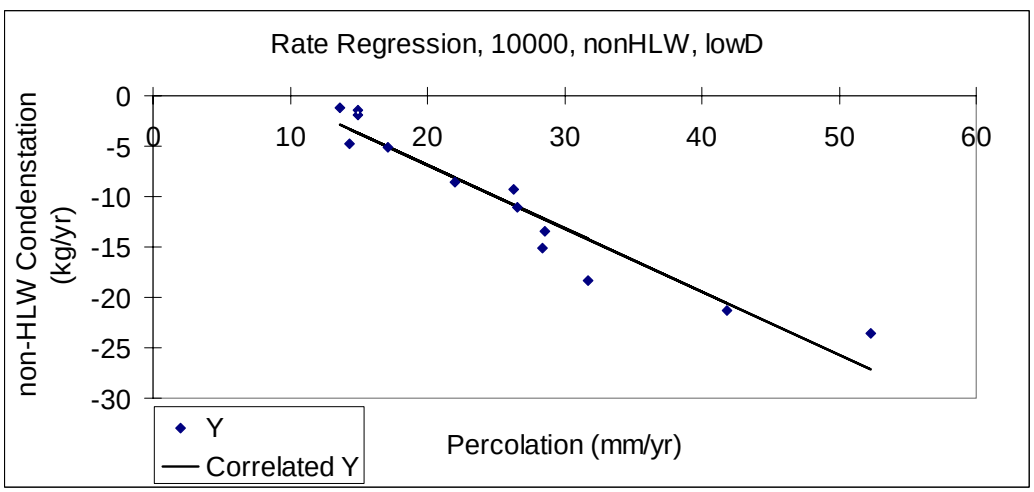

DTN: SN0403T0809903.005; file: Unmixed_High_Invert_10000_analysis.xls.

Figure I.2-17. Non-HLW Rate Regression, Low D, 10,000 Years, Unmixed High Invert Transport

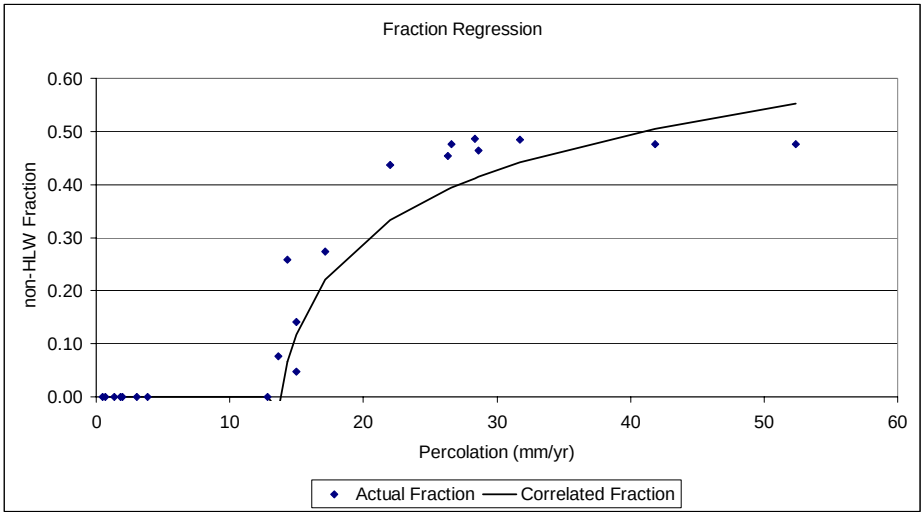

DTN: SN0403T0809903.005; file: Unmixed_High_Invert_10000_analysis.xls.

Figure I.2-18. Non-HLW Fraction Regression, Low D, 10,000 Years, Unmixed High Invert Transport

No condensate forms under the drip shield over non-HLW packages at 1,000 years for the high dispersion coefficient case.

At 3,000 years in the case of the high dispersion coefficient, condensation under the drip shield above non-HLW packages occurred for only the highest percolation value (52.34 kg/yr, at drift location 4). Consequently, condensation rate and fraction of condensation are not modeled by regression. Instead, fraction of condensation and condensation rate are conservatively modeled with step functions. For percolation rates ranging from 0.0 to 41.835, fraction of condensation and condensation rate are identically zero. For percolation rates above 41.835, fraction of condensation is 0.04 and condensation rate is –6.039. The percolation value 41.835 is the largest percolation value at which no condensation is observed.

Table I.2-10. Drip Shield Condensation: 10,000 Years, High Dispersion Coefficient, Non-HLW package – High Invert Transport

nonHLW, HighD	Slope	Y-intercept
Rate	-0.520365801	8.683769281
Rate R-Squared	0.861947027	
Std. Error on Rate Slope	0.085018946	
Std. Error on Rate Intercept	2.851530864	
	Slope	**Y-intercept**
Fraction	0.345140979	0.000565627
Fraction R-Squared	0.949060863	
Max Fraction	0.48	
Std. Error on Fraction Slope	0.018344188	
Std. Error on Fraction Intercept	0.012812397	
Max perc. With zero Fraction (m)	17.16	
Fraction Regression Model	Logarithmic with shift	
Fraction Model Equation	$\bar{P}_D = \begin{cases} 0 & \bar{p} < m \\ b + a\log_{10}\left(\bar{p} - m\right) & \bar{p} \geq m \end{cases}$	

DTN: SN0403T0809903.005; file: Unmixed_High_Invert_10000_analysis.xls.

The condensation rate under the drip shield over the non-HLW packages at 10,000 years for the high dispersion coefficient correlates reasonably well with percolation rate (Table I.2-10, Figures I.2-19 and I.2-20). The fraction of condensation under the drip shield correlates well with percolation rate, using the logarithmic with shift model. It is not necessary to sample the standard errors for the regression parameters at this time. (Note: percolation units are mm/yr; wall condensation rates are kg/yr where evaporation is positive in Table I.2-10 and Figure I.2-19).

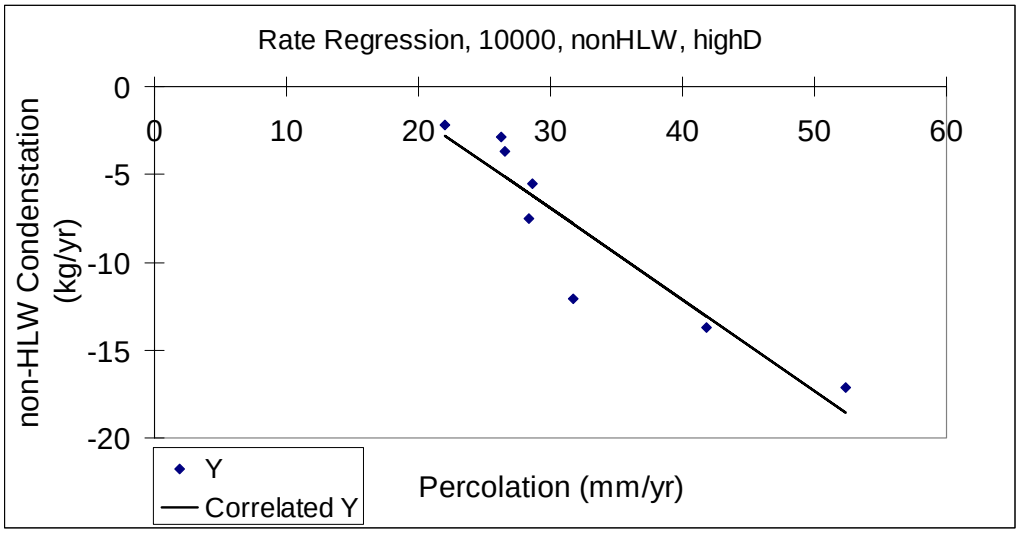

DTN: SN0403T0809903.005; file: Unmixed_High_Invert_10000_analysis.xls.

Figure I.2-19. Non-HLW Rate Regression, HighD, 10,000 Years, Unmixed High Invert Transport

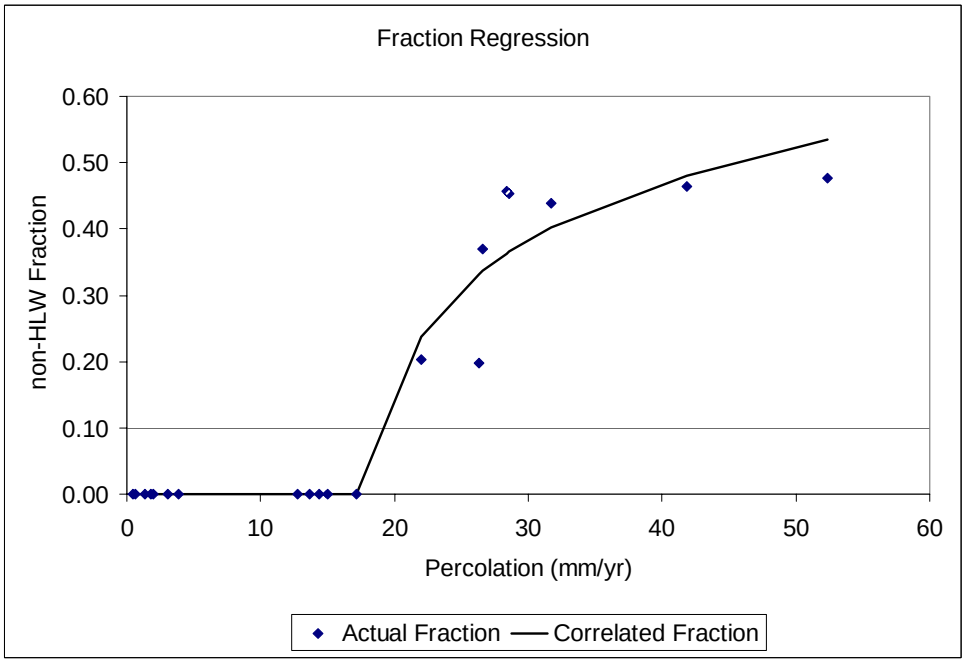

DTN: SN0403T0809903.005; file: Unmixed_High_Invert_10000_analysis.xls.

Figure I.2-20. Non-HLW Fraction Regression, HighD, 10,000 Years, Unmixed High Invert Transport

APPENDIX J

VERIFICATION OF TWO-DIMENSIONAL HEAT TRANSFER MODEL FOR STRUCTURES WITHIN THE DRIFT

The calculation of temperatures inside of the drift wall (Section 6.3.5.1.2) is based upon radial heat transport. The axial transport of energy in everything but the gas is ignored. The three basic structures (waste package, drip shield, and invert surface) are modeled with single nodes. Heat transfer mechanisms include both natural convection and thermal radiation. A comparison of the structure temperatures calculated by Equations 6.3-20 through 6.3-22 and those predicted by two-dimensional FLUENT calculations provides verification of this portion of the drift condensation model. The FLUENT calculations used in this comparison were created using the same mesh shown in Figure 6.4.5-2.

The four graphs below show the results of four two-dimensional FLUENT calculations for four different waste package powers (DTN: SN0406T0507803.024) as well as the predictions from the condensation model (**2D Comparison.mcd** file listed in Appendix D, Section D.7). The powers correspond approximately to the line-averaged powers at about 300 (Figure J-1), 1,000 (Figure J-2), 3,000 (Figure J-3), and 10,000 (Figure J-4) years (158.8, 67.67, 28.74, and 17.08 W/m from Table 4.1.3-7, line-averaged powers). The package diameter for these calculations is 1.714 m. The temperature at 5 m into the rock (radius of 7.75 m) is 350 K.

The four graphs look very similar. The vertical axis is the surface temperature; the horizontal axis is the horizontal distance from the vertical axis of symmetry. The dots are structure temperatures predicted by FLUENT. The red dots are the waste package temperatures. The bottom surface of the waste package is the hottest because it faces the insulating invert. The green dots are the invert surface. The invert surface temperature varies according to the proximity to the waste package. The blue dots are the drip shield temperatures. FLUENT predicts that the drip shield is nearly isothermal. The black dots are the wall temperatures. FLUENT predicts that the wall is nearly isothermal with a slightly cooler region near the invert surface where the flow is nearly stagnant.

The solid black horizontal lines are the averages of the drift wall temperatures predicted by FLUENT (indicated by black dots). These average wall temperatures are used in these comparisons as a boundary condition for the condensation model. The solid red horizontal lines are the predictions of the condensation model for waste package temperature. These are close to the temperatures of the top of the waste package predicted by FLUENT. The solid green horizontal lines are the invert temperatures predicted by the condensation model. They are roughly equal to the means of the invert temperatures calculated by FLUENT. The solid blue horizontal lines are the drip shield temperatures calculated by the condensation model. They are functionally identical to the drip shield temperatures calculated by FLUENT.

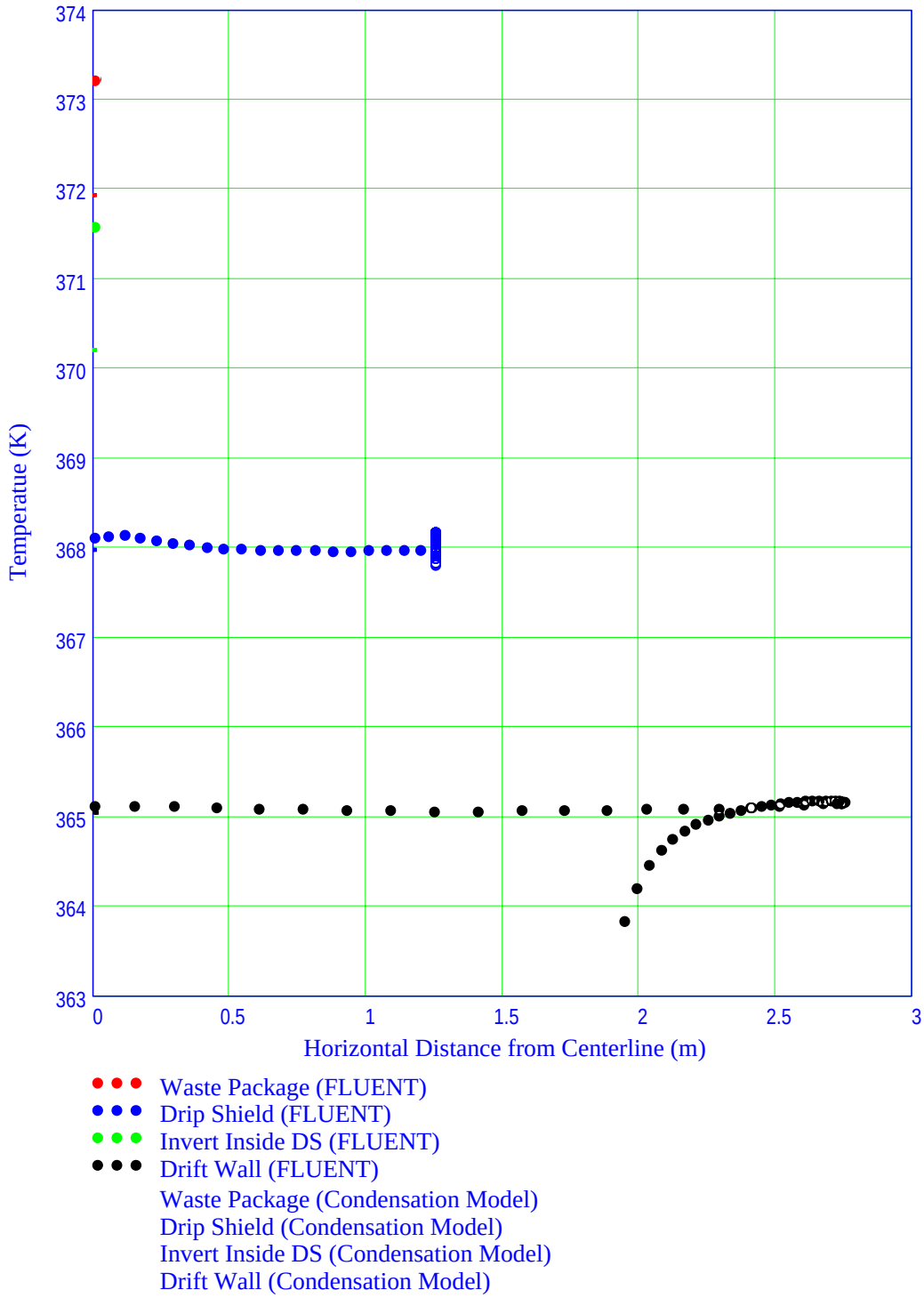

DTN: SN0408T0509903.007; file TOC.mcd; hyperlink 6.3.10, Verification of 2-D Heat Transfer Model for Structures within the Drift (Condensation Model).

DTN: SN0406T0507803.024 (FLUENT Temperatures).

Figure J-1. Comparison of Temperatures (FLUENT vs. Condensation Model) at about 300 Years

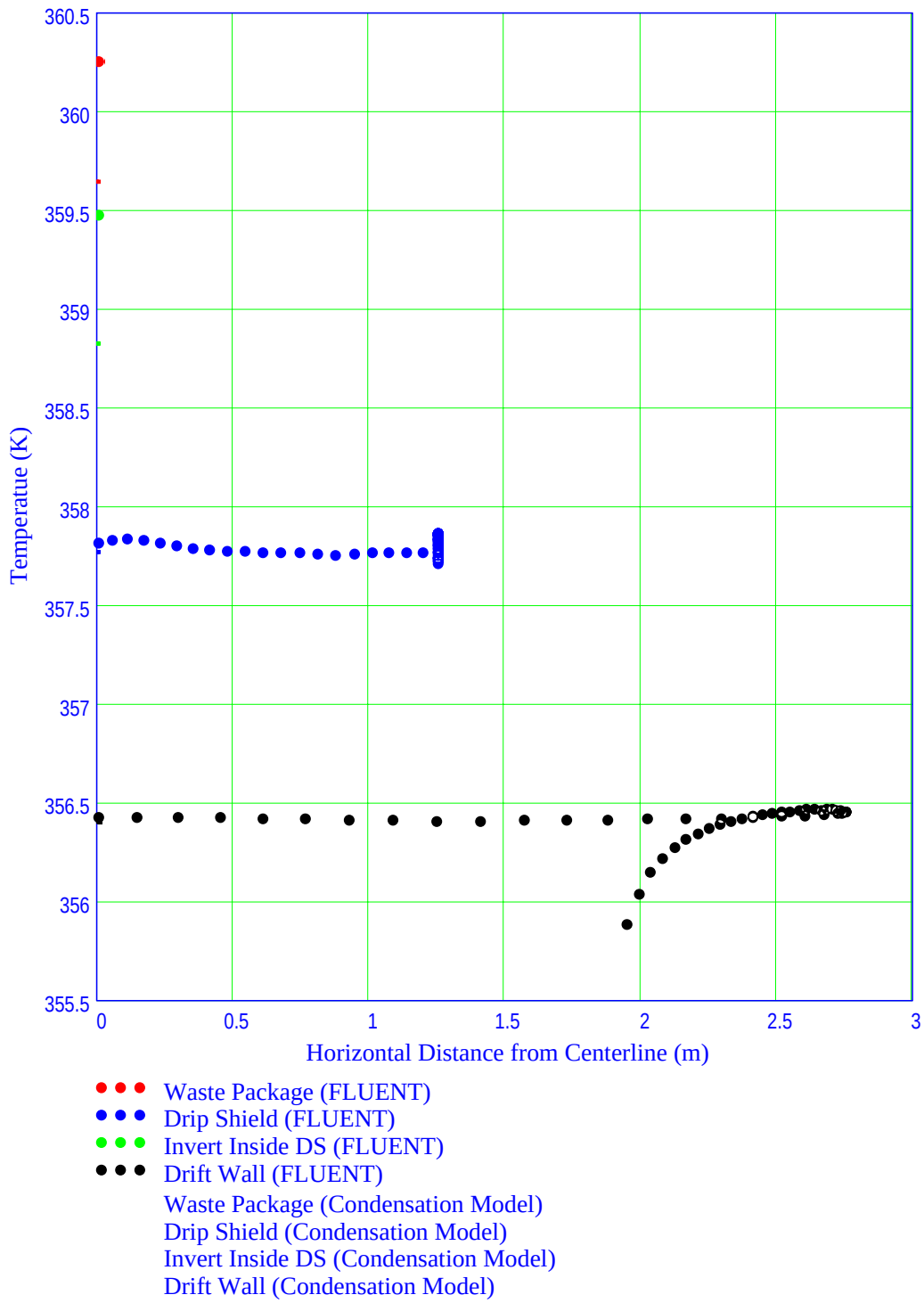

DTN: SN0408T0509903.007; file TOC.mcd; hyperlink 6.3.10, Verification of 2-D Heat Transfer Model for Structures within the Drift (Condensation Model)

DTN: SN0406T0507803.024 (FLUENT Temperatures).

Figure J-2. Comparison of Temperatures (FLUENT vs. Condensation Model) at about 1,000 Years

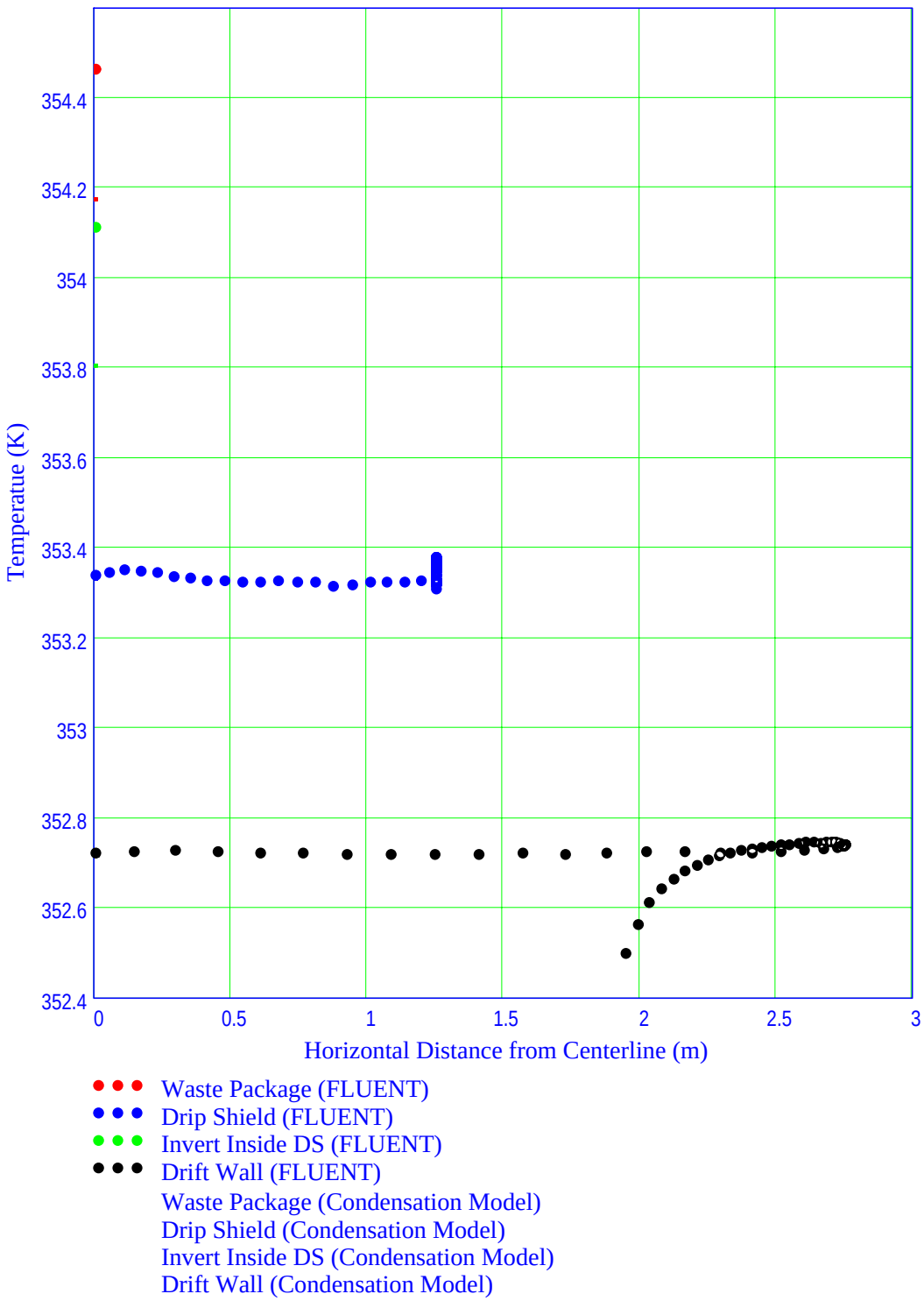

DTN: SN0408T0509903.007; file TOC.mcd; hyperlink 6.3.10, Verification of 2-D Heat Transfer Model for Structures within the Drift (Condensation Model)

DTN: SN0406T0507803.024 (FLUENT Temperatures).

Figure J-3. Comparison of Temperatures (FLUENT vs. Condensation Model) at about 3,000 Years

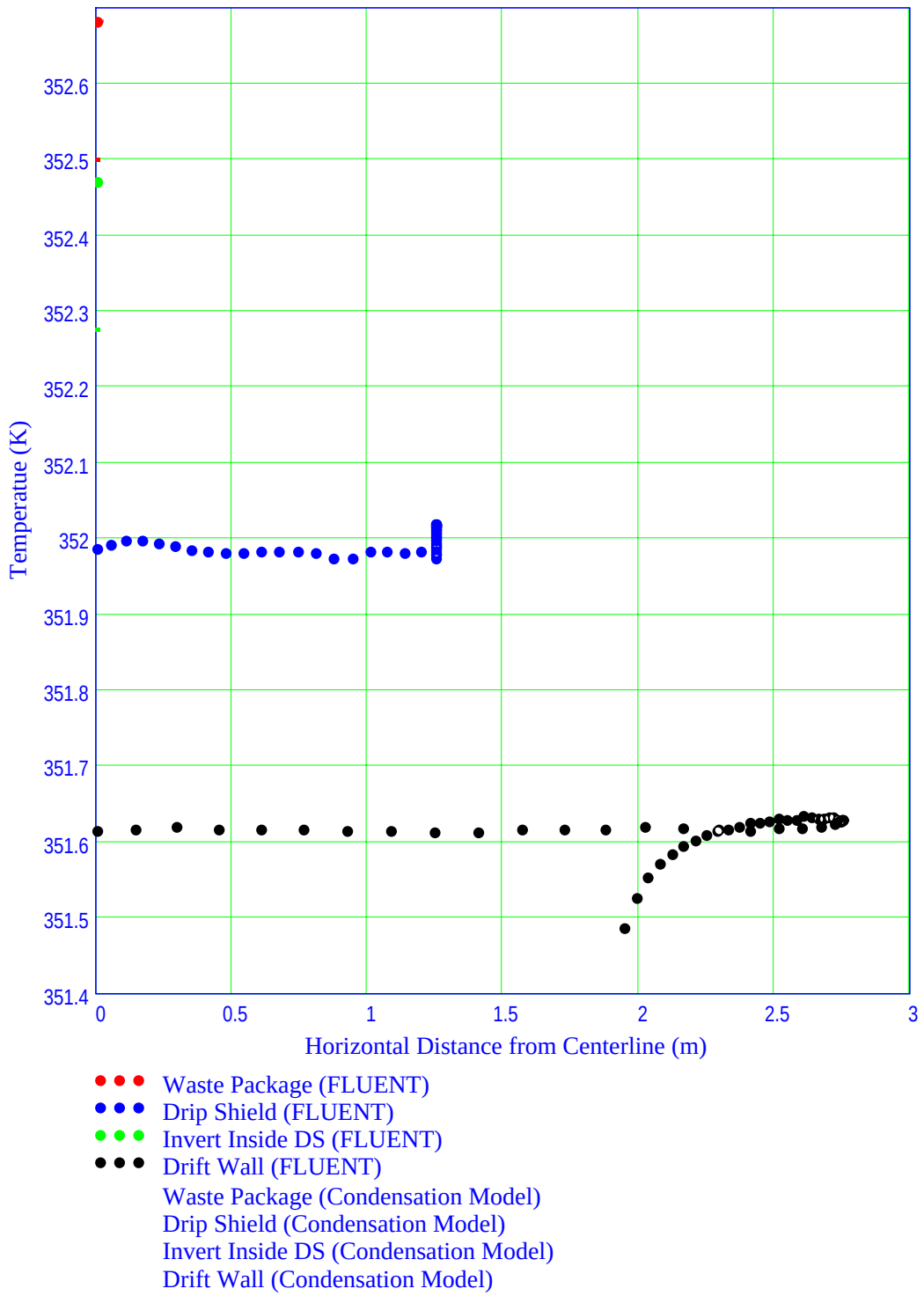

DTN: SN0408T0509903.007; file TOC.mcd; hyperlink 6.3.10, Verification of 2-D Heat Transfer Model for Structures within the Drift (Condensation Model)

DTN: SN0406T0507803.024 (FLUENT Temperatures).

Figure J-4. Comparison of Temperatures (FLUENT vs. Condensation Model) at about 10,000 Years

The comparison conducted above verified that the condensation model's prediction of surface temperatures interior to the drift wall is consistent with the two-dimensional CFD calculation, given the mean drift wall temperature. It is now appropriate to address the calculation of the mean drift wall temperature itself. The condensation model estimates the drift wall temperatures as a function of time and location using line source solutions. This temperature approximation does not include the influence of the invert on the mean wall temperature, which is included in the FLUENT simulations.

The influence of the insulating invert on the mean wall temperature is quantified by comparing the wall/boundary temperature differences in the FLUENT calculations to the temperature differences predicted by the line source solution. The FLUENT CFD calculation uses a temperature boundary condition of 350°C at 5 m into the rock. The difference between the computed mean wall temperature and this boundary temperature is tabulated in the second column of Table J-1 for the four times.

Equation 6.3-14 is the line source solution for the drift wall. By extending the radial depth, this equation is modified to compute the temperature 5 m into the rock:

$$T_{5m}(t, j, \Delta y) = \frac{1}{8\pi k} \int_0^t \frac{qL(t')}{t-t'} \sum_{n=1}^{N_{lines}} \left[\frac{e^{-\frac{\left(\Delta z_{C_{j,n}} + \frac{D_{drift}}{2} + 5\right)^2}{4\alpha(t-t')}} - e^{-\frac{\left(\Delta z_{C_{j,n}} + \frac{D_{drift}}{2} + 5 - 2ZG\right)^2}{4\alpha(t-t')}}}{e^{\frac{\left(\Delta x_{C_{j,n}}\right)^2}{4\alpha(t-t')}}} \left[\operatorname{erf} \frac{\left(\Delta y_{C_{j,n}} + \Delta y + \frac{L}{2}\right)}{\sqrt{4\alpha(t-t')}} - \operatorname{erf} \frac{\left(\Delta y_{C_{j,n}} + \Delta y - \frac{L}{2}\right)}{\sqrt{4\alpha(t-t')}} \right] \right] dt'$$

(Eq. J-1)

The difference in temperature across the 5 m of rock predicted by the line source solution is the difference between Equation 6.3-14 and Equation J-1. This difference is evaluated for the center of each of the chosen drifts and tabulated in Table J-1 in columns 3 thru 9. The temperature differences computed from the line source solution are only slightly smaller than those computed by FLUENT. This means that the presence of the invert does not adversely affect the accuracy of the line source solution.

Table J-1. Wall/Boundary Temperature Differences Computed by FLUENT and the Condensation Model

Time (yr)	**FLUENT Solution (^oC)**	**Line Source Solutions (^oC)**						
		Drift Choice #1	Drift Choice #2	Drift Choice #3	Drift Choice #4	Drift Choice #5	Drift Choice #6	Drift Choice #7
300	15.0	13.9	13.9	13.9	14.0	14.0	14.0	14.0
1000	6.4	6.0	6.0	6.0	6.0	6.0	6.0	6.0
3000	2.7	2.7	2.7	2.6	2.7	2.7	2.7	2.7
10,000	1.6	1.6	1.6	1.6	1.6	1.7	1.6	1.6

DTN: SN0408T0509903.007; file TOC.mcd; hyperlink 6.3.10, Verification of 2-D Heat Transfer Model for Structures within the Drift.

INTENTIONALLY LEFT BLANK

APPENDIX K

JUSTIFICATION OF SUPERSEDED DIRECT INPUT

During the preparation of this report, some of the design information was updated as several interface exchange drawings (IEDs) were superseded. These revisions resulted in small changes to the dimensions of the waste packages and drip shield as summarized in Table K.1-1. These small changes to the dimensions will have a negligible effect on the results of this report as evaluated below.

For internal natural convection in the problems of interest in this report, variations in waste package dimensions generally have a non-linear influence on governing model parameters. The effect of changes in dimensions can be evaluated using the k_{eq} correlation for the region under the drip shield developed in Section 6.4, or

$$k_{eq} = 0.142 Ra_{Lc}^{0.257} \qquad \text{(Eq. K-1)}$$

where

$$Ra_{Lc} = \frac{g\beta\Delta T L_c^{\ 3}}{\nu\alpha} \qquad \text{(Eq. K-2)}$$

where the characteristic length, L_c, varies depending on the problem of interest. For purposes of discussion, note that a change of 10 percent (0.10) in the characteristic length in the Rayleigh number represents less than a 8 percent change in the value of the equivalent thermal conductivity, k_{eq}. Due to the complex geometry and boundary conditions described in the main body of this report, it is not reasonable to devise more quantitative comparisons of the effects of changes to waste package dimension, spacing, and precise location. The driving force for the dispersion and condensation calculations is natural convection, so these same arguments apply to these models. Any difference of less than 10 percent in the natural convection heat transfer as indicated by the equivalent thermal conductivity correlation is well within the uncertainty of this model report results. The assessments for individual changes to physical inputs are based upon this reasonable assumption.

K.1 GEOMETRY UNDER THE DRIP SHIELD

The simulation geometry under the drip shield is different due to decreased waste package lengths (2.8 to 4.0 percent), increased waste package diameters (0.8 to 4.3 percent), larger drip shield dimensions (0.8 to 12.6 percent), and a slightly raised waste package (3.1 percent) as listed in Table K.1-1. The effect of these geometry changes will be evaluated for radial convective heat transfer and axial dispersion.

Radial convective heat transfer as quantified in equation K-1 is dependent on the characteristic dimension under the drip shield, which is proportional to the gap between the waste packages and the drip shield. The horizontal gap is the important dimension because the boundary layers develop in this area. The increased drip shield dimensions are partially offset by the increased waste package diameter. The horizontal gap for the 21-PWR waste package is the drip shield width minus the waste package diameter divided by two. Based on values in Table K-1, the simulation gap using the base drip shield width is 0.434 m, while the current value is 0.407 m, or a decrease of about 9.4 percent. Based on equation K-1, a decrease in the characteristic

dimension of 9.4 percent leads a decrease of 7 percent in the radial convective heat transfer, which is well within the uncertainty of the simulations.

The small differences in waste-package lengths will mostly affect the dispersion coefficient calculations. Because the input power to the waste packages remains the same, the total energy input to the in-drift air for mixing remains the same. However, the energy per unit length increases slightly due to the decreased waste package lengths. To a first order, the increase is Rayleigh number will be of order 2.8 to 4.0 percent, which results in an increase in the radial heat transfer of about 3 percent. The increase in axial heat transfer is approximately the same as the increase in radial heat transfer. Based on the heat transfer – mass transfer analogy, the increase in axial dispersion will be about 3 percent, which is well within the uncertainty of the simulations.

Note that these two effects partially offset each other. The radial geometry changes decrease the heat transfer rate, while the waste package length differences increase the heat transfer rate. Therefore, the net difference is expected to be about 4 percent based on simple addition of these two effects.

K.2 GEOMETRY OUTSIDE THE DRIP SHIELD

The simulation geometry outside the drip shield is different due to the larger drip shield dimensions (0.8 to 12.6 percent) as listed in Table K.1-1. The effect of these geometry changes will be evaluated for radial convective heat transfer and axial dispersion.

Similar to the evaluation under the drip shield, the change in the horizontal gap is evaluated. The horizontal gap width is the drift diameter of 5.5 m, which is unchanged, minus the drip shield width divided by two. Using the width at the bottom of the drip shield, the simulation gap is 1.494 m while the current gap is 1.484 m, or a decrease less than 1 percent in the dimension and in radial heat transfer. This change is insignificant for radial heat transfer.

The effects of changes in the waste package lengths on the dispersion coefficient is expected to be similar to that discussed for under the drip shield, or an increase of about 3 percent, which is well within the uncertainty of the simulations.

K.3 WASTE PACKAGE COORDINATES

The information used for the waste package coordinates has been updated since the analysis has been performed. The updated drawing shows some minor changes compared to the original source. These differences are detailed in Section 4.1.2.8 of the *Multiscale Thermohydrologic Model* (MSTHM) (BSC 2004 [DIRS 169565]). These changes are small and are of negligible consequence to the line-source temperature calculations.

Table K.1-1 Comparison of Design Inputs with Current Design Inputs

Cited Table in Document	Input Description	Superseded Input Cited in Section 4	Cited Value	Current Value of Parameter	Current Value	Comments	Percent Difference
Table 4.1.1-3	24 BWR Nominal Diameter	BSC 2003 [DIRS 164053]	1318 mm	BSC 2004 [DIRS 169472], Table 1	1375.4 mm		4.2%
	DHLW waste package Nominal diameter (largest)	BSC 2003 [DIRS 164053]	2110 mm	BSC 2004 [DIRS 169472], Table 1	2126 mm		0.8%
	Invert Height from Bottom of Drift	BSC 2003 [DIRS 164101]	0.806 m	BSC 2004 [DIRS 169503]	0.8636 m [2'10"]	Note that the invert height is reported in inches.	6.7%
	Outside Width of Drip Shield	BSC 2003 [DIRS 171024]	2.512 m	BSC 2004 [DIRS 169220]	2.53278 m		0.8%
	Height of Drip Shield	BSC 2003 [DIRS 171024]	2.521 m	BSC 2004 [DIRS 168067]	2.88562 m		12.6%
Table 4.1.2-5	Length of 21-PWR Waste Package	BSC 2003 [DIRS 165406]	5165 mm	BSC 2004 [DIRS 169472], Table 1	5024.4 mm		-2.8%
	21-PWR Waste Package Nominal Diameter	BSC 2003 [DIRS 165406]	1644 mm	BSC 2004 [DIRS 169472], Table 1	1718.3 mm		4.3%
	Length of 44 BWR Waste Package	BSC 2003 [DIRS 165406]	5165 mm	BSC 2004 [DIRS 169472], Table 1	5024.4 mm		-2.8%
	Length of 5-DHLW Short Waste Package	BSC 2003 [DIRS 165406]	3590 mm	BSC 2004 [DIRS 169472]	3452.8 mm		-4.0%
	Length of 5-DHLW Long Waste Package	BSC 2003 [DIRS 165406]	5217 mm	BSC 2004 [DIRS 169472]	5059.4 mm		-3.1%

Table 4.1.2-5 (cont.)	Invert Height from Bottom of Drift	BSC 2003 [DIRS 164101]	0.806 m	BSC 2004 [DIRS 169503]	0.8636 m [2'10"]	Note that the invert height is reported in inches.	-6.7%
	Distance from Top of Invert to Center of 21 PWR Package	BSC 2003 [DIRS 164069]	1018 mm	BSC 2004 [DIRS 168489]	1050.9 mm		3.1%
	Peak Height of Drip Shield	BSC 2003 [DIRS 171024]	2.521 m	BSC 2004 [DIRS 168067]	2.88562 m		12.6%
	Width of Drip Shield at Base	BSC 2003 [DIRS 171024]	2.512 m	BSC 2004 [DIRS 169220]	2.53278 m		0.8%
	Height of Vertical Section of Drip Shield	BSC 2003 [DIRS 171024]	1.875 m	BSC 2004 [DIRS 168067]	1.891 m		0.8%
Table 4.1.3-7	Waste Package Endpoint Coordinates	BSC 2003 [DIRS 161727]	See Text	BSC 2004 [DIRS 164519]	See text above.	Endpoint correspond with envelope dimensions	See Text
Table 4.1.3-8	Distance from Top of Invert to Center of 21 PWR Package	BSC 2003 [DIRS 164069]	1018 mm	BSC 2004 [DIRS 168489], Table 1	1050.9 mm		3.1%
	Length of 21-PWR Waste Package	BSC 2003 [DIRS 165406]	5165 mm	BSC 2004 [DIRS 169472], Table 1	5024.4 mm		-2.8%
	21-PWR Waste Package Nominal Diameter	BSC 2003 [DIRS 165406]	1644 mm	BSC 2004 [DIRS 169472], Table 1	1718.3 mm		4.3%
	Length of 44-BWR Waste Package	BSC 2003 [DIRS 165406]	5165 mm	BSC 2004 [DIRS 169472], Table 1	5024.4 mm		-2.8%
	44-BWR Waste Package Nominal Diameter	BSC 2003 [DIRS 165406]	1674 mm	BSC 2004 [DIRS 169472], Table 1	1756.4 mm		4.7%

Table 4.1.3-8 (cont.)	Length of 5-DHLW Short Waste Package	BSC 2003 [DIRS 165406]	3590 mm	BSC 2004 [DIRS 169472], Table 1	3452.8 mm		-4.0%
	5-DHLW Short Waste Package Nominal Diameter	BSC 2003 [DIRS 165406]	2110 mm	BSC 2004 [DIRS 169472], Table 1	2126.0 mm		0.8%
	Length of 5-DHLW Long Waste Package	BSC 2003 [DIRS 165406]	5217 mm	BSC 2004 [DIRS 169472], Table 1	5059.4 mm		-3.1%
	5-DHLW Long Waste Package Nominal Diameter	BSC 2003 [DIRS 165406]	2110 mm	BSC 2004 [DIRS 169472], Table 1	2126.0 mm		0.8%
Table 4.1.3-9	Invert Height from Bottom of Drift	BSC 2003 [DIRS 164101]	0.806 m	BSC 2004 [DIRS 169503]	0.8636 m [2'10"]	Note that the invert height is reported in inches.	6.7%
	Width of Drip Shield at Base	BSC 2003 [DIRS 171024]	2.512 m	BSC 2004 [DIRS 169220]	2.53278 m		0.8%
	Height of Vertical Section of Drip Shield	BSC 2003 [DIRS 171024]	1.875 m	BSC 2004 [DIRS 168067]	1.891 m		0.8%
	Peak Height of Drip Shield	BSC 2003 [DIRS 171024]	2.521 m	BSC 2004 [DIRS 168067]	2.88562 m		12.6%

[a] – A review of the IEDs shows both sources as being a controlled source of information for the invert height.

INTENTIONALLY LEFT BLANK

APPENDIX L

QUALIFICATION OF DIRECT INPUTS LISTED IN TABLE 4.1.5-1

Handbooks are considered to be compilations of established facts. However, handbooks in themselves derive or present no new information, they only present what has been published in the open literature, either by textbooks or publications. Thus when a textbook, source or a publication is referenced (or cited) by a handbook, the textbook, source or publication becomes reliable because it is part of the handbook, which in its entirety is established fact. Therefore, some of the following sources are demonstrated to be reliable for the intended use identified in Table 4.1.5-1 because the reliability of these sources (per AP-SIII.10Q, Section 5.2.1(k)) is demonstrated by being cited as references in the indicated handbook(s) and thus widely used in standard work practices by engineers and scientists. The other sources are demonstrated as being reliable by other specific methods as described. The extent to which the data (information or equations) demonstrate the properties (information or mathematics) of interest is also addressed.

Qualification of the use of information from Bejan A. 1995 [DIRS 152307]. The referenced source by A. Bejan, Convection Heat Transfer, was first published in 1984, and the second edition [DIRS 152307] was published in 1995. The second edition was reviewed by colleagues in the field of heat transfer from Rensselaer Polytechnic Institute, Air Force Office of Scientific Research, University of Cincinnati, Auburn University, State University of New York at Stony Brook, Seoul National University, IBM Corporation, and Texas A&M University. Other publications by Bejan on convective heat transfer are referenced in the handbook by Rohsenow et al. 1998 [DIRS 169241], reference numbers 15 and 16 in Chapter 4: Natural Convection. Therefore, the information from the source by A. Bejan is reliable and qualified for the intended use because it has been extensively reviewed and in publication for over two decades. His other works related to convective heat transfer are cited in a handbook on this subject, and thus are widely used in the standard work practices on this topic. The extent to which this source of information addresses the data and equations for the physical properties of air is considered adequate because these properties are well known, as documented here.

Qualification of the use of information from Bird, R.B.; Stewart, W.E.; and Lightfoot, E.N. 1960 [DIRS 103524]. The referenced source by Bird et al., was first published in 1960 and has been in publication ever since. This source is referenced by handbooks, specifically Rohsenow et al. 1998 [DIRS 169241], reference number 10 in Chapter 1: Basic Concepts of Heat Transfer, and Perry et al. 1984 [DIRS 125806], in the general references for Section 10: Heat Transmission. Therefore, the information from the source by Bird et al., is reliable and qualified for the intended use because it has been in publication for over four decades. This source is cited in two handbooks in the subject area of heat and mass transfer, and thus is widely used in the standard work practices on these topics. The extent to which this source of information addresses the heat and mass transfer relationships for dispersion/diffusion for air and conversion factors is considered adequate because these topics are well known, as documented here.

Qualification of the use of information from Carslaw, H.S. and Jaeger, J.C. 1959 [DIRS 100968]. The referenced source by Carslaw and Jaeger was first published in 1946. The second edition was first published in 1959 and has been reprinted 13 times. This source is referenced by two handbooks, specifically Rohsenow et al. 1998 [DIRS 169241], reference number 11 in Chapter 3: Conduction and Thermal Contact Resistances (Conductances), and Perry et al. 1984 [DIRS 125806], in the general references for Section 10: Heat Transmission. Therefore, the information from the source by Carslaw and Jaeger is reliable and qualified for the intended use because it has been in publication for over four decades, it is cited in two handbooks in the

subject area of heat conduction, and thus is widely used in the standard work practices on these topics. The extent to which this source of information addresses the analytical/mathematical results for conduction heat transfer is considered adequate because these topics are well known, as documented here.

Qualification of the use of information from Haar et al. 1984 [DIRS 105175]. The referenced source by Haar et al. 1984 [DIRS 105175] is a compilation of the thermophysical properties of water vapor/steam. This compilation tabulates, as one of the properties, the densities of the vapor and liquid. Thus this source is, in part, a density table. Also, this source is referenced in the handbook by Rohsenow et al. 1998 [DIRS 169241] as reference number 7 in Chapter 2: Thermophysical Properties. Therefore, the information from the source by Haar et al., is reliable and qualified for the intended use because it has been in publication for over two decades, it is cited in a handbook, and thus is widely used in the standard work practices using the physical properties of water vapor/steam. The extent to which this source of information addresses the thermophysical properties of liquid/vapor for water is considered adequate because this topic is well known, as documented here.

Qualification of the use of Equation 6.3-78 from Ho, C.K. 1997 [DIRS 141521]. The referenced equation is used to predict the temperature and pressure dependency of the diffusion coefficient. The inverse pressure dependence can also be seen from Perry et al. 1984 [DIRS 125806], equation 3-133, which shows the pressure dependency as 1/p. The temperature dependency to the power of 1.8 can also be seen from Perry et al. 1984 [DIRS 125806], equation 3-133, which shows a temperature dependency of T to the power of 1.75. These powers are sufficiently close to be considered to be the same (especially if 1.75 is rounded to 1.8). Therefore, equation 6.3-78 from Ho is considered reliable for its intended use of the prediction the pressure and temperature dependency of the diffusion coefficient because the mathematical form appears in a handbook. The extent to which this source of information addresses the temperature and pressure dependency of the diffusion coefficient is considered adequate because these dependencies are well known, as documented here.

Qualification of the view factor in equation 6.3-26 by Howell 1982 [DIRS 164711]. The referenced source by Howell, J.R. 1982 [DIRS 164711] is referenced in the handbook by Rohsenow et al. 1998 [DIRS 169241] as reference number 20 in Chapter 7: Radiation. Therefore, the information from the source by Howell is reliable and qualified for the intended use because it has been in publication for over two decades, this source is cited in a handbook on this topic, and thus is widely used in the standard work practices on the topic of radiation view factors. The extent to which this source of information addresses the radiant heat transfer relations and radiation view factors is considered adequate because these topics are well known, as documented here.

Qualification of the use of information from Siegel and Howell 1992 [DIRS 100687]. The referenced source by Siegel, R. and Howell, J.R. 1992 [DIRS 100687] on thermal radiation heat transfer is referenced in the handbook by Rohsenow et al. 1998 [DIRS 169241] as reference number 1 in Chapter 7: Radiation. Therefore, the information from the source by Siegel and Howell is reliable and qualified for the intended use because it has been in publication for over a decade, this source is cited in a handbook on this topic, and thus is widely used in the standard work practices for radiation heat transfer. The extent to which this source of information

addresses the radiant view factors for specific in-drift geometries is considered adequate because this topic is well known, as documented here.

Qualification of the use of information from Raithby and Hollands 1975 [DIRS 156726]. The referenced source by Raithby, G.D. and Hollands, K.G.T. 1975 [DIRS 156726] on a general method of obtaining approximate solutions to laminar and turbulent free convection problems is referenced in the handbook by Rohsenow et al. 1998 [DIRS 169241] as reference number 223 in Chapter 4: Natural Convection. Furthermore, Chapter 4 in this handbook is authored by Raithby and Hollands. Therefore, the information from the source by Raithby and Hollands is reliable and qualified for the intended use because it has been in publication for over three decades, this source is cited in a handbook on this topic, and thus is widely used in the standard work practices on convection problems. The extent to which this source of information addresses the use of natural-convection heat and mass transfer correlations is considered adequate because these topics are well known, as documented here.

Qualification of the references by Incropera and DeWitt, 1990 [DIRS 156693], 1996 [DIRS 108184], and 2002 [DIRS 163337]. The referenced source(s) by Incropera, F.P. and DeWitt, D.P. is referenced as the third edition in the handbook by Rohsenow et al. 1998 [DIRS 169241] as reference number 6 in Chapter 2: Thermophysical Properties. The later sources by Incropera, F.P. and DeWitt, D.P. 1996 [DIRS 108184] and 2002 [DIRS 163337] are the fourth and fifth editions of this publication. Therefore, the information from these sources by Incropera and DeWitt is reliable and qualified for the intended use because they have been in publication through five editions, the third edition is cited in a handbook, it is a textbook (including problems), and thus is widely used in the standard work practices on thermophysical properties and heat transfer topics. The extent to which these sources of information addresses the heat transfer relationships, physical properties of air, and emissivities of solids is considered adequate because these topics are well known, as documented here.

Qualification of the reference by Kuehn and Goldstein, 1976 [DIRS 100675]. The referenced source by Kuehn, T.H. and Goldstein, R.J. 1976 [DIRS 100675] is referenced in the handbook by Rohsenow et al. 1998 [DIRS 169241] as reference number 163 in Chapter 4: Natural Convection. Also, it is referenced in the textbook by Incropera, F.P. and Dewitt, D.P. 1996 [DIRS 108184], Chapter 9, Free Convection, as reference number 38. Therefore, the information from the source by Kuehn and Goldstein is reliable and qualified for the intended use because it is based on experimental data, has been in the open literature for over three decades, this source is cited in a handbook and textbook on this topic, and thus is widely used in the standard work practices on the topic of natural convection. The extent to which this source of information addresses natural convection heat transfer correlations between concentric cylinders is considered adequate because the correlation is well known and based on experimental measurements, as documented here.

Qualification of equations 9-5.1 and 9-5.2 from Reid et al. 1977 [DIRS 130310]. Equations 9-5.1 and 9-5.2 from Reid et al. 1977 [DIRS 130310] are used to calculate the viscosity of gas mixtures at low pressures. These equations also appear in the handbook by Perry et al. 1984 [DIRS 125806] as equations 3-87 and 3-88 in Section 3: Physical and Chemical Data in the subsection entitled Viscosity. The reference by Reid et al. 1977 [DIRS 130310] is also referenced by Perry in Section 3 as reference number 196. Thus the equations cited to calculate

the viscosity of gas mixtures are established fact because they appear in a handbook. The extent to which these equations address the properties of interest, gas-mixture viscosities, is adequate because equations are well known, as documented here.

Qualification of the information from Reynolds 1979 [DIRS 158410] appearing in Tables 4.1.3-3 and 4.1.3-4. The information appearing in Tables 4.1.3-3 and 4.1.3-4 from Reynolds, W.C. 1979 [DIRS 158410] appears in the handbook by Perry et al. 1984 [DIRS 125806] as follows. The molecular weight of water is 18.016 (Perry et al. 1984 [DIRS 125806], Table 3-1). The molecular weight of air is 28.96 (Perry et al. 1984 [DIRS 125806], footnote to Figure 3-16). This information, the molecular weights of water and air, are thus considered established fact because the values are corroborated in the cited handbook. The extent to which these data address the properties of interest is adequate because molecular weights are well known.

Qualification of the information from White 1986 [DIRS 111015] appearing in Table 7.4.2-8. The information presented in Table 7.4.2-8 (White 1986 [DIRS 111015]) is atmospheric pressure at two elevations. This type of information is known as the standard atmosphere. This information can also be found in Perry et al. 1984 [DIRS 125806], Table 3-214. The pressure given by White for an elevation of 1000 m is 89,889 Pa, and from Perry et al., the pressure is 0.89876 bar. The conversion from bar to Newtons per square meter is to multiply bar by 1×10^5 (Perry et al. 1984 [DIRS 125806], Table 1-6). The conversion factor for Newtons per square meter to Pa (Pascal) is unity (Rohsenow et al. 1998 [DIRS 169241], Table 2.4). Therefore the information referenced by White is considered established fact because it is corroborated in a handbook. The extent to which these data address the topic of interest is adequate because the standard atmosphere is well known, as documented here.

APPENDIX M

CALCULATION CORRECTION

During the checking of this report, two mistakes were found.

1. The equations for the capillary pressure (P_c, Equation 6.3-51) and the saturation derivative of the capillary pressure (Equation 6.3-52) were implemented incorrectly in the Mathcad file that calculates the capillary pumping contribution to the evaporation limit ($q_{matrix_limit_shp}$, Equation 6.3-60). Correction of this error changed the capillary pumping contribution from 0.79 mm/yr to 0.95 mm/yr. This is approximately a 20 percent increase in the water available by capillary pumping. The impact of this correction on the predicted condensation rates is small. At large percolation rates, the capillary pumping contribution is dwarfed by the percolation rate, which dominates the condensation rate. At small percolation rates, the condensation rate remains small, and the change due to the correction is of little consequence.

2. The equation for the view factor between the waste package and the invert (Eq. 6.3-26) was incorrectly programmed in the Mathcad files as:

$$F_{wp-invert} = \frac{1}{\pi}\tan^{-1}\left(\frac{\frac{D_{wp}}{2} + h_{wp}}{\frac{P_{invert}}{2}}\right) \qquad \text{(Eq. M-1)}$$

   The corrected view factor (correctly expressed in Mathcad as stated by Eq. 6.3-26) results in a slightly higher temperature for the invert surface resulting in a slightly higher heat and mass transport rate.

The changes in condensation rate that result from these two corrections are small compared to the intrinsic uncertainty in the predictions that is already captured by the bounds on invert performance, drip shield ventilation, and percolation rate. The comparatively small changes mean that the condensation abstraction (Section 8.3) prepared for inclusion into the TSPA model is adequate for its intended use.

The following tables document the impact of the correction on the condensation rates. Tables M-1 through M-5 contain the predictions of total drift wall condensation and are corrections of Tables 6.3.7-1 thru 6.3.7-5. The old values of the total length of the condensation zones and total condensation rate are included in parentheses where they differ from the corrected values. Tables M-6 and M-7 contain the corrected values for condensation under the drip shield. Again, the old values are included in parentheses where they differ from the corrected values.

Table M-1. Condensation on the Drift Walls: Well Ventilated Drip Shield Low Invert Transport, Low Dispersion Coefficient

Perc.	Drift	300 yrs		1,000 yrs		3,000 yrs		10,000 yrs	
Level	**Choice**	**Length (m)**	**Total Cond (kg/yr)**	**Length (m)**	**Total Cond (kg/yr)**	**Length (m)**	**Total Cond (kg/yr)**	**Length (m)**	**Total Cond (kg/yr)**
Low	# 1:	-	-	34	49 (40)	0	0	0	0
	# 2:	-	-	9	16 (15)	0	0	0	0
	# 3:	0	0	0	0	0	0	0	0
	# 4:	-	-	0	0	0	0	0	0
	# 5:	-	-	0	0	0	0	0	0
	# 6:	-	-	0	0	0	0	0	0
	# 7:	-	-	171 (152)	3206 (2834)	0	0	0	0
	Total:	**0**		**214 (195)**		**0**		**0**	
Mean	# 1:	-	-	55	110 (106)	0	0	0	0
	# 2:	-	-	44 (39)	74 (70)	0	0	0	0
	# 3:	0	0	0	0	0	0	0	0
	# 4:	-	-	147	1853 (1855)	0	0	0	0
	# 5:	-	-	81 (71)	597 (563)	0	0	0	0
	# 6:	-	-	19 (14)	18 (17)	0	0	0	0
	# 7:	-	-	277 (258)	5045 (4787)	0	0	0	0
	Total:	**0**		**624 (583)**		**0**		**0**	
Upper	# 1:	-	-	65	127	0	0	0	0
	# 2:	-	-	55	114	0	0	0	0
	# 3:	0	0	0	0	0	0	0	0
	# 4:	-	-	156	1915 (1921)	0	0	0	0
	# 5:	-	-	106	754 (748)	0	0	0	0
	# 6:	-	-	19	27 (26)	0	0	0	0
	# 7:	-	-	373	6011 (6026)	0	0	0	0
	Total:	**0**		**774**		**0**		**0**	

DTN: SN0408T0509903.008; file Mixed_LowInvertTransport\Summary Tables.mcd.

Table M-2. Condensation on the Drift Walls: Well Ventilated Drip Shield High Invert Transport, Low Dispersion Coefficient

Perc. Level	Drift Choice	300 yrs		1,000 yrs		3,000 yrs		10,000 yrs	
		Length (m)	Total Cond (kg/yr)	Length (m)	Total Cond (kg/yr)	Length (m)	Total Cond (kg/yr)	Length (m)	Total Cond (kg/yr)
Low	# 1:	-	-	104 (99)	455 (403)	424 (419)	691 (510)	505	1226 (1062)
	# 2:	-	-	50 (30)	242 (121)	424 (413)	793 (612)	514 (509)	1431 (1266)
	# 3:	0	0	108 (90)	79 (37)	343 (337)	1119 (1002)	385 (380)	1311 (1188)
	# 4:	-	-	0	0	137 (5)	31 (0)	491 (475)	810 (645)
	# 5:	-	-	0	0	266 (142)	108 (18)	500 (489)	931 (762)
	# 6:	-	-	0	0	211 (137)	91 (23)	364 (359)	777 (661)
	# 7:	-	-	171 (156)	4795 (4204)	632 (600)	927 (705)	671 (666)	2357 (2146)
	Total:	0		433 (374)		2438 (2055)		3430 (3383)	
Mean	# 1:	-	-	173	1416 (1309)	525	5695 (5522)	540	6384 (6212)
	# 2:	-	-	141 (131)	1187 (1120)	505	4832 (4667)	540	5651 (5479)
	# 3:	0	0	229 (219)	648 (555)	380	3665 (3541)	415	4107 (3975)
	# 4:	-	-	178	4488 (4389)	521	7976 (7805)	549	9367 (9193)
	# 5:	-	-	81 (76)	1421 (1288)	500 (495)	3743 (3576)	546 (540)	4869 (4697)
	# 6:	-	-	56	465 (433)	358	2842 (2722)	399	3907 (3780)
	# 7:	-	-	283 (263)	8349 (7724)	666	4860 (4643)	687	6410 (6192)
	Total:	0		1142 (1097)		3455 (3449)		3677 (3672)	
Upper	# 1:	-	-	270	3587 (3483)	535	13724 (13549)	560	14714 (14537)
	# 2:	-	-	182 (177)	2434 (2356)	525	9186 (9014)	555	10186 (10011)
	# 3:	0	0	313	2493 (2382)	410	7907 (7775)	435	8637 (8501)
	# 4:	-	-	217 (212)	6289 (6193)	535	16392 (16217)	565	18111 (17932)
	# 5:	-	-	140	2628 (2563)	526 (521)	7997 (7822)	556	9438 (9261)
	# 6:	-	-	65 (62)	656 (625)	374	4464 (4339)	399	5641 (5514)
	# 7:	-	-	415 (404)	12684 (12488)	677	10931 (10711)	707	12698 (12475)
	Total:	0		1602 (1577)		3582 (3577)		3777	

DTN: SN0408T0509903.008; file Mixed_HighInvertTransport\Summary Tables.mcd.

Table M-3. Condensation on the Drift Walls, Well Ventilated Drip Shield High Invert Transport, High Dispersion Coefficient

Perc. Level	Drift Choice	300 yrs		1,000 yrs		3,000 yrs		10,000 yrs	
		Length (m)	Total Cond (kg/yr)	Length (m)	Total Cond (kg/yr)	Length (m)	Total Cond (kg/yr)	Length (m)	Total Cond (kg/yr)
Low	# 1:	-	-	0	0	0	0	274 (228)	215 (112)
	# 2:	-	-	0	0	0	0	325 (288)	356 (242)
	# 3:	0	0	0	0	0	0	274 (263)	693 (601)
	# 4:	-	-	0	0	0	0	0	0
	# 5:	-	-	0	0	0	0	0	0
	# 6:	-	-	0	0	0	0	0	0
	# 7:	-	-	0	0	0	0	293 (208)	164 (75)
	Total:	**0**		**0**		**0**		**1165 (987)**	
Mean	# 1:	-	-	0	0	0	0	491 (486)	4532 (4369)
	# 2:	-	-	0	0	0	0	475	3902 (3744)
	# 3:	0	0	0	0	55	109	348	2923 (2809)
	# 4:	-	-	0	0	0	0	491	6452 (6293)
	# 5:	-	-	0	0	0	0	454	2775 (2625)
	# 6:	-	-	0	0	0	0	318 (313)	1665 (1562)
	# 7:	-	-	0	0	0	0	601 (586)	3271 (3079)
	Total:	**0**		**0**		**55**		**3178 (3153)**	
Upper	# 1:	-	-	0	0	134 (111)	217 (171)	519	12191 (12022)
	# 2:	-	-	0	0	0	0	500	8031 (7869)
	# 3:	0	0	0	0	196	1982 (1909)	378	6809 (6687)
	# 4:	-	-	0	0	0	0	519	14483 (14315)
	# 5:	-	-	0	0	0	0	505	6762 (6595)
	# 6:	-	-	0	0	0	0	344	3081 (2968)
	# 7:	-	-	0	0	0	0	652	8945 (8735)
	Total:	**0**		**0**		**330 (307)**		**3418**	

DTN: SN0408T0509903.008; file Mixed_HighInvertTransport\Summary Tables.mcd.

Table M-4. Condensation on the Drift Walls: Unventilated Drip Shield Low Invert Transport, Low Dispersion Coefficient

Perc. Level	Drift Choice	300 yrs		1,000 yrs		3,000 yrs		10,000 yrs	
		Length (m)	Total Cond (kg/yr)	Length (m)	Total Cond (kg/yr)	Length (m)	Total Cond (kg/yr)	Length (m)	Total Cond (kg/yr)
Low	# 1:	-	-	34	52 (45)	0	0	0	0
	# 2:	-	-	13	18 (16)	0	0	0	0
	# 3:	0	0	0	0	0	0	0	0
	# 4:	-	-	25 (5)	309 (46)	0	0	0	0
	# 5:	-	-	0	0	0	0	0	0
	# 6:	-	-	0	0	0	0	0	0
	# 7:	-	-	217 (198)	3424 (3064)	0	0	0	0
	Total:	**0**		**288 (249)**		**0**		**0**	
Mean	# 1:	-	-	55	97 (92)	0	0	0	0
	# 2:	-	-	50 (44)	72 (69)	0	0	0	0
	# 3:	0	0	0	0	0	0	0	0
	# 4:	-	-	152	1565 (1557)	0	0	0	0
	# 5:	-	-	92	550 (541)	0	0	0	0
	# 6:	-	-	19	19 (18)	0	0	0	0
	# 7:	-	-	314 (304)	4616 (4515)	0	0	0	0
	Total:	**0**		**682 (666)**		**0**		**0**	
Upper	# 1:	-	-	60	102	0	0	0	0
	# 2:	-	-	64	100	0	0	0	0
	# 3:	0	0	0	0	0	0	0	0
	# 4:	-	-	156	1598	0	0	0	0
	# 5:	-	-	106	640 (639)	0	0	0	0
	# 6:	-	-	25	23 (22)	0	0	0	0
	# 7:	-	-	378	5070 (5068)	0	0	0	0
	Total:	**0**		**788**		**0**		**0**	

DTN: SN0408T0509903.008; file Unmixed_LowInvertTransport\Summary Tables.mcd.

Table M-5. Condensation on the Drift Walls: Unventilated Drip Shield High Invert Transport, Low Dispersion Coefficient

Perc. Level	Drift Choice	300 yrs		1,000 yrs		3,000 yrs		10,000 yrs	
		Length (m)	Total Cond (kg/yr)	Length (m)	Total Cond (kg/yr)	Length (m)	Total Cond (kg/yr)	Length (m)	Total Cond (kg/yr)
Low	# 1:	-	-	34	52 (45)	0	0	0	0
	# 2:	-	-	13	18 (16)	0	0	0	0
	# 3:	0	0	0	0	0	0	0	0
	# 4:	-	-	25 (5)	309 (46)	0	0	0	0
	# 5:	-	-	0	0	0	0	0	0
	# 6:	-	-	0	0	0	0	0	0
	# 7:	-	-	217 (198)	3424 (3064)	0	0	0	0
	Total:	**0**		**288 (249)**		**0**		**0**	
Mean	# 1:	-	-	55	97 (92)	0	0	0	0
	# 2:	-	-	50 (44)	72 (69)	0	0	0	0
	# 3:	0	0	0	0	0	0	0	0
	# 4:	-	-	152	1565 (1557)	0	0	0	0
	# 5:	-	-	92	550 (540)	0	0	0	0
	# 6:	-	-	19	19 (18)	0	0	0	0
	# 7:	-	-	314 (304)	4616 (4514)	0	0	0	0
	Total:	**0**		**682 (666)**		**0**		**0**	
Upper	# 1:	-	-	60	102	0	0	0	0
	# 2:	-	-	64	100	0	0	0	0
	# 3:	0	0	0	0	0	0	0	0
	# 4:	-	-	156	1599	0	0	0	0
	# 5:	-	-	106	640 (639)	0	0	0	0
	# 6:	-	-	25	23 (22)	0	0	0	0
	# 7:	-	-	378	5070 (5069)	0	0	0	0
	Total:	**0**		**788**		**0**		**0**	

DTN: SN0408T0509903.008; file Unmixed_HighInvertTransport\Summary Tables.mcd.

Table M-6. Condensation under the Drip Shield: Unventilated Drip Shield High Invert Transport, Low Dispersion Coefficient

Perc.	Drift	300 yrs		1,000 yrs		3,000 yrs		10,000 yrs	
Level	**Choice**	**# WP's**	**Total Cond (kg/yr)**	**# WP's**	**Total Cond (kg/yr)**	**# WP's**	**Total Cond (kg/yr)**	**# WP's**	**Total Cond (kg/yr)**
Low	# 1:	-	-	0	0	21	983 (820)	29	1261 (1095)
	# 2:	-	-	0	0	22 (20)	1095 (938)	29 (28)	1451 (1285)
	# 3:	0	0	8	623 (507)	18	1131 (1009)	23 (22)	1341 (1216)
	# 4:	-	-	0	0	16 (14)	514 (352)	27	943 (784)
	# 5:	-	-	0	0	16 (14)	540 (379)	28 (27)	1017 (854)
	# 6:	-	-	0	0	14 (13)	549 (440)	21 (20)	949 (834)
	# 7:	-	-	0	0	35 (34)	2155 (1945)	39	2596 (2385)
	Total:	**0**		**8**		**142 (134)**		**196 (192)**	
Mean	# 1:	-	-	12 (11)	1564 (1421)	30	5868 (5692)	55	6430 (6252)
	# 2:	-	-	6	785 (648)	28	5071 (4907)	42 (36)	5674 (5500)
	# 3:	0	0	13	1475 (1352)	23	3776 (3644)	42	4214 (4077)
	# 4:	-	-	8 7	1889 (174)	30	8674 (8501)	73	9603 (8825)
	# 5:	-	-	0	0	28	4281 (4112)	32	4982 (4807)
	# 6:	-	-	2 (1)	110 (43)	22 (21)	3486 (3357)	36 (33)	4156 (4025)
	# 7:	-	-	9 (7)	1311 (1050)	38	6052 (5837)	56 (48)	6647 (6429)
	Total:	**0**		**50 (45)**		**199 (198)**		**336 (319)**	
Upper	# 1:	-	-	20	4988 (4831)	36 (35)	13893 (13712)	73	13997 (11694)
	# 2:	-	-	14	2844 (2690)	30	9377 (9206)	72 (71)	10322 (9318)
	# 3:	0	0	18	3595 (3459)	25	8109 (7975)	58	8856 (7540)
	# 4:	-	-	19	4868 (4704)	44 (41)	17090 (16805)	79 (73)	15895 (13037)
	# 5:	-	-	5	967 (856)	30	8575 (8399)	72	9633 (8932)
	# 6:	-	-	5	618 (519)	22	5169 (5043)	52	5956 (5682)
	# 7:	-	-	17 (16)	4696 (4461)	40	12079 (11855)	93	13038 (11728)
	Total:	**0**		**98 (96)**		**227 (223)**		**499 (492)**	

DTN: SN0408T0509903.008; file Unmixed_HighInvertTransport\Summary Tables.mcd.

Table M-7. Condensation under the Drip Shield: Unventilated Drip Shield High Invert Transport, High Dispersion Coefficient

Perc. Level	Drift Choice	300 yrs		1,000 yrs		3,000 yrs		10,000 yrs	
		# WP's	Total Cond (kg/yr)	# WP's	Total Cond (kg/yr)	# WP's	Total Cond (kg/yr)	# WP's	Total Cond (kg/yr)
Low	# 1:	-	-	0	0	18 (16)	788 (603)	27 (25)	1149 (990)
	# 2:	-	-	0	0	18 (16)	881 (719)	27 (26)	1332 (1173)
	# 3:	0	0	5 (4)	270 (166)	16 (15)	982 (860)	21	1241 (1121)
	# 4:	-	-	0	0	8 (1)	183 (12)	24 (23)	820 (666)
	# 5:	-	-	0	0	10 (6)	291 (141)	24	895 (734)
	# 6:	-	-	0	0	10 (8)	333 (233)	19 (18)	813 (703)
	# 7:	-	-	0	0	33 (31)	1856 (1657)	37	2451 (2243)
	Total:	**0**		**5 (4)**		**113 (93)**		**179 (174)**	
Mean	# 1:	-	-	8 (7)	981 (845)	28	5613 (5447)	32 (31)	6213 (6037)
	# 2:	-	-	2 (0)	74 (0)	28	4768 (4594)	31	5455 (5283)
	# 3:	0	0	10	1083 (962)	21	3592 (3468)	25 (24)	4024 (3893)
	# 4:	-	-	5	1105 (979)	30	8288 (8109)	69 (62)	9264 (8423)
	# 5:	-	-	0	0	26 (25)	3934 (3766)	31 (30)	4725 (4555)
	# 6:	-	-	0	0	20 (19)	3202 (3080)	23	3910 (3781)
	# 7:	-	-	2 (0)	82 (0)	37	5786 (5568)	40	6421 (6204)
	Total:	**0**		**27 (22)**		**190 (188)**		**251 (241)**	
Upper	# 1:	-	-	18	4267 (4100)	31	13537 (13362)	73 (72)	13627 (11333)
	# 2:	-	-	10 (9)	2055 (1916)	29	9047 (8874)	70	10043 (9003)
	# 3:	0	0	15	3109 (2990)	23	7835 (7706)	55 (54)	8535 (7247)
	# 4:	-	-	11	4117 (3997)	36 (34)	16637 (16367)	73	15487 (13016)
	# 5:	-	-	2 (0)	80 (0)	29	8166 (7793)	63 (49)	9301 (8574)
	# 6:	-	-	0	0	21	4834	40	5685
	# 7:	-	-	14 (13)	3508 (3246)	39	11763 (11541)	90 (88)	12678 (11272)
	Total:	**0**		**70 (66)**		**208 (206)**		**464 (443)**	

DTN: SN0408T0509903.008; file Unmixed_HighInvertTransport\Summary Tables.mcd.

The files containing the corrected calculations for the in-drift condensation model (DTN SN0408T0509903.008) are listed in the following tables. Table D.7-1 lists the calculation and documentation files that are common to all of the calculations documented in this report. The table of contents file (TOC.mcd) contains hyperlinks to the other files. Each file contains documentation describing the component of the calculation contained by that file. The linked Mathcad files serve as a descriptive document as well as a set of calculations files.

Table M-8. Common Documentation and Calculation Files

	Size (KB)	Date	Sections of Report
3. MS WORD FILES			
References.doc	68	8/30/2004	text
4. MATHCAD FILES			
Beginnings.mcd	2307	8/30/2004	text
Calculation Plots.mcd	16	8/30/2004	text
Calculation Results2.mcd	1910	8/30/2004	6.3.7.2
Correlations2.mcd	1015	8/30/2004	6.3.5.1.3
Cyl_vs_Line.mcd	57	9/1/2004	Appendix F
Differencing Test.mcd	503	8/30/2004	Appendix D.6
Dispersion Formulation.mcd	740	8/30/2004	6.3.5.1.2
Evaporation Limits.mcd	914	8/30/2004	6.3.5.1.4
Fluent Results.mcd	41	8/30/2004	6.3.4.1.2
Fluid Properties.mcd	322	8/30/2004	4.1.3 & 6.3.5.1.3
Repository Description LA 2.mcd	3194	8/30/2004	4.1.3 & 6.3.5.2
Repository Temperature Field 3.mcd	884	8/30/2004	6.3.5.1.1
Solution Algorithm Test Version.mcd	2071	8/30/2004	Appendix D.6
Solution Algorithm.mcd	2071	8/30/2004	Appendix D.5
Test Corelations.mcd	23	8/30/2004	Appendix D.6
TOC.mcd	374	8/30/2004	table of contents (hyperlinked)
2D Comparison.mcd	732	8/30/2004	Appendix J

Tables M-9 thru M-12 list the files that contain the calculation results for four parameter variations addressed by the analysis:

- Table M-9: Ventilated drip shield with high invert transport
- Table M-10: Ventilated drip shield with low invert transport
- Table M-11: Unventilated drip shield with high invert transport
- Table M-12: Unventilated drip shield with low invert transport

Each parameter variation is located in the subdirectory identified in the table.

Each subdirectory contains seven calculation files having file names of the form “Choice#.mcd,” where # is the number of the drift choice. These files are linked to the “driver” files listed in

Table M-8. Time, percolation rates, and axial dispersion are varied in each of these files. The results of the calculations are contained in embedded Excel workbooks. The results can be verified by the viewer by "enabling" the equation that was used to generate the results. Verification is performed by comparing the results of the calculation to the numbers contained in the Excel spreadsheet. Additionally, the graph of the convergence progression that appears at the end of the calculation can be compared to the picture of this graph that was stored at the time of the original calculation.

Each subdirectory also contains seven calculation files having file names of the form "Choice#Figures.mcd", where # is the number of the drift choice. These files contain plots of the results that are stored in the "Choice#Figures.mcd" files. In addition, the "Choice#Figures.mcd" files contain summary tables of condensation rates for individual drifts at individual times. These tables are saved as MS Excel files to the subdirectory "DIRs". The names of these Excel files contain the drift choice and the time (i.e. Choice#1_1000yrs.xls, etc.).

The Mathcad files named "Summary Tables.mcd" are linked to all of the Excel files in the underlying subdirectory. These four "Summary Tables" files assemble composite tables for condensation on the drift walls, condensation under the drip shield, and axial transport of energy. These composite tables are presented in Section 6.3.7 of this report.

Table M-9. Calculation Files: Well Ventilated Drip Shield; High Invert Transport

Subdirectory: Mixed_HighInvertTransport	**Size (KB)**	**Date**	**Sections of Report**
Choice 1.mcd	1472	8/30/2004	electronic file only
Choice 1Figures.mcd	1577	8/30/2004	electronic file only
Choice 2.mcd	1453	8/30/2004	electronic file only
Choice 2Figures.mcd	1582	8/30/2004	electronic file only
Choice 3.mcd	1779	8/30/2004	electronic file only
Choice 3Figures.mcd	2018	8/30/2004	electronic file only
Choice 4.mcd	1466	8/30/2004	electronic file only
Choice 4Figures.mcd	1582	8/30/2004	electronic file only
Choice 5.mcd	1467	8/30/2004	electronic file only
Choice 5Figures.mcd	1589	8/30/2004	electronic file only
Choice 6.mcd	1283	8/30/2004	electronic file only
Choice 6Figures.mcd	1508	8/30/2004	electronic file only
Choice 7.mcd	1620	8/30/2004	electronic file only
Choice 7Figures.mcd	1726	8/30/2004	6.3.7.2; Appendix E.1
Summary Tables.mcd	700	8/30/2004	M-1
Subdirectory: Mixed_HighInvertTransport\DTNs			
Choice#1_1000yrs.xls	240	8/30/2004	electronic file only
Choice#1_3000yrs.xls	243	8/30/2004	electronic file only
Choice#1_10000yrs.xls	243	8/30/2004	electronic file only
Choice#2_1000yrs.xls	243	8/30/2004	electronic file only
Choice#2_3000yrs.xls	245	8/30/2004	electronic file only
Choice#2_10000yrs.xls	244	8/30/2004	electronic file only
Choice#3_300yrs.xls	203	8/30/2004	electronic file only
Choice#3_1000yrs.xls	201	8/30/2004	electronic file only
Choice#3_3000yrs.xls	201	8/30/2004	electronic file only
Choice#3_10000yrs.xls	203	8/30/2004	electronic file only
Choice#4_1000yrs.xls	243	8/30/2004	electronic file only
Choice#4_3000yrs.xls	243	8/30/2004	electronic file only
Choice#4_10000yrs.xls	243	8/30/2004	electronic file only
Choice#5_1000yrs.xls	248	8/30/2004	electronic file only
Choice#5_3000yrs.xls	247	8/30/2004	electronic file only
Choice#5_10000yrs.xls	247	8/30/2004	electronic file only
Choice#6_1000yrs.xls	198	8/30/2004	electronic file only
Choice#6_3000yrs.xls	198	8/30/2004	electronic file only
Choice#6_10000yrs.xls	199	8/30/2004	electronic file only
Choice#7_1000yrs.xls	290	8/30/2004	electronic file only
Choice#7_3000yrs.xls	292	8/30/2004	electronic file only
Choice#7_10000yrs.xls	290	8/30/2004	electronic file only

Table M-10. Calculation Files: Well Ventilated Drip Shield; Low Invert Transport

Subdirectory: Mixed_LowInvertTransport	Size (KB)	Date	Sections of Report
Choice 1.mcd	1467	8/30/2004	electronic file only
Choice 1Figures.mcd	1577	8/30/2004	electronic file only
Choice 2.mcd	1483	8/30/2004	electronic file only
Choice 2Figures.mcd	1582	8/30/2004	electronic file only
Choice 3.mcd	1779	8/30/2004	electronic file only
Choice 3Figures.mcd	2018	8/30/2004	electronic file only
Choice 4.mcd	1456	8/30/2004	electronic file only
Choice 4Figures.mcd	1584	8/30/2004	electronic file only
Choice 5.mcd	1463	8/30/2004	electronic file only
Choice 5Figures.mcd	1596	8/30/2004	electronic file only
Choice 6.mcd	1283	8/30/2004	electronic file only
Choice 6Figures.mcd	1510	8/30/2004	electronic file only
Choice 7.mcd	1616	8/30/2004	electronic file only
Choice 7Figures.mcd	1731	8/30/2004	6.3.7.2; Appendix E.2
Summary Tables.mcd	701	8/30/2004	M-10
Subdirectory: Mixed_LowInvertTransport\DTNs			
Choice#1_1000yrs.xls	240	8/30/2004	electronic file only
Choice#1_3000yrs.xls	243	8/30/2004	electronic file only
Choice#1_10000yrs.xls	243	8/30/2004	electronic file only
Choice#2_1000yrs.xls	243	8/30/2004	electronic file only
Choice#2_3000yrs.xls	245	8/30/2004	electronic file only
Choice#2_10000yrs.xls	244	8/30/2004	electronic file only
Choice#3_300yrs.xls	203	8/30/2004	electronic file only
Choice#3_1000yrs.xls	201	8/30/2004	electronic file only
Choice#3_3000yrs.xls	201	8/30/2004	electronic file only
Choice#3_10000yrs.xls	203	8/30/2004	electronic file only
Choice#4_1000yrs.xls	243	8/30/2004	electronic file only
Choice#4_3000yrs.xls	243	8/30/2004	electronic file only
Choice#4_10000yrs.xls	245	8/30/2004	electronic file only
Choice#5_1000yrs.xls	248	8/30/2004	electronic file only
Choice#5_3000yrs.xls	244	8/30/2004	electronic file only
Choice#5_10000yrs.xls	244	8/30/2004	electronic file only
Choice#6_1000yrs.xls	198	8/30/2004	electronic file only
Choice#6_3000yrs.xls	194	8/30/2004	electronic file only
Choice#6_10000yrs.xls	198	8/30/2004	electronic file only
Choice#7_1000yrs.xls	290	8/30/2004	electronic file only
Choice#7_3000yrs.xls	292	8/30/2004	electronic file only
Choice#7_10000yrs.xls	290	8/30/2004	electronic file only

Table M-11. Calculation Files: Unventilated Drip Shield; High Invert Transport

Subdirectory: Unmixed_HighInvertTransport	Size (KB)	Date	Sections of Report
Choice 1.mcd	1554	8/30/2004	electronic file only
Choice 1Figures.mcd	1593	8/30/2004	electronic file only
Choice 2.mcd	1545	8/30/2004	electronic file only
Choice 2Figures.mcd	1583	8/30/2004	electronic file only
Choice 3.mcd	1831	8/30/2004	electronic file only
Choice 3Figures.mcd	2018	8/30/2004	electronic file only
Choice 4.mcd	1543	8/30/2004	electronic file only
Choice 4Figures.mcd	1583	8/30/2004	electronic file only
Choice 5.mcd	1530	8/30/2004	electronic file only
Choice 5Figures.mcd	1591	8/30/2004	electronic file only
Choice 6.mcd	1370	8/30/2004	electronic file only
Choice 6Figures.mcd	1509	8/30/2004	electronic file only
Choice 7.mcd	1680	8/30/2004	electronic file only
Choice 7Figures.mcd	1735	8/30/2004	6.3.7.2; Appendix E.3
Summary Tables.mcd	702	8/30/2004	M-5, M-6, M-7
Subdirectory: Unmixed_HighInvertTransport\DTNs			
Choice#1_1000yrs.xls	246	8/30/2004	electronic file only
Choice#1_3000yrs.xls	240	8/30/2004	electronic file only
Choice#1_10000yrs.xls	250	8/30/2004	electronic file only
Choice#2_1000yrs.xls	244	8/30/2004	electronic file only
Choice#2_3000yrs.xls	248	8/30/2004	electronic file only
Choice#2_10000yrs.xls	251	8/30/2004	electronic file only
Choice#3_300yrs.xls	203	8/30/2004	electronic file only
Choice#3_1000yrs.xls	203	8/30/2004	electronic file only
Choice#3_3000yrs.xls	205	8/30/2004	electronic file only
Choice#3_10000yrs.xls	209	8/30/2004	electronic file only
Choice#4_1000yrs.xls	244	8/30/2004	electronic file only
Choice#4_3000yrs.xls	247	8/30/2004	electronic file only
Choice#4_10000yrs.xls	252	8/30/2004	electronic file only
Choice#5_1000yrs.xls	248	8/30/2004	electronic file only
Choice#5_3000yrs.xls	250	8/30/2004	electronic file only
Choice#5_10000yrs.xls	253	8/30/2004	electronic file only
Choice#6_1000yrs.xls	198	8/30/2004	electronic file only
Choice#6_3000yrs.xls	201	8/30/2004	electronic file only
Choice#6_10000yrs.xls	203	8/30/2004	electronic file only
Choice#7_1000yrs.xls	291	8/30/2004	electronic file only
Choice#7_3000yrs.xls	296	8/30/2004	electronic file only
Choice#7_10000yrs.xls	300	8/30/2004	electronic file only

Table M-12. Calculation Files: Unventilated Drip Shield; Low Invert Transport

Subdirectory: Unmixed_LowInvertTransport	Size (KB)	Date	Sections of Report
Choice 1.mcd	1560	8/30/2004	electronic file only
Choice 1Figures.mcd	1579	8/30/2004	electronic file only
Choice 2.mcd	1536	8/30/2004	electronic file only
Choice 2Figures.mcd	1584	8/30/2004	electronic file only
Choice 3.mcd	3514	8/30/2004	electronic file only
Choice 3Figures.mcd	2017	8/30/2004	electronic file only
Choice 4.mcd	1530	8/30/2004	electronic file only
Choice 4Figures.mcd	1583	8/30/2004	electronic file only
Choice 5.mcd	1528	8/30/2004	electronic file only
Choice 5Figures.mcd	1590	8/30/2004	electronic file only
Choice 6.mcd	1366	8/30/2004	electronic file only
Choice 6Figures.mcd	1508	8/30/2004	electronic file only
Choice 7.mcd	1673	8/30/2004	electronic file only
Choice 7Figures.mcd	1726	8/30/2004	6.3.7.2; Appendix E.4
Summary Tables.mcd	701	8/30/2004	M-4
Subdirectory: Unmixed_LowInvertTransport\DTNs			
Choice#1_1000yrs.xls	240	8/30/2004	electronic file only
Choice#1_3000yrs.xls	243	8/30/2004	electronic file only
Choice#1_10000yrs.xls	239	8/30/2004	electronic file only
Choice#2_1000yrs.xls	243	8/30/2004	electronic file only
Choice#2_3000yrs.xls	242	8/30/2004	electronic file only
Choice#2_10000yrs.xls	243	8/30/2004	electronic file only
Choice#3_300yrs.xls	203	8/30/2004	electronic file only
Choice#3_1000yrs.xls	201	8/30/2004	electronic file only
Choice#3_3000yrs.xls	201	8/30/2004	electronic file only
Choice#3_10000yrs.xls	203	8/30/2004	electronic file only
Choice#4_1000yrs.xls	239	8/30/2004	electronic file only
Choice#4_3000yrs.xls	243	8/30/2004	electronic file only
Choice#4_10000yrs.xls	243	8/30/2004	electronic file only
Choice#5_1000yrs.xls	248	8/30/2004	electronic file only
Choice#5_3000yrs.xls	247	8/30/2004	electronic file only
Choice#5_10000yrs.xls	247	8/30/2004	electronic file only
Choice#6_1000yrs.xls	198	8/30/2004	electronic file only
Choice#6_3000yrs.xls	198	8/30/2004	electronic file only
Choice#6_10000yrs.xls	198	8/30/2004	electronic file only
Choice#7_1000yrs.xls	290	8/30/2004	electronic file only
Choice#7_3000yrs.xls	292	8/30/2004	electronic file only
Choice#7_10000yrs.xls	290	8/30/2004	electronic file only